

*NASA CR-174,366*

NASA-CR-174366  
19850010914

# **The Telecommunications and Data Acquisition Progress Report 42-80**

**October-December 1984**

**E.C. Posner  
Editor**

**LIBRARY COPY**

**February 15, 1985**

**1985**

**LANGLEY RESEARCH CENTER  
LIBRARY, NASA  
HAMPTON, VIRGINIA**



**National Aeronautics and  
Space Administration**

**Jet Propulsion Laboratory  
California Institute of Technology  
Pasadena, California**

# The Telecommunications and Data Acquisition Progress Report 42-80

October-December 1984

E.C. Posner  
Editor

February 15, 1985



National Aeronautics and  
Space Administration

Jet Propulsion Laboratory  
California Institute of Technology  
Pasadena, California

*N85-19224\**  
*thru N85-19248\**

The research described in this publication was carried out by the Jet Propulsion Laboratory, California Institute of Technology, under a contract with the National Aeronautics and Space Administration.

Reference herein to any specific commercial product, process, or service by trade name, trademark, manufacturer, or otherwise, does not constitute or imply its endorsement by the United States Government or the Jet Propulsion Laboratory, California Institute of Technology.

## Preface

This quarterly publication provides archival reports on developments in programs managed by JPL's Office of Telecommunications and Data Acquisition (TDA). In space communications, radio navigation, radio science, and ground-based radio astronomy, it reports on activities of the Deep Space Network (DSN) and its associated Ground Communications Facility (GCF) in planning, in supporting research and technology, in implementation, and in operations. Also included is TDA-funded activity at JPL on data and information systems and reimbursable DSN work performed for other space agencies through NASA. The preceding work is all performed for NASA's Office of Space Tracking and Data Systems (OSTDS).

In geodynamics, the publication reports on the application of radio interferometry at microwave frequencies for geodynamic measurements. In the search for extraterrestrial intelligence (SETI), it reports on implementation and operations for searching the microwave spectrum. The latter two programs are performed for NASA's Office of Space Science and Applications (OSSA).

Finally, tasks funded under the JPL Director's Discretionary Fund and the Caltech President's Fund which involve the TDA Office are included.

This and each succeeding issue of the TDA Progress Report will present material in some, but not necessarily all, of the following categories:

### OSTDS Tasks:

- DSN Advanced Systems
  - Tracking and Ground-Based Navigation
  - Communications, Spacecraft-Ground
  - Station Control and System Technology
  - Network Data Processing and Productivity
- DSN Systems Implementation
  - Capabilities for New Projects
  - Networks Consolidation Program
  - New Initiatives
  - Network Sustaining
- DSN Operations
  - Network Operations and Operations Support
  - Mission Interface and Support
  - TDA Program Management and Analysis
- GCF Implementation and Operations
- Data and Information Systems

### OSSA Tasks:

- Search for Extraterrestrial Intelligence
- Geodynamics
  - Geodetic Instrument Development
  - Geodynamic Science

### Discretionary Funded Tasks





# Contents

## OSTDS TASKS DSN Advanced Systems TRACKING AND GROUND-BASED NAVIGATION

<b>Arcsecond Positions for Milliarcsecond VLBI Nuclei of Extragalactic Radio Sources, Part III: 74 Sources</b> .....	1
D. D. Morabito R. A. Preston, R. P. Linfield, M. A. Slade, A. E. Wehrle, J. Faulkner, and D. L. Jauncey NASA Code 310-10-60-26-00	

## COMMUNICATIONS, SPACECRAFT-GROUND

<b>Microwave Surface Resistivity of Several Materials at Ambient Temperature</b> .....	8
H. F. Reilly, J. J. Bautista, and D. A. Bathker NASA Code 310-20-65-65-00	
<b>The Effects of Mode Impurity on Ka-Band System Performance</b> .....	12
D. J. Hoppe, W. A. Imbriale, and A. M. Bhanji NASA Code 310-20-64-22-00	
<b>Detection and Symbol Synchronization for Multiple-Bit per Photon Optical Communications</b> .....	24
W. K. Marshall NASA Code 310-20-67-59-00	
<b>Highly Efficient Nd:YAG Lasers for Free-Space Optical Communications</b> .....	31
D. L. Sipes, Jr. NASA Code 310-20-67-84-04	
<b>Condensed Antenna Structural Models for Dynamics Analysis</b> .....	40
R. Levy NASA Code 310-20-65-04-10	
<b>Interpolation Methods for GTD Analysis of Shaped Reflectors</b> .....	62
V. Galindo-Israel, W. Imbriale, Y. Rahmat-Samii, and T. Veruttipong NASA Code 310-20-65-04-00	
<b>Design Procedure for the New 70-Meter Antenna Subreflector Positioner</b> .....	68
R. D. Hughes NASA Code 310-20-65-62-00	
<b>Subreflector Focusing Techniques Applied to New DSS-15 and DSS-45 34-Meter Antennas</b> .....	83
R. D. Hughes and M. S. Katow NASA Code 310-20-65-62-00	

## STATION CONTROL AND SYSTEM TECHNOLOGY

<b>Reed-Solomon Code Synchronization Revisited</b> .....	91
L. J. Deutsch NASA Code 310-30-71-83-04	

<b>Further Results on Rate <math>1/N</math> Convolutional Code Constructions With Minimum Required SNR Criterion</b> .....	97
P. J. Lee	
NASA Code 310-30-71-83-02	

## NETWORK DATA PROCESSING AND PRODUCTIVITY

<b>Concepts and Tools for the Software Life Cycle</b> .....	103
R. C. Tausworthe	
NASA Code 310-40-72-10-00	

## DSN Systems Implementation CAPABILITIES FOR NEW PROJECTS

<b>Antenna Axis Drive Torques for the 70-Meter Antenna</b> .....	121
H. McGinness	
NASA Code 314-30-56-04-05	
<b>An Evaluation of the 64-Meter Antenna Radial Bearing for Use on the 70-Meter Antenna</b> .....	127
H. D. McGinness	
NASA Code 314-30-56-04-05	
<b>Elevation Bearing Maximum Load, 70-Meter Antenna</b> .....	142
H. D. McGinness	
NASA Code 314-30-56-04-05	
<b>Characteristics of the Elevation Drive Suspension of the 64-Meter Antennas</b> .....	146
H. D. McGinness	
NASA Code 314-30-56-04-05	
<b>Hydrostatic Bearing Pad Maximum Load and Overturning Conditions for the 70-Meter Antenna</b> .....	176
H. D. McGinness	
NASA Code 314-30-56-04-05	
<b>Performance of the DSA's Subcarrier Demodulation Digital Loop</b> .....	180
M. K. Simon and A. Mileant	
NASA Code 314-30-53-20-02	
<b>The Venus Balloon Project</b> .....	195
R. A. Preston, J. H. Wilcher, and C. T. Stelzried	
NASA Code 314-30-50-01-34	
<b>DSN 34-Meter Antenna Optics Analysis for Wideband SETI Investigations</b> .....	202
S. D. Slobin	
NASA Code 314-30-69-01-11	

## NETWORK SUSTAINING

<b>Historical Cost Curves for Hydrogen Masers and Cesium Beam Frequency and Timing Standards</b> .....	220
D. S. Remer and R. C. Moore	
NASA Code 314-40-31-30-09	

**DSN Operations**  
**MISSION INTERFACE AND SUPPORT**

<b>The Accuracy of Radio Interferometric Measurements of Earth Rotation</b> .....	229
T. M. Eubanks, J. A. Steppe, and M. A. Spieth	
NASA Code 314-40-22-70-11	

**Data and Information Systems**

<b>Codes With Parity Conditions on Subsets of Coordinates</b> .....	236
E. C. Posner and Z. Reichstein	
NASA Code 055-40-01-00-96	

**OSSA TASKS**  
**Geodynamics**  
**GEODETTIC INSTRUMENT DEVELOPMENT**

<b>Utilization of Mobile VLBI for Geodetic Measurements</b> .....	248
J. M. Davidson and D. W. Trask	
NASA Code 692-40-40-00-07	
<b>Author Index, 1984</b> .....	267

# Arcsecond Positions for Milliarcsecond VLBI Nuclei of Extragalactic Radio Sources, Part III: 74 Sources

D. D. Morabito, R. A. Preston, R. P. Linfield, and M. A. Slade  
Tracking Systems and Applications Section

A. E. Wehrle  
University of California, Los Angeles

J. Faulkner  
University of Southern California

D. L. Jauncey  
CSIRO, Sydney, Australia

*VLBI measurements at 2290 MHz and 8420 MHz on baselines of  $10^4$  km between Deep Space Network stations have been used to determine the positions of the milliarcsecond nuclei in 74 extragalactic radio sources. Estimated accuracies range from  $0''.1$  to  $4''.3$  in both right ascension and declination with typical accuracies of  $\sim 0''.3$ . The observed sources are part of an all-sky VLBI catalog of milliarcsecond radio sources. Arcsecond positions have now been determined for 819 sources. These positions are presently being used to identify optical counterparts in the Southern Hemisphere.*

## I. Introduction

A survey is underway to develop an all-sky catalog of radio sources with milliarcsecond components at 2.29 GHz. This is being accomplished by searching for compact components in known extragalactic sources (Refs. 1, 2, 3) with intercontinental baselines composed of Deep Space Network stations. We have used VLBI measurements of delay and fringe frequency at 2.29 GHz to determine the positions of the milliarcsecond nuclei. Previously we have presented the positions of 747 nuclei (Refs. 4 and 5). In this article, we present the positions of an additional 72 nuclei and include improved positions for P 1237-10 and P 0509+152 (Refs. 4 and 5, respectively).

Estimated accuracies for sources in this paper range from  $0''.1$  to  $4''.3$  in both right ascension and declination.

The observations were not performed primarily for position measurements, but were part of the development of an all-sky VLBI catalog of milliarcsecond radio sources at 2290 MHz. The delay observables were derived from single channel 2-MHz bandwidths resulting in arcsecond accuracy. However, these measurements constitute at least an order of magnitude improvement in positional accuracy for most of the sources.

Arcsecond positions serve as a useful starting point in the construction of a high-precision VLBI reference frame as well

as allowing unambiguous optical identifications to be made. Based on these positions, more than 100 optical counterparts have already been identified in the Southern Hemisphere (Refs. 6, 7). The positions from this article and Refs. 4 and 5, respectively, are presently being used as a first step in the formation of a precision reference frame of 100–200 sources in which relative radio positions should be determined to milliarcsecond accuracy (Refs. 8, 9).

## II. The Observations

The observations were performed with pairs of antennas on either California–Australia, or California–Spain baselines (see Table 1) during 12 separate observing sessions conducted between 1981 and 1983. A list of experiments appears in Table 2. The observations were performed at 2.29 GHz and 8.42 GHz with MK II VLBI recording systems as described in Ref. 4. The total number of sources whose positions were solved for is 157. Of these, there were 72 sources whose positions were not included in Refs. 4 and 5. The length of each observation was a few minutes with 65% of the sources being observed more than once.

## III. Method of Position Determination

The details of position determination for this set of sources closely follow the analysis given in Refs. 4 and 5. As in Refs. 4 and 5, observations of sources with well-known positions allowed instrumental delay and frequency offsets to be determined. At least three such calibration sources per experiment were spread in time among the program sources. A list of the 64 calibration sources appears in Table 3. Thirty of the calibration source positions have been determined with VLBI (Ref. 10) and can be referred to the FK4 reference frame (Ref. 11) with an accuracy of  $0''.1$ . Other calibration source positions came from Ref. 12 (33 sources,  $0''.1$  accuracy), and Ref. 13 (1 source,  $0''.2$  accuracy).

## IV. Results

The calculated positions of 74 sources and the corresponding uncertainties are shown in Table 4. The positions are referred to the equinox of 1950.0 and elliptical aberration terms are included, so as to agree with past astronomical convention. The source positions and position uncertainties for sources which were multiply observed were estimated from a weighted average over several observations. Therefore, individual uncertainties less than  $0''.3$  in Table 4 are due to averaging over multiple observations. Since the uncertainties for the vast majority of observations were dominated by the quadratically added  $0''.3$  error, correlations between right ascension and declination were not tabulated.

A total of 102 sources were observed two or more times, and the scatter in their position estimates is consistent with the estimated uncertainties. Figure 1 is a histogram of the ratio of the weighted rms scatter of the measurements to the weighted rms estimate of position coordinate uncertainty for both the right ascension and declination of each multiply observed source. For the 102 multiply observed sources, the rms value of this ratio is 0.7 for right ascension and 0.9 for declination.

In addition to the 74 sources listed in Table 4, we also re-observed 83 sources whose positions were reported in Refs. 4 and 5. For these 83 sources, Fig. 2 shows a histogram of the difference between the two measurements of each coordinate divided by the RSS error of the position coordinate uncertainties. For 85 sources including P 1237–10 and P 0509+152, this calculated ratio has a rms value of 1.5 for right ascension and 1.3 for declination. If we delete these two sources from this calculation, the rms value for right ascension becomes 1.0 and for declination becomes 0.9. For those two sources, P 1237–10, and P 0509+152, positions are given here which are improved from those cited in Refs. 4 and 5.

For 32 sources, we could compare our position estimates with other position estimates of better or similar accuracy (Refs. 10, 12, 14). Figure 3 displays a histogram of the ratio of the value of the difference between our source position estimate and the other catalog value to the RSS of the position uncertainties of both catalogs. For these 32 sources, the rms value of this ratio is 1.2 for right ascension and 1.2 for declination. For both right ascension and declination, the value of the ratio never exceeds 3.3. The bias offsets between our position estimates relative to those of the other catalogs for these 32 sources are  $-0''.05 \pm 0''.05$  in right ascension and  $-0''.03 \pm 0''.05$  in declination. Hence, these position estimate comparisons, along with the multiple observation comparisons, indicate our position uncertainty estimates are realistic.

Figures 4(a) and 4(b) show histograms of the number of sources versus estimated position uncertainty for declination and right ascension, respectively, for the 157 observed sources. Estimated accuracies range from  $0''.1$  to  $4''.3$  in both right ascension and declination.

## V. Summary

Positions for the milliarcsecond nuclei of 74 extragalactic sources have been determined to an accuracy of  $\sim 0''.1$  to  $4''.3$  in both right ascension and declination. The reliability of the determined positions has been demonstrated by testing the repeatability of multiple observations on the same source and by comparing the results with other radio catalogs. Arcsecond positions have now been determined for 819 milliarcsecond nuclei.

## Acknowledgement

We appreciate the assistance of L. J. Skjerve and the personnel of the Deep Space Network for aid in performing the observations.

## References

1. Morabito, D. D., Preston, R. A., Faulkner, J., 1981, *TDA Progress Reports*, 42-66, Sept. and Oct. 1981, Jet Propulsion Laboratory, Pasadena, Calif., pp. 30-36.
2. Preston, R. A., Morabito, D. D., NASA Conference Publication 2115, Proceedings of a Conference held at MIT, Cambridge, Massachusetts, June 19-21, pp. 173-179.
3. Preston, R. A., Morabito, D. D., Williams, J. G. Faulkner, J., Jauncey, D. L., and Nicolson, G. D., 1985, in preparation.
4. Morabito, D. D., Preston, R. A., Slade, M. A., Jauncey, D. L., 1982, *Astronomical Journal* 87, 517-527. Also published in *TDA Progress Report*, 42-66: September and October 1981, p. 37-48.
5. Morabito, D. D., Preston, R. A., Slade, M. A., Jauncey, D. L., and Nicolson, G. D., 1983, *Astronomical Journal*, 88, 1138-1145. Also published in *TDA Progress Report*, 42-77: January-March 1984, pp. 1-11.
6. Jauncey, D. L., Savage, A., Morabito, D. D., and Preston, R. A., 1985, in preparation.
7. Savage, A., Jauncey, D. L., Batty, M. J., Gulkis, S., Morabito, D. D., and Preston, R. A., IAU Colloquium No. 78, *Astronomy with Schmidt Type Telescopes*, Asiago, Italy, August-September 1983, pp. 481-487.
8. Fanselow, J. L., Thomas, J. B., Cohen, E. J., MacDoran, P. F., Melbourne, W. G., Mulhall, B. D., Purcell, G. H., Rogstad, D. H., Skjerve, L. J., Spitzmesser, D. J., Urech, J., Nicolson, G., 1979, *Time and the Earth's Rotation*, IAU Symp. 82, Reidel, pp. 199-209.
9. Fanselow, J. L., Sovers, O. J., Thomas, J. B., Purcell, G. H., Cohen, E. J., Rogstad, D. H., Skjerve, L. J., and Spitzmesser, D. J., 1984, *Astronomical Journal* 89, pp. 987-998.
10. Fanselow, J. L., Sovers, O. J., Thomas, J. B., Bletzacker, F. R., Kearns, T. J., Cohen, E. J., Purcell, G. H. Jr., Rogstad, D. H., Skjerve, L. J., Young, L. E., 1981, *Reference Coordinate Systems for Earth Dynamics*, 351-357, D. Reidel Publishing Company.
11. Fricke, W. and Kopff, A. 1963, *Veroeff. Astron. Rechen-Institut*, Heidelberg; No. 10, pp. 1-144.
12. Perley, R. A., 1982, *Astronomical Journal* 87, pp. 859-880.
13. Waltman, E., Johnston, K. J., Spencer, J. H., Pauliny-Toth, I., Schraml, J., and Witzel, A., 1981, *Astron. Astrophys.* 101, pp. 49-51.
14. Ulvestad, J., Johnston, K., Perley, R., and Fomalont, E., 1981, *Astronomical Journal* 86, pp. 1010-1035.

**Table 1. Participating observatories**

Location	Designation	Diameter, m	Baseline Length	
			Kilometers	Wavelengths
Tidbinbilla, Australia	DSS 43	64	$10.6 \times 10^3$	$8.1 \times 10^7$
Goldstone, California	DSS 13	26		
Madrid, Spain	DSS 63	64	$8.4 \times 10^3$	$6.4 \times 10^7$

**Table 2. Experiment list**

Experiment			DSS's Observing	
Yr	Mo	Dy		
81	01	31	13	43
81	10	23	13	43
81	10	24	13	43
81	10	26	13	43
81	11	01	13	43
82	05	18	13	43
82	05	30	13	43
82	06	05	13	43
82	09	03	13	43
82	09	08	13	43
83	06	21	13	43
83	11	25	13	63

**Table 3. List of calibrator sources**

Source	Position Reference	Source	Position Reference <sup>a</sup>
NRAO 5	2	B2 0745+24	2
P 0019+058	2	B2 0742+31	2
P 0038-020	2	DW 0742+10	2
P 0048-09	2	GC 0748+33	2
0056-001	2	GC 0759+18	2
P 0106+01	1	B2 0827+24	1
P 0111+021	2	GC 0839+18	1
P 0112-017	2	OJ 287	1
P 0119+11	2	AO 0952+17	1
GC 0119+04	2	0953+25	2
OC 079	2	P 1055+01	1
3C 48	1	P 1127-14	1
P 0201+113	2	P 1148-00	1
P 0202+14	2	3C 273	1
GC 0221+06	2	3C 274	1
CTD 20	2	DW 1335-12	1
		P 1351-018	2
GC 0235+16	1	OP-192	2
0316+162	2	P 1510-08	1
P 0317+188	2	NRAO 530	1
P 0332-403	1	P 1741-038	1
GC 0406+12	2	1803+73	3
P 0409+22	2	OV-236	1
P 0428+20	1	OV-198	1
3C 120	1	P 1936-15	2
P 0446+11	2	P 2008-159	2
P 0454+06	2	P 2134+004	1
3C 138	1	OX-192	1
DA 193	1	OY-172.6	1
OI 318	2	3C 454.3	1
P 0735+17	1	GC 2318+04	2
OI 363	1	P 2345-16	1
B2 0738+27	2		

<sup>a</sup>Position Reference Key:

1 Fanelow et al. 1981 (Ref. 10)

2 Perley 1982 (Ref. 12)

3 Waltman et al. 1981 (Ref. 13)



**Table 4. B1950.0 source positions**

Source Name	Right Ascension				Declination			
	Hr	Min	Sec	Error	Deg	Min	Sec	Error
P 0013-00	0	13	37.359	0.014	- 0	31	52.55	0.23
0032+276	0	32	4.590	0.028	+27	37	54.27	0.30
0047-051	0	47	49.001	0.011	- 5	8	39.63	0.24
P 0054-006	0	54	43.396	0.012	- 0	40	45.73	0.21
P 0114+07	1	14	49.523	0.016	+ 7	26	30.63	0.32
P 0127+145	1	27	15.025	0.016	+14	31	20.09	0.27
0131-001	1	31	38.936	0.028	- 0	11	35.27	0.48
P 0137+012	1	37	22.890	0.015	+ 1	16	35.74	0.51
GC 0147+18	1	47	5.622	0.024	+18	42	27.65	0.32
P 0149+21	1	49	31.739	0.017	+21	52	20.68	0.21
P 0158+031	1	58	5.156	0.012	+ 3	8	20.49	0.18
P 0159+034	1	59	15.644	0.016	+ 3	28	42.56	0.27
0229+262	2	29	33.586	0.029	+26	15	26.13	0.30
0242+238	2	42	23.589	0.027	+23	52	58.21	0.22
P 0253+13	2	53	50.168	0.015	+13	22	32.31	0.22
0305+039	3	5	49.193	0.048	+ 3	55	11.28	0.62
0322+222	3	22	40.840	0.023	+22	13	42.12	0.31
NRAO 140	3	33	22.405	0.024	+32	8	36.87	0.30
0338+074	3	38	12.716	0.046	+ 7	25	48.92	0.51
P 0338-214	3	38	23.260	0.017	-21	29	7.86	0.21
0344+199	3	44	36.530	0.029	+19	55	25.59	0.35
0423+233	4	23	54.706	0.029	+23	21	6.49	0.45
0426+273	4	26	47.384	0.029	+27	18	7.34	0.30
P 0458+138	4	58	55.545	0.032	+13	51	49.79	0.36
0459+252	4	59	54.256	0.018	+25	12	12.17	0.26
0502+049	5	2	43.802	0.011	+ 4	55	40.04	0.21
0506+056	5	6	45.747	0.021	+ 5	37	50.44	0.42
0507+179	5	7	7.483	0.011	+17	56	58.63	0.16
P 0509+152	5	9	49.447	0.010	+15	13	51.91	0.15
0518+165	5	18	16.513	0.022	+16	35	26.86	0.31
0620+389	6	20	51.521	0.015	+38	58	27.24	0.16
3C 166	6	42	24.662	0.014	+21	25	1.94	0.18
0743+25	7	43	23.055	0.010	+25	56	24.88	0.13
GC 0805+26	8	5	34.293	0.034	+26	55	24.20	0.33
0952+179	9	52	11.799	0.012	+17	57	44.49	0.21
GC 1004+14	10	4	59.769	0.010	+14	11	11.08	0.16
1011+250	10	11	5.647	0.020	+25	4	10.12	0.22
P 1012+232	10	12	0.513	0.016	+23	16	11.91	0.21
GC 1022+19	10	22	1.461	0.009	+19	27	34.72	0.14
P 1036-154	10	36	39.481	0.019	-15	25	28.24	0.22
1039+300	10	39	49.760	0.030	+30	5	28.29	0.31
P 1042+071	10	42	19.454	0.010	+ 7	11	25.10	0.19
P 1045-18	10	45	40.100	0.015	-18	53	44.08	0.21
P 1045+019	10	45	46.829	0.022	+ 1	58	5.49	0.33
P 1130+10C	11	30	25.131	0.023	+10	40	4.71	0.55
P 1142+052	11	42	47.069	0.036	+ 5	12	7.28	0.86
1144+352	11	44	45.505	0.026	+35	17	47.36	0.30
P 1149-084	11	49	43.831	0.018	- 8	24	21.92	0.23
P 1158+007	11	58	49.619	0.032	+ 0	45	8.78	0.50
P 1203+011	12	3	15.079	0.025	+ 1	10	21.02	0.40
1215-002	12	15	24.920	0.014	- 0	13	6.41	0.35
P 1228-113	12	28	20.042	0.021	-11	22	36.16	0.31
P 1237-10	12	37	7.280	0.017	-10	7	0.63	0.26
P 1310-041	13	10	15.621	0.010	- 4	8	56.47	0.16
P 1333-049	13	33	20.257	0.044	- 4	56	22.39	0.34
P 1340-17	13	40	54.456	0.024	-17	32	51.35	0.37

**Table 4. (contd)**

Source Name	Right Ascension				Declination			
	Hr	Min	Sec	Error	Deg	Min	Sec	Error
P 1418-064	14	18	29.578	0.073	- 6	30	14.83	0.68
1434+235	14	34	25.397	0.018	+23	34	3.14	0.22
P 1443-162	14	43	6.682	0.015	-16	16	26.65	0.23
1511+238	15	11	28.293	0.030	+23	49	43.69	0.32
P 1514-24	15	14	45.278	0.016	-24	11	22.56	0.22
OS-268	16	40	32.583	0.015	-23	10	33.50	0.22
1640+254	16	40	36.539	0.023	+25	28	43.63	0.22
1909+269	19	9	33.631	0.024	+26	53	10.01	0.33
OV-235	19	20	34.242	0.015	-21	10	24.72	0.21
P 1942-313	19	42	49.158	0.024	-31	18	59.05	0.23
P 2002-185	20	2	24.408	0.022	-18	30	38.76	0.33
2107-105	21	7	18.809	0.017	-10	33	12.52	0.23
P 2220-163	22	20	59.335	0.033	-16	22	17.68	0.32
P 2223-114	22	23	4.500	0.017	-11	28	56.52	0.27
P 2314-116	23	14	45.938	0.054	-11	38	46.90	0.40
P 2318-087	23	18	43.100	0.291	- 8	43	54.06	4.24
P 2338+000	23	38	33.144	0.020	+ 0	1	54.87	0.54
P 2340-036	23	40	22.498	0.016	- 3	39	4.88	0.38

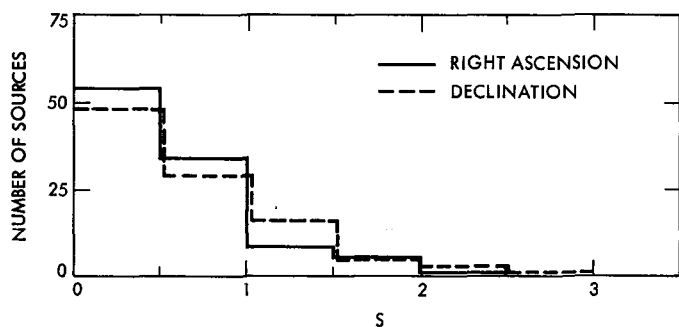


Fig. 1. Comparison of position estimates for 102 multiply observed sources.  $S$  is the ratio of the weighted rms scatter of the measurements to the weighted rms estimate of the uncertainty in that position coordinate.

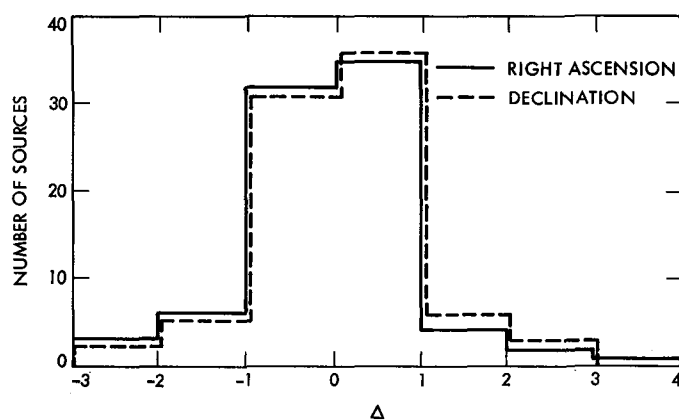


Fig. 2. Comparison of position estimates of 83 sources in common with Refs. 4 and 5. For each source,  $\Delta$  is the ratio of the difference between the source coordinate estimates to the weighted rms estimate of the uncertainty in that position coordinate.

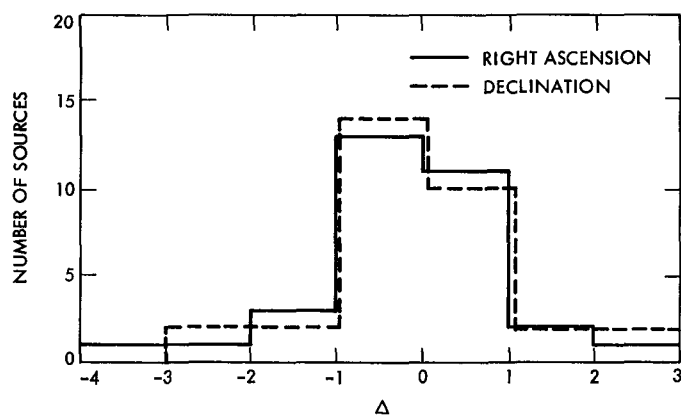


Fig. 3. Comparison of position estimates with other radio positional catalogs. For each source,  $\Delta$  is the ratio of the difference between our source coordinate estimate and the other catalog value to the RSS of the uncertainties of both catalogs.

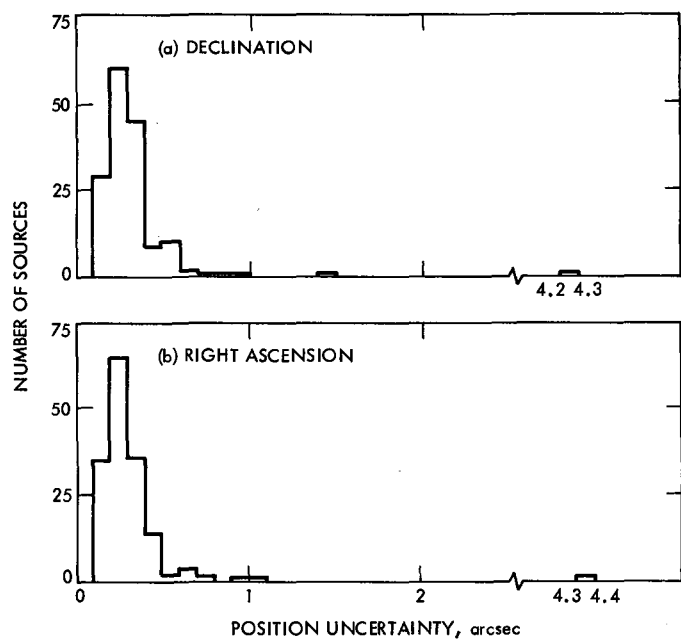


Fig. 4. Histogram of number of sources vs estimated position uncertainty

# Microwave Surface Resistivity of Several Materials at Ambient Temperature

H. F. Reilly, J. J. Bautista, D. A. Bathker  
Radio Frequency and Microwave Subsystems Section

*Microwave surface resistivity of a number of metal and other sample materials was measured at X-band, approximately 8400 MHz. The method of measurement uses a  $TE_{011}$  mode circular waveguide cavity resonator wherein the sample is used as one end of the cavity. This method has been used previously in JPL work with good results. Microwave reflection loss and noise arising from the dissipative loss are given, for materials having negligible transmission leakage.*

## I. Introduction

Previous work at JPL derived the properties of the  $TE_{011}$  resonator and demonstrated valid experimental results on a few materials (Ref. 1). Later work concentrated on an evaluation of various flame-spray metallized fiberglass-epoxy materials, accomplished with assistance from the Harris Corporation, Melbourne, Florida (Ref. 2). Later, Ford Aerospace, Palo Alto, California, under a work order issued by the Ground Antennas and Facilities Engineering Section, concentrated on understanding the dual carrier intermodulation generation characteristics of a different set of flame-spray samples. No serious attempt to obtain precise knowledge of the reflection loss of those samples was made at that time. More recently, in connection with the JPL 70-m Antenna Rehabilitation and Upgrade Project (Ref. 3), several questions arose with respect to resistivity and surface finish of candidate

materials for a proposed cast aluminum subreflector. This reporting covers (1) several control samples, (2) a collection of commonly available metals, (3) candidate 70-m subreflector materials, (4) a repeat of some of the earlier Harris Corporation samples which have been retained at JPL, and (5) a repeat of some of the earlier Ford Aerospace samples which have been retained at JPL. This reporting therefore represents an assemblage of new work and repeats of portions of older work. Some of the older flame-spray samples are approximately 36 months old.

## II. Experimental Setup

The experimental setup was essentially that shown in Ref. 2, with provision to switch the cavity in and out of the test channel, for rapid insertion loss measurement. Also, to

speed the measurement of the large number of samples, the signal generator was not synthesized for high-frequency stability; a frequency resolution of about 5 kHz was accepted. The estimated absolute accuracy of the results is about 15% on a high confidence basis; the observed repeatability and relative precision among various samples is about three times better than the absolute accuracy. We emphasize that this cavity method of resistivity measurement is capable of considerably better accuracy and precision if needed; the work reported herein had the goal of determining resistivity of a large collection of samples in short time rather than an accuracy/precision demonstration.

### III. Results

Table 1 gives measured resistivity in ohms (per square) and derived reflection loss and associated noise for some 30 samples. It should be appreciated that any material having some transmission (leakage) component, such as a mesh or other perforated material, will be overestimated. That is, a leaky material will cause the cavity technique to assess the reduced cavity loaded quality factor ( $Q_L$ ) as all due to surface resistivity whereas the truth is that an unknown portion of the assessment is due to resistivity and the balance due to leakage. Such materials are indicated in Table 1 as starred and footnoted. In Table 1 the control materials (Silver plate on brass, Copper sheet and OFHC Copper) were continually referred to during the course of the measurements. The aluminum series included two samples each of 70-m Project candidate machining techniques, having about 10 periods per lineal inch (25 mm) of 125, 250 and 500 microinch (0.003, 0.006, and 0.013 mm) RMS surface finishes. Such finishes arise from 3-axis milling machine treatment necessary for an asymmetric (not figure of revolution) shaped surface subreflector. It should be noted that the small scale surface finish (scale size  $<0.1$  inch or 2.5 mm) of these materials is perhaps 32 microinch ( $8 \times 10^{-4}$  mm), and as the measurements show, the resistivity appears consistent with this small scale size finish rather than the large scale size ( $\sim 1$  inch or 25 mm). The proposed casting alloy (Aluminum type 319-2F) appears suitable, although about 20% higher resistivity than Aluminum type 6061-T6.

Intentionally, we sought to demonstrate lossier materials such as stainless and mild steel as well as others. Some of the others were indeed very high resistance. In these cases the cavity resonant frequency was shifted considerably upwards (order of 100 MHz or 1.5%). Under these conditions, care must be exercised to remain with the intended  $TE_{011}$  mode.

Table 2 gives measured resistivity and derived reflection loss and associated noise for some 10 flame-sprayed samples. These samples include the lowest and highest expected resistivities from batches prepared by two different suppliers at two different times. The Harris Corporation (HARR) samples were prepared in 1981 (Ref. 2), and are all "as sprayed." The Ford Aerospace (FACC) samples were prepared in early 1984 and are similarly "as sprayed." The work accomplished earlier by Ford Aerospace included studies of buffed surfaces, in attempts to amalgamate individual flame-spray "beads" into a more continuous surface. Some indications were that buffing produced a lower intermodulation product generation. We did not test the buffed surfaces in the belief that any sizeable reflector could not be adequately quality controlled by such hand finishing. As can be seen in Table 2, flame-spray techniques are from two to four times higher resistivity than 6061 T6 Aluminum plate.

In DSN antenna service, with 400 KW CW X-band power incident upon a subreflector, the lowest resistivity material (Silver plate on brass) would dissipate about 100 watts. A good practical material (6061 T6 Aluminum) would dissipate about 160 watts. The best flame-spray (FACC 1/6) would dissipate about 300 watts while the highest resistivity sample (FACC 1/7) would dissipate 600 watts. The type 319-2F casting alloy will dissipate about 190 watts.

### IV. Summary

A previously developed and demonstrated technique for microwave surface resistivity measurement was applied to some 40 samples in a less sophisticated test setup. The object of these measurements departed from previous work in that highest accuracy and resolution were not the purpose, although very excellent results were nevertheless obtained. It was determined that the candidate material and processing method for the DSN 70-m subreflector is entirely acceptable at X-band. However, some caution is suggested with regard to frequency scaling (e.g., to 32 GHz), particularly for the 500 microinch sample. One may note that the 10 periods per lineal inch characteristics of this material will represent fewer ridges and valleys per wavelength at 32 GHz, compared to 8.4 GHz. For purposes of the 70-m subreflector machining, we would prefer the finer finishes, with eventual 32 GHz application in mind. Several flame-sprayed samples show a variation of a factor of two in resistivity, from twice to four times that of a 6061 T6 type Aluminum.

## References

1. Jet Propulsion Laboratory, 1972, *The Deep Space Network, Vol. 12*, JPL TR 32-1526, 59-67, Pasadena, Calif.
2. Thom, E. H., and T. Y. Otoshi, 1981, Surface resistivity measurements of candidate subreflector surfaces, *TDA Progress Report 42-65*, 142-150, Jet Propulsion Laboratory, Pasadena, Calif.
3. McClure, D. H., and F. D. McLaughlin, 64-meter to 70-meter antenna extension, *TDA Progress Report 42-79*, 160-164 Jet Propulsion Laboratory, Pasadena, Calif.

**Table 1. Resistivity, reflection loss and noise at 8400 MHz for various materials**

Material	R <sub>s</sub> , ohms per square	Refl. loss, dB	Noise, K
Silver Plate on Brass	0.0239	0.0011	0.07
Silver Plate on Brass	0.0243	↑	↑
Silver Plate on Brass	0.0244	↓	↓
Copper Sheet	0.0240		
Copper Sheet	0.0252		
Copper (OFHC)	0.0267	0.0011	0.07
Alum. 6061T6, 125 m/inch	0.0360	0.0018	0.12
Alum. 6061T6, 125 m/inch	0.0400	↑	↑
Alum. 6061T6, 250 m/inch	0.0378	↓	↓
Alum. 6061T6, 250 m/inch	0.0385		
Alum. 6061T6, 500 m/inch	0.0375		
Alum. 6061T6, 500 m/inch	0.0382		
Alum. 6061T6, Plate	0.0368		
Alum. 5052, Plate	0.0407	0.0018	0.12
Alum. 2024, Plate	0.0446	0.002	0.14
Alum. 319-2F, Cast Alloy	0.0446	↑	↑
Brass Plate	0.0481	↓	↓
Galvanized Steel (Zinc)	0.0464	0.002	0.14
Perf. Alum. Plate (1/8" × 40%)	0.115 <sup>a</sup>	0.005	0.36
Flame Spray (uncontrolled)	0.147	0.007	0.45
St. Steel 304	0.164	0.008	0.51
St. Steel 347	0.218	0.010	0.67
Titanium Plate	0.229	0.010	0.67
Mild Steel	0.332	0.015	1.03
St. Steel 321	0.347	0.016	1.07
St. Steel (unknown)	0.663	0.031	2.05
Rhomoglas on Balsa	3.49	0.164	11
Rhomoglas 1/2-3" fibres/2%/polyester	29.2 <sup>a</sup>	1.2	80
40% Alum. flakes/EMI X540 polycarb.	31.0 <sup>a</sup>	1.2	80
30% Carbon fibre DC-1006 polycarb.	50 <sup>a</sup>	1.75	120

<sup>a</sup>Partially transmissive (leaky)

**Table 2. Resistivity, reflection loss and noise at 8400 MHz for flame sprays**

Material <sup>a</sup>	R <sub>s</sub> , ohms per square	Refl. loss, dB	Noise, K
FACC 1/6 Pure Zinc	0.0712	0.0033	0.22
FACC 1/4 Pure Copper	0.0715	0.0033	0.22
FACC 1/5 Pure Silver	0.0779	0.0036	0.24
FACC 1/3 Pure Zinc-Tin	0.0909	0.0042	0.28
HARR 3 Std Al + Cu	0.0911	0.0042	0.28
HARR 2 Std Al + Cu	0.0936	0.0042	0.28
FACC 1/2 Pure Al	0.1356	0.0063	0.42
HARR 1 Std Al	0.1394	0.0063	0.42
HARR 2 Std Al	0.1413	0.0065	0.44
FACC 1/7 Std Al (10% impurity)	0.1490	0.0069	0.46

<sup>a</sup>FACC = Ford Aerospace. All using hi-temperature release agent.  
HARR = Harris Inc.

# The Effects of Mode Impurity on Ka-Band System Performance

D. J. Hoppe, W. A. Imbriale, and A. M. Bhanji  
Radio Frequency and Microwave Subsystems Section

*Problems associated with spurious mode generation in the proposed Ka-Band gyro-klystron transmitter tube, overmoded transmission line, and feed are discussed. A brief description of the overall problem is presented. The theory used to evaluate feed and antenna performance when spurious modes are present is given. Results for feed patterns and overall antenna patterns for various levels and types of spurious modes are presented. Worst case antenna efficiency is calculated as a function of spurious mode level. Conclusions are drawn regarding the results of this study and their application to specifications on the transmitter tube and transmission line system.*

## I. Introduction

A conceptual design for a 400 kW CW Ka-Band (34 GHz) transmitter system has been presented in a previous report (Ref. 1). Conventional klystron amplifiers and dominant mode transmission systems are not well suited for high-power millimeter wavelength systems since the small surface areas and high losses in these devices require cooling which is beyond the state of the art at this time. A solution to this problem is provided by using a gyroamplifier and overmoded transmission system (Ref. 2) which is shown in Fig. 1. In the proposed system, the microwave power is extracted from the beam in an overmoded cavity and delivered to the antenna feed in overmoded circular waveguide. Once the microwave power is extracted from the beam it enters a ripple wall mode converter which converts most of the power from the higher order  $TE_{12}$  mode into the  $TE_{11}$  mode. The microwave power then passes through a tapered collector region in the tube, out the vacuum window, through another taper and the transmission line, and

is radiated out the antenna feed. Each of these components allows multimode propagation; for example, the transmission line allows 66 waveguide modes to propagate. Although a well-designed tube and transmission system will minimize mode conversion in these components, the microwave power at the input to the feed will no longer be contained in the dominant  $TE_{11}$  waveguide mode. Since all of the microwave systems used previously in the DSN were single mode systems, this problem is particular to the Ka-band system. This report describes a theoretical study which was undertaken to determine the effect of mode purity on antenna performance.

The first section of the report describes the theory used and some of the basic equations involved, as well as the computer codes used to perform the calculations. The results of the calculations are presented, and conclusions are drawn regarding the results of this study and their application to system specifications.



## II. Theory

### A. Description of the Problem

The feed and Cassegrain system are shown schematically in Fig. 2. The problem we wish to solve is the following: Given a fixed amount of microwave power incident at the input of the overmoded feed at point  $A$ , how does the Effective Isotropically Radiated Power (EIRP) of the antenna system vary depending on the mode content of this incident microwave power?

The overall problem is solved by breaking it up into sections. First of all, the feed section is analyzed in a manner which gives, for any incident electric field  $E_A^i$  at point  $A$ , the resulting reflected field  $E_A^r$  at  $A$ , and the field present in the aperture of the feed  $E_B$ . The electric field in the feed is described as a combination of circular waveguide modes. The far field of the feed  $E_C$ , which is incident on the subreflector at surface  $C$ , is then determined from the feed aperture field  $E_B$ . The field incident on the subreflector is then scattered into the field illuminating the paraboloid,  $E_D$ , by using the geometrical theory of diffraction (GTD). Finally, the resulting far field  $E_E$  is determined from the fields on the paraboloid by physical optics using a Jacobi-Bessel expansion technique.

The question arises as to which types of spurious modes should be considered. The main part of the microwave power will be carried by a  $TE_{11}$  mode which is rotating in the right-hand sense. Symmetric diameter changes, i.e., tapers, couple this mode only to right-hand rotating  $TE_{1n}$  and  $TM_{1n}$  modes. These are the only types of spurious modes we would expect to be present at the field input if perfect circularity in the system were maintained, as well as perfect alignment and straightness. It is expected that although perfection will not be maintained with respect to these parameters the bulk of the spurious power will be contained in the  $TE_{1n}$  and  $TM_{1n}$  modes. Therefore, the detailed analysis will be limited only to modes with one azimuthal variation. Assuming the  $TE_{11}$  mode carries most of the microwave power, the modes most strongly coupled due to deformations other than symmetric radial deformations may be determined. The right-hand rotating  $TE_{11}$  mode is coupled to the  $TE_{01}$  mode through curvature, discrete waveguide tilts, and waveguide offsets. Ellipticity in the waveguide causes coupling to the left-hand rotating  $TE_{11}$  mode as well as right-hand rotating  $TE_{3n}$  and  $TM_{3n}$  modes. Approximate results for the effects of these modes on antenna performance will be given at the end of the results section.

### B. Feed Analysis

A cut-away view and cross sectional view of the antenna feed are shown in Fig. 3. The inside diameter of the overmoded transmission line was chosen to be 1.75 in. which is approximately the same size as the output of the X-band

hybrid horns when scaled to 34 GHz. Therefore the Ka-band system requires no flare angle horn, but merely a straight section of corrugated waveguide with varying slot depth. The slot depth profile is chosen to transform the  $TE_{11}$  mode of the smooth-walled waveguide into the balanced  $HE_{11}$  mode, which is one of the modes which exists in a corrugated waveguide with constant slot depth. Care must be taken in the design of this transition section since many other modes may also be excited in the 1.75-in. diameter corrugated waveguide at this frequency. The section's length and slot depth profile were adjusted to nearly optimally illuminate the subreflector when a pure  $TE_{11}$  mode was incident at point  $A$ . Along with the  $TE_{11}$  mode 8 other modes with one azimuthal variation may propagate in 1.75-in. diameter waveguide at 34 GHz. They are  $TE_{1n}$  ( $n = 2, 3, 4, 5$ ) and  $TM_{1n}$  ( $n = 1, 2, 3, 4$ ). The feed response to any combination of these modes at the input  $A$  is required.

The corrugated section is analyzed using a new computer code developed for the Ka-Band project.<sup>1</sup> The analysis follows the method of James (Ref. 3), expanding the fields inside each fin and slot in terms of circular waveguide modes, and matching the fields at each slot-fin boundary. All of the possible propagating modes, as well as a sufficient number of evanescent modes are matched at each edge, with results for successive edges and waveguide lengths being cascaded as one moves through the device. In this way the interaction between the fields of non-adjacent as well as adjacent slots is taken into account. The result of the calculation is a matrix equation relating the reflected and aperture modes to the input modes. If  $a_1$  is a vector containing the power normalized amplitudes of the input modes, then we may calculate the reflected modes  $b_1$ , and the aperture modes  $b_2$  using

$$b_2 = [S_{21}] a_1 \quad (1)$$

$$b_1 = [S_{11}] a_1 \quad (2)$$

Here  $[S_{21}]$  and  $[S_{11}]$  are the scattering matrices resulting from the computer run. They depend only on frequency and device dimensions, not input modes. We may therefore specify any input vector  $a_1$  and calculate the reflected and aperture fields.

Using the normalized amplitudes calculated above, and the normalized vector functions giving the field distributions for each mode, we find the aperture field  $E_B$ . The far field is then calculated by the method described by Silver and Ludwig (Ref. 4, 5).

<sup>1</sup> See D. J. Hoppe, "Scattering Matrix Program for Circular Waveguide Junctions," Interoffice Memorandum #3335-84-071 (internal document), Dec. 5, 1984, Jet Propulsion Laboratory, Pasadena, Calif.

$$\mathbf{E}_c = \frac{-1}{4\pi} \iint_S (-j\mu\omega(\mathbf{a}_n \times \mathbf{H}_B) \phi + (\mathbf{a}_n \times \mathbf{E}_B) \times \nabla \phi) ds \quad (3)$$

where

$\mathbf{E}_B$  = aperture electric field

$\mathbf{H}_B$  = aperture magnetic field

$\mathbf{a}_n$  = unit vector normal to aperture surface

$dS$  = incremented area on aperture surface

$\omega = 2\pi f$

$f$  = frequency

$\mu$  = free space permeability

$\nabla$  = gradient operator

$\phi = (\exp - jkr)/r$

$k = 2\pi/\lambda_0$

$r$  = far field point distance from origin (spherical radius)

When  $\mathbf{E}_B$  is represented in terms of circular waveguide modes the resulting integrals have already been evaluated by Silver (Ref. 5). Therefore, given an input vector and the scattering matrix, we determine the aperture modes and composite far field patterns. Throughout the analysis care must be taken to ensure proper normalization of the field amplitudes in terms of power.

### C. Dual Reflector Antenna Analysis

Given the feedhorn field  $\mathbf{E}_C$  which is incident on the subreflector, the GTD/Jacobi-Bessel Program (Ref. 6) was used to calculate the far field pattern of the composite Cassegrain system.

The field scattered to the parabolic main reflector from the ellipsoidal subreflector is calculated using GTD. The field incident on the paraboloid  $\mathbf{E}_D$ , is then integrated into the resulting final far field pattern of the antenna. In the final integral's evaluation a Jacobi-Bessel expansion technique is used (Ref. 7). In this study the far field patterns for the present 64-meter system were examined for arbitrary excitation of the feed. It should be pointed out that very accurate modeling of the 64-meter system is possible with the GTD/Jacobi-Bessel program, and effects such as the slight offsets of the feed placement and subreflector are included.

This completes the explanation of the analysis method. The total far field, including the on-axis field  $\mathbf{E}_E$ , may now be determined for arbitrary feed excitation.

### D. Gain and Orthogonality

Since the circular waveguide modes at the input to the feed are power orthogonal, we may calculate the far field for any arbitrary combination of mode amplitudes and phases by knowing the antenna pattern for each of the modes individually. An explanation follows.

Each waveguide mode incident on the feed generates a set of modes in the feed aperture. Since the feed and antenna are assumed to be lossless in the analysis, the set of aperture modes generated by any pure waveguide mode at the input is orthogonal to the set generated by any other pure waveguide mode at the input. This is a property of the scattering matrix determined from the fact that the device is lossless and power must be conserved (Ref. 8). Also antenna gain and directivity are equivalent. Power must also be conserved in the far field of the feed. That is, the far field generated by 1 watt of  $TE_{11}$  incident power contains 1 watt (neglecting reflections); the far field of 1 watt of  $TM_{11}$  incident also contains 1 watt; and since the two exciting modes are power orthogonal, the far field produced by the sum will contain 2 watts. This was confirmed by numerically integrating far-field patterns for single modes exciting the feed and arbitrary combinations. This result gives confidence in the correctness of the far-field calculations. Two different waveguide modes exciting the feed act like a two-element array with no mutual coupling.

Returning to the notation of part B we excite the feed with a single mode, mode number  $i$  ( $i = 1, 2, \dots, 9$ ). The fields are normalized so that we have for the input power  $P(i)$

$$P(i) = |a_1(i)|^2 \quad (4)$$

For this input signal we then calculate the feed pattern, subreflector pattern, and finally the electric field on the antenna axis,  $\mathbf{E}_E(i)$ . If we separate out the vector nature of the field, letting  $\mathbf{a}$  be a unit vector in the direction of the field,

$$\mathbf{E}_E(i) = \frac{\mathbf{E}_E(i)\mathbf{a}}{r\sqrt{4\pi}} \quad (5)$$

We may calculate the gain for the specific input mode,  $G(i)$

$$G(i) = \frac{|E_E(i)|^2}{\eta P(i)} = \frac{|E_E(i)|^2}{\eta |a_1(i)|^2} \quad (6)$$

or

$$E_E(i) = \eta |a_1(i)| G(i) \exp j\Phi(i) \quad (7)$$

where  $\Phi(i)$  is the phase of the far field which is given by the analysis but lost in the gain calculation. The gain for each

input mode may be calculated similarly. When an arbitrary combination excites the feed we have

$$P_{\text{sum}} = \sum_i |a_1(i)|^2 \quad (8)$$

$$E_{\text{sum}} = \sum_i E_E(i) = \sum_i \eta |a_1(i)| G(i) \exp j\Phi(i) \quad (9)$$

The antenna gain for any excitation of the feed is given by

$$G_{\text{sum}} = \frac{|E_{\text{sum}}|^2}{\eta P_{\text{sum}}} \quad (10)$$

or

$$G_{\text{sum}} = \frac{\left| \sum_i a_1(i) |G(i) \exp j\Phi(i)|^2 \right|}{\sum_i |a_1(i)|^2}$$

The next section will describe the results of the calculations described above.

### III. Results

#### A. Feed Patterns

The calculations described in Sec. II part B were carried out for a preliminary feed design. The feed radiation pattern for each possible input mode was determined. A few examples of the results of these calculations are depicted in Figs. 4-6. Figure 4 shows the  $E$  and  $H$  plane radiation patterns for the feed when it is excited by a pure  $TE_{11}$  mode. The calculated gain is 22.4 dBi, and fairly good pattern circular symmetry is obtained. A reduction of the  $H$  plane sidelobes, and improved pattern symmetry should be obtainable by further refinement of the corrugation profile. For a  $TE_{11}$  mode incident on the feed each of the reflected modes is found to be at a level of at least -43 dBc. (Here dBc references the power level to that of the forward traveling  $TE_{11}$  mode.) These small values for the reflected modes are due to the fact that the waveguide diameter is very large with respect to the wavelength. The feed radiation pattern for the case when the  $TM_{11}$  mode is incident on the feed is shown in Fig. 5. For this case we find that the pattern is grossly asymmetric, with the maximum gain of 17.7 dBi, occurring in the  $E$  plane at  $\Theta \cong 16^\circ$ . The on-axis gain of the feed is 13.7 dBi, or about 4 dB below the maximum. We may also note that when this pattern illuminates the subreflector  $|\Theta| \leq 15^\circ$ , much of the power is lost in spill-

over. The pattern for each spurious mode may be calculated similarly, and some general comments can be made. Higher order  $TM$  modes have maximum gain points in the  $E$  plane, and  $TE$  modes in the  $H$  plane. As the mode number increases, the point of maximum gain moves out further from the feed axis,  $\Theta = 0^\circ$ . For modes higher than  $TE_{13}$  less than 5% of the power in each mode is intercepted by the subreflector. This would indicate that the higher order spurious modes will have a smaller effect on the overall antenna gain than the lower order modes. Finally, an example of the feed pattern for the case when a mixture of modes excites the feed is shown in Fig. 6. The results are for a mode mixture where 6% of the incident power is carried by the  $TM_{11}$  mode, and 94% by the  $TE_{11}$  mode with the phase of  $TM_{11}$  mode with respect to the  $TE_{11}$  mode being  $145^\circ$ . The maximum gain occurs on the feed axis, and is 21.6 dBi, or about 0.8 dB below the gain for the case when a pure  $TE_{11}$  mode was incident. In a similar way, the feed pattern for an arbitrary combination of input modes may be calculated. It should be noted that modes without one azimuthal variation, that is, other than  $TE_{1n}$  and  $TM_{1n}$ , produce feed patterns which are hollow; i.e., no radiation on the feed axis is produced. The point of maximum gain moves further away from the axis as the mode number is increased.

#### B. Dual Reflector Patterns

The overall antenna patterns for the feed patterns of Figs. 4-6 were calculated using the method described in Sec. II Part C, and the results are plotted in Figs. 7-9. The calculated results are for the present 64-meter antenna system. The antenna far-field pattern in the  $E$  and  $H$  planes for a  $TE_{11}$  mode incident on the feed is shown in Fig. 7. The calculated gain is 86.15 dBi, and excellent pattern circular symmetry is obtained. The theoretical maximum gain of the system is 87.15 dBi. These calculations give an aperture efficiency, neglecting quadripod blockage and surface errors, of about -1 dB, or 79.5% for the  $TE_{11}$  mode. The calculated far field pattern for the  $TM_{11}$  case is shown in Fig. 8. The overall antenna pattern has a calculated on-axis gain of 62.1 dBi, with the maximum gain of 74.6 dBi occurring in the  $H$  plane at  $\Theta \cong 0.009^\circ$ . The resulting pattern contains many sidelobes, and is very asymmetric. The result for the composition of modes 94%  $TE_{11}$  plus 6%  $TM_{11}$  with the correct phasing of  $TE_{11}$  at  $0^\circ$  and  $TM_{11}$  at  $145^\circ$  is shown in Fig. 9. The calculated axis gain for this composition is 85.78 dBi, or a loss of 0.4 dB from the  $TE_{11}$  case. This shows that if a given amount of microwave power were distributed between  $TE_{11}$  and  $TM_{11}$  in this ratio of power and in this phasing we would experience a loss of 0.4 dB (8.75%) in effective isotropically radiated power (EIRP) from the case where all the power was in the  $TE_{11}$  mode. The parameter of major interest for the Ka-band system is the EIRP, or equivalently the on-axis antenna gain for a given mode composition.

The on-axis antenna gain was calculated for each input mode to the feed. The results of these calculations are summarized in Table 1. We see that in terms of on-axis field effects, the modes  $TE_{12}$ ,  $TM_{11}$ , and  $TM_{12}$  are of primary importance, the higher order modes being very poor on-axis radiators with respect to the  $TE_{11}$  mode. Modes of the type  $m \neq 1$ , i.e.,  $TE_{0n}$ ,  $TE_{2n}$ ,  $TM_{2n}$  etc., may be considered by making a few simplifications. If the Dual Reflector system were perfectly circularly symmetric it could be shown by symmetry considerations that modes with  $m \neq 1$  do not contribute to the on-axis gain, i.e., the entry in Table 1 for these modes is  $-\infty$ . Depending upon their level and phase with respect to the  $TE_{11}$  mode they could cause the maximum gain to appear off-axis, although the on-axis field value would be the same as for that of the  $TE_{11}$  mode alone. Although the 64-meter system is not perfectly symmetric, it is assumed that the on-axis gain for these modes will be very small.

### C. Efficiency Results

In this section we define an efficiency factor,  $\eta$ , which references the (EIRP) for a given mode content at the feed input to that for a pure  $TE_{11}$  mode incident on the feed. That is for a given RF power level,  $P_{RF}$ , and mode composition corresponding to an efficiency factor  $\eta$ , we have for the Effective Isotropically Radiated Power:

$$EIRP_{dBW} = P_{RF} (dBW) + 86.15 \text{ dB} + \eta(dB) \quad (12)$$

The factor  $\eta$  depends upon the percentage of  $P_{RF}$  in each mode, and the phases of these modes. For a pure  $TE_{11}$  mode composition  $\eta = 1.0 = 0 \text{ dB}$ . The results for  $\eta$  vs mode content are shown in Fig. 10. The horizontal axis represents the percent of  $TE_{11}$  mode present in the mode composition, or equivalently the total power level of the spurious modes with respect to the  $TE_{11}$  mode power. The vertical scale represents the efficiency factor  $\eta$ . Three curves are plotted,  $\eta_+$ ,  $\eta_-$ , and  $\eta_f$ . For a given total spurious mode level  $\eta_-$  gives the minimum possible value for  $\eta$  and  $\eta_+$  the maximum. The term  $\eta_f$  represents the effect of adding an ideal mode filter which dissipates all the spurious mode power and passes the  $TE_{11}$  power with no attenuation. In using Eq. (12) for this case,  $P_{RF}$  is the RF power measured before the filter.

For example, suppose the RF power is measured as 200 kW (53 dBW), and we also know that the RF power is 94%  $TE_{11}$  and 6% spurious modes (-12 dBc). Using Fig. 10 we find that for a spurious mode level of -12 dBc,

$$\begin{aligned} \eta_+ &= -0.12 \text{ dB} \\ \eta_- &= -0.4 \text{ dB} \end{aligned} \quad (13)$$

Then using Eq. (12), and realizing that the actual efficiency factor may fall anywhere between these two values, depending on which spurious modes are present and on their relative phases, we find

$$138.75 \text{ dBW} \leq EIRP \leq 139.03 \text{ dBW} \quad (14)$$

If an ideal mode filter is added to dissipate all of the power carried by the spurious modes then

$$\eta_f = -0.18 \text{ dB} \quad (15)$$

and

$$EIRP = 138.97 \text{ dBW} \quad (16)$$

If we can only guarantee that the mode purity ( $TE_{11}\%$ ) is at least 94% then we must find the maximum value for  $\eta_+$  and the minimum value for  $\eta_-$  for spurious mode levels less than -12 dBc (6%). Using Fig. 10 we find

$$\eta_+ = 0.02 \text{ dB}$$

and

$$\eta_- = -0.04 \text{ dB}$$

Using (12) we find

$$138.75 \text{ dBW} \leq EIRP \leq 139.17$$

The fact that  $\eta_+ = 0.02 \text{ dB}$  (1.004) for some spurious mode level  $\leq -12 \text{ dBc}$  deserves some comment. The result  $\eta_+ > 1.0$  merely implies that there is a combination of modes that may be put into the feed that achieves slightly better illumination of the subreflector and paraboloid than the pure  $TE_{11}$  mode. An analogous effect is used in the dual mode horn where the power incident in the  $TE_{11}$  mode is redistributed between the  $TE_{11}$  and  $TM_{11}$  modes, and more efficient antenna illumination is obtained.

### IV. Conclusions

The initial reason for performing this study was to determine some component specifications for the tube and transmission line making up the Ka-band system. Additional results regarding expected performance of the system were also provided by Varian Associates in the final report for the Ka-band feasibility study<sup>2</sup>. One of the comments made

<sup>2</sup>See D. Stone, R. Bier, M. Caplan, H. Huey, D. Pirkle, J. Robinson, and L. Thompson, *Feasibility Study for a 34 GHz (Ka-Band) Gyro-amplifier, Final Report*, prepared by Varian Associates, Inc., under JPL subcontract #956813, Sept. 1984.

by Varian in the report is that even with the most careful tube design spurious mode levels of about -12 dBc are expected and that further mode purity can only be obtained by absorbing some of the RF power in a lossy mode filter. In addition, calculations on the effect of tilt alignment of the transmission line show that in order to maintain a total spurious mode level of less than -15 dBc, an optical bench arrangement will be necessary to align the components. For the case analyzed in detail in Section III, 94%  $TE_{11}$  and 6% spurious power, it was shown that a net gain in EIRP of only 0.22 dB was possible (assuming the worst case phasing of the spurious modes) by adding an ideal mode filter. More detailed calculations of helix mode filter performance indicate that with reasonable values for tolerances of the device parameters the

insertion loss for the  $TE_{11}$  mode is about 0.1 dB, even with perfect conductivity assumed in the helical windings. Real life effects such as finite conductivity in these windings will also contribute to the  $TE_{11}$  insertion loss. Therefore, with real effects taken into account an optimistic estimate for the maximum increase in efficiency that could be expected by adding a filter is about 0.1 dB ( $\sim 2\%$ ).

For the reasons mentioned above, it has been decided that a more reasonable specification for mode purity to be given to the tube designer is -12 dBc (94%), rather than the original -30 dBc (99.9%). This would eliminate the need for an optical bench system and also eliminate the development of a  $TE_{11}$  mode filter.

## References

1. Bhanji, A., Hoppe, D., Hartop, R., Stone, E., Imbriale, W., Stone, D., and Caplan, M. High power Ka-band transmitter for planetary radar and spacecraft uplink, *TDA Progress Report 42-78* (April-June 1984), Jet Propulsion Laboratory, Pasadena, CA, pp. 24-48.
2. J. L. Hirshfield, Gyrotron, in *Infrared and Millimeter Waves*, Vol. 1, Academic Press, New York, pp. 1-54, 1979.
3. G. L. James, Analysis and design of  $TE_{11}$  to  $HE_{11}$ , corrugated cylindrical waveguide mode converters, *IEEE Trans. Microwave Theory and Tech.*, Vol. MTT-29, pp. 1059-1066, October 1981.
4. A. C. Ludwig, Radiation pattern synthesis for circular aperture horn antennas, *IEEE Trans. Antennas and Propagation*, Vol. AP-14, pp. 434-440, July 1966.
5. S. Silver, *Microwave Antenna Theory and Design*, Rad. Lab ser., Vol. 12, McGraw Hill, New York, pp. 336-338, 1949.
6. Veruttipong, T., Rochblatt, D., Imbriale, W., and Galindo, V., "Dual Shaped and Conic GTD/Jacobi-Bessel Analysis Programs," JPL-D-2096 (internal document), December 1984, Jet Propulsion Laboratory, Pasadena, CA.
7. Raj Mittra, Yahya Rahmat-Samii, Victor Galindo-Israel, and R. Norman, An efficient technique for the computation of vector secondary patterns of offset paraboloid reflectors, *IEEE Trans. Antennas and Propagation*, Vol. AP-27, pp. 294-304, May 1979.
8. R. E. Collin, *Foundations for Microwave Engineering*, McGraw Hill, New York, pp. 174-176, 1966.

**Table 1. On-axis antenna gain for various modes  
incident on the feed**

Input Mode	Gain, dBi	Gain Relative to the $TE_{11}$ Mode, dB
$TE_{11}$	86.15	0
$TM_{11}$	62.1	-24.05
$TE_{12}$	60.2	-25.95
$TM_{12}$	61.5	-24.65
$TE_{13}$	~44	~-42
$TM_{13}$	~40	~-46
$TE_{14}$	~30	~-56
$TM_{14}$	~53	~-33
$TE_{15}$	~46	~-40



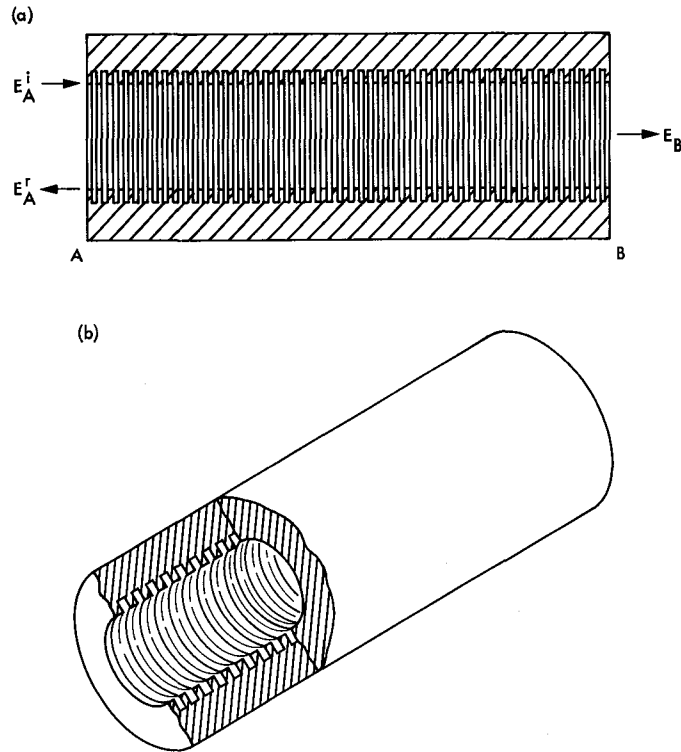


Fig. 3. Antenna feed, corrugated section with varying slot depth:  
(a) cross section view; (b) cut-away view

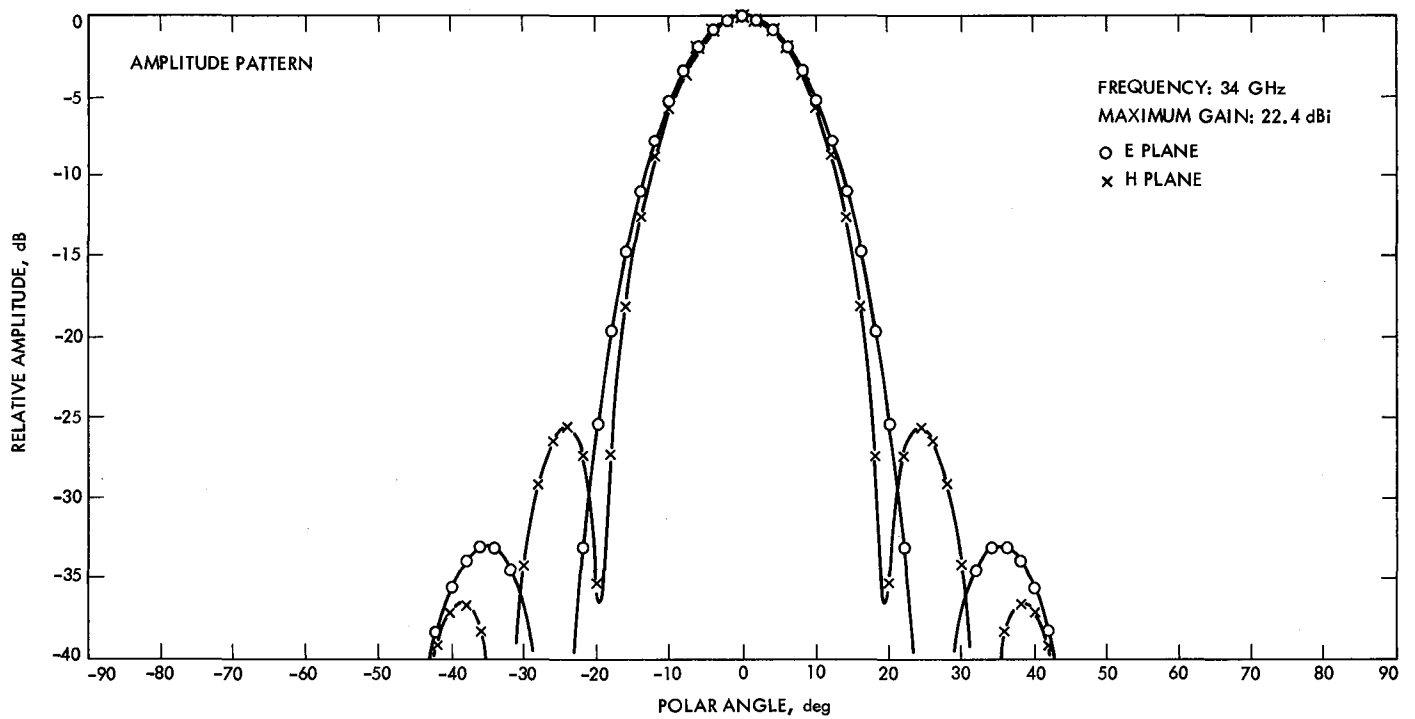


Fig. 4. Feed radiation patterns for a pure  $TE_{11}$  mode incident on the feed



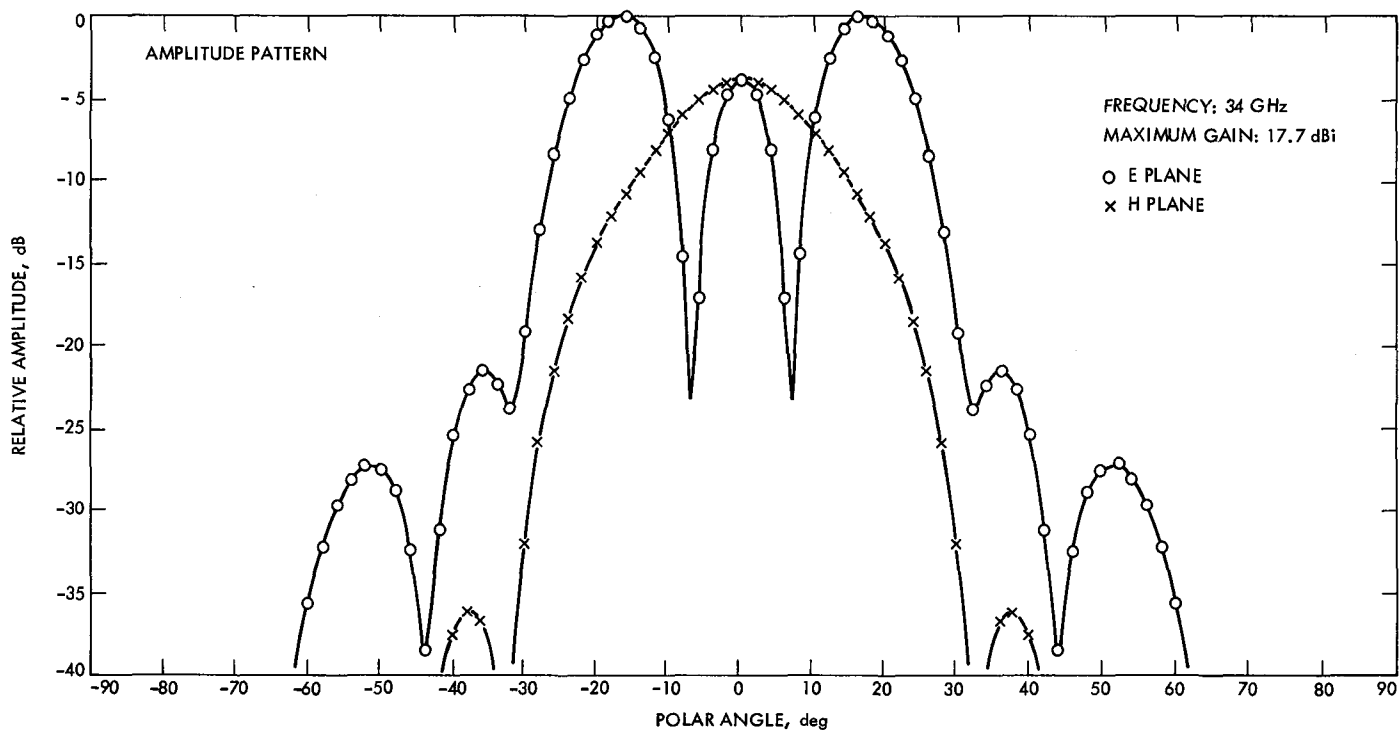


Fig. 5. Feed radiation patterns for a pure  $TM_{11}$  mode incident on the feed

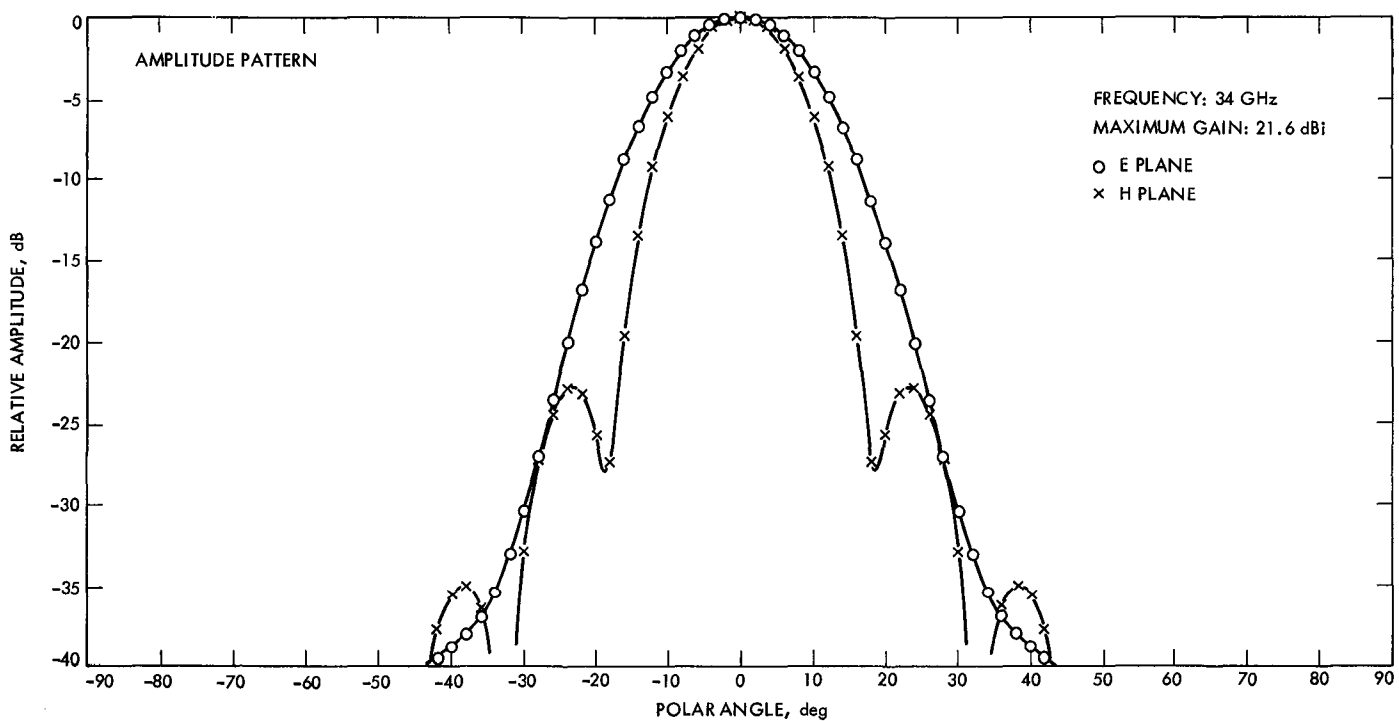


Fig. 6. Feed radiation patterns when a mixture of  $TE_{11}$  and  $TM_{11}$  modes is incident on the feed

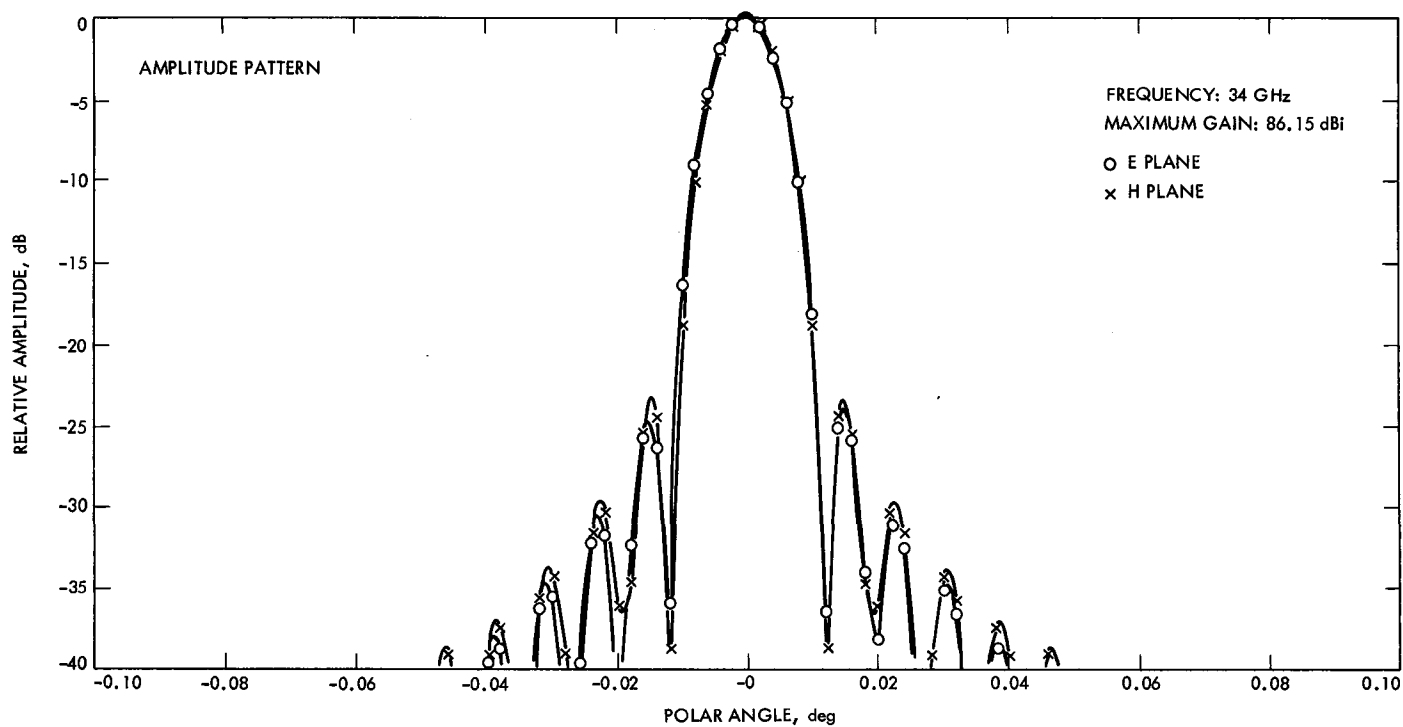


Fig. 7. Radiation patterns for the antenna when a pure  $TE_{11}$  mode is incident on the feed

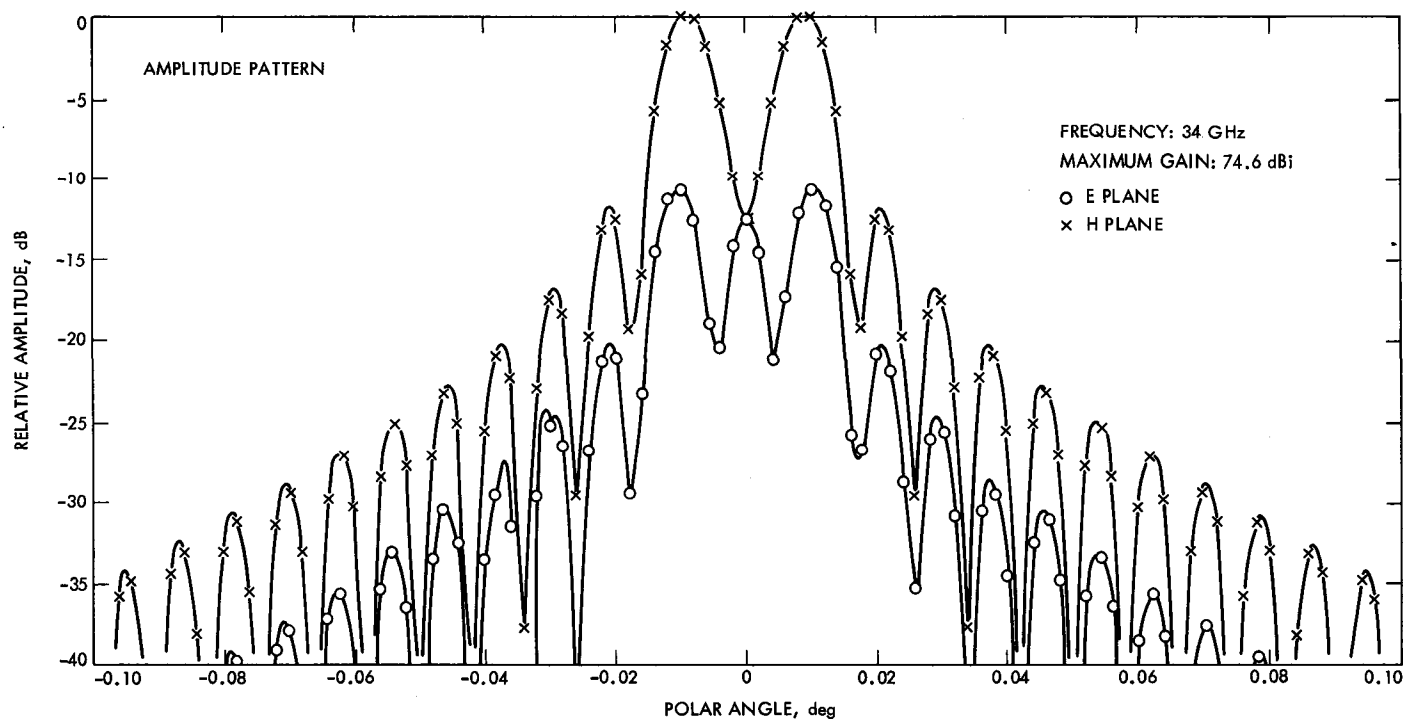


Fig. 8. Radiation patterns for the antenna when a pure  $TM_{11}$  mode is incident on the feed

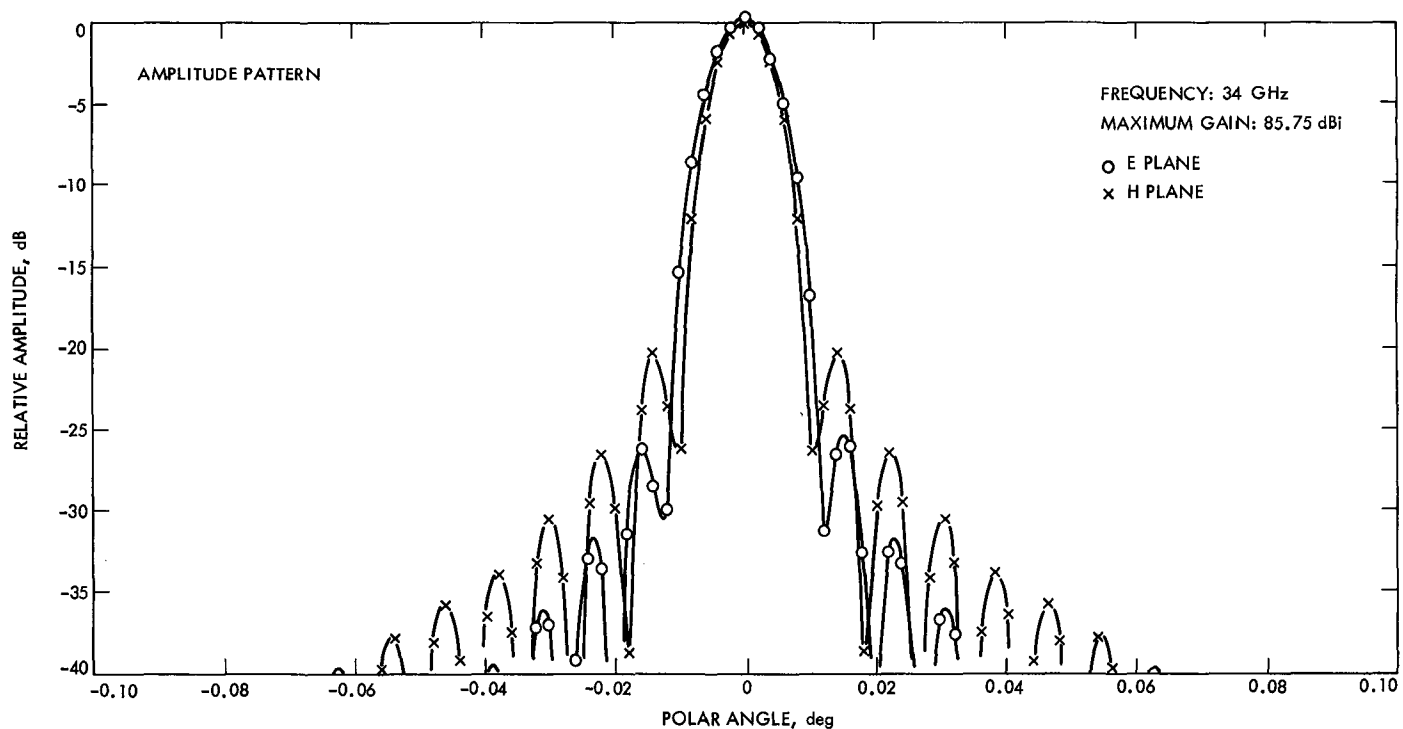


Fig. 9. Radiation patterns for the antenna when a mixture of  $TE_{11}$  and  $TM_{11}$  modes is incident on the feed

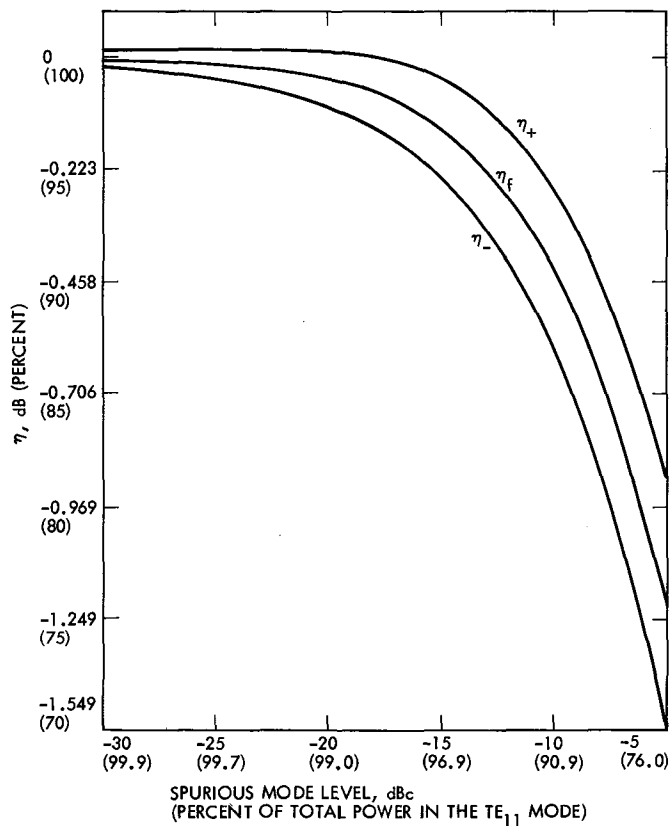


Fig. 10. Efficiency factors as a function of mode purity

# Detection and Symbol Synchronization for Multiple-Bit per Photon Optical Communications

W. K. Marshall

Communications Systems Research Section

*Methods of detection and synchronization in a highly efficient direct detection optical communication system are reported. Results of measurements on this moderate-rate demonstration system capable of transmitting 2.5 bits/detected photon in low-background situations indicate that symbol slot synchronization is not a problem, and that a simple symbol detection scheme is adequate for this situation. This system is a candidate for interplanetary optical communications.*

## I. Introduction

In a *signal limited* optical communication system, the data rate is determined by the number of received photons per second and the amount of data which can be communicated per received photon. The number of bits per received photon is a figure of merit of the efficiency of a given system and depends, in general, on the method of communications and on the quality of the receiver.

In a *photon counting* communication system information is sent by on-off modulating of a laser, with the laser output constant over a basic time interval called a *symbol slot*. The receiver estimates whether the laser was on or off during each symbol slot by counting the number of photon arrivals during that slot. A photon arrival is the result of extracting one quantum of energy (a photon) from the optical field incident on a detector to produce a photoelectron. The rate at which photoelectrons are generated is proportional to the incident optical intensity, but the actual number of photoelectrons is a random variable. A photon counting receiver has two tasks, symbol detection (estimating from the electrical output of the photon

counter whether the laser was on or off during a slot) and synchronization (determining the time position of symbol slots over which to count photons).

An efficient method of communicating with direct detection is to use  $M$ -ary pulse position modulation (PPM) (Ref. 1), in which the position of one *signal slot* (symbol slot in which the laser was "on") among  $M - 1$  *noise slots* (symbol slots in which the laser was "off") in a PPM word represents  $\log_2 M$  bits of information. In this article, the receiver section for a photon counting optical communication system which uses an average of less than 3 photon arrivals per signal slot with 256-ary PPM to achieve an efficiency of 2.5 bits/detected photon<sup>1</sup> is reported. The system communicates reliably (using Reed-Solomon error correction coding) at 300 kbps in low-background light situations.

---

<sup>1</sup>*Detected photons are different from received photons since the quantum efficiency of the photon counter is less than one. We use bits/detected photon to avoid the wavelength dependence of the efficiency of the photon counter (typically a PMT).*

In the first section below, the *symbol detector* which detects photon arrivals and assigns them to appropriate time slots is described. The following section discusses the performance of this detector and its use in calibrating the system at the very low optical signal levels used (typically less than 1 picowatt). The next section considers the slot synchronizer and its performance. Note that this report presents experimental results on the receiver section of a fully operational 2.5 bit/detected photon demonstration system; reports on other aspects of this system are listed in Refs. 2-4.

## II. Symbol Detection

The direct-detection receiver used in the 2.5 bit/detected photon demonstration program consists of a symbol detector and a phase-locked-loop slot synchronizer (Fig. 1). A photomultiplier tube (PMT) converts each photon arrival into a relatively large but random current pulse which drives the receiver. The symbol detector converts the (amplified) electrical output of the PMT into a signal indicating the reception of photons during time intervals (slots) determined by the slot synchronizer. The output of the detector is ultimately used by the PPM decoder to determine which of the  $M$  possible words (for  $M$ -ary PPM) was sent during each group of symbols which make up a PPM word.

In general, the problem of estimating photon arrivals from the electrical output of the PMT is quite difficult. For optimal PPM demodulation, the detector should be able to determine the number of photon arrivals during each of the symbol slots in a PPM word. Because of random PMT gain (i.e., PMT output pulses have variable height and width; Ref. 5), thermal noise in the amplified PMT output and limited time resolution (due to limited bandwidth), the estimation problem becomes quite difficult. However, in cases in which the channel is erasure-limited, (i.e., the probability of a background photon arrival during a PPM word is less than the probability that no signal photons are received due to the Poisson statistics of photon arrivals), the detection problem reduces to classifying slots only according to whether there were no photon arrivals (symbol detected as "0") or some photon arrivals (symbol detected as "1") during each slot. For the 2.5 bit/detected photon demonstration this erasure-limited condition is satisfied for background levels up to about 2000 noise counts/s (footnote 2); hence, the detector used here classifies slots only according to some photon arrivals or none.

The symbol detector used for these experiments is very simple and consists of a voltage threshold comparator and a

latch. If the (amplified 700X) output of the PMT crosses the voltage threshold during a symbol slot marked by rising edges on the estimated slot clock input, the latch output is "1" and a photon is declared to have arrived during that slot. Since the average height of the PMT pulses is much higher than the rms thermal noise voltage, almost all of the threshold crossings indicate photon arrivals. As shown in this next section, this detector circuit, although simple, performs satisfactorily in the few photons per signal slot regime.

## III. Detector Performance

In order to measure the performance of the detector independent of synchronization errors, the clock was initially hard-wired from the transmitter (with appropriate delays). The fraction of signal slots in which photons were detected (i.e., voltage threshold crossed) as a function of the detector threshold for three different signal intensities is shown in Fig. 2. The probability of detecting at least one photon during a signal slot,  $P_{ds}$ , is approximately constant over a wide range of thresholds (40-200 mV at the comparator input) but falls off quite rapidly at higher thresholds. The probability of detection in this constant  $P_{ds}$  region depends on the intensity in a way related to the Poisson distribution of the number of photon arrivals. In slots during which the laser is turned off (and the background intensity is essentially zero), there is still some probability that the threshold will be crossed due to thermal noise and due to the presence of PMT dark counts. The fraction of noise slots,  $(1 - P_{dn})$ , in which the threshold was crossed with no optical signal is shown in Fig. 3. This graph shows two distinct regions of operation. For  $V_{\text{thresh}} < \sim 50$  mV,  $(1 - P_{dn})$  decreases rapidly as the threshold is increased, due to the decreased probability that thermal noise will cause a threshold crossing. Above 50 mV, the fraction of false counts is almost constant at about  $2 \times 10^{-6}$ . This is the result of PMT dark counts which for the cooled RCA C31034 PMT used were about 20 per second.

The approximate shape of the  $P_{ds}$  versus threshold voltage curve can be predicted using the simple theory that a given photoelectron response pulse is detected if the (random) PMT gain seen by the pulse is greater than a gain threshold given by  $G_{\text{thresh}} = (V_{\text{thresh}}/700) T_{\text{pulse}}/R_{\text{term}}$  (electrons), where  $T_{\text{pulse}}$  is the (average) width of the amplified PMT single photoelectron response pulses and  $R_{\text{term}}$  is the PMT termination resistance. The probability of detecting a given single photoelectron response pulse is the probability that the gain is greater than  $G_{\text{thresh}}$ , given by

$$P(\text{Gain} > G_{\text{thresh}}) = \int_{G_{\text{thresh}}}^{\infty} p_G(x) dx \quad (1)$$

<sup>2</sup>For comparison, a diffraction-limited receiving telescope looking at Jupiter from Earth-orbit through a 10 angstrom filter at 0.9  $\mu\text{m}$  would produce  $10^3$  to  $10^4$  detected background photons per second.

where  $p_G(x)$  is the probability density of the PMT gain given approximately (Ref. 6) by

$$p_G(x) = \exp(-A/B) (\delta(x) + \frac{\exp(-x/B) \sqrt{A/x}}{B} I_1((2/B) \sqrt{A x})) \quad (2)$$

where for the PMT used,  $A = 10^6$  (the mean PMT gain) and  $B = 1.42 \times 10^5$ , and  $I_1$  is the modified Bessel function of the first kind. The overall  $P_{ds}$  is the probability of detecting a pulse containing a given number of photoelectron pulses averaged over the (Poisson) distribution of the number of photon arrivals in a signal slot. This curve is given in Fig. 4 and matches the experimental curve reasonably well for thresholds large enough to ignore thermal noise. The theory curve shows that for thresholds less than about 0.2 times the mean value, the detector should be nearly ideal, limited only by the Poisson photon erasure statistics, i.e.,

$$P_{ds} \cong 1 - \exp(-N_s) \quad (3)$$

where  $N_s$  is the mean number of photon arrivals per signal slot. Hence for a voltage threshold of 70 mV (used for measurements throughout the remainder of this report) the signal intensity,  $N_s$ , is given by

$$N_s \cong -\ln(1 - P_{ds}(70 \text{ mV})) \quad (4)$$

By using an additional photodetector to measure the laser output before it was attenuated (by  $\sim 80$  dB) and fed into the PMT, the value of  $N_s$  corresponding to various transmitter pulse widths and monitor photodiode voltages was measured (Fig. 5) and used to calibrate the received signal intensity. Note that the intensities given relate to the number of photoelectrons generated during a signal slot, and are therefore related to the actual (peak) optical intensity by the PMT quantum efficiency,  $\eta_{QE}$ , the energy per photon,  $h\nu$ , and the slot width,  $T$ , by

$$\text{Optical power} = \frac{N_s h\nu}{\eta_{QE} f T} \quad (5)$$

where  $f$  is the fraction of a symbol slot filled by a laser pulse. For a wavelength of  $0.85 \mu\text{m}$ ,  $h\nu = 2.3 \times 10^{-19}$  Joule, and  $\eta_{QE} = 0.2$ ,  $f = 0.7$ , and  $T = 100$  ns, the *peak* optical power incident on the PMT photocathode is

$$\text{Optical power} \cong 2 N_s \times 10^{-11} \text{ Watts} \quad (6)$$

For 256-ary PPM and  $N_s = 3$ , the *average* incident optical power would be  $\sim 0.25$  picowatts.

## IV. Symbol Slot Synchronization

Symbol slot synchronization in the direct-detection receiver is the reconstruction of the transmitter clock rate and phase to determine the intervals over which to count photon arrivals. The receiver must track the transmitter clock, using relatively few discrete photon arrivals (with random arrival times), where the primary noise sources are signal photon shot noise, shot noise due to background photons, and noise due to PMT gain fluctuations. Initial (linear) calculations for this case indicated that a PLL tracking loop would work, provided the loop bandwidth was sufficiently small. A symbol slot synchronizer using this approach was designed and constructed and operated with satisfactory results as discussed below.

The slot synchronizer portion of the receiver consists of a phase detector, an active low-pass filter and a precision voltage-controlled oscillator (VCO). The input to the loop is from the voltage comparator in the symbol detector, a binary signal which is "1" whenever the PMT output is above the voltage threshold. This signal is gated with the VCO output clock in the phase detector and filtered to produce the error input to the VCO.

The closed loop response of the PLL is (approximately)

$$H(s) = K(1 + s T_2)/(s^2 T_1 + K(1 + s T_2)) \quad (7)$$

where  $K = (K_\phi K_{VCO})$  is the combined gain of the phase detector and the VCO, and  $T_1 = (R_1 C_2)$ ,  $T_2 = (R_2 C_2)$  are the loop filter time constants. The phase detector gain  $K_\phi$  is a function of the signal level  $N_s$  and the fraction of slots during which the laser is on ( $= 1/M$  for  $M$ -ary PPM). Although  $K_\phi$  is actually a non-linear function of the signal level, for small  $N_s$  it can be (empirically) approximated by

$$K_{\phi} \cong 0.06 \frac{N_s}{M} \text{ volts/radian} \quad (8)$$

The VCO gain was

$$K_{VCO} = 750 \text{ radians/sec/volt} \quad (9)$$

so that the combined gain was

$$K \cong 50 \frac{N_s}{M} \text{ sec}^{-1} \quad (10)$$

By an extension of the results in Ref. 7, the steady-state rms timing error due to shot noise is given approximately by

$$\frac{T_{rms}}{T} = f \sqrt{\frac{B(N_s) M T}{2 N_s} \left(1 + \frac{N_b M}{N_s}\right)} \quad (11)$$

where  $B(N_s)$  is the one-sided loop noise bandwidth,  $M$  is the number of symbols in a PPM word, and  $N_b$  is the mean number of photon arrivals per noise slot. For the transfer function  $H(s)$  given in Eq. (7) and the gain given by Eq. (10), the noise bandwidth is given (Ref. 8) by

$$B(N_s) = B_1 + B_2 N_s \quad (12)$$

where  $B_1 = 1/(4 T_2)$  and  $B_2 = (50/M) T_2/(4 T_1)$ , so that the expected rms timing error is given by

$$\frac{T_{\text{rms}}}{T} = f \sqrt{\frac{M T}{2} \left( \frac{B_1}{N_s} + B_2 \right) \left( 1 + \frac{N_b M}{N_s} \right)} \quad (13)$$

Measured values of  $T_{\text{rms}}$  versus signal level are shown for three different loop filters in Fig. 6, for four pulse width fractions in Fig. 7, and for three values of  $N_b$  in Fig. 8. Symbol tracking down to better than 1/50 of a symbol slot (i.e.,  $< 2$  ns) was achieved using an appropriately narrow loop ( $B_1 = 16/\text{sec}$ ,  $B_2 = 6/\text{sec}$ ). The results show the expected dependence on loop bandwidth, pulse width, and background intensity, but the actual values of  $T_{\text{rms}}/T$  were two to four times greater than predicted by Eq. (10). Likely sources of error are inaccuracies in estimating the phase detector gain  $K_\phi$  and the loop filter response to pulsed input.

Acquisition performance of the demonstration system was determined experimentally, although there are no theoretical results to compare them with. Since the loop idled at the

upper frequency limit, unaided acquisition required that the loop pull-in from the VCO limit of 1 kHz above the slot frequency of 10 MHz. This occurred for loop filter 1 (as listed in Fig. 6) almost instantaneously (fractions of a second), but not for the other filters which produced narrower loops. However, by pulling the VCO down to -1 kHz and letting it drift upward towards the center frequency (simulating swept acquisition), all the filters used produced reliable acquisition.

## V. Conclusions

The intent in constructing the receiver described in this article and the rest of the 2.5 bit/detected photon system was to demonstrate that the concepts of multiple bit per photon direct detection communications were valid, and to show that a practical system could be built. This goal was successfully accomplished.

The 300 kbps rate of the system was chosen to outperform existing deep space links which use microwaves; a factor of 10 improvement in rate could be made by employing faster electronics, but at a cost of higher average laser power (since the number of bits/photon is constant). Alternatively, faster electronics in the receiver only would allow the symbol detector to run at 10 times the slot rate. This would allow the PPM demodulator to make soft decisions (based on the number of sub-symbols in which photons were counted) to determine which PPM word was sent, resulting in substantial improvement of the system's performance in higher background light situations.

## References

1. J. R. Pierce, Optical channels: practical limits with photon counting, *IEEE Trans. Commun. COM-26*, pp. 1819-1821, Dec. 1978.
2. J. R. Lesh, Optical communications research to demonstrate 2.5 bits/detected photon, *IEEE Communications Magazine* 20, No. 6, pp. 35-37, Nov. 1982.
3. J. Katz, 2.5 bit/detected photon demonstration program: Phase II and III experimental results, *TDA Progress Report 42-70*, pp. 95-104, Jet Propulsion Laboratory, California (1982).
4. W. K. Marshall, A PPM modulator and demodulator for the 2.5 bit/detected photon demonstration, *TDA Progress Report 42-68*, pp. 50-54, Jet Propulsion Laboratory, California (1982).
5. R. W. Engstrom, *RCA Photomultiplier Handbook PMT-62*, Ch. 4, RCA Solid State Division, Lancaster, PA, 1980.
6. H. H. Tan, A statistical model of the photomultiplier gain process with applications to optical pulse detection, *TDA Progress Report 42-68*, pp. 55-67, Jet Propulsion Laboratory, Pasadena, CA, 1982.
7. V. A. Vilnrotter, et al., A synchronization technique for optical PPM signals, submitted to *IEEE Transactions on Communications*.
8. W. C. Lindsey, *Synchronization Systems in Communications and Control*, Ch. 4, Prentice-Hall, Englewood Cliffs, NJ, 1972.



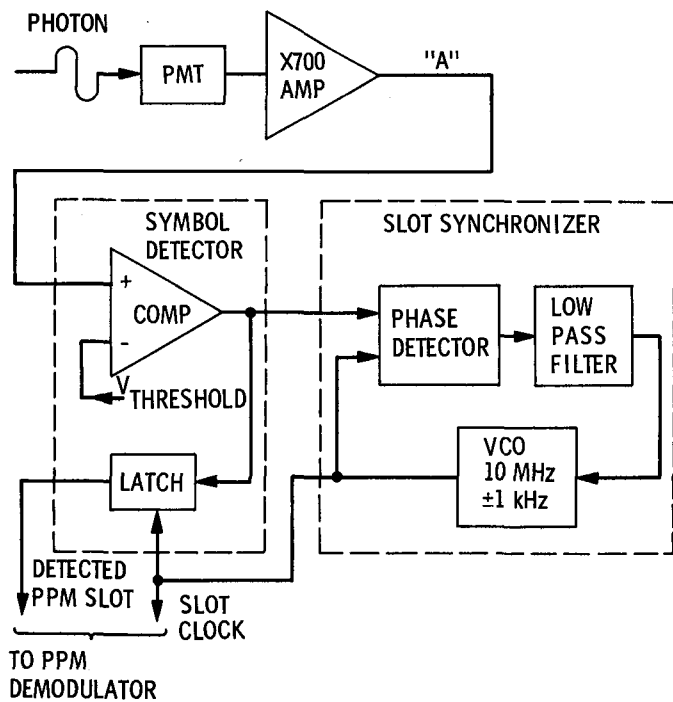


Fig. 1. Direct-detection receiver

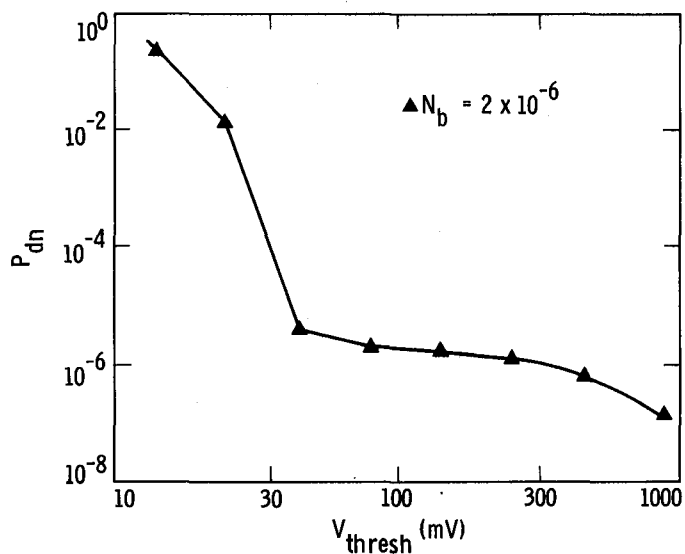


Fig. 3. Relative frequency of detected symbol "1" during noise slots ( $1 - P_{dn}$ ) vs threshold voltage,  $V_{\text{thresh}}$  (mV)

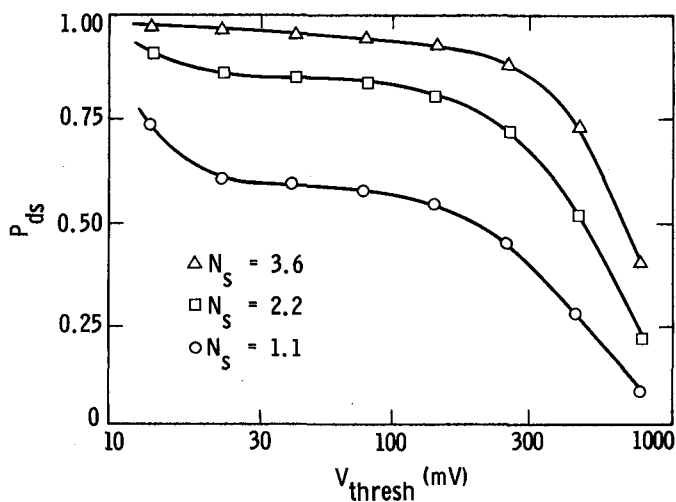


Fig. 2. Relative frequency of detected symbol "1" during signal slots,  $P_{ds}$ , vs threshold voltage,  $V_{\text{thresh}}$  (mV)

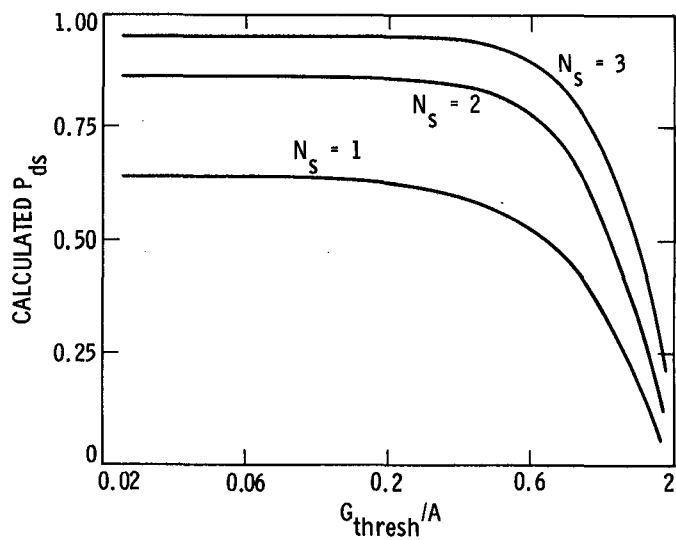


Fig. 4. Calculated  $P_{ds}$  vs normalized gain threshold,  $(G_{\text{thresh}}/A)$

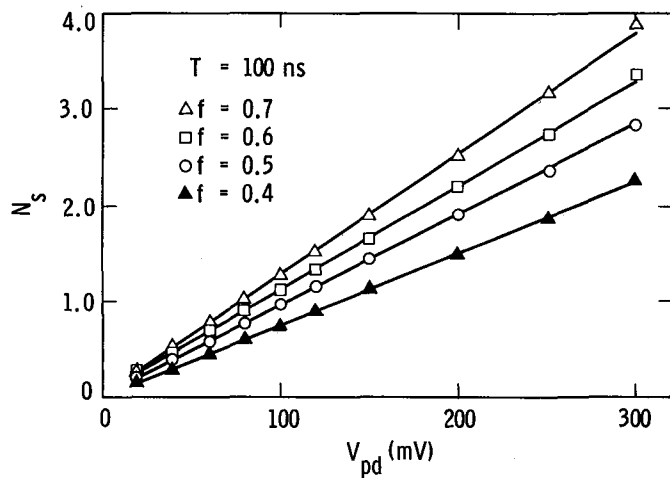


Fig. 5. Detected photons per signal slot,  $N_s$ , vs monitor photodiode voltage,  $V_{pd}$  (mV)

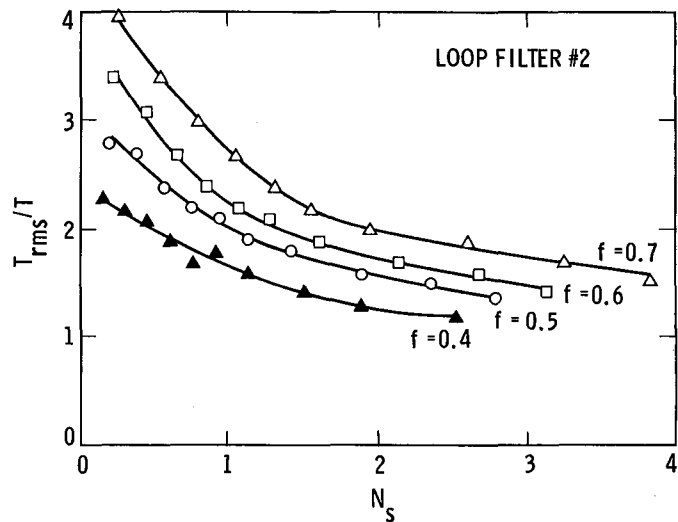


Fig. 7.  $T_{rms}/T$  vs  $N_s$  for different laser pulse width fractions,  $f$

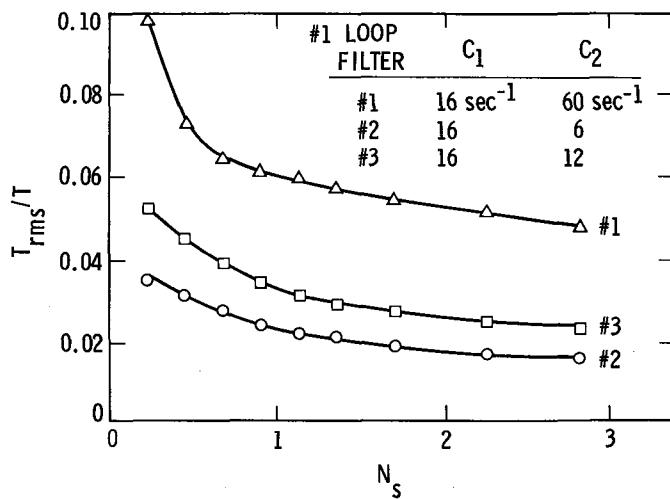


Fig. 6.  $T_{rms}/T$  vs  $N_s$  for  $f = 0.6$  and various loop filters

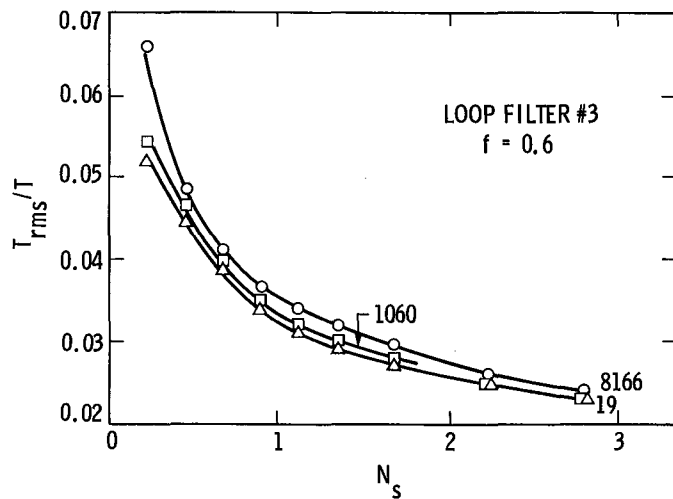


Fig. 8.  $T_{rms}/T$  vs  $N_s$  for different background levels,  $N_b$

# Highly Efficient Nd:YAG Lasers for Free-Space Optical Communications

D. L. Sipes, Jr.

Communications Systems Research Section

*The concept of a highly efficient Nd:YAG laser end-pumped by semiconductor lasers as a possible free-space optical communications source is discussed. Because this concept affords high pumping densities (thus high photon-to-photon conversion efficiencies), a long absorption length, and excellent mode-matching characteristics, it is estimated that electrical-to-optical efficiencies greater than 5% could be achieved. Several engineering aspects such as resonator size and configuration, pump collecting optics, and thermal effects are also discussed. Finally, possible methods for combining laser-diode pumps to achieve higher output powers are illustrated.*

## I. Introduction

The DSN is currently interested in optical communications as a means of increasing telemetry capabilities while reducing costs. Optical communication over interplanetary distances (10 AU or more) with transmitting apertures of practical diameters (i.e., on the order of 20 cm) requires approximately 1 W of optical power to achieve data rates on the order of several megabits per second (Ref. 1). One of the major obstacles to realizing such a system is the lack of an efficient single-mode source operating in the visible region of the electromagnetic spectrum with the required output power. Two candidates have been proposed for use as an optical source, the semiconductor laser and the Nd:YAG laser. While being relatively efficient, the semiconductor (e.g., GaAlAs) laser is primarily a low-power device, producing only about 20-mW, single-mode operation. Although arrays of individual laser diodes have

produced output powers above 2 W (Ref. 2), a long-lived, high-power, communications-quality (i.e., single-lobed radiation pattern) device has yet to be realized. Nd:YAG (pumped by lamps), which emits light at the wavelength of  $1.064\ \mu\text{m}$ , has been operated continuous wave at power levels of well into the hundreds of watts regime, and up to several tens of watts of its second harmonic radiation (at  $0.532\ \mu\text{m}$ ) have been produced. However, low efficiency — typically 0.1% in present day systems — is the main disadvantage of Nd:YAG lasers.

Much effort has been put into the development of a source that is a hybrid of these two lasers, namely the GaAlAs semiconductor laser-pumped Nd:YAG laser. In this arrangement, many GaAlAs laser diodes or diode arrays can be combined to optically pump the Nd:YAG laser medium. Moreover, the multimode operation of GaAlAs laser arrays is not a problem

because they act only as a pump source, rather than a communications source, and hence their coherence, modal structure, and spectral purity are of lesser importance.

Figure 1 illustrates this laser with conventional side-pumping geometry. In this configuration, the diodes are placed along the length of the Nd:YAG rod and pump perpendicularly to the direction of propagation of the laser resonator mode. As more power is required, more diodes can be added along and around the laser rod. This hybrid laser, however, is only about 0.5% efficient, which is still too low for a deep-space optical transmitter (about 5% to 10% is necessary). The side-pumped geometries' large inefficiencies result from the small absorption length (only about 3 mm), relatively large pumped volume (so the pumping density is low), and the small cross section of the resonator mode (there are pumped regions of the rod where energy is wasted because of mode mismatch).

In this article, a highly efficient laser-diode-pumped Nd:YAG laser employing an end-pumped geometry is proposed. In this configuration, shown in Fig. 2, diode pump sources are placed at the ends of the Nd:YAG rod and, through the use of suitable optics, the pump light is collected and focused to a small spot (typically 50 to 100  $\mu\text{m}$ ) that matches the resonator mode. It is immediately apparent that this geometry rectifies virtually all the inefficiencies that plague the side-pumped scheme. First, the absorption length can be made as long as necessary to absorb practically all of the pump light. Second, the pump light can be focused to provide the intensities needed for efficient lasing. Finally, the beams can be adjusted to overlap for optimum mode matching.

This end-pumping concept has been demonstrated in the mid-1970s on miniature Nd-doped lasers end pumped by light emitting diodes and laser diodes for use as transmitters in optical fiber communications (Refs. 3 through 6). This work, however, was primarily concerned with achieving a low lasing threshold and not with efficient operation above threshold, as is the focus of this article.

In Section II, the various inefficiencies associated with laser operation needed to calculate the overall efficiency of this proposed device are identified and quantified. In Section III, some engineering aspects of this laser, such as the resonator, focusing elements, and temperature effects, are addressed, and, in Section IV, some possible pumping configurations are illustrated.

## II. Efficiency

To accurately estimate the overall efficiency of such a device, all factors that give rise to energy loss must be iden-

tified. First, there is the quantum efficiency,  $\eta_q$ , which is the ratio of the lasing photon energy to the pumping photon energy. The quantum efficiency represents the maximum theoretical limit for laser efficiency. Next,  $\eta_0$ , the operating efficiency, includes the resonator losses and conversion efficiency of pump photons into lasing photons. The mode-matching efficiency,  $\eta_m$ , is the fraction of the pumped cross-section area that lies within the oscillating mode volume. The fraction of light incident at the laser rod end that is absorbed in the gain medium (assuming all of the laser diode light falls within the pump absorption bands) is designated  $\eta_{abs}$ , while  $\eta_i$  and  $\eta_c$  describe the interface and pump light coupling efficiencies respectively. Finally  $\eta_{LD}$  is the electrical-to-optical laser-diode efficiency. In the following sections, these factors will be discussed in greater detail.

### A. Operation Efficiency ( $\eta_p$ )

The efficiency with which pump photons are converted to lasing photons can be calculated as a function of input pump power, cavity loss, and beam radius. We start with the steady-state rate equations describing the spatial evolution of the inversion and photon energy densities:

$$\frac{dS^+}{dz} = [\beta N - \alpha] S^+ \quad (1a)$$

$$\frac{dS^-}{dz} = [\beta N - \alpha] S^- \quad (1b)$$

$$0 = R_p - \frac{N}{\tau_s} - \nu \beta N [S^+ + S^-] \quad (2)$$

where  $S^+$  and  $S^-$  are the forward and backward propagating photon energy densities respectively ( $\text{J}/\text{cm}^3$ ),  $N$  is the inversion energy density ( $\text{J}/\text{cm}^3$ ),  $\alpha$  is the loss coefficient per unit length of material ( $\text{cm}^{-1}$ ),  $\beta$  is the stimulated emission coefficient ( $\beta = \sigma/h\nu_l$  where  $\sigma$  is the stimulated emission cross section ( $\text{cm}^2$ )),  $\tau_s$  is the spontaneous emission lifetime (s),  $\nu$  is the group velocity of the wave in the medium, and  $R_p$  is the pumping power density ( $\text{W}/\text{cm}^3$ ). Any radial dependence is included in the mode matching efficiency  $\eta_m$  and so is neglected here.

These equations can be solved numerically (Ref. 7) to find the output power efficiency as a function of the mirror reflectivity for various input power intensities. Figure 3 illustrates that for an input intensity of 10  $\text{kW}/\text{cm}^2$ , the photon-to-photon conversion efficiency exceeds 90% (where a single pass loss of 1% and  $\sigma$  given by Ref. 8 were assumed). Figure 3 shows efficiency as a function of output mirror reflectivity for various input power intensities, and Fig. 4 relates efficiency to input power for various modal radii.

Another factor considered is that due to the absorption of pump light along the rod (i.e., as  $R_p$  is a function of  $z$ ), with the most basic case being the exponential decay of a single-ended pump. This problem has been analyzed (Ref. 9), and for the pump intensities and emission cross sections relevant to our application, it was found to be of no consequence.

It is well known that high pumping densities result in more efficient laser operation. By focusing the light of the diode pump, high pumping densities can be created even with low levels of pump power.

## B. Mode Matching Efficiency ( $\eta_m$ )

For the efficient use of pump light for stimulated emission, the pump light must fall within the Gaussian mode of the resonator and not be wasted as spontaneous emission. Because the pump beam cross section may be elliptical and not circular, and because the gain along the laser rod is nonuniform, laser efficiency varies with pump and laser mode parameters in a complex way. In their analysis, Hall et al. (Ref. 10) showed that efficiency is maximized for the matched mode case: i.e.,  $R_0 \cong W_0$ , where  $R_0$  and  $W_0$  are the pump- and laser-mode Gaussian beam waist radii respectively. Although their analysis did not take into account high-gain operation, nonuniform gain distribution, or the divergent nature of Gaussian beams,  $R_0 \cong W_0$  is still a good design starting point. Further analysis and experimentation are being conducted to determine exact conditions for optimum performance.

## C. Absorption Efficiency ( $\eta_{abs}$ )

Figure 5 shows the absorption spectrum of a 1-cm sample of 1% Nd<sup>3+</sup> in YAG and the corresponding emission spectrum of the laser diode pump source. It can be seen from this figure that the laser diode source spectrum falls well within the main Nd:YAG pump band centered at 807 nm. As illustrated, the Nd:YAG absorption spectrum is fine structured, so experimentation is needed to determine how precisely the laser diode spectrum needs to be controlled. From Fig. 5 one can calculate the length of the YAG rod needed to absorb virtually all of the pump light. For example, a 1- to 2-cm-long crystal will absorb over 90% of the incident pump light.

## D. Interface Efficiency ( $\eta_i$ )

To achieve sufficient feedback, the gain medium in a laser must be placed between two mirrors of high reflectivity. The high reflectivity is usually obtained by coating the mirrors with a multilayer dielectric coating. Since the pump light must pass through this coating (or interface) to pump the medium, it is important that the coating be highly reflective at the lasing wavelength yet highly transmissive at the pump wave-

length. By using properly designed dielectric coatings, one can produce a mirror that reflects 99.8% of the light at 1.06  $\mu\text{m}$ , yet transmits over 95% of the pump light at 0.810  $\mu\text{m}$  (A. Zook, Z.C.R. Optical Coating Company, private communication).

## E. Coupling Efficiency ( $\eta_c$ )

For the device to operate efficiently, the pump light must be collected and focused onto the gain medium efficiently. The focusing system must be small, have a short working distance, and have a minimum number of optical components to ensure high throughput and less sensitivity to motion (displacements). Figure 6 shows how collection efficiency varies with the  $f$  number of the collecting lens for standard laser diodes. Systems with over 90% efficiency (collection and transmission) are available commercially.

## F. Total Optical Conversion Efficiency

The total optical conversion efficiency can now be calculated by simply taking the product of all the subsystem efficiencies previously mentioned:

$$\begin{aligned} \text{quantum efficiency: } \eta_q &= 76.7\% \\ \text{operation efficiency: } \eta_o &\geq 90\% \\ \text{mode matching efficiency: } \eta_m &\approx 100\% \\ \text{absorption efficiency: } \eta_{abs} &\geq 90\% \\ \text{interface efficiency: } \eta_i &\geq 95\% \\ \text{collection efficiency: } \eta_c &\geq 90\% \\ \therefore \eta_{opt} = \eta_q \eta_o \eta_m \eta_{abs} \eta_i \eta_c &\geq 50\% \end{aligned}$$

The laser is therefore expected to convert over half of the pump power into laser light at the Nd:YAG fundamental wavelength.

## G. Overall Electrical Efficiency

The total overall electrical-to-optical efficiency is just the optical efficiency  $\eta_{opt}$  times the power efficiency of the laser diode pump source,  $\eta_{LD}$ . For commercially available diode lasers,  $\eta_{LD}$  is 10% or more, so overall efficiencies of up to and greater than about 5% can be expected. This value is over 10 times better than the efficiency of previous side-pumped lasers. It is also to be noted that laser diode efficiency becomes the limiting factor for highly efficient operation. Since over 35% overall efficiency has already been achieved in laboratory devices (Ref. 11), the total efficiency is expected to go up as laser diode technology matures.

### III. Engineering Aspects

Although this proposed device seems very promising in terms of highly efficient operation, questions regarding its feasibility from an engineering standpoint need to be answered. In this section, some of the pertinent engineering aspects are discussed.

#### A. Resonator

To achieve the small spot sizes necessary for efficient operation, the dimensions of a simple (i.e., 2-mirror) and stable resonator must be small. For example, the confocal resonator, the most stable, requires mirrors with radii of curvature of 5 cm and a separation of 5 cm to achieve beam waist radii of approximately 50  $\mu\text{m}$ . This is advantageous in that it reduces the overall size of the optical transceiver package – a prime consideration in space optical communications systems development.

#### B. Focusing Subsystem

The focusing subsystem needs to have an  $f$  number smaller than 1 to efficiently collect and deliver the pump light (see Fig. 6). Since only on-axis performance is required, commercially available aspheric lenses with  $f$  numbers as low as 0.6 can be used for this purpose. A working distance (i.e., the distance from the optics to the focal plane) of 1 to 2 cm is required. For a given working distance, there is a minimum diameter that the incident beam possess in order to be focused to the desired size. For Gaussian beams, the minimum focused spot size is given by:

$$2W_0 = \frac{1.27 \lambda f}{d} \quad (3)$$

where  $W_0$  is the radius of the focused spot,  $d$  is the diameter of the incident beam,  $f$  is the focal length of the lens, and  $\lambda$  is the wavelength. Hence, for  $W_0 = 50 \mu\text{m}$  and  $f = 2 \text{ cm}$ ,  $d$  equals 0.02 cm. What this shows is that extremely small optics can be used to collect and deliver the pump light, thus keeping the overall size and weight of the laser small.

It is not altogether clear whether or not the pump beam needs to be anamorphically transformed from its elliptical shape at the laser diode source to the circular beam of the resonator mode. The analysis of Hall (Ref. 12) seems to indicate that pump profile shape does not matter much as long as all of the pump light falls within the resonator mode area. There is a problem with applying this analysis because it does not take into account the divergent nature of Gaussian beams. Further experiments and analysis are being conducted to determine the required pump beam manipulation. Even so, to accomplish this requires only the addition of a cylindrical lens.

#### C. Temperature Effects

As noted earlier, efficient laser operation of Nd:YAG requires pump intensities on the order of 10 kW/cm<sup>2</sup>. With such high optical intensities, thermo-optical effects must be taken into account. Thermo-optical distortions of a laser beam arise because of temperature-induced changes in the index of refraction. The major effects include thermal lensing, spherical and higher-order aberrations, and thermal depolarization. The main process by which the material heats up is through the nonradiative electronic transitions that take place from the pump band to the upper laser level and from the lower laser level to the ground state. These transitions are illustrated in Fig. 7.

Since the pump beam is Gaussian, the material will be heated in a nonuniform manner. If we assume that the heat flows mainly in the radial direction (i.e., neglecting laser-rod edge effects), the heat conduction equation can be replaced by the one-dimensional heat equation in radial coordinates

$$\frac{d^2 T}{dr^2} + \frac{1}{r} \frac{dT}{dr} + \frac{q_0}{k} \exp \frac{-r^2}{R_0^2} = 0 \quad (4)$$

where the source term contains the Gaussian heat profile. In Eq. (4),  $q_0$  is the thermal power density on axis ( $q_0 = P_a / \pi R_0^2 l$ ),  $R_0$  is the pump beam waist,  $l$  is the length of the material,  $k$  is the coefficient of thermal conductivity, and  $P_a$  is the fraction of pump power that goes into heating the material ( $P_a = P_{abs} (1 - \eta_q)$ ). The complete analysis of this problem is quite involved and will be published later. This heat transfer equation has been solved for local beam heating in nonlinear crystals (Refs. 13 and 14), and we can use these results to estimate the magnitude of the relevant thermal effects.

We now consider the thermal loading effects on the operation of a 1-W Nd:YAG laser utilizing the end pumping concept. From the efficiency estimates in Section II, we see that approximately 2 W of optical pump power are required to produce 1 W of Nd:YAG radiation. From this we calculate the power absorbed to be  $P_{abs} = P_{out} / \eta_0 \eta_m \eta_q \cong 1.4 \text{ W}$ . Of this, the fraction  $P_a = P_{abs} (1 - \eta_q) \cong 0.3 \text{ W}$  goes into heating the rod. If we assume this power is absorbed uniformly along a 1-cm rod (in reality the absorption is nonuniform: for estimation purposes, the uniform approximation will suffice), then the thermal load is well below the 115-W/cm fracture limit for Nd:YAG. In addition, the power focused onto the end of the laser rod ( $P_{abs} = 1.4 \text{ W}$ ) to achieve the necessary 10 kW/cm<sup>2</sup> pumping intensity for efficient operation is more than a factor of 3 below the optical damage threshold of Nd:YAG and even further below the coating damage threshold at the rod facet.

The first thermo-optical effect we consider is thermal lensing. This occurs when radial temperature gradients produce stress-induced distortion in the laser material such that the cylindrical laser rod takes on the form of a thick lens. Preliminary calculations indicate that the focal length of any lensing that occurs will be longer than the length of the laser resonators under consideration. This result is important because it shows that stable laser resonators with small mode dimensions can be configured with the appropriate choice of mirrors.

Another thermo-optical distortion that can be quite debilitating, especially in situations where a polarized laser output is required, is stress-induced birefringence. This has the effect of introducing a birefringence into the crystal that tends to depolarize the beam. If we assume uniform pumping over a volume bounded by the pump beam waist  $R_0$ , and if we assume that the resonator mode waist radius  $W_0$  equals  $R_0$ , then we can estimate the loss due to stress-induced birefringence by the fraction of the light rejected when an analyzer is placed in the path of the depolarized beam. This loss is given by (Ref. 15).

$$L_{\text{depol}} = 1/4 \left( 1 + \frac{16}{C^2 P_a^2} \right)^{-1} \quad (5)$$

where  $C$  is a material constant ( $C = 8.1 \times 10^{-2} \text{ W}^{-1}$  for Nd:YAG). If we use the value of  $P_a = 0.3 \text{ W}$  in our example, then we calculate  $L_{\text{depol}} \cong 10^{-5}$ , which is an insignificant amount. Further analysis is being conducted to compute these values more accurately.

#### IV. Pumping Configurations

In all the analyses presented thus far, we have neglected the problem of concentrating the diode pump power to produce sufficient laser output power. The area into which the laser diodes themselves must be packed to ensure proper mode matching over the length of the rod is governed by conservation of brightness:  $A_1 \Omega_1 = A_2 \Omega_2$ , where  $A_1$  and  $A_2$  are the object and image source areas respectively, and  $\Omega_1$  and  $\Omega_2$  are the divergent and convergent solid angles respectively. Since the diode pump source is anamorphic, the packing requirements for directions perpendicular to the junction are different than those for directions parallel to the junction. As was mentioned in Section II, the relationship between pump beam and laser-mode size is quite complicated, but estimates based on conservation of brightness seem to indicate that pump diodes must be placed within  $100 \mu\text{m}$  for efficient operation. Further analysis is needed to resolve this point. An alternative

to simple stacking, which has been used in pumping very short Nd<sup>3+</sup> lasers, is fiber-optical pump coupling. In this scheme, the pump light is transmitted from the diodes to the gain medium through multimode fibers as shown in Fig. 8. Such fiber couplers have been built with only 1.5-dB insertion loss (Ref. 16).

Since the single pass gain of the laser is the integral of the gain per unit length, several laser rods can be cascaded together so that the packing requirement goes down by a factor of  $1/N$  compared to a simple double-ended pump ( $N$  is the number of rods, assuming each rod can be pumped from both ends, cascaded together). This novel concept is illustrated in Fig. 9. A traveling wave laser consisting of four laser rods pumped by eight sources of 200 mW each produces 1.6 W of pump power, and, from Section II, 800 mW of output power at  $1.06 \mu\text{m}$ . Unidirectional power flow in this ring cavity can be insured in several ways, for example by an InGaAlAsP laser operating at  $1.06 \mu\text{m}$  acting as an injection locking device. The scale in Fig. 9 is drawn to show that it is possible to achieve high output powers in very small packages.

Although none of the devices described in this section have been built yet, they illustrate that efficient lasers producing approximately 1 W could be built today using off-the-shelf technology with the end-pumping concept. Furthermore, extensive industry efforts are now being invested in developing high-power laser diode arrays for pumping second harmonic Nd:YAG lasers, so that an order of magnitude increase in the available pump power from a single array can probably be expected in the near future.

#### V. Conclusions

In this article, a highly efficient Nd:YAG laser end-pumped by GaAlAs lasers has been proposed. The overall efficiency of such a device was estimated by evaluating the efficiency of each component, and the optical-to-optical efficiency  $\eta_{opt}$  was found to exceed 50%. Next, engineering aspects such as resonator design and coupling optics were discussed and the degradation of the device operation due to thermo-optical effects was calculated and found to be minimal. Finally, several ways for combining and arraying pump sources to increase power output were presented. It was concluded that output power levels close to the goal of 1 W could be achieved with existing technology, with the prospect of increased power virtually assured. An experimental program is now underway to demonstrate key concepts with the goal of developing such a high-efficiency device.

## References

1. Vilnrotter, V. A., and Gagliardi, R. M., *Optical-Communication Systems for Deep-Space Applications*, JPL Publication 80-7. Jet Propulsion Laboratory, Pasadena, Calif., March 15, 1980.
2. Scifres, D. R., Lindstrom, C., Burnham, R. D., Strifer, W., and Paoli, T. L., "Phase-Locked (GaAl) As Laser Diode Emitting 2.6 W cw From a Single Mirror," *Electron Letters*, Vol. 19, No. 5, March 1983, p. 169-171.
3. Rosenkrantz, L. J., "GaAs Diode Pumped Nd:YAG Laser," *J. Appl. Phys.*, Vol. 43, No. 11, November 1972, p. 4603-4605.
4. Chesler, R. B., and Draegert, D. A., "Miniature Diode Pumped Nd:YAG Lasers," *Appl. Phys. Lett.*, Vol. 23, No. 5, 1 Sept 1973, p. 235-236.
5. Saruwatari, M., Kimura, T., and Otsuka, K., "Miniaturized cw LiNdP<sub>4</sub>O<sub>12</sub> Laser Pumped with a Semiconductor Laser," *Appl. Phys. Lett.*, Vol. 29, No. 5, September 1, 1976, p. 291-293.
6. Washio, K., Iwanto K., Inove, K., Hino, I., Natsumoto, S., and Saito, F., "Room Temperature cw Operation of an Efficient Miniatured Nd:YAG Laser End Pumped by a Super Luminescent Diode," *Appl. Phys. Lett.*, Vol. 29, No. 11, December 1976, p. 720-723.
7. Katz, J. "Power Efficiency of Semiconductor Injection Lasers," *TDA Progress Report 42-66*, Jet Propulsion Laboratory, Pasadena, Calif., pp. 94-100, September-October 1981.
8. Birnbaum, M., Tucker, A., and Fincher, C., "Laser Emission Cross Section of Nd:YAG at 1064  $\mu\text{m}$ ," *J. Appl. Phys.*, Vol. 52, No. 3, March 1981, p. 1212-1214.
9. Sipes, D., Katz, J., "Laser Efficiency Under Conditions of Nonuniform Gain Distribution," to be published.
10. Hall, D. G., Smith, R. J., and Rice, R. R., "Pump Size Effects in Nd:YAG Lasers," *Appl. Opt.*, Vol. 19, No 18, 1980, p. 3041-3043.
11. Chinone, N., Scoto K., Ito, R., Aiki, K., and Shige, N., "Highly Efficient (GaAl) As Buried Heterostructure Lasers With a Buried Optical Guide," *Appl. Phys. Lett.*, Vol. 35, No. 7, October 1979, p. 515-516.
12. Hall, D. G., "Optimum Mode Size Criterion for Low Gain Lasers," *Appl. Optics*, Vol. 20, No. 9, 1 May 1981, p. 1579-1583.
13. Stein, A., "Thermo-Optically Perturbed Resonators," *IEEE J. Quant. Electron.*, Vol. QE-10, pp. 427-434, April 1974.
14. Barry, J. D., and Kennedy, C. J., "Thermo-Optical Effects of Intracavity Ba<sub>2</sub>Na(NbO<sub>3</sub>)<sub>5</sub> on a Frequency Doubled Nd:YAG Laser," *IEEE Quant. Electron.*, Vol. QE-11, No. 8, 1975, pp. 575-579.
15. Kochener, W., *Solid State Laser Engineering*, Springer-Verlag, New York, 1976, p. 360.
16. Kubodera, K., and Noda, J., "Pure Single Mode LiNdP<sub>4</sub>O<sub>12</sub> Solid State Laser Transmitter for 1.3  $\mu\text{m}$  Fiber Optic Communications," *Appl. Opt.*, Vol. 21, No. 19, p. 3466-3468.



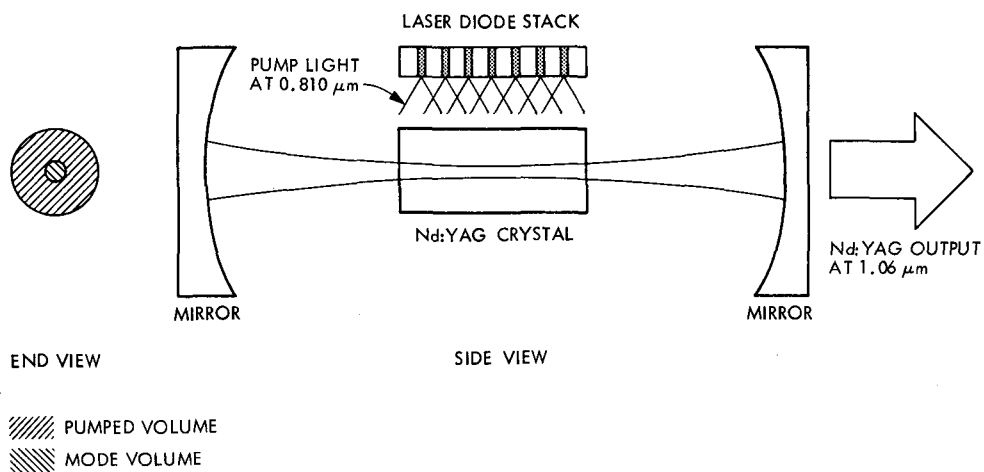


**Fig. 1. Semiconductor-laser-diode-pumped Nd:YAG with side pumping geometry; end view illustrates mode mismatch.**

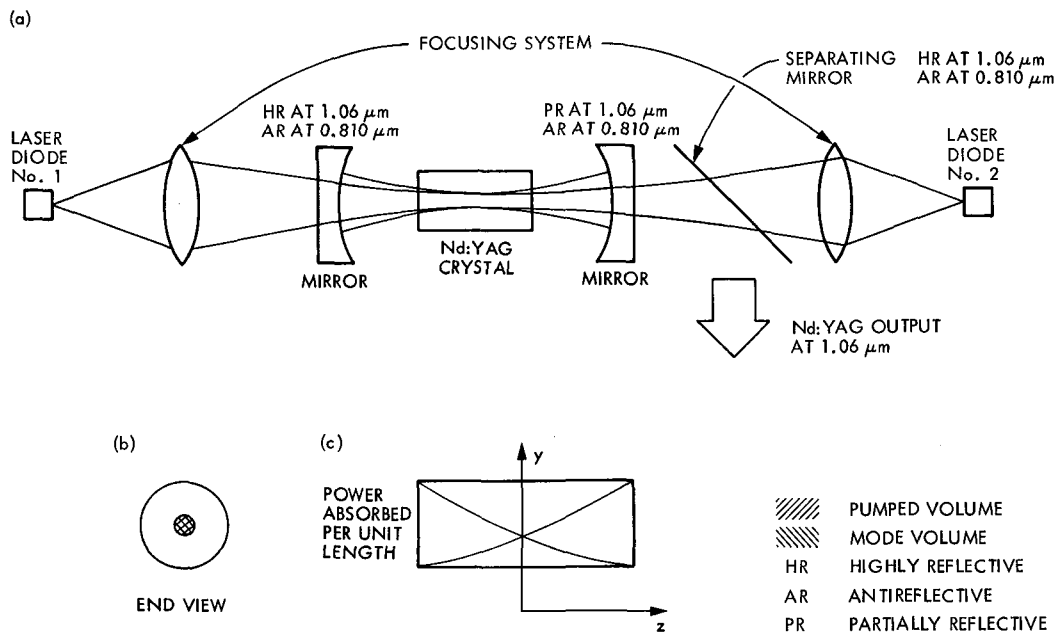


**Fig. 2. Semiconductor-laser-pumped Nd:YAG: (a) end-pumping geometry; (b) end view of mode matching properties; (c) side view of nonuniform pumping along length of rod.**

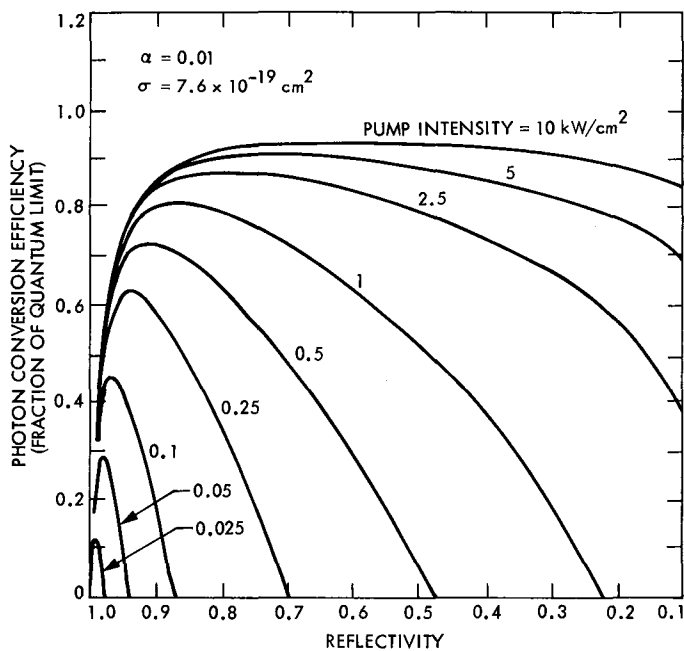


Fig. 3. Calculated values of semiconductor-laser-pumped Nd:YAG efficiency as a function of mirror reflectivity for several values of input pump intensity (for the case of perfect mode matching).

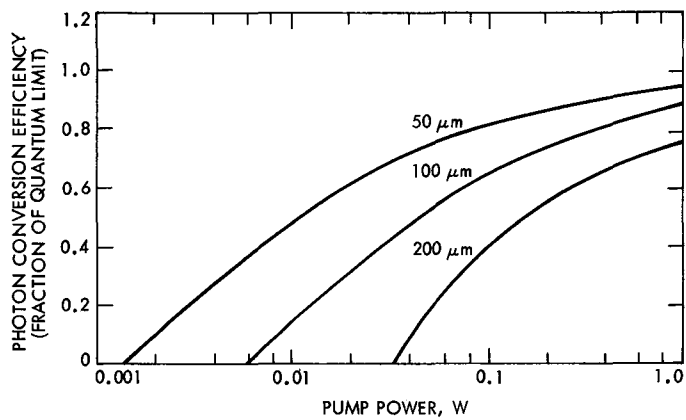


Fig. 4. Semiconductor-laser-pumped Nd:YAG: end-pumped configuration. Calculated efficiency as a function of input pump power for several values of minimum pump beam radii.

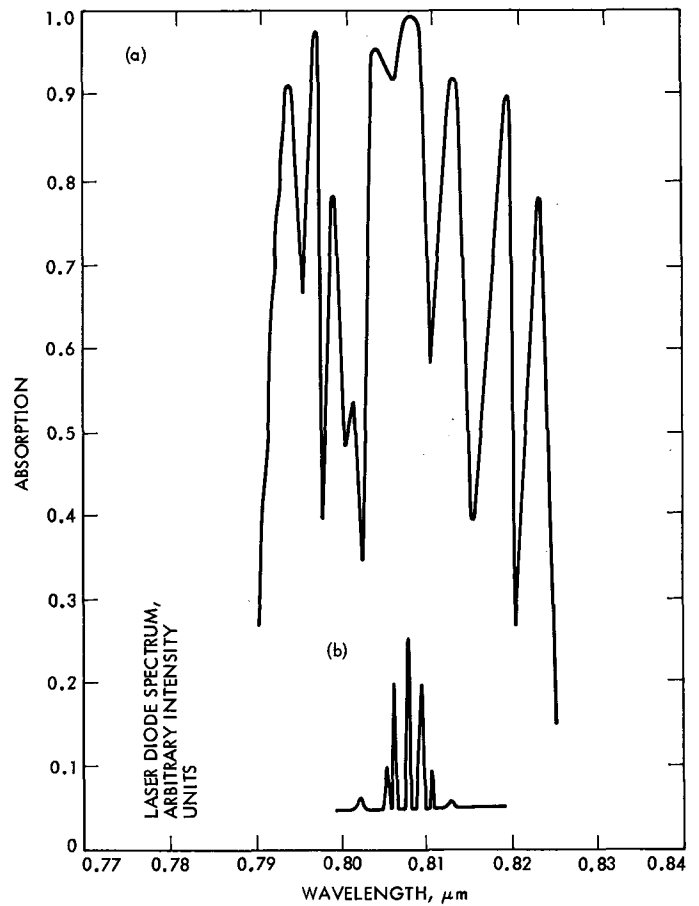
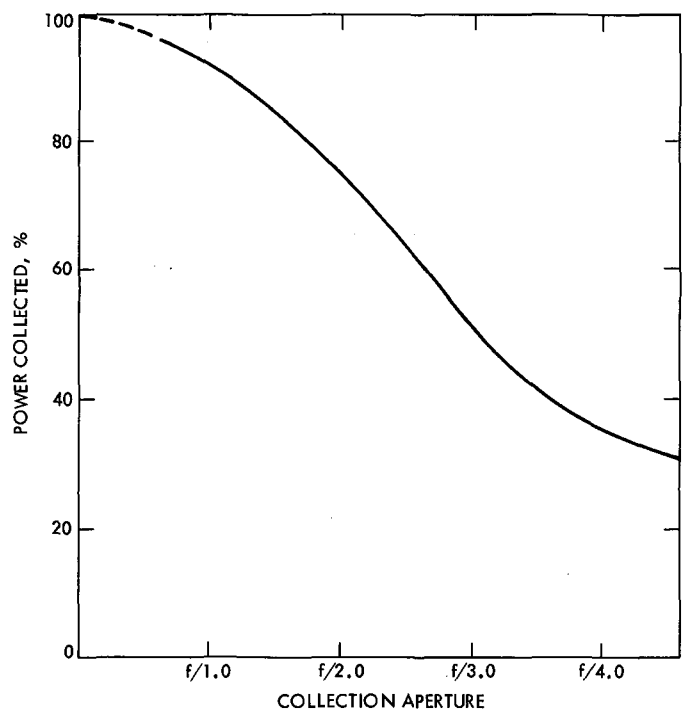
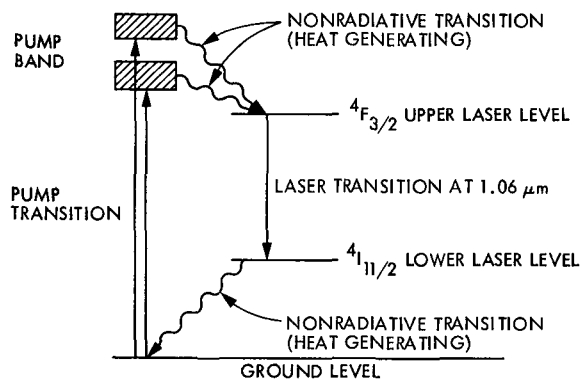


Fig. 5. Spectral properties of diode-pumped Nd:YAG: (a) 0.81- $\mu\text{m}$  absorption band in a 1-cm sample of 1% Nd:YAG; (b) emission spectrum of semiconductor laser pump array.



**Fig. 6. Power collection efficiency for standard semiconductor lasers**



**Fig. 7. Energy diagram of four-level laser operation and heat generation process in Nd:YAG**

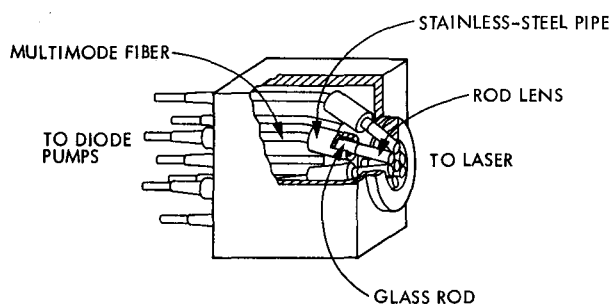


**Fig. 8. Optical pump fiber coupler (after Ref. 16)**

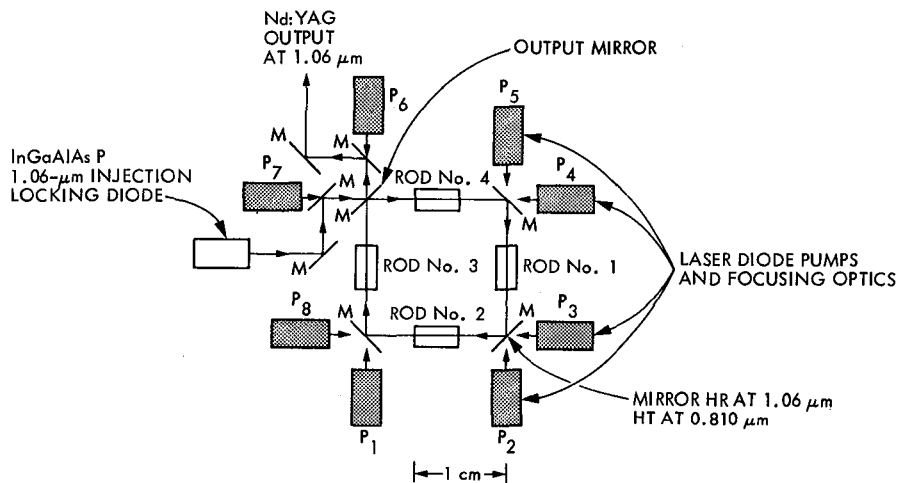


**Fig. 9. Schematic of unidirectional Nd:YAG ring laser comprised of four Nd:YAG rods pumped by eight sources**

# Condensed Antenna Structural Models for Dynamics Analysis

R. Levy

Ground Antenna and Facilities Engineering Section

*Condensed degree-of-freedom (effective-mass) models are compared with large degree-of-freedom finite-element models of a representative antenna-tipping and alidade structure, for both "locked" and "free-rotor" configurations. It is shown that: a) the effective-mass models accurately reproduce the lower-mode natural frequencies of the finite element model; b) frequency responses for the two types of models are in agreement up to at least 16 rad/s for specific points; and c) transient responses computed for the same points are in good agreement. It is concluded that the effective-mass model, which best represents the five lower modes of the finite-element model, is a sufficient representation of the structure for future incorporation with a total servo control-structure dynamic simulation.*

## I. Introduction

The finite-element computer models of a typical large antenna-tipping structure and alidade comprise many more degrees of freedom, than can, or need be represented in a practical simulation of a combined structure and control-system dynamic response. Consequently, a drastic reduction of the structural finite-element model, to only a few equivalent degrees of freedom, is a necessary and a common practice. There are many known ways to achieve this reduction. Although differing in details of implementation, each of these ways are essentially equivalent in accurately representing only the low-frequency vibration modes and ignoring higher fre-

quencies that are presumed to be outside of the operational control-system bandwidth.

The method of reduction used here is to represent each low-frequency vibration mode by an equivalent spring-mass single degree-of-freedom oscillator that is independent of the other modal oscillators. The formulation, which is given in Ref. 1, ensures that the reactions that result from independent rigid body acceleration of the structure foundation are the same for both the many degrees-of-freedom model and for the corresponding equivalent oscillators. This formulation is accomplished by matching the terms of the rigid-elastic modal coupling matrices of both the full structural model and the

equivalent oscillator model that represents the same modes. It can be shown that this condition also makes the kinetic energy of each oscillator equal to that of the corresponding structural mode for steady-state foundation motion. The inertia of higher-frequency modes, not represented by spring-mass oscillators, is contained in a residual mass placed at the foundation. Consequently, the mass of the full structure is accounted for; the approximation of this representation is only due to omitting the elasticity of the higher-frequency modes not represented by additional individual oscillators. It follows that the accuracy increases with larger numbers of effective oscillators. In the limit, a large set of oscillators provides a mathematically exact duplication of the dynamics of the original finite-element model.

This reduction method is chosen because of its accuracy, the simple representation it provides for the structure within a complete structure-servo control dynamics simulation program, and the ease of developing the effective oscillator properties. The equivalent oscillators are determined from special output provided by the JPL-IDEAS program eigenvalue analysis (Ref. 2). The output consists of a summary of the computations according to the algorithms of Ref. 1 for which principal relationships are restated and included here for reference in Appendix A. A restriction, that the equivalent representation applies only to systems that have statically determinate foundation reactions, is satisfied by the antenna structure.

## II. Structure Models

The azimuth-axis drive control of an example 34-m diameter at the zenith position (elevation =  $90^\circ$ ) will be considered. The elevation-axis drive model is similar with respect to representation of the tipping structure, but a separate treatment is necessary for the alidade representation. Figure 1 shows a representative tipping structure and alidade. The global Z-axis is the vertical axis. At zenith elevation, the reflector local Z (pointing) axis coincides with the global axis and at horizon elevation the local reflector Y-axis coincides with the global Z-axis.

The effective mass oscillators are derived from a JPL-IDEAS eigenvalue analysis of the finite-element model. The structure is foundation-grounded at the alidade base. Since we are concerned with the azimuth-axis drive, the only ground motion of interest is the alidade rotation about the Z-axis and the corresponding inertia term is the mass moment of inertia about this axis. Consequently, the effective "mass" model becomes an effective "mass moment of inertia" model with a torsional, rather than linear, spring constant. In the following discussions, references to "mass" and "inertia" will be used interchangeably to imply the "mass moment of inertia."

Figure 2(a) shows five effective mass oscillators that are established after screening the lowest 16 natural vibration modes found from the eigenvalue analysis. The screening eliminated modes with insignificant azimuth rotation and reduced the number of oscillators to the five that represent the first through the fourth and the thirteenth modes of the constrained model. These oscillators are combined with the residual inertia of the remaining unrepresented natural modes and with the azimuth gearbox springs. Motion of the alidade base (point B) is allowed, and Fig. 2(a) represents a "locked rotor" model grounded at the azimuth motor rotors. Figure 2(b) is the "free rotor" model with unconstrained azimuth rotors and with the reflected rotor inertia included at the two motor points (M1 and M2). Each motor point is associated with the azimuth drive consisting of the two motors and two gearboxes at each of the two corners of the alidade base. The control-system model transfer function for the effective-mass oscillators is described in Appendix B.

The conventional normal coordinates of the associated natural modes are related to the five effective oscillator coordinates by easily determined individual scale factors. These modal normal coordinates can be employed within the conventional method of modal analysis (Ref. 3) as "combining factors" that operate on the eigenvectors to synthesize the dynamic displacement response of the finite-element model by superposition. However, since the effective-mass coordinates are relative to the alidade base, the displacement of the base must be added to each displacement obtained from modal superposition.

## III. Numerical Results

Table 1 provides the inertia and stiffness properties of the condensed models of Figs. 2(a) and 2(b). The five frequency numbers tabulated are from the eigenvalue analysis of the finite-element model grounded at the alidade base (no gearbox springs) and are a subset of the first sixteen modes, as described previously. Notes in this table show how the residual inertia is determined for the azimuth base point of the model, and also show the calculations for reflected motor-rotor inertias and gearbox springs.

### A. Natural Frequencies

Table 2 shows comparisons of the natural frequencies obtained from analysis of the models of Figs. 2(a) and 2(b), and the 12 lowest modes obtained from analysis of 3700 degree-of-freedom finite-element models that also contained the azimuth gearbox springs and the free rotor reflected motor inertias. There apparently is a spurious highest-mode frequency of the equivalent models, but otherwise the agreement with the full models ranges from excellent to good. The second mode

(4.9 rad/s) free-rotor natural frequency is not significant and represents a mode shape that consists essentially of the two motor rotors moving in opposition. This mode would be excited only in the case of a conflicting input command. Note that the lowest-mode frequency of the full model for the free-rotor case is almost, but not quite, equal to the ideal value of zero. This is because at the time of this investigation the IDEAS program did not accommodate a singular stiffness matrix except by the artifice of including an almost zero stiffness spring. More recently, however, a program update has been provided to treat the singular condition. Figure 3 shows a plot of the lowest 12 finite-element model natural frequencies to facilitate comparison of the "locked" and "free" rotor configurations. Where frequencies are almost the same for either configuration, it can be assumed that the mode does not entail significant rotation about the azimuth axis.

An additional NASTRAN program natural frequency analysis was made for the "free-rotor" finite-element model for comparison with the IDEAS "soft-spring" analysis. Table 3 shows the NASTRAN natural frequencies and repeats the values from Table 2 that were obtained with IDEAS. The frequencies compare well from the first through fifth modes and also for the seventh and eighth modes. The generalized masses computed for the eigenvectors of these same modes have also been found to be similar. There is no eigenvalue agreement after the eighth mode, and NASTRAN does not show several of the lower frequencies (which have been identified as local quadripod modes, found by IDEAS). Some differences between results of the two programs are expected because of small differences in the stiffness matrix formulation for membrane plate finite elements.

## B. Steady-State Response

Forced steady-state frequency response calculations were made for the effective-mass models of Figs. 2(a) and 2(b) and also by conventional modal superposition analysis of the 12 lowest modes of complete finite-element models with gearbox springs and motor rotors. Damping was assumed to be negligible in these calculations. The natural frequencies of all of these models have been presented in Table 2.

The input to the "locked-rotor" models is a fixed amplitude, variable frequency sinusoidal torque applied at the alidade base. It can be shown that a similar dynamic response will occur when the torque excitation is replaced by prescribed equal sinusoidal displacements at the motor grounding points. Figure 4 shows the "locked-rotor" steady-state response for the alidade base  $\phi_B$ , azimuth encoder  $\phi_E$ , and alidade  $\phi_A$  at forcing frequencies of up to 16 radians per second. The alidade response shown is defined as the rotation of the line between the elevation-bearing support points at the

top of the alidade. Four sets of data are shown on each of the curves of Fig. 4: the full-model 12-mode response superposition computed by both the mode-displacement (M-D) and mode-acceleration (M-A) methods (Ref. 3); the response of the six degree-of-freedom (6 DOF) model of Fig. 2(a); and the response of a model (2 DOF) similar to that of Fig. 2(a), but with only one equivalent modal mass instead of five.

It can be seen that the full-model mode-acceleration method and the model of the responses of Fig. 2(a) are in agreement. These responses also are assumed to be the most accurate, based upon a check that can be made for zero forcing frequency. The mode-displacement and mode-acceleration methods' responses appear to converge at higher frequencies. The single effective-mass (2 DOF) model accuracy degenerates at frequencies above the 10.7 rad/s lowest-mode resonance. At forcing frequencies beyond the second mode resonance of 14.6 rad/s, this 2 DOF model is no longer valid.

The torque input to the "free-rotor" models is an equal pair applied at the two motors. The frequency response is shown in Figs. 7 through 10. Figures 7 through 9 show the responses for the same points as Figs. 4 through 6. Figure 10 shows the response curve for either one of the same motor points that were grounded for Figs. 4 through 6. The model 12-mode response is computed only by the mode-displacement method. As in Figs. 4 through 6, the response of the effective-mass model (8 DOF) is identical to the full-model response to within the scale of the figures. The response of a single effective-mass model (4 DOF) compares in accuracy to the response of the similar model (2 DOF) of Figs. 4 through 6. It is reassuring to observe that the motor response exhibits the conventional anti-resonances at the locked-rotor natural frequencies.

## C. Transient Response

Transient responses of full structure and effective mass models are shown in Figs. 11 and 12. The rigid body motion of the free rotor models has been subtracted in Fig. 12. Time histories are shown for impulse-type forcing functions that consist of step torques of 0.02 seconds duration (instead of the sinusoidal functions used in the frequency response analysis in Figs. 4 through 10).

The solid lines in Figs. 11 and 12 are the responses for the effective-mass models determined by the Advanced Continuous Simulation Language (ACSL) program. The ACSL program was used to solve the differential equations for the models of Figs. 2(a) and 2(b) directly, although it could also use transfer function inputs. The broken lines represent the response superposition for the lowest 12 modes of the full finite-element model, which were obtained by an in-house program written for this purpose. In both "locked" and "free" rotor models, damping of 0.5% was applied for the lowest

significant elastic modes (10.7 and 11.3 rad/s) and the damping for the higher modes increased (damping matrices were proportional to stiffness matrices) in proportion to the natural frequency.

The above figures typically show essentially similar wave forms, although there are occasional differences in the amplitude peaks. These differences tend to be restricted to the initial half of the time histories. At the later times of the figures the full model and effective-mass model agreement improves. The differences in the earlier portion of the time histories is attributed to the presence of more higher-mode frequency content in the full model, which becomes attenuated later on by damping. Despite some differences in the transient response curve, the transient response agreement of

the five effective modal-mass representations with the full model response is estimated to be adequate.

#### IV. Summary

The lower-mode natural frequencies have been shown to be identical in large finite-element models and condensed effective-mass models. Furthermore, the control-system band-pass cut-off frequency, usually less than about 2 rad/s, is within the range of frequencies for which the effective-mass models have shown good agreement with the full finite-element models for steady-state response. Consequently, the numerical results justify employing the effective-mass representation within the control-structure simulation model.

### Acknowledgment

The author wishes to thank John Cucchissi for developing the computations and executing the computer models, and Douglas Strain who provided the software for the computer graphics.

### References

1. Wada, B. K., Bamford, R., and Garba, J. A., "Equivalent Spring-Mass System: A Physical Interpretation," *The Shock and Vibration Bulletin*, No. 42, Part 5, pp. 215-225, January 1972.
2. Levy, R., "Optimization of Antenna Structure Design," *Eighth Conference on Electronic Computation*, ASCE, Houston, Texas, February 1983.
3. Bisplinghoff, R. L., Ashley, H., and Halfman, R. L., *Aeroelasticity*, Addison-Wesley Publishing Co., Reading, Massachusetts, Ch. 3, 1955.

**Table 1. Equivalent-mass model data**

Point	Mode* Simulated		Inertia in-lbf-s <sup>2</sup> × 10 <sup>-7</sup>	Stiffness in-lbf/rad × 10 <sup>-9</sup>
	No.	Rad/s		
1	1	13.59	3.686	6.808
2	2	15.71	0.186	0.429
3	3	15.26	1.486	3.458
4	4	15.90	0.725	1.831
5	13	35.53	3.652	46.090
	Sum		9.734 <sup>(1)</sup>	
B	Alidade base frame		3.878 <sup>(2)</sup>	
M1	One drive corner		51.200 <sup>(3)</sup>	12.800 <sup>(4)</sup>
M2	One drive corner		51.200 <sup>(3)</sup>	12.800 <sup>(4)</sup>

\*In first 16 modes of finite-element model grounded at base frame.

Notes:

1. Total structure and parasitic inertia about azimuth axis =  $1.3612 \times 10^8$  in-lbf/s<sup>2</sup>.
2. Residual inertia of B =  $1.3612 \times 10^8 - 9.734 \times 10^7 = 3.878 \times 10^7$  in-lbf/sec<sup>2</sup>.
3. Inertia of one motor armature and gearbox = 0.0907 lbf-ft-sec<sup>2</sup> at high speed =  $0.0907 \times 12 \times (15.339)^2 = 2.56 \times 10^8$  in-lbf-sec<sup>2</sup> at 1 × speed =  $5.12 \times 10^8$  in-lbf sec<sup>2</sup> for 2 motors.
4. Spring constant, one gearbox =  $0.963 \times 10^7$  at pinion  $\times (386.7'' \text{ radius}/15'' \text{ wheel})^2 = 6.4 \times 10^9$  in-lbf/rad of 1 × speed =  $12.8 \times 10^9$  in-lbf/rad for 2 boxes.

**Table 2. Full and condensed model natural frequencies, rad/s**

Natural frequencies, rad/s				
Locked Rotor		Free Rotor		
Finite-element model (IDEAS)	Equivalent 6 DOF model (RESPONMAP)	Finite-element model (IDEAS)	Equivalent 8 DOF model (RESPONMAP)	
1	10.70	10.71	0.17	0.00
2	14.64	14.65	4.89	4.99
3	15.10	15.21	11.28	11.28
4	15.74	15.74	14.67	14.67
5	19.00	22.05	15.10	15.21
6	19.10	55.12	15.75	15.74
7	21.70		21.88	22.23
8	23.05		23.05	55.15
9	25.54		25.53	
10	26.05		26.07	
11	26.37		26.31	
12	29.65		29.22	

**Table 3. NASTRAN vs. IDEAS, finite-element model, free-rotor natural frequencies**

NASTRAN model			IDEAS model		
Mode	Rad/s	General mass	Mode	Rad/s	General mass
1	0.00	2,592	1	0.11	2,589
2	4.88	11,393	2	4.89	11,380
3	11.32	103	3	11.28	103
4	14.89	272	4	14.67	119
5	15.51	129	5	15.10	113
6	20.39	23	6	15.75	22
7	21.99	124	7	21.88	114
8	23.68	715	8	23.05	651
			9	25.53	8
			10	26.07	6
			11	26.31	5
			12	29.22	84
9	33.79	69			
10	39.13	344			
11	40.89	51			
12	41.51	299			



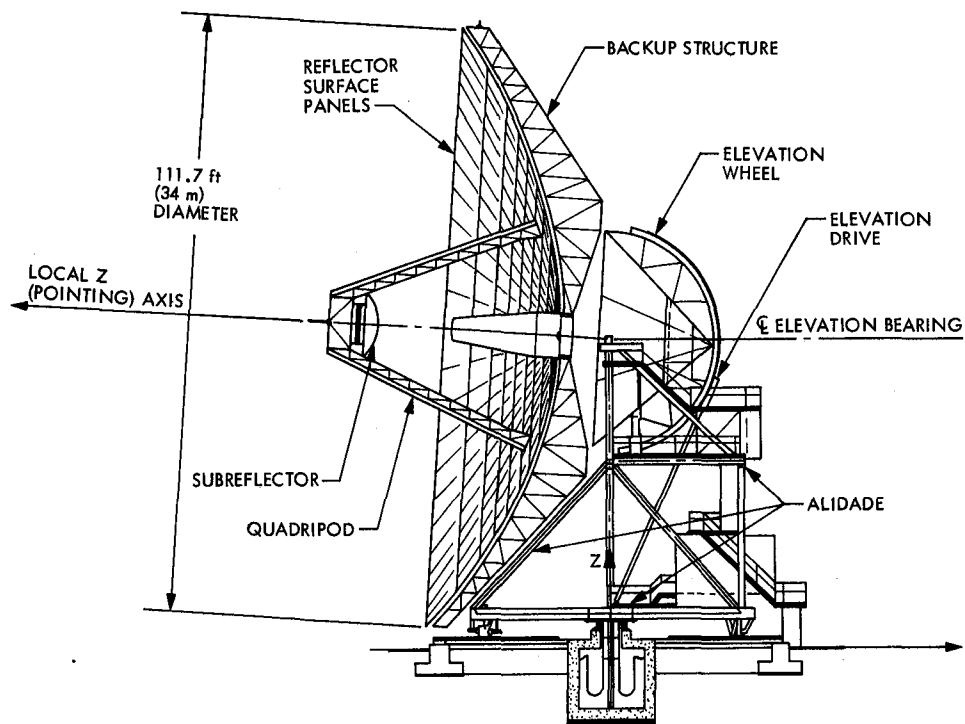


**Fig. 1. Example antenna structure (34-m diameter)**

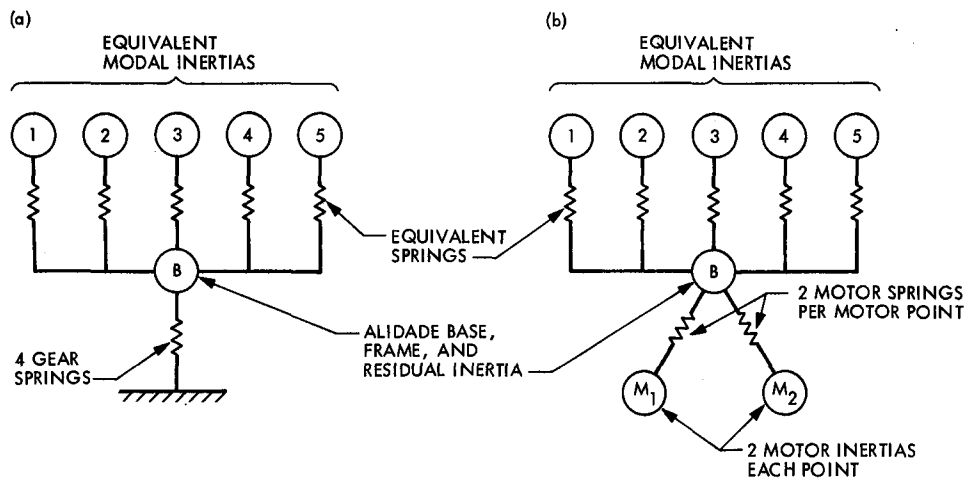


**Fig. 2. Equivalent-mass models: (a) locked rotor; (b) free rotor**

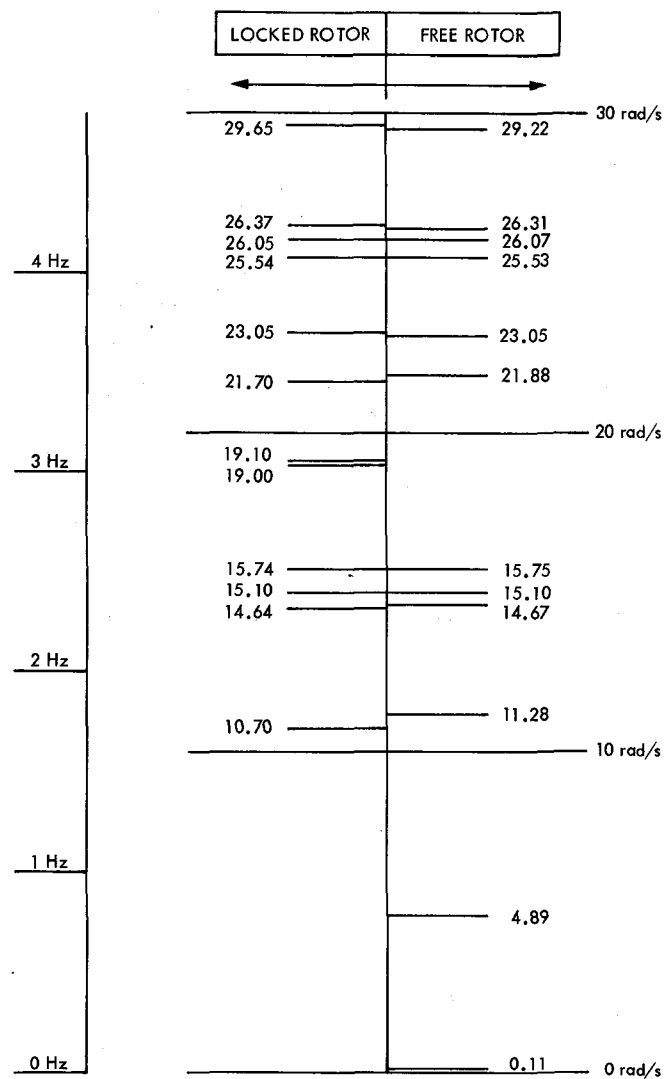


**Fig. 3. Tipping and alidade structure natural frequencies, azimuth model (reflector at 90° elevation)**

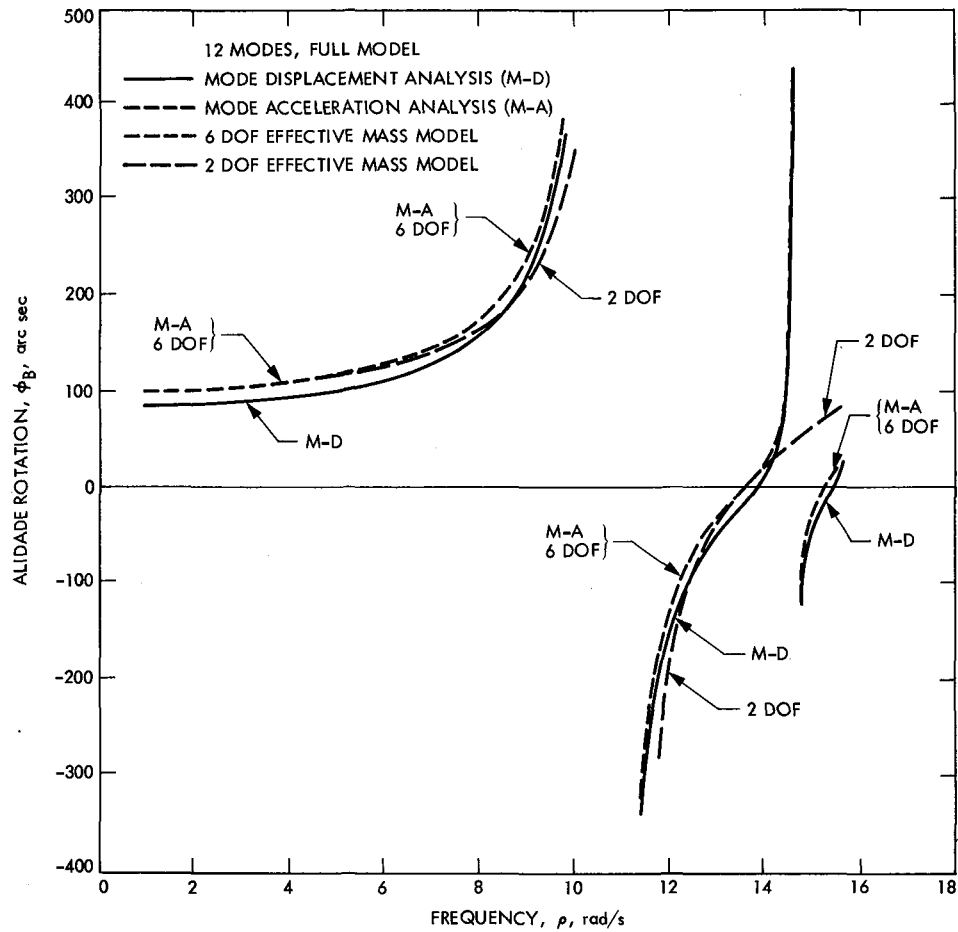


Fig. 4. Alidade base "locked-rotor" frequency response ( $K_s = 2.5518 \times 10^{10}$  in-lbf/rad)

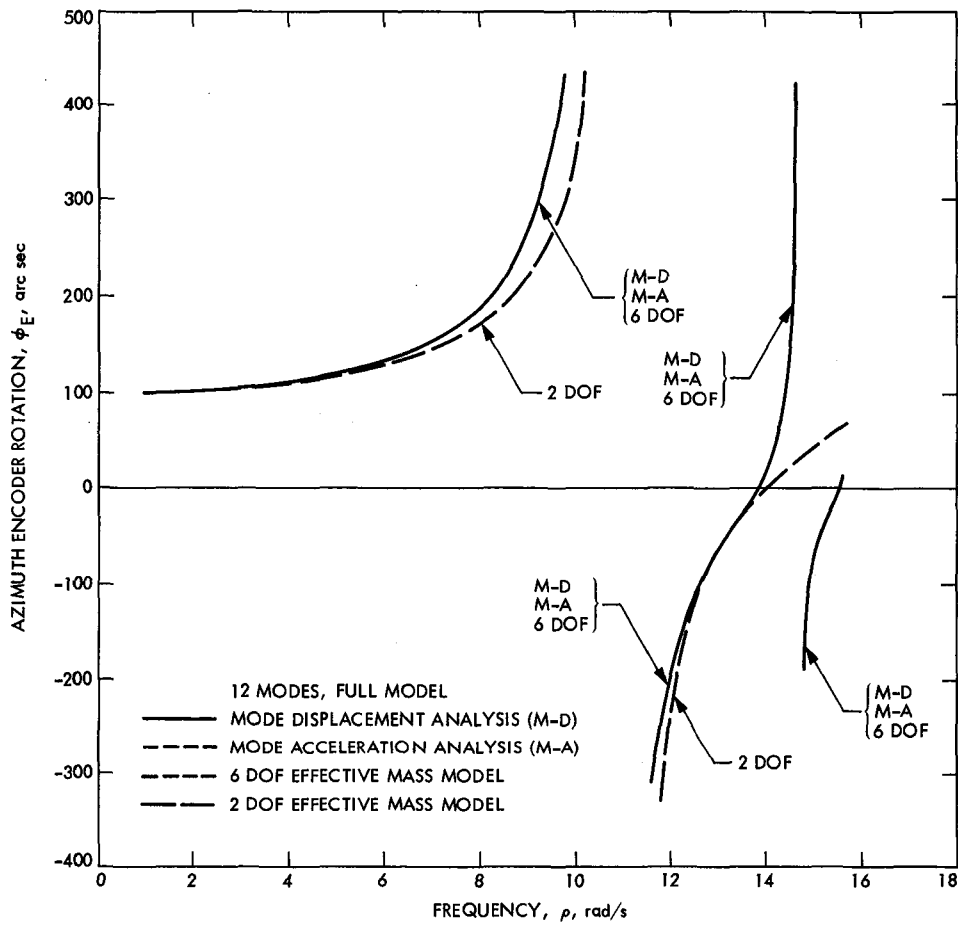


Fig. 5. Azimuth encoder "locked-rotor" frequency response ( $K_s = 2.5518 \times 10^{10}$  in-lbf/rad)

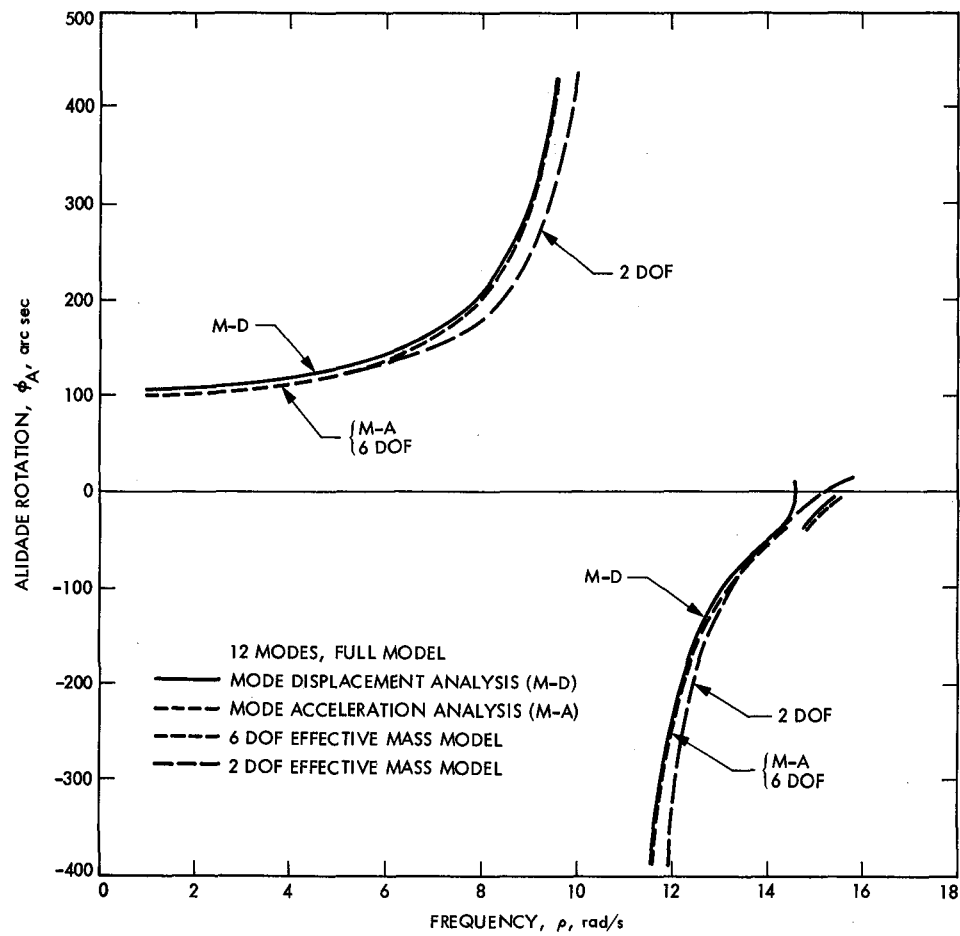


Fig. 6. Alidade "locked-rotor" frequency response ( $K_s = 2.5518 \times 10^{10}$  in-lbf/rad)

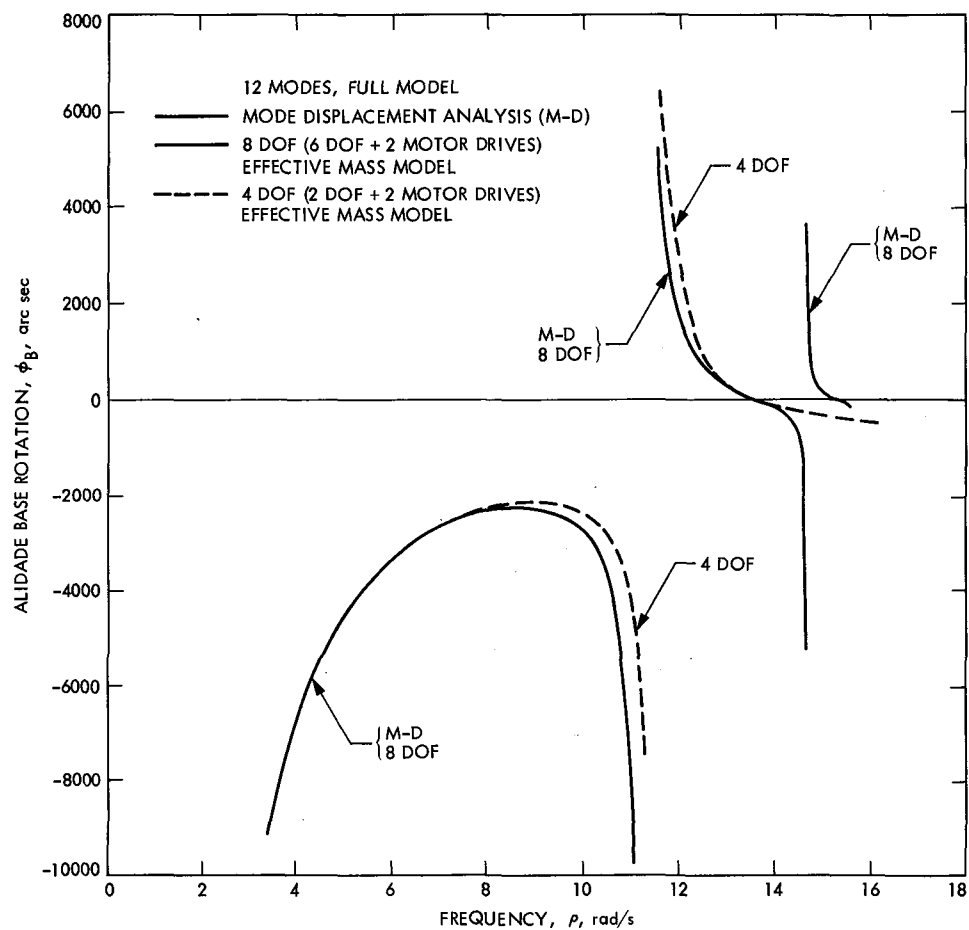


Fig. 7. Alidade base "free-rotor" frequency response ( $K_s = 2.5518 \times 10^{10}$  in-lbf/rad)



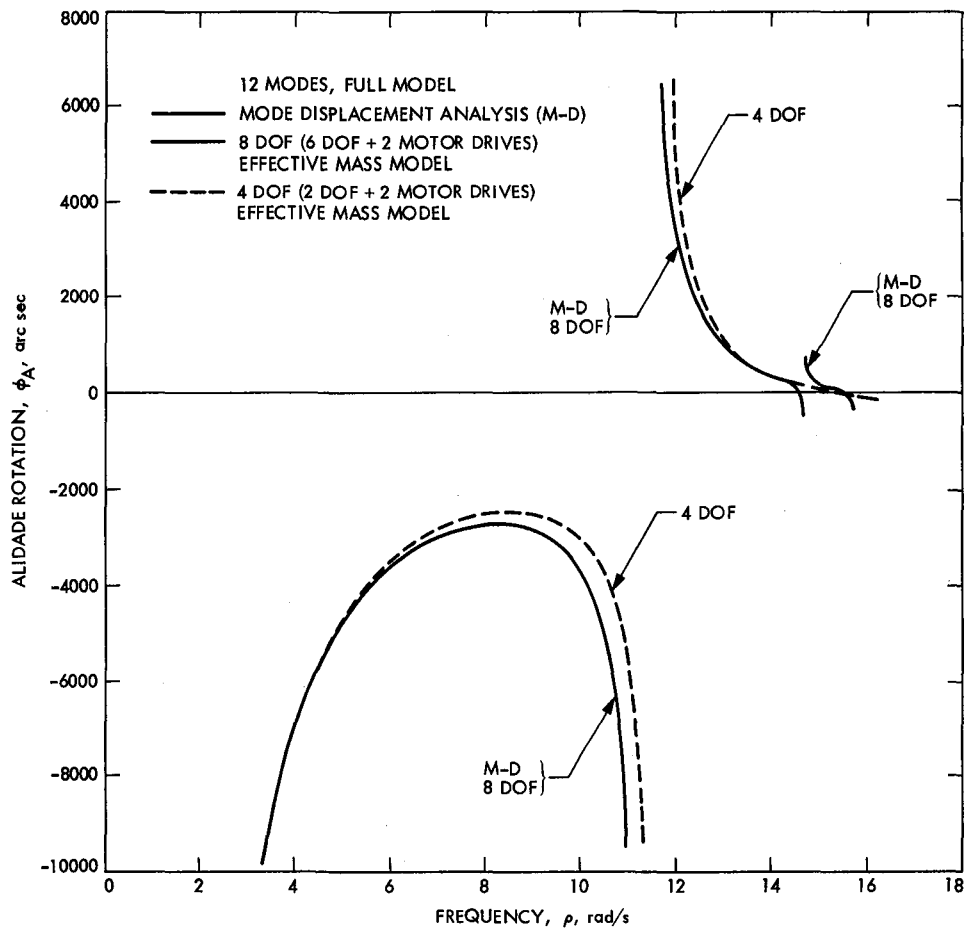


Fig. 9. Alidade "free-rotor" frequency response ( $K_s = 2.5518 \times 10^{10}$  in-lbf/rad)



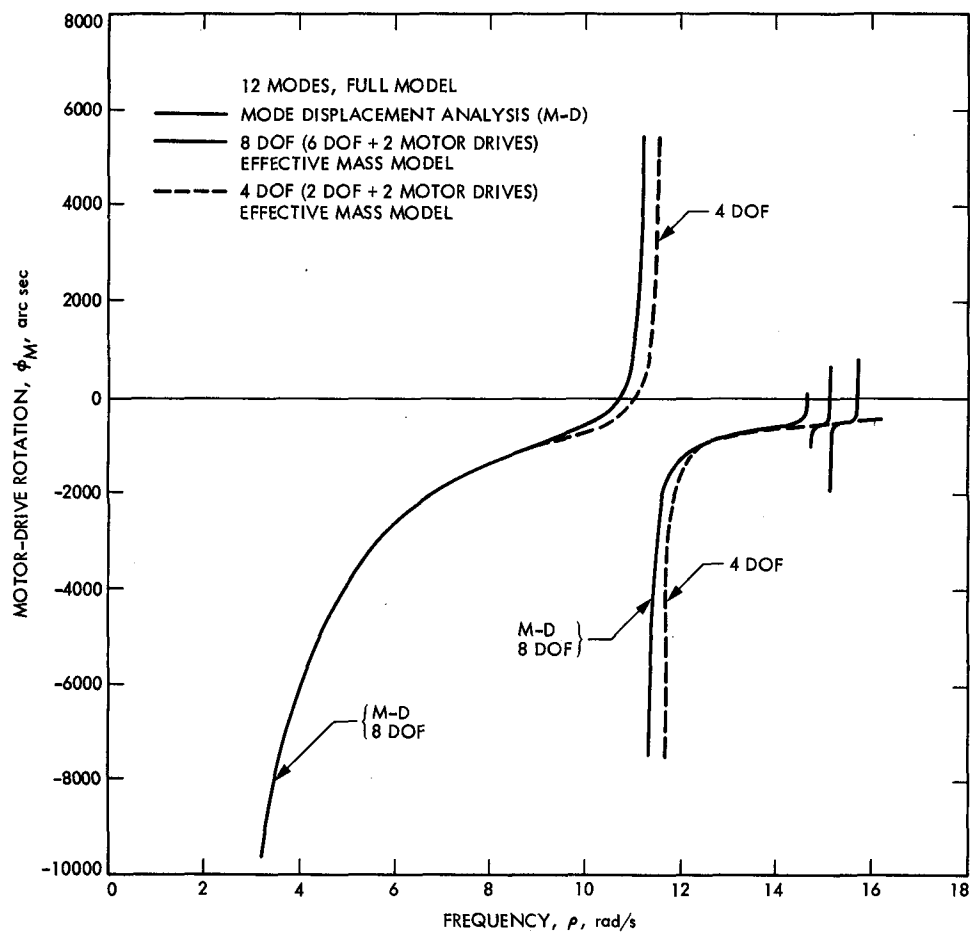
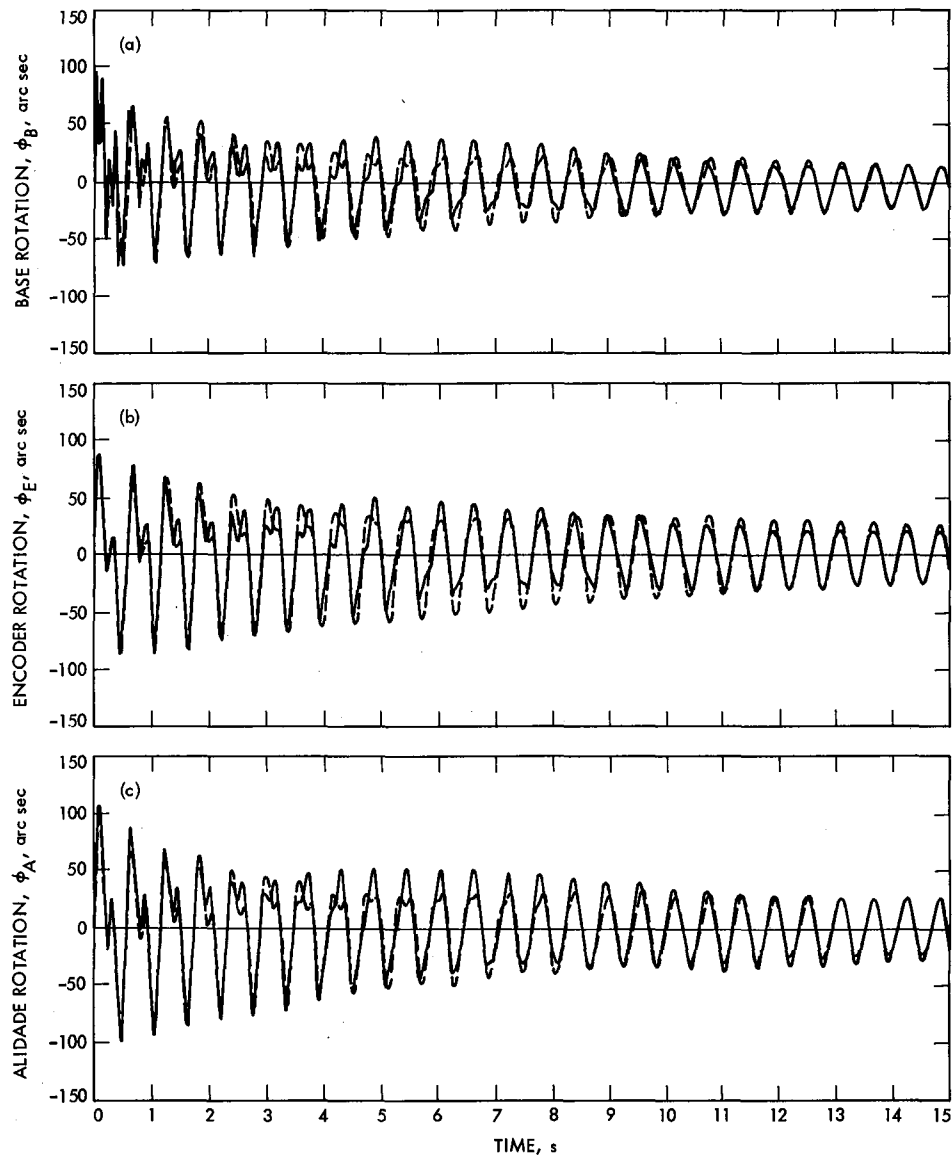
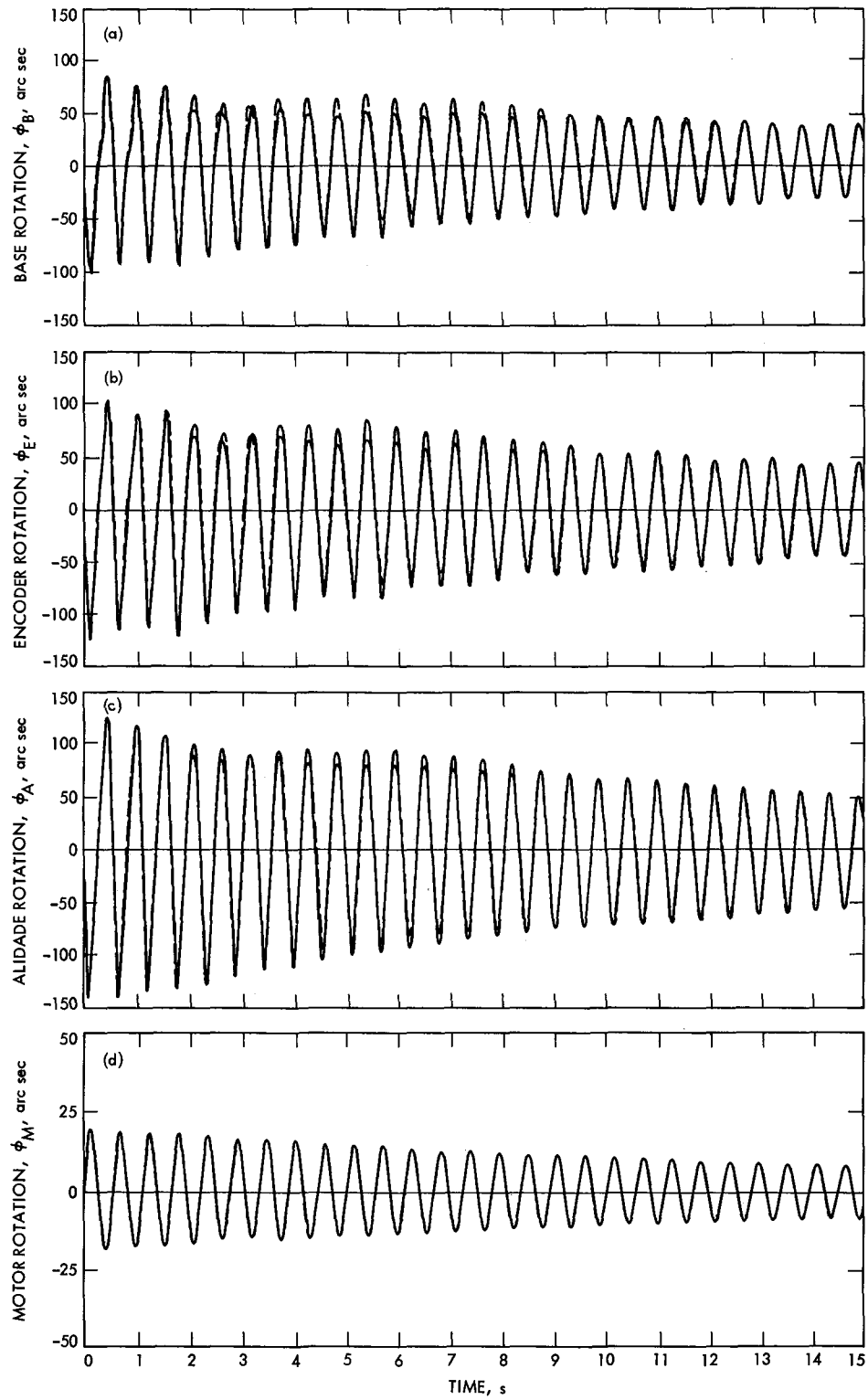


Fig. 10. Motor "free-rotor" frequency response ( $K_s = 2.5518 \times 10^{10}$  in-lbf/rad)



**Fig. 11. ACSL versus modal-superposition, "locked rotor": (a) base; (b) encoder; (c) alidade**



**Fig. 12. ACSL versus modal-superposition, "free rotor": (a) base; (b) encoder; (c) alidade; (d) motor**

## Appendix A

### Equivalent Oscillators Computations

The equations of motion of a linear, undamped elastic structure are:

$$\mathbf{M}\ddot{\mathbf{u}} + \mathbf{K}\mathbf{u} = \mathbf{f} \quad (\text{A-1})$$

$$\begin{Bmatrix} \mathbf{u} \end{Bmatrix} = \begin{Bmatrix} \mathbf{x} \\ \mathbf{g} \end{Bmatrix} \quad (\text{A-2})$$

in which

$\mathbf{M}$  = mass matrix

$\mathbf{K}$  = stiffness matrix

$\mathbf{f}$  = vector of forcing functions

$\mathbf{u}$  = set of all displacements

$\mathbf{x}$  = all displacements excluding the foundation

$\mathbf{g}$  = foundation displacements

When the structure has a statically determinate connection to the foundation, the displacements can be expressed as a combination of elastic and rigid body terms, e.g.

$$\mathbf{x} = \mathbf{y} + \phi_{\mathbf{R}}\mathbf{g} \quad (\text{A-3})$$

in which the foundation displacement has, at most, six components consisting of the three translations and three rotations that are listed in the following notation:

$$\mathbf{g} = [g_x \ g_y \ g_z \ g_{\theta_x} \ g_{\theta_y} \ g_{\theta_z}]$$

and

$\mathbf{y}$  = set of elastic displacements

$\phi_{\mathbf{R}}$  = rigid body transformation; depends only on the geometry of nodes and the center of the foundation rotation

Each six rows of  $\phi_{\mathbf{R}}$  correspond to the six degrees of freedom at each physical node of the structure model, and are of the form:

$$\begin{array}{l} \text{typical} \\ \text{rows} \\ \text{of } \phi_{\mathbf{R}} \end{array} = \begin{matrix} (g_x) & (g_y) & (g_z) & (g_{\theta_x}) & (g_{\theta_y}) & (g_{\theta_z}) \\ \begin{bmatrix} 1 & 0 & 0 & 0 & Z' & -Y' \\ 0 & 1 & 0 & -Z' & 0 & X' \\ 0 & 0 & 1 & Y' & -X' & 0 \\ 0 & 0 & 0 & 1 & 0 & 0 \\ 0 & 0 & 0 & 0 & 1 & 0 \\ 0 & 0 & 0 & 0 & 0 & 1 \end{bmatrix} \end{matrix}$$

where  $X'$ ,  $Y'$ , and  $Z'$  are the difference in the  $X$ ,  $Y$ , and  $Z$  coordinates of the particular node and the center of the foundation rotation.

In the special case of a structure model that omits rotational degrees of freedom and contains only the three translations at each node, the last three rows of the above form are omitted. Beyond this, the remainder of the following development applies without other modifications.

For a structure with  $N$  nodes, we can write  $\phi_{\mathbf{R}}$  as the following six column partitions

$$\phi_{\mathbf{R}} = [\{\phi_x\} \{\phi_y\} \{\phi_z\} \{\phi_{\theta_x}\} \{\phi_{\theta_y}\} \{\phi_{\theta_z}\}] \quad (\text{A-4})$$

where the form of each column repeats the six row (or three row, as explained) expression shown above.

Substituting Eq. (A-3) in Eq. (A-2), we have

$$\mathbf{u} = \begin{Bmatrix} \mathbf{x} \\ \mathbf{g} \end{Bmatrix} = \begin{bmatrix} \mathbf{I}_{yy} & \phi_{\mathbf{R}} \\ 0 & \mathbf{I}_{gg} \end{bmatrix} \begin{Bmatrix} \mathbf{y} \\ \mathbf{g} \end{Bmatrix} \quad (\text{A-5})$$

in which  $\mathbf{I}_{yy}$  and  $\mathbf{I}_{gg}$  are identity matrices of the size of  $\mathbf{y}$  and of  $\mathbf{g}$ .

From conventional synthesis of normal modes, the elastic displacements are

$$\mathbf{y} = \phi_{\mathbf{N}}\xi \quad (\text{A-6})$$

in which

$\phi_{\mathbf{N}}$  = matrix of eigenvectors ("modal matrix")

$\xi$  = vector of "normal" modal coordinates

By substituting Eq. (A-5) in Eq. (A-6), we have

$$\mathbf{u} = \begin{Bmatrix} \mathbf{x} \\ \mathbf{g} \end{Bmatrix} = \begin{bmatrix} \phi_N & \phi_R \\ 0 & \mathbf{I}_{gg} \end{bmatrix} \begin{Bmatrix} \xi \\ \mathbf{g} \end{Bmatrix} \quad (\text{A-7})$$

By partitioning Eq. (A-1) to conform with Eq. (A-7), making that substitution, and considering only the mass matrix  $\mathbf{M}_{yy}$  associated with the elastic displacements, we have

$$\begin{bmatrix} \mathbf{M}_{yy} & 0 \\ 0 & 0 \end{bmatrix} \begin{bmatrix} \phi_N & \phi_R \\ \mathbf{u} & \mathbf{I}_{gg} \end{bmatrix} \begin{Bmatrix} \ddot{\xi} \\ \ddot{\mathbf{g}} \end{Bmatrix} + \begin{bmatrix} \mathbf{K}_{yy} & \mathbf{K}_{yg} \\ \mathbf{K}_{gy} & \mathbf{K}_{gg} \end{bmatrix} \begin{bmatrix} \phi_N & \phi_R \\ 0 & \mathbf{I}_{gg} \end{bmatrix} \begin{Bmatrix} \xi \\ \mathbf{g} \end{Bmatrix} = \begin{Bmatrix} \mathbf{f}_y \\ \mathbf{f}_g \end{Bmatrix} \quad (\text{A-8})$$

where  $\mathbf{K}_{yy}$ ,  $\mathbf{K}_{yg}$ ,  $\mathbf{K}_{gy}$ ,  $\mathbf{K}_{gg}$ ,  $\mathbf{f}_y$ , and  $\mathbf{f}_g$  are the conforming partitions of the mass matrix and of the forcing function.

Equation (A-8) is premultiplied by the transpose

$$\begin{bmatrix} \phi_N^t & \phi_R^t \\ 0 & \mathbf{I}_{gg}^t \end{bmatrix} = \begin{bmatrix} \phi_N^t & 0 \\ \phi_R^t & \mathbf{I}_{gg} \end{bmatrix} \quad (\text{A-9})$$

with the result

$$\begin{aligned} & \begin{bmatrix} \phi_N^t & \mathbf{M}_{yy} & \phi_N & | & \phi_N^t & \mathbf{M}_{yy} & \phi_R \\ \hline \phi_R^t & \mathbf{M}_{yy} & \phi_N & | & \phi_R^t & \mathbf{M}_{yy} & \phi_R \end{bmatrix} \begin{Bmatrix} \xi \\ \mathbf{g} \end{Bmatrix} \\ & + \begin{bmatrix} \phi_N^t & \mathbf{K}_{yy} & \phi_N & | & \phi_N^t & \mathbf{K}_{yy} & \phi_R + \phi_N^t & \mathbf{K}_{yg} \\ \hline \phi_R^t & \mathbf{K}_{yy} & \phi_N & | & \phi_R^t & \mathbf{K}_{yy} & \phi_R + \phi_R^t & \mathbf{K}_{yg} \\ + & \mathbf{K}_{gy} & \phi_N & | & + & \mathbf{K}_{gg} & + & \mathbf{K}_{gy} & \phi_R \end{bmatrix} \begin{Bmatrix} \xi \\ \mathbf{g} \end{Bmatrix} \\ & = \begin{Bmatrix} \phi_N^t & \mathbf{f}_y \\ \hline \phi_R^t & \mathbf{f}_y + \mathbf{f}_g \end{Bmatrix} \quad (\text{A-10}) \end{aligned}$$

The second coefficient matrix on the left-hand side of Eq. (A-10) can be significantly simplified. The simplification is obtained by considering only cases of rigid body displacements of the structure and foundation. In this case, all elastic displacements and displacement derivatives are zero, and only the foundation displacements can be non-zero. Then it can be

concluded, from the principle that forces and reactions are zero for rigid body displacements, that only the upper-left partition of this matrix is not null. Therefore, we can rewrite Eq. (A-10) as

$$\begin{bmatrix} \mathbf{M}_{NN} & \mathbf{M}_{ER} \\ \mathbf{M}_{RE} & \mathbf{M}_{RR} \end{bmatrix} \begin{Bmatrix} \xi \\ \mathbf{g} \end{Bmatrix} + \begin{bmatrix} \mathbf{K}_{NN} & 0 \\ 0 & 0 \end{bmatrix} \begin{Bmatrix} \xi \\ \mathbf{g} \end{Bmatrix} = \begin{Bmatrix} \phi_N^t & \mathbf{f}_y \\ \phi_R^t & \mathbf{f}_y + \mathbf{f}_g \end{Bmatrix} \quad (\text{A-11})$$

in which

$\mathbf{M}_{NN} = \phi_N^t \mathbf{M}_{yy} \phi_N$ , the elastic-structure generalized mass matrix

$\mathbf{M}_{ER} = \phi_N^t \mathbf{M}_{yy} \phi_R$ , the elastic-rigid coupling matrix

$\mathbf{M}_{RE} = \mathbf{M}_{ER}^t$ , the rigid-elastic coupling matrix

$\mathbf{M}_{RR} = \phi_R^t \mathbf{M}_{yy} \phi_R$ , the rigid-body mass matrix

$\mathbf{K}_{NN} = \phi_N^t \mathbf{K}_{yy} \phi_N$ , the elastic-structure generalized stiffness matrix

Note from the orthogonality of the normal modes, that  $\mathbf{M}_{NN}$  and  $\mathbf{K}_{NN}$  are diagonal.

Equation (A-11), except for differences in notation and ordering, is identical to Eq. (A-4) of the reference.

When a full set of the maximum of six independent foundation displacements is considered, the elastic-rigid coupling matrix  $\mathbf{M}_{ER}$  has one row for each normal mode included and one column for each of the six foundation displacements. A specific row of  $\mathbf{M}_{ER}$  corresponding to the  $j^{\text{th}}$  normal mode can be written as

$$\mathbf{M}_{ERj} = \begin{bmatrix} M_j^x & M_j^y & M_j^z & M_j^{yx} & M_j^{yz} & M_j^{zx} \end{bmatrix} \quad (\text{A-12})$$

in which, for example

$$M_j^x = \phi_{Nj}^t \mathbf{M}_{yy} \phi_x$$

where  $\phi_{Nj}$  is the  $j^{\text{th}}$  natural mode eigenvector and  $\phi_x$  is the first column of the column-partitioned form of  $\phi_R$ , as described following Eq. (A-3) and in Eq. (A-4). The remaining righthand-side terms are computed similarly by substituting the corresponding column of  $\phi_R$ . Furthermore, the generalized mass of the  $j^{\text{th}}$  normal mode follows from the definition of the  $\mathbf{M}_{NN}$  matrix Eq. (A-11) as

$$\mathbf{M}_{NNj} = \phi_{Nj}^t \mathbf{M}_{yy} \phi_{Nj} \quad (\text{A-13})$$

The notation of Eqs. (A-12) and (A-13) allows, as an example, the following term to be defined:

$$M_{Exj} = (M_j^x)^2 / M_{NNj} \text{Sgn}(M_j^x) \quad (\text{A-14})$$

Obviously, five more terms ( $M_{Eyj}$ ,  $M_{Ezj}$ ,  $M_{E\theta xj}$ ,  $M_{E\theta yj}$ , and  $M_{E\theta zj}$ ), similar in form to Eq. (A-14), can be generated by employing the second through sixth right-hand terms of Eq. (A-12) to replace, in turn, the  $M_j^x$  term of Eq. (A-14). Algebraic manipulations can show that forming the sum of the absolute values of the first three terms generated this way provides the  $j^{\text{th}}$  mode equivalent (effective) mass as defined in the reference. That is,

$$M_{Ej} = \text{abs}(M_{Exj}) + \text{abs}(M_{Eyj}) + \text{abs}(M_{Ezj}) \quad (\text{A-15})$$

It can also be shown that the six terms,  $M_{Exj}$  through  $M_{E\theta zj}$ , are the reductions to the diagonals of the residual mass matrix  $\mathbf{M}_{\text{RES}}$  produced by the  $j^{\text{th}}$  normal mode. As a specific example, the  $k^{\text{th}}$  diagonal term of the residual mass matrix when  $\mathbf{M}$  normal modes are included is given by

$$\mathbf{M}_{\text{RES}}(k, k) = \mathbf{M}_{\text{RR}}(k, k) - \sum_{j=1}^M \text{abs}(M_{E pj}) \quad (\text{A-16})$$

where  $p = x, y, z, \theta x, \theta y$ , and  $\theta z$  for  $k = 1, 2, 3, 4, 5$ , and  $6$ , respectively.

Evidently, if all natural modes are considered, the residual mass matrix will be zero. Also, if a diagonal term of  $\mathbf{M}_{\text{RES}}$  is relatively large in comparison with the same diagonal of  $\mathbf{M}_{\text{RR}}$ , most of the inertia is being treated as rigid, and very little of it is being recognized as flexible. Nevertheless, such a representation could be appropriate if the  $\mathbf{M}$  modes included adequately cover the spectrum of the structure frequencies that could be excited by the control system. Furthermore, if no normal (elastic) modes are considered, the following equality holds:

$$\mathbf{M}_{\text{RES}} = \mathbf{M}_{\text{RR}} \quad (\text{A-17})$$

When the mechanical control-system model is for an azimuth-elevation antenna, we are concerned with, at most, two rotational components of the foundation displacement vector. As a specific example, say we are concerned only with the azimuth-drive axis, which is identified here as the  $Z$ -axis. Then, the pertinent foundation displacement is  $g_{\theta x}$ . The significant terms of the rigid body and residual mass matrices are  $\mathbf{M}_{\text{RR}}(6,6)$  and  $\mathbf{M}_{\text{RES}}(6,6)$ . Of the six terms that can be generated on the form of Eq. (A-14), only the last term  $M_{E\theta zj}$  is needed. This latter term becomes the  $j^{\text{th}}$  mode equivalent inertia which is employed instead of the equivalent mass of Eq. (A-15).

The JPL-IDEAS computer program eigenvalue analysis performs the following related operations:

- (1) Computes eigenvalues, eigenvectors, and generalized mass for the  $\mathbf{M}$  user denoted lowest-frequency natural modes.
- (2) Computes the six components of  $\mathbf{M}_{\text{ER}}$  (see Eq. A-14) for each of the modes.
- (3) Computes and tabulates the six reduction components to the diagonals of the residual mass matrix (see Eq. A-14) and equivalent mass (see Eq. A-15) for each mode.
- (4) Computes and prints the  $6 \times 6$  rigid-body mass matrix  $\mathbf{M}_{\text{RR}}$  (see Eq. A-11).
- (5) Computes and prints coordinates to locate the equivalent effective mass of each mode. The computations are not described here, but are consistent with formulations shown in the reference paper.
- (6) Lists the sum of reductions to each of the diagonals of the residual mass matrix and the diagonals of the residual mass matrix for the  $\mathbf{M}$  modes.

## Appendix B

### Transfer Function of Equivalent Modal Inertia Structure Model

A complex elastic structure can be simply represented within a mechanical control-system simulation model by the "candelabra" diagram of Fig. B-1. Here the parallel branches represent equivalent effective oscillators derived from the normal modes of the structure, and the stem represents physical coordinates of the output pinion of the gearbox that drives the system and of the motor that applies driving torques through the gearbox. The remainder of the control system, which interfaces with the motor and pinion, does not permit such simple generalization and is omitted from the figure.

The following notations are used in conjunction with Fig. B-1:

$q_1, \dots, q_M$  = generalized elastic-effective modal coordinates derived from the "locked-rotor" (fixed at pinion) natural modes of the structure

$J_1, \dots, J_M$  = equivalent inertia of the effective coordinates

$K_1, \dots, K_M$  = equivalent stiffness of the effective coordinates

$\omega_{ni}$  =  $i^{\text{th}}$  mode structure natural circular frequency  $(K_i/J_i)^{1/2}$

$\theta_P$  = gearbox pinion coordinate

$J_P$  = gearbox inertia (includes residual inertia of structure, which is the inertia not included in  $J_1$  through  $J_M$ )

$K_G$  = gearbox spring constant

$\theta_{MTR}$  = coordinate of motor (input end of gearbox)

$J_{MTR}$  = motor inertia

The typical equation of motion for the  $i^{\text{th}}$  modal oscillator is

$$J_i \ddot{q}_i + K_i (q_i - \theta_P) = 0, \quad i = 1, 2, \dots, M \quad (\text{B-1})$$

The pinion equation of motion is

$$J_P \ddot{\theta}_P + \sum_{i=1}^M K_i (\theta_P - q_i) + \sum_{j=1}^L K_G (\theta_P - \theta_{MTR_j}) = 0 \quad (\text{B-2})$$

in which it has been assumed that there are  $L$  motors (with generic index,  $j$ ) and gearboxes all attached to the same pinion.

The motor equation of motion is of the form

$$J_{MTR_j} \ddot{\theta}_{MTR_j} + K_G (\theta_{MTR_j} - \theta_P) + \text{Control System Terms} = \text{Motor Input Torque} \quad (\text{B-3})$$

In Eqs. (B-1), (B-2), and (B-3) we have assumed an undamped structure and gearbox ratios of unity. These are not essential assumptions and are made here only to condense the discussions.

It is convenient to recast the equations of motion into relative oscillator coordinates. To do this, let  $e_i$  be the coordinate for the  $i^{\text{th}}$  oscillator relative to its base  $\theta_P$ . That is

$$e_i = q_i - \theta_P$$

or

$$q_i = e_i + \theta_P \quad (\text{B-4})$$

Then Eq. (B-1) becomes

$$J_i \ddot{e}_i + K_i e_i = -J_i \ddot{\theta}_P, \quad i = 1, 2, \dots, M \quad (\text{B-5})$$

Using the Laplace operator  $S$ , the associated transfer functions become

$$e_i(S) = \frac{-S^2}{S^2 + \omega_{ni}^2} \theta_P(S) \quad (\text{B-6})$$

Equation (B-2) can be written as

$$J_P \ddot{\theta}_P - \sum_{i=1}^M K_i e_i + \sum_{j=1}^L K_G (\theta_P - \theta_{MTR_j}) = F_P$$

or

$$J_P \ddot{\theta}_P = \sum_{i=1}^M K_i e_i + \sum_{j=1}^L K_G \theta_{MTR_j} - \sum K_G \theta_P \quad (\text{B-7})$$

so that the transfer function becomes

$$\theta_P(S) = \frac{\sum_{i=1}^M K_i e_i(S) + \sum_{j=1}^L K_G \theta_{MTR_j}(S) - \sum K_G \theta_P(S)}{J_P S^2} \quad (B-8)$$

The inertia, spring constant, and natural frequency of each  $e_i$  is the effective value associated with the  $i^{\text{th}}$  normal mode. If  $\xi_i$  is the normal coordinate of the  $i^{\text{th}}$  mode, it can be shown

$$\xi_i = \alpha_i e_i \quad (B-9)$$

where

$$\alpha_i = \sqrt{\frac{J_i}{JG_i}}$$

and  $JG_i$  is the generalized mass of the  $i^{\text{th}}$  mode, arbitrarily normalized according to the normalization of the eigenvector. Then let  $\phi_{Ei}$  equal the value of the eigenvector of the encoder

in the  $i^{\text{th}}$  mode, and  $\theta_E$  equal the encoder displacement (in physical coordinates). It then follows from conventional modal analysis and the conversion here to relative coordinates that

$$\theta_E = \sum_{i=1}^M \phi_{Ei} \xi_i + \theta_P \quad (B-10)$$

By introducing the new constants

$$A_{Ei} = \phi_{Ei} \alpha_i \quad (B-11)$$

we have, from Eqs. (B-9), (B-10), and (B-11),

$$\theta_E = \sum_{i=1}^M A_{Ei} e_i + \theta_P \quad (B-12)$$

A servo-block diagram equivalent to Fig. B-1 is shown in Fig. B-2. This figure incorporates the relationships of Eqs. (B-6), (B-8), and (B-12), a non-unity gear ratio  $N$ , and four independent drive motors.





# Interpolation Methods for GTD Analysis of Shaped Reflectors

V. Galindo-Israel, W. Imbriale, Y. Rahmat-Samii, and T. Veruttipong

Radio Frequency and Microwave Subsystems Section

*It is often required to find "smooth" analytic representations for antenna reflector surfaces which are prescribed only by discretized data obtained by various synthesis methods. Frequently the data are distributed in a nonuniform grid and contain noise. The "smoothness" required is to  $C_1$  for physical optics diffraction analysis and to  $C_2$  for Geometrical Theory of Diffraction (GTD) analysis. Furthermore, the GTD analysis approach requires a surface description which returns data very rapidly. Two methods of interpolation, the global and the local methods, are discussed herein. They each have advantages and disadvantages – usually complementary. These characteristics are discussed and examples are presented.*

## I. Introduction

The diffraction analysis of reflector surfaces which are described only at a *discrete* set of locations usually leads to the requirement of an *interpolation* to determine the surface characteristics over a continuum of locations. Such discretized surface descriptions can come about from a set of point measurements for example. Another common source of such a description is the dual offset shaped reflector synthesis (Refs. 1 and 2), which may involve numerical difference type solutions over a discretized field.

The physical optics analysis of a reflector antenna requires an accurate description of the point characteristics (e.g.,  $[x, y, z]$  or  $[r, \theta, \phi]$ ) of the surface, and it also requires a reasonably accurate description of the slopes (e.g.,  $[\partial z/\partial x = z_x, z_y]$  or  $[r_\theta, r_\phi]$ ) at the same points. The GTD analysis requires, further, an accurate knowledge of the second derivatives at the same points. The second derivatives provide the scattered amplitude for both the GO and the diffraction parts

of GTD. Hence the GTD analysis of shaped reflectors with discretized raw data requires an accurate and often time consuming interpolation process.

In dual reflector antennas, it is usually desirable to analyze the subreflector by GTD since more near-zone observation points are required on the main reflector than far field observation points of the main reflector. (We analyze the main reflector by the Jacobi-Bessel method [Refs. 3 and 4].) The interpolation techniques to be described are applicable to both reflectors, but we will describe results found for a shaped subreflector synthesized for high gain.

High gain shaped subreflectors represent a more than average difficult surface to describe because the surface curves more rapidly and often possesses inflection points (Refs. 1 and 5). A profile description of such a dual reflector is shown in Fig. 1. Also illustrated are the projected (on the  $[\theta, \phi]$  plane) discretized raw data locations at equal  $(\Delta\theta, \Delta\phi)$  increments. In some synthesis methods (Ref. 1), the raw data

consists of  $r$ ,  $r_\theta$ , and  $r_\phi$  at each  $(\theta, \phi)$  discretized location. However, the derivative data of at least one derivative (in Ref. 1 the  $r_\phi$  derivative) are *unstable* since they are computed by difference techniques which do not permit very small increments.

A method for evaluating the accuracy and stability of a surface description is to compute the “distance” function derivatives  $D_\phi$  and  $D_{\phi\phi}$ . The distance  $D$  is the the distance from the source to a point on the reflector and then to the observation point. When  $D$  is a minimum (Fermat) we have a GO or an edge diffraction spectral point. In our evaluation method, we allow the point on the subreflector to vary in position with  $\phi$  ( $\theta$  fixed). Usually we take  $\theta = \theta_{\text{MAX}}$  along the edge of the reflector, although all  $\theta$  values should be evaluated.

The results for a particular set of raw data (Ref. 5) are shown in Fig. 2. Note the erratic second derivative behavior ( $D_\phi = 0$  implies a diffraction spectral point — there are two).

## II. Global Interpolation

A global interpolation representation is a closed form or series expression valid over the entire surface. The coefficients of a series expression are found by an integration of the raw data. Since far fewer coefficients are used to describe the surface than raw data points, the integration effectively provides a smoothing of the raw data.

For example, the Jacobi polynomial-sinusoidal (Ref. 3) expansion was found (Ref. 6) to provide a fast converging representation of the offset shaped subreflector discussed. The representation is

$$r(\theta, \phi) = \sum_{n=0}^{N-1} \sum_{m=0}^{M-1} a_{mn} F_m^n(\theta) \begin{Bmatrix} \cos n\phi \\ \sin n\phi \end{Bmatrix}$$

where the Jacobi polynomial

$$F_m^n(\theta) = \sqrt{2(n+2m+1)} P_m^{(n,0)}(1-2\theta^2) \cdot \theta^n$$

$$P_m^n(s) = \frac{(-1)^m (1-s)^{-n}}{2^m M!} \frac{d^m}{ds^m} \left[ \frac{(1-2)^{m+n}}{(1+s)^{-m}} \right]$$

and the  $a_{mn}$  are found by using the orthogonality properties of the expansion functions.

In Fig. 3, the distance function  $D_{\phi\phi}$  is found to be perfectly smoothed in the global description of the reflector. In Fig. 4 we observe the convergence of the  $D_\phi$  and the  $D_{\phi\phi}$  functions

with  $N \times M$  terms. Although  $N \times M = 4 \times 4 = 16$  terms are totally adequate for  $D_\phi$  (at the edge), several more terms are required for  $D_{\phi\phi}$ . Actually the derivatives with respect to  $\theta$  demand some extra terms. The GTD diffraction pattern for the same shaped subreflector is shown in Figs. 5 and 6. The depicted patterns are taken in the plane of offset of the subreflector which possesses left-right symmetry. A feed with -16 dB taper at the subreflector edge was used. The pattern increases with  $\theta$  because it is shaped to compensate for the space loss that results when feeding a main offset shaped reflector for high gain. The amplitude is dependent directly upon the second derivatives of the reflector surface.

Figure 5 illustrates the convergence of the pattern with increasing number of global coefficients to represent the surface. We find  $4 \times 4 = 16$  terms are adequate except for some cross polarization introduced near  $\theta \approx -3^\circ$ . There is no cross polarization with  $5 \times 5 = 25$  terms. In Fig. 6, we observe the same GTD pattern obtained for  $5 \times 5$  global terms and the results obtained directly from the raw data.

The *advantages* of the global representation can be briefly summarized:

- (1) It converges rapidly and uses a small computer core to describe the entire reflector (16-50 real numbers).
- (2) It is analytically smooth through the second derivatives.
- (3) It can be readily used as a synthesis tool with optimization techniques since few terms are involved.

The principle *disadvantage* of the global representation is that it is computationally much slower than closed form expressions such as the hyperboloid formula. In GTD analysis, the search for the GO and edge spectral points (for many observation points) may require many thousands of surface evaluations. Hence a very fast local interpolation (which may use a large set of data and core) is desirable.

## III. Local Interpolation

A local interpolation provides a closed form expression for only a small area of the reflector surface. In Fig. 7, we divide the subreflector into three (or more) sectors where each have constant  $(\Delta\theta, \Delta\phi)$  discretized data. Each area *segment* is then described by a two-dimensional quadratic surface — locally:

$$z = a_1 + a_2x + a_3y + a_4x^2 + a_5xy + a_6y^2$$

The six coefficients are found locally from six data points and stored for that particular  $(\theta, \phi)$  location. Although the second derivatives  $z_{xx}$ ,  $z_{xy}$ , and  $z_{yy}$  can be found from the quadratic expression above, we choose to find an *average*  $z_{xx\text{AVG}}$ ,

$z_{xyAVG}$ ,  $z_{yyAVG}$  over the area segment. We thus store nine instead of six real numbers for each segment. We found this averaging necessary because our computer word size (36 bits) would not allow a sufficiently small ( $\Delta\theta, \Delta\phi$ ) to be used so as to calculate the second derivatives accurately from the quadratic expression above. The averaging method worked successfully.

A quadratic expression was used instead of a higher order local expression because of our required "maximum speed possible" computation. Furthermore, we required our surface to return ( $X, Y, Z_x, Z_y; Z_{xx}, Z_{xy}, Z_{yy}$ ) data from a  $(\theta, \phi)$  input. The required computation is fast and simple for a quadratic expression but rapidly becomes more complex as the order of the local surface is increased.

The disadvantages of the local interpolation are essentially the same as the advantages of the global interpolation. In particular, a large core is required for the local interpolation. The advantage is the higher speed and "turn-around" time for computations. The speed is

- (1) Independent of the surface complexity (or the number of terms required by the global method)
- (2)  $>20 \times$  global for 50 global terms  
 $>10 \times$  global for 25 global terms

The local interpolation does require "smooth" raw data. We found it useful to first obtain a global expression and then do our diffraction analysis rapidly with the local interpolation.

## References

1. Galindo-Israel, V., Mittra, R., and Cha, A., "Aperture Amplitude and Phase Control of Offset Dual Reflectors," *IEEE Trans. on Antennas and Propagation*, pp. 154-164, March 1979.
2. Galindo-Israel, V., and Mittra, R., "Synthesis of Offset Dual Shaped Subreflector Antennas for Control of Cassegrain Aperture Distributions," *IEEE Trans. on Antennas and Propagation*, pp. 86-92, Jan. 1984.
3. Galindo-Israel, V., and Mittra, R., "A New Series Representation for the Radiation Integral With Application to Reflector Antennas," *IEEE Trans. on Antennas and Propagation*, pp. 631-641, Sept. 1977 (see also *IEEE 1977 International Symposium Digest*, pp. 599-602).
4. Rahmat-Samii, Y., and Galindo-Israel, V., "Shaped Reflector Analysis Using the Jacobi-Bessel Series," *IEEE Trans. on Antennas and Propagation*, pp. 425-435, July 1980.
5. Cha, A., "An Offset Dual Shaped Reflector With 84.5% Efficiency," *IEEE Trans. on Antennas and Propagation*, pp. 896-902, Nov. 1983.
6. Rahmat-Samii, Y., and Galindo-Israel, V., "A Novel Global Surface Interpolation for Reflector Antenna Applications," paper presented at the National Radio Science Meeting, Boulder, Colo., Jan. 1982.

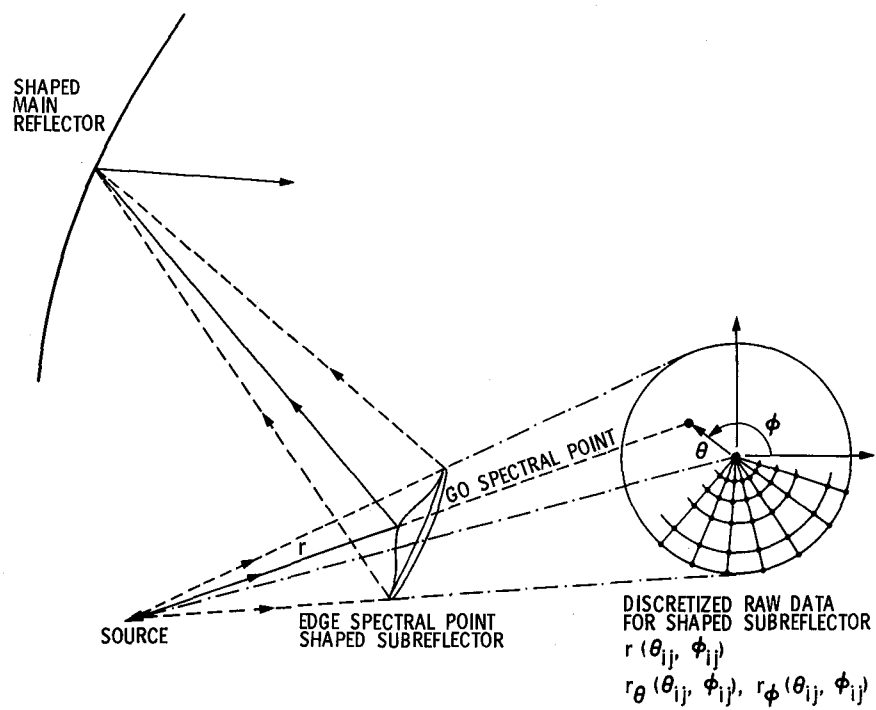


**Fig. 1. Dual offset shaped (high gain) reflectors**

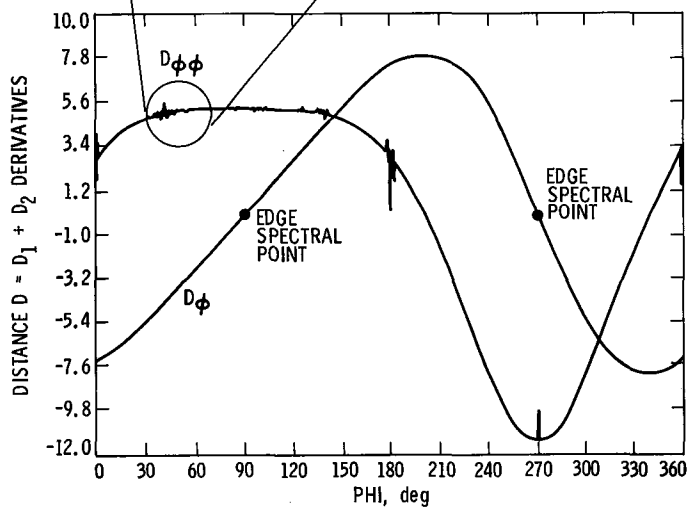
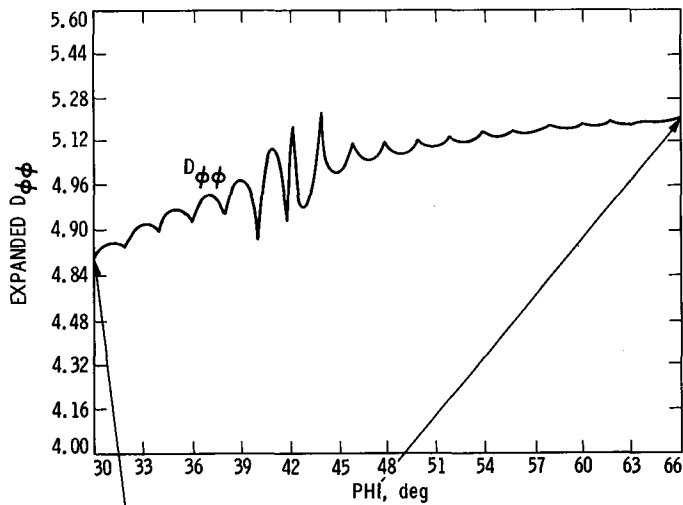


Fig. 2. Distance function derivatives for "raw data"

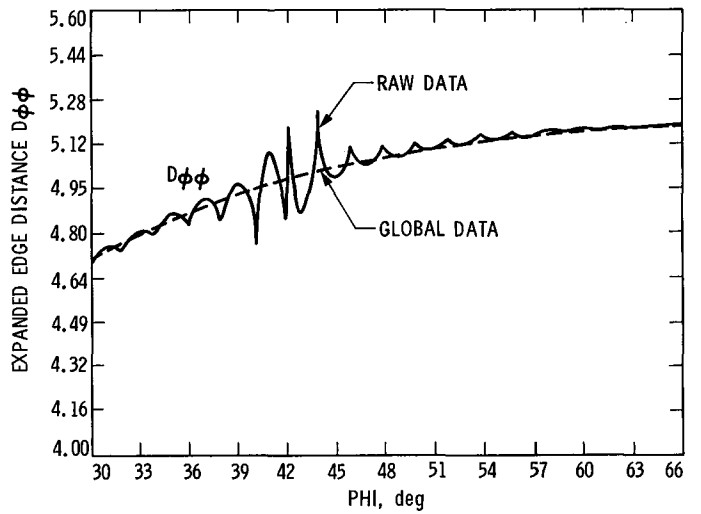


Fig. 3. Distance function  $D_{\phi\phi}$  for raw data and global data shaped subreflector (along edge)

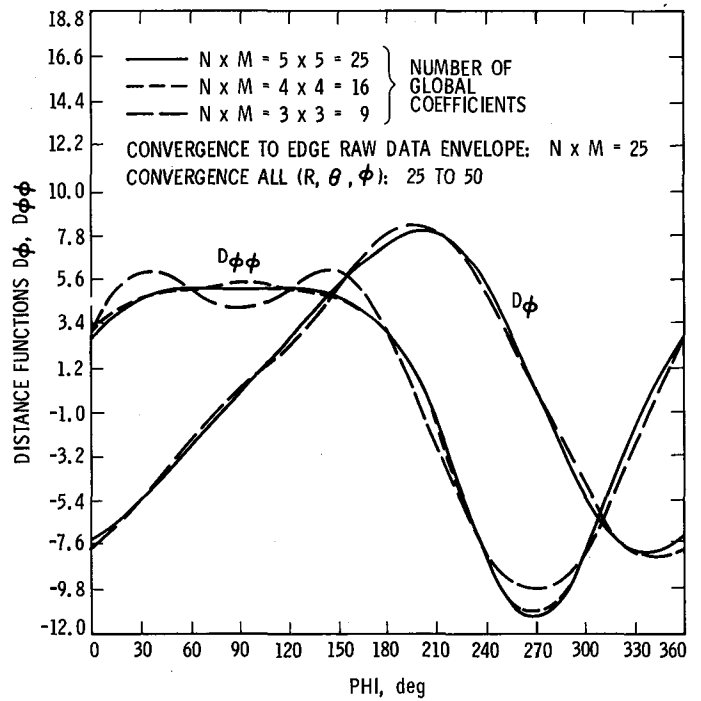


Fig. 4. Distance functions  $D_{\phi}$ ,  $D_{\phi\phi}$

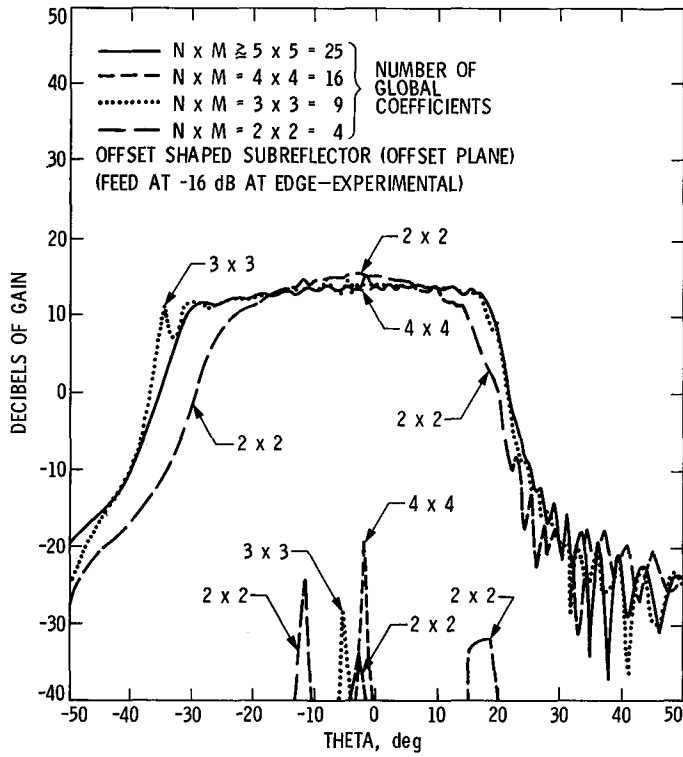


Fig. 5. Scattered field (GO + diffraction) vs global representation

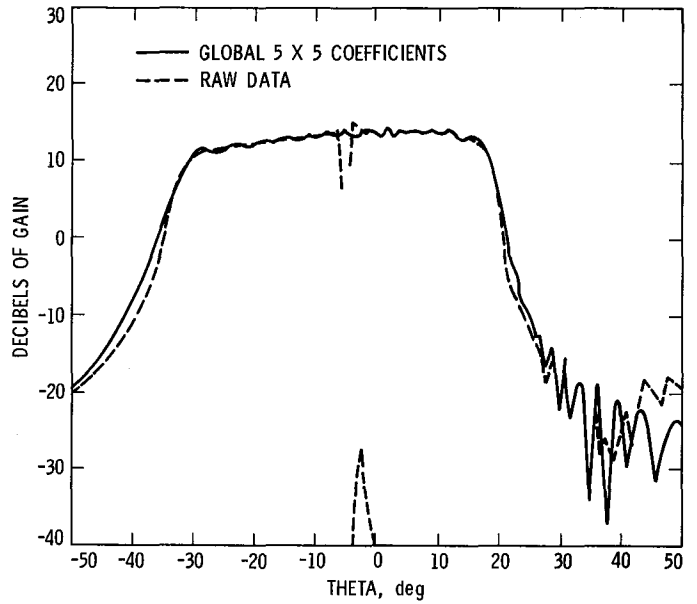


Fig. 6. Scattered field (GO + diffraction) raw data vs global surfaces

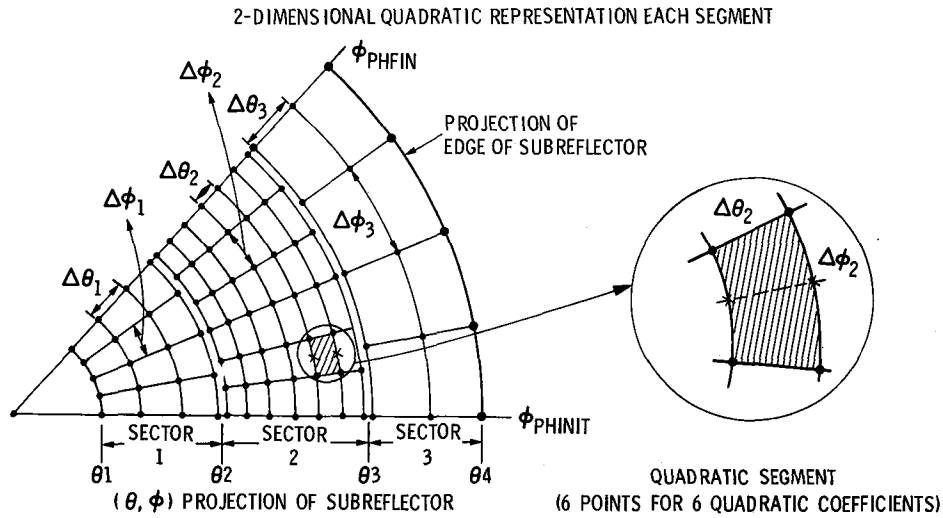


Fig. 7. Local interpolation

# Design Procedure for the New 70-Meter Antenna Subreflector Positioner

R. D. Hughes

Ground Antenna and Facilities Engineering Section

*Design procedures are developed for determining Cassegrain-type antenna subreflector positioner strength and displacements under wind and gravity loading conditions. The procedures are applied to the JPL 70-m antenna subreflector design, and the resulting design details are presented. The generalized analysis can be adapted to other antenna and subreflector-positioners. The results show that the new design meets the strength and displacements criteria under worst-case loading.*

## I. Introduction.

Under the 64-meter to 70-meter Antenna Upgrade and Rehabilitation Project, the three existing 64-meter antennas of JPL at DSS-14 (Goldstone, California) DSS-43, (Tidbenbilla, Australia) and DSS-63 (Madrid, Spain) will undergo major modifications which will increase the antenna gain by 1.9 dB at X-band and extend the aperture diameter from 64 to 70 meters. Although the antenna will remain essentially Cassegrainian, the main reflector will be "shaped" to a slightly non-parabolic surface contour to provide a uniform RF radiation pattern. A uniform radiation pattern would increase the antenna gain and efficiency; and when added to other gain increases realized by extending the antenna diameter, resurfacing the main reflector by using high-precision surface panels, reduced quadripod blockage, and better subreflector controllers, will reach the 1.9 dB gain differential.

A new subreflector needed to be designed, therefore, which is larger in diameter and "shaped" also in such a manner that it will complement the main reflector shape to keep a constant beam path length and improve the RF performance. This sub-

reflector, hereafter referred to as the new 70-m antenna subreflector, will be heavier, subject to greater wind loading due to its increased surface area, and will be located in a different position relative to the quadripod apex when compared to the original 64-m antenna subreflector.

Thus, the need to re-design the subreflector positioner for the new 70-m antenna was inevitable. An analytical procedure was developed which characterizes the subreflector surface and its positioner as one assembly having load-displacement relationships described by a "structural flexibility matrix." This flexibility matrix formulation then allows calculation of deflections and/or rotations of various components of the assembly for any given set of loading conditions. In this fashion, any component possessing excessive "compliance" will be noted, and the overall deflections and/or rotations of the subreflector relative to the apex will be determined.

Another part of the redesign process involved determining the new loads in each of the subreflector support shafts which connect the subreflector to the quadripod structure. The worst case loads were then used as criteria for the support shaft



design. This part of the design is presented in this report in terms of general analytical procedures which can be applied to other subreflector configurations in the antenna network.

In this report we present also the formulation of the subreflector loading conditions, the flexibility matrix, the general formulation of the procedure for the new 70-m subreflector positioner, a comparison of the strength versus loading of the subreflector support system, and the resulting key design details.

## II. Design Procedure

For economic reasons, the new 70-m antenna subreflector positioner design was constrained such that the new positioner should resemble the existing 64-m antenna positioner in both configuration and mechanical details as closely as possible. Several alternative configurations were considered, primarily to provide a new, more flexible five degree-of-freedom subreflector motion (two lateral [ $x$  and  $y$ ], one axial [ $z$ ], and two tilting motions) as opposed to the three-degree-of-freedom motion with the existing 64-m antenna subreflector positioner (two lateral [ $x$  and  $y$ ] and one axial [ $z$ ]). However, the project cost and schedule requirements forced the new 70-m subreflector positioner design to have minimal impact on existing control system hardware and/or software. These have dictated further the installation of only a new three-degree-of-freedom positioner which can have provisions for future addition of a tilting mechanism.

Figure 1 shows the existing 64-m antenna subreflector-positioner configuration relative to the quadripod apex. The significant changes for the new 70-m antenna subreflector concern the new larger subreflector design and its new mounting provision. Details of the 70-m antenna subreflector design which will impact the positioner, e.g., new subreflector weight and size, were taken into account in this analysis. Figures 2 and 3 show the axial and lateral motion mechanisms which are analogous between the 64-m and 70-m designs. The major portion of the redesign effort has centered around determining adequacy of strength and magnitude deflections of all major components of the positioner under the worst cases of wind and/or gravity loading conditions.

### A. Gravity and Wind Loads

The resultant loading matrix combining various antenna elevation angles and wind velocities and directions was calculated in two ways: first in terms of equivalent loads and moments at the subreflector and positioner centers-of-gravity, the results of which are used with the flexibility matrix to determine deflections and rotations of the subreflector relative to the apex; and second in terms of forces at the positioner support

shafts,  $z_1, z_2, z_3, y_1, y_2$ , and  $x_1$  shown in Figs. 2 and 3, the results of which are applied to the component strength analysis.

The sign conventions used for wind and gravity loading are shown in Fig. 4. For a given subreflector weight,  $W_s$ , and a given positioner suspended weight,  $W_p$ , the following relations express loads due to gravity:

$$\left. \begin{aligned} F_z &= -W_s \sin \alpha \\ F_y &= -W_s \cos \alpha \\ P_z &= -W_p \sin \alpha \\ P_y &= -W_p \cos \alpha \end{aligned} \right\} \quad (1)$$

where  $\alpha$  = antenna elevation angle;  $F_y, F_z$  = loads at the subreflector center-of-gravity (c.g.) in the directions indicated by the subscripts corresponding to the coordinates system defined in Figs. 1-3;  $P_y, P_z$  = loads at the positioner c.g., analogous to  $F_y, F_z$ . For the 70-m antenna subreflector,  $W_s = 10,400$  lb (46.26 kN) and  $W_p = 6800$  lb (30.25 kN).

Wind loads were determined<sup>1</sup> and compiled from subsonic wind-tunnel experiments using a paraboloid dish in a uniform air stream. This wind loads computation approach is conservative, since for all antenna orientations, the subreflector is partially shielded (by the quadripod legs or the positioner) from direct wind, implying that actual wind loads are likely to be less than those calculated by wind-tunnel coefficients. Table 1 lists the force and moment coefficients and the resulting forces and moments for a 70 mph (112 km/h) wind, which is the survival wind velocity limit for any arbitrary antenna attitude.

For determining forces and moments from the wind coefficients data we use, for example:

$$\begin{aligned} F_D &= C_D q A \\ M_p &= C_m q A D \end{aligned} \quad (2)$$

where

$F_D$  = drag force

$q$  = dynamic pressure of wind ( $= [1/2] \rho V^2$  where  $\rho$  is the air density and  $V$  is the wind velocity)

<sup>1</sup>N. L. Fox, et al., Preliminary Report on Paraboloidal Reflector Antenna Wind Tunnel Tests (JPL Internal Memorandum), JPL - CP3 (Reorder No. 62-709), Jet Propulsion Laboratory, Pasadena, Calif., 1962.

$A$  = subreflector aperture area

$D$  = subreflector diameter

$C_D$  = drag coefficient

$M_p$  = pitch moment

$C_m$  = moment coefficient

For the 70-m subreflector positioner,  $A = 512.7 \text{ ft}^2$  ( $47.63 \text{ m}^2$ ) and  $D = 25.55 \text{ ft}$  ( $7.79 \text{ m}$ ).

Note that since the wind tunnel test data convention was that moments were considered about the subreflector vertex, and since the loading analysis requires moments about the torus c.g. (assumed to be at the intersection of the  $z$ -axis and the  $x$ -plane passing through the centerline of the torus), the equivalent moments were calculated from the data in Table 1 according to:

$$M_t = M_{SR} - LF \quad (3)$$

where

$M_{SR}$  = a moment (pitch or yaw) about the subreflector vertex

$M_t$  = equivalent moment at torus c.g.

$L$  = axial distance between subreflector vertex and torus c.g.

$F$  = lateral force at subreflector vertex

Combined wind and gravity equivalent loads are found significant, as shown in Table 2, for a wind velocity of 30 mph (48 km/h) which is the operational limit wind velocity.

For the second method in which loading conditions were expressed as forces in the positioner support shafts, the following gives the shaft forces for *gravity* loading:

$$\left. \begin{aligned} y_1 = y_2 &= \left( \frac{W_s + W_p}{2} \right) \cos \alpha \\ z_1 &= \frac{W_s L_3 \cos \alpha + (W_p + W_s) L_1 \cos \alpha}{L_1 + L_2} \\ z_2 = z_3 &= 1/2 \left[ \frac{W_s L_3 \cos \alpha + (W_p + W_s) L_2 \sin \alpha}{L_1 + L_2} \right] \end{aligned} \right\} \quad (4)$$

where the variables are as defined in Fig. 4. For the 70-m positioner,  $L_1 = 39.0 \text{ in.}$  ( $0.991 \text{ m}$ ),  $L_2 = 56.0 \text{ in.}$  ( $1.422 \text{ m}$ ) and

$L_3 = 31.75 \text{ in.}$  ( $0.806 \text{ m}$ ). The following expressions give the shaft forces for *wind* loading:

$$\left. \begin{aligned} y_1 &= -F_L/2 + (L_2/L_5) F_y \\ y_2 &= -F_L/2 - (L_2/L_5) F_y \\ z_1 &= \frac{L_1}{L_1 + L_2} F_D + \frac{M_N}{L_1 + L_2} \\ z_2 &= 0.5 \left[ \frac{L_2 F_D}{L_1 + L_2} + \frac{M_N}{L_4} - \frac{M_N}{L_1 + L_2} \right] \\ z_3 &= 0.5 \left[ \frac{L_2 F_D}{L_1 + L_2} - \frac{M_N}{L_4} - \frac{M_N}{L_1 + L_2} \right] \end{aligned} \right\} \quad (5)$$

where

$F_L$  = lift force

$F_D$  = drag force

$F_y$  = lateral force

$M_p$  = pitch moment

$M_N$  = yaw moment, according to Fig. 4

For the 70-m positioner,  $L_4 = 53.0 \text{ in.}$  ( $1.35 \text{ m}$ ) and  $L_5 = 110.0 \text{ in.}$  ( $2.79 \text{ m}$ ).

Shaft forces for combined gravity and wind loads are listed in Table 3 for a 70 mph (112 km/h) wind velocity at various antenna attitudes, and in Table 4 for a 100 mph (160 km/h) wind velocity at stow attitude (antenna at zenith, elevation angle =  $90^\circ$ ). These conditions comprise the survivability limits in design. Worst-case loads from Tables 3 and 4 indicate a design load of 9953 lbs (443 kN) tension for the axial ( $z$ ) positioner mechanism shafts, and 4482 lb (199 kN) tension and compression for the lateral ( $x$ -axis) positioner shaft. For design purposes, these loads were rounded off to 10,000 and 4500 lbs (445, 200 kN), respectively.

## B. Strength of Mechanical Components

The mechanical components which connect the positioner-subreflector assembly to the quadripod structure comprise the positioner support system, and must withstand the loads due to gravity and wind. These loads are transmitted through the shaft assemblies for each of the three ( $x$ ,  $y$ , and  $z$ ) directions of positioner travel, according to the coordinate system shown in Figs. 1-3.

A shaft assembly consists of a rod, two universal joints, connecting hardware, and a ball-screw jack. The load-bearing

strength of each of these components was calculated by classical strength-of-materials methods, using simplifying assumptions where applicable. In some cases the manufacturer's rating is used for determining the strength of off-the-shelf components. Table 5 shows the load, strength, and factor of safety for support components. The only component having a marginal factor of safety (F. S.) is the y-axis screw jack, for which F. S. = 2.0. Since the strength of this component is based on the manufacturer's rating, which includes an additional factor of safety, the calculated factor of safety is considered adequate.

### C. Design Details

All remaining components that are part of the positioner assembly were designed according to the previously discussed loading conditions. The following is a list of significant differences in subreflector design details between the old 64-m antenna and the new 70-m antenna positioners:

- (1) The lateral and axial support rod lengths will increase to conform to the new 70-m antenna geometry.
- (2) The y-axis lateral support shaft assembly will be upgraded to have mechanical strength equivalent to that of the z-axis assembly.
- (3) The y-axis drive motor assembly will be upgraded to provide 18 ft-lb (24.4 N-m) of torque at the output shaft (vs 12 ft-lb or 16.3 N-m) and output velocity of 0.90 rpm (vs. 0.45 rpm).
- (4) The gear reducer box, which is part of the positional readout assembly, will be modified to provide the proper synchro rotation rate.
- (5) The axial motion mechanism drive shaft which is parallel to the y-axis (Fig. 2, top view) will be segmented to allow for possible future modification of the axial drive to tilt the subreflector about the elevation axis.
- (6) The rotational drive mechanism and the index pin actuator will be changed from a pneumatically-driven to a mechanically-driven device.

## III. Compliance Analysis

The motions of the subreflector relative to the main reflector which are induced by both gravity and wind loadings must be quantified for two reasons relating to improving the antenna performance:

- (1) Correctable motions will be compensated for by the subreflector positioner mechanism as controlled by the antenna servo controller. In the case of the new 70-m antenna positioner, z and y translations are

presently controlled to compensate for gravity-induced deflections, and the x-axis lateral motion mechanism is only used for manual alignment.

- (2) The remaining motions which are not correctable, such as the subreflector rotation, must not be excessive.

The results of a structural analysis using finite element computer models (such as JPL's IDEAS program) predict displacements of the quadripod apex relative to a best-fit paraboloid representing the main reflector. These displacements may be superimposed with the results of the positioner analysis to give overall relative motions required for the two reasons mentioned above. Thus, the required subreflector translations can be determined as a function of antenna elevation angle, and the resulting antenna performance may be estimated as described in Ref. 1.

### A. Load-Displacement Relationship

Using the "force method" of structural analysis, the flexibility matrix of the positioner-subreflector assembly was computed to describe the load-displacement relationship for each component. The force method expresses the load-displacement relationship as:

$$\{\delta\} = [F] \{P\} \quad (6)$$

where  $\{\delta\}$  is the displacement vector, consisting of translations and rotations of each major element of a structure (in this case, the positioner and the subreflector are the major elements);  $[F]$  is the flexibility matrix, whose elements represent the displacements at a given point of the structure caused by the application of a *unit load* at any other point of the structure;  $\{P\}$  is the load vector which consists of forces and moments at designated points on the structure.

Reference 2 describes the formulation of the flexibility matrix by summing the total strain energy contained in an externally loaded structure. The relationship described is written as:

$$[F] = [B]^T [f] [B] \quad (7)$$

where the matrix  $[B]$  is the "static transformation matrix" given by:

$$\{p\} = [B] \{P\} \quad (8)$$

and where  $[f]$  is a diagonal block matrix composed of elemental flexibility matrices; for example, for a system composed of three structural elements:

$$[f] = \begin{bmatrix} [f_a] & [0] & [0] \\ [0] & [f_b] & [0] \\ [0] & [0] & [f_c] \end{bmatrix} \quad (9)$$

For element  $a$ , for example,  $\{\delta_a\} = [f_a] \{P_a\}$  where  $\{\delta_a\}$  and  $\{P_a\}$  are the displacement and load vectors pertaining particularly to element  $a$ . In Eq. (8), the vector  $\{p\}$  is the vector of stress resultants which are caused by the application of loads  $\{P\}$ . The static transformation matrix is constructed by inspection such that Eq. (8) is satisfied.

## B. New Positioner-Subreflector Displacements

The displacement and load vectors of Eq. (6) are given for the positioner subreflector assembly as:

$$\begin{aligned} \{\delta\}^T &= \{U_s \quad V_s \quad W_s \quad V_p \quad W_p \quad \theta_x \quad \theta_y\} \\ \{P\}^T &= \{F_x \quad F_y \quad F_z \quad P_y \quad P_z \quad M_x \quad M_y\} \end{aligned} \quad (10)$$

where  $U_s, V_s, W_s$  = displacements of the subreflector vertex in the  $x, y$ , and  $z$  directions;  $\theta_x, \theta_y$  are rotations of the subreflector about the  $x$ -axis and  $y$ -axis, respectively;  $F_x, F_y, F_z$  are loads at the subreflector c.g. caused by wind forces and subreflector weight;  $P_y, P_z$  = loads of the positioner c.g. due to positioner weight;  $M_x, M_y$  = moment about positioner c.g. caused by lateral loads at subreflector c.g.

The positioner-subreflector assembly was viewed as consisting of two structural elements: one element included the subreflector, the backup structure, and bearing adaptor ring; the other element consisted of the remaining positioner components up to the point of attachment to the apex. The stiffnesses of the major components in these elements were calculated either by classical strength-of-materials methods, or by computer model for the more complex items. Table 6 indicates the spring constants for translation and rotation of the subreflector, and Figs. 1-3 identify the components.

The spring constants were used to assemble the elements of the flexibility matrices, and the above procedure was applied to determine the overall flexibility matrix shown in Table 7. The calculated subreflector displacements relative to the apex are shown in Table 8 for both the gravity and 30 mph (48 km/h) wind loading conditions described in Table 2. To quantify the effect of wind loading, Table 9 is presented, giving displacements for gravity loading with no wind.

Note that worst cases of lateral translation, axial translation, and rotation were unchanged because the effect of wind

loading at 30 mph (48 km/h) was not sufficient to surpass the effect of worst-case gravity loading. This situation is due to the fact that worst-case wind loading occurs at orientations other than those at which worst-case gravity loading occur. A case with greater wind velocity will indicate worst-case displacements occurring at different antenna orientations.

For worst-case deflections. The method of calculating gain losses due to subreflector translation and rotation is as follows: The RMS equivalent gain loss for lateral ( $y$ ) subreflector deflections is given by:

$$\text{RMS} = \frac{R_{\text{lat}} V_s}{m} \quad (11)$$

and for axial ( $z$ ) subreflector deflections by:

$$\text{RMS} = \frac{R_{\text{ax}} W_s}{m} \quad (12)$$

where  $R_{\text{lat}}$  and  $R_{\text{ax}}$  are proportionality constants obtained from curves developed by radiation pattern analysis for a range of antenna configurations (Ref. 3),  $m$  is the magnification factor:

$$m = (c + a)/(c - a) \quad (13)$$

where

- $a$  = distance from the subreflector origin to the vertex (subreflector treated as a hyperboloid)
- $c$  = distance from the subreflector vertex to the virtual focus (hyperboloid focal length)

For the 70-m antenna,  $a = 202.92$  in. (515.42 cm),  $c = 272.37$  in. (691.82 cm), giving  $m = 6.84$ .

The gain loss in decibels is given by the relation developed by Ruze:

$$\text{dB} = -4.3429 \left( \frac{4 \pi \text{RMS}}{\lambda} \right)^2$$

For X-band operation,  $\lambda = 1.396$  in. (3.546 cm). The pointing error is given by:

$$\theta_{px} = \frac{2 \theta_x (c - a) K}{f} \quad (14)$$

where  $\theta_x$  = subreflector rotation,  $f$  = antenna focal length, and  $K$  = the beam deviation factor (Ref. 1). For the 70-m antenna,  $f = 1072.0$  in. (2723 cm) and  $K = 0.76$ .

The equivalent gain losses corresponding to the root-mean-square (RMS) value of the main reflector surface distortion caused by subreflector translations, and the pointing error caused by subreflector rotation are indicated in Tables 8 and 9.

Displacements relative to the apex were used in calculating these performance parameters. Some subreflector displacements may actually be canceled by other antenna distortions. However, these RMS losses and pointing error values indicate relative subreflector-positioner structural integrity under various loading conditions.

## IV. Summary

The method of analysis that was developed for determining adequacy of strength of the subreflector supports and displacements of the subreflector vertex under various antenna loading conditions were described in general. The method can be extended to other antenna designs, although some minor details may have to be modified to apply to other subreflector-positioner configurations.

The design of the new 70-m antenna subreflector-positioner has generated an additional product, the determination of subreflector motions relative to the quadripod apex, which will be used in the antenna alignment and pointing error reduction analysis.

## References

1. Hughes, R. D. and Katow, M. S., Subreflector focussing techniques applied to new DSS-15 and DSS-45 34-m antennas, *TDA Progress Report 42-80*, Jet Propulsion Laboratory, Pasadena, Calif., October-December, 1984.
2. Levy, R. I., *Nuclear Weapons Effects on Shipboard Electronic Systems*, Department of the Navy, Washington D.C., May 24, 1962.
3. Katow, M. S., 34-meter antenna subreflector translations to maximize RF gain, *TDA Progress Report 42-62*, 112-120 January-February, 1981, Jet Propulsion Laboratory, Pasadena, CA.

**Table 1. Net subreflector wind coefficients, forces, and moments at 70 mph (112 km/h) wind**

Elev Angle, (deg)	Azimuth Angle, (deg)	Coefficients					Forces/Moments				
		$C_D$	$C_L$	$C_Y$	$C_N$	$C_P$	$F_{D'}$ klb (kN)	$F_{L'}$ lb (kN)	$F_{Y'}$ lb (kN)	$M_N$ ft. lb (Nm)	$M_P$ ft. lb (Nm)
0	0	1.5	0	0	0	0	9.4 (42)	0 (0)	0 (0)	0 (0)	0 (0)
0	60	1.58	0	0.29	-0.088	0	9.9 (44)	0 (0)	1.8 (8.1)	-14,133 (-19,164)	0 (0)
0	120	-0.20	0	0.39	0.138	0	-1.3 (-5.6)	0 (0)	2.5 (11)	22,163 (30,053)	0 (0)
30	0	1.46	-0.02	0	0	-0.04	9.2 (41)	-0.1 (-0.6)	0 (0)	0 (0)	-6,424 (-8,711)
45	0	1.48	0.11	0	0	-0.042	9.3 (41)	0.7 (3.1)	0 (0)	0 (0)	-6,745 (-9,146)
60	0	1.58	0.29	0	0	-0.088	9.9 (44)	1.8 (8.1)	0 (0)	0 (0)	-14,133 (-19,164)
90	0	-0.03	0.38	0	0	0.129	-0.2 (-0.8)	2.4 (11)	0 (0)	0 (0)	20,717 (28,092)

Notes: See Fig. 4 for definitions.

Antenna faces into wind for azimuth angle = 0.

**Table 2. Equivalent subreflector loads: gravity + 30 mph (48 km/h) wind**

Elev Angle, deg	Azimuth Angle, deg	$F_x$ , lb (kN)	$F_y$ , lb (kN)	$F_z$ , lb (kN)	$P_y$ , lb (kN)	$P_z$ , lb (kN)
0	0	0 (0)	-10 (-46)	-1.7 (-7.7)	-6.8 (-30)	0 (0)
0	60	-2.0 (-8.9)	-10 (-46)	-1.8 (-8.1)	-6.8 (-30)	0 (0)
0	120	0.2 (0.7)	-10 (-46)	0.2 (1.0)	-6.8 (-30)	0 (0)
30	0	0 (0)	-8.6 (-38)	-6.9 (-31)	-5.9 (-26)	-3.4 (-15)
45	0	0 (0)	-6.5 (-29)	-9.1 (-40)	-4.8 (-21)	-4.8 (-21)
60	0	0 (0)	-3.2 (-14)	-10.8 (-48)	-3.4 (-15)	-5.9 (-26)
90	0	0 (0)	-0.1 (-0.5)	-10.4 (-46)	0 (0)	-6.8 (-30)

Note:  $F_x$ ,  $F_y$ ,  $F_z$  are forces acting at the subreflector c.g., including the effect of moments.  $P_y$ ,  $P_z$  are forces acting at the positioner c.g.

**Table 3. 70-m antenna subreflector positioner support loads: gravity + 70 mph (112 km/h) wind**

Elev, deg	Azimuth, deg	Forces in Support Rods, klb (kN)					
		$Z_1$	$Z_2$	$Z_3$	$Y_1$	$Y_2$	$X_1$
0	0 <sup>a</sup>	7.4 (33)	1.0 (4.4)	1.0 (4.4)	8.6 (38)	8.6 (38)	0
0	60	7.6 (34)	-1.5 (-6.7)	3.9 (17)	9.5 (42)	7.7 (34)	1.8 (8.0)
0	120	3.0 (13)	-1.1 (-4.9)	-3.1 (-14)	9.9 (44)	7.4 (33)	2.5 (11)
30	0 <sup>a</sup>	9.6 (43)	4.1 (18)	4.1 (18)	7.5 (33)	7.5 (33)	0
45	0 <sup>a</sup>	10.0 (44)	5.8 (26)	5.8 (26)	5.7 (25)	5.7 (25)	0
60	0 <sup>a</sup>	8.9 (40)	8.0 (36)	8.0 (36)	2.6 (12)	2.6 (12)	0
90	0 <sup>a</sup>	8.0 (36)	6.5 (29)	6.5 (29)	-1.2 (-5.3)	-1.2 (-5.3)	0

<sup>a</sup>At AZ = 0, antenna points directly into wind.

**Table 4. 70-m antenna subreflector positioner support loads: gravity + 100 mph (160 km/h) wind (stow condition)**

Elev, deg	AZ, Deg	Forces in Support Rods, klb (kN)					
		$Z_1$	$Z_2$	$Z_3$	$Y_1$	$Y_2$	$X_1$
90	0	8.9 (39.7)	4.0 (17.6)	4.0 (17.6)	-2.4 (-10.9)	-2.4 (-10.9)	0
90	90	6.9 (30.7)	6.8 (30.0)	3.2 (14.0)	2.5 (11.1)	-2.5 (-11.1)	4.5 (19.9)
90	180	5.2 (23.2)	6.2 (27.5)	6.2 (27.5)	2.4 (10.9)	2.4 (10.9)	0
90	270	7.2 (32.1)	3.4 (15.1)	6.9 (30.7)	-2.5 (-11.1)	2.5 (11.1)	-4.5 (-19.9)

**Table 5. 70-m antenna subreflector positioner support component strength**

Component	Load, klb (kN)	Strength <sup>a</sup> klb (kN)	Factor of Safety
S/R Rotation Bearing	58.6 (260.5)	744.0 (3309.3) (R)	12.7
Axial Rods	10.0 (44.5)	68.4 (304.2) (Y)	6.8
Axial Universal Joint	10.0 (44.5)	54.0 (240.2) (R)	5.4
Axial U-Joint Pin	10.0 (44.5)	51.2 (227.8) (Y)	5.1
Lateral (y) Rod	10.0 (44.5)	45.0 (200.2) (Y)	4.5
Lateral (y) Universal Joint	10.0 (44.5)	39.0 (173.5) (R)	3.9
Lateral (y) U-Joint Pin	10.0 (44.5)	51.2 (227.8) (Y)	5.1
Lateral (x) Rod	4.5 (20.0)	45.0 (200.2) (Y)	10.0
Lateral (x) Universal Joint	4.5 (20.0)	39.0 (173.5) (R)	8.7
Lateral (x) U-Joint Pin	4.5 (20.0)	51.2 (227.8) (Y)	11.4
Axial Screw Jack	10.0 (44.5)	40.0 (177.9) (R)	4.0
Lateral (y) Screw Jack	10.0 (44.5)	20.0 (89.0) (R)	2.0
Lateral (x) Screw Jack	4.5 (20.0)	20.0 (89.0) (R)	4.4

<sup>a</sup>Based on tensile yield stress (y) or rated capacity (r).

**Table 6. 70-m antenna subreflector positioner spring constants**

Component	Rotational (N/rad) $\times 10^8$			Translational (N/m) $\times 10^6$		
	$K_{x-x}$	$K_{y-y}$	$K_{z-z}$	$K_x$	$K_y$	$K_z$
Axial Adjustment Mech.	4.49	4.10	--	---	---	267.9
Torus + Lateral Adjustment Mechanism	3.38	1.47	1.78	31.5	131.3	210.1
Torus-to-Bearing Adaptor	22.15	22.15	--	---	---	6129.1
Rotation Bearing	21.0	21.0	--	3502.4	3502.4	7004.7
Bearing-to-S/R Adaptor	58.70	58.70	--	3467.3	3467.3	53060.8
Subreflector + Back-up Structure	9.10	9.10	--	218.9	218.9	646.2

NOTE: Unlisted items are considered infinitely stiff. See Figs. 1-3 for definitions.



**Table 7. 70-m antenna subreflector/positioner flexibility matrix load-displacement relationship (Eq. 6) given by:  $\{\delta\} = [F]\{P\}$**

(displacement vector = flexibility matrix • load vector)

$\left\{ \begin{array}{l} U_s, \text{ in. (m)} \\ V_s, \text{ in. (m)} \\ W_s, \text{ in. (m)} \\ V_p, \text{ in. (m)} \\ W_p, \text{ in. (m)} \\ \theta_x, \text{ rad} \\ \theta_y, \text{ rad} \end{array} \right\}$	=	$\begin{bmatrix} 9.33 \times 10^{-6} \\ (5.33 \times 10^{-8}) & 0 & 0 & 0 & 0 & 0 & 5.47 \times 10^{-8} \\ & (1.23 \times 10^{-8}) & & & & & \\ 0 & 3.96 \times 10^{-6} & 0 & 2.24 \times 10^{-5} & 0 & 3.67 \times 10^{-8} & 0 \\ & (2.26 \times 10^{-8}) & & (1.28 \times 10^{-7}) & & (8.25 \times 10^{-9}) & \\ 0 & 0 & 1.81 \times 10^{-6} & 0 & 1.54 \times 10^{-6} & 0 & 0 \\ & & (1.03 \times 10^{-8}) & & (8.79 \times 10^{-9}) & & \\ 0 & 2.24 \times 10^{-6} & 0 & 1.38 \times 10^{-6} & 0 & 2.72 \times 10^{-8} & 0 \\ & (1.28 \times 10^{-8}) & & (7.88 \times 10^{-9}) & & (6.12 \times 10^{-9}) & \\ 0 & 0 & 1.54 \times 10^{-6} & 0 & 1.54 \times 10^{-6} & 0 & 0 \\ & & (8.79 \times 10^{-9}) & & (8.79 \times 10^{-9}) & & \\ 0 & 3.67 \times 10^{-8} & 0 & 2.72 \times 10^{-8} & 0 & 1.80 \times 10^{-10} & 0 \\ & (8.25 \times 10^{-9}) & & (1.55 \times 10^{-10}) & & (1.59 \times 10^{-9}) & \\ 5.47 \times 10^{-8} & 0 & 0 & 0 & 0 & 0 & 1.8 \times 10^{-10} \\ (1.23 \times 10^{-8}) & & & & & & (1.59 \times 10^{-9}) \end{bmatrix}$	$\left\{ \begin{array}{l} F_x, \text{ lb (N)} \\ F_y, \text{ lb (N)} \\ F_z, \text{ lb (N)} \\ P_x, \text{ lb (N)} \\ P_y, \text{ lb (N)} \\ P_z, \text{ lb (N)} \\ M_x, \text{ in-lb (N-m)} \\ M_y, \text{ in-lb (N-m)} \end{array} \right\}$
--	---	---	--

**Table 8. Subreflector displacements relative to apex gravity + 30 mph (48 km/h) wind**

Elev., deg	Azim, deg	$10^{-3} U_{s'} \text{ in. (mm)}$	$10^{-3} V_{s'} \text{ in. (mm)}$	$10^{-3} W_{s'} \text{ in. (mm)}$	$\theta_x, 10^{-3} \text{ rad}$	$\theta_y, 10^{-3} \text{ rad}$
0	0	0	-56 <sup>(1)</sup> (-1.42)	-3 (-0.08)	-0.567	0
0	60	-19 (-0.48)	-56 (-1.42)	-3 (-0.08)	-0.567	-0.109 <sup>(3)</sup>
0	120	2 (0.05)	-56 (-1.42)	-0.4 (-0.01)	-0.567	$9.14 \times 10^{-3}$
30	0	0	-47 (-1.19)	-18 (-0.46)	-0.477	0
45	0	0	-37 (-0.94)	-24 (-0.61)	-0.369	0
60	0	0	-20 (-0.51)	-29 <sup>(2)</sup> (-0.74)	-0.210	0
90	0	0	-0.4 (-0.01)	-29 (-0.74)	$-3.74 \times 10^{-3}$	0

**NOTES:**

(1) RMS Equivalent Gain Loss =  $1.5 \times 10^{-4}$  in. ( $3.70 \times 10^{-4}$  cm) or  $7.48 \times 10^{-6}$  db at X-band  $\lambda = 3.546$  cm

(2) RMS Equivalent Gain Loss =  $2.2 \times 10^{-3}$  in. ( $5.59 \times 10^{-4}$  cm) or  $1.8 \times 10^{-3}$  db at X-band  $\lambda = 3.546$  cm

(3) Pointing Error =  $1.07 \times 10^{-5}$  rad (0.037 arc-minutes)

**Table 9. Subreflector displacements relative to apex gravity only**

Elev., deg	$10^{-3} U_{s'} \text{ in. (mm)}$	$10^{-3} V_{s'} \text{ in. (mm)}$	$10^{-3} W_{s'} \text{ in. (mm)}$	$\theta_x, 10^{-3} \text{ rad}$	$\theta_y, 10^{-3} \text{ rad}$
0	0	-56 <sup>(1)</sup> (-1.42)	0	-0.567 <sup>(3)</sup>	0
30	0	-49 (-1.24)	-15 (-0.38)	-0.491	0
45	0	-40 (-1.02)	-21 (-0.53)	-0.401	0
60	0	-28 (-0.71)	-25 (-0.64)	-0.283	0
90	0	0	-29 <sup>(2)</sup> (-0.74)	0	0

**NOTES:**

(1) RMS Equivalent Gain Loss =  $1.5 \times 10^{-4}$  in. ( $3.70 \times 10^{-4}$  cm) or  $7.48 \times 10^{-6}$  db at X-band  $\lambda = 3.546$  cm

(2) RMS Equivalent Gain Loss =  $2.2 \times 10^{-3}$  in. ( $5.59 \times 10^{-4}$  cm) or  $1.8 \times 10^{-3}$  db at X-band  $\lambda = 3.546$  cm

(3) Pointing Error =  $5.56 \times 10^{-5}$  rad (0.19 arc-minutes)

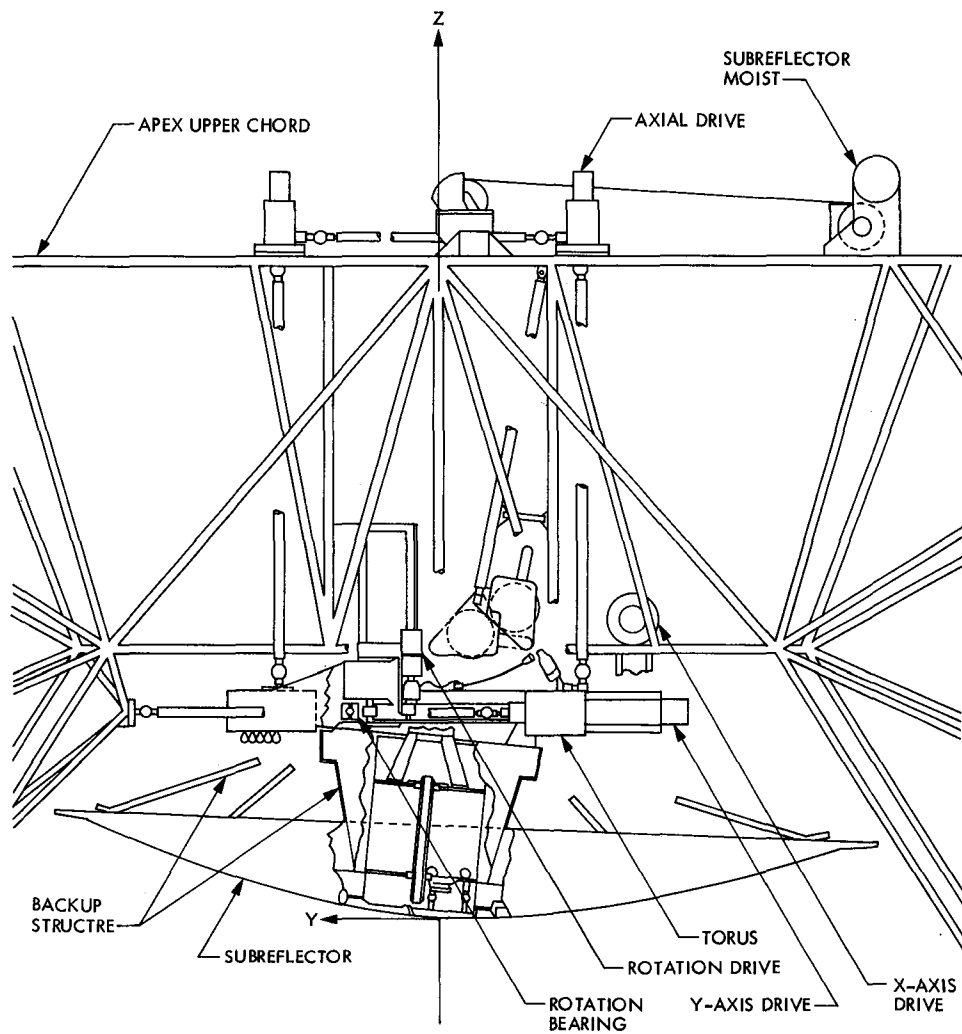


**Fig. 1. Subreflector positioner mechanism**

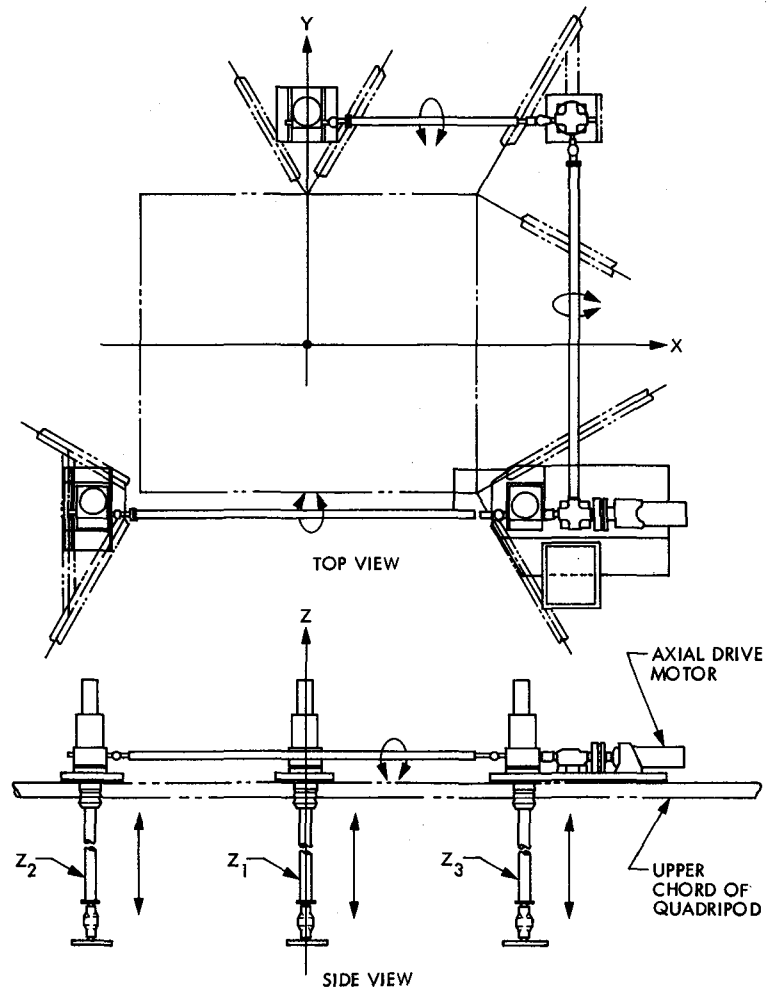


**Fig. 2. Subreflector positioner axial motion mechanism**

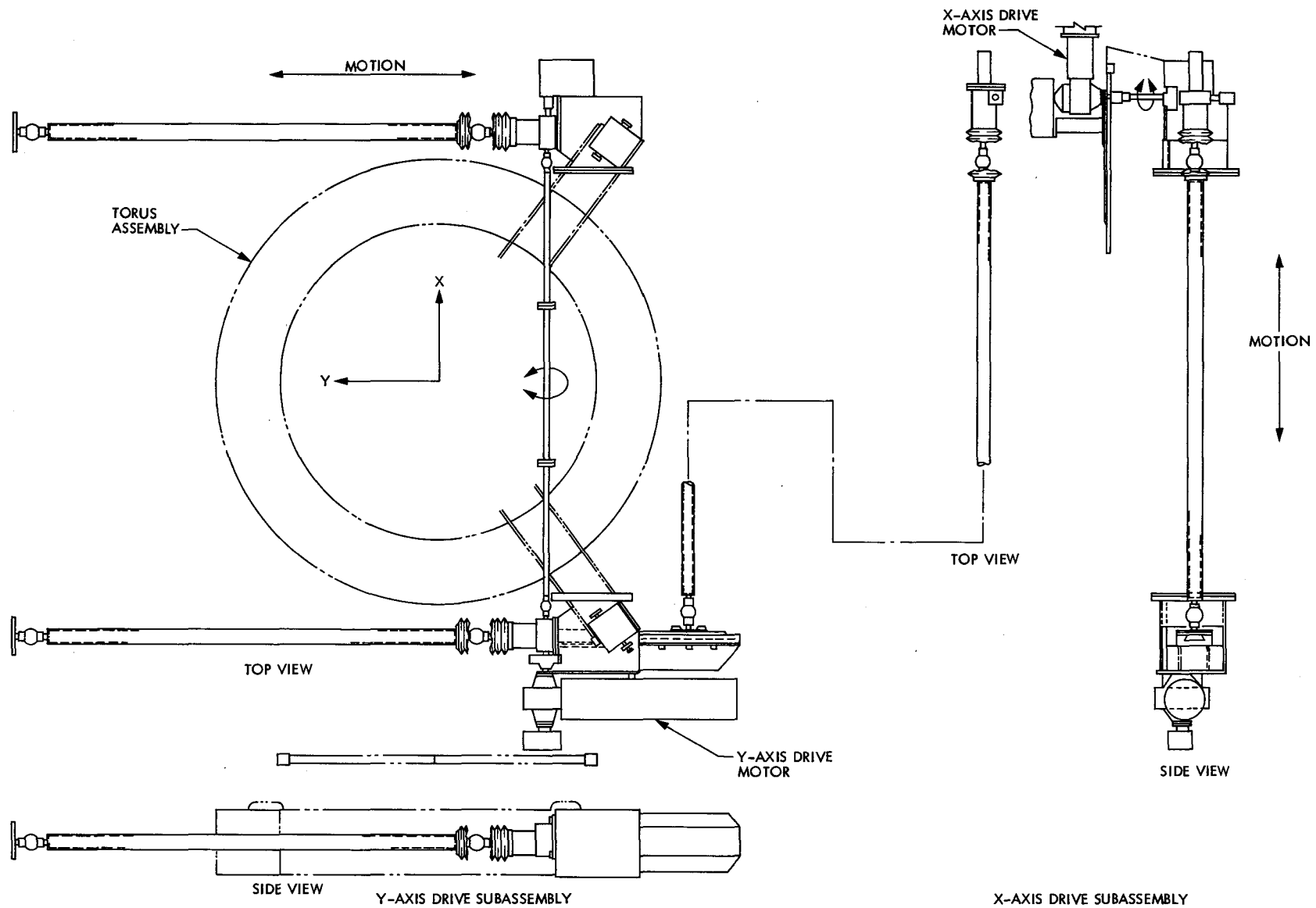
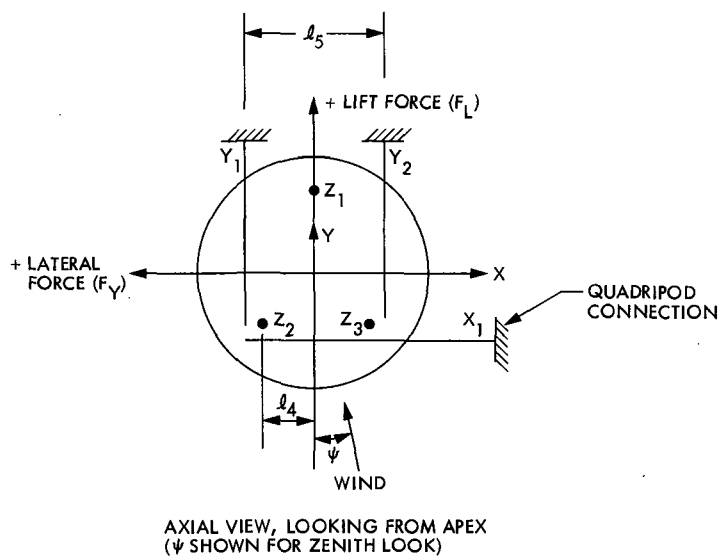


**Fig. 3. Subreflector positioner lateral motion mechanism**



NOTE:  $\psi$  = AZIMUTH ANGLE  
 $\alpha$  = ELEVATION ANGLE

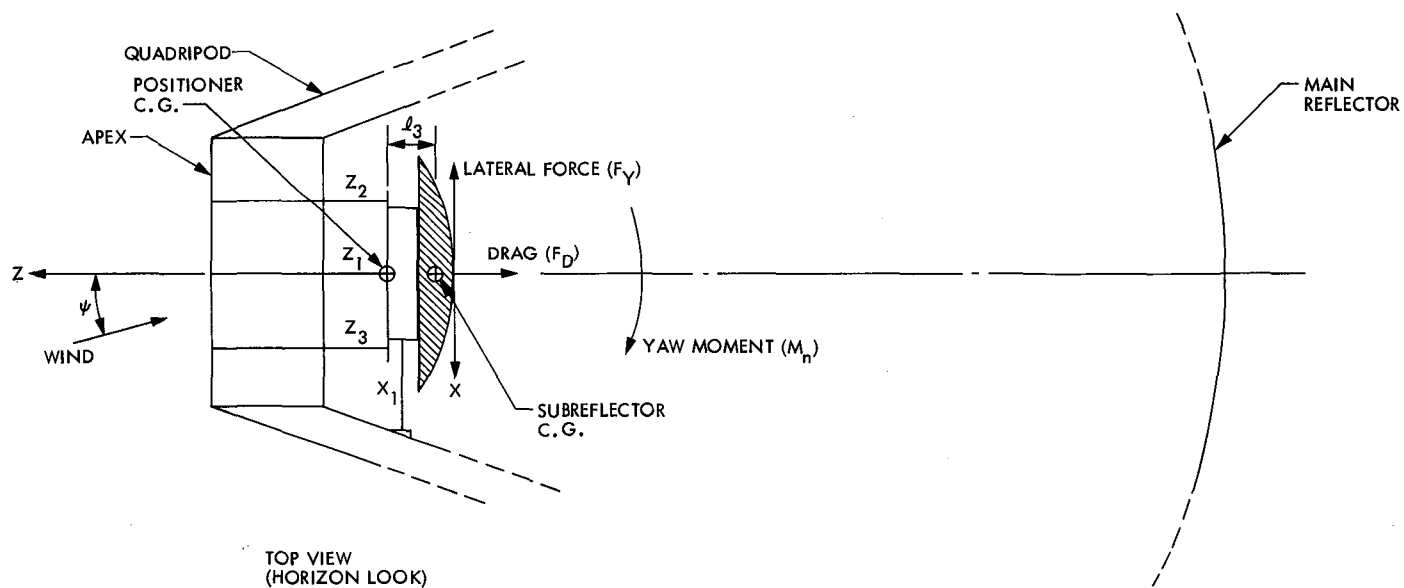
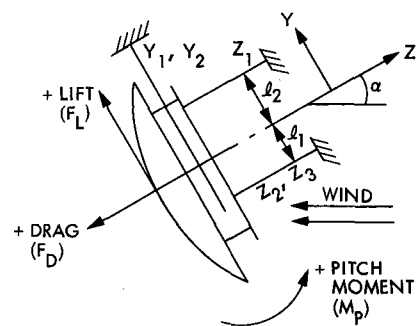


Fig. 4. Wind and gravity force conventions

# Subreflector Focusing Techniques Applied to New DSS-15 and DSS-45 34-Meter Antennas

R. D. Hughes and M. S. Katow  
Ground Antennas and Facilities Engineering Section

*An improved technique for determining the subreflector translations required to properly focus a Cassegrainian antenna, under gravity loading, at a full range of elevation angles, is presented. This technique is applied to the 34-m antenna configuration installed at stations DSS-15 (Goldstone, California) and DSS-45 (Australia). The subreflector lateral and axial translations, to be stored into the antenna-control systems, are computed and tabulated. The relationships that govern the main parameters are also presented for future subreflector focusing analysis under wind and thermal loadings.*

## I. Introduction

Future upgrades and the improved gain/noise ratio (G/T) operation of the Deep Space Network (DSN) antennas at X-band and at higher frequencies has created stringent requirements for maintaining minimum dimensional tolerances of various major components for precision motion. The subreflector position controller (s) is a key component in improving focusing. A refined technique has been developed to accurately determine the subreflector focusing motions as a function of the antenna elevation angle. The resulting subreflector motions are effected by the microprocessor-controlled subreflector servo-positioner mechanism in order to maximize antenna gain by compensating for gravity-induced deformations as the elevation angle changes.

As with techniques conventionally used in the past, the new technique involves ray tracing using geometric optics to compute the required subreflector motions through the full range of elevation angles. However, new procedures have been

included such that the antenna's secondary virtual focus coincides, after focusing is completed, with the main reflector's "best-fit" focus, as shown in Fig. 1. The system's "best-fit" parameters are determined according to the best-fit reflector configuration (still a paraboloid). The latter is the best approximation, by the least-squares method, of the deformed main reflector at a given elevation angle (Ref. 1). Figure 1 also shows the reference coordinate-system orientation used in our analysis. Tables 1 and 2 show lateral ( $Y$ ) and axial ( $Z$ ) subreflector offsets as a function of the antenna elevation angle. (The results of the IDEAS structure program analysis will be entered into the subreflector control logic.) These offset tables will provide initial positioning data which may be refined in the future as the antennas are calibrated using the known star-tracking procedure.

Although the 34-m antennas have "shaped" main and subreflectors, the use of a close-fitting paraboloid for the analysis in this study should provide accurate answers.

## II. Analysis

The 34-m AZ-EL antenna design for both stations is structurally identical. The parameters describing the deformed antenna configuration under varying gravity loadings were studied both analytically and experimentally. First, structural deflections were modeled by the finite-element method using JPL's IDEAS computer program (Ref. 2). Relative motions of major antenna components with respect to the computed best-fit paraboloid were determined (Ref. 1). Second, subreflector motions relative to the quadripod apex, which were due to the subreflector positioner mechanism deflections, were determined by measurements. A test fixture was constructed, by the vendor (TIW at Sunnyvale, California), to carry the subreflector and the positioner mechanism. This fixture was tipped at various angles, simulating elevation angle changes of the antenna and/or the subreflector. Use of this test fixture data is discussed later on for individual loading cases.

The results of the IDEAS computer program were obtained for two cases: (1) Y-gravity loading with a unit gravity load (1.0g, where  $g$  is the acceleration of gravity) is applied in the Y-direction to simulate antisymmetric loading conditions when the antenna is oriented in the horizon position ( $E = 0$ , where  $E$  is the elevation angle); and (2) Z-gravity loading with unit gravity load (1.0g) applied in the Z-direction to simulate the symmetric loading conditions when the antenna is in the zenith-look position ( $E = 90^\circ$ ).

The major components of the Cassegrainian antenna, with the exception of the subreflector positioner mechanism, act together as a single elastic structure under gravity loading. Therefore, the principle of superposition may be applied, and the following relationships exist for subreflector positioning:

$$\text{Axial correction} = \Delta Z = \Delta Z_0 (\sin E - \sin E_r) \quad (1)$$

$$\text{Lateral correction} = \Delta Y = \Delta Y_0 (\cos E - \cos E_r) \quad (2)$$

where

$\Delta Z_0$  = axial correction required for unit (1.0g) Z-direction load

$\Delta Y_0$  = lateral correction required for unit (1.0g) Y-direction load

$E$  = antenna elevation angle

$E_r$  = antenna-rigging angle, the elevation angle at which the main reflector panels are set in the field to ideally form an undistorted paraboloid surface

The beam deviation or reflection ratio,  $K$ , is defined as the "cumulative" ratio of the angle of reflection to the angle of

incidence of the "transmitted" beam rays. This ratio,  $K$ , is not equal to unity due to the nature of the RF radiation pattern in this type of antenna. The beam deviation or reflection ratio,  $K$ , is determined from Fig. 2, taken from Ref. 3. Figure 2 relates various antenna performance parameters to the ratio of the main reflector focal length to the aperture diameter ( $F/D$ ), and was constructed using the JPL Radiation Program as described in detail in Ref. 3. For the 34-m antenna, under study,  $F/D = 0.324$ , which gives  $K = 0.775$ . The following two extreme gravity-loading cases are presented in order to determine the subreflector focusing parameters at any elevation angle between  $0^\circ$  and  $90^\circ$ .

### A. Gravity Loading at Zenith Look

Figure 3 illustrates the geometry of the deflections involved in the Z-gravity loading case. The known parameters in Fig. 3, obtained from the design configuration and the computer model are:

$f$  = design focal length = 1102.36 cm (434.0 in.)

$f'$  = "best-fit" focal length = 1101.93 cm (433.83 in.)

$U$  = "best-fit" main-reflector vertex axial offset = 0.373 cm (0.147 in.)

$V$  = subreflector vertex axial offset = 0.417 cm (0.164 in.)

$W$  = axial displacement of the main reflector focus =  $(f - f' - U) = 0.058$  cm (0.023 in.)

$Z$  = required axial subreflector translation for unit (1.0g) gravity load in +Z-direction =  $e + d = 0.475$  cm (0.187 in.)

To illustrate the concept of having an effective gravity load in the +Z-direction, suppose that the antenna was "rigged" at zenith, then moved to horizon. The net change in gravity loading would be 1.0g in the +Z-direction, and the subreflector would have to be moved axially, toward the main reflector, for proper focusing since the main reflector becomes deeper. Equation (1) follows this behavior.

Table 1 lists the required total axial-focusing translations as a function of the elevation angle, for a rigging angle of  $45^\circ$ . The tabulated values were obtained by adding the measured positioner-mechanism axial deflections to the  $\Delta Z$  values obtained by using Eq. (1) at each elevation angle (with  $\Delta Z_0 = 0.475$  cm). Since the positioner-mechanism deflections were originally measured relative to horizon-loading conditions, the measured values indicated in Table 1 have been redefined in terms of a  $45^\circ$  rigging angle. Linear interpolation was used to determine the positioner-deflection corrections at intermediate angles. Note that the net  $\Delta Z$  from the horizon to zenith positions (0.686 cm or 0.270 in.) indicated in Table 1 is equal to



the sum of  $\Delta Z_0$  and the net positioner deflection, i.e., (0.475 + 0.0457 + 0.1651) cm.

## B. Gravity Loading at Horizon Look

Figure 4 illustrates the geometry of the antenna deflections in the Y-gravity loading case. The known design parameters are:

- $a$  = length from subreflector vertex to primary design focus = 541.54 cm (213.206 in.)
- $b$  = length from subreflector vertex to secondary design focus = 69.35 cm (27.305 in.)
- $f$  = design reflector focal length = 1102.36 cm (434.0 in.)
- $d$  = feed lateral displacement = 0.983 cm (0.387 in.)
- $e$  = main reflector vertex lateral displacement = 3.439 cm (1.354 in.)
- $\beta$  = angular displacement of "best-fit" focal axis = 0.002577 rad

From the combined computer model deflections and measured deflections of the subreflector positioner one obtains

- $c$  = subreflector vertex lateral translation = 3.084 cm (1.214 in.)
- $\alpha$  = subreflector focal axis angular displacement = 0.00169 rad

Focal length changes for this case are relatively small and are considered negligible. From the geometry shown in Fig. 4, the remaining parameters may be calculated as follows:

- $m = \alpha a = 0.914$  cm (0.360 in.)
- $n = c + m - d = 3.015$  cm (1.187 in.)
- $\delta = n/a = 0.00557$  rad
- $W = \delta b = 0.386$  cm (0.152 in.)
- $P = b\alpha = 0.1171$  cm (0.0461 in.)
- $q = c - p - w = 2.581$  cm (1.016 in.)
- $r = \beta f = 2.840$  cm (1.118 in.)
- $s = e - r = 0.599$  cm (0.236 in.)
- $t = q + s = 3.180$  cm (1.252 in.)
- $h = tk = 2.464$  cm (0.970 in.)
- $\gamma = (r - h)/f = 0.000341^\circ$  (1.17 arc sec)

The angle,  $\gamma$ , is the boresight-pointing error due to subreflector lateral misalignments. The computational procedure performed above may be applied in general to AZ-EL antennas

to determine the boresight-pointing error due to lateral subreflector misalignments.

The focused antenna configuration for the y-gravity loading case is shown in Fig. 5, where  $\Delta y_0$  is the required subreflector translation. The known quantities in the figure are:  $a$ ,  $b$ ,  $d$ ,  $s$ , and  $\alpha$ . There are three unknown quantities:  $\theta$ ,  $\ell$ , and  $g$ . By simple geometric analysis, the following equations may be derived:

$$\theta = (g - d)/a \quad (3)$$

$$\ell = \alpha(a + b) - g \quad (4)$$

$$\theta = (s - \ell)/b \quad (5)$$

Since  $\ell$  is the only unknown pertaining directly to  $\Delta y_0$ , Eqs. (3), (4), and (5) were combined so that  $\theta$  and  $g$  were eliminated, and the following expression for  $\ell$  is obtained:

$$\ell = \frac{1}{1 - a/b} [\alpha(a + b) - \frac{a}{b} S - d] \quad (6)$$

For this case,  $\ell = 0.681$  cm (0.268 in.). The required subreflector translation is:

$$\Delta y_0 = \ell + c - p \quad (7)$$

By referring to Figs. 4 and 5, then

$$\Delta y_0 = 3.647 \text{ cm (1.436 in.)}$$

It should be noted that in this case, the subreflector vertex lateral deflection ( $c = 3.084$  cm) was calculated by taking into account the measured deflection and rotation of the subreflector due to positioner-mechanism flexibilities, as well as the computer model results for apex translation and rotation. The required subreflector lateral translations, as a function of the elevation angle, were obtained using Eq. (2), and are presented in Table 2. The measured positioner-mechanism lateral deflections were taken into account by incorporation of the zenith-to-horizon deflection in  $\Delta y_0$ , instead of by reperforming the entire computational procedure at each elevation angle. This modified approach avoids unnecessary computations and provides accurate results, since the positioner-mechanism lateral deflection trend changes similar to  $\cos \theta$  as the elevation angle changes.

## III. Summary

For two 34-m diameter AZ-EL-type Cassegrainian antennas, a refined analysis was made to determine the boresight-pointing error, lateral, and axial translations required to properly focus the subreflector as a function of the antenna elevation angle. Deformations of the components comprising the

antenna must be quantified for zenith and horizon gravity-loading conditions. This analysis was applied to the 34-m antenna configuration most recently installed at the two tracking stations DSS-15 and DSS-45.

By utilizing Eqs. (1) and (2) with the appropriate geometric relationships the required subreflector translations for other types of loads, e.g., wind or thermal, may be determined in a similar fashion using this new procedure.

## References

1. Katow, M. S., and Schmele, L. W., "Antenna structures: Evaluation Techniques of Reflector Distortions," *Space Programs Summary*, Special Publication Summary 37-40, Vol. IV, pp. 176-184, Jet Propulsion Laboratory, Pasadena, CA, September, 1968.
2. Levy, R., "Optimization of Antenna Structure Design," *Eighth Conference on Electronic Computation*, ASCE, pp. 114-129, Houston, Texas, Feb., 1983.
3. Katow, M. S., "34-Meter Antenna - Subreflector Translations to Maximize RF Gain," *TDA Progress Report 42-62*, pp. 112-120, Jet Propulsion Laboratory, Pasadena, CA, January and February, 1981.

**Table 1. Required axial (Z) subreflector correction as a function of the elevation angle (rigging angle = 45°)**

Elevation angle (deg)	Positioner correction (measured) cm (in.)		Total correction cm (in.)	
90 (zenith)	0.0457	(0.018)	0.185	(0.073)
85	0.0203	(0.017)	0.180	(0.071)
80	0.0406	(0.016)	0.173	(0.068)
75	0.0381	(0.015)	0.161	(0.063)
70	0.0330	(0.013)	0.144	(0.057)
65	0.0254	(0.010)	0.120	(0.047)
60	0.0203	(0.008)	0.096	(0.038)
55	0.0127	(0.005)	0.066	(0.026)
50	0.0076	(0.003)	0.035	(0.014)
45	0	(0)	0	(0)
40	-0.0178	(-0.007)	-0.048	(-0.019)
35	-0.0356	(-0.014)	-0.099	(-0.039)
30	-0.0533	(-0.021)	-0.152	(-0.060)
25	-0.0711	(-0.028)	-0.206	(-0.081)
20	-0.0914	(-0.036)	-0.264	(-0.104)
15	-0.1118	(-0.044)	-0.325	(-0.128)
10	-0.1270	(-0.050)	-0.381	(-0.150)
5	-0.1473	(-0.058)	-0.442	(-0.174)
0 (horizon)	-0.1651	(-0.065)	-0.501	(-0.197)
Net, horizon-to-zenith motion	0.2108	0.083	0.686	0.270

**Table 2. Required lateral (Y) subreflector corrections as a function of the elevation angle (rigging angle = 45°)**

Elevation angle (deg)	Correction cm (in.)	
90 (zenith)	-2.578	(-1.015)
85	-2.261	(-0.890)
80	-1.943	(-0.765)
75	-1.633	(-0.643)
70	-1.331	(-0.524)
65	-1.036	(-0.408)
60	-0.754	(-0.297)
55	-0.488	(-0.192)
50	-0.234	(-0.092)
45	0	0
40	0.211	(0.083)
35	0.409	(0.161)
30	0.579	(0.228)
25	0.726	(0.286)
20	0.851	(0.335)
15	0.945	(0.372)
10	1.013	(0.399)
5	1.054	(0.415)
0 (horizon)	1.069	(0.421)

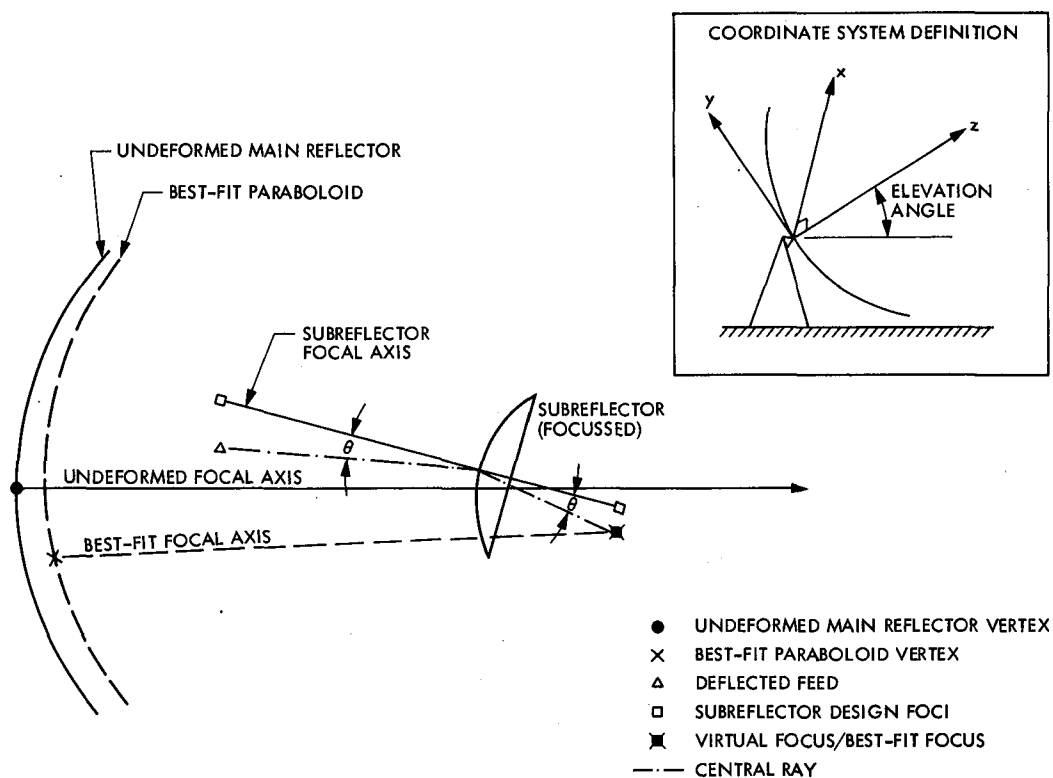


Fig. 1. Focused Cassegrainian geometry, with best-fit parabola

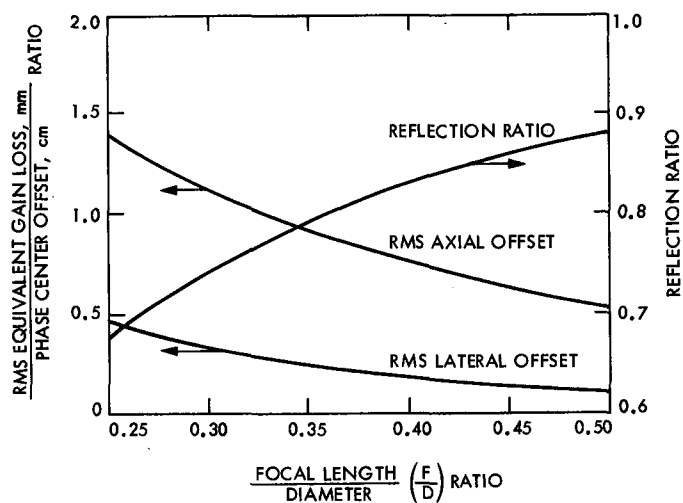


Fig. 2. Antenna gain reduction and reflection ratio as a function of the subreflector offset and paraboloid F/D ratio

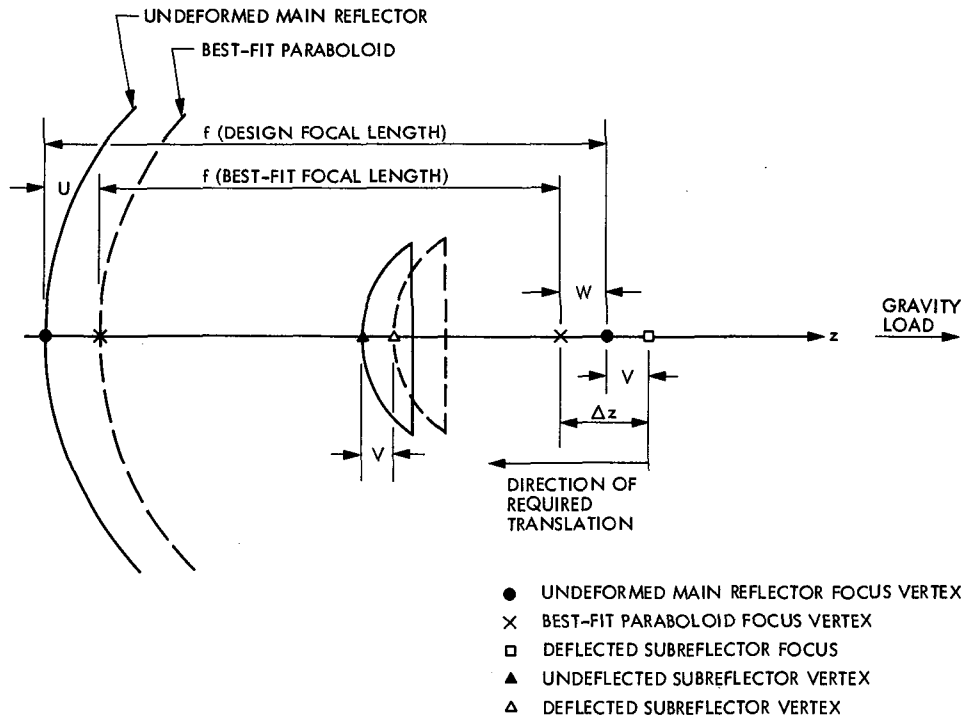


Fig. 3. Deflections and translations for zenith loading

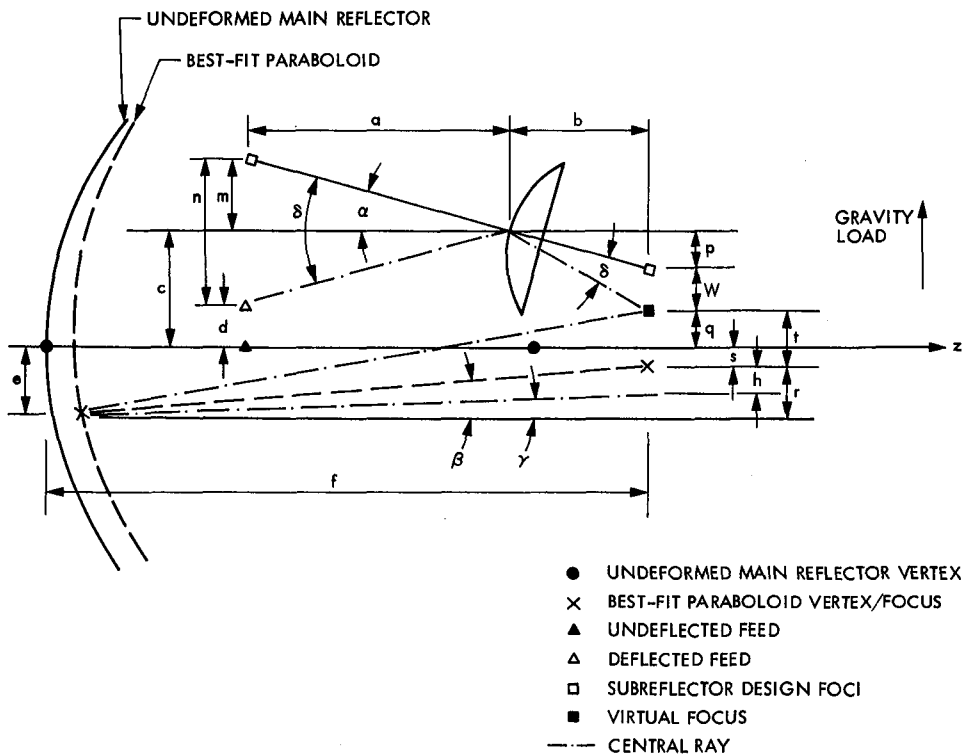
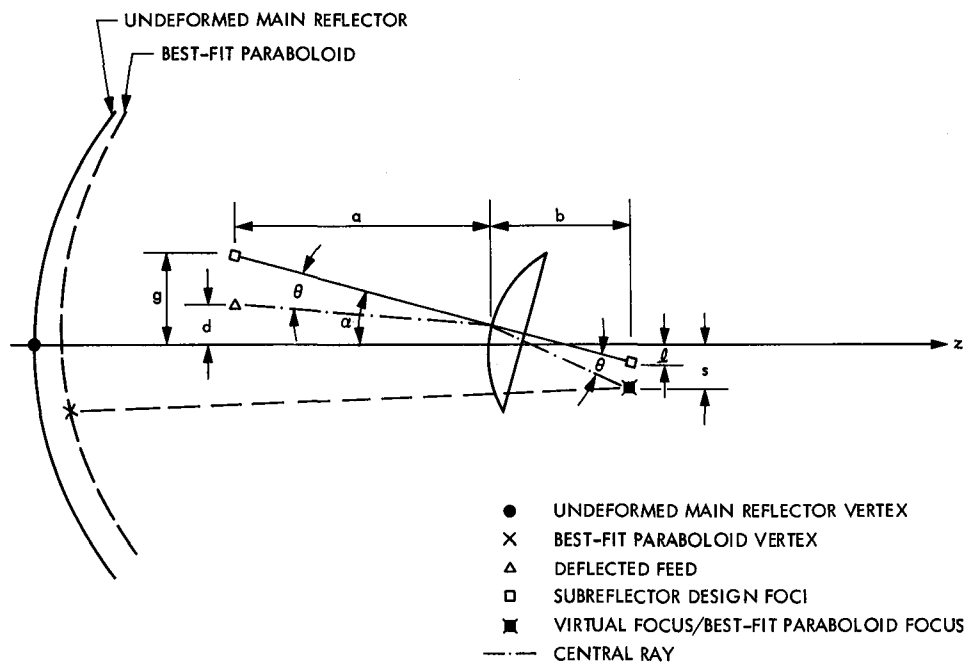


Fig. 4. Deflections for horizon loading



**Fig. 5. Focused configuration for horizon loading**

# Reed-Solomon Code Synchronization Revisited

L. J. Deutsch

Communications Systems Research Section

*A concatenated coding scheme consisting of an inner (7, 1/2) convolutional code and an outer (255, 223) Reed-Solomon code has been recommended by the Consultative Committee for Space Data Systems for cross-supported space missions. The Reed-Solomon code that was chosen makes use of the Berlekamp encoding algorithm. This report examines some peculiarities of this code that could give rise to synchronization problems. Suggestions are given to alleviate these problems.*

## I. Introduction

Concatenated coding for deep space missions was developed in response to a need for a relatively error-free channel for high digital data rates. Such a channel is required, for example, when source data compression is to be used. There is a long history of work here at JPL on such concatenated systems both with and without data compression (Refs. 1-3).<sup>1</sup> In recent years it has become evident that such concatenated coding systems will be required by many future missions both by NASA and by foreign space agencies. For this reason, the Consultative Committee on Space Data Systems (CCSDS), which is formed of members from many space agencies throughout the world, has published a set of guidelines for

concatenated coding systems. (These guidelines appear in the CCSDS publication *Telemetry Channel Coding*, a draft "blue book," February, 1984.)

The CCSDS-recommended system consists of an inner (7, 1/2) convolutional code and an outer (255, 233) Reed-Solomon code with 8-bit symbols. These are the same parameters as are used by the Voyager project. However, a new implementation of the Reed-Solomon code due to Berlekamp (Ref. 4) was chosen for the standards. This code has a symmetric code generator polynomial that can significantly reduce the amount of hardware needed to implement an encoder. Berlekamp also described a bit-serial algorithm for an encoder that further reduces its size and weight. Perlman and Lee (Ref. 5) worked with Berlekamp to produce a flight-qualifiable prototype for this encoder. As a result of their work, the CCSDS has adopted the Berlekamp Reed-Solomon code as a recommended standard. In Ref. 6 a very large scale integrated (VLSI) implementation of the Berlekamp encoder is described.

<sup>1</sup>See also J. P. Odenwalder, *Concatenated Reed-Solomon/Viterbi Channel Coding for Advanced Planetary Missions: Analysis, Simulations, and Tests*, Submitted to the Jet Propulsion Laboratory by Linkabit Corporation, San Diego, Calif., Contract No. 953866, December, 1974.

In order to reduce the error rate of the system still farther, Reed-Solomon codewords will be interleaved to a depth of  $I$  ( $I = 5$  in most proposed applications). Interleaving occurs on the Reed-Solomon symbol level and is performed in such a way that the order of information symbols is preserved by the encoding process.<sup>2</sup> A set of  $I$  interleaved codewords is called a Reed-Solomon frame. Since the Reed-Solomon code is a block code, codeword synchronization is required before the decoding process can begin. This will be done by placing a fixed set of symbols, called a frame synchronization marker (or simply a frame marker), at the beginning of each Reed-Solomon frame. An analysis of this synchronization technique can be found in Ref. 7.

This report examines two phenomena that are peculiar to the Reed-Solomon code that could lead to code synchronization problems if they are not treated correctly. They are both fairly well known effects to those who work with Reed-Solomon codes but may be unknown to others who design systems that will use the codes.

The first effect arises from the fact that the recommended code generator polynomial is symmetric. Consider the case in which all the data symbols to be encoded are zero. Before encoding takes place, the synchronization marker is placed at the beginning of the frame. Suppose that there are  $n$  symbols in this marker (i.e., there are less than or equal to  $8n$  bits in the marker) and that  $n$  is at most equal to  $I$ . Then the encoded frame has the form shown in Fig. 1. Notice that, since the code generator polynomial is symmetric, the 224th column of the frame is identical to the first. This can be easily seen by the fact that the Reed-Solomon code is cyclic and each row is just the cyclic rotation of the codeword formed by a constant multiplied by the generator polynomial. In particular, the synchronization marker appears in both the first and 224th column. This can result in false synchronization of the frame. In fact, this was observed in systems tests performed by the European Space Agency (ESA).

The second effect considered in this report is that repeated sequences of symbols of certain periods are Reed-Solomon codewords. This effect includes the special case of the constant codeword as well as (in the case of the CCSDS code) cycles of length 3, 5, and 15. This can produce only a very rare case of synchronization failure but it is a very useful fact in the testing of encoders and decoders. This effect was observed by C. Lahmeyer while implementing the decoders that will be eventually used by the Voyager project. R. L. Miller presented an explanation in an internal memorandum. This report presents a proof of the effect that can easily be generalized to other code sizes.

<sup>2</sup>See J. P. Odenwalder, op. cit.

## II. False Synchronization of Constant Data Sequences

As mentioned in Section I, if the data source produces a constant symbol value, then there is a possibility of false frame synchronization in the 224th column. Since the (255, 223) Reed-Solomon code can correct only 16 symbol errors, a false synchronization in this case will cause the decoder to fail to decode — even in the case of a noiseless channel. This condition can be reported automatically by the decoder and, in fact, this is how ESA first noticed the problem. There are several possible solutions to this problem.

Since the false image of the marker is separated from the actual marker by exactly  $32 \cdot I$  symbols, the frame synchronization system can keep track of both images and easily distinguish between them. Alternatively, the marker can be taken out of the frame and inserted, instead, between the frames. In this way, the marker is not encoded and the false image is never formed.

Another solution is to use "virtual zero fill." This is an algorithm by which a shortened Reed-Solomon code (Ref. 8) is used with the same hardware by assuming that all the missing symbols are zeros. For implementation reasons, the missing symbols are always assumed to be the first ones in each codeword. Code shortening has the effect of moving the marker from the first column of the frame to another one. This suppresses, in most cases, the formation of a false image. Table 1 shows the number of false images that are produced as a function of the information block length of the shortened code. The numbers in this table were produced by computer simulation of the Reed-Solomon encoding process. All the lengths not shown represent cases in which no false images are formed. In particular, shortening by only one symbol (information length 222) alleviates the false image problem and produces an undetectable degradation in performance in most cases.

It should be noted that the case of constant data is rather uninteresting. In fact, a good source encoding algorithm would probably never let this happen. However, the above solutions may prove useful in a case where there is no data compression.

## III. Periodic Codewords

In this section, the case of Reed-Solomon codewords that are made up of periodic sequences of symbols is examined.

Consider a (255, 223) Reed-Solomon codeword (not necessarily the CCSDS code) that consists of a periodic sequence of symbols. Let the smallest period of the symbols be  $n$ . Then clearly  $n \mid 225$  or  $n \in \{1, 3, 5, 15, 17, 51, 85, 255\}$ . It will be



shown that, in fact, the only possible values are 1, 3, 5, 15, and 255. We will ignore the rather uninteresting (and trivial) case of  $n = 255$ .

Let  $p(x)$  be a polynomial over  $\text{GF}(256)$  of the form

$$p(x) = \sum_{k=0}^{(255/n)-1} x^{nk}$$

where  $n$  is an integral divisor of 255. The polynomial  $p(x)$  can be considered a codeword in a (255, 223) Reed-Solomon code if it is divisible by the code generator polynomial. Another way of saying this is that all the roots of the generator polynomial are also roots of  $p(x)$ . Notice that  $p(x)$  may also be written as

$$p(x) = \frac{(x^{255} - 1)}{(x^n - 1)}.$$

Hence the roots of  $p(x)$  are just those 255th roots of unity that are not also  $n$ th roots of unity. Let  $\alpha$  be a primitive 255th root of unity. Then the roots of the CCSDS Reed-Solomon generator polynomial,  $g(x)$ , are

$$\alpha^{112}, \alpha^{113}, \alpha^{114}, \dots, \alpha^{143}$$

and a simple check will show that none of these are either 1st, 3rd, 5th, or 15th roots of unity. This means that all the roots of  $g(x)$  are also roots of  $p(x)$  for  $n \in \{1, 3, 5, 15\}$  and hence  $p(x)$  is a multiple of  $g(x)$ . This is just another way of saying  $p(x)$  is a Reed-Solomon codeword. However,

$$\alpha^{120}$$

is a 17th root of unity so  $n$  cannot be a multiple of 17 if  $p(x)$  is to be a codeword. Clearly, all periodic sequences of these periods can be built linearly by combining polynomials of the form  $p(x)$  and hence these will also be codewords. It should be noted that the Voyager Reed-Solomon code which has roots

$$\alpha^1, \alpha^2, \alpha^3, \dots, \alpha^{32}$$

in its code generator polynomial also exhibits this property.

The phenomenon of periodic codewords does not present a problem in frame synchronization except in the unlikely case that the frame marker is similar to part of a periodic data sequence. If the frame contains some nonconstant data (such as a time tag or frame identification code) then the problem will never exist.

## IV. Conclusions

The two effects that have been described in this report are well understood and well known by those who routinely work with Reed-Solomon codes. The issue of false frame marker images is, nonetheless, an important consideration in the design of an overall coded telemetry system. Any of the various solutions that are cited in Section II will alleviate that problem. The best solution, however, would probably be to remove the frame synchronization marker from within the Reed-Solomon code block and place it, instead, between adjacent code blocks. In this way, not only would the false image problem be solved, but the wasted overhead that is created by the Reed-Solomon encoding of the frame marker would be eliminated.

## References

1. Miller, R. L., Deutsch, L. J., and Butman, S. A., *On the Error Statistics of Viterbi Decoding and the Performance of Concatenated Codes*, Publication 81-9, Jet Propulsion Laboratory, Pasadena, Calif., September, 1981.
2. Liu, K. Y., and Lee, J. J., *An Experimental Study of the Concatenated Reed-Solomon/Viterbi Channel Coding System Performance and Its Impact on Space Communications*, Publication 81-58, Jet Propulsion Laboratory, Pasadena, Calif., August, 1981.
3. Rice, R. F., *Channel Coding and Data Compression Systems Considerations for Efficient Communication of Planetary Imaging Data*, Technical Memorandum 33-695, Jet Propulsion Laboratory, Pasadena, Calif., June, 1974.
4. Berlekamp, E. Bit-serial Reed-Solomon encoders, *IEEE Trans. Information Theory*, IT-28, No. 6, November, 1982, pp. 869-874.
5. Perlman, M. and Lee, J. J., *Reed-Solomon Encoders – Conventional vs Berlekamp's Architecture*, Publication 82-71, Jet Propulsion Laboratory, Pasadena, Calif., December, 1982.
6. Truong, T. K., Deutsch, L. J., and Reed, I. S., *The VLSI Design of a Single Chip Reed-Solomon Encoder*, Publication 82-84, Jet Propulsion Laboratory, Pasadena, Calif., November, 1982.
7. Swanson, L., *A Comparison of Frame Synchronization Methods*, Publication 82-100, Jet Propulsion Laboratory, Pasadena, Calif., December, 1982.
8. Deutsch, L. J., The effects of Reed-Solomon code shortening on the performance of coded telemetry systems, *TDA Progress Report 42-75*, Jet Propulsion Laboratory, Pasadena, Calif., November, 1983, pp. 14-20.

**Table 1. Number of frame marker images as a function of information block length**

Information Block Length	Number of Marker Images	Information Block Length	Number of Marker Images
1 (shortest)	2	117	2
24	2	122	2
26	2	126	2
34	2	129	2
35	2	135	2
37	2	147	2
54	2	152	2
55	3	155	2
61	2	163	2
69	2	169	3
72	2	170	2
77	2	187	2
89	2	189	2
95	2	190	2
98	2	198	2
102	2	200	2
107	2	223 (full length)	2
112	3		

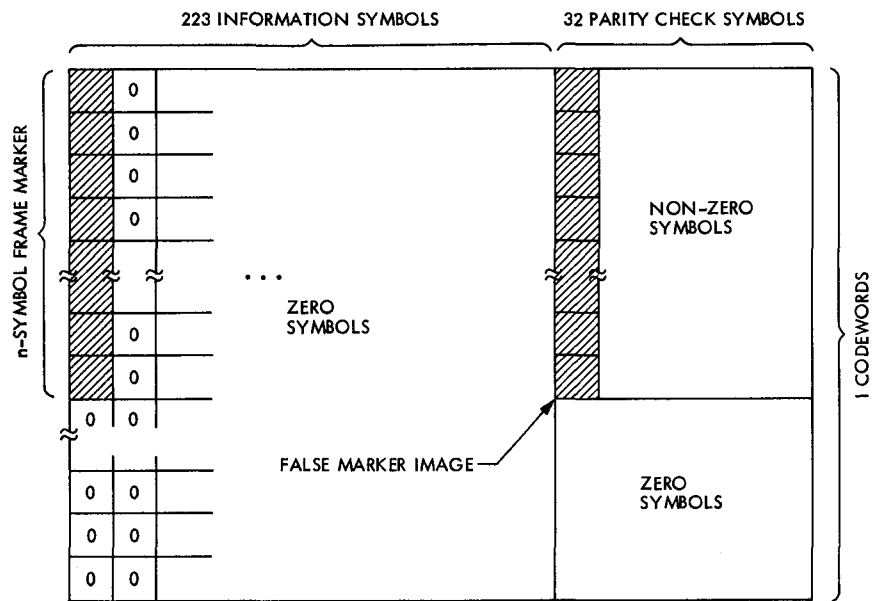


**Fig. 1. Encoded Reed-Solomon frame with false frame marker image**

# Further Results on Rate 1/N Convolutional Code Constructions With Minimum Required SNR Criterion

P.J. Lee

Communications Systems Research Section

*New good  $(K, 1/N)$  convolutional codes for  $8 \leq K \leq 13$  and  $2 \leq N \leq 8$  were found and tabulated which require minimum signal-to-noise ratio (SNR) for given desired bit error rates (BER) with Viterbi decoding. The transfer function bound was used for the BER evaluations.*

## I. Introduction

For a convolutional coding system employing a Viterbi decoder, the decoded bit error rate (BER) is well upper-bounded by the transfer function bound (Refs. 1; 2, Chapter 4)

$$\text{BER} \leq c_o \cdot \frac{\partial}{\partial Z} T(D, Z) \bigg|_{D=D_o, Z=1} = c_o \cdot \sum_{i=d_f}^{\infty} a_i \cdot D_o^i \quad (1)$$

where the coefficient  $c_o$  and transfer function  $T(D, Z)$  depend on the code and type of channel used.  $D_o$  is the Bhattacharyya bound (Ref. 2, p. 63) which depends on the channel only, and  $d_f$  is the free distance of the code. For an additive white Gaussian noise channel with BPSK signaling (BPSK/AWGN channel) without quantization.  $D_o$  and  $c_o$  are given by  $D_o = \exp(-E_s/N_o)$  and

$$c_o = Q(\sqrt{2d_f \cdot E_s/N_o}) \exp(d_f \cdot E_s/N_o)$$

(Refs. 1; 2, p. 248) where  $N_o$  is the one-sided noise power spectral density,  $E_s$  is the received signal energy per channel symbol, and

$$Q(w) = \int_w^{\infty} \exp(-t^2/2) \cdot dt / \sqrt{2\pi}$$

Many researchers (e.g., Refs. 3-7) have used the maximum  $d_f$  criterion or the criterion of maximum  $d_f$  together with minimizing the first few  $a_i$ 's in Eq. (1), for determining the goodness of a code in their code search procedures. However, another criterion (Ref. 8) of minimizing required signal-to-noise ratio (SNR) for a given desired BER with the direct use of Eq. (1) for BER evaluation provides much better results. For effective partial code searches in Ref. 8, some known facts were used with a very useful idea that "good codes generate

good codes.” That is, good rate  $1/(N+1)$  codes can be found by extending the code generators of good rate  $1/N$  codes. Moreover, the theoretically predicted benefit of coding bandwidth expansion was confirmed with our new codes, whereas the previously reported codes did not uniformly confirm this property.

However, in order to test a code under the above criterion, we have to evaluate the transfer function bound which requires a matrix inversion. Hence, even for a code with short constraint length, considerable amount of computing time has been required. Therefore in Ref. 8 we stopped the code search at constraint length  $K=7$ . More recently (Ref. 9), a very efficient algorithm for finding the transfer function bound was devised; the algorithm is very fast and requires a much smaller amount of computer memory storage since all the unnecessary operations, such as multiplication-by-zero, etc., are eliminated. This technique enabled us to search for longer constraint length codes.

In the next section, after introducing necessary notations, the partial code searching techniques discussed in Ref. 8 are briefly reviewed. Some additional restrictions which were applied to the searches for longer codes are explained. In the last section, the code search results are summarized in a table and figure where their performance is compared with previously reported codes.

## II. Notations and Partial Code Searching Techniques

A typical nonsystematic, constraint length  $K$ , rate  $1/N$  convolutional encoder, denoted by  $(K, 1/N)$  code, is shown in Fig. 1. The code connection box is often represented by an  $N \times K$  binary matrix  $G$ . Let  $G(n)$  and  $g(k)$  be the  $n$ th row and  $k$ th column vectors of matrix  $G$ , and  $G(n, k)$  be the element of  $n$ th row and  $k$ th column of  $G$  for  $n = 1, 2, \dots, N$  and  $k = 1, 2, \dots, K$ . The  $n$ th bit in the  $t$ th output vector  $y_n^t$  (see Fig. 1), for  $t=1, 2, \dots$ , is given by:

$$y_n^t = \text{mod} \left\{ \sum_{k=1}^K G(n, k) \cdot x^{t-k+1}, 2 \right\} \quad (2)$$

where  $\text{mod}\{u, v\}$  is the remainder when  $u$  is divided by  $v$ ,  $x^t \in \{0, 1\}$ ,  $t = 1, 2, \dots$  is the encoder input sequence and  $x^t = 0$  for  $t < 1$  by convention.

The code generator matrix is often represented by  $(G(1), G(2), \dots, G(N))$  with the  $G(n)$ 's in octal form. We also adopt this notation. For given  $K$  and  $N$ , this code generator  $G$  determines the code performance. By “code search” we imply

the search for a  $G$  which provides good performance. The transfer function bounding technique on the BER at the Viterbi decoder output will not be discussed here.

In previous code searches for shorter constraint length codes, we restricted the search space to codes having  $g(1) = g(K) = (1, 1, \dots, 1)$  and eliminated equivalent codes using the obvious facts that “changes in the orders of the  $G(n)$ 's” or “reversing the order of the  $g(k)$ 's” gives the same performance. The search space for  $(K, 1/N)$  codes was limited by deleting catastrophic codes and codes with too small free distance (smaller than the maximum achieved  $d_f$  value of  $(K, 1/(N-1))$  codes, or smaller than that of  $(K-1, 1/2)$  codes for  $N=2$  cases).

For a given pair of  $K$  and  $N$ , we estimated the values of SNR at which we believed the best code(s) could achieve the prespecified desired values of BER. Search results were listed with the best code at the top. A code was considered to be better than another if the weighted sum of the logarithm of two calculated BER values was smaller. For  $N=2$  cases, the codes in the restricted search space were exhausted. For  $N \geq 3$  cases, roughly  $2^{K-2}$  of the good  $(K, 1/(N-1))$  code generators (in the upper portion of the list) were used as seeds to generate the  $(K, 1/N)$  code search space. This last restriction was adopted from the observation that “good codes generate good codes.”

In the searches for longer constraint length codes, the unquantized BPSK/AWGN channel was assumed as before and the previous procedure was adopted with some minor changes. The first change was in the target values of BER. For shorter codes, the values were  $10^{-6}$  and  $10^{-3}$ . But since the transfer function bound is known to be tight only when the operating SNR is far from the cutoff rate limit, we chose the target BER values to be  $10^{-9}$  and  $10^{-6}$  for longer codes. Smaller target BER values also reduce the effort in testing a code.

Since, for large  $K$ , the number of codes in the reduced search space is still too large (it increases exponentially with  $K$ ), we had to further reduce the search space size. In searches for  $(K, 1/N)$  codes, codes with  $d_f$  smaller than the mid-point between the maximum  $d_f$  for  $(K, 1/(N-1))$  codes and the upper bound on the  $d_f$  for  $(K, 1/N)$  codes were deleted. Also the number of seeds was limited to 100 rather than  $2^{K-2}$ . These limitations increase the possibility of losing better codes, but were required to obtain results in a reasonable length of time.

From the shorter code search results, we made another interesting observation. That is, the number of 1's in the code generator of a good code is equal to, or at most slightly more than, the value of its free distance. This observation was

employed for further reducing the search space for longer codes.

### III. Code Search Results and Conclusions

Our code search results are summarized in Table 1 where the code generators and corresponding performances are shown. These are best in the sense of minimizing the required SNR for the upper bound on desired BER of  $10^{-9}$  and  $10^{-6}$  among the codes searched. Notice that the values of bit SNR ( $E_b/N_o$ ,  $E_b = E_s \cdot N$ ) shown in the table are upper bounds on the required bit SNR for actual target BER values. Also, previously found codes with maximum free distance (Refs. 3-7)

are compared to our codes. If more than one code was reported with the same  $K$  and  $N$ , the best one was chosen for comparison. For visual comparisons, the required bit SNR bounds are plotted in Fig. 2 as a function of  $N$  ( $= 1/\text{code rate}$ ). The benefit of coding bandwidth expansion becomes more evident with longer constraint length codes.

In conclusion, we have found (1) good codes for values of  $N$  and  $K$  where no good code had been obtained, and (2) better codes than previously known "best" codes for many of other values of  $K$  and  $N$ . These low-rate codes are expected to have a number of applications, especially for systems having large bandwidth-bit time products such as deep space and spread spectrum communication systems.

## Acknowledgement

The author wishes to express his appreciation to Dr. J.R. Lesh and to many colleagues for helpful discussions.

## References

1. A. J. Viterbi, "Convolutional codes and their performance in communication systems," *IEEE Trans. Commun. Tech. COM-19*, pp. 751-772, Oct. 1971.
2. A. J. Viterbi and J.K. Omura, *Principles of Digital Communication and Coding*, McGraw-Hill Book Co., New York, NY, 1979.
3. J. P. Odenwalder, *Optimal Decoding of Convolutional Codes*, Ph.D. Thesis, Univ. of Calif. at Los Angeles, L.A., CA, 1970.
4. K. L. Larsen, "Short convolutional codes with maximal free distance for rates  $1/2$ ,  $1/3$ , and  $1/4$ ," *IEEE Trans. Info. Theory IT-19*, pp. 371-372, May 1973.
5. R. Johannesson and E. Paaske, "Further results on binary convolutional codes with an optimum distance profile," *IEEE Trans. Info. Theory IT-24*, pp. 264-268, March 1978.
6. D. G. Daut, J. W. Modestino, and L. D. Wismer, "New short constraint length convolutional code constructions for selected rational rates," *IEEE Trans. Info. Theory IT-28*, pp. 794-800, Sept. 1982.
7. R. Palazzo, *Analysis of Periodic Nonlinear Trellis Codes*, Ph.D. Thesis, Univ. of Calif. at Los Angeles, L.A., CA, 1984.
8. P. J. Lee, "New short constraint length, rate  $1/N$  convolutional codes which minimize the required  $E_b/N_o$  for given bit error rate," *TDA Progress Report 42-77*, pp. 41-56, Jet Propulsion Laboratory, Pasadena, CA, May 1981.
9. P. J. Lee, "A very efficient transfer function bounding technique on bit error rate for Viterbi decoded, rate  $1/N$  convolutional code," *TDA Progress Report 42-79*, pp. 114-123, Jet Propulsion Laboratory, Pasadena, CA, Nov. 1984.

Table 1. Code search results

$(K, 1/N)$	Required bit SNR, dB for		$d_f$	Notes	Code Generator G in Octal									
	1.E-9	1.E-6												
(8, 1/2)	5.987	4.481	10	9,O	371,	247								
(8, 1/2)	5.998	4.462	10	6,A	363,	255								
(8, 1/3)	5.609	4.115	16	9,6,O	357,	251,	233							
(8, 1/4)	5.552	4.008	22	9,A	353,	335,	277,	231						
(8, 1/4)	5.553	4.005	22	6,A	365,	337,	271,	233						
(8, 1/4)	5.634	4.070	22	L	357,	313,	275,	235						
(8, 1/5)	5.517	3.960	28	9,A	367,	337,	263,	251,	235					
(8, 1/5)	5.522	3.956	27	6,A	351,	331,	265,	257,	237					
(8, 1/5)	5.659	4.067	28	D	357,	323,	271,	257,	233					
(8, 1/6)	5.499	3.929	33	9,A	363,	351,	331,	265,	257,	237				
(8, 1/6)	5.520	3.926	32	6,A	365,	351,	337,	273,	263,	221				
(8, 1/6)	5.574	4.008	34	D	375,	357,	331,	313,	253,	235				
(8, 1/7)	5.490	3.916	39	9,A	373,	353,	345,	335,	277,	251,	231			
(8, 1/7)	5.513	3.906	37	6,A	367,	331,	311,	277,	253,	235,	215			
(8, 1/7)	5.553	3.976	40	D	375,	357,	331,	313,	275,	253,	235			
(8, 1/8)	5.472	3.892	44	9,A	371,	353,	331,	323,	275,	267,	237,	225		
(8, 1/8)	5.473	3.889	44	6,A	373,	353,	335,	315,	277,	251,	231,	227		
(8, 1/8)	5.581	3.994	45	D	371,	357,	331,	313,	275,	275,	253,	235		
(9, 1/2)	5.573	4.129	12	9,O	753,	561								
(9, 1/2)	5.603	4.122	11	6,A	731,	523								
(9, 1/3)	5.299	3.840	18	9,6,A	665,	537,	471							
(9, 1/3)	5.388	3.898	18	L	711,	663,	557							
(9, 1/4)	5.184	3.714	24	9,A	765,	671,	513,	473						
(9, 1/4)	5.219	3.709	24	6,A	733,	645,	571,	437						
(9, 1/4)	5.289	3.786	24	L	745,	733,	535,	463						
(9, 1/5)	5.158	3.648	29	9,A	751,	665,	543,	537,	471					
(9, 1/5)	5.160	3.647	29	6,A	755,	651,	637,	561,	453					
(9, 1/5)	5.284	3.768	31	P	747,	675,	535,	531,	467					
(9, 1/6)	5.138	3.609	35	9,6,A	765,	721,	663,	571,	513,	467				
(9, 1/6)	5.181	3.659	37	P	727,	711,	677,	553,	545,	475				
(9, 1/7)	5.126	3.590	42	9,6,A	763,	737,	665,	551,	531,	475,	427			
(9, 1/7)	5.229	3.671	44	P	755,	751,	737,	673,	525,	463,	457			
(9, 1/8)	5.116	3.572	48	9,6,A	767,	735,	665,	637,	571,	551,	461,	453		
(9, 1/8)	5.202	3.653	50	P	775,	717,	671,	647,	625,	567,	553,	513		
(10, 1/2)	5.307	3.916	12	9,A	1753,	1151								
(10, 1/2)	5.315	3.905	12	6,J	1755,	1363								
(10, 1/3)	5.024	3.595	19	9,A	1735,	1261,	1117							
(10, 1/3)	5.025	3.589	19	6,A	1735,	1261,	1163							
(10, 1/3)	5.126	3.690	20	L	1633,	1365,	1117							
(10, 1/4)	4.885	3.445	26	9,A	1753,	1547,	1345,	1151						
(10, 1/4)	4.902	3.443	26	6,A	1753,	1557,	1345,	1151						
(10, 1/4)	4.985	3.549	27	L	1653,	1633,	1365,	1117,						
(10, 1/5)	4.836	3.385	33	9,A	1731,	1537,	1323,	1217,	1135					
(10, 1/5)	4.844	3.376	32	6,A	1731,	1621,	1535,	1337,	1123					
(10, 1/6)	4.812	3.342	40	9,6,A	1755,	1651,	1453,	1371,	1157,	1067				
(10, 1/7)	4.797	3.322	46	9,A	1747,	1731,	1651,	1535,	1337,	1261,	1123			
(10, 1/7)	4.809	3.315	46	6,A	1713,	1551,	1461,	1365,	1277,	1167,	1075			
(10, 1/8)	4.785	3.294	52	9,6,A	1731,	1621,	1575,	1433,	1327,	1277,	1165,	1123		



Table 1. (contd)

(K, 1/N)	Required bit SNR, dB for		$d_f$	Notes	Code Generator G in Octal							
	1.E-9	1.E-6										
(11, 1/2)	5.060	3.701	14	9,A	3643,	2671						
(11, 1/2)	5.070	3.699	13	6,A	3723,	2151						
(11, 1/2)	5.088	3.731	14	J	3645,	2671						
(11, 1/3)	4.712	3.352	22	9,6,A	3165,	2671,	2373					
(11, 1/3)	4.814	3.420	22	L	3175,	2671,	2353					
(11, 1/4)	4.605	3.216	28	9,A	3453,	3077,	2755,	2351				
(11, 1/4)	4.620	3.213	29	6,A	3453,	3157,	2755,	2351				
(11, 1/4)	4.722	3.293	29	L	3175,	2671,	2353,	2327				
(11, 1/5)	4.554	3.157	36	9,A	3673,	3161,	2575,	2363,	2265			
(11, 1/5)	4.566	3.146	35	6,A	3721,	3165,	2671,	2477,	2153			
(11, 1/6)	4.522	3.107	42	9,A	3275,	3165,	2671,	2423,	2277,	2173		
(11, 1/6)	4.537	3.099	42	6,A	3663,	3327,	3161,	2575,	2251,	2177		
(11, 1/7)	4.500	3.073	49	9,A	3625,	3261,	3151,	2733,	2457,	2375,	2167	
(11, 1/7)	4.505	3.068	49	6,A	3721,	3223,	3165,	2671,	2527,	2277,	2173	
(11, 1/8)	4.492	3.054	57	9,6,A	3651,	3453,	3375,	3167,	2763,	2361,	2265,	2155
(12, 1/2)	4.784	3.504	14	9,A	6765,	4627						
(12, 1/2)	4.800	3.503	15	6,J	7173,	5261						
(12, 1/3)	4.482	3.163	22	9,A	7473,	5611,	4665					
(12, 1/3)	4.487	3.161	23	6,A	6755,	5271,	4363					
(12, 1/3)	4.512	3.180	24	L	6265,	5723,	4767					
(12, 1/4)	4.361	3.013	30	9,A	7635,	6733,	5221,	4627				
(12, 1/4)	4.363	3.011	30	6,A	7725,	6671,	5723,	4317				
(12, 1/4)	4.431	3.054	32	L	7455,	6265,	5723,	4767				
(12, 1/5)	4.299	2.950	38	9,A	7725,	6711,	5723,	5513,	4317			
(12, 1/5)	4.305	2.937	38	6,A	7725,	6671,	5723,	5321,	4317			
(12, 1/6)	4.258	2.893	45	9,A	7725,	6671,	5723,	5161,	4553,	4317		
(12, 1/6)	4.266	2.890	45	6,A	7725,	7341,	6711,	5723,	4533,	4317		
(12, 1/7)	4.235	2.859	54	9,6,A	7721,	7325,	6711,	5723,	5337,	4713,	4317	
(12, 1/8)	4.223	2.841	61	9,A	7721,	7325,	6711,	6545,	5723,	5337,	4713,	4317
(12, 1/8)	4.225	2.838	62	6,A	7725,	7121,	6711,	6277,	5723,	5333,	4735,	4317
(13, 1/2)	4.572	3.337	16	9,6,J	16461,	12767						
(13, 1/3)	4.251	2.993	24	9,A	16331,	12277,	11565					
(13, 1/3)	4.253	2.981	23	6,A	14331,	13523,	10747					
(13, 1/3)	4.363	3.043	24	L	17661,	10675,	10533					
(13, 1/4)	4.119	2.841	33	9,A	17227,	14331,	13277,	11165				
(13, 1/4)	4.145	2.827	32	6,A	16353,	14751,	13157,	10255				
(13, 1/4)	4.222	2.883	33	L	16727,	15573,	12477,	11145				
(13, 1/5)	4.055	2.753	41	9,6,A	17633,	14471,	12337,	11275,	10565			
(13, 1/6)	4.016	2.705	49	9,6,A	16365,	14331,	13277,	12467,	11275,	10473		
(13, 1/7)	3.996	2.671	58	9,6,A	17661,	16365,	14331,	13277,	12467,	11275,	10473	
(13, 1/8)	3.979	2.652	65	9,A	17467,	16751,	15345,	14331,	13277,	12475,	11261,	10473
(13, 1/8)	3.986	2.650	64	6,A	17623,	16365,	15221,	14331,	13277,	12467,	11275,	10473

## Notes:

- 9 Code which minimizes the upperbound on the required SNR for desired BER = 1.E-9 (among searched)
- 6 Code which minimizes the upperbound on the required SNR for desired BER = 1.E-6 (among searched)
- O Found by Odenwalder (Ref. 3)

- L Found by Larsen (Ref. 4)
- J Found by Johannesson and Paaske (Ref. 5)
- D Found by Daut, et. al. (Ref. 6)
- P Found by Palazzo (Ref. 7)
- A Found by the author

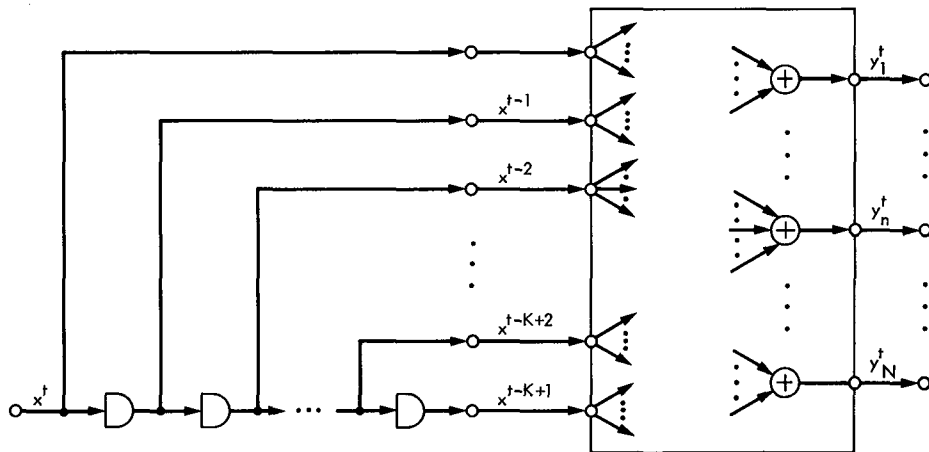


Fig. 1. A nonsystematic, constraint length  $K$ , rate  $1/N$  convolutional encoder structure

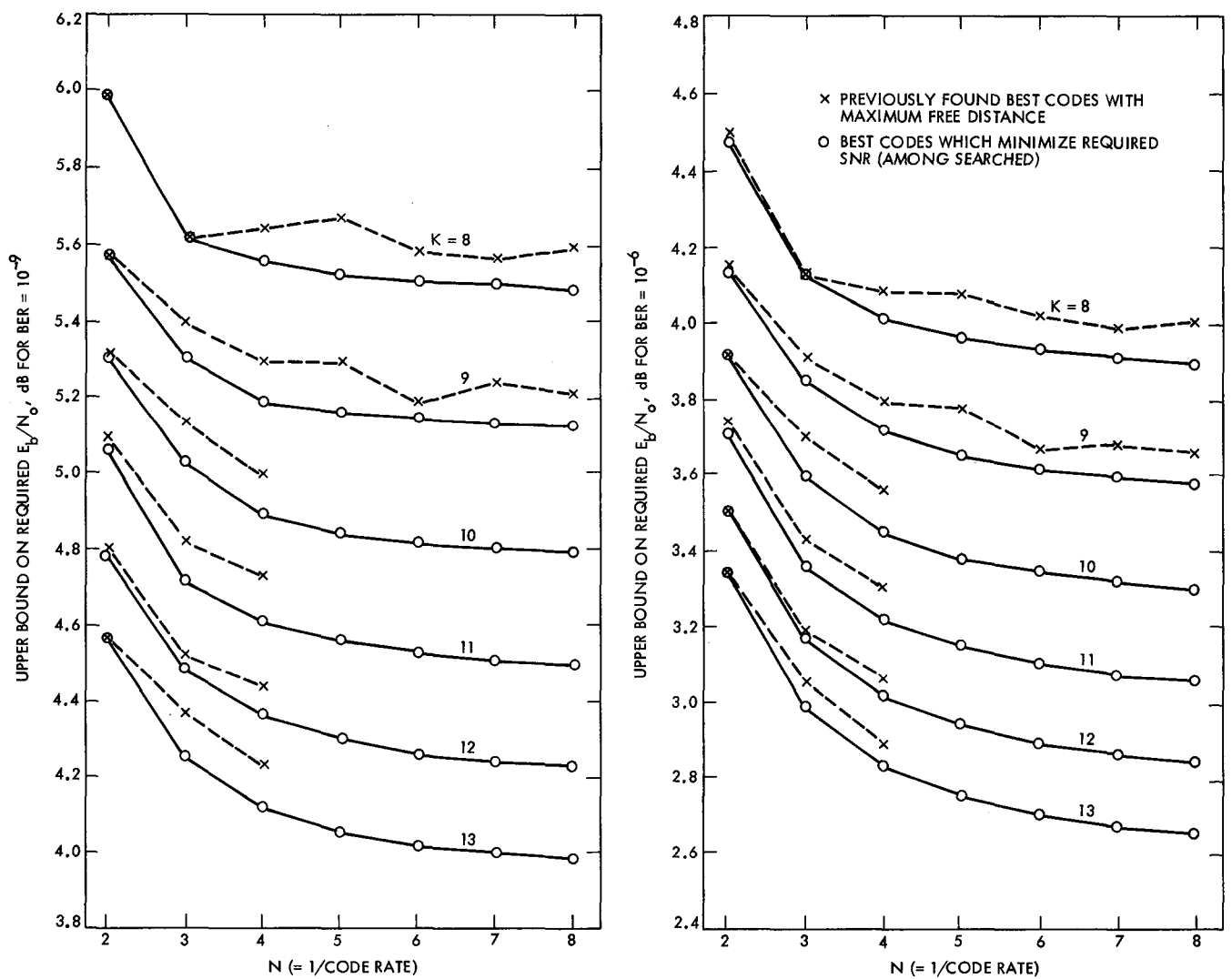


Fig. 2. Performance comparisons of  $(K, 1/N)$  codes

# Concepts and Tools for the Software Life Cycle

R. C. Tausworthe  
DSN Data Systems

*The Tools, techniques, and aids needed to engineer, manage, and administrate a large software-intensive task are themselves parts of a large software base, and are incurred only at great expense. This article focuses on the needs of the software life cycle in terms of such supporting tools and methodologies. The concept of a distributed network for engineering, management, and administrative functions is outlined, and the key characteristics of localized subnets in high-communications-traffic areas of software activity are discussed. A formal, deliberate, structured, systems-engineered approach for the construction of a uniform, coordinated tool set is proposed as a means to reduce development and maintenance costs, foster adaptability, enhance reliability, and promote standardization.*

## I. Introduction and Background

In 1979 it was recognized that more than half of the United States' National Aeronautics and Space Administration (NASA) budget was required to sustain labor-intensive, routine services and operations, and that fraction was rising. In 1980, the NASA study committee on machine intelligence and robotics identified the potential of computer science for increasing the productivity and the affordability of future space operations. Computer science was identified as the most critical supporting technology requiring an intensive NASA research and development involvement. The committee recommended that NASA develop a long-term commitment and a centralized, coordinated effort to alleviate the budget drain, support a higher-caliber personnel skill mix, and enable productivity breakthroughs that would enable expanded mission sophistication.

The world's entire industry is rapidly becoming information-intensive, silicon-based, and software-driven<sup>1</sup>. The trends in modern information systems are toward very large data bases, distributed systems, computer networks, less expensive hardware, complex applications, and automated workplaces and factories. The space effort administered by NASA, in many respects, is but a particular example of this tendency. Although its progress may not, perhaps, be as pronounced as some research organizations within the USA and elsewhere abroad (Ref. 1) have reported, NASA, nevertheless, has recognized the need to capitalize on computer technology advances to increase the affordability of its coming missions.

---

<sup>1</sup> Reifer, Donald, session-opening comment at COMPSAC-79, Chicago, Ill., November 1979.

People-costs are rising at inflationary rates — 5% to 15% per year — while computer logic costs are decreasing some 25% per year and computer memory costs are decreasing about 40% per year. Overcoming the labor-intensive nature of building and maintaining large, complex information systems increasingly rests on raising the productivity of personnel responsible for the *software* (i.e., programs, data bases, and documentation) within the system. Software efforts are not yet mechanized to the point that their products are “manufactured” in production-line fashion.

## A. Software Problems

Software, from its beginnings, has been immersed in the same kinds of problems any new kind of industry undergoes. Software products have too often been late and over-budget, often have not fulfilled the needs of users, often have been unreliable, often are difficult to modify to meet new user needs, and often cannot be adapted to accommodate evolving technology. The useful lifetime of that software is therefore often shorter than planned, usually at low salvage value upon its retirement.

Even though many “software problems” are, in reality, perhaps better classified as “systems engineering problems,” the fact is that systems are becoming so complex that the elaboration and management of system details are becoming literally impossible without computational aid. That is, system engineering relies on being able to find solutions to system problems via software. Hence, software problems permeate the entire application system in which they reside and the entire development system in which they are created.

If software problems could be localized, or related to simple, noninteracting influences, or could be found to be coupled to simple, fundamentally wrong underlying principles, perhaps they could be attacked with more sweeping results. But the large software project operates within an entangled socio-economic system that must respond to intangible or subjective requirements, accommodate an uncertain discovery/development process, communicate excruciatingly detailed information through an imprecise, ambiguous human medium, and perform within sometimes severe fiscal and schedule constraints to build or maintain a very large, technically complex, intricate application system. Consequently, there is almost a complete fabric of austere, tightly interwoven technical and managerial problems entangling each programming project in the large.

Because software costs are rising, this rise being primarily related to labor, software costs often dominate the system costs. For a number of reasons, cost and schedule performances in software tasks have been regarded as poor in comparison with hardware tasks. Software tasks are also generally

acknowledged to be harder to manage than hardware tasks. Furthermore, qualified software implementation and management personnel are scarce.

Labor-intensive efforts are reduced by improvement in methodology, environments, tools, and aids — what we shall refer to in the current context as *software engineering technology*. Software engineering is a disciplined approach to software-intensive efforts whose goal is to solve software and related technological and administrative problems in an organized, responsible, professional way. Software engineering also seeks to improve the quality, performance, and usability of computational facilities, as well.

A recent study (Ref. 2) by the University of Maryland reported the results of a survey of state-of-the-art technology and its utilization in the United States and Japan. Its principal conclusion was that, while researchers in these two countries took advantage of, and further expanded the state of the art, the large production programming projects within the same organizations did not. Cited as reasons for not using up-to-date tools and methodology were unawareness and lack of training, poor human engineering of the tools, lack of good documentation and support, unreliability, and cost overheads.

As a result, the conclusions of the NASA study committee still seem to describe most of the software industry today. True, progress may have been made in the interim, but it appears outwardly that resultant productivity has been little affected, perhaps counteracted by rising applications and systems complexity. There still seems to be about a 10-year lag between state-of-the-art software engineering technology and its propagation into accepted practice. And software organizations need an injection of new technology in excess of 10% per year just to remain 10 years behind!

The software situation may be becoming increasingly more serious. It was described in the 1960s and early 1970s as “the software problem,” but the term escalated to “the software crisis” in the late 1970s and early 1980s. The “continuing software crisis” is now expected to be with us throughout the 1990s (Ref. 3).

## B. Critical Near-Term Needs

Some of the critical needs within the state of the art are: establishment of broader funding bases of support within organizations for the acquisition and integration of software engineering technology; improvement in the usage, quality, and effectiveness of software tools; betterment of the software implementation and management processes; provisions for better education and training in the use of software technology; and adoption of standard practices in software efforts.

Training of software personnel in the application of modern software engineering methods and standard practices throughout the entire software life cycle is certainly needed, but very costly to perform on the job. Implementing software tools for technology transfer by giving proper attention to portability, human engineering, adaptability, and product standards requires particular emphasis, but again requires objectivity, training, and monitored adherence. Improved hardware facilities, support software and operating systems, and networked work stations are incurred also at extra cost and complexity.

Means of coping with problems that are not inherently software-caused may also be relieved to some degree by increased understanding and automated support. Problems attributable to uncertain, ambiguous, and unstable user or system requirements may cause less frustration if risks could be quantitatively assessed and compensations made in costs, schedule, and program design. Some software engineering methods and tools, such as those for software requirements analysis and structural design, may be extensible, to some degree, to systems design and systems engineering tasks, even those not involving imbedded software.

### **C. Goals and Directions**

Increased manpower effectiveness is essential to lowering computing costs and mission costs over the remainder of this century. To maintain affordability amid the increasing information system complexity that will accompany its coming space missions, NASA is considering the goal of a 500% increase in manpower effectiveness over the next 20 years.

Manpower effectiveness is increased primarily by methods and tools. Because software costs are not concentrated in any one particular phase of activity, it will be necessary to provide such means throughout the entire software life cycle. Tools concentrated in a particular phase can have only limited benefit. For example, the existence and use of a miraculous language that could render the coding activity instantaneous by itself would yield a cost benefit of only about 20%, because only about 20% of the current software effort is coding.

The 1980 NASA study committee cited the following development needs: the expansion of on-line, interactive, and automatic programming to increase productivity; a modern data-structuring language; symbolic models and computer representations of application areas of knowledge-based usage systems for these application areas; and the use of an integrated design, programming, documentation, and management data base. They concluded that the systematic, thorough application of automation technology to NASA was essential to the agency's cost effectiveness; that current technology

could significantly reduce staff and response time; and that the use of computer-based machine intelligence could further increase productivity and utility of acquired information.

A number of efforts in private industry and government, both in the United States and abroad, have for some time now focused growing concern on software problems. There are three current concerted efforts led by the Department of Defense, and conjoined by NASA and certain constituents of private industry, to provide a common programming language (Ada<sup>2</sup>, Ref. 4), to provide Software Technology for Adaptable, Reliable Systems (STARS) (Ref. 5), and to integrate Ada and other software technology into practice (the Software Engineering Institute). These efforts are oriented not only toward developing better software engineering technology, but also toward accelerating its propagation into the software industry.

A current study sponsored by the U.S. Air Force (Ref. 3) is evaluating the needs, issues, costs, benefits, and risks of a comprehensive standardized software engineering life-cycle support environment for the STARS program. Such an environment, when implemented, states the report, should have a dramatic positive impact on the continuing software crisis. However, the costs of the STARS program are large, about \$300 million.

Unfortunately, a single standard environment and set of support tools may not work for everyone. The computing field may be just too diverse for that. The costs of a custom, complete programming environment for each application area are probably prohibitive for all except the large software houses. The development of a modern environment of the STARS variety is beyond the capital resources of even the large software houses.

Others must therefore content themselves with commercial, STARS-fallout, public-domain, or government-supplied environments, plus the smaller special tools that they must have and can develop for themselves. It therefore behooves organizations to adopt standards that will promote the infusion of this technology at the least cost. An example in which this approach was successfully applied has been recently reported by TRW (Ref. 6) in its Software Productivity System.

## **II. Software Technology Improvement Areas**

As new software engineering tools or techniques emerge, they may or may not become a part of a particular software engineering environment. If they are not integrated into an

<sup>2</sup>Ada is a trademark of the U.S. Government (Ada Joint Program Office).

environment and properly used, they are ineffective, regardless of their potential. Improvements to the general software situation will therefore come about primarily through improved software engineering environments. Let us, for a moment, ponder some possible candidates for this environment and certain of their characteristics.

### **A. Near-Term Improvement Areas**

Since most software organizations are not currently benefiting from existing technology anywhere near the maximum extent possible, probably the least expensive alternative for productivity and quality improvement is making off-the-shelf tools and techniques usable. This alternative requires awareness and existence of a spectrum of compatible, proven tools and techniques, training in their usage, perhaps better human-machine interfaces, and good vendor support.

In addition, there may be other worthwhile concepts within the current state of technology that can be readily implemented, given funding and the same engineering care as referred to above. Regardless of the alternatives, timeliness, benefits, and costs will determine the members of the tool set acquired.

Tools in this term may be likened to ordinary "hand tools," in that they are primarily automated instances of the routine kinds of things that people do. Their mechanical advantage is significant, but not outstanding.

Items in this category include programmer's toolkits, workbenches, and operating systems; management planning and status-monitoring tools; prototypes of requirements and design languages and analyzers; code and documentation auditors; software life-cycle mathematical models; design and documentation data bases; interactive environments for programming and management; test-case generators and test-path monitors; assertion validation monitors; reliability assessment models; regression data bases; and software engineering standard practices.

### **B. Medium-Term Improvement Areas**

In a somewhat longer time frame, more ambitious and more costly "power tools" of the "computer-assisted, intuition-guided" variety may become generally available. The technical problems for such tools are definable today, but the solutions may require some technology development. Most tools in this class will probably be characterized by knowledge of the application built into (or available to) each tool. In such cases, this knowledge-assist is expected to yield a good mechanical advantage.

Tools in this category include such things as context-knowledgeable programming and document generation tools;

software application data bases and reuse tools; sophisticated, accurate software life-cycle process phenomenology models; coordinated software production and task management tools; automated configuration management tools; program design quality analyzers; test and validation tools; requirement-code-test-configuration traceability tools; and friendly requirements capture-and-analysis tools. Many of these are in the process of being perfected today.

### **C. Long-Term Improvement Areas**

The application of artificial intelligence techniques, specifically knowledge-based expert systems, to increase the automation of specification, design, implementation, and testing and validation processes probably yields the best hope of improving productivity and software reliability by at least an order of magnitude. But such tools will be very expensive to develop.

A knowledge-based system for software production would contain sets of software engineering rules integrated into an environment that would permit application of the rules to embryo software systems through the full range of life-cycle disciplines, technical and managerial. Tools of this type would play the role of an automated assistant in software development and maintenance, and would provide such services as conversational requirements capture and analysis; expert design consulting; expert software management decision support; self-coding documentation; automatic validation, failure analysis, and work-arounds; and direct requirements-to-product synthesis.

### **D. Prognosis**

Use of the computer as a means to solve the problems caused by its own existence (as well as those thrust upon it by system engineering deficiencies) will necessarily be evolutionary, because the developed technology, being software, will only add to the problems it is aimed at curing. But it is believed that, within the STARS program, the technology-bootstrapping process will eventually converge to provide a considerable improvement in software productivity in general, and perhaps an order of magnitude in some areas, by the end of the century.

Current and near-term software engineering technology, if developed and *used*, can do much toward improving the production and management of software applications. Medium-term technology will potentially relieve programmers and managers of most burdensome activities that can be automated. If long-term technology is successful in removing currently known machine-intelligence limitations, programmers and managers, as we conceive of them today, may be put out of work; such individuals might be needed only for consulting and very special applications during the acquisition of requirements.

The effort in requirements capture seems to be a fundamental limitation, linked to the human discovery of need, uncertainty of the true form of the satisfaction needed, and the decision to act. Someday, perhaps someone will discover that the human channel capacity for requirements definition can be quantified by some Shannon-type (Ref. 7) information-theoretic limit. Then, just as the communications engineer now knows how to design communication systems optimally within this capacity, the software engineer will be able to fabricate systems to compensate for disruptive requirements, and software managers will plan for this uncertainty as a matter of course.

Of course, it is also possible that software engineering as a discipline, if not wisely administered, will die a horrible, lingering death — poisoned by wasted and fragmented efforts, crushed by an evolving enormity too great to be compatible within itself, strangled by overcontrolling managers, or starved by sponsors unwilling to invest capital to cut labor. Steps must be taken and attitudes must be adjusted to see that these kinds of things do not happen. Technological improvements must be planned, developed, capitalized, nurtured, and integrated into practice when they are ready. They will not come about by themselves; it will take continuing effort to make large software application systems affordable.

### III. Software Production Information System

At this point, let us focus on a particular software environment, that in which the DSN Data Systems are implemented. The "Mark IVa" configuration for 1985 (Fig. 1), now in implementation, will contain some 145 computers of various kinds, and perhaps about 1.3 million lines of source code. The software resides in interconnected subsystems for deep-space tracking and data acquisition, spacecraft command, network performance validation, and communication system control and data routing.

The software production activity to support this configuration appears, at its upper abstraction, as a highly orchestrated, information-intensive process; the participants and their informational needs are shown in Fig. 2. From this viewpoint, the DSN environment perhaps looks fairly normal, much the same as any other environment.

However, within the environmental "black box," one finds a more complex, high-communications-traffic beehive of activity. For many reasons, partly inheritance, partly evolution, and partly because of operational constraints, software is developed on a number of different hosts, with the documentation and source code data base spread out over many types of media in different formats and on different machines. The flow of information and products in the implementation process

is depicted in Fig. 3. This awkward, disconnected kind of environment, too, may look familiar to many. The reader will note that, while certain aspects of the development are automated, the communications among the various parts represent a serious deterrent to productivity.

The DSN therefore is developing a rationale and an architectural concept to restructure the software engineering environment for improved software throughput. That rationale and architecture are the subjects of the remainder of this article.

The software engineering environment is envisioned as an information system, an integrated set of processing and data federated around common interface considerations into an overall design that is balanced to serve the informational needs of all of its users. However, there are some constraints that prevent a drastic change from the current host mainframes and operating systems being used for software development and task management into a more modern development environment rife with tools, such as the UNIX<sup>3</sup> system. Changes must be made gradually (budgetary and training restrictions) and within the environment as it is being used for Mark IVa development.

The users of this information system for a given project include programmatic and institutional management, supervisors, system engineers, software engineers, quality assurance, administrative, and clerical personnel, user organization representatives, operations personnel, and various support staff, as well as those charged with implementing and maintaining the environment itself. Each has computational and communicational needs served by the environment.

Figure 4 shows the potential simplification in traffic obtained by providing users with workstations and other computational elements interconnected by local area networks, and providing object-oriented "servers" for major resources. Figure 5 shows how the management and administrative data bases can be organized around generic life-cycle functions and Fig. 6 shows how the same kind of organization can be applied to the software products and technical information. We have termed this configuration the Management and Development Network (MADNET). Prototype demonstrations of MADNET concepts were performed by Fouser<sup>4</sup>.

The software engineering environment is envisioned as a layered architecture in which the user interface, at the top, is

<sup>3</sup>UNIX is a trademark of American Telephone and Telegraph, Inc.

<sup>4</sup>Fouser, T. J., Management and Development Local Area Network Concept Report, Report D-857, Jet Propulsion Laboratory, Pasadena, Calif., April 1983 (JPL internal document).

insulated from hardware, system software, and communications vagaries, and, at the bottom, by levels of virtual machines (Fig. 7). The user interacts with the system seemingly at the tool level using standard tool interfaces, although the tools themselves may be distributed within the system. Existing and purchased-off-the-shelf tools can be made more effective by imbedding them thus in a richer environment, by increasing their availability and accessibility, and by insulating the users from particular details of the host operating system(s).

A spectrum of tools is required to cover the range of users throughout the life cycle. Whereas the long-term goal is to build a fully integrated environment, short-term needs and limited resources make it necessary to provide first for integration of the tools available and readily acquirable. Thus, tools have been ported and purchased that are not 100% compatible with each other, but still serve users fairly well. Many of the Kernighan and Plauger Software Tools (Ref. 8) have been installed, and are in use.

Table 1 lists the kinds of tools that are needed and available (or could be made available in the near term) to development, management, and administrative personnel through the life-cycle phases. It also shows, upon analysis, where tools are absent and better tools are needed. (The Kernighan and Plauger Software Tools are not shown). Current tools tend to be clustered around the production phase for use by developers.

## IV. Environment for Tool Development

The environment for building software tools need not be the same as the environment used to run the tools, nor is either of these necessarily the application software environment. We may thus make a distinction among software engineering environment, applications environment, and tools engineering environment. Each may be optimized toward its own ends.

The applications software, when operational, is mostly imbedded within a real-time data-acquisition system, and its lifetime is coupled to the lifetime of the space mission and the surrounding deep-space station hardware. Only in the event of a major redesign of the network would the transport and reuse of software in new computers be of concern.

However, a software tool that is generally useful over a number of projects needs to present the same user interface, regardless of its host or the application target machine. Toolware thus needs to be transportable to, or available on (or through), any workstation. In the interests of reducing retraining costs, learning to use a new tool, e.g., a new text editor or

a radically different language dialect, just to work with a different host machine, should not be required.

A software layering technique can be applied to the construction of toolware, as indicated in Fig. 8. The figure shows a set of user tools built on a machine-independent set of functions written in an efficient machine-independent subset of a high-level language. These functions and language subset form a virtual machine, the *tool-builder's interface*. Below this interface, there will be a layer of functions with some degree of system dependency, which can be customized by suitable parameterization and minor modifications to present a stable *virtual machine layer interface*. At the next layer are the core toolset language and core system interface library of functions that form a *system and network layer interface*. This layer interfaces directly with the operating system, stabilizing many of the system dependencies into mere idiosyncracies that can be necessary to augment the existing operating system with "primitives," or host-dependent, application-independent code at the system-dependency level (Ref. 8).

Current investigations within the DSN are considering the use of the C language and the UNIX operating system (or UNIX-look-alikes) for building the DSN tools and tool interfaces. (Ada is not yet available on any of the machines in the current environment.) Non-UNIX-like operating systems tend to present problems only in certain file-access routines, which can be softened, to some extent, by the addition of auxiliary functions to create UNIX-like directories. Functions at the portable and customizable layers are maintained in source form and installed on each host to form a common library, so as to ensure the same operation of tools. Selectable options within the source media permit tools to capitalize on features of terminals, printers, and file systems, and yet not destroy the commonality of the user interface.

## V. Tool Design Goals and Criteria

User-interface compatibility and, therefore, transportability are mentioned above as driving considerations in tool design. But a tool must primarily be *effective*. If making a tool portable also renders it ineffective, nothing is gained. Trade-offs among design goals must be made when conflicts occur.

There is a high priority for tools giving a significant and *measurable benefit* to the software engineering process. Since various factors tend to demotivate those in charge of funding the improvements to the software process, the benefits must be clear and capable of being demonstrated, and the expenditure must be justifiable.

In addition, tools should *interface well with other tools* and with the implementation methodology being applied within



the software organization. When tools are built in-house or under contract, their interfaces can be prespecified. However, acquisition of off-the-shelf items do not afford this opportunity, but it may be possible to adapt the tool via special install-options, or patches, or by way of a special version from the vendor, to the interface needs of the environment. In some cases, a special separate server may be developed to provide the input/output or function interface required. Figure 9 shows a layering of computational elements arrayed for server equalization of user interfaces.

Each tool should provide *wide-spectrum benefit* to the developer, to task management, to configuration management, and to quality assurance. For example, a good program design language tool can be used by the programmer to develop the structure, data flow, and detail design of program parts; it also serves to document this design; the manager may use statistics gathered by the tool as a status base for controlling the task; change detection algorithms in the analyzer assist configuration management; measurements of design complexity and automatic checks for completeness, for traceability to requirements, and for conformance to standards aid in quality assurance.

Tools should provide *status and quality information* relative to the object being worked on. This status should be unobtrusively extracted, as an integral part of the tool design (Fig. 10), and should automatically be made available to the management tools by way of a status data base.

Tools should be capable of being operated *interactively* through an appropriate friendly interface where intimate contact with a particular tool is required, such as when the details of an object are being worked out. There should also be a *non-interactive mode* to suppress all the details, once worked out. For example, a tool that has a set of interactive options for operation may skip the option-selection step the next time it is executed with the same object. Another approach is that of scripts executed by the operating system, as by the UNIX shell.

Tools should *have good life-cycle support*, and be as well engineered and documented as the products they support, or perhaps better. They should be built with usability and quality as goals. User manuals should be particularly well written and operation reliable. Moreover, since the tool (and documentation) will no doubt adapt to new applications, new methodologies, and new interfaces with other tools, it is important that the tool software be designed and documented for maintainability.

To the extent possible, *intermediate results and routine decisions should be hidden* from the user; final results should be immediate. For example, the edit-compile-link-execute-observe-re-edit cycle could conceivably (with sufficient computing power) be all integrated together merely into edit and observe windows, with all the intermediate compiling and linking steps suppressed, and with observed results almost simultaneously displayed.

## VI. Summary

As information systems become more sophisticated and complex, the very means to make them affordable becomes an enabling technology. The tools that serve these means will themselves generally be sophisticated, complex, and costly. Thus, tool costs will generally have to be amortized across many projects tools to justify their capital expenditure.

Software tools then, perhaps more urgently than applications programs, require focused attention and concentrated effort to make them rehostable among many environments or to make them generally available within a distributed environment. The payoffs, however, can be significant in utility, training costs, tool acquisition costs to individual projects, schedules, and product quality. The layered-interface object-oriented approach in tool construction is one way to promote this rehosting, and standard network layering of protocols can help make the tools available throughout a distributed implementation environment.

## References

1. Kim, K. H., "A Look at Japan's Development of Software Engineering Technology," *Computer*, Vol. 16, No. 5, May 1983, pp. 26-37.
2. Zelkowitz, Marvin B., et al., "Software Engineering Practices in the US and Japan," *IEEE Computer Magazine*, Vol. 17, No. 6, June, 1984, pp. 57-66.
3. Vick, Charles R., et al., *Methods for Improving Software Quality and Life Cycle Cost*, Report of the Committee on Methods for Improving Software Quality and Life Cycle Cost, Air Force Studies Board Commission on Engineering and Technical Systems, Washington, D.C., May 18, 1984 (draft).
4. Barnes, J. G. P., *Programming in Ada*, Addison-Wesley Publishers, Ltd., London, 1982.
5. Druffel, Larry E., et al., "The DoD STARS Program," *IEEE Computer Magazine*, Vol. 16, No. 11, November, 1983, entire issue.
6. Boehm, Barry W., et al., "A Software Development Environment for Improving Productivity," *IEEE Computer Magazine*, Vol. 17, No. 6, June, 1984, pp. 30-42.
7. Shannon, Claude E., "Communications in the presence of noise," *Proc. IRE*, Vol. 37, No. 1, January 1949, pp. 10-21.
8. Kernighan, Brian W., and Plauger, P. J., *Software Tools in Pascal*, Addison-Wesley, Reading, Mass., 1980.

**Table 1. Support for software implementation**

Personnel level	Implementation phase					
	Software planning and requirements	Software design definition	Software design and production	Section combined subsystem test	Acceptance test and transfer	Operation and maintenance
Administrative	WAD, SRM, MAIL	MAIL, SRM	MAIL, SRM	MAIL, SRM	MAIL, SRM	MAIL, SRM
	Action items	Action items	Action items	Action items	Action items	Action items
	Procurement	Procurements	Travel, calendar	Travel, calendar	Travel, calendar	Procurements
	Travel, calendar	Travel, calendar				Calendar
Management	WAD, SRM, MAIL	WBS, MAIL	WBS, MAIL, ARS, DVCS	WBS, MAIL, ARS, DVCS	WBS, MAIL, ARS, DVCS	ARS, MAIL, Action items
	Action items	Action items				
	Requirements capture	Software visibility	Action items	Action items	Action items	ECR/ECO
	Requirements analysis	Productivity metrics	Software visibility	Software visibility	Software visibility	Transfer
	ECR/ECO	Traceability metrics	Productivity metrics	Productivity metrics	Productivity metrics	status
	Procurements	Design quality metrics	Traceability metrics	Traceability metrics	Traceability metrics	DB
	Review preparation aids	Review preparation aids	Design quality metrics	QA metrics	QA metrics	
	Softcost		Review preparation aids			
Development	Word processing	Word processing	EDIT, POL, CRISP, PASCAL, HAL/S, PL/M, MODCOMP assembly, DVCS	EDIT, PASCAL, HAL/S, PL/M MODCOMP assembly DVCS, STAR test generator	EDIT, PASCAL, HAL/S, PL/M, MODCOMP assembly DVCS, STAR test generator	ARS ECR/ECO
	Requirements capture	Requirements analysis				
	Requirements analysis	PDL, CRISP				
	ECR/ECO	ECR/ECO				
	SPMC documentation/graphics	SPMC documentation/graphics	SPMC documentation/graphics	SPMC documentation/graphics	SPMC documentation/graphics	
	Graphics		Simulated test environment	Simulated test environment	Regression tests	
			Debuggers			

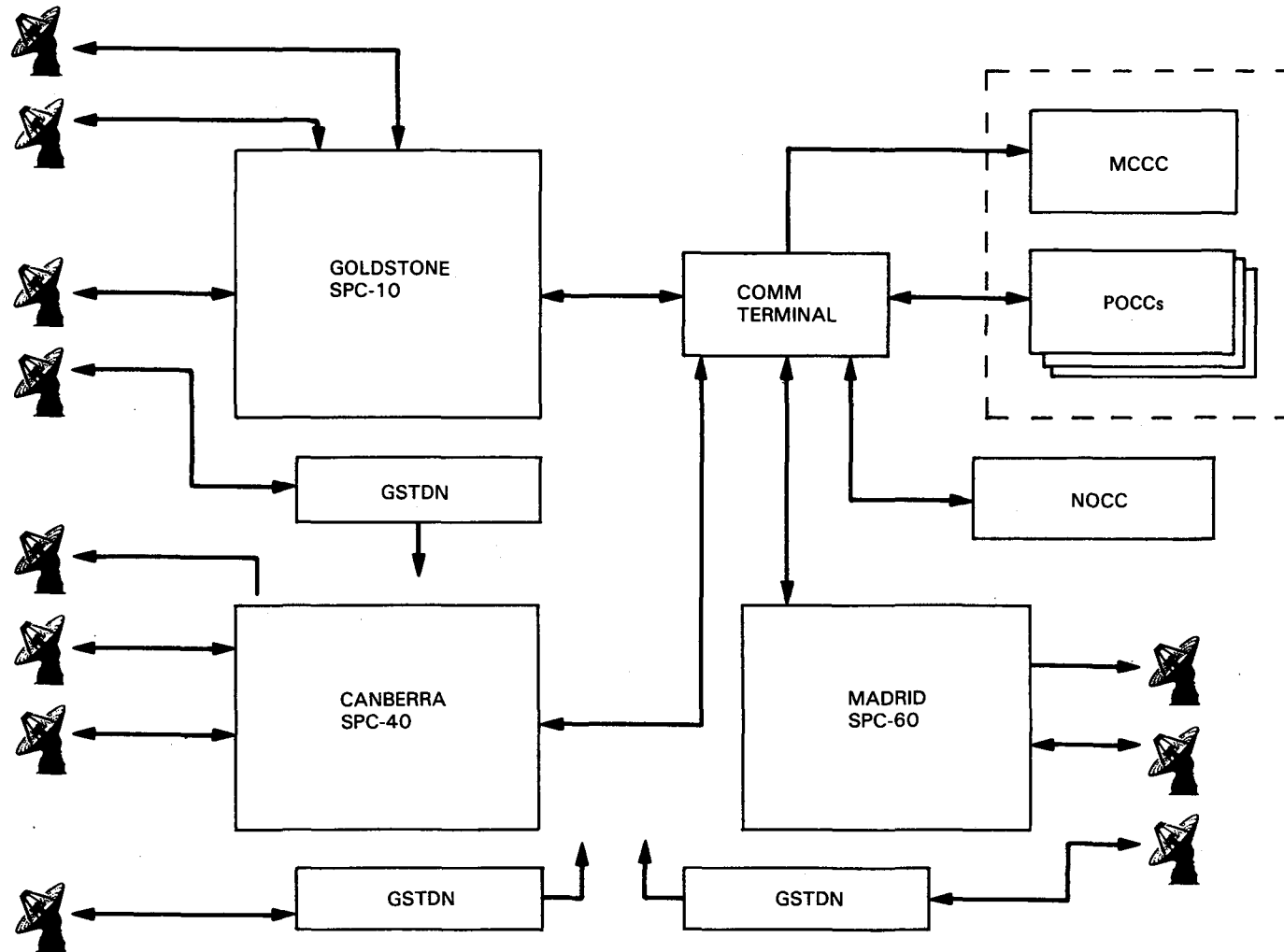


Fig. 1. Deep Space Network, Mark IVa, 1985

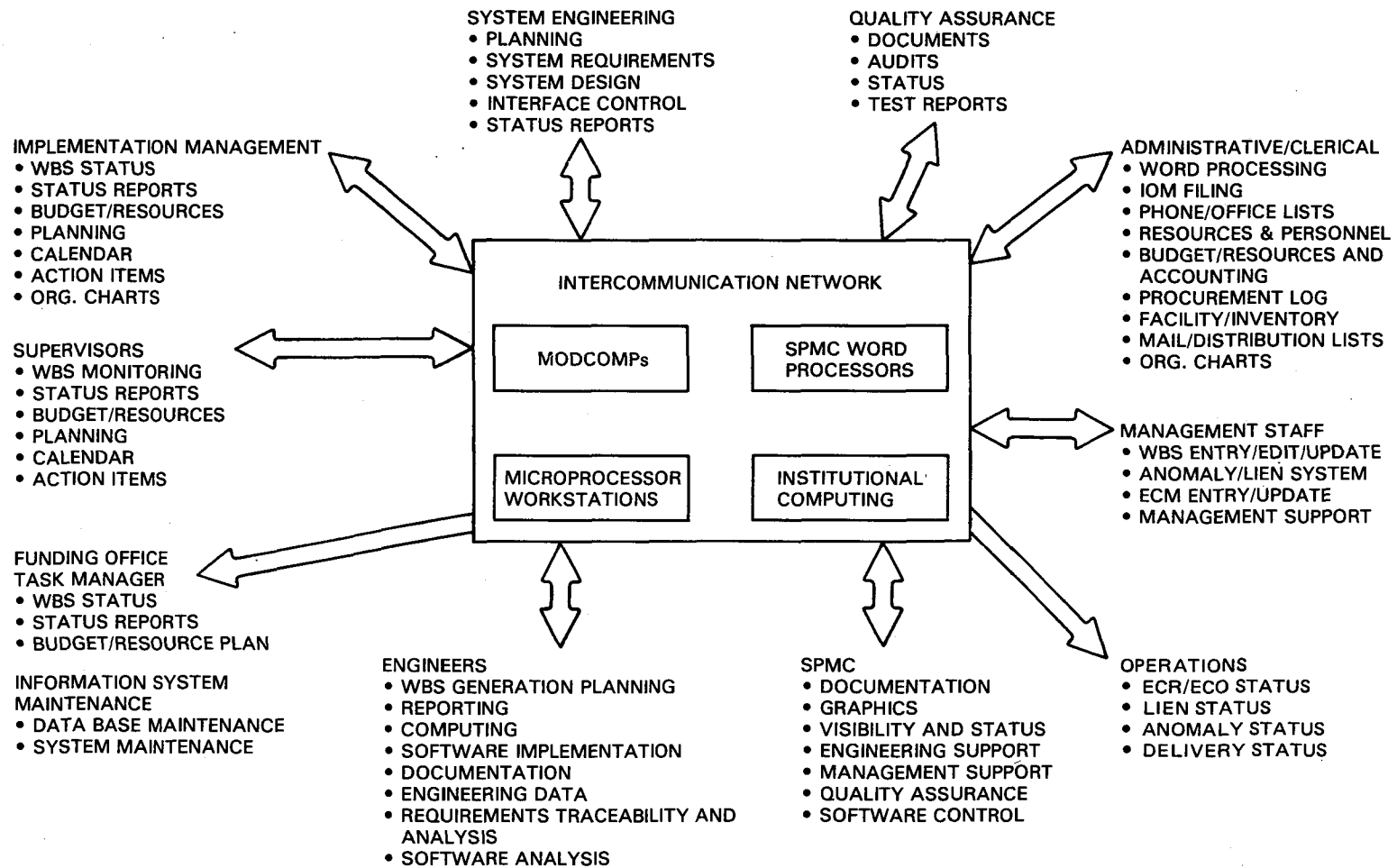


Fig. 2. DSN production information system

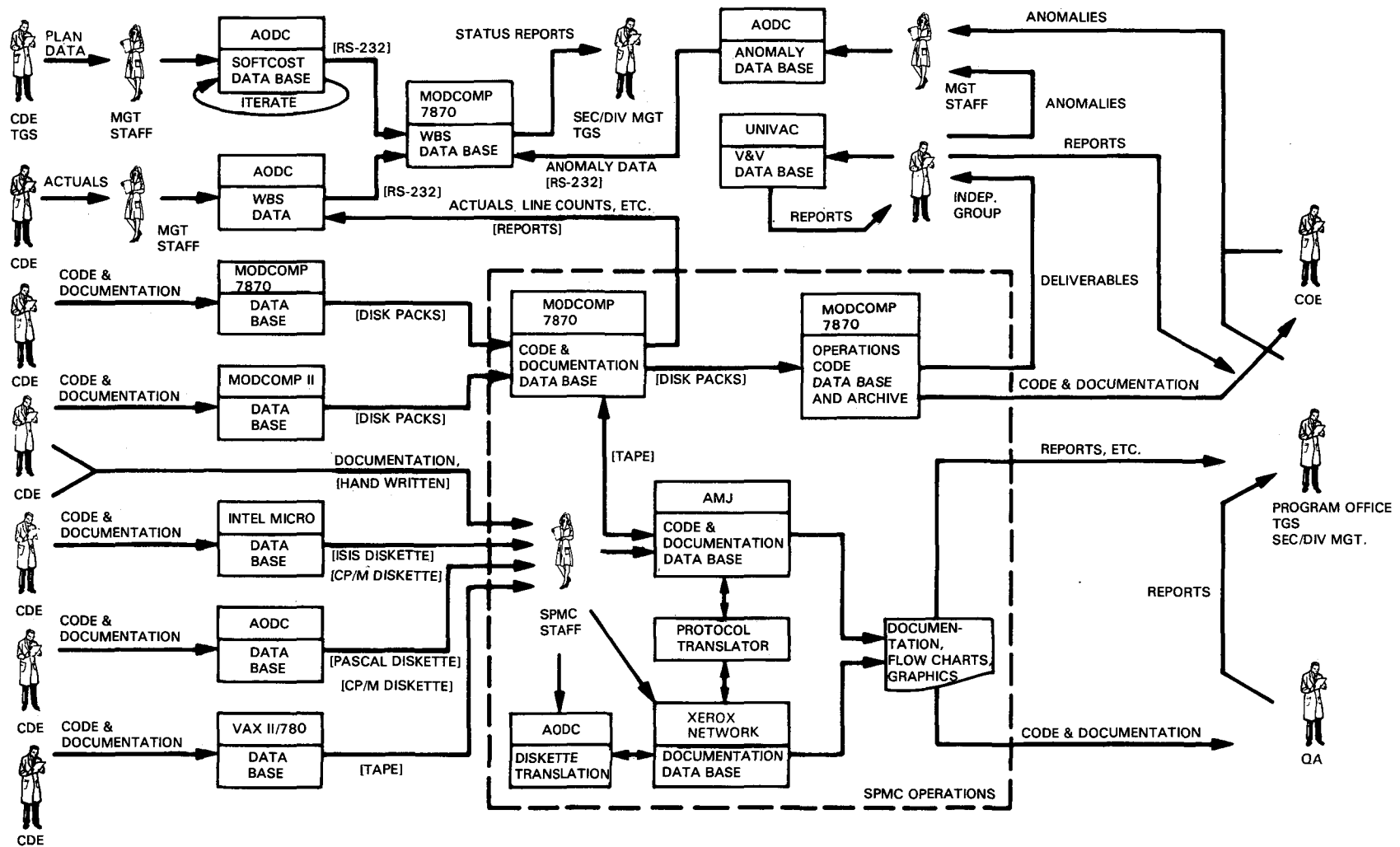


Fig. 3. Early DSN Mark IVa implementation process flow (from footnote 4)

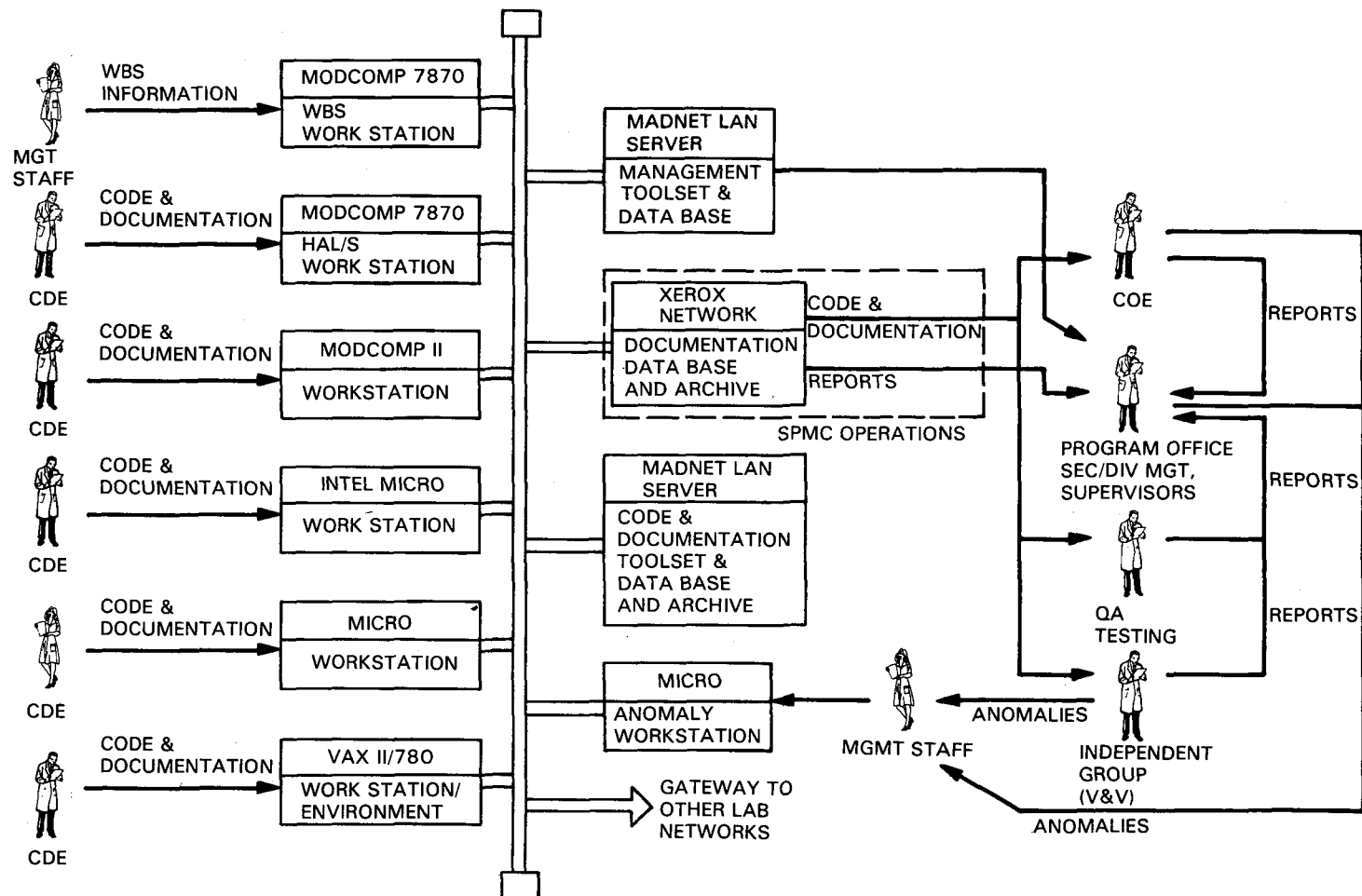


Fig. 4. Conceptual MADNET implementation process flow (from footnote 4)

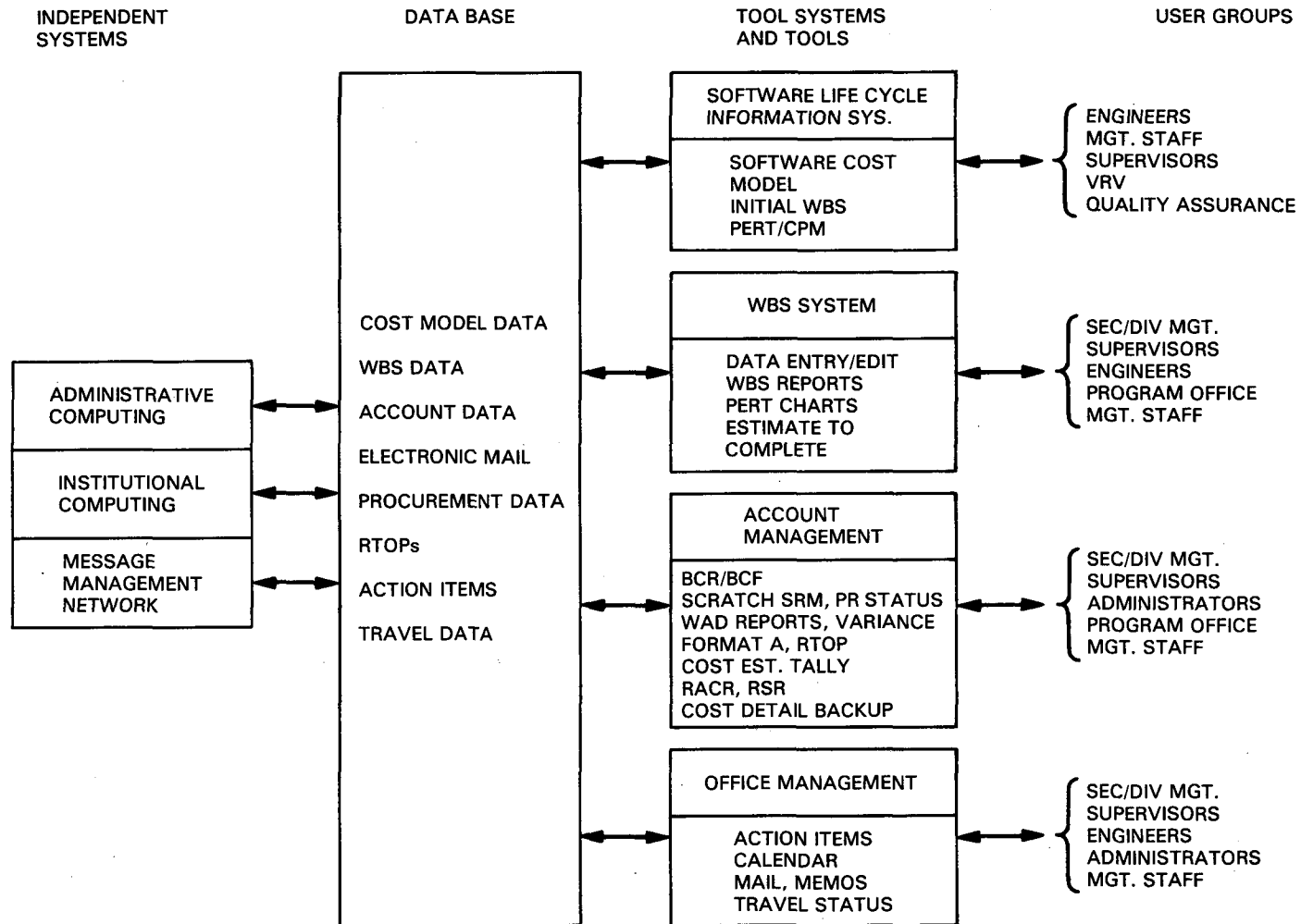


Fig. 5. Implementation data base (management components) (from footnote 4)



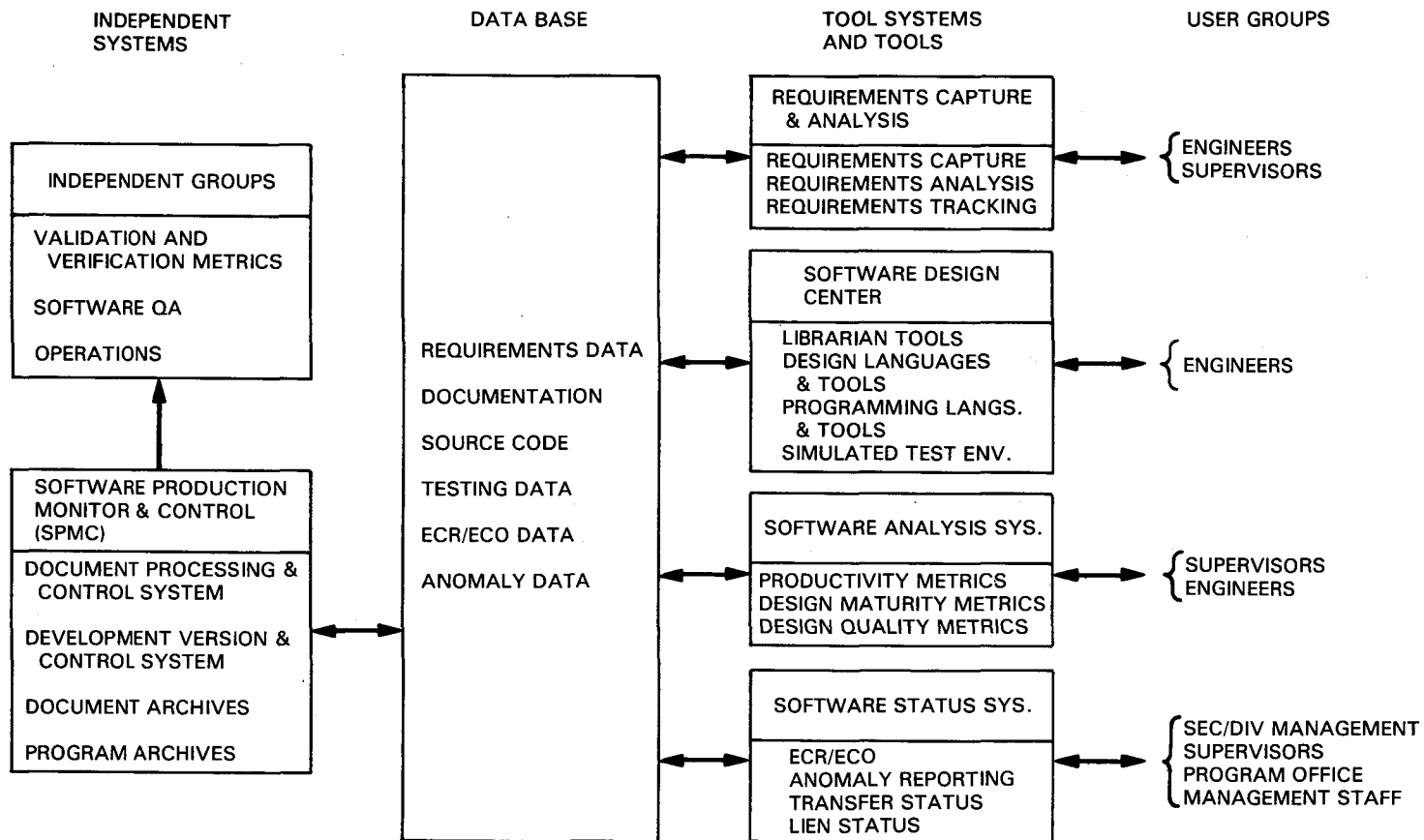


Fig. 6. Implementation data base (engineering components) (from footnote 4)

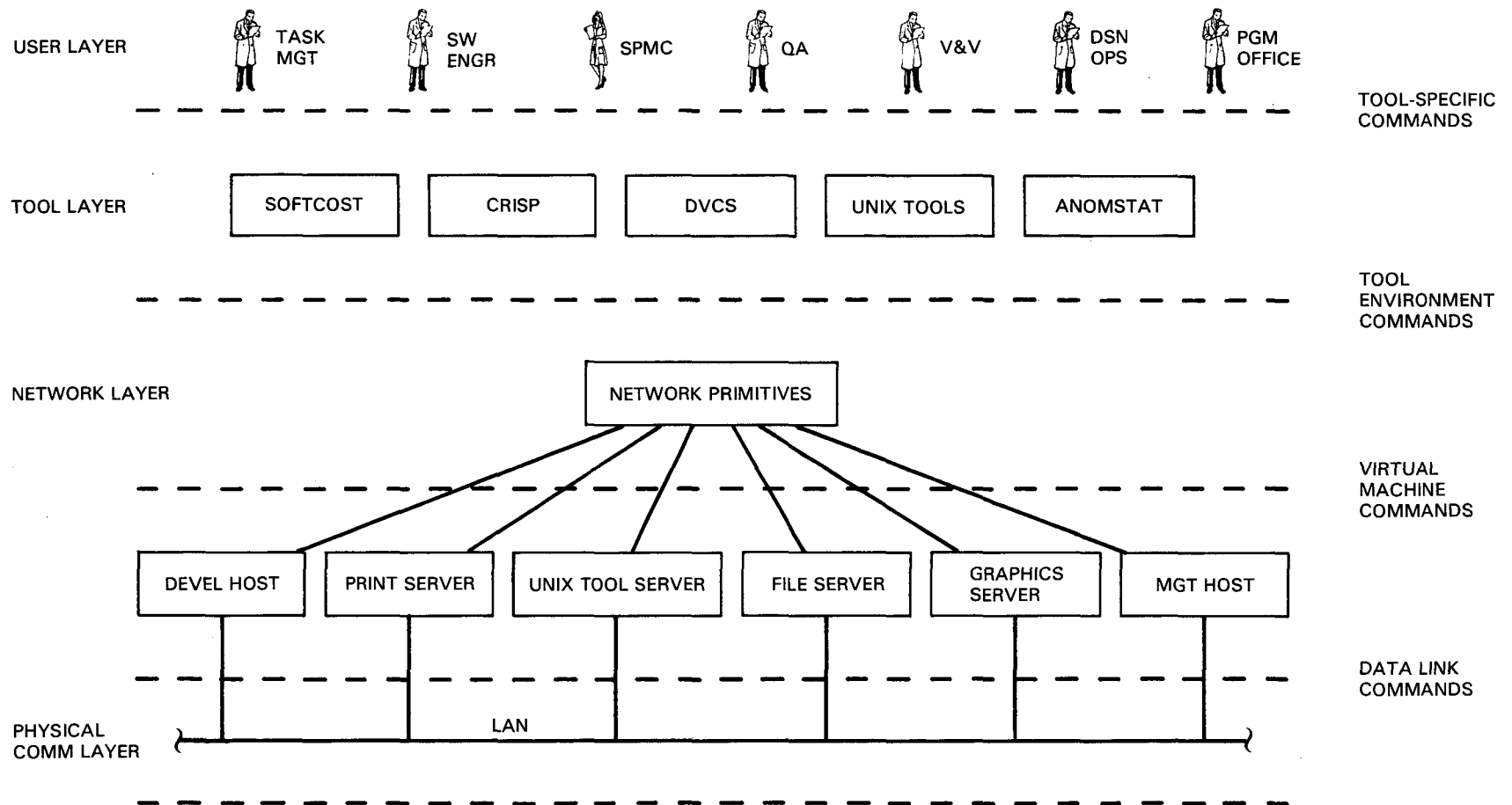


Fig. 7. Command layering via network protocols

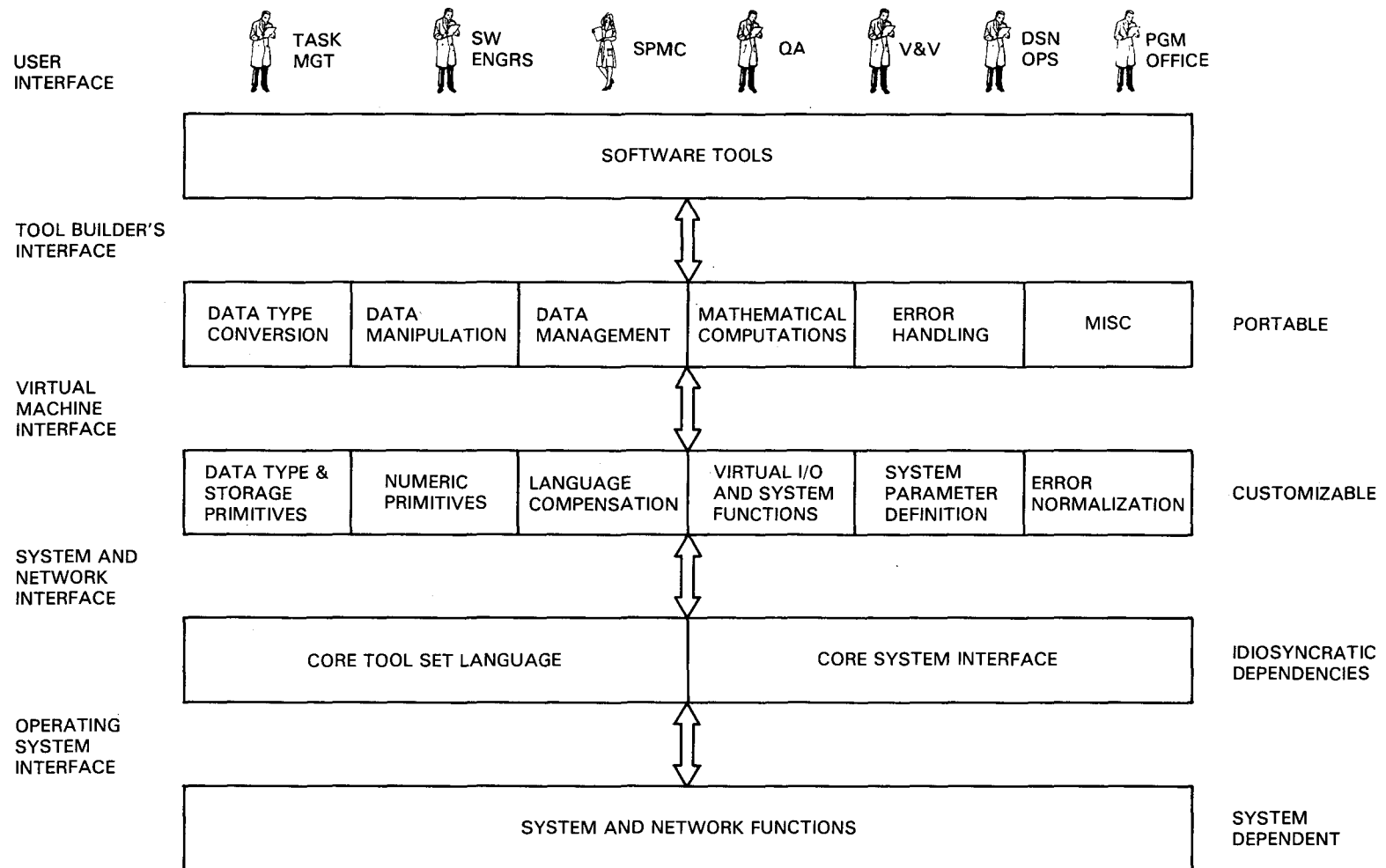
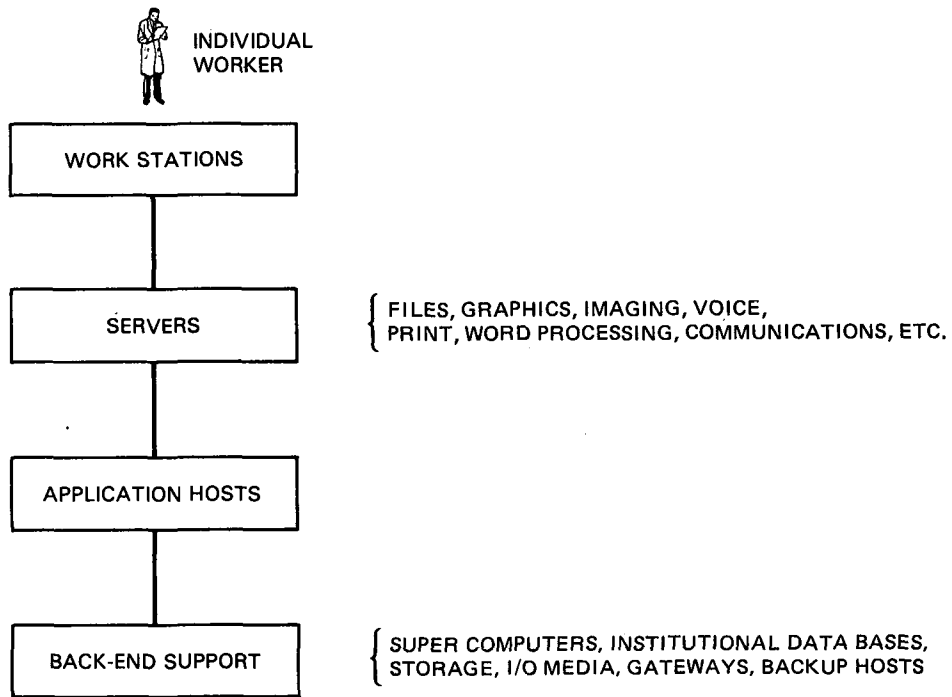
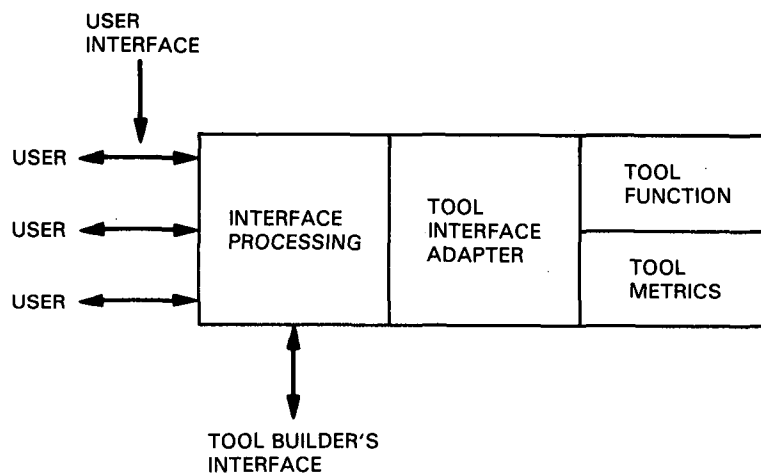


Fig. 8. Layered approach for software tools



**Fig. 9. Integrated distributed facilities**



**Fig. 10. Generalized tool architecture**

# Antenna Axis Drive Torques for the 70-Meter Antenna

H. McGinness

Ground Antennas and Facilities Engineering Section

*Antenna axis speeds versus wind speeds are given in terms of dish size, hydraulic-motor size, and the number of servo valves.*

## I. Introduction

An increase in the dish diameter of an antenna is usually accompanied by increases in the axis torques required to drive the antenna against wind. The proposed increase in the diameters of the 64-m antenna dishes to 70 m (plus a noise shield) does require increased axis torques. This report shows the effect of these increased torques on the axis speeds.

## II. Description of the Axis Drives

The azimuth-axis drive is composed of a large bull gear, four speed reducers, each of which is driven by two hydraulic motors, a brake, a servo valve, and the necessary hydraulic power source.

The elevation-axis drive is similar, but has two bull gears in parallel, each of which is driven by two speed-reducer units. One hydraulic motor on the input end of each speed reducer applies a constant torque which is equilibrated by an equal and opposite torque from a hydraulic motor on one of the other speed reducers. These countertorquing motors serve to keep the drive system free of backlash. Each speed reducer also has

a second motor attached to its input end, and these motors are termed the torquing motors. The torquing motors of each axis drive are controlled by a single servo valve. Figure 1 is a schematic of two drive units and a bull gear. In actuality the motors connect to the output pinion through a multistage gear reduction. Figure 1 demonstrates that the countertorquing hydraulic system is independent of the torquing hydraulic system, and that only the torquing motors resist wind or inertia torques.

## III. Drive Torque Analysis

The maximum torques, induced by wind, about the azimuth and elevation axes are taken from Table VI of Ref. 1, and are as follows, where  $T_A$  is the maximum azimuth torque and  $T_E$  is the maximum elevation torque (the subscripts 64 and 72 pertain to the 64-m and 70-m antennas, respectively):

$$T_{A64} = 0.117 q \frac{\pi}{4} D^3 \quad (1)$$

$$T_{A72} = 0.122 q \frac{\pi}{4} D^3 \quad (2)$$

$$T_{E64} = 0.122 q \frac{\pi}{4} D^3 \quad (3)$$

$$T_{E72} = 0.123 q \frac{\pi}{4} D^3 \quad (4)$$

where

$q = 1/2 \rho V^2$  = the dynamic pressure of the wind

$\rho$  = the air density

$V$  = the wind speed

$D$  = the antenna dish diameter

The ratios between the maximum torques of the two antennas may be obtained directly from Eqs. (1), (2), (3), and (4), and are

$$\frac{T_{A72}}{T_{A64}} = \frac{0.122 \left(\frac{72}{64}\right)^3}{0.117 \left(\frac{72}{64}\right)^3} = 1.476 \quad (5)$$

$$\frac{T_{E72}}{T_{E64}} = \frac{0.123 \left(\frac{72}{64}\right)^3}{0.122 \left(\frac{72}{64}\right)^3} = 1.432 \quad (6)$$

The maximum azimuth torque occurs at an elevation angle of  $5^\circ$  and a wind azimuth angle of  $120^\circ$ . The maximum elevation torque occurs at an elevation angle of  $60^\circ$  and a wind azimuth of  $180^\circ$ .

The torque of either antenna axis may be written

$$T_{ANT} = C q \frac{\pi}{4} D^3 = C \frac{1}{2} \rho V^2 \frac{\pi}{4} D^3 = C \frac{\pi}{8} \rho V^2 D^3 \quad (7)$$

where  $C$  is the pertinent numerical coefficient appearing in Eqs. (1), (2), (3), and (4).

The pressure drop  $\Delta P$  across the servo valve, see Fig. 1, is obtained from Ref. 2 and is

$$\Delta P = \left[ 1 - \left( \frac{Q_L}{Q_{NL}} \right)^2 \right] \frac{P_S}{1.15} \quad (8)$$

where

$P_S$  = the supply pressure to the servo valve

$Q_L$  = the load flow through the valve

$Q_{NL}$  = the no-load flow through the valve and is a function of the supply pressure,  $P_S$

The factor, 1.15, allows for line and motor losses.

The load flow,  $Q_L$ , can be expressed in terms of the antenna-axis angular speed, since the angular speed is proportional to the flow through the hydraulic motors.

$$Q_L = \frac{\alpha r n d}{360} \text{ volume per unit time} \quad (9)$$

where

$\alpha$  = the axis speed in degrees per unit time

$r$  = the speed ratio between the hydraulic motor and antenna axis

$n$  = the number of motors supplied by one servo valve

$d$  = the motor displacement per turn

Substitute Eq. (9) into Eq. (8) and obtain

$$\Delta P = \left[ 1 - \left( \frac{\alpha r n d}{360 Q_{NL}} \right)^2 \right] \frac{P_S}{1.15} \quad (10)$$

The output torque from one hydraulic motor,  $T_{HM}$ , is

$$T_{HM} = \frac{\Delta P d}{2\pi} \quad (11)$$

Since there are four torquing motors per antenna axis, the motor torque also must be

$$T_{HM} = \frac{T_{ANT}}{4r\eta} \quad (12)$$

where  $\eta$  is the efficiency of the speed reducer. Equate Eq. (11) to Eq. (12) and obtain

$$\frac{\Delta P d}{2\pi} = \frac{T_{ANT}}{4r\eta} \quad (13)$$

Substitute Eqs. (10) and (7) into Eq. (13) and obtain

$$\left[ 1 - \left( \frac{\alpha r n d}{360 Q_{NL}} \right)^2 \right] \frac{P_S}{1.15} \frac{d}{2\pi} = \frac{C \pi \rho V^2 D^3}{32 r \eta} \quad (14)$$

Solve Eq. (14) for  $\alpha$  and obtain

$$\alpha = \frac{360 Q_{NL}}{r n d} \left[ 1 - \frac{C \pi^2 1.15 \rho V^2 D^3}{16 r \eta d P_S} \right]^{1/2} \quad (15)$$

For a particular servo valve, the no-load flow,  $Q_{NL}$ , is a certain function of the valve-supply pressure,  $P_S$ . From Fig. 1 of Ref. 4, which pertains to the servo valve now used on the 64-m antennas (namely MOOG 72-163), the value of  $Q_{NL}$  is given graphically as a function of  $P_S$ . The displacement per turn of this motor is  $.0000395 \text{ m}^3$  ( $2.41 \text{ in.}^3$ ) and the  $Q_{NL}$  value is  $.00580 \text{ m}^3/\text{s}$  ( $354 \text{ in.}^3/\text{s}$ ) for  $P_S = 2069 \cdot 10^4 \text{ N/m}^2$  (3000 psi); the  $Q_{NL}$  is  $.00567 \text{ m}^3/\text{s}$  ( $346 \text{ in.}^3/\text{s}$ ) for  $P_S = 1724 \cdot 10^4 \text{ N/m}^2$  (2500 psi).

From Fig. 133 of Ref. 2 the efficiency of the speed reducer,  $\eta$ , is given as .90 for high torques. From Table 5 of Ref. 2, the speed ratio between motor and antenna axis,  $r$ , is 28724 for the azimuth axis and 28730 for the elevation axis. Of the three 64-m antennas, the one at DSS-43 is the closest to sea level, namely 670 m. At this elevation the air density is approximately 96% of the standard sea-level air density. Substituting the foregoing parametric values into Eq. (15), together with the appropriate  $C$  values from Eqs. (1), (2), (3), and (4), the curves of Figs. 2 and 3 have been drawn. These curves show the maximum antenna-axis speeds plotted against the wind speed for the antenna attitudes which produce the maximum axis torques.

The error band shown for one of the curves of both Figs. 2 and 3 is based upon a wind moment coefficient error of  $\pm 15\%$ .

The elevation axis torque caused by bearing friction is less than 1% of that coming from a 18 m/s (40 mph) wind. The elevation axis imbalance tends to aid the drive to the stow position; however, it is also of negligible significance.

The azimuth axis torque caused by the hydrostatic bearing and by the cable wrap is less than 1% of that coming from a 18 m/s (40 mph) wind.

## IV. Conclusions

The increased dish diameter causes the maximum azimuth and elevation torques to increase 48% and 43%, respectively.

In Fig. 2 the maximum elevation axis speeds are plotted against the wind speed for various values of the parameters appearing in Eq. (13). For the case of the 70-m antenna with a noise shield, abbreviated 72 m, using the same hydraulic drive equipment as now used with the 64-m antenna, but having the hydraulic supply pressure increased, the curve is given with an error band shown cross-hatched. The left edge of the error band intersects the 0.25/s axis speed at a wind speed value of 18.33 m/s (41 mph). This means that at the critical antenna attitude, an elevation axis speed of 0.25/s might be limited to wind speeds less than 18.33 m/s. The left boundary of the error band also shows that at the critical antenna attitude, no elevation drive would be possible at winds greater than 21.7 m/s (48.5 mph). Although the substitution of larger hydraulic motors would extend the driving range at low speeds, the driving range at greater speeds would be reduced. Only by combining an additional servo valve with larger motors can the driving range be increased for all speeds.

In Fig. 3 the maximum azimuth-axis speeds are plotted against the wind speed for various values of the parameters of Eq. (13). The results are similar to those pertaining to the elevation axis.

## References

1. McGinness, H., *The Effects of Wind Loading on the Bearing and Drives of the 64m and 72m Antennas*, unpublished, Reorder Number 84-2, Jet Propulsion Laboratory, Pasadena, California, May, 1984.
2. *The NASA/JPL 64m Diameter Antenna at Goldstone, California: Project Report*, Tech. Memorandum 33-671, Jet Propulsion Laboratory, Pasadena, California, July 15, 1974.
3. *MOOG Technical Bulletin 122*, Moog Inc., Controls Division, East Aurora, New York, 1969.
4. *MOOG Catalog 721979*, Moog Inc. Controls Division, East Aurora, New York, 1979.

REF JPL DWG 9435981

CONDITION SHOWN  
 $P_{\text{COUNTER}} > P_{\text{TORQUE}}$   
TORQUE

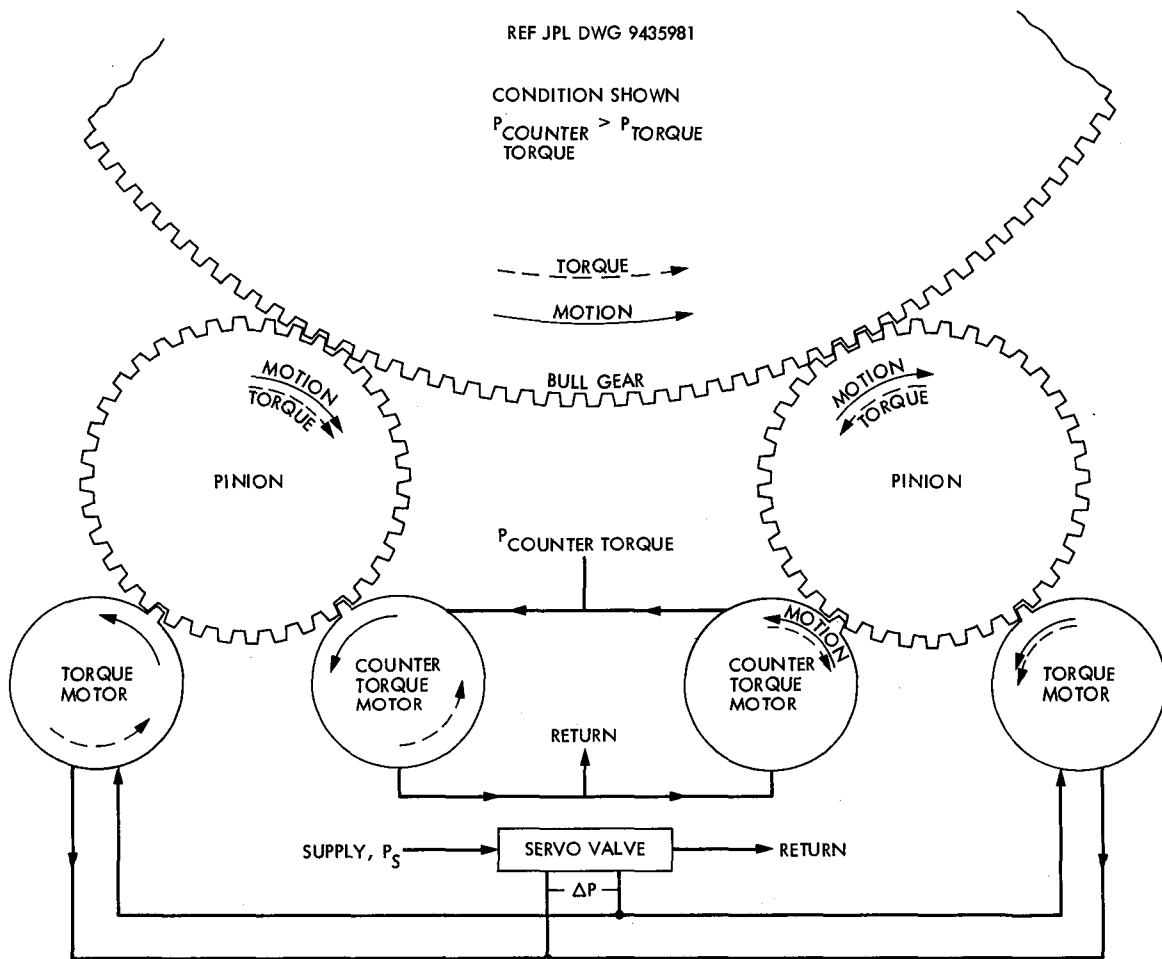


Fig. 1. Schematic of bull gear, pinion, hydraulic motors, and servo valve



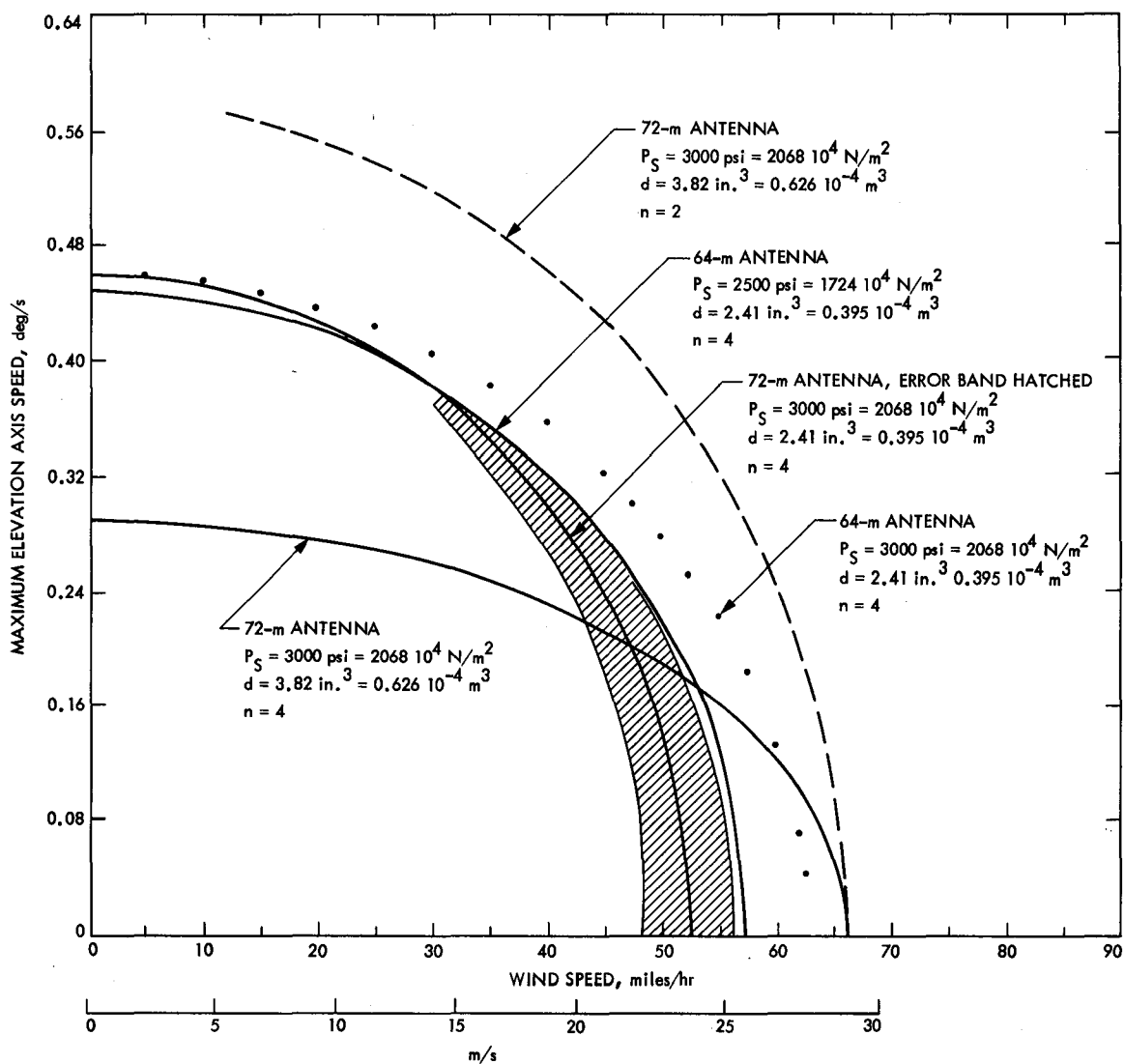


Fig. 2. Maximum elevation axis speed versus wind speed at critical configuration (elevation = 60°, azimuth = 180°, air density = 96% of standard sea-level density)

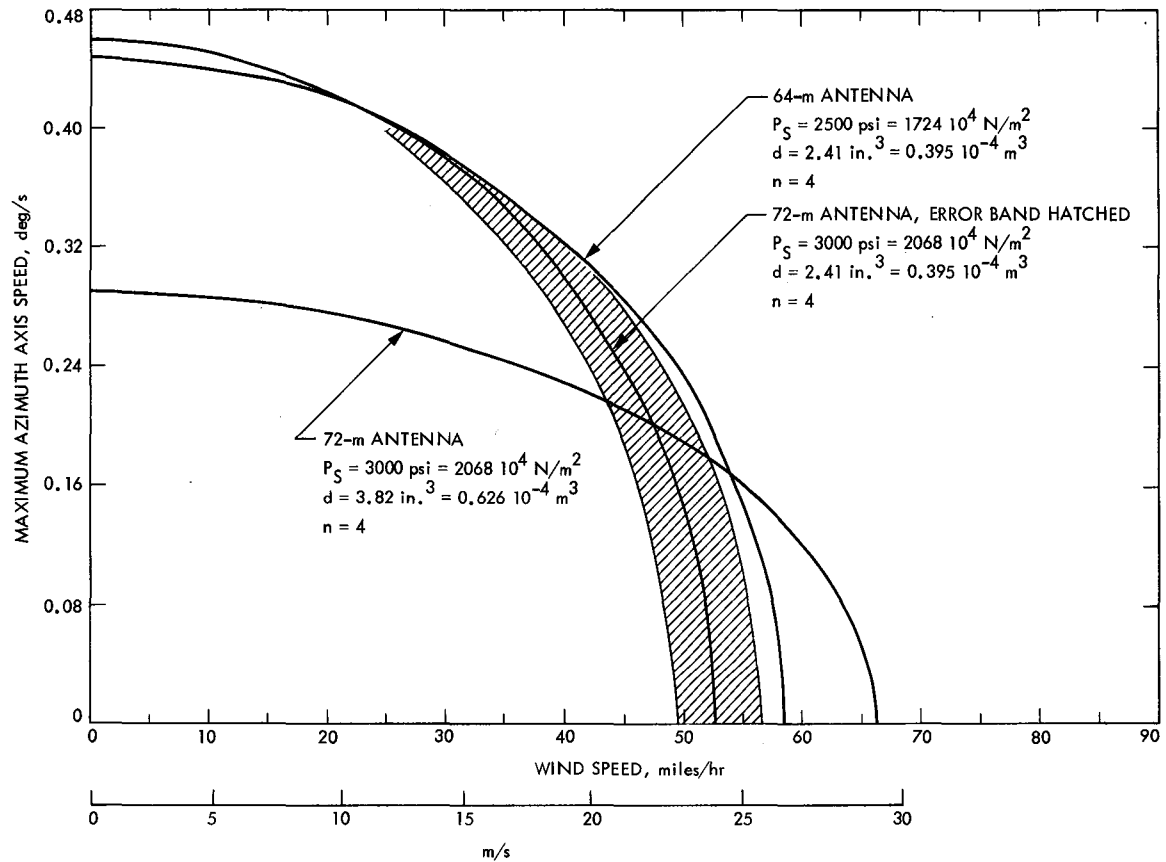


Fig. 3. Maximum azimuth axis speed versus wind speed at critical configuration (elevation = 5°, azimuth = 120°, air density = 96% of standard sea-level density)

# An Evaluation of the 64-Meter Antenna Radial Bearing for Use on the 70-Meter Antenna

H. D. McGinness

Ground Antennas and Facilities Engineering Section

*An analysis of the 64-m antenna radial bearing shows that it will be satisfactory for the increased loads brought about by increasing the antenna dish to a diameter of 70-m.*

## I. Introduction

During the autumn and winter of 1983 and 1984 a new radial bearing runner assembly was installed at DSS-14. The runner was made in accordance with JPL drawing 9474446G. The problems associated with the old runner and their causes have been reported in Ref. 1. Figure 1 shows a cross section of the installed runner, its alignment bolts, anchor nuts, and grout. Before the old runner was removed it was not known whether the anchor nuts embedded in the concrete would be reusable for the new runner; that is, it was uncertain whether the old alignment bolts could be removed from the anchor nuts. Fortunately all of the bolts were removed without damaging the anchor nuts, thereby eliminating the need for the laborious task of chipping out concrete and embedding new anchor nuts.

Reference 1 describes the reference ring which was used for monitoring the changes in the old runner which had become distorted. This same reference ring was used for adjusting the new runner for roundness. Figure 2 shows the method of aligning the runner to the reference ring.

In late 1983 the radial bearing wheel assemblies were removed and thoroughly inspected. It was decided to grind

the rolling surfaces true to the bearing journals, and this was accomplished to concentricity and cylindricity accuracies of approximately 0.025 mm (0.001 in.). For the convenience of subsequent alignment, the upper outer edges of all wheels were made perpendicular to the rolling surfaces to within 0.025 mm (0.001 in.). This permits the wheel alignment to be made or checked simply by placing a precision level on the upper outer edge of the wheel. Figure 3 shows the plan view of the radial bearing and the three truck assemblies which are attached to the alidade base structure. The individual wheel bearing housings can be shimmed to adjust dimensions  $b$  and  $t$  as shown in Fig. 3. Since the bearings are self-aligning spherical rollers, such shimming can achieve near perfect alignment of the wheels. Figure 4 shows the wheel and bearing assembly. Even when the wheels are preloaded against the runner, a precision level can be placed on the upper edge of a wheel, aligned either in a radial or tangential direction. Since the runner surface forms a vertical cylinder, such level measurements detect any slight misalignment of the wheel, and corrective shim thickness can be calculated promptly.

The critical loads on the wheels are determined by the wind direction and magnitude, the preload in the azimuth drive links, imperfections in the runner (bumps or indentations), and the initial preload applied to the truck assemblies.

## II. Truck Load From Non-Circular Track

The wheel truck load caused by an imperfectly round runner depends upon the stiffnesses of the several components constituting the elastic system. These components are the alidade base triangle, the girder connecting the truck assembly to the corner weldment of the base triangle, the pedestal supporting the runner, the runner, the wheels, the wheel bearings, the truck frame, the stem, and the pivot pin. Most of these components are identified in Fig. 5. The details of the truck assembly can be obtained from JPL drawing 9437995.

An attempt was made to calculate the above mentioned stiffness components. The corresponding deflections are listed in Table 1. Since there are three trucks involved, the deflections per truck must be multiplied by 3 to obtain the amount to be combined with the single alidade base triangle. The calculated stiffness,  $k_c$ , is the reciprocal of the total deflection per unit load; hence the calculated stiffness is

$$\frac{10^{10}}{17.91} = 0.0558 \times 10^{10} \text{ N/m } (3.19 \times 10^6 \text{ lb/in.})$$

An experiment was made wherein the deflection  $\delta$  was measured for a series of hydraulic jack forces, applied as indicated in Fig. 5. The resulting measured stiffness,  $k_m$ , was  $0.0606 \times 10^{10} \text{ N/m } (3.46 \times 10^6 \text{ lb/in.})$ . This value of the stiffness will be used in estimating the effect of an out-of-round runner on the wheel load.

The amount that the runner is out of round is determined by making a series of radial measurements when there is no preload in the trucks. From a pivot point inside the instrument tower, measurements can be made to the inside of the reference ring at every  $15^\circ$ . Then measurements are made from the reference ring to the runner, as shown in Fig. 2, and the sums are the desired radial measurements which can be plotted as shown in Fig. 6.

The variation in truck preload can be established as follows:

- (1) Determine at what antenna azimuth angle the wheels are to be preloaded and locate the six wheel positions on Fig. 6(a). Denote the ordinates of the wheels of truck No. 1 as  $Y_{1B}$  and  $Y_{1A}$  in accordance with the wheel identification per Fig. 3. Denote the ordinates of the other wheels as  $Y_{2F}$ ,  $Y_{2E}$ ,  $Y_{3D}$ ,  $Y_{3C}$ .
- (2) Form the sum of the ordinates of all six wheels at the preload position and denote it as  $Y_p$ .
- (3) Let the wheels traverse a distance of  $120^\circ$ , as on Fig. 6(a) and denote the sum of all six wheel ordinates as  $Y_\theta$ .

(4) Plot  $Y_\theta$  versus azimuth angle as per Fig. 6(b).

(5) Determine  $Y_\theta$  maximum and  $Y_\theta$  minimum.

(6) Denote the initial truck preload by  $P_i$ .

(7) The maximum increase from  $P_i$  is  $+\Delta P_i$ ,

$$+\Delta P_i = (Y_{\theta \text{ MAX}} - Y_p) k_m \quad (1)$$

(8) The maximum decrease from  $P_i$  is  $-\Delta P_i$ ,

$$-\Delta P_i = (Y_p - Y_{\theta \text{ MIN}}) k_m \quad (2)$$

(9) The total excursion of the preload,  $\Delta P$ , is

$$\Delta P = (Y_{\theta \text{ MAX}} - Y_{\theta \text{ MIN}}) k_m \quad (3)$$

## III. Truck Load Induced by Azimuth Drive

The azimuth axis wind torque is resisted by four azimuth drive units, which effectively are four links connecting the corners of the alidade base triangle to tangent points on the azimuth bullgear. In Fig. 7 these four links are represented by the dashed vectors labeled  $P_D$ , where  $P_D$  is the preloaded value of the link load and exists at this value only when the azimuth torque is zero. When the wind torque is finite, the link loads are of different magnitudes such that the torque produced equilibrates the applied wind torque. Since the maximum and minimum truck loads occur when the wind blows directly into the dish at a  $5^\circ$  elevation angle, a condition for which the azimuth torque is zero, the effect of the link loads on the trucks will be analyzed only for the preloads,  $P_D$ .

The link preloads,  $P_D$ , are exactly statically equivalent to their resultant components shown in Fig. 7, namely the force  $0.816 P_D$  applied at joint 3, and the forces  $0.995 P_D$  and  $0.103 P_D$  applied at joints 1 and 2. The elastic structure composed of the base triangle and the truck assemblies is statically indeterminate under this loading; hence, the truck loads will involve a consideration of the stiffnesses of the members. Denote the truck load at joint number 3 as  $\beta P_D$  and denote the load in truck number 1 as  $F_1$ . The load in each of the triangle legs meeting at joint 3 is  $[(0.816 - \beta)/(2 \cos 30^\circ)] P_D$ .

Consider the horizontal equilibrium of joint 1 and obtain the following equation:

$$\left( \frac{0.816 - \beta}{2 \cos 30^\circ} \right) P_D \cos 30^\circ + F_1 \cos 60^\circ = 0.995 P_D \quad (4)$$

Solve Eq. (4) for  $F_1$  and obtain:

$$F_1 = \frac{P_D \left[ 0.995 - \left( \frac{0.816 - \beta}{2} \right) \right]}{\cos 60^\circ} = P_D (1.174 + \beta) \quad (5)$$

Consider the vertical equilibrium of joint 1 and obtain:

$$F_v + P_D (1.174 + \beta) \cos 30^\circ + P_D \frac{(0.816 - \beta)}{2 \cos 30^\circ} \cos 60^\circ + 0.103 P_D = 0 \quad (6)$$

Solve Eq. (6) for  $F_v$  and obtain:

$$F_v = -P_D [0.103 + 1.174 (0.866) + 0.866 \beta + 0.236 - 0.289 \beta] = -P_D [1.355 + 0.577 \beta] \quad (7)$$

The loads in terms of  $\beta$  are now known for all the members of the elastic system and are marked in Fig. 7.

The strain energy,  $V$ , of a prismatic member loaded axially is:

$$V = \frac{1}{2} \left( \frac{F^2 L}{EA} \right) \quad (8)$$

where  $F$  is the axial load;  $E$  is the elastic modulus; and  $L/A$  is the ratio of member length to member cross sectional area. For the base triangle legs,  $L/A = 797/272 = 2.93$  1/in. (115.35 1/m). Based upon the measured  $k_m$  of  $3.46 \times 10^6$  lb/in. ( $0.0606 \times 10^{10}$  N/m), the effective  $L/A$  for the truck assemblies is 2.05 1/in. (80.7 1/m). Using these  $L/A$  values together with the member loads marked on Fig. 7, sum the strain energy in the entire elastic system and obtain:

$$V = \frac{P_D^2}{2E} \left\{ (1.355 + 0.577 \beta)^2 2.93 + 2 (0.471 - 0.577 \beta)^2 2.93 + \beta^2 (2.05) + 2 (1.174 + \beta)^2 2.05 \right\} \quad (9)$$

Simplifying there is obtained:

$$V = \frac{P_D^2}{2E} [12.329 + 11.0232 \beta + 9.076 \beta^2] \quad (10)$$

By the principle of minimum strain energy, the derivative of  $V$  with respect to the parameter  $\beta$  must be zero; hence,

$$\frac{\partial V}{\partial \beta} = \frac{P_D^2}{2E} [11.0232 + 18.152 \beta] = 0 \quad (11)$$

$$\beta = -0.6187 \quad (12)$$

For this value of  $\beta$  the member loads are marked in Fig. 8.

The value of the link preload,  $P_D$ , is proportional to the hydraulic motor supply pressure,  $p$ , and can be adjusted over a large range. The value of  $P_D$  is:

$$P_D = \frac{DR\eta p}{2\pi r} \quad (13)$$

where

$D$  = the displacement of the hydraulic motor per turn

$R > 1$  = the speed ratio of the gear box drive

$\eta$  = the gear box efficiency

$r$  = the pitch radius of the output pinion

Substituting the appropriate values into Eq. (13) there is obtained:

$$P_D = \frac{2.41 (610) (0.90) p}{2\pi 8.912} = 23.63 (p_{\text{psi}}) \text{ lb} \quad (14)$$

If the current value of 550 psi for  $P$  is used, the value of  $P_D$  is:

$$P_D = 23.63 (550) = 12996 \text{ lb (57804 N)} \quad (15)$$

This value of  $P_D$  produces 8045 lb (35782 N) of tension in truck 3 and 7213 lb (32082 N) of compression in trucks 1 and 2.

The preceding analysis is based on the assumption that the link preloads are tension loads. It is possible to reverse the hydraulic motor connections and obtain compressive link preloads, in which case the senses of the truck loads would reverse.

## IV. Truck Loads From Wind

The maximum and minimum truck loads occur when the wind blows directly into the dish at an elevation angle of  $5^\circ$ . Figure 9 shows the symmetrical loading on the alidade base triangle in terms of the unknown parameter  $\alpha$ . It is assumed that the truck compressive preload is sufficient to enable truck number 3 to carry the tension load induced by the wind.

The unknown truck forces are denoted as  $Q$  for truck number 3 and as  $P$  for trucks 1 and 2. Static equilibrium requires that:

$$W = Q + 2P \sin 30^\circ = Q + P \quad (16)$$

In Fig. 9 the forces in the six members of the elastic structure are shown in terms of  $\alpha$ ,  $W$ , and  $Q$ .

The strain energy,  $V$ , of a prismatic member axially loaded is:

$$V = \frac{1}{2} \left( \frac{F^2 L}{EA} \right)$$

where

$F$  = the axial load

$E$  = the elastic modulus

$L/A$  = the ratio of length to cross sectional area

The total strain energy in the elastic structure is:

$$V = \frac{1}{2E} \left\{ \frac{Q^2 L_s}{A_s} + 2(W - Q)^2 \frac{L_s}{A_s} + \frac{2(Q - \alpha W)^2}{3} \frac{L}{A} \right. \\ \left. + \left[ (3 - \alpha) \frac{W}{2} - Q \right]^2 \frac{1}{3} \left( \frac{L}{A} \right) \right\} \quad (17)$$

where  $L_s/A_s$  pertains to the equivalent truck member and  $L/A$  pertains to the triangle base members.

By the principle of minimum strain energy, the derivative of  $V$  with respect to  $Q$  must be zero; hence,

$$\frac{\partial V}{\partial Q} = \frac{1}{2E} \left\{ 2 \frac{L_s}{A_s} Q + (4Q - 4W) \frac{L_s}{A_s} + \left( \frac{4}{3} Q - \frac{4}{3} \alpha W \right) \frac{L}{A} \right. \\ \left. + \left[ \frac{2}{3} Q + \left( \frac{\alpha}{3} - 1 \right) W \right] \frac{L}{A} \right\} = 0 \quad (18)$$

Simplifying Eq. (18) there is obtained:

$$\frac{Q}{W} = \frac{4 \frac{L_s}{A_s} + (1 + \alpha) \frac{L}{A}}{6 \frac{L_s}{A_s} + 2 \frac{L}{A}} \quad (19)$$

For the particular case of  $\alpha = 1/3$ , when the wind load is applied equally to the three corners of the base triangle, Eq. (19) becomes:

$$\frac{Q}{W} = \frac{4 \frac{L_s}{A_s} + \frac{4}{3} \frac{L}{A}}{6 \frac{L_s}{A_s} + \frac{2}{3} \frac{L}{A}} = \frac{4 \left( \frac{L_s}{A_s} + \frac{1}{3} \frac{L}{A} \right)}{6 \frac{L_s}{A_s} + \frac{1}{3} \frac{L}{A}} = \frac{2}{3} \quad (20)$$

which shows that for the particular  $\alpha = 1/3$ ,  $Q/W$  is independent of the relative stiffnesses of the members.

Estimates for  $L/A$  and  $L_s/A_s$  are respectively 2.93 and 2.05 in.<sup>-1</sup>

Substituting these into Eq. (19), there is obtained:

$$\frac{Q}{W} = \frac{4(2.05) + 2.93 + 2.93 \alpha}{6(2.05) + 2(2.93)} = 0.613 + 0.161 \alpha \quad (21)$$

Even if  $\alpha$  is substantially different from 1/3, the value of  $Q/W$  is not strongly affected; therefore the value of 1/3 for  $\alpha$  shall be assumed, thus producing:

$$Q = (2/3) W \quad (22)$$

$$P = (1/3) W \quad (23)$$

## V. Truck Preload

The minimum truck preload must be enough to insure that truck No. 3 is in compression at a wind speed of 70 mph (31.3 m/s) when the antenna is at the critical attitude of zero wind azimuth and 5° elevation angle. Denote the truck loads as  $F_1$ ,  $F_2$ , and  $F_3$ . Each of these will be the algebraic sum of the loadings caused by preload, drive link load, wind, and out of roundness of the track. The values for these components are set out in Table 2. The values of  $F_3$  and  $F_1$  for the 64-m and 70-m antennas in terms of the truck preload  $P$  and the track out of roundness factors are:

$$F_{364} = 8044 + 285866 + (Y_{\theta \text{MAX}} - Y_{\theta \text{MIN}}) 3.46 \times 10^6 - P \quad (24)$$

$$F_{372} = 8044 + 386667 + (Y_{\theta \text{MAX}} - Y_{\theta \text{MIN}}) 3.46 \times 10^6 - P \quad (25)$$

$$F_{164} = -7212 - 142933 + (Y_{\theta \text{MAX}} - Y_{\theta \text{MIN}}) 3.46 \times 10^6 - P \quad (26)$$

$$F_{172} = -7212 - 193333 + (Y_{\theta \text{MAX}} - Y_{\theta \text{MIN}}) 3.46 \times 10^6 - P \quad (27)$$

Equations (24), (25), (26), and (27) apply for the critical condition of a 70-mph (31.3-m/s) wind at zero wind azimuth and an elevation angle of 5°. For these conditions it is necessary that  $F_3$  be greater than zero. From Eqs. (24) and (25) the required values of the truck preloads  $P$  are:

$$P_{64} > 8044 + 258866 + (Y_{\theta \text{MAX}} - Y_{\theta \text{MIN}}) 3.46 \times 10^6 \text{ lb} \quad (28)$$

$$P_{72} > 8044 + 386667 + (Y_{\theta\text{MAX}} - Y_{\theta\text{MIN}}) 3.46 \times 10^6 \text{ lb} \quad (29)$$

where the factor  $(Y_{\theta\text{MAX}} - Y_{\theta\text{MIN}})$  must be measured in accordance with the instructions previously given.

The substitution of Eqs. (28) and (29) into Eqs. (26) and (27), respectively, yields the following minimum values for  $F_1$  at the critical configuration:

$$\begin{aligned} F_{164} &= -7212 - 142933 - 8044 - 285866 \\ &= -444055 \text{ lb } (-1975255 \text{ N}) \end{aligned} \quad (30)$$

$$\begin{aligned} F_{172} &= -7212 - 193333 - 8044 - 386667 \\ &= -595256 \text{ lb } (-2647830 \text{ N}) \end{aligned} \quad (31)$$

The value of the preload,  $P$ , should exceed the minimum value by some amount,  $\Delta P$ , to be determined. Then the value of  $F_1$  would be increased by  $\Delta P$ .

## VI. Truck and Wheel Alignment

In the past it has been difficult to align the trucks and wheels so that each has a lateral runout hysteresis loop within the desired amount. Past practice has been to jack the trucks into the correct vertical position, align the wheels to be parallel to the runner, and then apply the preload. Oftentimes one truck would have a satisfactory hysteresis loop, whereas others would not. It might be that vertical equilibrium of forces on the wheel required a vertical friction force; that is, at the time the preload was applied, the temporary forces from the vertical alignment jacks were not zero. A cylindrical roller, in general, does not have one definite rolling radius over the entire width of the roller when the elastic roller is pressed against an elastic track. The result is that over most of the roller width there is a finite amount of slippage as the rolling motion progresses. Small geometrical imperfections in the roller or track can cause the narrow no-slip regions to change. The effect can be that the vertical frictional resistance reduces drastically, thus allowing the wheel to seek a lower equilibrium position.

It is recommended that the truck stems be aligned so that when the wheels are barely clearing the track, and not supported by vertical jacks, the wheels are centered on the track wear strip and are parallel to it. This means that the structure supporting the truck stems be shimmed or modified so that the natural cantilevered position of the wheels is at the desired elevation. When such a position is obtained, the clearances between the track and wheel edges can be measured. This is

best done by measuring the level of the wheel upper edge in the radial direction. The wheel can then be shimmed at the spherical bearing housings until uniformity of clearance has been obtained. Then the wheel level can be measured in the track tangential direction and the bearing housings shimmed appropriately. Note that there is a small interaction between the radial and tangential alignments (the shimming surfaces are not quite perpendicular to radial and tangential lines), and this should be taken into account when striving for best alignment. When shimming for radial alignment, if dimension  $t$  of Fig. 3 is increased by a unit amount, dimension  $b$  must be decreased by 0.135 times the unit amount. When shimming for tangential alignment, if dimension  $b$  is increased by a unit amount, dimension  $t$  must be increased by 0.135 times the unit amount.

The hysteresis loop tests have been run over a  $\pm 120^\circ$  azimuth range. The usual result is that the lateral runout is more or less linear for a certain distance and then remains approximately constant for the rest of the distance. Upon direction reversal, the linear lateral motion commences and is followed by a constant displacement, the sum of which approximately equals the first half of the cycle.

It is believed that the linear portion of the lateral runout obtains until the induced side force caused by tangential misalignment is equilibrated by the elastic restoring force of the truck considered as a cantilevered beam. If this is true, the amount of lateral runout is proportional to the truck load since the induced side force is proportional to the truck load. Therefore, it is desirable to keep the truck preload no higher than is required by previous considerations. Furthermore, the contact stresses increase with the square root of the truck load. The minimum value of the truck preload,  $P$ , is obtained for the condition of a perfectly circular track for which the  $(Y_{\theta\text{MAX}} - Y_{\theta\text{MIN}})$  factor of Eqs. (28) and (29) would be zero. For the case of the 70-m antenna Eq. (29) may be written as follows:

$$P_{72} = 394711 + \Delta P + (Y_{\theta\text{MAX}} - Y_{\theta\text{MIN}}) 3.46 \times 10^6 \text{ lb} \quad (32)$$

where  $\Delta P$  is the increment above zero at the critical condition. If  $\Delta P$  is arbitrarily set at 5% of the first right hand term of Eq. (32), then  $P_{72}$  becomes:

$$P_{72} = 1.05 (394711) + (Y_{\theta\text{MAX}} - Y_{\theta\text{MIN}}) 3.46 \times 10^6 \text{ lb} \quad (33)$$

If the second right hand term of Eq. (33) is set at, say, 15% of the first right hand term, then the value of  $(Y_{\theta\text{MAX}} - Y_{\theta\text{MIN}})$  becomes:

$$(Y_{\theta\text{MAX}} - Y_{\theta\text{MIN}}) = \frac{1.05 (394711) (0.15)}{3.46 \times 10^6}$$

$$= 0.018 \text{ in. (0.456 mm)} \quad (34)$$

This apparently is a practical track alignment goal to strive for when setting the circularity of the runner, since the initial measurements made at DSS-14 on the new track gave approximately this result. It seems remarkable that such a large diameter bearing can be set to this accuracy.

If the value of Eq. (34) is substituted into Eq. (33) there is obtained:

$$P_{72} = 1.05 (394711) + 0.018 (3.46 \times 10^6)$$

$$= 476727 \text{ lb (2120585 N)} \quad (35)$$

$$P_{64} = 1.05 (293910) + 0.018 (3.46 \times 10^6)$$

$$= 370885 \text{ lb (1649781 N)} \quad (36)$$

Taking  $\Delta P_{64} = 0.05 (293910) = 14695 \text{ lb}$  and  $\Delta P_{72} = 0.05 (394711) = 19736 \text{ lb}$  and adding these respectively to Eqs. (30) and (31) there are obtained:

$$F_{164} = 444055 + 14695 = 458750 \text{ lb (2040622 N)} \quad (37)$$

$$F_{172} = 595256 + 19736 = 614992 \text{ lb (2735621 N)} \quad (38)$$

These can be taken as tentative values, but they should be revised if final track roundness values differ from the initial ones used here.

## VII. Contact Stresses in Wheels and Wear Strip

For the case of contact between a uniformly loaded cylindrical wheel and a cylindrical track of ten times the wheel diameter, the Hertz stress,  $\sigma_H$ , and the maximum shear stress,  $\tau$ , are, from Ref. 2:

$$\sigma_H = 0.605 \sqrt{\frac{FE}{DL}} \quad (39)$$

$$\tau = 0.183 \sqrt{\frac{FE}{DL}} \quad (40)$$

where

$F$  = the normal force between cylinder and plane

$E$  = the common modulus of elasticity of the materials

$D$  = the roller diameter

$L$  = the roller width

For the case of a triangularly distributed load across the width of the wheel, the load intensity per unit length at the heavily loaded edge would be twice as much as for the uniformly loaded case. Since the stresses of Eqs. (39) and (40) vary as the square root of the load per unit length, the Hertz stress,  $\sigma_H$ , and maximum shear stress,  $\tau$ , for this loading will be  $\sqrt{2}$  times those for the uniformly distributed case, thus,

$$\sigma_{HT} = 0.855 \sqrt{\frac{FE}{DL}} \quad (41)$$

$$\tau_T = 0.259 \sqrt{\frac{FE}{DL}} \quad (42)$$

In Table 3 are listed the maximum shear stresses corresponding to truck preloads and truck maximum loads for both the 64-m and 70-m antennas. It is assumed that the contact wearstrip has a minimum tensile yield strength of 68950 N/cm<sup>2</sup> (100000 psi) which corresponds to a shear yield strength of 39991 N/cm<sup>2</sup> (58000 psi). From Table 3 it may be seen that all shear stresses are well below this shear yield value. The wheels are case hardened and have considerably more strength than the wear strips.

## VIII. Wheel Bearings Loads

As Fig. 4 shows, each wheel is supported by two spherical roller bearings which are spaced 0.546 m (21.5 in.) apart. When the wheel is uniformly loaded across its width, the bearing radial loads are the same and each bearing radial load is equal to one-fourth the truck load since there are two wheels on each truck. For the case of triangularly distributed loading across the wheel width, the radial load on the more highly loaded bearing is two-thirds the wheel load or one-third the truck load. As Fig. 4 shows, only the upper wheel bearing can resist axial load. With the tangential wheel alignment required to achieve the desired hysteresis loop value, it is believed that the axial bearing load will not exceed 10% of the bearing radial load. From Ref. 3 the equivalent bearing load,  $P_E$  is:

$$P_E = F_r + 2.2 F_a \quad (43)$$



where  $F_r$  is the radial load and  $F_a$  is the axial load. For  $F_a = 0.10 F_r$ , Eq. (43) becomes:

$$P_E = F_r + 2.2 (0.10) F_r = 1.22 F_r \quad (44)$$

In Table 4 there are set out the equivalent bearing loads for the various loading conditions mentioned above. In all cases it is assumed that the axial load is 10% of the radial load. From Ref. 3 the bearing static and dynamic load ratings are respectively 2068320 N (465000 lb) and 1845920 N (415000 lb). These are substantially more than any of the entries of Table 4.

## IX. Conclusion

This report has discussed the derivation of the proper truck preload and has shown that it is dependent upon the azimuth drive preload direction, the wind direction and magnitude, and the out of roundness of the track. The resulting wheel and track contact stresses have been evaluated and found to be satisfactory for either the 64-m or 70-m antenna. The wheel bearing loads have been found to be quite satisfactory for the larger 70-m antenna.

Methods for evaluating the effects of track out of roundness and for aligning the wheel and truck assemblies have been presented. It is believed that these methods are practical and that the increased loadings on the parts will not affect the expected long life of the azimuth bearing.

## References

1. McGinness, H., and G. Gale, Rehabilitation of 64-m antenna radial bearing, *TDA Progress Report 42-65*, July 1981, pp. 151-161, Jet Propulsion Laboratory, Pasadena, Calif.
2. Timoshenko, S., *Theory of Elasticity*, McGraw Hill, 1934, First Edition, p. 349.
3. SKF Industries, Catalogue Reg. No. 47122, 1981, p. 30.

**Table 1. Stiffness components and corresponding deflections**

Component	Deflection per Truck, $10^{-10}$ m/N	Deflection per Set of Three Trucks, $10^{-10}$ m/N
Pedestal	0.354	1.062
Girder to Corner Weldment	1.598	4.796
Truck Pivot Pin	0.513	1.542
Truck Stem	0.194	0.582
Truck Frame	0.268	0.805
Wheel Contact	0.600	1.799
Wheel Bearings	0.519	1.557
Alidade Triangle Base		5.767
Total Deflection		17.910

**Table 2. Truck load components**

Load Source	$F_3$		$F_1$	
	N	lb	N	lb
Drive link load from Fig. 8 for $p = 550$ psi	35,781 TENSION	8,044	32,080 COMP	7,212
Wind Load from Eqs. (22), (23) and Fig. 9 for $W_{64} = 428800$ lb <sup>a</sup>	1,271,595	285,866	635,798	142,933
$W_{72} = 580000$ lb <sup>a</sup>	1,719,980 TENSION	386,667	859,988 COMP	193,333
Track out of roundness from Eq. (3) $\Delta P = (Y_{\theta \text{ MAX}} - Y_{\theta \text{ MIN}}) 3.46 \times 10^6$		$(Y_{\theta \text{ MAX}} - Y_{\theta \text{ MIN}}) 3.46 \times 10^6$ TENSION		
Preload	$P$ COMP	$P$	$P$ COMP	$P$

<sup>a</sup>From *The effects of wind loading on the bearings and drives of the 64-m and 72-m antennas* (unpublished), by H. D. McGinness, 1984, Table VI, Reorder No. 84-2, Jet Propulsion Laboratory, Pasadena, CA.

**Table 3. Wheel and track contact stresses**

	64-m Antenna		70-m Antenna	
Truck preload	1,649,781 N	(370,885 lb)	2,120,585 N	(476,727 lb)
Maximum shear stress from wheel preload uniform distribution (Eq. [40])	$14,704 \times 10^4 \text{ N/m}^2$	(21,326 psi)	$16,671 \times 10^4 \text{ N/m}^2$	(24,178 psi)
Truck maximum load	2,040,622 N	(458,750 lb)	2,735,621 N	(614,992 lb)
Maximum shear stress from wheel maximum load uniform distribution (Eq. [40])	$16,354 \times 10^4 \text{ N/m}^2$	(23,718 psi)	$18,936 \times 10^4 \text{ N/m}^2$	(27,461 psi)
Maximum shear stress from wheel maximum load triangular distribution (Eq. [42])	$23,145 \times 10^4 \text{ N/m}^2$	(33,568 psi)	$26,798 \times 10^4 \text{ N/m}^2$	(38,866 psi)

**Table 4. Equivalent wheel bearing loads for axial load = 10% radial load**

Loading Condition (See Table 3 for truck load values)	64-m Antenna		70-m Antenna	
	N	lb	N	lb
Preload uniformly distributed across wheel	503,157	113,120	646,747	145,402
Preload triangularly distributed across wheel	670,877	150,827	862,329	193,869
Maximum truck load uniformly distributed across wheel width	622,359	139,919	834,323	187,573
Maximum truck load triangularly distributed across wheel width	829,811	186,558	1,112,430	250,097

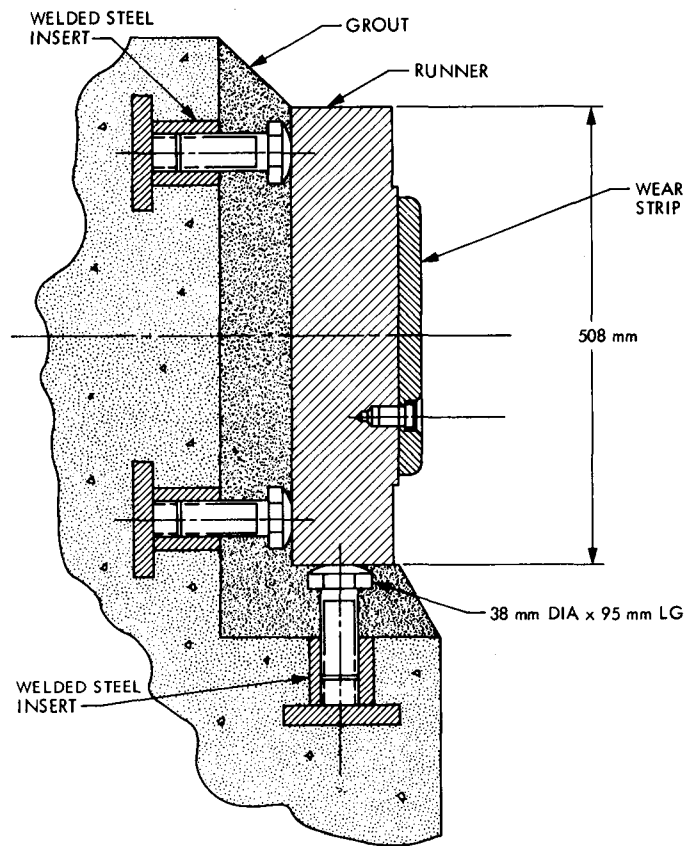


**Fig. 1. Cross section of runner showing alignment bolts and grout**

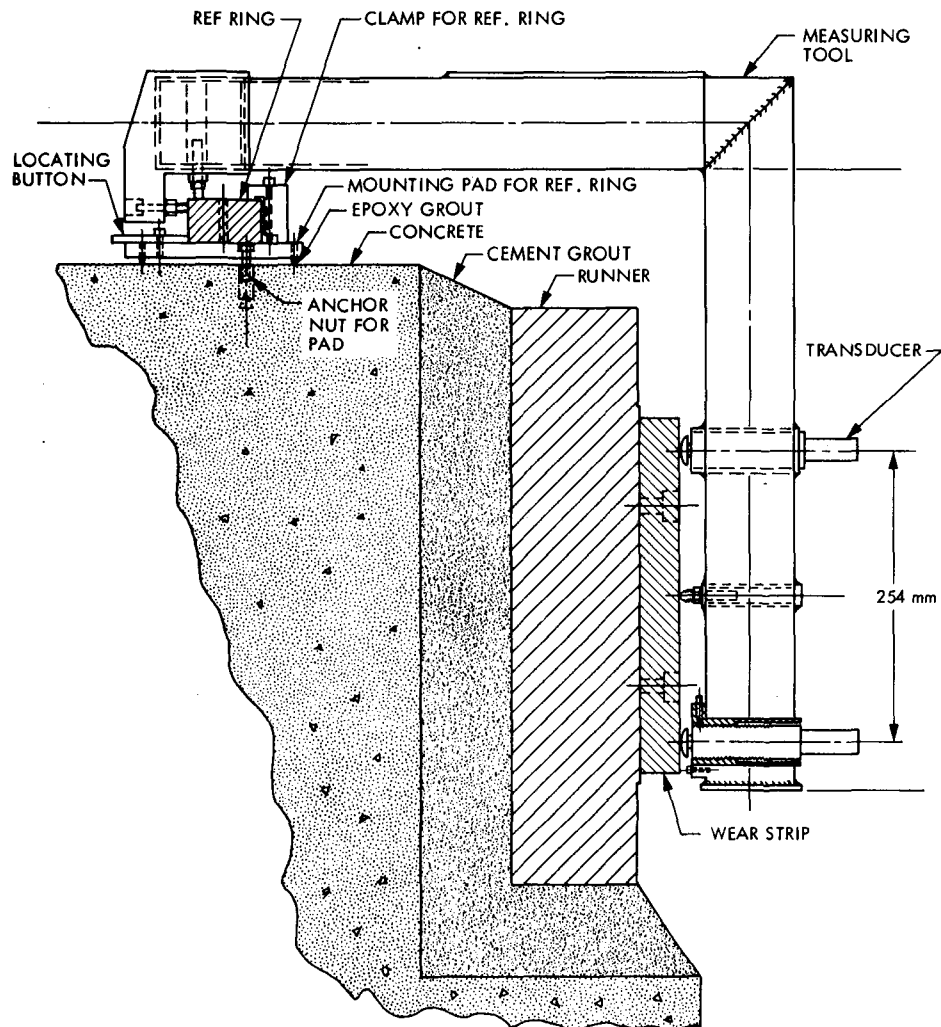
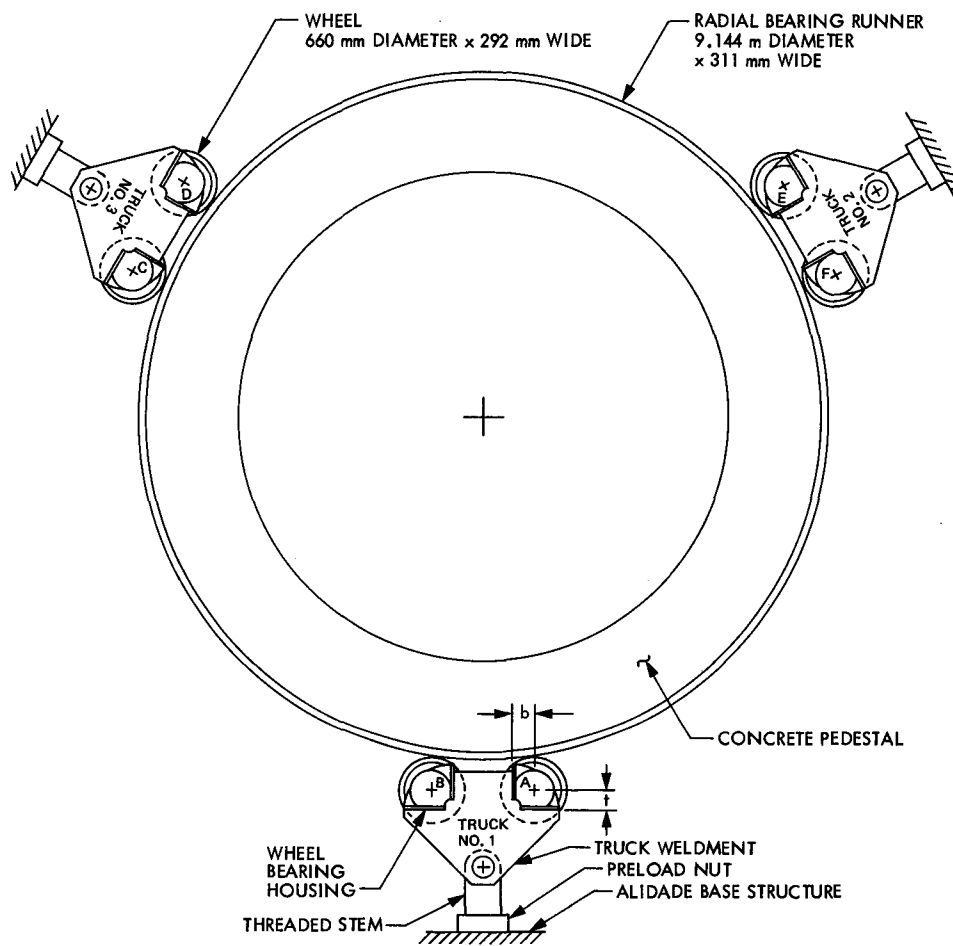
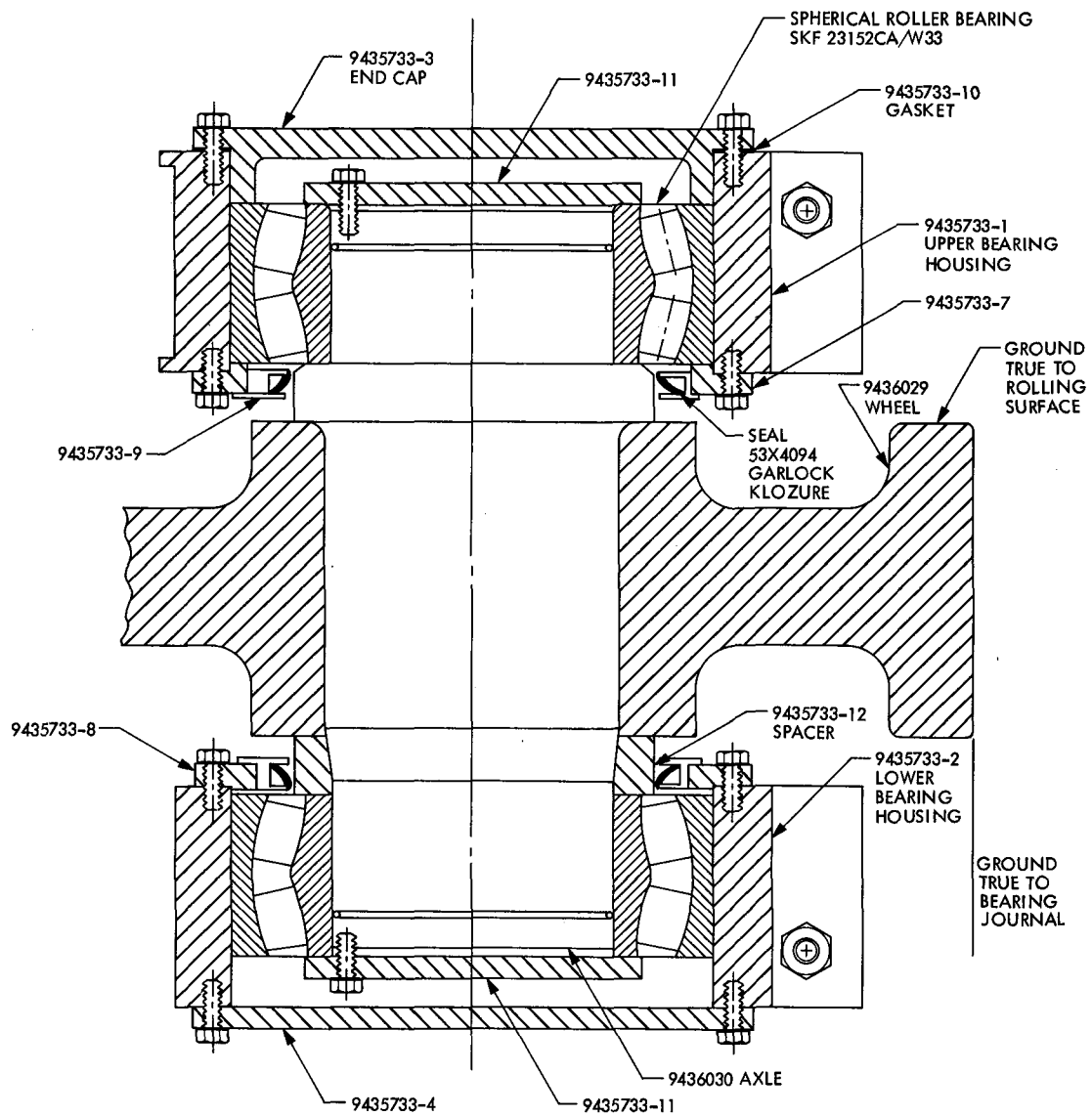


Fig. 2. Method of aligning runner to reference ring



**Fig. 3. Plan view of radial bearing runner and trucks**



**Fig. 4. Wheel and bearing assembly**

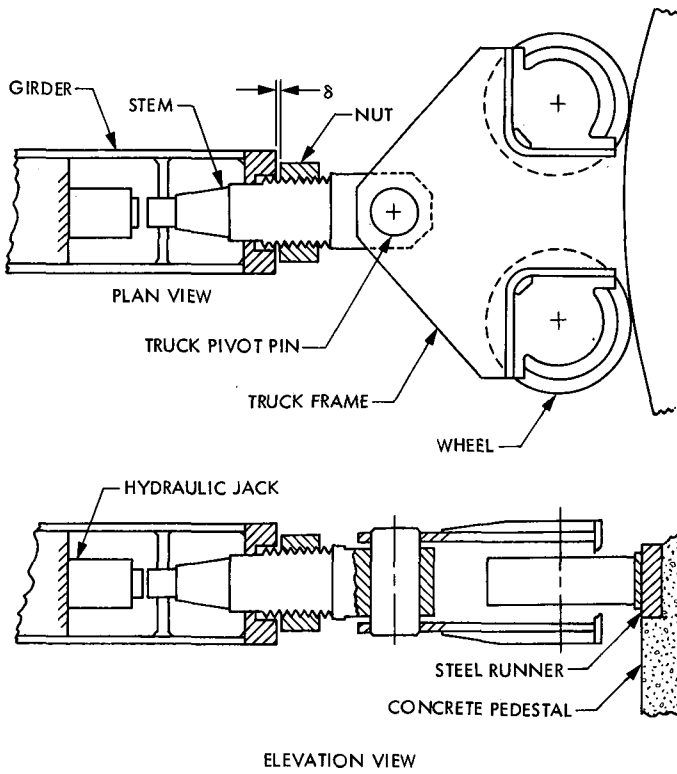


Fig. 5. Truck assembly, method of preloading

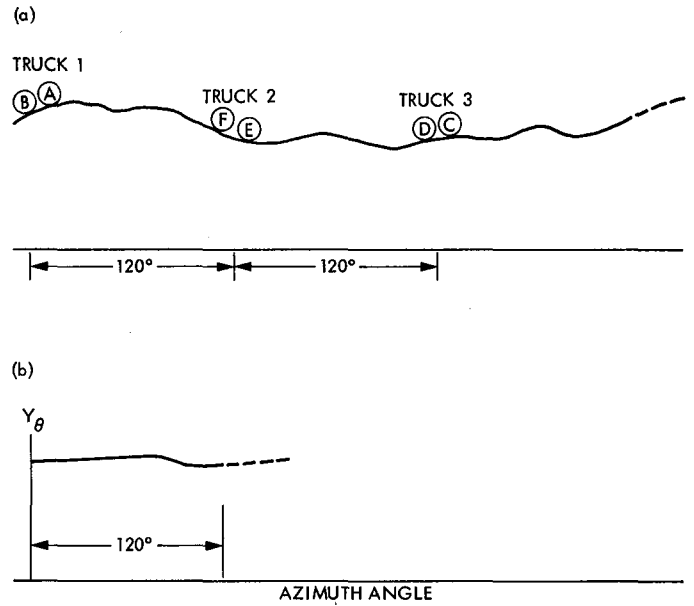


Fig. 6. Method of measuring runner roundness

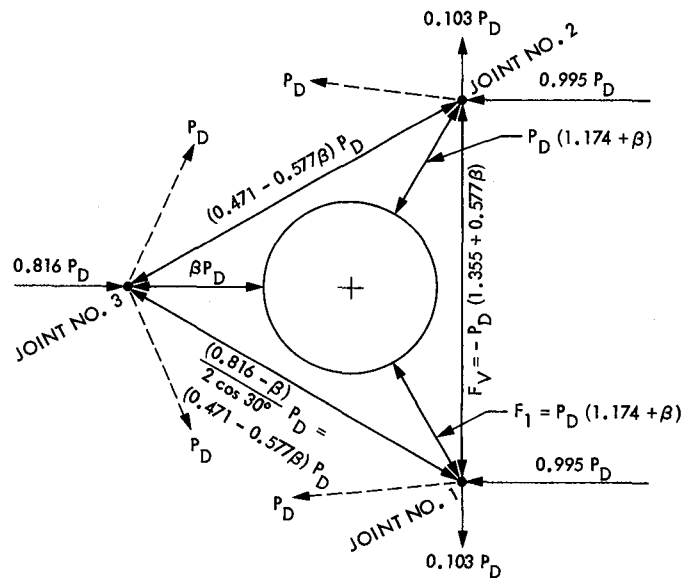


Fig. 7. Effect of azimuth drive preload



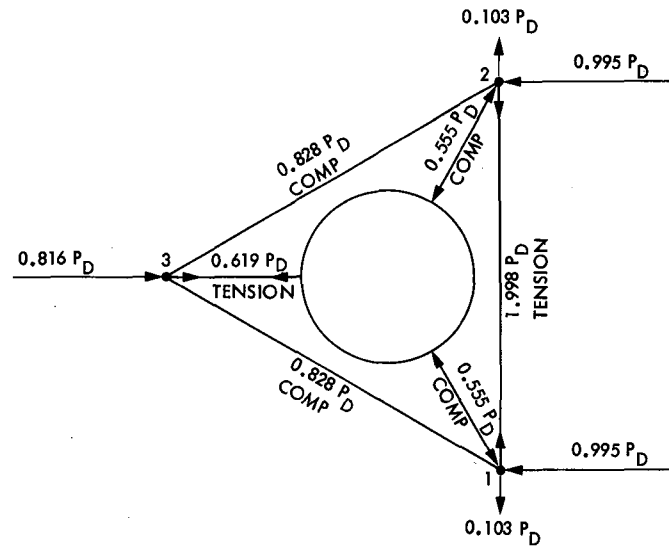


Fig. 8. Truck loads caused by azimuth drive preloads

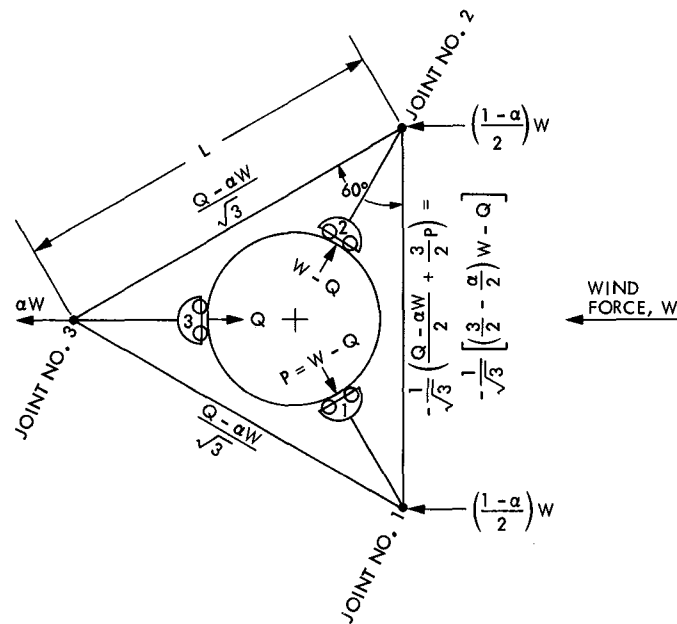


Fig. 9. Truck loads from wind

# Elevation Bearing Maximum Load, 70-Meter Antenna

H. D. McGinness

Ground Antennas and Facilities Engineering Section

*The elevation bearing loads of the 70-m antenna are presented and shown to be within the bearing safe loading limits.*

## I. Introduction

One of the preliminary frequency analyses of the 64-m antenna disclosed that considerable flexibility was attributable to the structure adjacent to the elevation bearings. In order to reduce this compliance, this adjacent structure and the bearings were made substantially larger. The result is that the stresses in these parts are small when used with the 64-m reflector and will remain sufficiently small when used with the larger 70-m reflector, which has an extended one-meter noise shield at its outer edge. This report serves to document the loads on the elevation bearings of the larger 70-m reflector and to compare these loads to the corresponding ones of the 64-m antenna.

## II. Design Description

The antenna elevation axis bearings are composed of two trunnion assemblies attached to the antenna tipping structure, four spherical roller bearings, and four bearing housings attached to the alidade. Each trunnion assembly is composed of a large steel casting (JPL Dwg. 9437476) having a forged steel shaft (JPL Dwg. 9435754) pressed into it. The centers of these trunnions are spaced 17.07-m (672 in.) apart, and the two spherical roller bearings at each trunnion assembly are sym-

metrically spaced 0.914 m (36 in.) from the trunnion centerline. Figures 1 and 2 show the general arrangement of the principal structural elements of the bearing installation. Appropriate seals, bearing retainers, etc. are not shown in these figures but are shown on JPL Dwg. 9436183 and 9437997.

## III. Bearing Maximum Loads

The loads on the elevation bearing assemblies are caused by the weight of the antenna tipping structure and by the wind loading acting on this structure.<sup>1</sup> The maximum radial load acting on one trunnion assembly,  $F_R$ , is given by the following equation, where the numerical subscripts 64 and 72 identify the antenna size:

$$F_{R_{64}} = \left\{ \left[ \frac{W_T}{2} + q \frac{\pi}{4} D^2 (0.345) \right]^2 + \left[ q \frac{\pi}{4} D^2 (0.451) \right]^2 \right\}^{1/2} \quad (1)$$

<sup>1</sup>The wind loading is derived in Appendix III and summarized in Table VI of *The Effects of Wind Loading on the Bearings and Drives of the 64-m and 70-m Antennas* (unpublished), H. McGinness, 1984, Reorder No. 84-2, Jet Propulsion Laboratory, Pasadena, Calif.

$$F_{R_{72}} = \left\{ \left[ \frac{W_T}{2} + q \frac{\pi}{4} D^2 (0.332) \right]^2 + \left[ q \frac{\pi}{4} D^2 (0.439) \right]^2 \right\}^{1/2} \quad (2)$$

The axial load on one trunnion assembly,  $F_A$ , is equal to half the side force load on the antenna, and for either the 64- or 72-m antenna is:

$$F_A = 0.144 q \frac{\pi}{4} D^2 \quad (3)$$

where

- $W_T$  = the total weight of the antenna tipping structure
- $q$  = the dynamic pressure of the wind
- $D$  = the antenna dish diameter

The dimensionless numerical coefficients in Eqs. (1), (2), and (3) correspond to antenna elevation and azimuth angles of  $60^\circ$  each. This antenna attitude produces the maximum bearing loads.

Since there are two bearings per trunnion assembly, the radial and axial loads per bearing are less than that given by Eqs. (1), (2), and (3) but could be more than half of the amount. It will be assumed that the maximum load per bearing is  $2/3$  the total amount. These maximum bearing loads  $P_R$  and  $P_A$  are:

$$P_{R_{64}} = \frac{2}{3} \left\{ \left[ \frac{W_{64}}{2} + q \frac{\pi}{4} D_{64}^2 (0.345) \right]^2 + \left[ q \frac{\pi}{4} D_{64}^2 (0.451) \right]^2 \right\}^{1/2} \quad (4)$$

$$P_{R_{72}} = \frac{2}{3} \left\{ \left[ \frac{W_{72}}{2} + q \frac{\pi}{4} D_{72}^2 (0.332) \right]^2 + \left[ q \frac{\pi}{4} D_{72}^2 (0.439) \right]^2 \right\}^{1/2} \quad (5)$$

$$P_A = \frac{2}{3} \left[ 0.144 q \frac{\pi}{4} D^2 \right] \quad (6)$$

The tipping structure estimated weights for the 64- and 70-m diameter antennas are 11,991,800 N (2,696,000 lb) and

16,439,800 N (3,696,000 lb), respectively. At a wind speed of 31.3 m/s (70 mph) the wind dynamic pressure,  $q$ , has the value

$$q = 1/2 \rho V^2 = 1/2 (1.22) (31.3)^2 = 598 \text{ N/m}^2 \quad (7)$$

where  $\rho$  is the air density and  $V$  is the windspeed. For these values of  $W$  and  $q$ , Eqs. (4), (5), and (6) become:

$$P_{R_{64}} = \frac{2}{3} \left\{ [5995900 + 663698]^2 + [867616]^2 \right\}^{1/2} = 4477250 \text{ N (1006576 lb)} \quad (8)$$

$$P_{R_{72}} = \frac{2}{3} \left\{ [8219900 + 808340]^2 + [1068860]^2 \right\}^{1/2} = 6060860 \text{ N (1362600 lb)} \quad (9)$$

$$P_{A_{64}} = \frac{2}{3} \left[ 0.144 (598) \frac{\pi}{4} (64)^2 \right] = 184680 \text{ N (41520 lb)} \quad (10)$$

$$P_{A_{72}} = \frac{2}{3} \left[ 0.144 (598) \frac{\pi}{4} (72)^2 \right] = 233733 \text{ N (52548 lb)} \quad (11)$$

A comparison of the numbers in Eqs. (8) and (9) shows that the wind loading at 31.3 m/s is approximately 12% of the weight loading.

In order to compare the bearing applied loads to the rated static capacity,  $C_0$ , of the bearing, an equivalent load  $P_E$  is calculated in conformance with Ref. 2, which is:

$$P_E = 1.00 P_R + 2.3 P_A \quad (12)$$

Evaluating  $P_E$  for the two antenna sizes, there are obtained:

$$P_{E_{64}} = 4477250 + 2.3 (184680) = 4902014 \text{ N (1102070 lb)} \quad (13)$$

$$P_{E_{72}} = 6060860 + 2.3 (233733) = 6598445 \text{ N (1483463 lb)} \quad (14)$$

The rated static capacity,  $C_0$ , of the SKF 231/600 spherical roller bearing is 9,892,300 N (2,240,000 lb) per Ref. 1. The ratios between the static capacities and equivalent loads are as follows:

$$\frac{C_0}{P_{E_{64}}} = \frac{9892300}{4902014} = 2.018 \quad (15)$$

$$\frac{C_0}{P_{E_{72}}} = \frac{9892300}{6598445} = 1.499 \quad (16)$$

It should be recognized that the static capacity is that load which produces a permanent deformation less than 0.0001 times the diameter of the rolling element. The static load required to fracture the bearing is usually more than 8  $C_0$ . From the standpoint of safety, the factor is very high,  $1.5 \times 8$  or 12. Spherical roller bearings oftentimes operate at 2 or 4 times the  $C_0$  value without there being any noticeable increase in the friction coefficient.

The basic bearing rating,  $C$ , is that load under which at least 90% of a large number of bearings will survive 1,000,000

rotations without any evidence of fatigue damage. For these elevation bearings the  $C$  value, from Ref. 1, is 7,695,000 N (1,730,000 lb). The ratios between the basic ratings and the equivalent loads are as follows:

$$\frac{C}{P_{E_{64}}} = \frac{7695000}{4902014} = 1.570 \quad (17)$$

$$\frac{C}{P_{E_{72}}} = \frac{7659000}{6598445} = 1.166 \quad (18)$$

The number of revolutions of the elevation bearings over a 50-year period might be approximately 60,000. Since this is a small portion of 1,000,000 rotations, on which the  $C$  factor is based, the probability of fatigue damage is extremely small. Bearing damage is much more likely to result from improper lubrication and corrosion than from being overloaded when used on the 70-m antenna.

## Reference

1. SKF Industries, *SKF Spherical Roller Bearings Catalog*, 1960, Form 591-B/15M-773-SED.

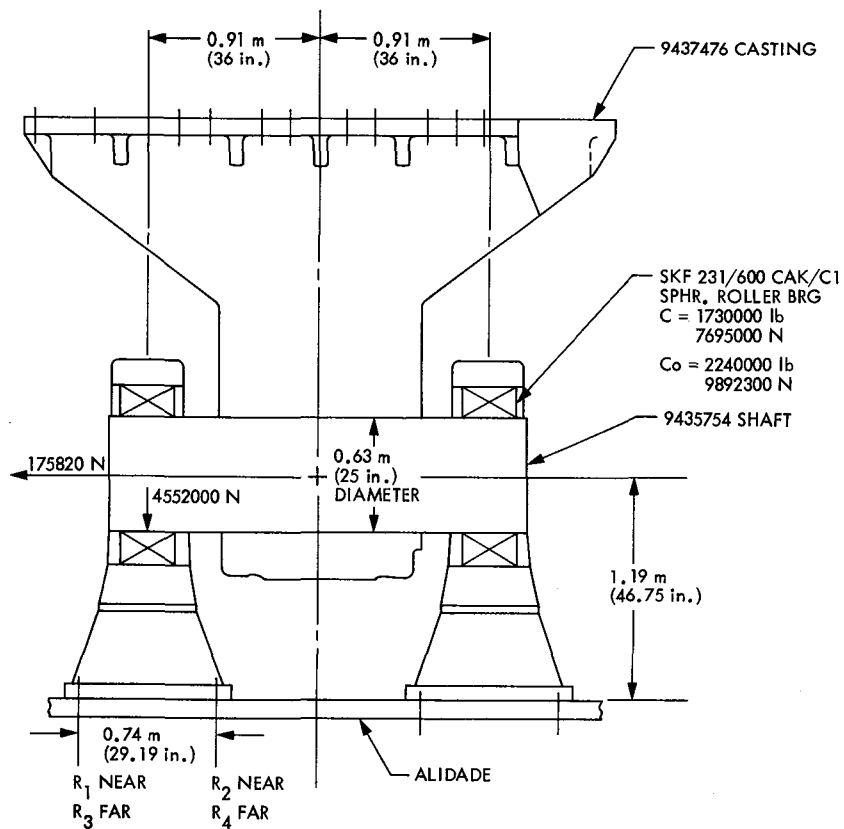


**Fig. 1. Side view of elevation bearing installation**

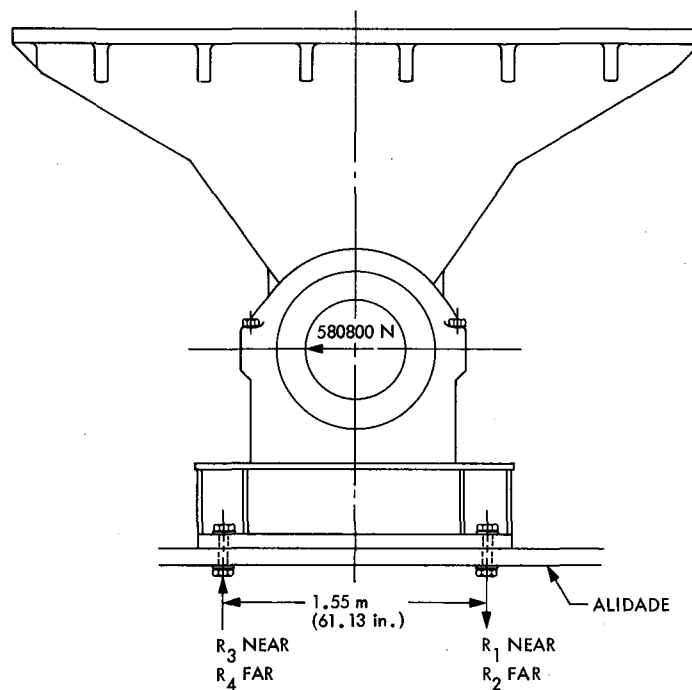


**Fig. 2. End view of elevation bearing installation**

# Characteristics of the Elevation Drive Suspension of the 64-Meter Antennas

H. D. McGinness

Ground Antennas and Facilities Engineering Section

*The elevation axis drive unit of the DSN 64-m antennas is arranged so that its output pinion can self-align to the bull gear. The design is described and conflicting desiderata are discussed.*

## I. Introduction

The elevation drives for the 64-m antennas at DSS 14, 43, and 63 have been in operation for 18, 12, and 11 years respectively. During these periods only a moderate amount of maintenance has been required. There has gradually developed, however, an unusual wear pattern on both the pinions and bull gears. It is the intent of this report to review some of the design features of the elevation drive suspension and to discuss why certain changes were made and whether these changes are related to the gear wear.

## II. Description of the Drive System

A pair of bull gear segments of 12.65-m radii are concentric with the elevation axis and spaced approximately 5.4 m apart. The output pinions of two drive units mesh with each bull gear and are counter-torqued against each other so that backlash in the gear system is eliminated. Reference 2 contains a good general description of the drive system. Figures 1 and 2 show schematic views of the upper and lower drive units and their

relationship to the bull gear. From these figures it may be seen that the output pinions are self-aligning to the bull gear. Such a large bull gear is likely to have radial and lateral runouts as well as twist. A fixed drive pinion would be subjected to misalignment and perhaps excessive change in gear contact ratio. A perfect self-aligning arrangement would obviate these undesirable features.

From Fig. 1 it may be seen that the lower end of the drive unit is ball-joint mounted to the antenna alidade and that this ball joint lies on a tangent line to the bull gear-pinion pitch line. The reaction roller is directly opposite the output pinion and rolls on the inside surface of the bull gear ring so as to keep the pinion properly spaced with respect to the bull gear teeth. The load on the reaction roller ideally is equal to the separating force between the pinion and bull gear. The dead weight of the drive unit, or gear box, is carried ideally by the alidade ball joint and by the two vertical spring-loaded struts labeled  $F_1$  and  $F_2$  in the figures. Horizontal stability is provided by the horizontal spring-loaded strut labeled  $S$ . With respect to the alidade ball joint and the tangent line, the gear box can pitch, yaw, and roll, as the bull gear runs out radially,

laterally, and in a twisting fashion. As these aberrant displacements occur, the reaction roller force and the strut forces change.

### III. Characteristics of These Self-Aligning Gear Boxes

The gear box is installed by hoisting it to a position near its final position, attaching the ball-joint pivot to the alidade, placing auxiliary jacks appropriately to support the remaining weight, and installing the horizontal and vertical spring loaded struts which have been set to a calculated length by displacement of the springs by auxiliary bolts. Then the auxiliary jacks are removed, thus allowing the weight to be transferred to the reaction roller and the vertical struts. The auxiliary bolts holding the springs are removed and the strut lengths adjusted until the load is removed from the reaction roller. To limit the amount of strut length adjustment to a practical value requires that the vertical strut spring constants not be too low. On the other hand it is desirable to have low spring constants in the vertical struts so that when the bull gear runs out radially, there will not be an excessive transfer of load to the reaction roller. Additionally, it is desirable that the ratio of the stiffness of the vertical struts be a particular value such as to allow gear box pitch unaccompanied by gear box roll. For example, if the bull gear runs out radially but does not twist, the vertical struts should extend (or compress) by amounts which do not induce gear box roll, since unwanted roll represents a misalignment. The correct extension ratio is a function of the strut configuration, and extension ratio is proportional to the strut stiffness ratio.

There are schematic drawings of the three struts in Fig. 3. The horizontal strut,  $S$ , is preloaded to 1156 N and has a spring constant of 38876 N/m in either tension or compression. In order to allow gear box yaw to accommodate tooth misalignment, the horizontal strut stiffness should be low. On the other hand, it must be high enough to insure stability against the gear box running off the bull gear when the bull-gear motion is directed from pinion to alidade ball joint. The Number 1 gear box ran off the bull gear twice in 1966. Most of the time this gear box was stable and none of the other three ever ran off. A probable explanation of why this gear box ran off the bull gear is given in the analysis of Appendix A, the result of which defines a critical lateral displacement (see Figs. 30 and 31).

The derivation of the proper ratio between the vertical strut extensions, and the related stiffness ratio, is given in the analysis of Appendix B (see Figs. 4 and 5).

An outline of the method of installing the struts and aligning the gear boxes is given in Appendix C.

### IV. Results of the Analyses

The analysis of Appendix A suggested that the value of the critical lateral displacement,  $x_{CR}$  for gear box No. 1 was abnormally small because there was an excessive amount of dead weight loading on the reaction roller. The analysis of Appendix B showed that the stiffness ratio between the original vertical struts was not very close to the ideal value. In order to reduce the dead weight loading on the reaction roller, it would have been necessary to change the strut lengths slightly. Although length adjustments were built into the original struts, it was found that the adjusting nut on the large vertical compressive strut could not be turned. A study was conducted to decide whether new and properly designed spring loaded struts or servo controlled constant force hydraulic struts should be employed. It was decided that properly designed spring loaded struts would be more reliable and less expensive. Such struts were fabricated and tested for stiffness at the fabricator's plant. The new compression strut is shown schematically in Fig. 3(c). It incorporates a ball bearing on the upper end of the bronze adjusting nut. Length adjustment of 4.233 mm per turn can be made with moderate torque. The new tension strut shown in Fig. 3(b) also employs a bronze adjusting turnbuckle nut one turn of which changes the strut length by 4.233 mm. These were installed at DSS 14 in July of 1982 and at DSS 43 and DSS 63 later in the same year.

The load-deflection curves of all the new compression and tension struts are shown in Figs. 6 through 29. The Belleville spring elements used in the vertical struts were selected from catalogs. An advantage of Belleville disks is that the stiffness of the assembly can be altered by adding or subtracting disks. The test performance of the tension struts was generally very good and corresponded fairly well with calculations made in accordance with Ref. 3. The first tests on the compression struts, which contained much larger disks, were very erratic and unrepeatable. Many of these elements had to be sent back to the manufacturer for rework which consisted of grinding true flats near the outer and inner edges. Without these small edge flats there was the tendency for one or more elements to move laterally and wedge against the housing, thereby producing unrepeatable results. The final performance of the compression struts was very good as is indicated in Figs. 6 through 17. Because of the tendency of some of the spring elements to wedge against the housing, it is recommended that if a strut unit must be disassembled, that each spring element be marked for angular orientation and position in the stack, and upon reassembly this sequence and angular orientation be reestablished.

Table 2 of Appendix B lists the stiffness ratios of all the vertical strut pairs,  $K_1/K_2$ . From this table it may be seen that all the ratios are within the ranges judged to be satisfactory

from the standpoint of preventing unwanted roll when the gear box must move to accommodate bull gear radial runout.

The gear box weights, center of gravity position, and the strut locations given in Figs. 1 and 2 are believed to be accurate because they were determined by measurement. In December 1981 one upper and one lower gear box were suspended by a cable harness so that the tangent line angles of  $42.25^\circ$  and  $7.683^\circ$  of Figs. 1 and 2 were obtained. The harness was attached to a load cell which determined the total weight. The center of gravity lay directly beneath the single cable supporting the load cell. The strut locations were verified by surveying methods.

An outline of how the new struts were installed and how the reaction roller was aligned is given in Appendix C. After the new struts were so installed and aligned the antenna was driven back and forth many times through the  $85^\circ$  elevation range and lateral runout of the pinion with respect to the bull gear was observed to be less than 4 mm.

## V. Conclusion

The new elevation drive vertical struts allow the roll alignment of the drive pinion and reaction roller to be made perfect at any particular elevation angle. The stiffness ratio of the two vertical struts is such that the roll alignment should remain perfect even though the bull gear has radial runout. The ease of adjusting the strut lengths allows the reaction roller to be set so that it carries no dead weight load at the elevation angle at which it was adjusted. Moderate amounts of bull gear radial runout or twist will not cause the reaction roller to be overloaded.

The original vertical struts were very difficult to adjust and best alignment was not maintained. This probably caused some excessive wear of the gear teeth near their edges; however, it is believed that such misalignment is not the primary cause of the strange wear pattern which exists over the entire width of the gear teeth and that other reasons should be sought.

## References

1. McGinness, H., 1982, Lateral and drag forces on misaligned cylindrical rollers, *TDA Progress Report 42-69*, 174-178, Jet Propulsion Laboratory, Pasadena, Calif.
2. The NASA/JPL 64-m Diameter Antenna at Goldstone, CA: Project Report TM 33671, 19XX, pp. 66-108 (internal document).
3. Almen, I. O., and A. Laszlo, 1936, The Uniform Section Disc Spring, *ASME Trans.* 58, 305-314.



**Table 1. Ideal ratio between strut stiffness**

$\lambda = \frac{K_1}{K_2}$		$\frac{h}{l_R}$
Lower	0.694	0.01554
	0.460	-0.01535
Upper	0.760	0.01533
	0.446	-0.01558

**Table 2. Stiffness ratios of vertical struts**

Elevation Gear Drive No.	Tension Strut Serial No.	Comp. Strut Serial No.	$K_1$ Comp., lb/in.	$K_2$ Tension, lb/in.	$\frac{K_1}{K_2}$
DSS-14 I L	2	5	3055	5438	0.46 < 0.562 < 0.694
DSS-14 II U	1	1	2829	5510	0.44 < 0.513 < 0.760
DSS-14 III L	4	3	2837	5142	0.46 < 0.552 < 0.694
DSS-14 IV U	3	2	2878	5117	0.44 < 0.562 < 0.760
DSS-43 I L	11	12	3243	5172	0.46 < 0.626 < 0.694
DSS-43 II U	12	11	3144	5177	0.44 < 0.607 < 0.760
DSS-43 III L	10	4	3125	5056	0.46 < 0.618 < 0.694
DSS-43 IV U	9	10	3504	5312	0.44 < 0.660 < 0.760
DSS-63 I L	8	6	3472	5113	0.46 < 0.679 < 0.694
DSS-63 II U	7	8	3315	5172	0.44 < 0.641 < 0.760
DSS-63 III L	6	7	3760	5420	0.46 < 0.693 < 0.694
DSS-63 IV U	5	9	3488	5357	0.44 < 0.651 < 0.760

**Table 3. Vertical strut alignment dimensions at DSS-14**

Elevation Angle at Which Struts Were Adjusted, deg	Elevation Drive Gear Box No.	Comp. Strut Serial No.	Dimension A, mm	Dimension B, mm	Ten. Strut Serial No.	Dimension a, mm	Dimension b, mm
65	I	5	53.6	139.7	2	68.1	60.5
60	II	1	63.0	152.4	1	71.9	57.2
71	III	3	59.4	106.4	4	66.8	63.5
71	IV	2	63.5	136.7	3	64.8	73.2

REF. JPL DWG. 9435115  
9435112  
DIMENSIONS IN inches (mm)

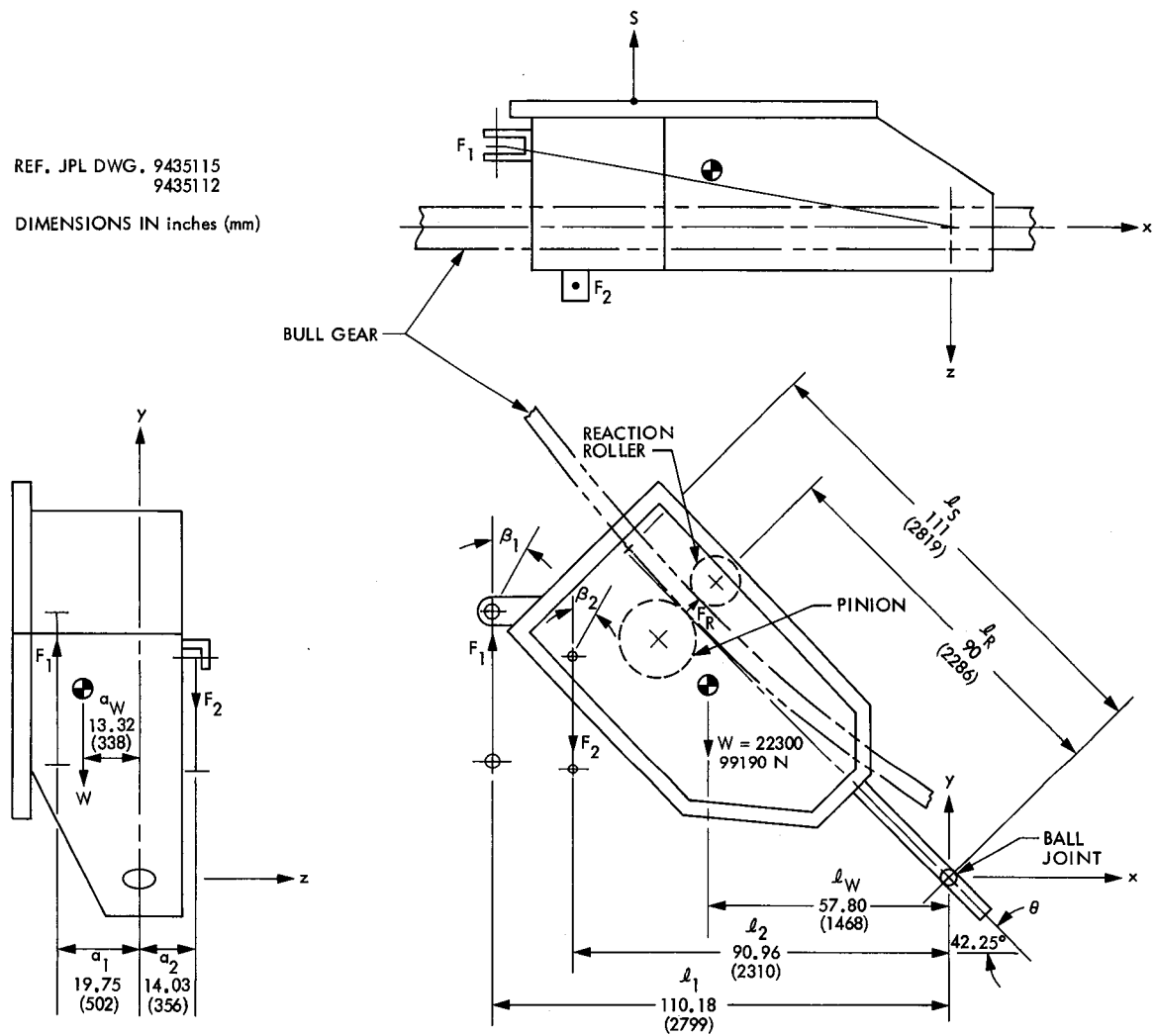


Fig. 1. Upper elevation drive gear box no. 2

REF. JPL DWG. 9435115  
 9435110  
 DIMENSIONS IN inches (mm)

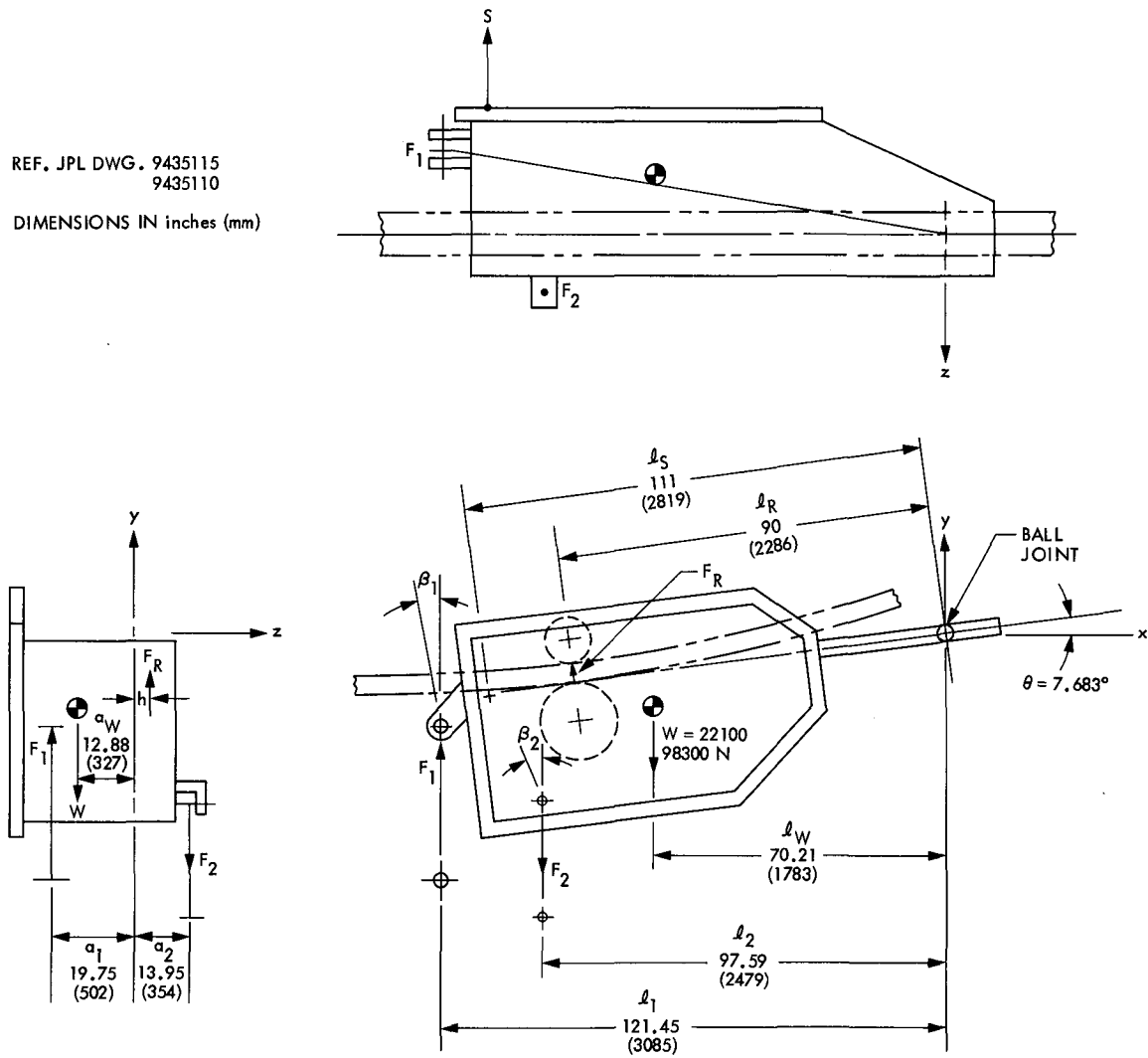
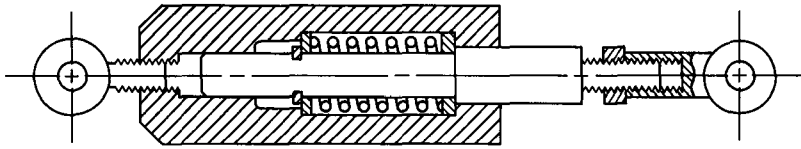
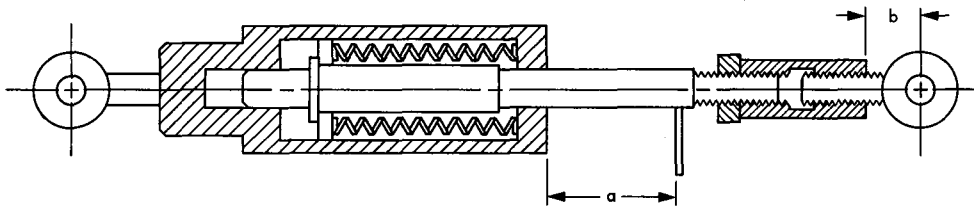


Fig. 2. Lower elevation drive gear box no. 3

(a) HORIZONTAL STRUT S TENSION OR COMPRESSION  
(SEE JPL 9436181)



(b) VERTICAL STRUT  $F_2$  TENSION ONLY  
(SEE JPL 9477064)



(c) VERTICAL STRUT  $F_1$  COMPRESSION ONLY  
(SEE JPL 9477064)

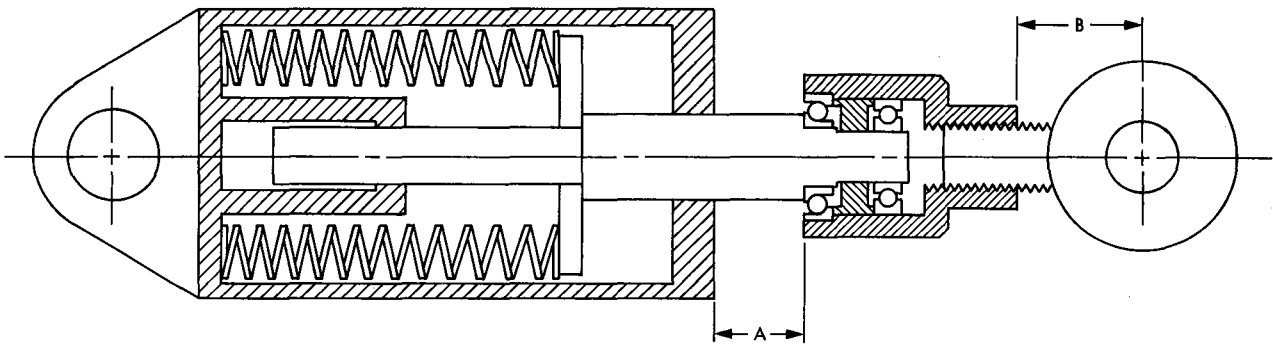


Fig. 3. Schematic drawings of elevation drive spring loaded support struts

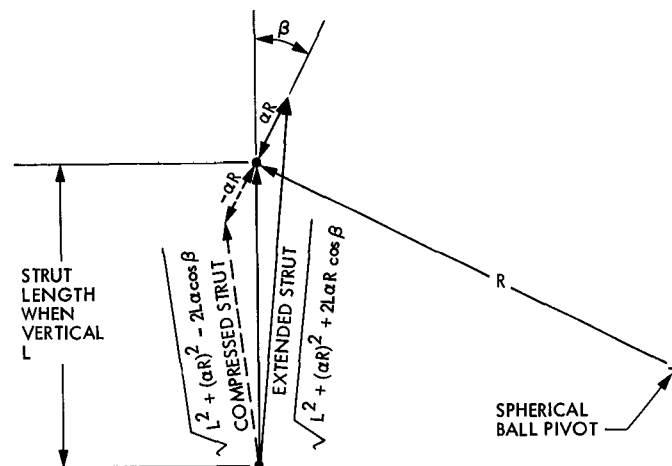


Fig. 4. Vertical strut length geometry

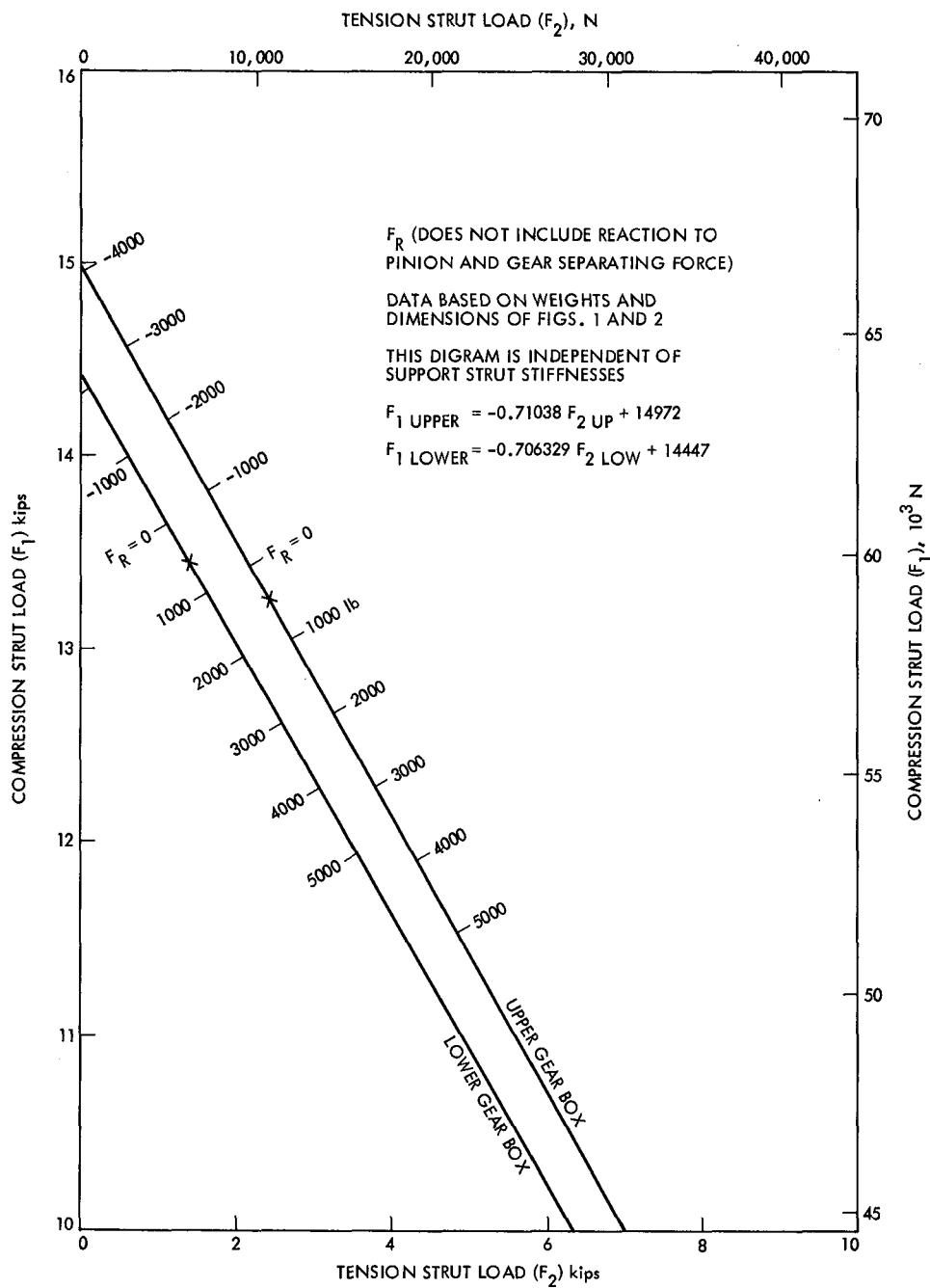


Fig. 5.  $F_1$  versus  $F_2$  for various values of roller reaction force  $F_R$  centered at mid-point of roller

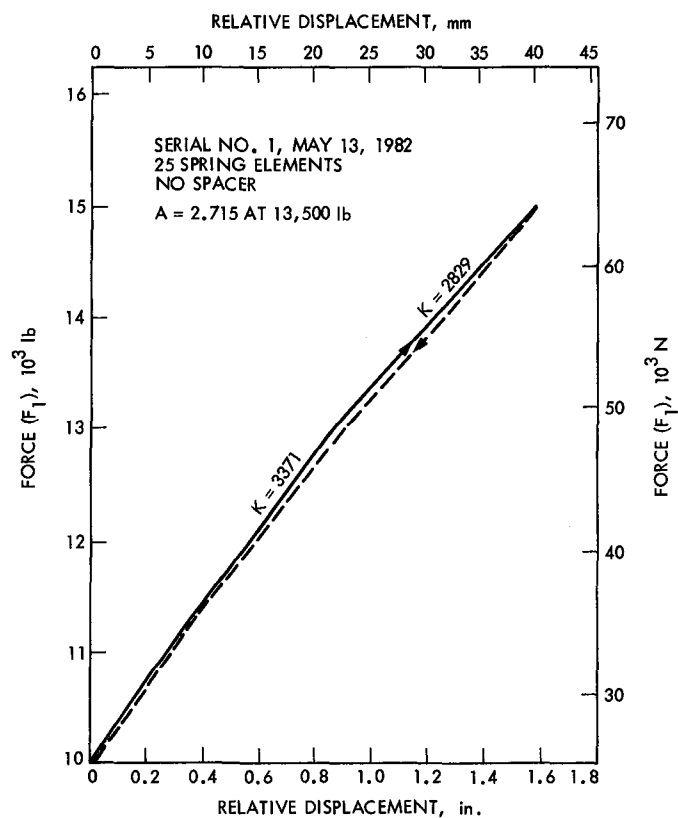


Fig. 6. Force versus deflection, measured, compression serial 1

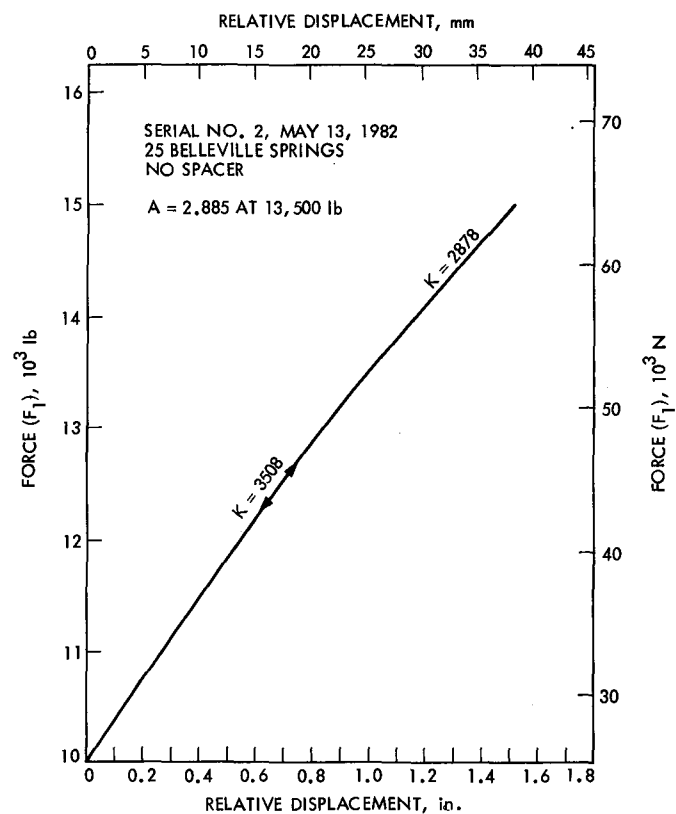


Fig. 7. Force versus deflection, measured, compression serial 2

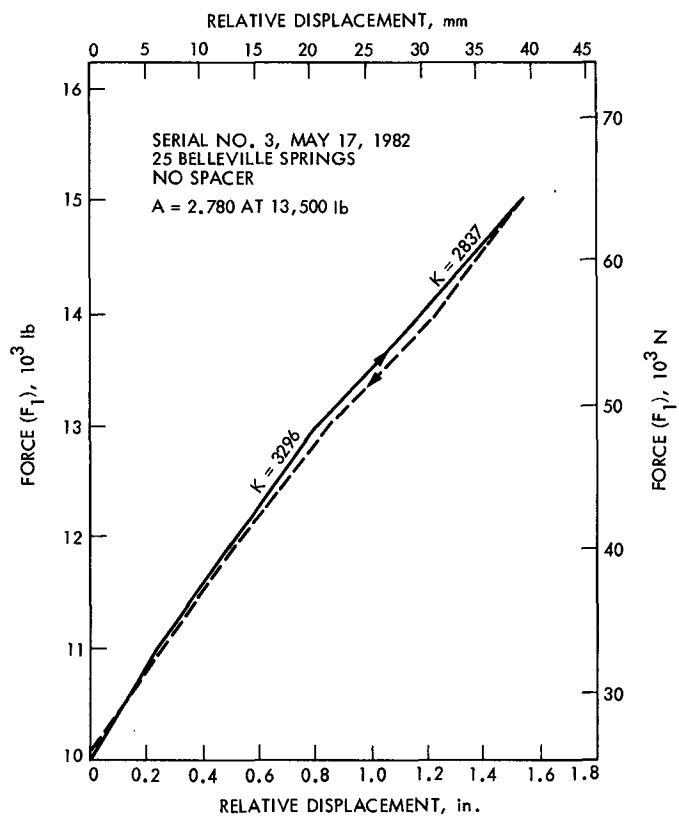


Fig. 8. Force versus deflection, measured, compression serial 3

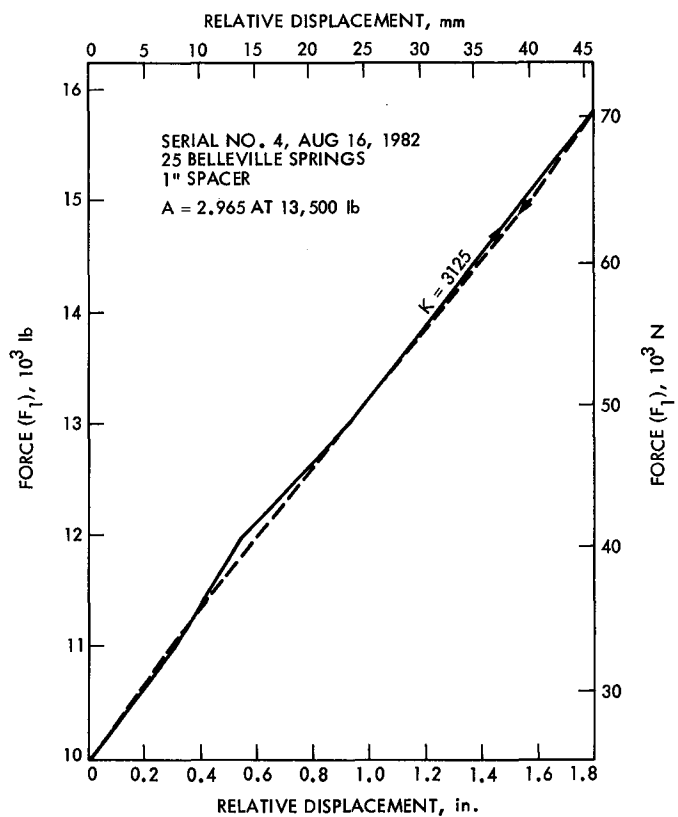


Fig. 9. Force versus deflection, measured, compression serial 4

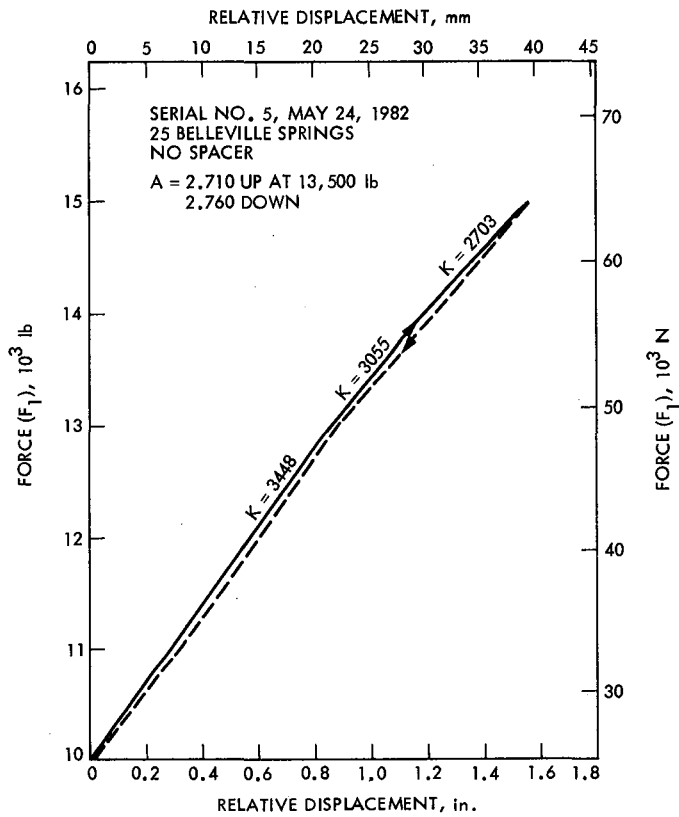


Fig. 10. Force versus deflection, measured, compression serial 5

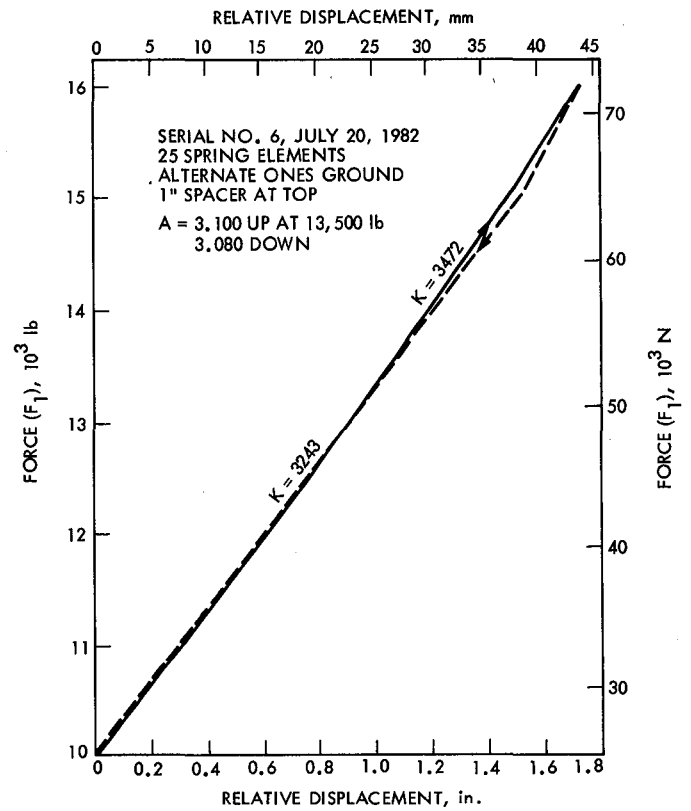


Fig. 11. Force versus deflection, measured, compression serial 6



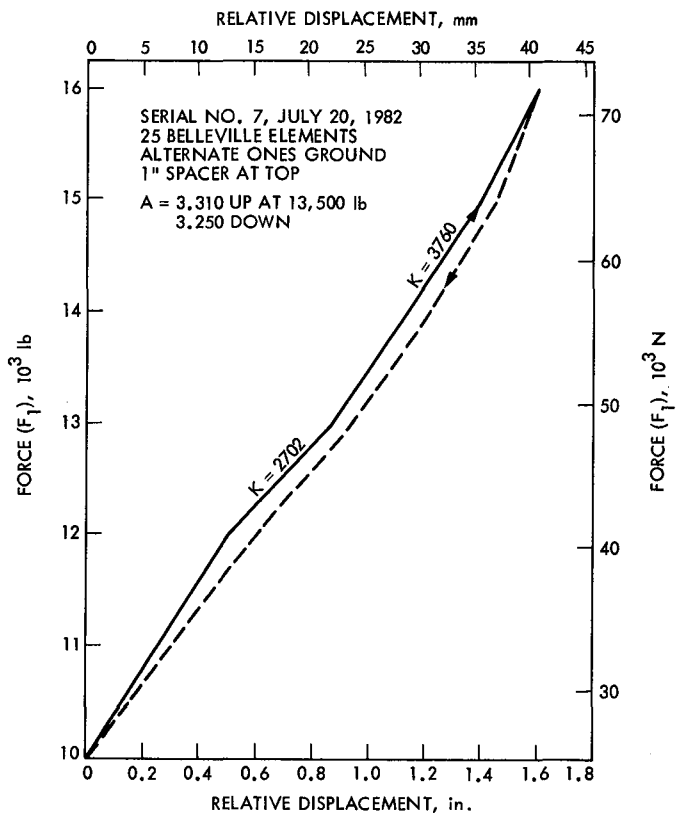


Fig. 12. Force versus deflection, measured, compression serial 7

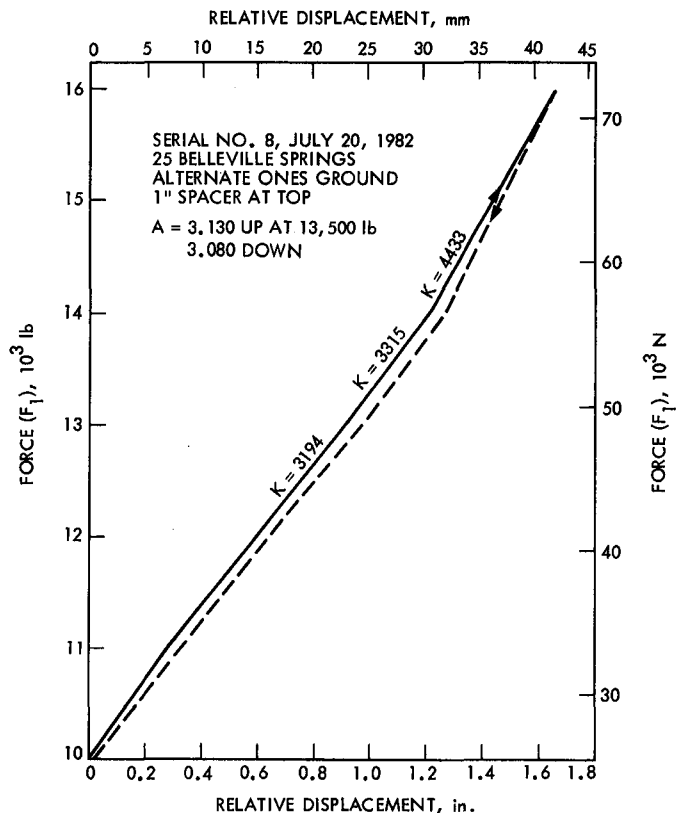


Fig. 13. Force versus deflection, measured, compression serial 8

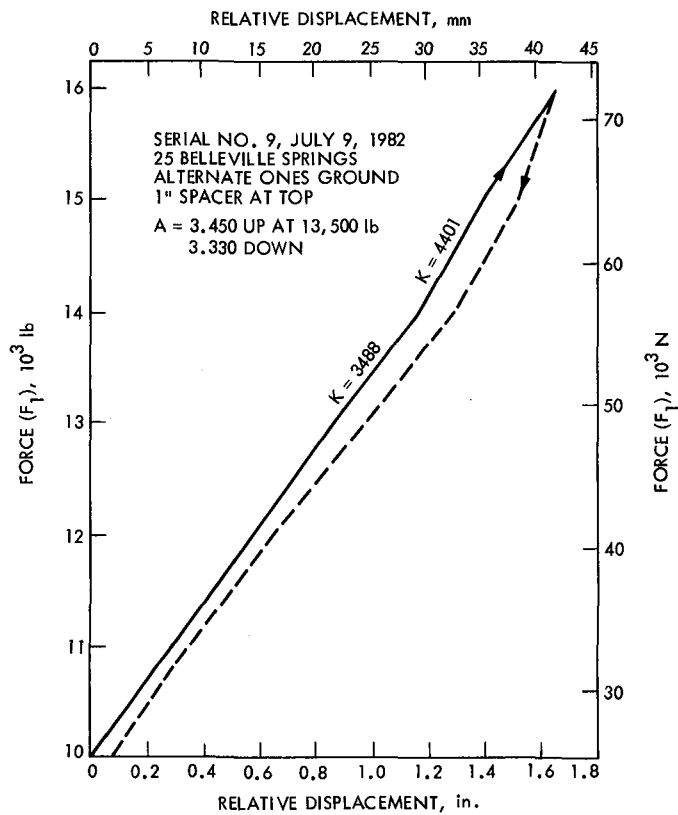


Fig. 14. Force versus deflection, measured, compression serial 9

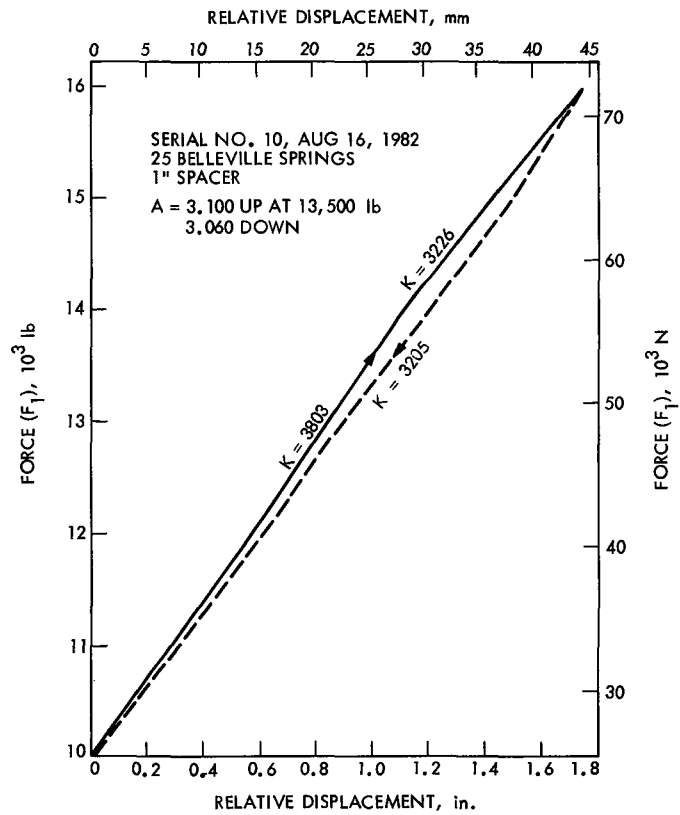


Fig. 15. Force versus deflection, measured, compression serial 10

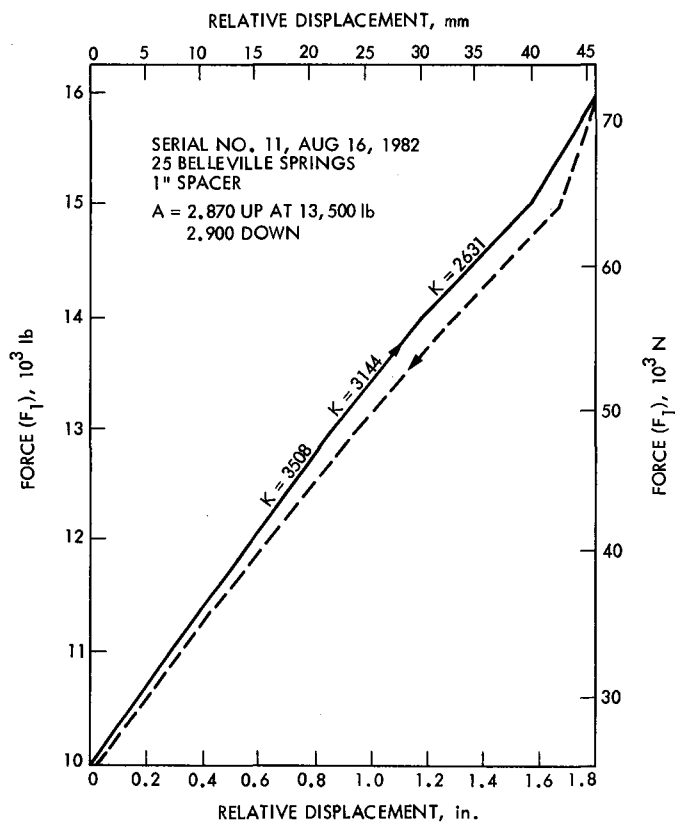


Fig. 16. Force versus deflection, measured, compression serial 11

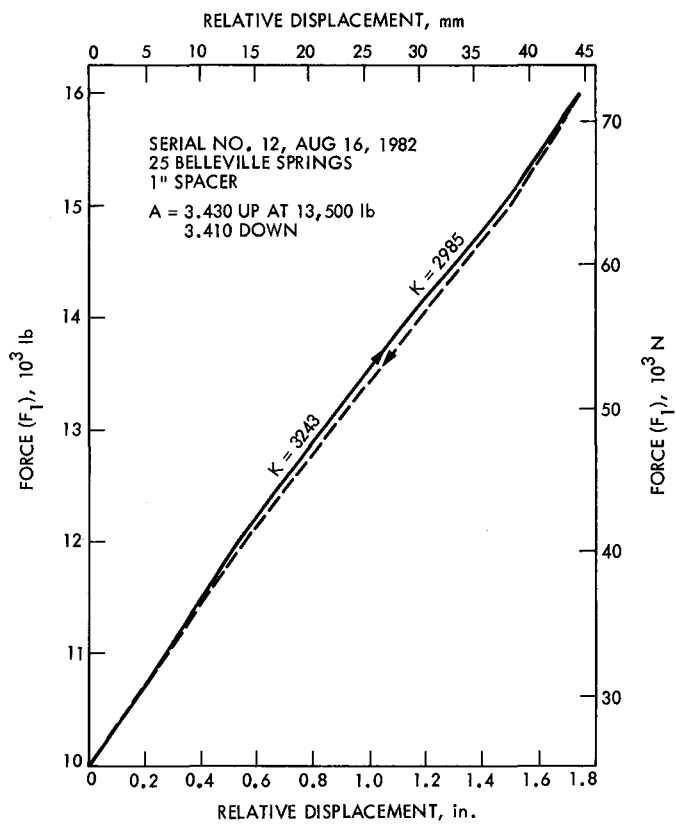


Fig. 17. Force versus deflection, measured, compression serial 12

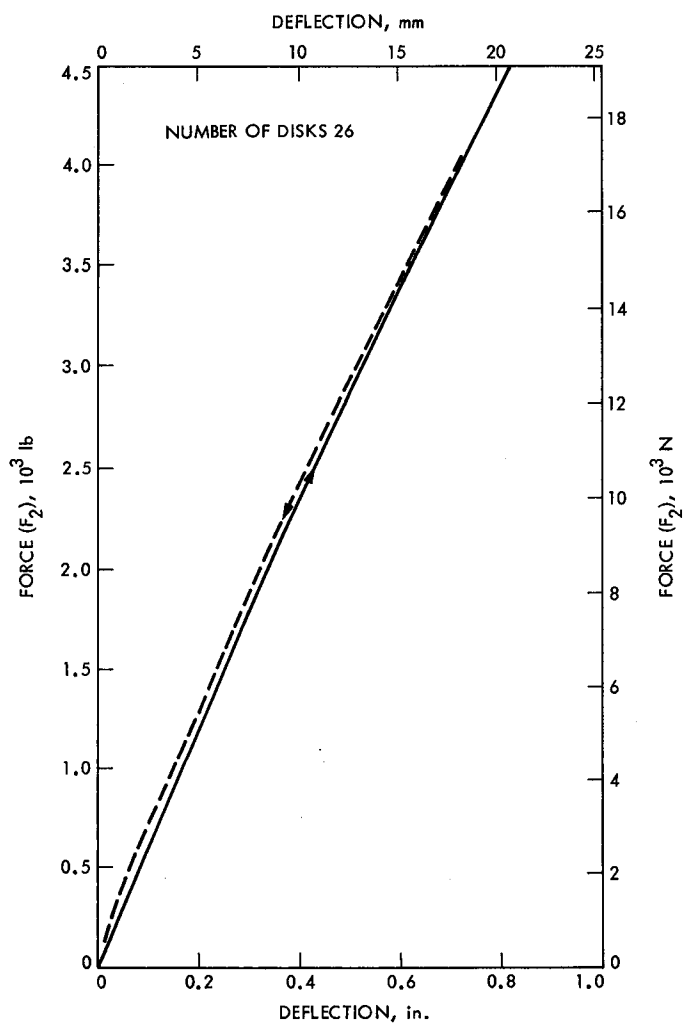


Fig. 18. Force versus deflection, measured, tension serial 1

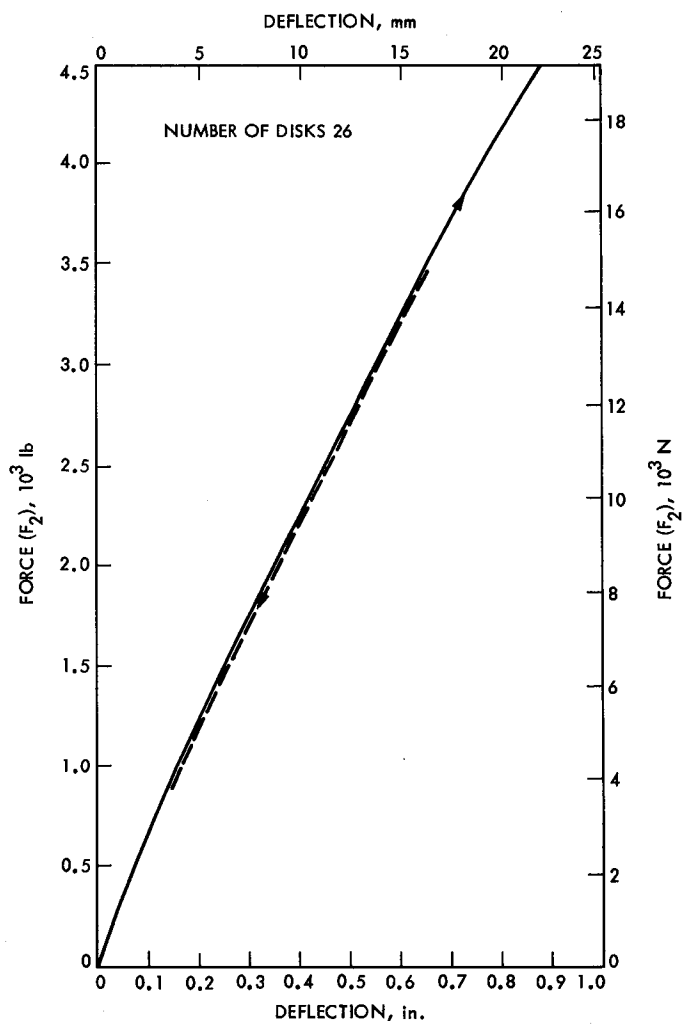


Fig. 19. Force versus deflection, measured, tension serial 2

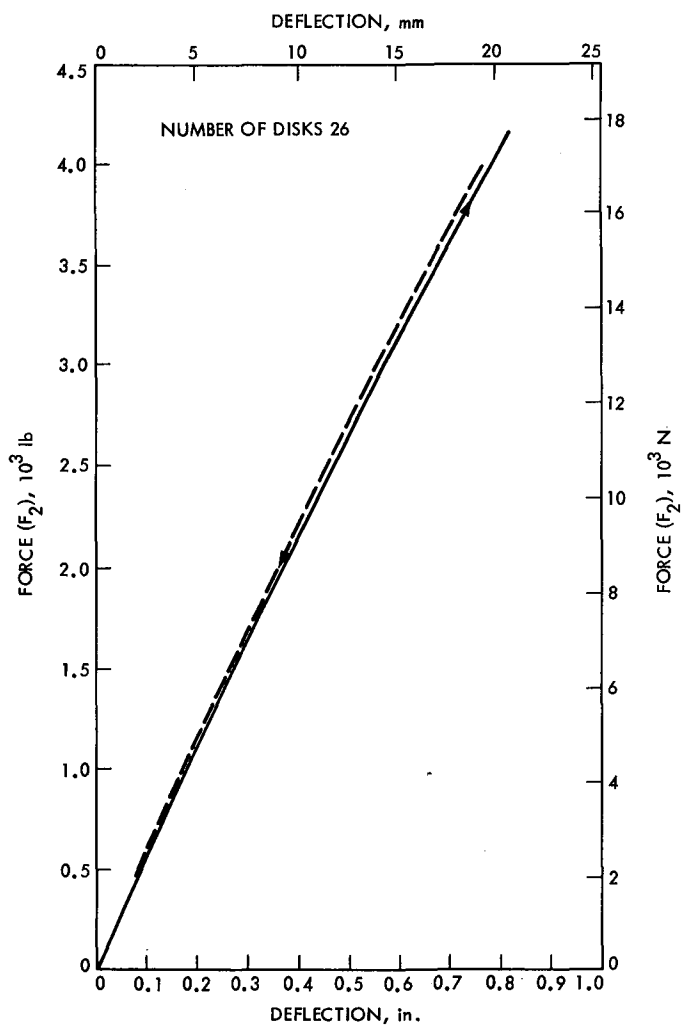


Fig. 20. Force versus deflection, measured, tension serial 3

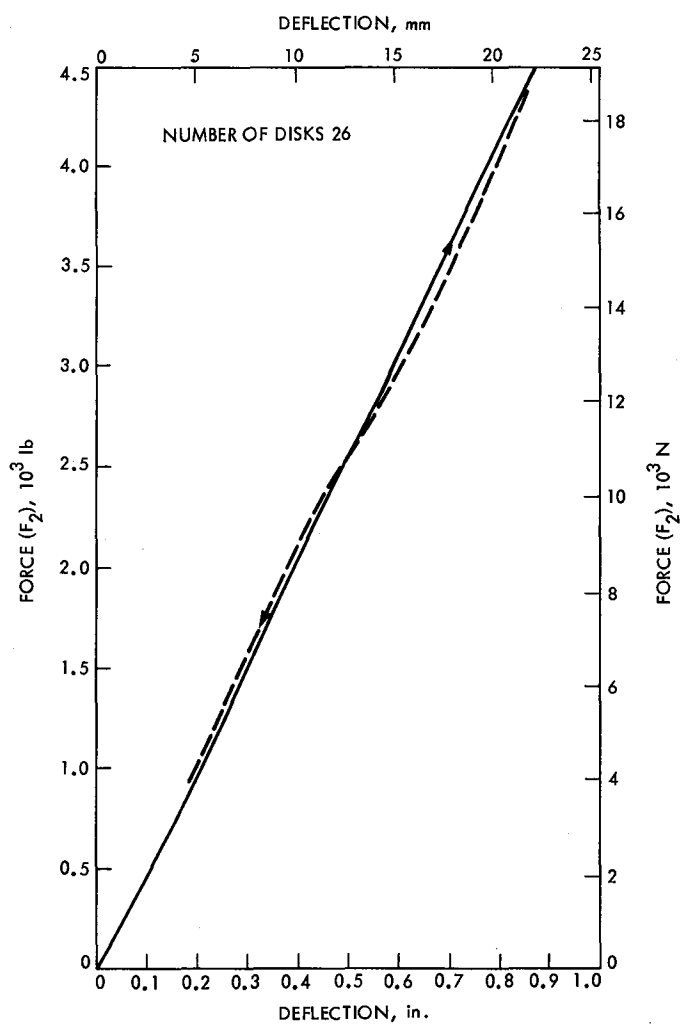


Fig. 21. Force versus deflection, measured, tension serial 4

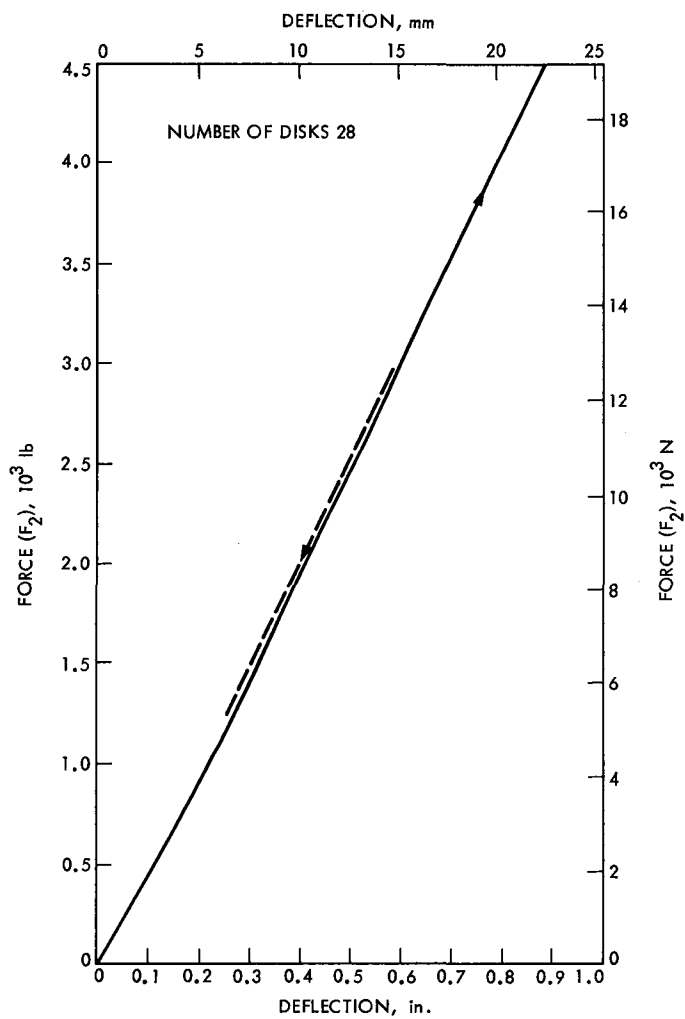


Fig. 22. Force versus deflection, measured, tension serial 5

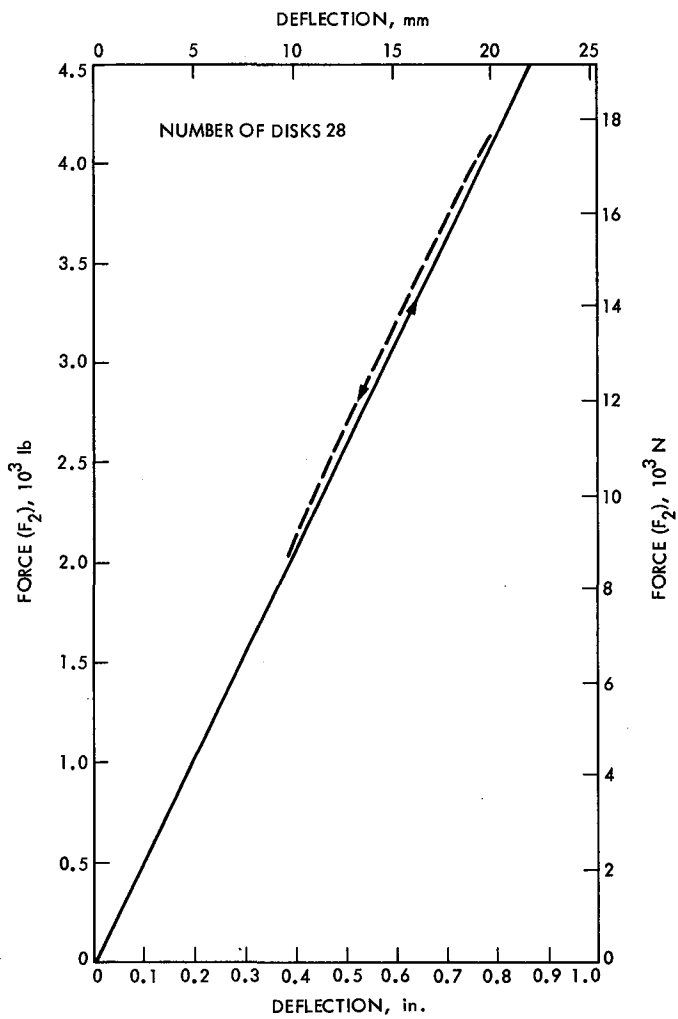


Fig. 23. Force versus deflection, measured, tension serial 6

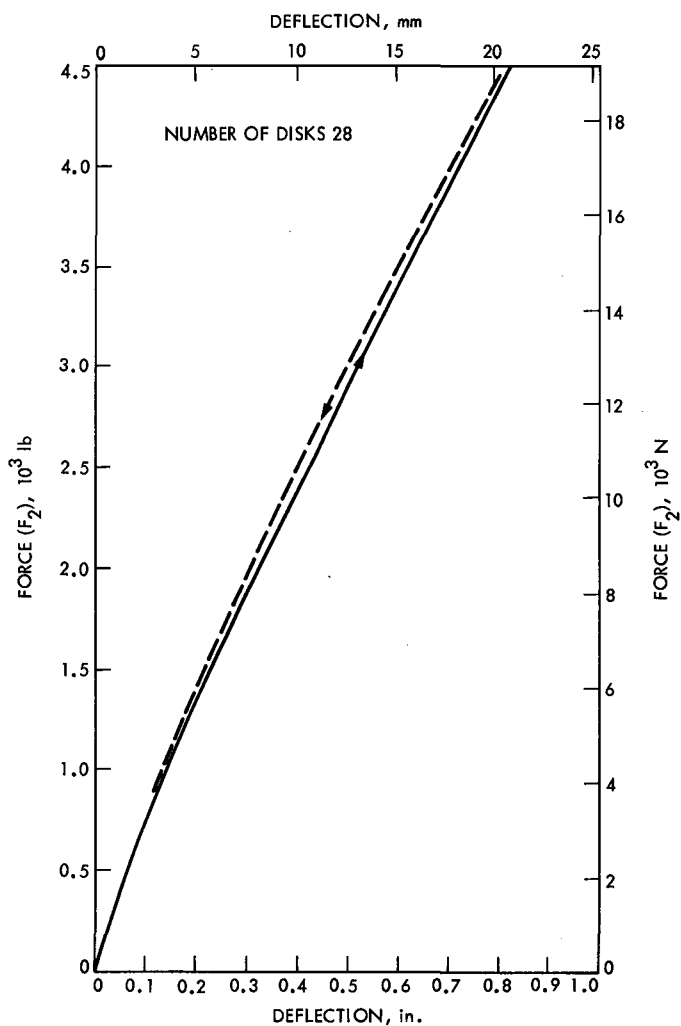


Fig. 24. Force versus deflection, measured, tension serial 7

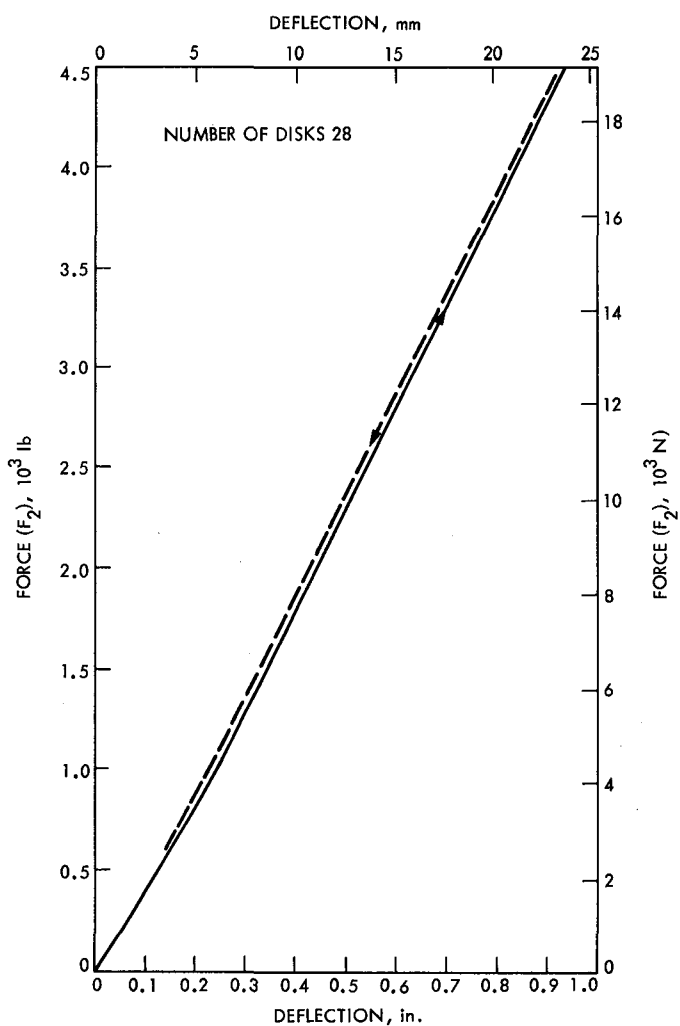


Fig. 25. Force versus deflection, measured, tension serial 8

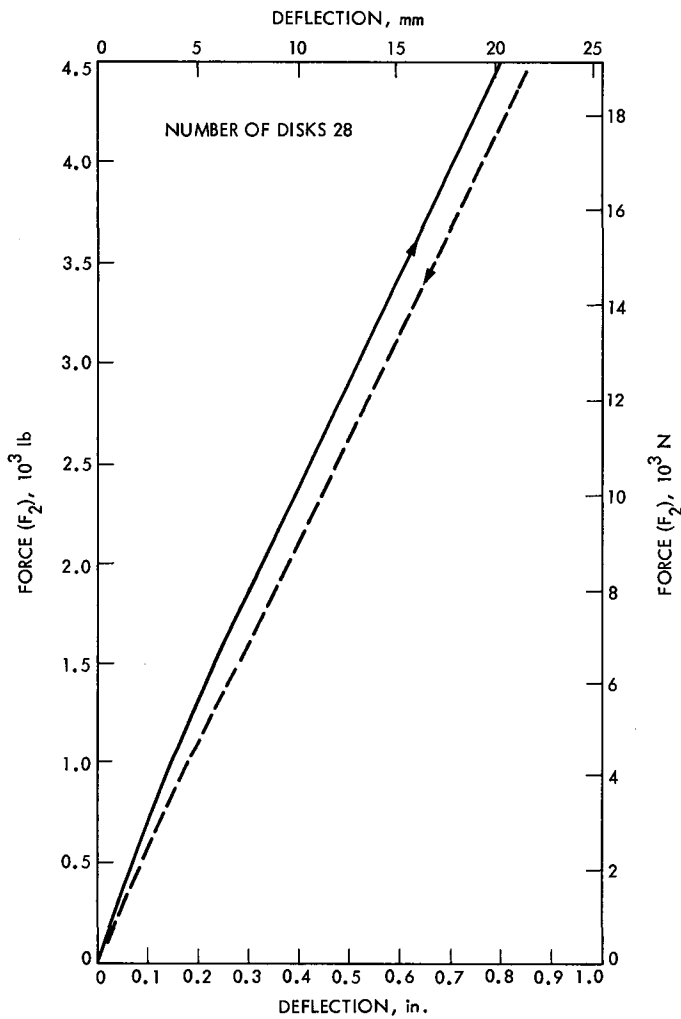


Fig. 26. Force versus deflection, measured, tension serial 9

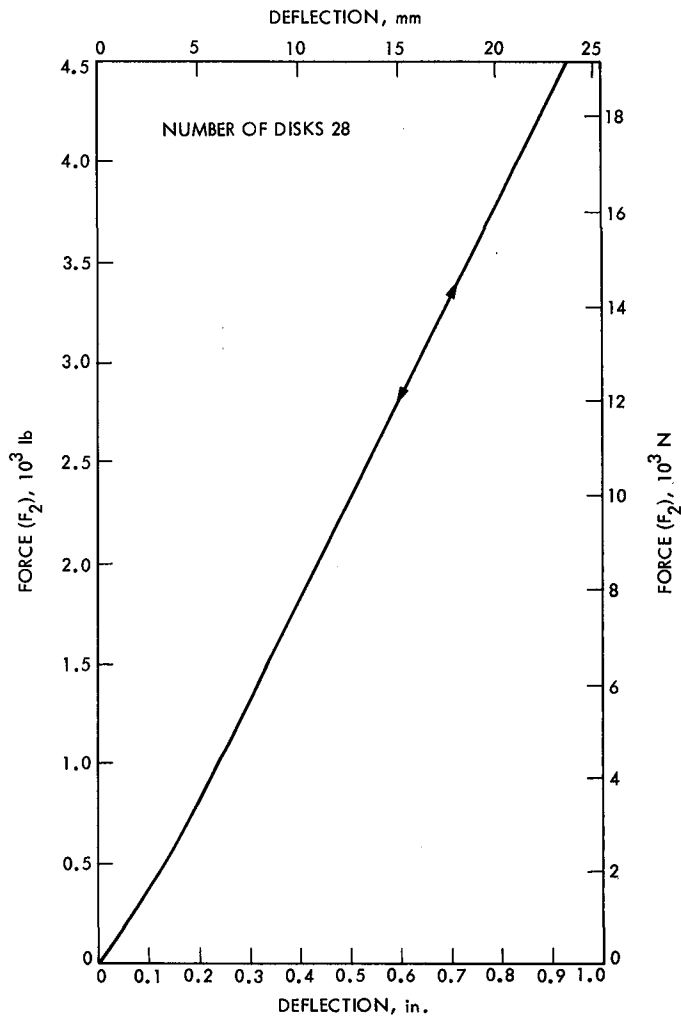


Fig. 27. Force versus deflection, measured, tension serial 10



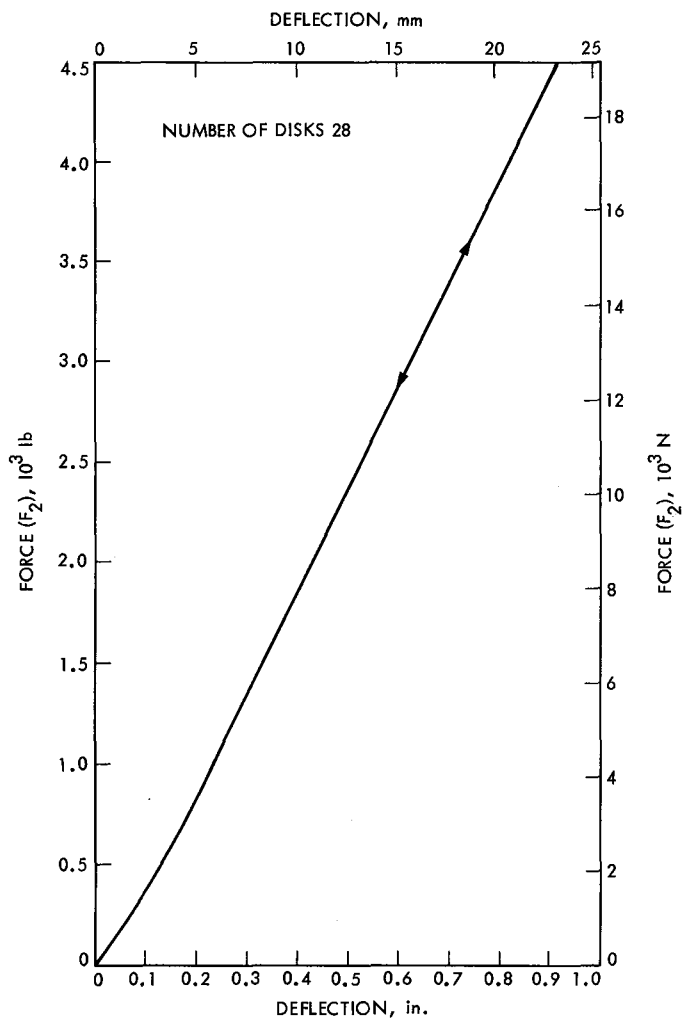


Fig. 28. Force versus deflection, measured, tension serial 11

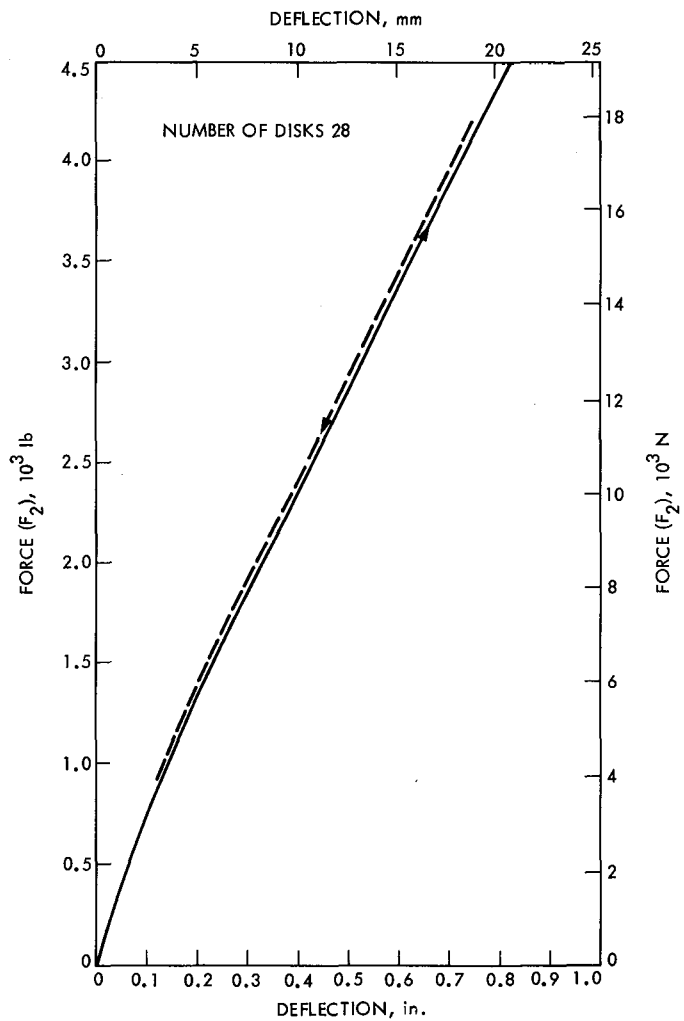


Fig. 29. Force versus deflection, measured, tension serial 12

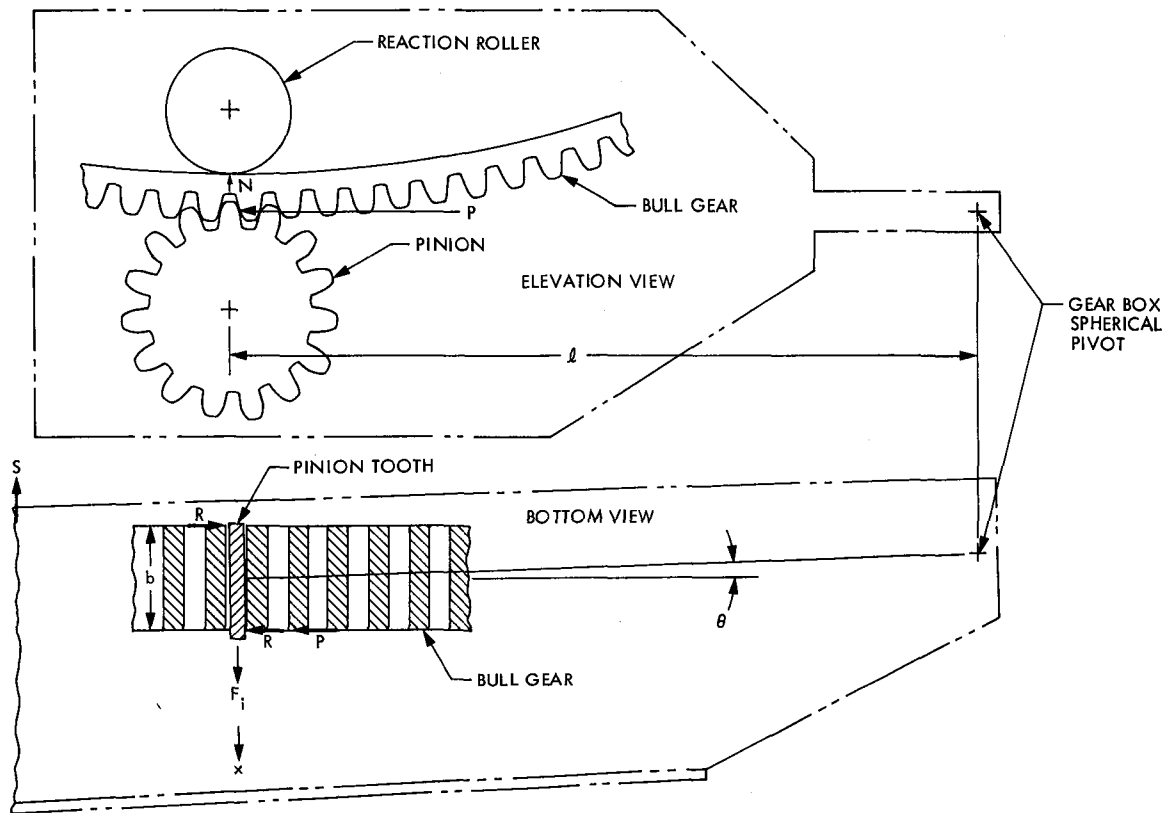
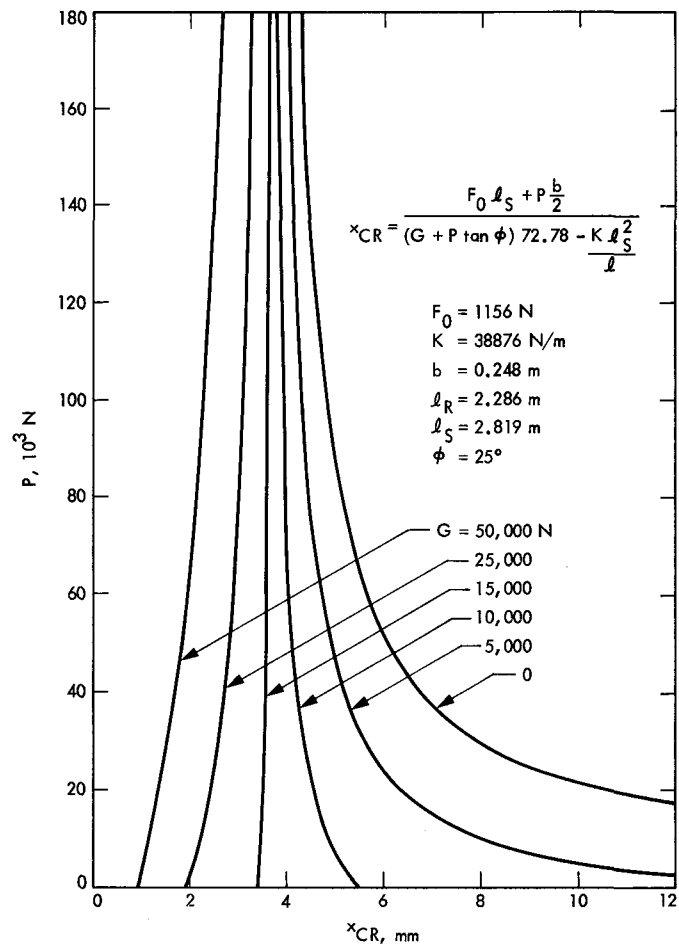


Fig. 30. Schematic of the elevation drive gears, showing forces considered



**Fig. 31. Critical displacement,  $x_{CR}$ , versus tangential load  $P$**

## Appendix A

### Static Stability Criterion for Elevation Drive of the 64-Meter Antenna

In 1966, shortly after the completion of the 64-m antenna at DSS 14, the No. 1 elevation drive pinion ran off the bull gear. To prevent a recurrence, bronze shoes or rubbing blocks were added to the drive housing so as to bear against the edge of the bull gear whenever conditions promoted a tendency for the pinion to run off. The arrangement and support of the gear boxes, as shown in Figs. 1 and 2, is such as to allow the pinion to align itself perfectly with the teeth of the bull gear. There is a spherical joint at one end of the gear box and two vertical and one horizontal spring loaded struts near the other end. This provision for gear self-alignment also allows the possibility of instability. The tendency for instability comes from induced lateral forces acting on a misaligned roller, which for the case at hand is the back-up roller or gear separation reaction roller. The bull gear teeth are on the outside of a ring structure. The inside surface of the ring is smooth and accurately spaced radially from the gear tooth pitch cylinder. The reaction roller, which is attached to the gear box and is nominally parallel to the drive pinion, constrains the pinion to near perfect radial alignment with the bull gear teeth. Ideally the contact force on the reaction roller is equal to the gear separation force, but if there is a variation in the bull gear radius, the vertical spring loaded support struts are deflected, and the spring force is equilibrated by a change in the roller reaction.

The induced side force on a misaligned roller can be large as described in Ref. 1. If large enough, the roller side force can predominate over restoring forces with the result that instability occurs. The following analysis discusses the conditions which promote static instability. Such instability is possible only when the motion of the bull gear is from pinion to gear box pivot. The reverse motion cannot produce instability.

Figure 30 shows two views of a gear box. By summing moments about the pivot point, the stabilizing and unstabilizing effects can be compared. For the case where the misalignment is small enough so that both edges of the gear teeth are not grounded out against the mating gear, the  $R$  forces do not exist, and the instability inequality is:

$$F_i \ell_R > S \ell_s + P m \quad (1)$$

where  $P$  is the tangential force at the pitch line caused by pinion torque

$$S = F_0 + k x \frac{\ell_s}{\ell_R} \quad (2)$$

is the horizontal spring loaded strut force

$F_0$  is the initial preload spring force

$k$  is the spring constant

$x$  is lateral displacement of pinion or roller

$\ell_R$  is distance from pivot to roller or pinion

$\ell_s$  is distance from pivot to horizontal strut

$m$  is distance from center of gear to force  $P$

$F_i = NC$ , the induced side force

$N$  is the normal force on the roller

$C$  is the side force coefficient

The normal force on the roller,  $N$ , is:

$$N = G + P \tan \phi \quad (3)$$

where  $G$  is the portion of  $N$  caused by gear box weight and  $\phi$  is the pressure angle of the spur gear teeth. Substitute Eqs. (2) and (3) into (1) and obtain:

$$(G + P \tan \phi) C \ell_R > F_0 \ell_s + k \frac{\ell_s^2}{\ell_R} x + P m \quad (4)$$

It is desirable to express  $C$  as a function of  $x$  and this can be done by using the straight line portion of Fig. 3 of Ref. 1 which is a plot of  $C$  versus the misalignment angle of a cylindrical roller. The result is:

$$C = 72.78 \theta \quad (5)$$

where  $\theta$  is the misalignment in radians. For the elevation drive,

$$\theta = \frac{x}{\ell_R} \quad (6)$$

Hence,

$$C = 72.78 \frac{x}{\ell_R} \quad (7)$$

Substitute Eq. (7) into Eq. (4) and obtain:

$$(G + P \tan \phi) 72.78 x > F_0 \ell_s + k \frac{\ell_s^2}{\ell_R} x + P m \quad (8)$$

If the load on the misaligned pinion is triangularly distributed along the tooth width,  $b$ ,  $m_1$  is equal to  $b/6$ , whereas if the load is concentrated at the edge,  $m_2 = b/2$ . Both cases will be considered. The horizontal spring loaded strut (JPL Dwg. 9436181) has an  $F_0$  value of 1156 N (260 lb) and a  $k$  value of 38876 N/m (222 lb/in.). A cursory check of the stiffness of the structure to which the horizontal strut attaches shows that practically all the flexibility is constituted by the spring loaded strut; therefore the small deflection of the structure will be ignored. When  $x$  is zero the left side of Eq. (8) is zero and the expressed inequality is not true; hence if Eq. (8) is converted to an equality, for finite values of  $x$ , and solved for  $x$ , the  $x$  value, called  $x_{CR}$ , represents the condition of neutral static stability. If an incidental displacement of the gear box should exceed  $x_{CR}$ , the displacement would increase, whereas an incidental displacement less than  $x_{CR}$  would be reduced.

$$x_{CR} = \frac{F_0 \ell_s + P m}{(G + P \tan \phi) 72.78 - k \frac{\ell_s^2}{\ell_R}} \quad (9)$$

Equation (9) is valid providing there is sufficient gear tooth backlash to allow one edge of tooth to be free. When instability occurs the lateral displacement,  $x$ , increases until both edges of the tooth are in contact and additional forces are developed. This will be discussed later.

It is desirable that  $x_{CR}$  be large from a static stability standpoint. From Eq. (9) it is clear that large  $F_0$  promotes large  $x_{CR}$ . The quantity  $(G + P \tan \phi)$  must not be negative or the roller would not be in contact with its track; hence large  $k$  also promotes large  $x_{CR}$ . Large  $m$  value also promotes large  $x_{CR}$ . If a small  $m$  value existed such that instability occurred, an increase in displacement would cause the small  $m$  value to shift to the larger  $m$  value; therefore it is proper to consider only the larger one, namely,  $m_2 = b/2$ . In other words the triangular distribution of tooth load will shift to corner loading as  $x$  increases. Equation (9) becomes

$$x_{CR} = \frac{F_0 \ell_s + P \frac{b}{2}}{(G + P \tan \phi) 72.78 - k \frac{\ell_s^2}{\ell_R}} \quad (10)$$

Equation (10) is plotted in Fig. 31 as  $x_{CR}$  versus  $P$  for various values of  $G$  for the particular values given in the figure which

pertain to the elevation drive. The effect of  $G$  obviously is to reduce substantially the value of  $x_{CR}$ . Therefore it is extremely important that the vertical struts of the elevation drive be easily adjustable so that little dead weight portion of the gear box is resisted by the roller. If the bull gear has radial run-out, as surely such a large gear will, then as the vertical struts change length, a finite  $G$  force will develop. Adjustments should be made to minimize the  $G$  force value.

The 64-m antenna elevation drives are counter-torqued against each other to give  $P$  values of approximately 66720 N at zero wind condition. At this  $P$  value  $x_{CR}$  is 5 mm for zero  $G$  and reduces to 3.7 mm for a  $G$  value of 10000 N. It is interesting to notice from Fig. 31 that a reduction in  $P$  increases the critical displacement,  $x_{CR}$ , for the smaller  $G$  values but decreases  $x_{CR}$  for the larger  $G$  values.

For the case of static instability, the lateral displacement,  $x$ , increases under the action of the forces considered above, until diagonal corners of the pinion are hard against adjacent teeth of the bull gear. At this time the corner forces  $R$  come into existence. Referring to Fig. 30 and summing moments about the gear box pivot, there is obtained the following balance of moments if equilibrium exists:

$$F_i \ell_R = S \ell_s + P \frac{b}{2} + R b \quad (11)$$

The normal force,  $N$ , on the roller is now increased by the additional corner forces,  $R$ , and becomes:

$$N = G + P \tan \phi + 2R \tan \phi \quad (12)$$

The induced force  $F_i$  is, as before,

$$\begin{aligned} F_i &= NC = N(72.78) \frac{x}{\ell_R} \\ &= 72.78 \frac{x}{\ell_R} [G + P \tan \phi + 2R \tan \phi] \end{aligned} \quad (13)$$

Substitute Eqs. (2) and (13) into Eq. (11) and obtain:

$$(G + P \tan \phi + 2R \tan \phi) (72.78) x \geq F_0 \ell_s + k \frac{\ell_s^2}{\ell_R} x + P \frac{b}{2} + R b \quad (14)$$

Equation (14) is identical to Eq. (8) except for the addition of the terms containing  $R$ . Since instability is assumed to exist up to the time the  $R$  forces come about, Eq. (14) will be an inequality as indicated if the left side  $R$  term is greater than the right side  $R$  term, that is, if

$$2(72.78) x \tan \phi > b \quad (15)$$

the value of the lateral displacement  $x_3$  at the time the  $R$  forces come about is a function of the gear backlash,  $\epsilon$ , the gear width  $b$ , and the distance from pinion to pivot,  $\ell_R$ . The value of this  $x_3$  is:

$$x_3 = \frac{\ell_R \epsilon}{b} \quad (16)$$

The backlash range is 0.001020 to 0.000635 m,  $\ell_R$  is 2.286 m, and  $b$  is 0.248 m, thus

$$x_3 = \frac{2.286}{0.248} \epsilon = 9.217 \epsilon \quad (17)$$

which equals 0.0094 m to 0.00585 m. Substitute the smaller value of Eq. (17) into Eq. (15) and obtain:

$$2(72.78) (0.00585) (0.466) > 0.248 \quad (18)$$

$$0.396 > 0.248 \quad (19)$$

which shows that equilibrium does not exist for these conditions. The existence of  $R$  as a restoring moment causes the induced side force moment,  $F_i \ell_R$ , to increase by a greater amount than the restoring moment  $Rb$ . The result is that if an incidental lateral displacement exceeds  $x_{CR}$ , the displacement will continue and cause the pinion to run off the bull gear if pinion rotation continues, unless there are additional constraints such as the bronze rubbing shoe.

It is believed that this is the explanation for the pinion run-off that occurred in 1966 at DSS 14, and only a relatively small incidental lateral displacement was required because there was an excessive portion of the gear box dead weight being carried by the roller, that is, the  $G$  value of Fig. 31 was excessive.

## Appendix B

### Derivation of Strut Stiffness Ratios

The configurations of the elevation drives, lower and upper are shown respectively in Figs. 1 and 2. These figures show the locations of the spherical pivot, center of gravity, weight, vertical strut locations which are designated  $F_1$  and  $F_2$ ,  $\beta$  angles which represent direction displacements of strut upper ends as the drive unit rotates about the  $z$  axis, pinion position, and reaction roller. Schematic drawings of the spring loaded support struts are shown in Fig. 3.

Ideally the dead weight of the drive unit, or gear box, is supported by the spherical joint and the two vertical struts. The reaction roller, which rests against the inner surface of the bull gear ring, ideally reacts only the separating force between the pinion and bull gear, but if the bull gear has radial runout, as surely it will, the gear box is caused to rotate about its pivot, and this will change both the reaction roller load and the vertical strut loads. The primary objective of this analysis is to determine the proper ratio between the stiffnesses of the vertical struts so that when the gear box is forced to rotate slightly about the  $z$  axis, there will be no concomitant roll about the  $x$  axis. Such  $x$  axis roll would tend to misalign the pinion and roller. However, the stiffnesses of both vertical struts must be low enough to allow the gear box to align itself to the bull gear, if the bull gear should roll from its nominal position, without inducing large forces.

First the extension (or compression) ratio between the struts, such that gear box roll is avoided, must be calculated. This is done by referring to Fig. 4 which shows the lengths of extended and compressed struts in terms of the gear box rotation and other parameters identified in the figure.

Let  $\delta$  be the bull gear radial runout. The gear box rotation  $\alpha$  is:

$$\alpha = \frac{\delta}{\ell_R} \quad (1)$$

where  $\ell_R$  is distance from pivot to roller. Substituting Eq. (1) into the expressions of Fig. 4 representing the lengths of the extended and compressed struts, it is easy to show that for small  $\alpha$  values, extension and contraction both can closely be approximated by:

$$\Delta L = \frac{R}{\ell_R} \delta \cos \beta \quad (2)$$

For the expected bull gear runout of  $\delta < 5$  mm, the vertical strut will tilt only a negligible amount; thus the effect on the horizontal moment arms of the struts may be ignored.

The  $\Delta L$ 's for the struts will be identified with the subscripts 1 and 2, for  $F_1$  and  $F_2$ , and with subscripts  $L$  and  $U$ , for lower and upper gear boxes.

$$\Delta L_{1L} = \frac{123.5}{90} (\cos 10.35) \delta = 1.350 \delta \quad (3)$$

$$\Delta L_{2L} = \frac{105}{90} (\cos 22.28) \delta = 1.080 \delta \quad (4)$$

$$\Delta L_{1U} = \frac{128}{90} (\cos 30.15) \delta = 1.230 \delta \quad (5)$$

$$\Delta L_{2U} = \frac{106}{90} (\cos 30.70) \delta = 1.013 \delta \quad (6)$$

The required extension (or compression) ratios are:

$$\frac{\Delta L_{1L}}{\Delta L_{2L}} = \frac{1.350}{1.080} = 1.250 \quad (7)$$

for the lower gear box and

$$\frac{\Delta L_{1U}}{\Delta L_{2U}} = \frac{1.230}{1.013} = 1.214 \quad (8)$$

for the upper gear box, which are the required extension ratios for no roll of the gear boxes.

For the condition of perfect roller alignment, the roller force  $F_R$  produces no moment about the  $x$  axis. If the gear box is rotated about the  $z$  axis without rolling about the  $x$  axis, as is desired, the moment equilibrium equation about the  $x$  axis is:

$$a_1 \Delta F_1 = a_2 \Delta F_2 \quad (9)$$

where the moment arms  $a_1$  and  $a_2$  are identified in Figs. 1 and 2 and  $\Delta F_1$  and  $\Delta F_2$  are force increments in vertical struts No. 1 and No. 2 respectively, and are:

$$\Delta F_1 = K_1 \Delta L_1 \quad (10)$$

$$\Delta F_2 = K_2 \Delta L_2 \quad (11)$$

Divide Eq. (11) by (10) and obtain:

$$\frac{K_2}{K_1} = \frac{\Delta F_2 \Delta L_1}{\Delta F_1 \Delta L_2} \quad (12)$$

Substitute  $\Delta F_2/\Delta F_1$  from Eq. (9) into (12) and obtain:

$$\frac{K_2}{K_1} = \frac{a_1 \Delta L_1}{a_2 \Delta L_2} \quad (13)$$

as the desired ratio between the stiffnesses of the two vertical struts.

Now the strut forces  $F_1$  and  $F_2$  will be calculated. Again assume that the roller reaction,  $F_R$ , is uniformly distributed so that it does not produce a moment about the  $x$  axis. Sum moments about axes  $x$  and  $z$  and obtain:

$$a_1 F_1 + a_2 F_2 = a_w W \quad (14)$$

where  $W$  is gear box weight

$$\ell_1 F_1 - \ell_2 F_2 = \ell_w W - \ell_R F_R \quad (15)$$

From Eq. (14)

$$F_2 = \frac{a_w}{a_2} W - \frac{a_1}{a_2} F_1 \quad (16)$$

A plot of Eq. (16) is in Fig. 5. Substitute Eq. (16) into (15) and obtain:

$$\ell_1 F_1 - \ell_2 \left[ \frac{a_w}{a_2} W - \frac{a_1}{a_2} F_1 \right] = \ell_w W - \ell_R F_R \quad (17)$$

Solve Eq. (17) for  $F_1$  and obtain:

$$F_1 = \left[ \frac{\ell_w + \ell_2 \frac{a_w}{a_2}}{\ell_1 + \ell_2 \frac{a_1}{a_2}} \right] W - \left[ \frac{\ell_R}{\ell_1 + \ell_2 \frac{a_1}{a_2}} \right] F_R \quad (18)$$

From Eq. (14)

$$F_1 = \frac{a_w W}{a_1} - \frac{a_2}{a_1} F_2 \quad (19)$$

Substitute Eq. (19) into Eq. (15) and obtain:

$$F_2 = \left[ \frac{\ell_1 \frac{a_w}{a_1} - \ell_w}{\ell_2 + \ell_1 \frac{a_2}{a_1}} \right] W + \left[ \frac{\ell_R}{\ell_2 + \ell_1 \frac{a_2}{a_1}} \right] F_R \quad (20)$$

Various values of  $F_R$  have been calculated from Eq. (20) and are shown in Fig. 5.

From Eqs. (18) and (20) it can be seen that as  $F_R$  becomes finitely positive,  $F_1$  reduces and  $F_2$  increases. From Figs. 1 and 2 it is clear that as the gear boxes rotate clockwise about the  $z$  axis, both  $F_1$  and  $F_2$  struts must extend. Since  $F_1$  is a compression strut its extension represents a reduction in load;  $F_2$  is a tension strut and so its extension represents an increase in load. If the gear box has been perfectly aligned so that the reaction roller uniformly clears the bull gear by an infinitesimal amount,  $F_R$  is zero and  $F_1$  and  $F_2$  can be calculated from Eqs. (18) and (20). From this condition let the bull gear run out radially by the amount  $\delta$ . The quantities  $\Delta F_1$  and  $\Delta F_2$  can be calculated using Eqs. (3), (4), (5), and (6) together with Eqs. (10) and (11) obtaining:

$$\Delta F_{1L} = K_{1L} 1.350 \delta \quad (21)$$

$$\Delta F_{2L} = K_{2L} 1.080 \delta \quad (22)$$

$$\Delta F_{1U} = K_{1U} 1.230 \delta \quad (23)$$

$$\Delta F_{2U} = K_{2U} 1.013 \delta \quad (24)$$

The roller reaction force,  $F_R$ , may be calculated by substituting these values of  $\Delta F$  for  $F_1$  and  $F_2$  of Eqs. (18) and (20) respectively, with  $W$  set to zero since incremental loading due to runout is now being considered. There are obtained:

$$F_{RL} = 2.2005 K_{2L} \delta \quad (25)$$

$$F_{RU} = 1.9048 K_{2U} \delta \quad (26)$$

Since the dimensionless coefficients of Eqs. (25) and (26) vary only about 7% from their mean value, it is feasible to select a common value for  $K_{2L}$  and  $K_{2U}$ . The important feature is that the ratio between  $K_2$  and  $K_1$  be in accordance with Eq. (13) which when evaluated becomes:

$$\left( \frac{K_2}{K_1} \right)_L = 1.770 \quad (27)$$



$$\left(\frac{K_2}{K_1}\right)_U = 1.709 \quad (28)$$

where the subscripts  $L$  and  $U$  designate lower and upper gear boxes respectively.

These stiffness ratios are the ideal ones which would both prevent gear box roll about the  $x$  axis and insure uniform loading along the reaction roller length. From practical considerations it is impossible to obtain these stiffness ratios exactly. The following analysis will show over what range the stiffness ratio can vary without allowing  $x$  axis roll but by allowing nonuniform loading along the roller length. The roller loading now being considered is caused by bull gear radial runout only. (The primary load on the roller is caused by the gear separation force and this will be discussed later.)

Consider that the roller force,  $F_R$ , is a concentrated force applied to the gear box at the roller position but displaced the distance  $h$  (see Fig. 2) along the roller axis from the mid-point of the roller length. The three supports of the gear box are the spherical pivot and the  $F_1$  and  $F_2$  struts which have reactions  $\Delta F_1$  and  $\Delta F_2$  respectively. Sum moments about the  $x$  axis and obtain:

$$\Delta F_1 a_1 - \Delta F_2 a_2 = \frac{F_R h}{\cos \theta} \quad (29)$$

Sum moments about the  $z$  axis and obtain:

$$\Delta F_1 \ell_1 + \Delta F_2 \ell_2 = F_R \ell_R \quad (30)$$

Substitute Eq. (30) into (29) and obtain:

$$h = \frac{(\Delta F_1 a_1 - \Delta F_2 a_2) \ell_R \cos \theta}{(\Delta F_1 \ell_1 + \Delta F_2 \ell_2)} \quad (31)$$

Using Eqs. (10) and (11) together with Eqs. (3), (4), (5), and (6), and letting  $\lambda = K_1/K_2$ ,  $h$  is evaluated for the lower and upper gear boxes as:

$$\begin{aligned} \frac{h_L}{\ell_R} &= \frac{(1.350 a_1 \lambda - 1.080 a_2) \cos 7.683^\circ}{(1.350 \ell_1 \lambda + 1.080 \ell_2)} \\ &= \frac{26.423 \lambda - 14.931}{163.957 \lambda + 105.397} \end{aligned} \quad (32)$$

$$\begin{aligned} \frac{h_U}{\ell_R} &= \frac{(1.230 a_1 \lambda - 1.013 a_2) \cos 45.25^\circ}{(1.230 \ell_1 \lambda + 1.013 \ell_2)} \\ &= \frac{17.102 \lambda - 10.006}{135.521 \lambda + 92.142} \end{aligned} \quad (33)$$

From Eqs. (32) and (33) the corresponding values of  $\lambda$  and  $h_L/\ell_R$  shown in Table 1 are obtained. The length of the cylindrical part of the roller is 71.43 mm and  $\ell_R$  is 2286 mm. Thus if the concentrated force  $F_R$  were located 71.43/2 mm from the roller center,  $h/\ell_R$  would be 0.01562. The maximum value of  $h$  for which stability prevails is 35.71 mm, since if  $h$  exceeded this, the concentrated force would be beyond the cylindrical part of the roller and tilting would occur. Therefore if the stiffness ratio of the lower struts,  $K_1/K_2$ , lies between 0.460 and 0.694, tilting would not occur. If the stiffness ratio of the upper struts,  $K_1/K_2$ , lies between 0.446 and 0.760, tilting will not occur. The stiffnesses of the actual compression struts are given by the slopes of the force versus deflection curves shown in Figs. 6 through 17. The stiffnesses of the actual tension struts are given by the slopes of the force versus deflection curves shown in Figs. 18 through 29. These curves do not necessarily have constant slopes; therefore it is necessary to know the approximate values of  $F_1$  and  $F_2$  and these can be taken from Fig. 5 for the appropriate values of the reaction roller force  $F_R$ . The  $F_R$  values can be calculated from Eqs. (25) and (26) if the bull gear radial runout,  $\delta$ , is known. From measurements made at DSS 14 in March 1980, at DSS 43 in 1980, and at DSS 63 in June 1980, the total excursions of the bull gear radial runouts were respectively 5.1 and 4.3 mm at DSS 14, 2.79 and 5.80 mm at DSS 43, and 1.14 and 1.65 mm at DSS 63. Using half the largest of these together with the  $K_2$  value from Fig. 28, namely 18000/0.02005 Newtons per meter, Eqs. (25) and (26) yield

$$F_{RL} = \frac{2.2}{2} \frac{18000}{0.02005} 0.0058 = 5728 \text{ N}$$

or 1288 lb and

$$F_{RU} = \frac{1.9}{2} \frac{18000}{0.02005} 0.0058 = 4947 \text{ N}$$

or 1112 lb as approximations for the maximum  $F_R$  value caused by bull gear runout only. Taking the means between these estimated maximum  $F_R$  values and zero  $F_R$  values, there are obtained 644 lb and 556 lb respectively for the lower and upper gear boxes. For these mean values the  $F_1$  and  $F_2$  coordinates from Fig. 5 are:

$$F_{1L} = 13450 \text{ lb}$$

$$F_{2L} = 1400 \text{ lb}$$

$$F_{1U} = 13280 \text{ lb}$$

$$F_{2U} = 2400 \text{ lb}$$

It is for the foregoing  $F$  values that the strut spring constants will be compared to determine if the gear boxes will be free of rolling displacement as the bull gear undergoes radial run-out. These stiffness ratios are set out in Table 2 from which it may be seen that all ratios are within the desired range.

## Appendix C

### Outline for Removing, Installing, and Adjusting the Vertical Struts

The new vertical compression strut (JPL Dwg. 9477047) and the new vertical tension strut (JPL Dwg. 9477064) were installed and aligned essentially as per the following outline.

- (1) Bull gear radial runout measurements made at DSS-63 were approximately one millimeter total excursion. For such small runouts the vertical struts may be installed and adjusted at any elevation angle. At DSS 43 the radial runout is 3 mm for one bull gear and 6 mm for the other. The mean compression or extension of the struts should be determined by measuring dimensions  $a$  and  $A$  of Fig. 3 for each gear box, over the elevation angle range. The adjustment of the new struts should be made at the elevation angle corresponding to the mean lengths. At DSS 14 the bull gear radial runouts are 4.3 mm and 5.1 mm. The proper DSS 14 elevation angles for adjusting the vertical struts are  $65^\circ$ ,  $60^\circ$ ,  $71^\circ$ , and  $71^\circ$  for gear boxes numbers 1, 2, 3, and 4 respectively.
  - (2) To remove a compression strut, the compressive load must be locked in by screwing in four 25.4-mm-diameter bolts until their ends contact the spring piston, thus preventing sudden expansion of the strut upon release of the gear box weight loading. The gear box must safely be supported by auxiliary jacks or hoists. Then the strut attachments may be removed. The new compression struts were compressed to 60000 N (13500 lb) and the corresponding  $A$  dimensions are shown in Figs. 6 through 17. Four 25.4-mm-diameter bolts locked in this compressive force, and in this condition the new compressive struts were installed by adjusting the large bronze nut as required. The tension strut was installed by adjusting its bronze nut as required.
  - (3) The auxiliary supports were removed allowing the gear box weight to be transferred to the new vertical struts and the reaction roller.
  - (4) To insure that there was no load on the drive pinion, the gear box input shaft was set near the middle of its backlash range. The four 25.4-mm-diameter bolts which locked in the compressive load were retracted.
- Then the bronze nuts of the compressive and tension struts were adjusted until a clearance was obtained between the reaction roller and bull gear back side. This was determined by using a thickness gage to verify clearance.
- (5) The reaction roller was removed and the bronze nuts of the compression and tension struts further adjusted so that when the reaction roller was reinstalled, its clearance with the back side of the bull gear would be uniform. This was done by making measurements between the bull gear and the roller shaft housings.
  - (6) The dimensions  $a$  and  $A$  for the tension and compression struts respectively were measured. Dimension  $a$  for the unloaded tension strut had been previously recorded. A comparison of dimensions  $A$  and  $a$  with the force deflection curves shown respectively in Figs. 6 through 17 and Figs. 18 through 29, allow the forces in the struts to be determined for the condition of no load on the reaction roller.
  - (7) The reaction roller was reinstalled and the adjusting bronze nuts of the tension and compressive struts were safetied.
  - (8) The final adjustments of the gear boxes were made by adjusting the horizontal strut so as to optimize the pinion to bull gear teeth alignment. Further adjustments to the vertical struts would be necessary only if their springs should change their stiffnesses or if additional weight were added to the gear boxes. Such can be determined by setting the elevation angle at the proper position as given in step 1 and with the servo drive turned off, determining whether a clearance exists between the reaction roller and the bull gear back side.
  - (9) After the final adjustment, the change in lengths of the compression and tension struts, dimensions  $A$  and  $a$ , as a function of elevation angle, were measured and recorded.
- The initial alignment dimensions for the new vertical struts at DSS-14 are shown in Table 3.

# Hydrostatic Bearing Pad Maximum Load and Overturning Conditions for the 70-Meter Antenna

H. D. McGinness

Ground Antennas and Facilities Engineering Section

*The maximum hydrostatic bearing loading is shown to be sufficiently small and the ratios of stabilizing to overturning moments are ample.*

## I. Introduction

A project has been established to increase the reflector diameters of the 64-m antennas to 70-m (Ref. 1). In order to evaluate the minimum film thickness of the hydrostatic bearing which supports the antenna weight, it is first necessary to have a good estimation of the maximum operational load on the most heavily loaded bearing pad. The most heavily loaded pad is the Number 3 pad, and this is identified in Figs. 1 and 2. It is also essential to know the stabilizing moment and overturning moment caused, respectively, by weight and wind loading.

$$R_{3_{64}} = 1.519 q \frac{\pi}{4} D^2 \quad (1)$$

and for the 70-m antenna

$$R_{3_{72}} = 1.627 q \frac{\pi}{4} D^2 \quad (2)$$

where

$q = 1/2 \rho V^2$  = the dynamic pressure of the wind

$\rho$  = the air density

$V$  = the wind speed

## II. Bearing Pad Load Calculation

The maximum reactions on the Number 3 pads of the 64- and 70-m antennas, caused by wind loading only, are<sup>1</sup> for the 64-m antenna.

These maximum reactions occur at an elevation angle of 5° and a wind azimuth of zero.

The measured weight loading on pad Number 3 of the 64-m antenna was 9,719,604 N(2,185,054 lb) and was obtained by measuring the pressure in hydraulic jacks when the alidade was raised for repair of the hydrostatic bearing runner in 1983. It is estimated that the 70-m reflector will add from 3,333,750

<sup>1</sup> See Table VI in *The effects of wind loading on the bearings and drives of the 64-m and 72-m antennas* (unpublished), by H. D. McGinness, 1984, Reorder No. 84-2, Jet Propulsion Laboratory, Pasadena, CA.

to 4,445,000 N (750,000 to 1,000,000 lb) to the weight reaction at Pad Number 3. The total reactions,  $R_{T3}$ , at the Number 3 pads, using one third the larger of the estimated increment for the 70-m antenna and a wind speed of 22.35 m/s (50 mph), are:

$$R_{T3_{64}} = 9,719,604 + \left(\frac{1}{2}\right) 1.171 (22.35)^2 \frac{\pi}{4} (64)^2$$

$$= 10,660,000 \text{ N (2,396,463 lb)} \quad (3)$$

$$R_{T3_{72}} = 11,202,343 + \left(\frac{1}{2}\right) 1.171 (22.35)^2 \frac{\pi}{4} (72)^2$$

$$= 12,392,533 \text{ N (2,785,952 lb)} \quad (4)$$

where  $1.172 \text{ kg/m}^3$  is the air density 670 m above sea level. Thus, the Pad Number 3 loading of the 70-m antenna is  $(12392533/10,660,000) = 1.163$  times that of the 64-m antenna pad. From elementary laminar flow through a slot theory, the film thickness,  $h$ , should vary inversely with the cube root of the load. When applied to the load factor 1.163

$$h_{72} = h_{64} \frac{1}{(1.163)^{1/3}} = 0.95 h_{64} \quad (5)$$

A more accurate analysis taking account of the disposition of the pad recesses, and the deflection of the runner, produced a somewhat smaller value of  $h_{72}/h_{64}$ , namely 0.85, as the ratio of the film thicknesses at one corner of the pad.

### III. Overturning Calculations

The ratio of stabilizing moment,  $M_s$ , to overturning moment,  $M_o$ , for two conditions may be obtained.<sup>2</sup>

During operation of the antenna the minimum ratio of stabilizing to overturning moment occurs at elevation angle  $5^\circ$  and wind azimuth zero. For this case the ratios of the two antennas are:

$$\left(\frac{M_s}{M_o}\right)_{64} = \frac{W_3}{1.516 q \frac{\pi}{4} D^2} = \frac{W_3}{1.516 \left(\frac{1}{2}\right) \rho V^2 D^2} \quad (6)$$

$$\left(\frac{M_s}{M_o}\right)_{72} = \frac{W_3}{1.612 q \frac{\pi}{4} D^2} = \frac{W_3}{1.612 \left(\frac{1}{2}\right) \rho V^2 D^2} \quad (7)$$

where  $W_3$  is the weight loading on Pad Number 3 at zero wind. Evaluate Eqs. (6) and (7) for  $V = 31.29 \text{ m/s (70-mph)}$  and obtain:

$$\frac{M_s}{M_o} = \frac{9,719,604}{1.516 \left(\frac{1}{2}\right) 1.171 (31.29)^2 \frac{\pi}{4} (64)^2} = 3.478 \quad (8)$$

$$\frac{M_s}{M_o} = \frac{11,202,343}{1.612 \left(\frac{1}{2}\right) 1.171 (31.29)^2 \frac{\pi}{4} (72)^2} = 2.979 \quad (9)$$

Overturning impends when  $M_s/M_o = 1$ . From Eqs. (8) and (9) the overturning wind speeds are:

$$V_{64} = \left[ \frac{9,719,604}{1.516 \frac{1}{2} 1.171 \frac{\pi}{4} (64)^2} \right]^{1/2} = 58.36 \text{ m/s (131 mph)} \quad (10)$$

$$V_{72} = \left[ \frac{11,202,343}{1.612 \frac{1}{2} 1.171 \frac{\pi}{4} (72)^2} \right]^{1/2} = 54.00 \text{ m/s (121 mph)} \quad (11)$$

At the stow position of elevation angle  $90^\circ$  and wind azimuth  $180^\circ$ , the  $M_s/M_o$  ratios are:

$$\left(\frac{M_s}{M_o}\right)_{64} = \frac{W_3}{1.079 \left(\frac{1}{2}\right) \rho V^2 D^2} \quad (12)$$

$$\left(\frac{M_s}{M_o}\right)_{72} = \frac{W_3}{1.124 \left(\frac{1}{2}\right) \rho V^2 D^2} \quad (13)$$

Evaluating Eqs. (12) and (13) for  $V = 44.7 \text{ m/s (100 mph)}$  there are obtained:

$$\left(\frac{M_s}{M_o}\right)_{64} = \frac{9,719,604}{1.079 \left(\frac{1}{2}\right) 1.171 (44.7)^2 \frac{\pi}{4} (64)^2} = 2.394 \quad (14)$$

$$\left(\frac{M_s}{M_o}\right)_{72} = \frac{11,202,343}{1.124 \left(\frac{1}{2}\right) 1.171 (44.7)^2 \frac{\pi}{4} (72)^2} = 2.093 \quad (15)$$

<sup>2</sup>See Table VI, H. D. McGinness, *op. cit.*

Overturning impends when  $M_s/M_o = 1$ . From Eqs. (12) and (13) the overturning wind speeds for the two antennas at stow are:

$$V_{64} = \left[ \frac{9,719,604}{1.079 \left(\frac{1}{2}\right) 1.171 \frac{\pi}{4} (64)^2} \right]^{1/2} = 69.17 \text{ m/s (155 mph)} \quad (16)$$

$$V_{72} = \left[ \frac{11,202,343}{1.124 \left(\frac{1}{2}\right) 1.171 \frac{\pi}{4} (72)^2} \right]^{1/2} = 64.67 \text{ m/s (145 mph)} \quad (17)$$

## IV. Conclusion

The minimum film thickness at Pad Number 3 corner of the 70-m antenna is not less than 0.85 times the corresponding thickness of the 64-m antenna and this is considered satisfactory. Additional pumping power for the hydrostatic bearing system is not required.

The stabilizing to overturning ratios, as given by Eqs. (9) and (15), namely 2.979 and 2.093, respectively, are deemed to be ample. The wind speed required to overturn at the worst operating attitude is 54 m/s (121 mph), whereas drive to stow will start at 22.35 m/s (50 mph). At stow the overturning wind speed is 64.67 m/s (145 mph), whereas survival specifications for the 64-m antenna was 53.64 m/s (120 mph).

## Reference

1. McClure, D. H., and F. D. McLaughlin, 64-meter to 70-meter antenna extension, *TDA Progress Report 42-79*, Jet Propulsion Laboratory, Pasadena, CA, pp. 160-164.

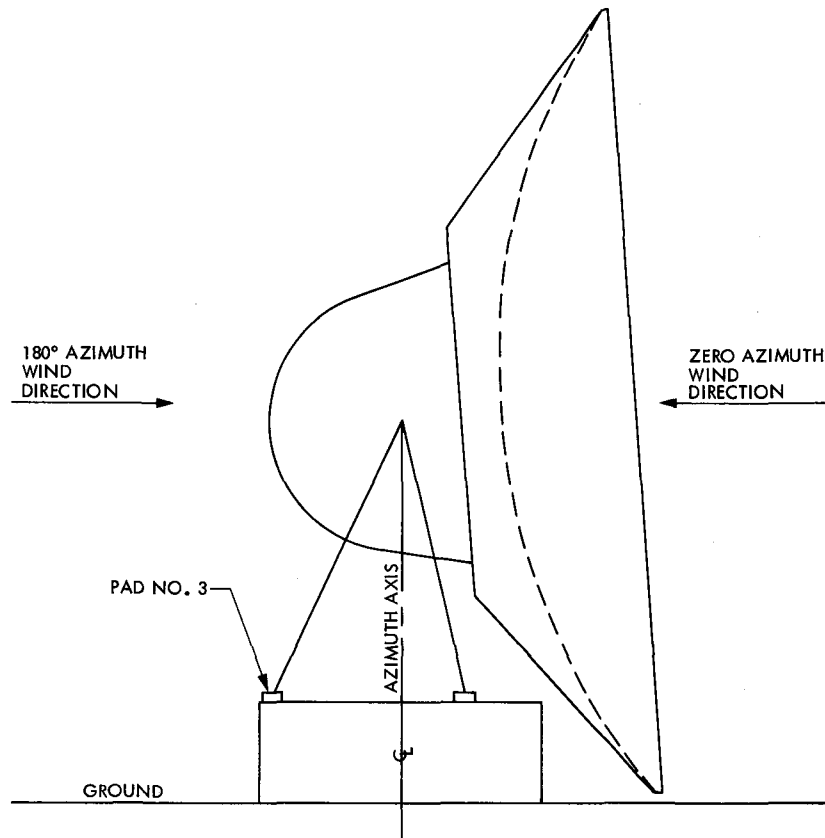


**Fig. 1. Attitude of antenna for critical load on Pad 3 during operation, wind azimuth zero; critical overturning, wind azimuth 180°**

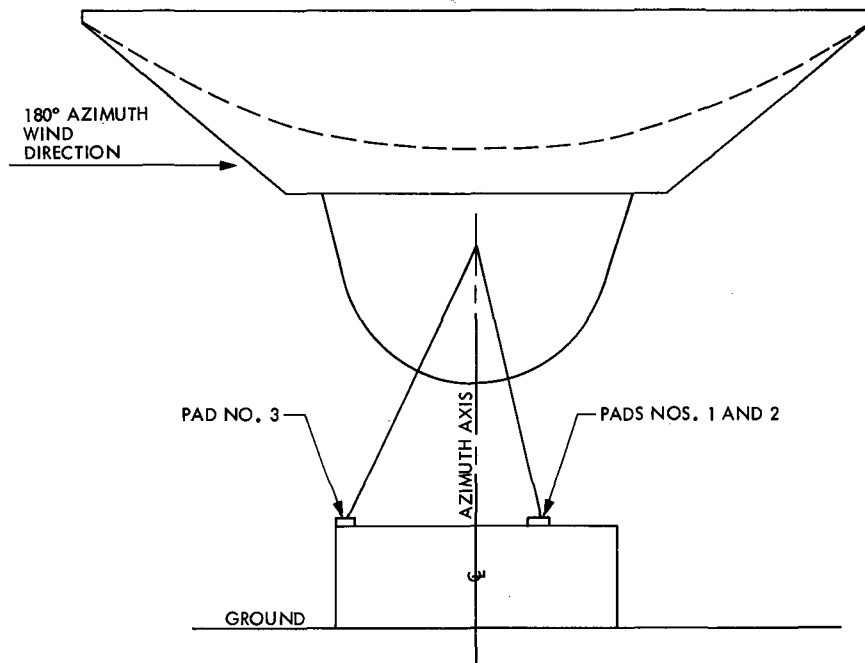


**Fig. 2. Stow position of antenna; overturning critical at wind azimuth 180°**

# Performance of the DSA's Subcarrier Demodulation Digital Loop

M. K. Simon

A. Mileant

Telecommunication Systems Section

*The subcarrier demodulation digital loop is part of the Baseband Assembly. The subcarrier demodulator is a fourth-order Costas-type loop. It corresponds to a "type 2" analog loop in terms of steady state response. In this article, the expected value and the variance of the error signal are determined as functions of the input SNR. A Nyquist sampling rate of the input signal is assumed. From the integro-difference equations a mixed  $s/z$  domain block diagram is obtained. From the loop's transfer function a set of gains for the loop filter is obtained. Also, a set of state equations is presented for future reference. Finally, the noise-equivalent bandwidths are calculated for normalized computation times of 0, 0.25 and 0.5.*

*The subcarrier demodulator analyzed in this article tracks a parabolic phase input with finite steady state error. Since at each update instant the loop gains are adjusted to compensate for the variations in SNR of the input signal, the noise-equivalent bandwidth is maintained constant.*

## I. Introduction

The subcarrier demodulation digital loop is part of the Baseband Assembly (Ref. 1). The subcarrier is demodulated by a Costas-type fourth-order digital loop. The input to this loop, which comes from the real-time combiner (RTC), consists of a string of unitless numbers whose values are proportional to the signal and noise amplitudes. For analysis purposes, it is convenient to assume that sampling of the input signal occurs at the Nyquist rate. This is justified by the fact that, according to

measurements made by Larry Howard (private communication), oversampling does not appear to improve or degrade the SNR of the loop's error signal.

In this article, the topics are subdivided as follows:

- (1) Error Signal Statistics
- (2) DCO Board Transfer Function
- (3) Phase Detector Averages



- (4) Closed Loop Transfer Function
- (5) Determination of Gains A, B, C, and D
- (6) Steady State Error
- (7) Derivation of the State and Output Equations
- (8) Noise-Equivalent Bandwidth

## II. Error Signal Statistics

The input to the subcarrier demodulation loop (Fig. 1) comes from the RTC. This input can be modeled as a string of samples as follows:

$$y_i = s_i + n_i \quad (1)$$

where  $s_i$  is a unitless random variable whose value is proportional to the signal amplitude of the  $i^{\text{th}}$  sample, and  $n_i$  is a unitless random variable whose value is proportional to the noise amplitude of the  $i^{\text{th}}$  sample.

The signal tracked by the loop is a squarewave subcarrier of  $N_{sc}$  Nyquist samples per cycle BPSK modulated by binary random data with  $N_s$  Nyquist samples per symbol. The mean of the  $i^{\text{th}}$  sample is given by

$$E\{s_i\} = b_j \sqrt{S} \cos \theta_i \quad (2)$$

where  $b_j = \pm 1$  is a random variable equal to the sign of the  $j^{\text{th}}$  binary data symbol.

The noise is modeled as a random process with zero mean and variance per sample  $\sigma_n^2$ . The instantaneous phase of the input signal is  $\theta_i$ .

In the tracking mode, the subcarrier digital phase-locked loop produces an estimate of the input phase,  $\hat{\theta}_i$ , with an instantaneous error

$$\phi_i = \hat{\theta}_i - \theta_i \quad (3)$$

To proceed with this analysis, it will be convenient to define the normalized phase error

$$u_i = \frac{\phi_i}{\pi/2} \quad (4)$$

with half symbol average

$$u_k = \frac{1}{N_s/2} \sum_{i=1}^{N_s/2} u_i \quad (5)$$

and one update period average ( $K$  symbols per update)

$$u_n = \frac{1}{2K} \sum_{k=1}^{2K} u_k$$

$$= \frac{1}{T_L} \int_{t_n - T_c}^{t_n + T_R} u(t) dt \quad (6)$$

Here  $T_L$  is the update time interval.

Referring to Fig. 1, the expected value of the outputs of the in-phase and quadrature arms will be, respectively (assuming loop operation in the linear region),

$$\bar{x}_{Ii} = b_j K_1 \sqrt{S} (1 - |u_i|) \quad (7)$$

$$\bar{x}_{Qi} = b_j K_2 \sqrt{S} u_i \quad (8)$$

The outputs of the  $I$  and  $Q$  summers, which add up  $N_s/2$  samples, will have means

$$\bar{x}_{Ik} = b_j K_1 \sqrt{S} \frac{N_s}{2} (1 - |u_k|) \quad (9)$$

$$\bar{x}_{Qk} = b_j K_2 \sqrt{S} \frac{N_s}{2} u_k; \quad k = 1, 2, \dots, 2K \quad (10)$$

and variances due to thermal noise

$$\sigma_{Ik}^2 = K_1^2 \frac{N_s}{2} \sigma_n^2 \quad (11)$$

$$\sigma_{Qk}^2 = K_2^2 \frac{N_s}{2} \sigma_n^2; \quad k = 1, 2, \dots, 2K \quad (12)$$

Finally, the error signal  $e_n$  at the output of the third summer, which adds up  $2K$  half-symbol samples, will have mean value

$$e_n = 2K \bar{x}_{I1} \bar{x}_{Q2} = \frac{K}{2} K_1 K_2 K_3 N_s^2 S (1 - |u_n|) u_n \quad (13)$$

because  $b_j^2 = 1$  for all  $j$ .

The variance at the input to the third summer will be

$$\sigma_{IQk}^2 = E[(x_{Ik} x_{Qk})^2 - (\bar{x}_{Ik} \bar{x}_{Qk})^2] K_3^2 \quad (14)$$

$$= (\sigma_{Ik}^2 \sigma_{Qk}^2 + (\bar{x}_{Ik})^2 \sigma_{Qk}^2 + (\bar{x}_{Qk})^2 \sigma_{Ik}^2) K_3^2 \quad (15)$$

The variance of the output of the third summer will be

$$\sigma_\epsilon^2 = \sum_{k=1}^{2K} \sigma_{IQk}^2 \quad (16)$$

$$\begin{aligned} &= \frac{K}{2} K_1^2 K_2^2 K_3^2 N_s^2 \sigma_n^4 \\ &+ \frac{K_1^2}{8} K_2^2 K_3^2 SN_s^3 \sigma_n^2 \left( \sum_{k=1}^{2K} (1 - |u_k|)^2 \right) \\ &+ \frac{K_1^2}{8} K_2^2 K_3^2 SN_s^3 \sigma_n^2 \left( \sum_{k=1}^{2K} u_k^2 \right) \end{aligned} \quad (17)$$

Since the assumption of operation in the linear region implies a high loop SNR condition (small values of  $u_k$ ), then it is convenient to let  $u_k = 0$  in (17), which gives the approximation

$$\begin{aligned} \sigma_\epsilon^2 &= \frac{K}{2} K_1^2 K_2^2 K_3^2 N_s^2 \sigma_n^4 + \frac{K}{4} K_1^2 K_2^2 K_3^2 SN_s^3 \sigma_n^2 \\ &= \frac{K}{2} K_1^2 K_2^2 K_3^2 N_s^2 \sigma_n^4 \left[ 1 + \frac{SN_s}{2\sigma_n^2} \right] \end{aligned} \quad (18)$$

Furthermore, for small  $u_n$  the normalized loop tracking curve

$$g(u_n) = (1 - |u_n|) u_n \quad (19)$$

can be approximated by

$$g(u_n) = u_n \quad (20)$$

whereupon the mean of the error signal at the third summer output, as given by (13), becomes

$$\bar{\epsilon}_n = G'_Q u_n \quad (21)$$

with

$$G'_Q \triangleq KK_1 K_2 K_3 N_s^2 S/2 \quad (22)$$

### III. DCO Board Transfer Function

Referring to Fig. 1, the CPU reads the error signal  $\epsilon_n$  every  $T_L$  seconds (i.e.,  $N_s K$  samples), and at the input of the DCO

board produces increments of phase rate according to the following algorithm:

$$\Delta \hat{\theta}_n = A \epsilon_n + B \epsilon_{n-1} + C \Delta \hat{\theta}_{n-1} + D \Delta \hat{\theta}_{n-2} + E \hat{\theta}_n \quad (23)$$

where  $A$ ,  $B$ ,  $C$ , and  $D$  are gains to be determined, and  $\hat{\theta}_n$  is the estimate of the phase acceleration and is an external input to the digital loop. In this analysis, it will be assumed that  $E = 0$ .

Assuming zero initial conditions, Eq. (23) can be expressed in the  $z$ -domain as

$$\Delta \hat{\theta}(z) (1 - Cz^{-1} - Dz^{-2}) = \epsilon(z) (A + z^{-1}B) \quad (24)$$

It should be noted that Eq. (24) assumes zero computation time; i.e., as soon as the CPU reads  $\epsilon_{n-1}$ , it produces  $\hat{\theta}_n$ . The actual delay between reading  $\epsilon_{n-1}$  and producing  $\Delta \hat{\theta}_n$  will be accounted for further on in this analysis.

The transfer function  $F(z)$  of the blocks designated in our analysis as the "loop filter" is, from Eq. (24),

$$F(z) = \frac{\Delta \hat{\theta}(z)}{\epsilon(z)} = \frac{(Az + B)z}{(z^2 - Cz - D)} \quad (25)$$

The phase rate of the DCO's output is constant during one update period, and its sampled value equals (see Fig. 2(b))

$$\hat{\theta}_n = \hat{\theta}_0 + \sum_{j=1}^n \Delta \hat{\theta}_j \quad (26)$$

The transfer function for a DCO is

$$\frac{\hat{\theta}(s)}{\hat{\theta}(z)} = \frac{1 - e^{-sT_L}}{s^2} \quad (27a)$$

Our subcarrier demodulation loop has, in addition, a summer built on the DCO board. Taking this into account, the total "DCO board" transfer function becomes

$$\frac{\theta(s)}{\Delta \hat{\theta}(z)} = \left( \frac{1 - e^{-sT_L}}{s^2} \right) \frac{z}{z - 1} \quad (27b)$$

### IV. Phase Detector Averages

The phase rate error process  $\phi(t)$  is shown in Fig. 2(a). At frequency update instants, it is expressed by the following difference equation

$$\dot{\phi}_n = \dot{\phi}_{n-1} + T_L \ddot{\phi}_{n-1} - \Delta \hat{\theta}_n \quad (28) \quad \text{or}$$

with

$$T_L = T_R + T_c \quad (29)$$

where

$T_L$  = the frequency update period in seconds, and

$T_c = T_L g$ , the computation time, in seconds, with

$$0 \leq g < 1. \quad (30)$$

The phase error process  $\phi(t)$  at frequency update instants is obtained by integrating  $\phi(t)$  between  $t_{n-1}$  and  $t_n$ , namely

$$\phi_n = \phi_{n-1} + \dot{\phi}_{n-1} T_L + \ddot{\phi}_{n-1} \frac{T_L^2}{2} \quad (31)$$

Referring to Fig. 2, we want to find the integrated phase error over one update period

$$\bar{\phi}_n = \left[ \int_{t_n - T_c}^{t_n} \phi(t) dt + \int_{t_n}^{t_n + T_R} \phi(t) dt \right] \quad (32)$$

The algebra in finding  $\bar{\phi}_n$  is straightforward but a little lengthy.

It can be shown that

$$\begin{aligned} \bar{\phi}_n = T_L \left( \phi_n + \frac{1}{2} T_L (1 - 2g) \dot{\phi}_n \right. \\ \left. + \frac{1}{6} T_L^2 (1 - 3g + 3g^2) \ddot{\phi}_n - \frac{T_L}{2} g^2 \Delta \hat{\theta}_n \right) \end{aligned} \quad (33)$$

where the normalized computation time  $g$  is defined by (30).

Using (33) together with (4), the normalized average phase error corresponding to Eq. (6) is

$$\begin{aligned} u_n &= \frac{2}{\pi T_L} \bar{\phi}_n \\ &= \left( \frac{2}{\pi T_L} \right) T_L \\ &\quad \times \left[ 1 - \frac{T_L}{2} (1 - 2g) - \frac{T_L^2}{6} (1 - 3g + 3g^2) - \frac{T_L}{2} g^2 \right] \begin{bmatrix} \phi_n \\ \dot{\phi}_n \\ \ddot{\phi}_n \\ \Delta \hat{\theta}_n \end{bmatrix} \end{aligned} \quad (34)$$

$$u_n = \left( \frac{2}{\pi T_L} \right) \bar{T}' \cdot \bar{\Phi}_n \quad (35)$$

where  $\bar{T}'$  is the row vector of (34) including the multiplication by  $T_L$ , and  $\bar{\Phi}_n$  is the rightmost column vector.

## V. Closed Loop Transfer Function

Combining Eqs. (21), (32) and (35), we get

$$\bar{\epsilon}_n = G'_Q \frac{2}{T_L \pi} \int_{t_n - T_c}^{t_n + T_R} \phi(t) dt \quad (36)$$

$$= G'_Q \frac{2}{T_L \pi} \bar{T}' \cdot \bar{\phi}_n \quad (37)$$

The  $z$ -transform of the output  $C_n$  of an integrate-and-dump device with gain  $G$  and continuous input  $R(t)$  is, according to Ref. 2,

$$C(z) = G \frac{z-1}{z} \left( \frac{R(s)}{s} \right)^* \quad (38)$$

where  $R(s)$  is the Laplace transform of  $R(t)$  and the asterisk denotes a  $z$ -transform. Letting

$$G_Q = G'_Q \frac{2}{T_L \pi} = \frac{KK_1 K_2 K_3 N_s^2 S}{T_L \pi} \quad (39)$$

then from (37) and (38), we obtain

$$\bar{\epsilon}(z) = G_Q \frac{z-1}{z} \left( \frac{\Phi(s)}{s} \right)^* \quad (40)$$

where  $\Phi(s)$  is the Laplace transform of  $\phi(t)$ .

The time delay between the instants in which the error signal  $\epsilon_n$  is read and the phase rate update  $\Delta \theta_n$  is produced, is modelled as

$$D(s) = e^{-gT_L s} \quad (41)$$

Equations (25), (27), (40) and (41) now can be combined to give the block diagram of Fig. 3, which is a hybrid Laplace  $z$ -transform equivalent representation of the subcarrier demodulation loop.

Referring to Fig. 3,

$$X(s) = \frac{\phi(s)}{s} = \frac{\theta(s)}{s} - \Delta\hat{\theta}(z) \frac{e^{-gT_L s}}{s^3} (1 - e^{-sT_L}) \frac{z}{z-1} \quad (42)$$

$$= \frac{\theta(s)}{s} - \Delta\hat{\theta}(z) \frac{e^{-gT_L s}}{s^3} \quad (43)$$

because  $e^{-sT_L} \triangleq z^{-1}$ .

Taking the z-transform on both sides of (43),

$$X(z) = \left( \frac{\phi(s)}{s} \right)^* = \left( \frac{\theta(s)}{s} \right)^* - \Delta\hat{\theta}(z) \left( \frac{e^{-gT_L s}}{s^3} \right)^* \quad (44)$$

In general, given a function  $L(s)$ , we always have

$$[e^{-gT_L s} L(s)]^* = L(z, m), \quad m = 1 - g \quad (45)$$

where  $L(z, m)$  is the modified z-transform of  $L(s)$ .

Using this property in (44),

$$X(z) = \left( \frac{\theta(s)}{s} \right)^* - \frac{T_L^2 [m^2 z^2 + (2m - 2m^2 + 1)z + (m - 1)^2]}{2(z - 1)^3} \Delta\hat{\theta}(z) \quad (46)$$

or

$$= \left( \frac{\theta(s)}{s} \right)^* - \frac{T_L^2 [(1 - g)^2 z^2 + (1 + 2g - 2g^2)z + g^2]}{2(z - 1)^3} \Delta\hat{\theta}(z) \quad (47)$$

Combining Eqs. (25), (40) and (47), the block diagram shown in Fig. 4 is obtained.

The open loop transfer function corresponding to Fig. 4 is

$$G(z) = \frac{\hat{\theta}_1(z)}{X(z)} = G \frac{((1 - g)^2 z^2 + (1 + 2g - 2g^2)z + g^2)(zA + B)}{(z - 1)^2 (z^2 - zC - D)} \quad (48)$$

where

$$G = \frac{T_L^2}{2} G_Q \quad (49)$$

The closed loop transfer function is

$$H(z) = \frac{\hat{\theta}_1(z)}{\theta_1(z)} = \frac{G(z)}{1 + G(z)} \quad (50)$$

$$H(z) = \frac{G((1 - g)^2 z^2 + (1 + 2g - 2g^2)z + g^2)(zA + B)}{z^4 + z^3 (GA(1 - g)^2 - C - 2) + z^2 (1 + 2C - D + GA(1 + 2g - 2g^2) + GB(1 - g)^2) + z(2D - C + GAg^2 + GB(1 + 2g - 2g^2)) - D + GBg^2} \quad (51)$$

The denominator of (51) is designated as the characteristic polynomial of the loop, which we define as  $C(z)$ .

## VI. Determination of Gains A, B, C and D

For stability, we want the poles of  $H(z)$  to be inside the unit circle. To avoid instability and oscillation problems when the gain  $G$  changes slightly for whatever reasons, we choose to place all four poles on the real axis such that

$$p_1 = p_2 = \text{small negative number}$$

and

$$p_3 = p_4 \text{ between } 0.3 \text{ and } 0.7. \quad (52)$$

As such, poles  $p_3$  and  $p_4$  will determine the transient response of the closed loop. Using (52), let

$$\begin{aligned} C(z) &= (z - p_1)^2 (z - p_3)^2 \\ &= z^4 + 2(-p_1 - p_3)z^3 + (p_3^2 + 4p_1p_3 + p_1^2)z^2 \\ &\quad + 2(-p_1p_3^2 - p_1^2p_3)z + p_1^2p_3^2 \end{aligned} \quad (53)$$

Equating the coefficients of equal powers in the polynomials of Eq. (53) and the denominator of (51), we obtain four equations with four unknowns which can be written in the following matrix form

$$\begin{bmatrix} G(1-g)^2 & 0 & -1 & 0 \\ G(1+2g-2g^2) & G(1-g)^2 & 2 & -1 \\ Gg^2 & G(1+2g-2g^2) & -1 & 2 \\ 0 & Gg^2 & 0 & -1 \end{bmatrix} \begin{bmatrix} A \\ B \\ C \\ D \end{bmatrix} = \begin{bmatrix} a_3 + 2 \\ a_2 - 1 \\ a_1 \\ a_0 \end{bmatrix} \quad (54)$$

where, from (53), we have

$$\begin{aligned} a_0 &= p_1^2 p_3^2 \\ a_1 &= -2(p_1 p_3^2 + p_1^2 p_3) \\ a_2 &= p_3^2 + 4p_1 p_3 + p_1^2 \\ a_3 &= -2(p_1 + p_3) \end{aligned} \quad (55)$$

Table 1 gives values for the gains  $A, B, C$  and  $D$  when  $G = 1.0$ ,  $p_1 = -0.1$ ,  $p_3 = 0.6$  and  $g = 0, 0.25$  and  $0.5$ .

The root locus diagrams for  $g = 0$  and  $g = 0.5$  for  $G$  changing between 0 (open loop) to 2 (unstable loop) are shown in Fig. 5. As we see from this figure, when nominal total loop gains  $GA, GB$  are selected, two pairs of poles at  $-0.1$  and two pairs of poles at  $0.6$  are obtained. In both cases ( $g = 0$  and  $g = 0.5$ ) the loop will lock without oscillations. The settling time,  $t_s$ , will be determined by  $p_3$  and  $p_4$  and will be, in our case,

$$t_s \approx \frac{4T_L}{-\ln p_3} = 7.8 \text{ seconds} \quad (56)$$

if  $T_L = 1$  second.

The Nyquist plot corresponding to the selected nominal gains for  $g = 0$  is shown in Fig. 6 and the Bode diagram in Fig. 7. For nominal loop gain, the

$$\begin{aligned} \text{Gain margin} &= -20 \log_{10} |G(z)| \Big|_{\substack{\cong 10 \text{ dB} \\ |G(z)| = 180^\circ}} \end{aligned} \quad (57)$$

and

$$\begin{aligned} \text{Phase margin} &= 180 - \angle G(z) \Big|_{\substack{\cong 50 \text{ deg} \\ |G(z)| = 0 \text{ dB}}} \end{aligned} \quad (58)$$

To doublecheck the stability of our loop, let

$$C'(z) = a_4 z^4 + a_3 z^3 + a_2 z^2 + a_1 z + a_0 \quad (59)$$

be the polynomial of the denominator of the closed loop transfer function  $H(z)$  given by (51). The Jury stability test (Ref. 3) requires that the following conditions be met:

- (1)  $C'(1) > 0$
- (2)  $C'(-1) > 0$
- (3)  $|a_0| < a_4 = 1$
- (4)  $|b_0| > |b_3|$
- (5)  $|C_0| > |C_2|$

where

$$b_k = \begin{vmatrix} a_0 & a_{4-k} \\ a_4 & a_k \end{vmatrix} \quad (61)$$

$$C_k = \begin{vmatrix} b_0 & b_{3-k} \\ b_3 & b_k \end{vmatrix}$$

Using the nominal gain values of Table 1 to compute  $a_0, a_1, a_2, a_3$ , and  $a_4$ , it is straightforward to show that these conditions are met.

## VII. Steady State Error

For a parabolic input

$$\theta(t) = \ddot{\theta}_p t^2, \quad (62)$$

the  $z$ -transform of the equivalent input in Fig. 4 is

$$\theta_1(z) = \left( \frac{\theta(s)}{s} \right)^* = \frac{\ddot{\theta}_p T_L^3 z(z^2 + 4z + 1)}{6(z-1)^4} \quad (63)$$

Our transfer function now is defined as

$$H_e(z) = \frac{\epsilon(z)}{\theta_1(z)} \quad (64)$$

From Fig. 4,  $H_e(z)$  is

$$H_e(z) = \frac{z-1}{z} \times \frac{G_Q}{1 + \frac{G_Q((1-g)^2 z^2 + (1+2g-2g^2)z + g^2)(zA+B)}{(z-1)^2(z^2 - zC - D)}} \quad (65)$$

The steady state error is defined as

$$\begin{aligned} \bar{\epsilon}_{ss} &= \lim_{n \rightarrow \infty} \bar{\epsilon}_n \\ &= \lim_{z \rightarrow 1} \left( \frac{z-1}{z} \right) H_e(z) \theta_1(z) \end{aligned} \quad (66)$$

Inserting (63) and (65) into (66) and letting  $z$  go to one, the steady state error signal at sampling instants due to a parabolic input is

$$\bar{\epsilon}_{ss} = \frac{\ddot{\theta}_p T_L (1-C-D)}{(A+B)} \quad (67)$$

Equation (67) says that our subcarrier demodulation loop can track a parabolic input with a finite steady state error which is independent of the normalized computation time,  $g$ .

### VIII. Derivation of the State and Output Equations

Using (33) in (37), the error signal evaluated at sample time  $n-1$  is

$$\begin{aligned} \epsilon_{n-1} &= G_Q \left( T_L \phi_{n-1} + \frac{1}{2} T_L^2 (1-2g) \dot{\phi}_{n-1} \right. \\ &\quad \left. + \frac{1}{2} T_L^3 \left( \frac{1}{3} - g + g^2 \right) \ddot{\phi}_n - \frac{T_L^2}{2} g^2 \Delta \hat{\theta}_{n-1} \right) + \eta_{n-1} \end{aligned} \quad (68)$$

The error signal at time  $n-2$  can be expressed in terms of its value at time  $n-1$ , namely,

$$\begin{aligned} \epsilon_{n-2} &= G_Q \left( T_L \phi_{n-1} - \frac{1}{2} T_L^2 (1+2g) \dot{\phi}_{n-1} \right. \\ &\quad \left. + \frac{T_L^3}{2} \left( \frac{1}{3} + g + g^2 \right) \ddot{\phi}_n - \frac{T_L^2}{2} (1+2g) \Delta \hat{\theta}_{n-1} \right. \\ &\quad \left. - \frac{T_L^2}{2} g^2 \Delta \hat{\theta}_{n-2} \right) + \eta_{n-2} \end{aligned} \quad (69)$$

Inserting (68) and (69) into (23) and combining terms gives

$$\begin{aligned} \Delta \hat{\theta}_n &= G_Q T_L (A+B) \phi_{n-1} \\ &\quad + \frac{G_Q T_L^2}{2} [A(1-2g) - B(1+2g)] \dot{\phi}_{n-1} \\ &\quad + \frac{T_L^3}{2} G_Q \left[ A \left( \frac{1}{3} - g + g^2 \right) - B \left( \frac{1}{3} + g + g^2 \right) \right] \ddot{\phi}_n \\ &\quad + \left[ C - G_Q \frac{T_L^2}{2} (Ag^2 + B(1+2g)) \right] \Delta \hat{\theta}_{n-1} \\ &\quad + \left( D - \frac{G_Q}{2} T_L^2 g^2 B \right) \Delta \hat{\theta}_{n-2} + A\eta_{n-1} + B\eta_{n-2} \end{aligned} \quad (70)$$

Let

$$X = G_Q T_L (A+B)$$

$$V = G_Q \frac{T_L^2}{2} [A(1-2g) - B(1+2g)]$$

$$Y = C - G_Q \frac{T_L^2}{2} [Ag^2 + B(1+2g)]$$

$$W = \frac{T_L^3}{2} G_Q \left[ A \left( \frac{1}{3} - g + g^2 \right) - B \left( \frac{1}{3} + g + g^2 \right) \right]$$

$$U = D - \frac{G_Q T_L^2}{2} g^2 B \quad (71)$$

Then, Eq. (70) can be rewritten as

$$\begin{aligned}\hat{\Delta\theta}_n &= X\phi_{n-1} + V\dot{\phi}_{n-1} + W\ddot{\phi}_{n-1} \\ &+ Y\hat{\Delta\theta}_{n-1} + U\hat{\Delta\theta}_{n-2} + A\eta_{n-1} + B\eta_{n-2}\end{aligned}\quad (72)$$

Referring to Fig. 3, we have

$$x_2(k+1) = x_1(k)$$

or

$$\hat{\Delta\theta}_{n-2+1} = \hat{\Delta\theta}_{n-1}\quad (73)$$

Inserting (72) into (28) gives

$$\begin{aligned}\dot{\phi}_n &= -X\phi_{n-1} - Y\hat{\Delta\theta}_{n-1} - U\hat{\Delta\theta}_{n-2} + (1-V)\dot{\phi}_{n-1} \\ &+ (T_L - W)\ddot{\phi}_{n-1} - A\eta_{n-1} - B\eta_{n-2}\end{aligned}\quad (74)$$

Combining Eqs. (31), (74), (72) and (73) in matrix form, we obtain the State Equation:

$$\begin{pmatrix} \phi_n \\ \dot{\phi}_n \\ \hat{\Delta\theta}_n \\ \hat{\Delta\theta}_{n-1} \end{pmatrix} = \begin{pmatrix} 1 & T_L & 0 & 0 \\ -X & 1-V & -Y & -U \\ X & V & Y & U \\ 0 & 0 & 1 & 0 \end{pmatrix} \begin{pmatrix} \phi_{n-1} \\ \dot{\phi}_{n-1} \\ \hat{\Delta\theta}_{n-1} \\ \hat{\Delta\theta}_{n-2} \end{pmatrix} + \begin{pmatrix} T_L^2/2 & 0 & 0 & 0 \\ T_L - W & -A & -B & 0 \\ W & A & B & 0 \\ 0 & 0 & 0 & 0 \end{pmatrix} \begin{pmatrix} \ddot{\phi}_{n-1} \\ \eta_{n-1} \\ \eta_{n-2} \\ 0 \end{pmatrix}\quad (75)$$

which is of the form

$$x(k+1) = Ax(k) + Bu(k)\quad (76)$$

The Output Equation is (rewriting (68) in vector form):

$$\begin{aligned}\epsilon_n &= G_Q \begin{pmatrix} T_L & \frac{1}{2}T_L^2(1-2g) & -\frac{T_L^2}{2}g & 0 \end{pmatrix} \begin{pmatrix} \phi_n \\ \dot{\phi}_n \\ \hat{\Delta\theta}_n \\ \hat{\Delta\theta}_{n-1} \end{pmatrix} \\ &+ \begin{pmatrix} G_Q & \frac{T_L^3}{2}(\frac{1}{3}-g+g^2) & 1 & 0 & 0 \end{pmatrix} \begin{pmatrix} \ddot{\phi}_n \\ \eta_n \\ \eta_{n-1} \\ 0 \end{pmatrix}\end{aligned}\quad (77)$$

which is of the form

$$\epsilon(k) = \bar{D}x(k) + \bar{E}u(k)\quad (78)$$

The characteristics polynomial  $C(z)$  is

$$C(z) = \det(zI - A)\quad (79)$$

where  $A$  is the matrix defined in (76). Inserting  $A$  into (79), we obtain

$$\begin{aligned}C(z) &= \det \begin{bmatrix} z-1 & -T_L & 0 & 0 \\ X & z-V-1 & Y & U \\ -X & -V & z-Y & -U \\ 0 & 0 & -1 & z \end{bmatrix} \\ &= z^4 + z^3(V-Y-2) + z^2(2Y-V-U+1+T_LX) \\ &\quad + z(2U-Y) - U\end{aligned}\quad (80)$$

Using the definitions of (71), we obtain

$$\begin{aligned}C(z) &= z^4 + [GA(1-g)^2 - 2 - C]z^3 \\ &\quad + [2C - D + 1 + GA(1+2g-2g^2) + GB(1-g)^2]z^2 \\ &\quad + [2D - C + GA g^2 + GB(1+2g-2g^2)]z - D + GB g^2\end{aligned}\quad (81)$$

Comparing (81) to the denominator of  $H(z)$  in Eq. (51), we see that both polynomials are identical, as they should be.

The state equation given by (75) will be needed to derive the steady state values of  $\phi$ ,  $\dot{\phi}$  and  $\Delta\theta$ .

## IX. Noise-Equivalent Bandwidth

Referring to Fig. 4, the closed loop transfer function  $H(z)$  is given by Eq. (51). The one-sided noise-equivalent bandwidth is defined as

$$B_L = \frac{1}{2T_L} \frac{1}{H^2(1)} \frac{1}{2\pi j} \oint H(z) H(z^{-1}) \frac{dz}{z} \quad (82)$$

It can be shown that

$$H^2(1) \equiv 1 \quad (83)$$

for all values of  $A, B, C, D, g$  and  $G$ .

To evaluate (82), we express  $H(z)$  of (51) as a ratio of polynomials,

$$H(z) = \frac{b_0 z^4 + b_1 z^3 + b_2 z^2 + b_3 z + b_4}{a_0 z^4 + a_1 z^3 + a_2 z^2 + a_3 z + a_4} \quad (84)$$

and then make use of the results in Table III.4 of Ref. 3.

If we define

$$I_4 = \frac{1}{2\pi j} \oint H(z) H(z^{-1}) \frac{dz}{z} \quad (85)$$

then, from Ref. 4 we have

$$I_4 = \frac{a_0 B_0 Q_0 - a_0 B_1 Q_1 + a_0 B_2 Q_2 - a_0 B_3 Q_3 + B_4 Q_4}{a_0 [(a_0^2 - a_4^2) Q_0 - (a_0 a_1 - a_3 a_4) Q_1 + (a_0 a_2 - a_2 a_4) Q_2 - (a_0 a_3 - a_1 a_4) Q_3]} \dots \quad (86)$$

where

$$B_0 = b_0^2 + b_1^2 + b_2^2 + b_3^2 + b_4^2$$

$$B_1 = 2(b_0 b_1 + b_1 b_2 + b_2 b_3 + b_3 b_4)$$

$$B_2 = 2(b_0 b_2 + b_1 b_3 + b_2 b_4)$$

$$B_3 = 2(b_0 b_3 + b_1 b_4)$$

$$B_4 = 2b_0 b_4$$

$$Q_0 = a_0 e_1 e_4 - a_0 a_3 e_2 + a_4 (a_1 e_4 - e_3 e_4)$$

$$Q_1 = a_0 a_1 e_4 - a_0 a_2 a_3 + a_4 (a_1 a_2 - a_3 e_4)$$

$$Q_2 = a_0 a_1 e_2 - a_0 a_2 e_1 + a_4 (a_2 e_3 - a_3 e_2)$$

$$Q_3 = a_1 (a_1 e_2 - e_3 e_4) - a_2 (a_1 e_1 - a_3 e_3) + a_3 (e_1 e_4 - a_3 e_2)$$

$$Q_4 = a_0 [e_2 (a_1 a_4 - a_0 a_3) + e_5 (a_0^2 - a_4^2)]$$

$$+ (e_2^2 - e_5^2) [a_1 (a_1 - a_3) + (a_0 - a_4) (e_4 - a_2)]$$

$$e_1 = a_0 + a_2$$

$$e_2 = a_1 + a_3$$

$$e_3 = a_2 + a_4$$

$$e_4 = a_0 + a_4$$

$$e_5 = a_0 + a_2 + a_4 \quad (87)$$

Using the above results, the one-sided noise-equivalent bandwidths for given values of  $g, A, B, C, D$  and  $G$  are listed in Table 2.

## X. Conclusion

The BBA's subcarrier demodulation digital loop, a fourth-order Costas-type loop, has been analyzed in this article. The mean value and variance of the error signal have been found. A block diagram in the  $z$ -domain has been obtained from which optimum gains of the loop filter have been found. These gains will keep the four poles of the transfer function on the real axis inside the unit circle. The loop is able to track a parabolic input with finite steady state error, as it is a type-2 analog loop. One-sided noise-equivalent bandwidths for given values of normalized computation time and gain values have been given.



## References

1. "DSN/Flight Project Interface Design Handbook," JPL 810-5, Rev. D, Volume II, Module TLM-10, p. 4.
2. Winkelstein, R. A., "Analysis of the Signal Combiner for Multiple Antenna Arraying," Deep Space Network Progress Report 42-26, January and February 1975, pp. 102-118.
3. Jury, E. I., "Theory and Applications of the Z-Transform Method," R. E. Krieger Publishing Co., Malabar, Florida, 1982.

**Table 1. Loop gains for given pole locations<sup>a</sup>**

Filter Gains	Computation Time Factor		
	$g = 0.0$	$g = 0.25$	$g = 0.5$
<i>A</i>	0.5248	0.5390	0.5632
<i>B</i>	-0.4180	-0.4422	-0.4664
<i>C</i>	-0.4852	-0.6968	-0.8592
<i>D</i>	-0.0036	-0.0312	-0.1202

<sup>a</sup> $p_1 = p_2 = -0.1.$   $p_3 = p_4 = 0.6.$   $G = 1.0.$

**Table 2. Noise-equivalent one-sided bandwidth in Hz for gains *A*, *B*, *C* and *D* given in Table 1**

Gain <i>G</i>	Computation Time Factor		
	$g = 0.0$	$g = 0.25$	$g = 0.5$
1.0	0.3324	0.3858	0.4395
0.5	0.1696	0.1744	0.1814
0.1	0.0792	0.0768	0.0748
0.01	0.0620	0.0604	0.0589
0.001	0.0603	0.0588	0.0573

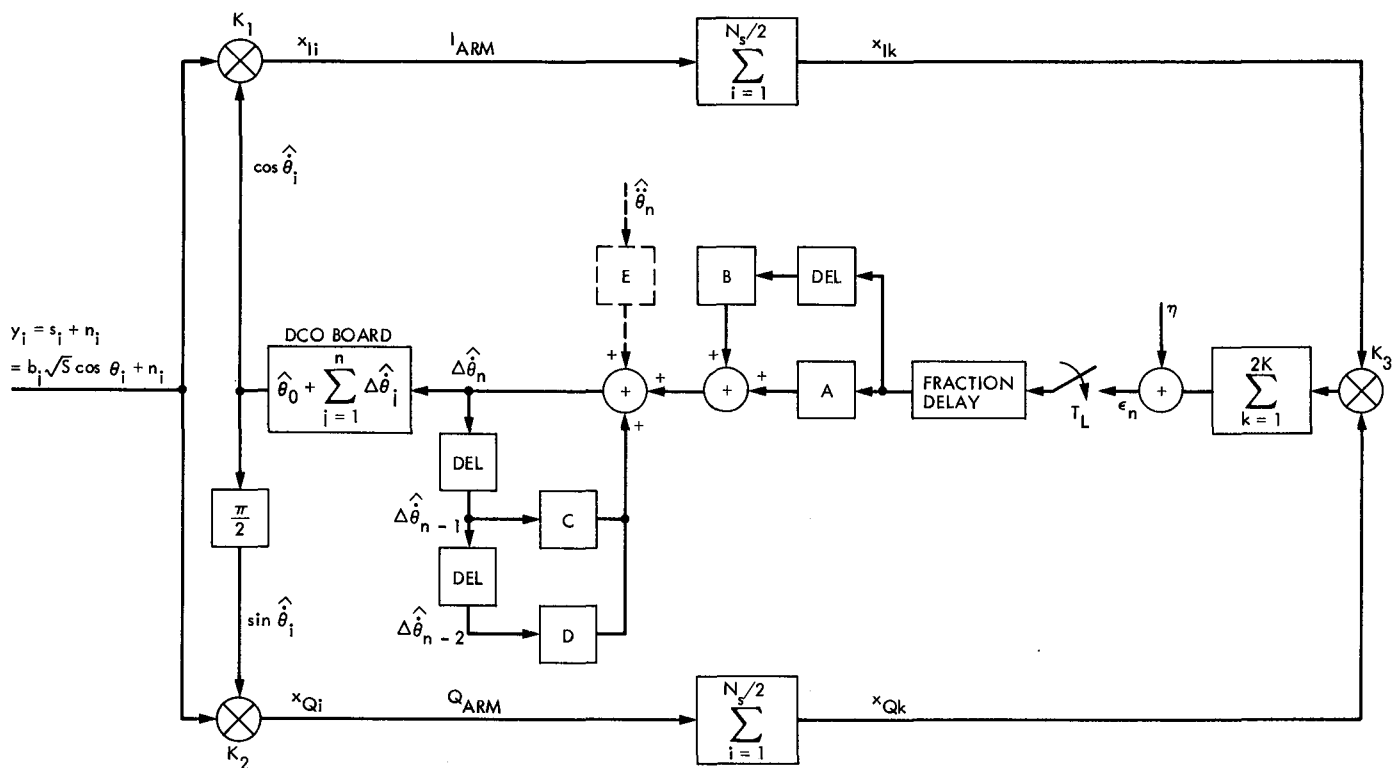


Fig. 1. Subcarrier demodulation loop

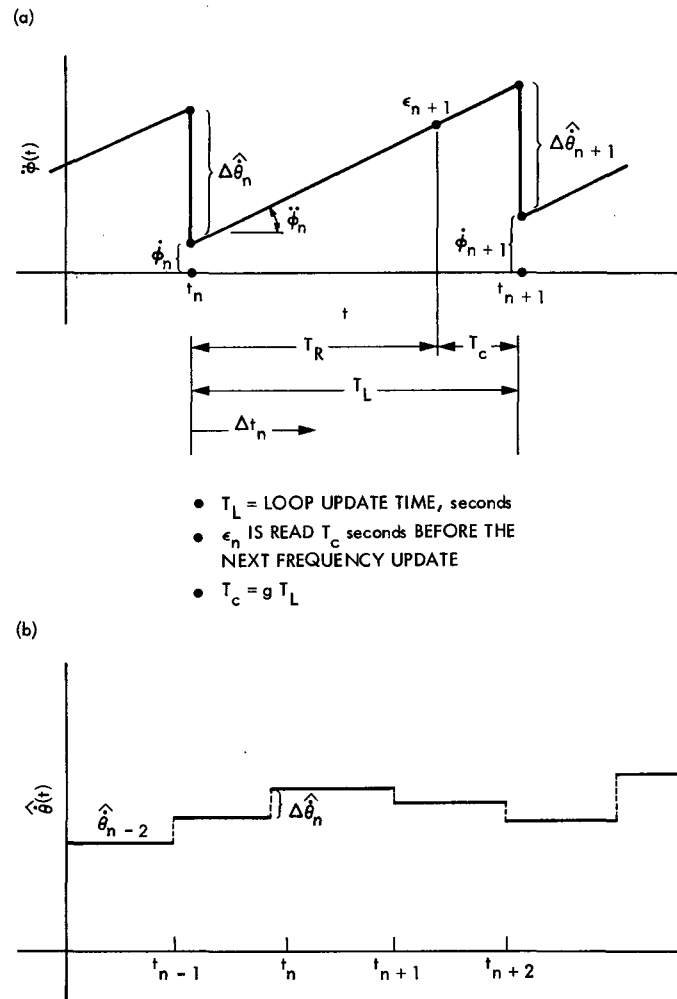


Fig. 2. Phase rate (a) error, and (b) DCO output

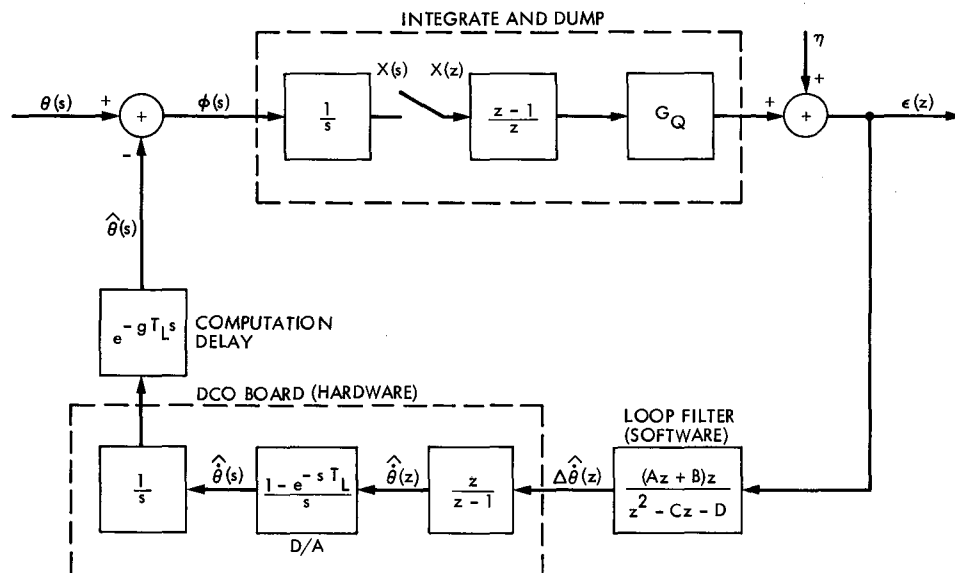


Fig. 3. Closed loop hybrid s/z diagram. Note that a conventional DCO does not include the  $z/(z-1)$  transfer function as shown here as an integral part of the DCO board.

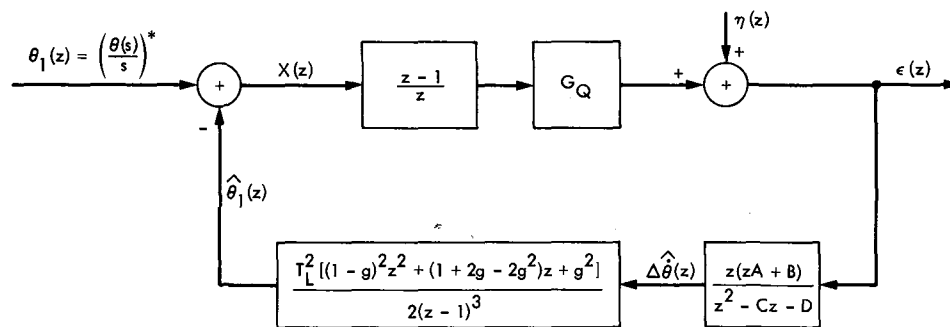


Fig. 4. Equivalent z-domain block diagram

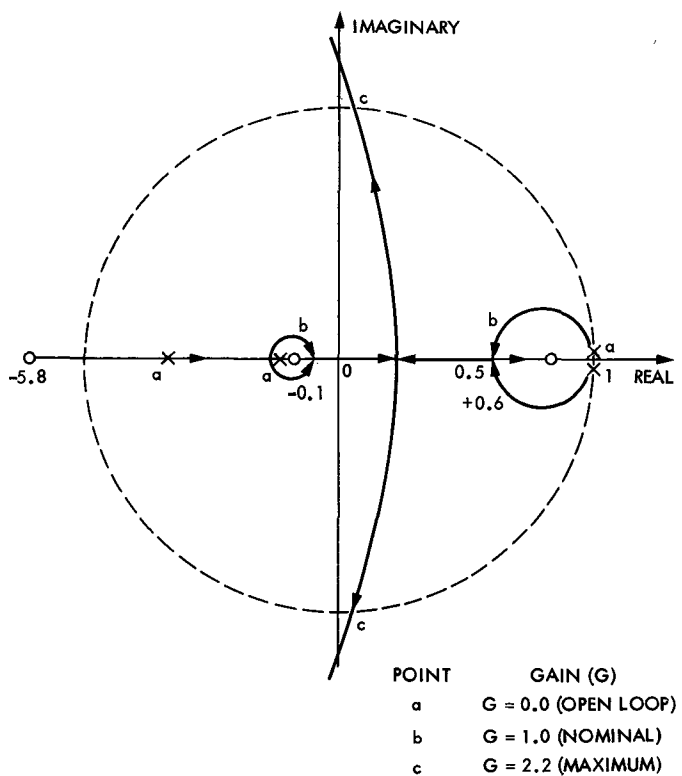
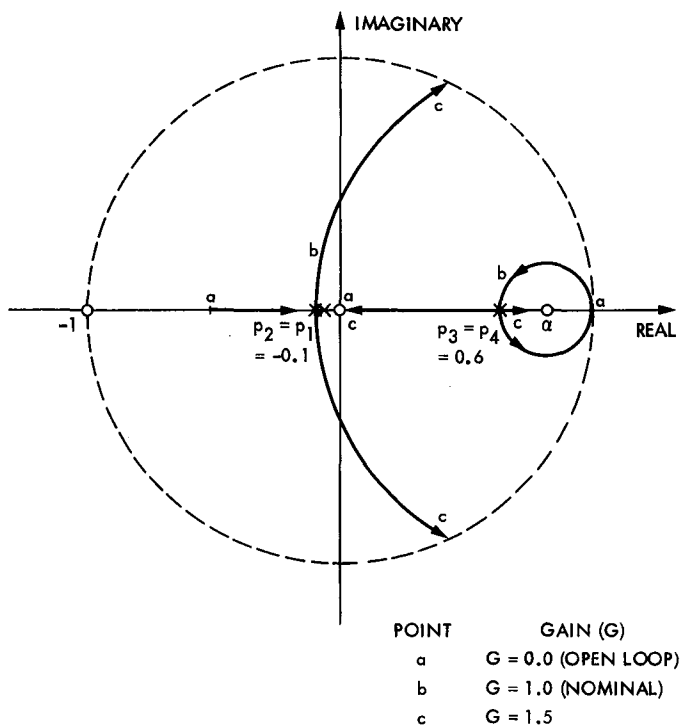


Fig. 5. Root locus diagram for (a)  $g = 0.0$ , and (b)  $g = 0.5$

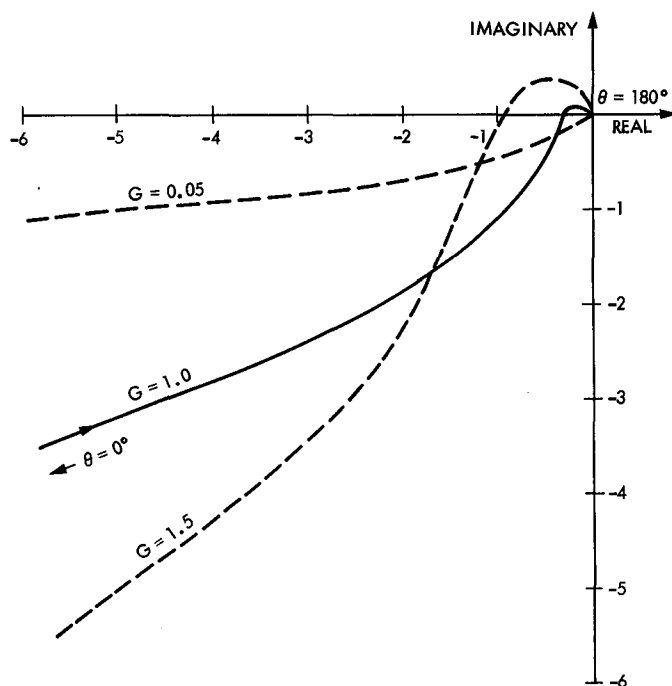


Fig. 6. Frequency response loci of  $G(z)$  for a sample frequency of  $\omega_s = 2/T_L$  and  $g = 0.0$

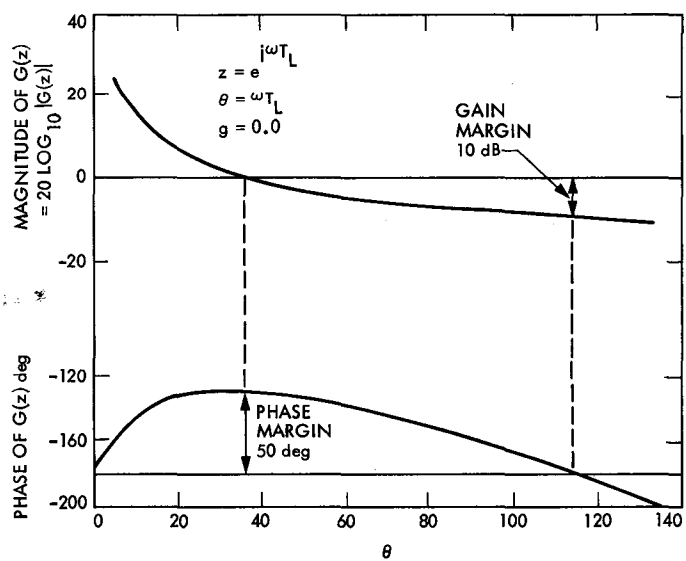


Fig. 7. Bode diagram of  $G(z)$  for nominal gains

# The Venus Balloon Project

R. A. Preston and J. H. Wilcher  
Tracking Systems and Applications Section

C. T. Stelzried  
TDA Mission Support and DSN Operations Office

*During the Soviet Vega Mission to Venus and Comet Halley, two instrumented balloons will be placed into the Venusian atmosphere in June 1985. These Soviet/French balloons will be used to study the structure and dynamics of the Venusian atmosphere by means of in situ measurements and earth-based VLBI determination of balloon position and velocity. The DSN 64-meter subnet will be part of an international network of antennas organized by the French to support this mission. The DSN is installing new L-band receiving systems for this task. All scientific data from the balloons will be analyzed by a joint Soviet/French/U.S. science team.*

## I. Introduction

Two Soviet spacecraft were launched in December 1984, and will arrive in the vicinity of Venus in mid-June 1985. Upon arrival, each spacecraft bus will release an entry module containing both a lander and a balloon, then continue on to Comet Halley. Each balloon and associated gondola will drift along the Venusian equator at an altitude of about 55 km for a lifetime of 24 to 60 hours. Since the Venus encounters are separated by about four days, the balloons will not transmit simultaneously. L-band (1668 Mhz) downlinks from the balloon and spacecraft bus will provide three types of information:

- (1) Spacecraft bus trajectory from delta differential one-way ranging ( $\Delta$ DOR) and one-way doppler data taken by the NASA Deep Space Network (DSN).
- (2) Balloon position and velocity obtained from  $\Delta$ VLBI measurements between the spacecraft bus and balloon taken by an international network of ground antennas.
- (3) Venusian in situ atmospheric data from the balloon telemetry data.

The balloon experiment is a cooperative French/Soviet venture. The French space agency, CNES, is responsible for organizing an international network of about a dozen antennas to track the balloons and flyby spacecraft bus. The DSN plays a key role in this international network. The Soviets will also provide more limited tracking with an internal Soviet network. All data will be analyzed by the joint Soviet/French/U.S. science team.

## II. The Balloon Experiment

The purpose of the balloons is to study the structure and dynamics of the Venusian atmosphere. The Pioneer Venus probes and previous Soviet missions have obtained nearly instantaneous vertical profiles of physical characteristics of the Venusian atmosphere. The balloons will provide an extended

temporal history of the atmospheric parameters at a nearly constant altitude. The combination of in situ measurements from the balloon gondola and earth-based VLBI determination of the Venusian winds (i.e., balloon velocity) will allow a study of the transport of momentum and heat in the atmosphere by means of eddy motions. Cloud characteristics will also be studied.

Figure 1 shows the path of the balloons across the face of Venus as viewed from the earth. At the time of encounter, the Sun-Venus-Earth angle is about 90 degrees, causing the terminator to appear near the center of the visible hemisphere. The balloons will be injected into the Venusian atmosphere near the equator and at almost Venusian midnight, just visible on the limb as seen from Earth. The balloons will drift across the equator during their 24 to 60 hour lifetimes, reaching the terminator after about 40 hours.

The configuration of the balloon and gondola are shown in Fig. 2. The small, 1.5-meter-high gondola is suspended 15 meters below the 3.4-meter-diameter, helium-filled, pressurized balloon. The gondola contains sensors to measure pressure, temperature, vertical wind velocity, cloud density, and the frequency of lightning flashes. On the top of the gondola is a helical L-band antenna for one-way transmission of the sensor telemetry as well as VLBI tones. The onboard frequency and timing reference for the transmissions is a temperature-controlled crystal oscillator (ultra-stable oscillator).

### III. Concept of VLBI Determination of Balloon Position and Velocity

At least three antennas must simultaneously observe the balloon and flyby spacecraft to determine a complete set of three-dimensional position and velocity components relative to Venus. Utilizing the technique of VLBI, transverse velocity information is provided by measurements of the differential received RF frequency of the balloon signals at widely separated antennas. This is essentially the same method as that used in the Pioneer Venus Wind Experiment. The transverse position is obtained by using bandwidth synthesis to effectively yield observations of the balloon differential range.

Simultaneous observations of the balloon and flyby spacecraft are algebraically differenced to cancel common errors, such as those resulting from unknown station clock offsets, baseline uncertainties, and troposphere and ionosphere delays. Knowledge of the flyby trajectory is used to tie the balloon position and velocity to a Venus-centered reference frame. The trajectory will be determined by VLBI measurements at L-band taken over a 2-week period around the time of balloon insertion into the Venusian atmosphere. For flyby orbit determination, cancellation of observation errors will be

achieved by differencing the spacecraft measurements with those acquired on an angularly nearby natural radio source ( $\Delta$ DOR).

To obtain measurements of the line-of-sight balloon position and velocity, VLBI data from the balloon will be augmented by one-way Doppler data extracted from the VLBI recording at a single antenna, and by estimates of altitude and altitude rates obtained from in situ measurements of pressure. The line-of-sight velocity is provided by the one-way Doppler data (not differenced with flyby), which is dependent on knowledge of the balloon reference oscillator frequency. A calibration of this reference frequency will be based on balloon altitude rate information. The altitude is required to provide line-of-sight position, which is not sensed by VLBI.

Because of the low power of the balloon signal, and the frequency instabilities introduced by the balloon reference oscillator and by the erratic balloon motion, continuous coverage by sensitive, 64-meter DSN antennas will be required to detect the signal phase with integration times shorter than the coherence time of the balloon signal. Using models based on the phase observed at the 64-meter antennas, the data from the less sensitive antennas of the international French network can be processed with longer integration times to achieve adequate SNR.

### IV. L-Band Transmissions

The spectra of balloon and spacecraft bus one-way L-band transmissions are essentially identical. The spectra consist of sequenced pure carrier, telemetry, or VLBI tones. The L-band carrier is transmitted at a frequency of  $1667.92 \pm 0.01$  Mhz. The telemetry is transmitted on subcarriers of 254.5 Hz at a rate of 1 or 4 bits/second. The spacecraft bus transmits dummy telemetry for testing purposes. The carrier signal is used for the VLBI determination of balloon velocity relative to the flyby. The spacecraft bus transmits continuously during the lifetime of the associated balloon, but the balloon transmits at most 11 minutes out of every hour in order to conserve its batteries. During some of the balloon transmissions, the only signals emitted are two sideband tones spaced at  $\pm 3.25$  Mhz from the highly suppressed carrier. These tones are used in the bandwidth synthesis VLBI determination of balloon position relative to the flyby spacecraft and for the  $\Delta$ DOR determination of the flyby spacecraft orbit with respect to Venus.

Two days prior to Venus encounter the Soviets can predict the timing of the balloon transmissions to within 1 or 2 minutes and will set the phasing of the flyby spacecraft transmissions so that the flyby and balloon signals always display a similar spectra. The flyby and balloon L-band transmitters are



identical in design. The radiated power is about 4.5 watts with left-hand circular polarization. The antenna gain for the spacecraft bus is about 9, while that of the balloon ranges from 0.4 to 1. The maximum balloon antenna gain is achieved when the balloon is near the center of the Venusian disk as viewed from Earth.

The Soviets will be in two-way communication with the spacecraft bus at their new space communication frequency of 6 GHz. Each spacecraft bus will be commanded to turn the L-band transmitter on for short periods during the cruise phase to Venus for network testing and training.

## **V. DSN Involvement**

### **A. DSN Tracking Requirements**

The major implementation requirements of the DSN for the Venus Balloon Project are as follows:

- (1) Modify the 64-m antenna subnet for receiving the RF carrier and VLBI tone signals in the 1668 MHz (L-band) range and subsequent upconversion to S-band.
- (2) Modify the VLBI Block 0 subsystem to be compatible with the wide frequency separation of the Venus balloon project VLBI tones.

The major operational requirements for the DSN are as follows:

- (1) Receive the following L-band data from the two spacecraft bus/balloon pairs:
  - (a) Doppler data from the spacecraft bus.
  - (b)  $\Delta$ DOR data from the spacecraft bus and an angularly nearby quasar (Block 1 recording system).
  - (c) Telemetry data from the balloon (radio science recording system).
  - (d)  $\Delta$ VLBI data from a balloon/flyby pair (Block 0 recording system).
- (2) Provide near real-time demodulation/decoding of the telemetry spectrum for operational verification purposes.

### **B. DSN Signal Paths**

The L-band 1668 MHz configuration will contain an L-band microwave feed-horn subsystem mounted to the 64-m antennas at DSS 14, DSS 43, and DSS 63 (Fig. 3). Another subsystem will contain a low-noise amplifier (LNA) and frequency

upconverter to convert the L-band spectrum to a DSN-compatible S-band spectrum for inputting the signal into the S-band microwave subsystem (see Fig. 4).

The S-band microwave subsystem will deliver the signal to the existing DSCC VLBI, radio science, and doppler tracking system receivers. The doppler tracking system will use the Block IV closed-loop receiver-exciter subsystem to obtain one-way doppler data.

The radio science receiver will downconvert the S-band spectrum to an intermediate frequency (IF) spectrum centered about 300 MHz. The 300 MHz IF signal will be power-divided at the DSCC Signal Processing Center (SPC) to provide signals to existing DSCC VLBI (Block 0 and Block 1) and radio science subsystems.

Both the VLBI Block I and radio science subsystems will be capable of acquiring VLBI and telemetry data directly without hardware modification to their assemblies. The VLBI Block 0 subsystem will require minor modification of the IF-video downconversion stage to allow the received tones, which are spread over a 6.5-MHz bandwidth, to be compressed into the 2-MHz bandwidth of the Block 0 subsystem. Near real-time demodulation/decoding of the telemetry spectrum for operational verification purposes will be provided.

### **C. Balloon Telemetry**

Telemetry data are required to be provided to the project in the form of non-real-time detected, demodulated, and decoded telemetry streams recorded on computer-compatible magnetic tape. While the balloons are in the Venusian atmosphere, the DSN will record (in open-loop mode) the telemetry spectrum, including the carrier and the data-modulated subcarrier. At the conclusion of each balloon telemetry transmission, the participating DSN station will detect the carrier for selected portions of the transmission to obtain an SNR measurement of the received spacecraft signal. The recorded spectrum will then undergo carrier detection, demodulation, and decoding at the DSN station or at JPL. Both the original recorded spectrum data and the decoded data will be sent to the project.

### **D. VLBI Determination of Flyby Orbit**

The DSN will determine the trajectories of both the Vega 1 and 2 spacecraft during the Venus flyby phase. To establish the flyby trajectories, DSN L-band one-way doppler and  $\Delta$ DOR will be acquired from encounter (E) -10 days to E + 8 days. The  $\Delta$ DOR data require identification of sufficiently strong (greater than 0.5 Jy) L-band Extra-Galactic Radio Sources (EGRS) in the vicinity of the Vega spacecraft trajectories. Such sources are needed for both the cruise phase and the Venus encounter phase. Candidate L-band radio

sources will be selected from the DSN EGRS S-band source catalog. Source strengths for the candidate S-band sources at L-band will be validated by scheduling observing sessions from February through May 1985. Also during this cruise phase,  $\Delta$ DOR and doppler data acquisition is required for test and training, and navigation data validation.

### **E. Balloon/Flyby VLBI**

As part of the international network, the DSN 64-meter stations will provide coverage for the acquisition of VLBI data. The DSN 64-m stations will provide VLBI data from each balloon/spacecraft bus pair while the two are in the same antenna beam (a period of approximately two days near each Venus encounter). During balloon transmission, the DSN will

record the L-band spectra of the balloon and the spacecraft bus simultaneously. During cruise, VLBI data will also be acquired for network testing and calibration.

The DSN will also provide the following VLBI processing capabilities for these data:

- (1) "Local model" correlation of Block 0 VLBI recordings of spacecraft signals.
- (2) Cross-correlation of single-channel quasar VLBI data in Block 0 formats.
- (3) Post-correlation processing of single-channel quasar VLBI data to yield the clock offset and received phase.

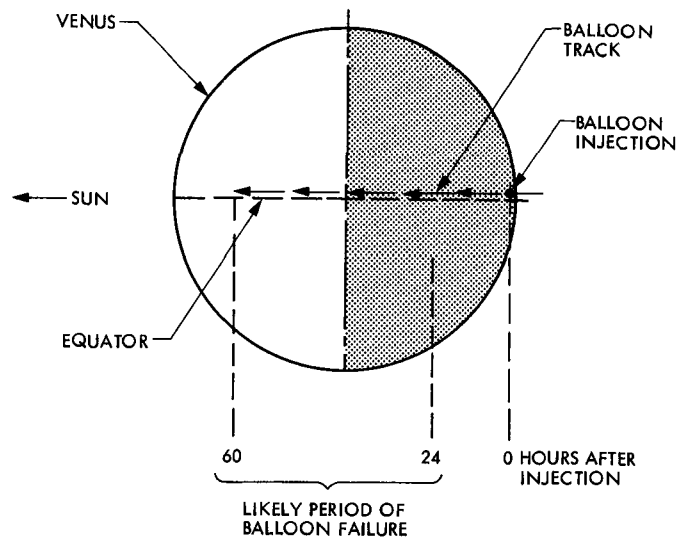


**Fig. 1. Balloon path as viewed from Earth**

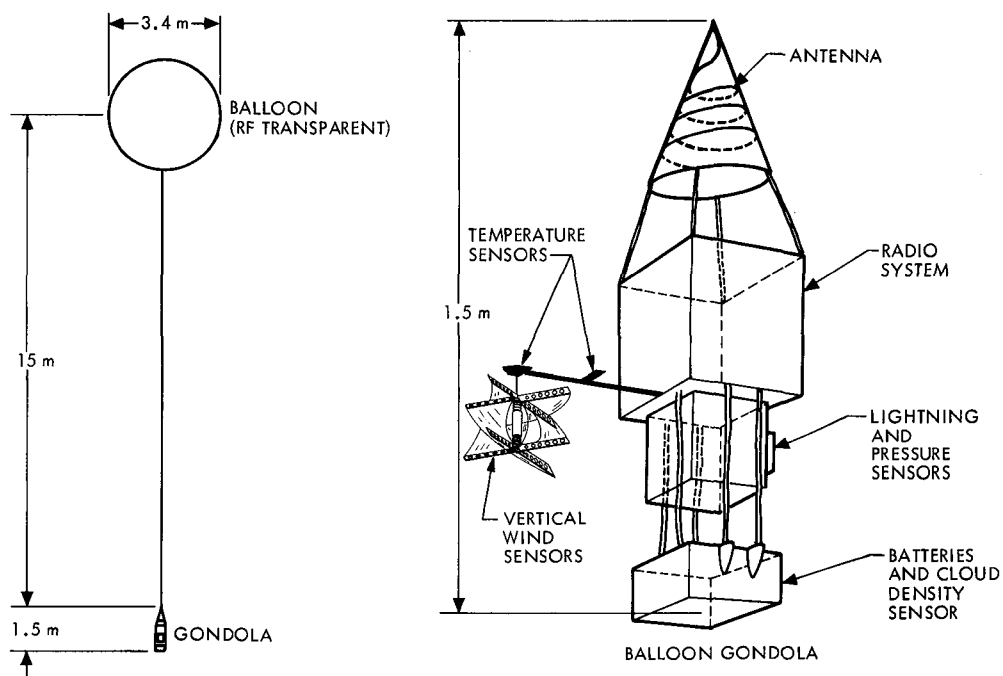


**Fig. 2. Configuration of balloon and gondola**

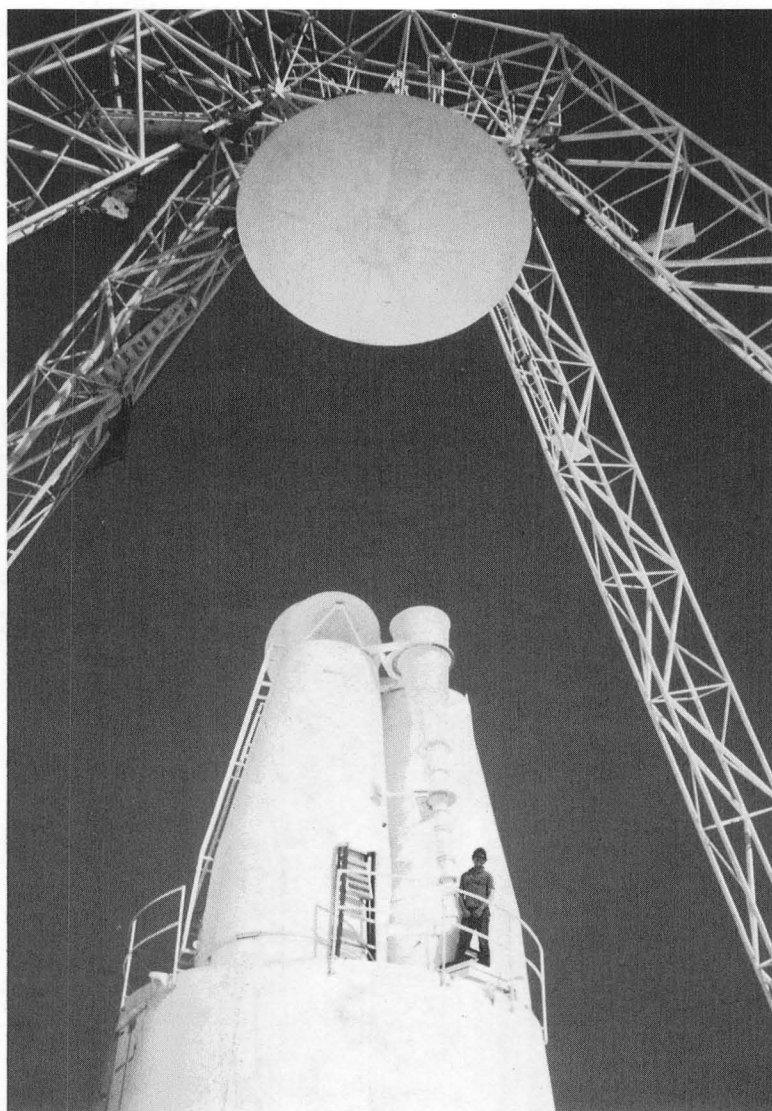


**Fig. 3. L-band feed installed on the Goldstone DSCC 64-m antenna**

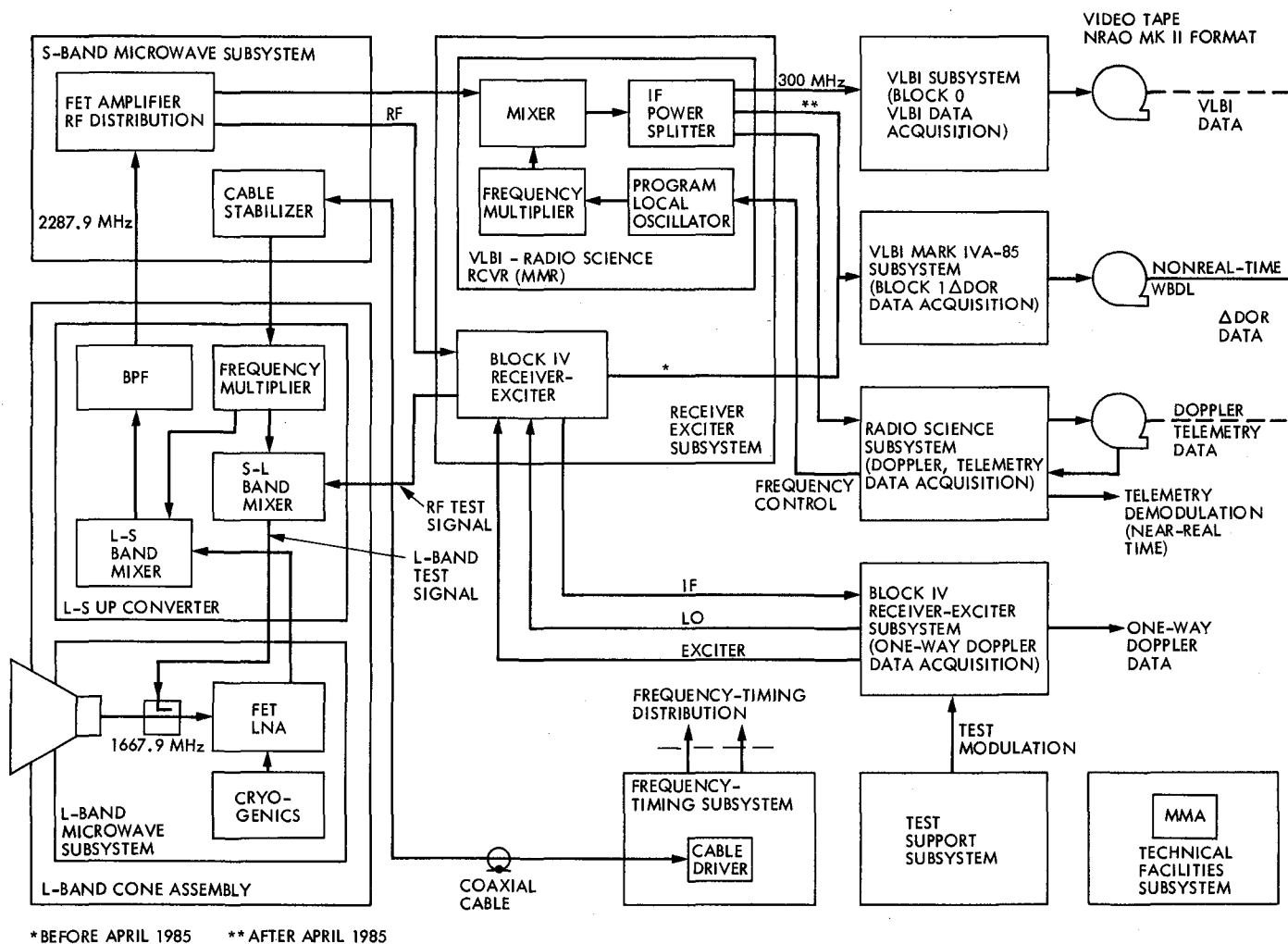


Fig. 4. DSN L-band implementation configuration

# DSN 34-Meter Antenna Optics Analysis for Wideband SETI Investigations

S. D. Slobin

Radio Frequency and Microwave Subsystems Section

*A DSN 34-meter symmetric Cassegrain antenna configuration is examined for wide-band use over the frequency range of 1 to 10 GHz, rather than only at the narrow-band operational design frequencies of 2.295 GHz (S-band) and 8.448 GHz (X-band). Aperture efficiency and surface efficiency are calculated as the components determining the gain of the antenna. Noise temperature contributions arise from the ground, atmosphere, and quadripod scattering. These components are calculated as a function of frequency and elevation angle to determine a G/T (gain/system noise temperature) figure-of-merit for a nominal 34-meter antenna configuration. A computational method has been developed which will enable design of a multi-horn antenna feed system to optimally cover the 1 to 10 GHz frequency range.*

## I. Introduction

The SETI Project (Search for Extra-Terrestrial Intelligence, Refs. 1 and 2) is planning to investigate a small region of the microwave spectrum in its search for signals possibly indicative of life elsewhere in our galaxy. In particular, it has been decided that the region 1 to 10 GHz may be a particularly fruitful frequency band, based on considerations of galactic noise interference below 1 GHz, atmospheric noise above 10 GHz, and “philosophical” arguments regarding the “water-hole” communication frequency region from 1.4 to 1.7 GHz.

Clearly, the use of the Deep Space Network antennas would be of great value to SETI, as the cumulative collecting area of the 10 large antennas (ranging in size from 26-meter diameter to 70-meter diameter as of 1987) will be greater than that of any other assembly in the world, except those of the VLA (Very Large Array) in New Mexico. The three DSN

antennas in Australia give access to the southern skies for declinations less than about  $-45^\circ$ , a region unreachable by most of the world's large antennas. (An arbitrary southern elevation angle limit of 10 degrees is chosen to limit atmospheric effects and horizon mask noise contributions.)

The particular SETI search strategy contemplated is to use the 64-/70-meter antennas to look at particular stars (approximately 1000) in the frequency range 1 to 3 GHz. The 34-meter (or 26-meter) antennas will be used for an all-sky survey over the frequency range 1 to 10 GHz.

The DSN antennas, however, have been designed and built to operate at the specific narrow-band microwave frequencies used to communicate with “deep space” spacecraft, almost exclusively those launched by the United States. (“Deep space” is used to denote a distance from the earth generally beyond the orbit of the moon, 400,000 km.) Those

particular narrow-band (0.2 GHz) frequencies are L-band (1.7 GHz), S-band (2.3 GHz), and X-band (8.4 GHz); and L-band is presently carried only upon the 64-meter subnet.

## II. Antenna and Feed Description

A typical 34-meter antenna is the DSS-12 instrument at Goldstone (Fig. 1). This antenna is a HA-DEC antenna; i.e., it is constructed to track in hour angle and declination, rather than in azimuth and elevation (AZ-EL). The 64-meter antennas (DSS-14, -43, -63) and new high-efficiency shaped-reflector 34-meter antennas (e.g. DSS-15) are of the AZ-EL configuration. A general description of all DSN antennas and microwave systems is given in Ref. 3. DSS-12 has a reflex feed type of microwave optics system whereby simultaneous S-band and X-band signals can be transmitted and received by use of the ellipsoidal reflector at the S-band feedhorn and a dichroic plate located over the X-band feedhorn. A complete description of this system is given in Ref. 4.

Because the dichroic plate is an inherently narrow-band device (8.3–8.5 GHz), use of the reflex feed system is contraindicated for SETI X-band investigations. The present analysis of the 34-meter microwave optics system then assumed that modification to the antenna would be necessary for wide-band use — certainly the reflex feed system would be eliminated. Possibly, a complete new series of feedcones and horns might be developed to cover the 1 to 10 GHz band.

In the reflex feed system, the subreflector is both tilted and of asymmetric shape. This design does not easily lend itself to use in configurations other than that for which it is specifically designed. The use of off-axis feedhorns in the asymmetric system would result in greatly reduced antenna gain and increased spillover and ground noise contribution.

A symmetric antenna with a single frequency corrugated feedhorn does not exist in the DSN. Modifications to existing antennas could create one; and for SETI use it may become necessary to operate in some slightly modified version of this simple antenna optics scheme. The basis of the analysis presented here was the 34-meter symmetric antenna design because it is very representative of performance obtained in both the asymmetric 34-meter and 64-meter reflex-feed antennas, and symmetric 26-meter antenna with an S-X common aperture feedhorn. Naturally, the gain differences between these different size antennas must be accounted for in the analysis.

An “equivalent” symmetric Cassegrain antenna was chosen for analysis. This antenna closely matches the DSS-12 34-meter design. Figure 2 and Table 1 show the actual antenna

dimensions used in the analysis. Figure 3 and Table 2 show the dimensions of the subreflector, including the two-segment vertex plate used to direct reflected energy away from the feedcone area, and the peripheral flange used to control rear spillover and ground noise contribution.

The X-band feedhorn used in this analysis is identical to the X-band corrugated horn actually used in the reflex feed design. The S-band horn analyzed here is scaled (in size) by frequency (8.448/2.295) from the X-band dimensions. It is assumed in this analysis that the horns can be mounted separately with their phase centers (at the nominal design frequencies of 2.3 and 8.4 GHz) at the identical location relative to the antenna reflecting surfaces.

Most figures and tables in this report have dimensions given in inches. Although use of the English system of units is not a TDA reporting policy, these dimensions are already on design documents and blueprints, and comparison with existing documents is facilitated. Use of the metric system in this instance is not recommended.

## III. Description of Computational Techniques

A description of the computational methods used to characterize antenna performance can be more easily understood by reference to Figs. 2 and 3. The goal of the analysis is to determine a G/T (gain/system noise temperature) for the antenna system at various frequencies and elevation angles. Table 3 shows the pertinent components of G and T.

It was decided to reference the computed G/T figures-of-merit to the G/T at the nominal S- and X-band frequencies (rounded off to 2.3 and 8.4 GHz) and elevation angle (90°), since the actual gains and system noise temperatures are published (Ref. 5) and presumably well known for these conditions. For a DSN 34-meter antenna of the DSS-12 type, the gain and zenith system noise temperature are 56.1 dBi and 21.5 K at S-band, and 66.2 dBi and 25.0 K at X-band. Actual system noise temperatures may be lower than these published numbers, especially in the case of a non-reflex antenna configuration. The G/T figure-of-merit can be expressed as (cf. Table 3)

$$G/T \sim \frac{\eta_{\text{aperture}} \times \eta_{\text{surface}}}{T_{\text{ground}} + T_{\text{atmosphere}} + T_{\text{quadripod}} + T_{\text{base}}} \quad (1)$$

Aperture efficiency is calculated as a percentage of the gain achieved by a (theoretically optimum) uniformly illuminated aperture, equal in size to the physical area of the antenna; or,

in other words, the gain of a uniformly illuminated aperture reduced by corrections for forward and rear spillover, non-uniform amplitude illumination, non-uniform phase illumination, cross polarization, and subreflector blockage. Quadripod blockage is not considered, as it is considered constant with frequency and elevation angle and is only a multiplicative constant in the numerator of Eq. (1) (an additive constant in terms of decibels). Quadripod blockage is already included in the published gain values for the DSN antennas.

Surface efficiency shows the effect of antenna main reflector surface roughness and deviation from a true paraboloidal shape as a result of gravity deformation. Ground noise arises from the "hot" earth's surface being reflected principally from the hyperboloidal subreflector into the feedhorn. Atmospheric noise (clear air) arises from oxygen and water vapor emission being reflected from the subreflector into the feedhorn (as in the case of ground noise) or from the atmosphere in the main antenna beam. Quadripod scatter noise results from the ground emission reflecting from the quadripod truss structure, and through one or more reflections entering the feedhorn.

The baseline system noise temperature is a constant for each microwave band and represents the "non-changing" contributions from the maser, waveguide (including horn), and cosmic background noise temperatures. The baseline values used here are 14.81 K (S-Band) and 18.25 K (X-Band).

All these components of G/T will be described further in more detail. The computational method proceeds as follows.

## A. Corrugated Horn Patterns

Horn patterns are calculated from JPL Telecommunications Division computer programs known generically as "hybrid mode" programs. Geometrical inputs to these programs are given in Table 4. First, the illumination pattern of the existing X-band horn is calculated at 8.4 GHz using the physical dimensions of the horn. A subroutine in the program calculates a best-fit phase center of the horn pattern over a far-field polar angular extent of 16 degrees, the angle subtended by the subreflector (32 degrees from side-to-side). In the 8.4 GHz case, the far-field phase center is found to be located 2.2129 inches inside the horn aperture; and on the real DSS-12 antenna (and on our hypothetical antenna) the horn is physically located so that the phase center is coincident with the focus of the hyperboloidal subreflector (cf. Fig. 2). Calculations are made at other frequencies in the X-band range, and the calculated phase centers change from that at 8.4 GHz. These positions vary from 1.2 inches at 7.0 GHz to 3.4 inches at 9.4 GHz. The S-band positions vary from 3.6 inches to 15.7 inches over the frequency range 1.8 to 2.7 GHz. The analysis presented here assumes that the feedhorns cannot be

repositioned to accommodate the changing phase center positions. Adjusting the subreflector position will not properly solve this misfocusing problem. The only proper solution is to accurately position the feedhorn as a function of frequency.

The S- and X-band frequency ranges are chosen to reflect the inherent bandwidth limitations of these particular DSN corrugated horns. The actual S-band range (modeled from X-band) would be 1.9 to 2.6 GHz, slightly narrower than that investigated here.

The changing phase center positions (which are not compensated for by repositioning the horn from its bolted-in 8.4 GHz or 2.3 GHz location) result in over- and under-illumination of the subreflector in addition to phase errors of up to a wavelength.

Figure 4 shows a typical X-band horn pattern at 8.4 GHz. Patterns at other frequencies (both X-band and S-band) are quite similar and are characterized by nearly identical E- and H-plane gain, and very low side and backlobes. Table 5 shows the 3-dB beamwidth, hyperboloid edge illumination, and phase center position for all S-band and X-band cases. Note that as the frequency increases from the nominal design frequency, the beamwidth decreases and the hyperboloid edge illumination decreases, resulting in under-illumination of the main reflector and decreased aperture efficiency. At frequencies lower than the design frequency, beamwidth and illumination increase, and rear spillover increases, thus increasing contribution from ground emission. For all cases, the horn patterns are stored in computer files and are used in the next step of the analysis process, scattering of the horn fields from the subreflector.

## B. Subreflector Shape

First, however, the exact shape of the subreflector surface must be mathematically described. Figure 3 shows the schematic view of the subreflector with its hyperboloid section, two-segment vertex plate, and peripheral flange. The use of the computer program describing the subreflector shape is given in Ref. 6. The output of this program (the subreflector shape) is also used as an input to the subreflector scattering program.

A series of calculations was made at 8.4 GHz to examine the effect of a changing flange angle (Fig. 3, angle BE3) on noise temperature contribution from rear spillover and ground emission. The full use of this program is described later. The results are shown in Table 6. It is seen that unless the outer portion of the subreflector is "turned in" toward the main reflector, an unacceptably large amount of rear spillover results and substantially increases the system noise temperature. The existing design angle is 63.226°. The calculations



leading to the Table 6 values were made using subreflectors with no vertex plates. The effect on rear spillover (of neglecting the vertex plates) is negligible.

### C. Scattering Program

The scattering program calculates the scattered field resulting from the corrugated horn (Section III.A) illuminating the subreflector (Section III.B). The scattered field contains components of the horn pattern also, so that the sidelobes of the horn pattern should not be disregarded even though they do not strike the subreflector. These sidelobes may be sensitive to a source of RFI within 20 degrees of the main antenna beam. This problem will be discussed later. In other words, the field sensitive to noise from the sky and ground exists in all space, in both the forward and rearward directions. A description of the scattering program is given in Ref. 7. This program is known in the Telecommunications Division as the Rusch Scattering Program, after W. V. T. Rusch, the originator.

Table 7 gives some of the pertinent input values used in the Rusch Scattering Program. A large number of the other input values are "administrative" and refer to the calculation technique rather than the geometry of the problem. Data file inputs to this program are the subreflector shape and the corrugated horn pattern. It is important to remember that input horn patterns at frequencies other than 2.3 or 8.4 GHz are from *misfocused* horns.

Figures 5 and 6 show the S-band and X-band amplitude patterns of the hyperboloid-scattered fields. A polar angle equal to 0° is toward the vertex of the main reflector as seen from the hyperboloid. A polar angle of 180° corresponds to the direction behind the subreflector; and the region 140° to 180° contains the sidelobes and diffracted pattern of the feedhorn.

It can be seen from Figs. 5 and 6 that RFI sources (e.g., radio stars) located approximately 20 degrees (polar angle 160 degrees) and 100 degrees (polar angle 80 degrees) from the main antenna beam (polar angle 180 degrees) may cause system noise temperature increases. The 20° peak of the scattered pattern is "forward spillover" and is caused primarily by power from the feedhorn passing beyond the edge of the subreflector. The 100° peak is "rear spillover" and comes about from scattered energy passing beyond the edge of the main reflector. The location of known radio noise sources must be monitored during SETI search procedures to avoid confusion and misinterpretation. Table 8 gives the amplitude and location ( $\pm 0.5^\circ$ ) of the strong scattered side-lobe at 160 degrees polar angle (cf. Figs. 5 and 6).

The dip near the center of each pattern shows the effect of the vertex plate removing and redirecting energy which would otherwise strike the central cone and feed system. The steep taper in the 70°-80° range shows the effect of both the normal Cassegrain optics and the additional flange around the edge of the subreflector. The polar angle to the edge of the main reflector is 75.525°; the edge illumination power level is down approximately 15 dB at this angle.

The output of the scattering program is the far-field amplitude and phase of the field scattered from the subreflector. This field exists in all space (polar angle 0° to 180°); and a portion of it (that with the greatest amplitude) is intercepted by the main reflector. Also calculated by the program are numerous efficiencies pertaining to forward and rear spillover, non-uniform amplitude and phase illumination, and cross polarization. Quadripod blockage is neglected, as it is considered common to all frequencies and elevation angles. For each frequency, an overall aperture efficiency is calculated. This efficiency is not a function of elevation angle, and represents "how well" the illuminated main reflector utilizes the incident energy compared to a uniformly illuminated circular aperture of the same diameter.

The aperture efficiency is directly related to gain and is used as one of the gain components in the G/T figure-of-merit. The calculations yield typical aperture efficiencies in the range 70 to 80 percent for the frequencies studied. The aperture efficiencies (which are a function of frequency only) appear as the term, " $\eta_{\text{aperture}}$ " in Eq. (1).

### D. Surface Efficiency

The effects of main reflector roughness and deviation from paraboloidal shape are accounted for by an "equivalent" Ruze formula (Ref. 8):

$$\frac{G}{G_0} = \exp \left[ - \left( \frac{4\pi\epsilon}{\lambda} \right)^2 \right] \quad (2)$$

where

$G/G_0$  = fractional gain reduction

$\epsilon$  = rms surface roughness

$\lambda$  = wavelength

A surface tolerance  $\epsilon$  is chosen *a priori* to give the measured or expected gain reduction seen on the DSS-12 34-meter-type antenna. This equivalent surface tolerance is given in Table 9. The antenna surface is adjusted to have best shape at 30° elevation. Due to the behind-dish support structure, the worst shape occurs at 90° elevation. Typical fractional gains range

from 99% at low frequencies down to 80% at high frequencies and worst attitude shape. A nominal X-band fractional gain given in Ref. 4 for the specific case of a 34-meter reflex-feed antenna (e.g., DSS-12) is 0.88 for a 1-mm rms surface distortion due to wind, thermal, and gravity effects. The surface efficiency values determined as a function of frequency and elevation angle are directly related to the antenna gain and appear as the term " $\eta_{\text{surface}}$ " in Eq. (1).

## E. Ground and Atmosphere Noise Temperature

Figure 7 shows typical antenna rays which contribute to noise from the ground and atmosphere. Ray 1 is scattered from the subreflector edge and sees the hot ground. Ray 2 is part of the horn pattern and sees the atmosphere. Ray 3 (part of the main antenna beam) strikes the surface of the main reflector and is reflected upward at the elevation angle of the antenna. Ray 4 is scattered from the subreflector edge and sees the sky. The net noise temperature from the effect of all these rays can be calculated from the expression

$$T_{\text{noise}} = \frac{\iint T_{\text{source}}(\theta, \phi) G(\theta, \phi) dA}{\iint G(\theta, \phi) dA} \quad (3)$$

where

$T_{\text{source}}$  = ground or atmosphere equivalent blackbody noise temperature

$G$  = scattered field strength (gain) in direction of source

$dA$  = unit area in direction of source

The geometry is complex, but the results obtained as a function of elevation angle (at 2.3 or 8.4 GHz) agree quite well with experiment and simpler estimates.

The ground is considered to have an average equivalent blackbody noise temperature of 240 K. The equivalent blackbody noise temperature of the ground is a function of its emissivity, which in turn is a complex function of the dielectric constant of the ground, grazing angle of the impinging ray, polarization, and frequency. For rough surfaces, frequencies greater than 1 GHz, and grazing angles greater than  $10^\circ$ , reflection coefficients of 0.0 to 0.4 are found. This would yield blackbody temperatures of 300 K down to 180 K, respectively. Ground emissivity is discussed in much detail in Ref. 9.

The atmosphere is modeled to have a zenith noise temperature contribution (for an antenna at approximately 1 km above sea level) at S-band of 2.0 to 2.1 K and at X-band of 2.5 to 2.75 K from lowest to highest frequencies. The clear-sky atmospheric noise contribution arises from oxygen (predominantly, below 10 GHz) and water vapor. The elevation angle

dependence of atmospheric noise temperature is modeled as the inverse sine of the elevation angle, up to a maximum of 19.1 airmasses (equivalent to an elevation angle of  $3^\circ$ ), to account for the round earth.

## F. Quadripod Scatter Noise Temperature

Some amount of power received by the feedhorn arrives from the ground via scattering from the quadripod structure. This ground contribution is considered separately from the spillover ground noise described previously. Estimates of the noise temperature contribution from this source have been made by Potter (Ref. 10) for a 64-meter antenna. By a careful process of measurement and subtraction of known effects, the elevation angle effects were determined. It is felt that these values will apply to the 34-meter antenna system also. This component of noise temperature has not been measured separately; however, overall system noise temperature measurements at various elevation angles confirm the results obtained in Ref. 10. It should be mentioned again that quadripod noise temperature is assumed to be a function of elevation angle only, not frequency, to within experimental error. The noise contribution ranges from 2.5 K at zenith to 6 K at  $10^\circ$  elevation.

## G. Baseline Noise Temperature

Part of the figure-of-merit calculation (Eq. [1]) is the determination of the non-changing portion of the system noise temperature, due to preamplifier, waveguide, and cosmic noise contributions. Since the baseline system noise temperatures are known, it is a simple matter to subtract out the ground, atmosphere, and quadripod contributions calculated here in order to arrive at the non-changing component. The baseline values used here are 14.81 K (S-band) and 18.25 K (X-band).

Tables 10 through 14 show sample calculated results of the G/T components described above. Complete listings for all frequencies and elevation angles are too lengthy to present here. These tables show the general variations of the components over extreme ranges of frequency and elevation angle.

## IV. Results

As discussed in Section III, a G/T figure-of-merit was calculated for each frequency and elevation angle considered. This figure-of-merit was normalized to the value obtained at zenith and 2.3 (S-band) or 8.4 (X-band) GHz. Table 15 contains the complete relative G/T figures-of-merit (in dB) as a function of frequency and elevation angle. It can be seen that for the X-band case at the higher elevation angles ( $50^\circ$ - $80^\circ$ ), G/T performance is increased over that at zenith. This is due primarily to the decreased ground contribution and increased surface

efficiency. The maximum G/T increase is found to be about 0.3 dB. For S-band above 30° elevation, and X-band above 20° elevation, G/T degradation is found to be less than about 1 dB. Figures 8 through 12 show the aperture and surface efficiency, ground and atmospheric noise, and quadripod scatter noise, respectively, for the nominal 2.3 and 8.4 GHz frequencies. Figure 13 shows the G/T figures-of-merit at S-band for various elevation angles. Figure 14 shows the same for X-band.

From Figs. 13 and 14, it can be seen that given elevation angle limits and signal-to-noise ratio margins above some desired threshold, an estimate can be made of the number of feedhorns needed to cover the 1 to 10 GHz frequency range. Fortunately, feed system performance is not a strong function of frequency over the operating range of a single horn. The primary causes of G/T degradation are the three elevation-

dependent noise temperature contributions from the ground, atmosphere, and quadripod scatter.

It may be concluded that the DSN 34-meter HA-DEC subnet (or 26-meter antennas) could, at least down to the feed-horn output, provide significant bandwidth and high G/T performance, even using the somewhat restrictive DSN standard corrugated horn design. Techniques to achieve wider bandwidth horns are now available, but not yet proven on a DSN antenna. The reader should note, however, that the design of wideband (1.4:1 or greater bandwidth) low-noise preamplifier, polarizer, and orthomode components is not well understood. The above analysis defers performance study of these important components. Further studies will provide a "balanced" design capable of 1 to 10 GHz bandwidth coverage in a cost effective way. Meanwhile, certain planning functions for SETI can proceed, based on the analysis presented here.

## Acknowledgment

The author wishes to thank Eduardo Andres who carried out the numerous computer calculations and generated all the plots. Carole Devereux typed this report and graciously tolerated my numerous revisions. Dan Bathker and Bill Williams generously provided much needed technical support and guidance.

## References

1. F. Drake, J. H. Wolfe, and C. L. Seeger, SETI Science Working Group Report, NASA Tech. Paper 2244, 1984.
2. S. Gulkis, Note on the Optimum Search Strategy for Uniformly Distributed CW Transmitters, *TDA Progress Report 42-77*, Jet Propulsion Laboratory, Pasadena, Calif., 1984, pp. 144-150.
3. N. A. Renzetti, C. T. Stelzried, et al., The Deep Space Network — A Radio Communications Instrument for Deep Space Exploration, *JPL Publication No. 82-104*, Jet Propulsion Laboratory, Pasadena, Calif., July 15, 1983.
4. D. L. Nixon and D. A. Bathker, S-/X-Band Microwave Optics Design and Analysis for DSN 34-Meter-Diameter Antenna, *DSN Progress Report 42-41*, Sept. 15, 1977, Jet Propulsion Laboratory, Pasadena, Calif., pp. 146-165.
5. Jet Propulsion Laboratory, DSN/Flight Project Interface Design Document 810-5, Rev. D., TCIs-10, -20, -30 (internal document), November 1984, Pasadena, Calif.
6. A. Ludwig, editor, Computer Programs for Antenna Feed System Design and Analysis, Vol. I, *JPL Technical Report No. 32-979*, April 15, 1967, Jet Propulsion Laboratory, Pasadena, Calif., pp. 27-29.
7. A. Ludwig and W. V. T. Rusch, Digital Computer Analysis of a Subreflector of Complex Shape, *JPL Technical Report No. 32-1190*, November 15, 1967, Jet Propulsion Laboratory, Pasadena, Calif.
8. J. Ruze, Antenna Tolerance Theory — A Review, *Proc. IEEE*, Vol. 54, No. 4, April 1966, pp. 633-640.
9. H. Reed and C. Russell, *Ultra High Frequency Propagation*, Wiley and Sons, New York, 1953.
10. P. D. Potter, Efficient Antenna Systems: Calibration of the Mars Deep Space Station 64-m Antenna System Noise Temperature Degradation Due to Quadripod Scatter, *JPL Technical Report 32-1526*, Vol. XVI, August 15, 1973, Jet Propulsion Laboratory, Pasadena, Calif., pp. 22-29.

**Table 1. Dimensions for 34-meter symmetric antenna configuration (cf. Fig. 2)**

Parameter	Dimension
Diameter	149.532 in.
A	101.6233 in.
C	138.000 in.
V	158.468 in.
TH1	75.5 deg
TH2	75.525 deg
AL2	13.500 deg
AL3	15.675 deg
BE3	63.226 deg

**Table 2. Dimensions for 34-meter symmetric subreflector with vertex plate and peripheral flange (cf. Fig. 3)**

Parameter	Dimension
C	138.000 in.
A	101.6233 in.
D	0.873 in.
AL1	0.92065 deg
AL2	13.500 deg
AL3	15.675 deg
BE1	81.903 deg
BE2	81.175 deg
BE3	63.226 deg

**Table 3. Components of gain and noise temperature calculated for G/T figure-of-merit determination**

Components	Function of:	
	Frequency	Elevation Angle
Gain		
Aperture efficiency	Yes	No
Surface efficiency	Yes	Yes
Noise Temperature		
Ground noise	Yes	Yes
Atmospheric noise	Yes	Yes
Quadripod scatter noise	No	Yes
Maser, waveguide, cosmic background ( $T_{\text{base}}$ )	Constant for each band	

**Table 4. S- and X-band corrugated horn design values**

Parameter	S-Band	X-Band
Phasing section length	0.0 in.	0.0 in.
Diameter of phasing section and small end of flare	5.039 in.	1.369 in.
Flare length	95.928 in.	26.06 in.
Aperture diameter	26.051 in.	7.077 in.
Groove depth in phasing section and flare	1.583 in.	0.430 in.
Frequency <sup>a</sup>	1.8–2.7 GHz <sup>b</sup>	7.0–9.4 GHz
Phase center position inside horn aperture at nominal design frequency	8.3874 in. at 2.3 GHz	2.2129 in. at 8.4 GHz

<sup>a</sup>The frequency is chosen to reflect the inherent bandwidth limitations of the DSN corrugated horns.

<sup>b</sup>The modeled range would be 1.9–2.6 GHz

**Table 5. Characteristics of corrugated horn illumination patterns**

Frequency, GHz	E-Plane 3 dB Beamwidth Half-Angle, deg	E-Plane Taper at 16° (Subreflector Edge), dB	Phase Center Position Inside Aperture, in.
1.8	9.6	-8.8	3.605
1.9	9.1	-10.1	4.305
2.0	8.5	-11.5	5.113
2.1	8.1	-13.0	6.046
2.2	7.7	-14.6	7.128
2.3 (Design freq.)	7.3	-16.3	8.387
2.4	7.0	-18.0	9.852
2.5	6.7	-19.6	11.556
2.6	6.4	-20.8	13.506
2.7	6.2	-21.6	15.721
7.0	9.0	-10.1	1.173
7.2	8.8	-10.9	1.288
7.4	8.5	-11.7	1.414
7.6	8.3	-12.5	1.548
7.8	8.0	-13.3	1.695
8.0	7.8	-14.2	1.854
8.2	7.6	-15.1	2.026
8.4 (Design freq.)	7.4	-16.0	2.213
8.6	7.2	-17.0	2.416
8.8	7.1	-17.9	2.636
9.0	6.9	-18.8	2.875
9.2	6.7	-19.6	3.131
9.4	6.6	-20.3	3.404

**Table 6. Ground noise temperature contribution for zenith-pointing antenna, as a function of subreflector flange angle**

Flange Angle, deg	Ground Noise Temperature, K
71.5	1.413
65.0	1.126
63.226 (34-m design value)	1.339
58.984 (tangent to hyperboloid)	8.348

**Table 7. Input values for Rusch Subreflector Scattering Program**

Parameter	Meaning, value
DIST	Subreflector focal length (2C), 276.0 in.
BLK	Half blockage angle of subreflector shadow at vertex of main reflector, 9.780°
X1	Lower limit of integration (subreflector edge), 164.21°
X2	Intermediate limit of integration, 172.0°
X3	Upper limit of integration, 180.0°

**Table 8. Sidelobe characteristics near the main beam of the 34-meter antenna**

Frequency, GHz	Sidelobe Position Relative to Main Beam, deg ( $\pm 0.5^\circ$ )	Amplitude of Sidelobe Peak, dBi
1.8	20	6.0
1.9	19	4.9
2.0	20	4.0
2.1	19	3.3
2.2	19	2.7
2.3	18	2.6
2.4	19	2.5
2.5	18	2.6
2.6	19	2.1
2.7	17	2.4
7.0	19	7.5
7.2	19	7.0
7.4	19	6.3
7.6	18	5.7
7.8	18	5.1
8.0	18	4.2
8.2	18	3.4
8.4	18	3.1
8.6	18	3.0
8.8	18	2.6
9.0	18	2.1
9.2	18	1.8
9.4	18	1.9

**Table 9. Equivalent surface tolerance for 34-meter HA-DEC antenna, e.g., DSS-12**

Elevation Angle, deg	RMS Surface Tolerance, in.
0	0.0375
10	0.0330
20	0.0300
30	0.0293 (3/4 mm)
40	0.0300
50	0.0315
60	0.0345
70	0.0375
80	0.0420
90	0.0465

**Table 10. Aperture efficiency as a function of frequency and elevation angle**

Frequency, GHz	Elevation Angle, deg			
	10	20	30	90
1.8	0.760	0.760	0.760	0.760
2.3	0.785	0.785	0.785	0.785
2.7	0.707	0.707	0.707	0.707
7.0	0.710	0.710	0.710	0.710
8.4	0.739	0.739	0.739	0.739
9.4	0.711	0.711	0.711	0.711

**Table 11. Surface efficiency as a function of frequency and elevation angle**

Frequency, GHz	Elevation Angle, deg			
	10	20	30	90
1.8	0.996	0.997	0.997	0.992
2.3	0.993	0.995	0.995	0.987
2.7	0.991	0.993	0.993	0.982
7.0	0.941	0.951	0.953	0.887
8.4	0.916	0.930	0.933	0.841
9.4	0.896	0.914	0.917	0.805

**Table 12. Ground noise temperature (K) as a function of frequency and elevation angle**

Frequency, GHz	Elevation Angle, deg			
	10	20	30	90
1.8	11.05	5.28	3.89	5.86
2.3	4.33	1.87	1.35	1.84
2.7	2.79	0.59	0.32	0.28
7.0	7.93	2.45	1.52	1.94
8.4	3.66	1.54	0.96	1.34
9.4	2.67	0.92	0.56	0.68

**Table 13. Atmospheric noise temperature (K) as a function of frequency and elevation angle**

Frequency, GHz	Elevation Angle, deg			
	10	20	30	90
1.8	12.77	7.05	4.79	2.91
2.3	12.32	6.47	4.39	2.35
2.7	12.40	6.37	4.29	2.14
7.0	15.50	8.27	5.49	2.91
8.4	15.73	8.22	5.57	2.92
9.4	16.18	8.38	5.67	2.89

**Table 14. Quadripod scatter noise temperature (K) as a function of frequency and elevation angle**

Frequency, GHz	Elevation Angle, deg			
	10	20	30	90
1.8	6.00	5.70	4.70	2.50
2.3	6.00	5.70	4.70	2.50
2.7	6.00	5.70	4.70	2.50
7.0	6.00	5.70	4.70	2.50
8.4	6.00	5.70	4.70	2.50
9.4	6.00	5.70	4.70	2.50

**Table 15. G/T figures-of-merit (dB) relative to nominal values at zenith and 2.3 GHz (S-Band) or 8.4 GHz (X-Band)**

Frequency, GHz	Elevation Angle, deg									
	0	10	20	30	40	50	60	70	80	90
1.8	-5.487	-3.272	-1.935	-1.272	-0.959	-0.784	-0.695	-0.707	-0.955	-0.956
1.9	-5.227	-2.935	-1.696	-1.071	-0.768	-0.596	-0.497	-0.494	-0.706	-0.696
2.0	-5.035	-2.684	-1.498	-0.894	-0.595	-0.413	-0.307	-0.288	-0.466	-0.439
2.1	-4.925	-2.509	-1.359	-0.764	-0.462	-0.282	-0.164	-0.130	-0.275	-0.244
2.2	-4.879	-2.420	-1.281	-0.696	-0.390	-0.205	-0.079	-0.036	-0.150	-0.113
2.3	-4.883	-2.385	-1.242	-0.663	-0.351	-0.163	-0.026	0.032	-0.043	0.000
2.4	-4.941	-2.405	-1.252	-0.679	-0.361	-0.163	-0.022	0.052	0.012	0.045
2.5	-5.033	-2.464	-1.301	-0.733	-0.415	-0.215	-0.062	0.017	-0.002	0.027
2.6	-5.155	-2.551	-1.381	-0.816	-0.494	-0.290	-0.130	-0.044	-0.042	-0.012
2.7	-5.316	-2.678	-1.495	-0.930	-0.605	-0.397	-0.237	-0.145	-0.126	-0.106
7.0	-4.936	-2.490	-1.060	-0.417	-0.102	0.068	0.163	0.176	0.036	-0.045
7.2	-4.834	-2.335	-0.969	-0.341	-0.045	0.125	0.211	0.229	0.084	-0.001
7.4	-4.776	-2.231	-0.914	-0.302	-0.005	0.159	0.244	0.249	0.104	0.017
7.6	-4.737	-2.158	-0.885	-0.275	0.027	0.190	0.273	0.283	0.143	0.046
7.8	-4.711	-2.099	-0.859	-0.256	0.039	0.201	0.282	0.284	0.134	0.036
8.0	-4.696	-2.048	-0.834	-0.236	0.062	0.218	0.300	0.302	0.155	0.052
8.2	-4.718	-2.039	-0.842	-0.240	0.054	0.212	0.290	0.287	0.140	0.033
8.4	-4.747	-2.047	-0.860	-0.263	0.031	0.192	0.265	0.261	0.113	0.000
8.6	-4.792	-2.065	-0.876	-0.286	0.011	0.171	0.244	0.243	0.095	0.012
8.8	-4.855	-2.104	-0.910	-0.325	-0.029	0.130	0.202	0.199	0.052	-0.066
9.0	-4.905	-2.125	-0.935	-0.354	-0.053	0.106	0.172	0.171	0.025	-0.096
9.2	-4.972	-2.168	-0.974	-0.390	-0.093	0.067	0.136	0.131	-0.017	-0.151
9.4	-5.082	-2.258	-1.045	-0.464	-0.163	-0.008	0.056	0.050	-0.094	-0.238



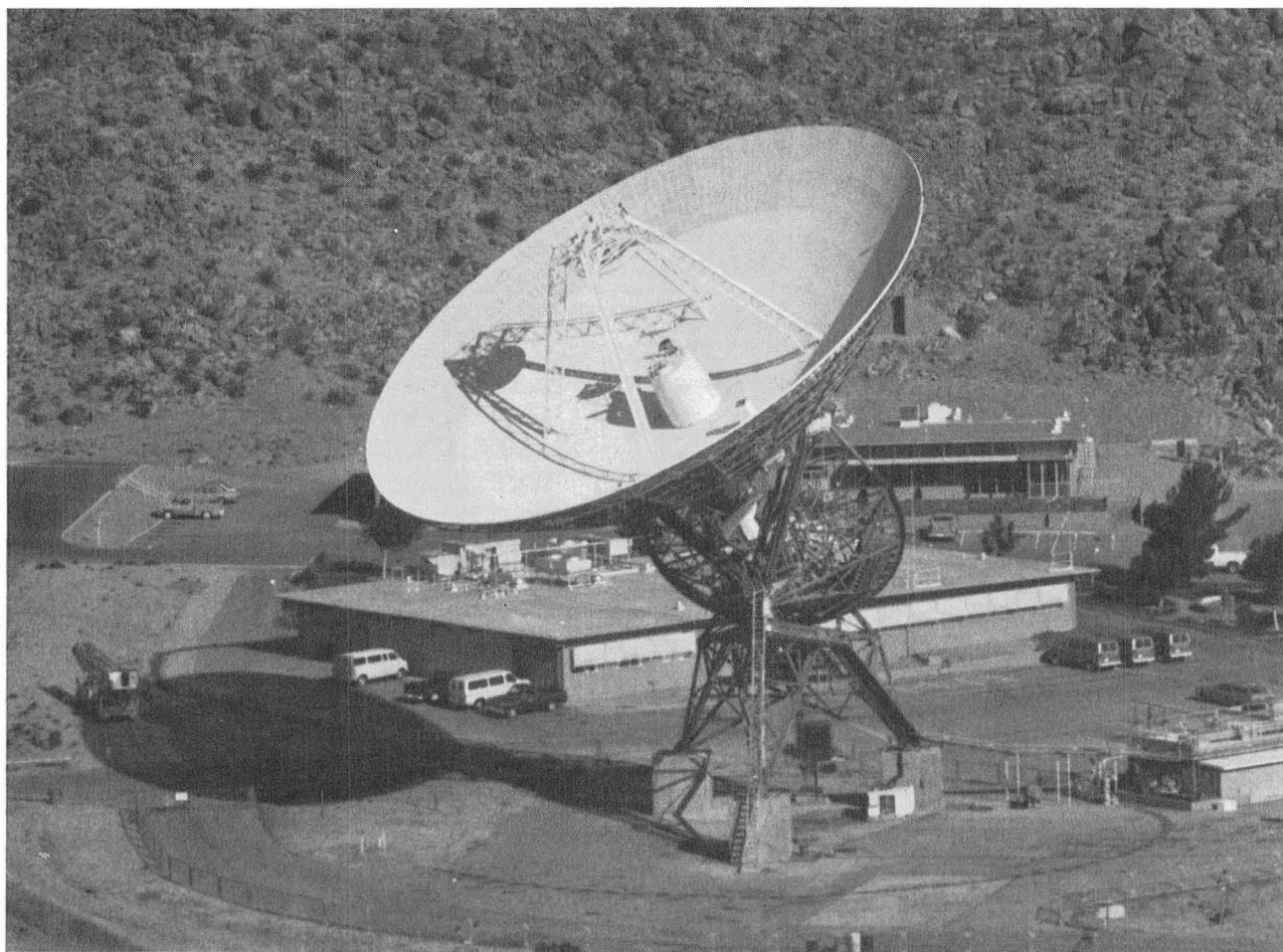


Fig. 1. DSS-12 34-meter antenna at Goldstone, in S/X reflex feed configuration

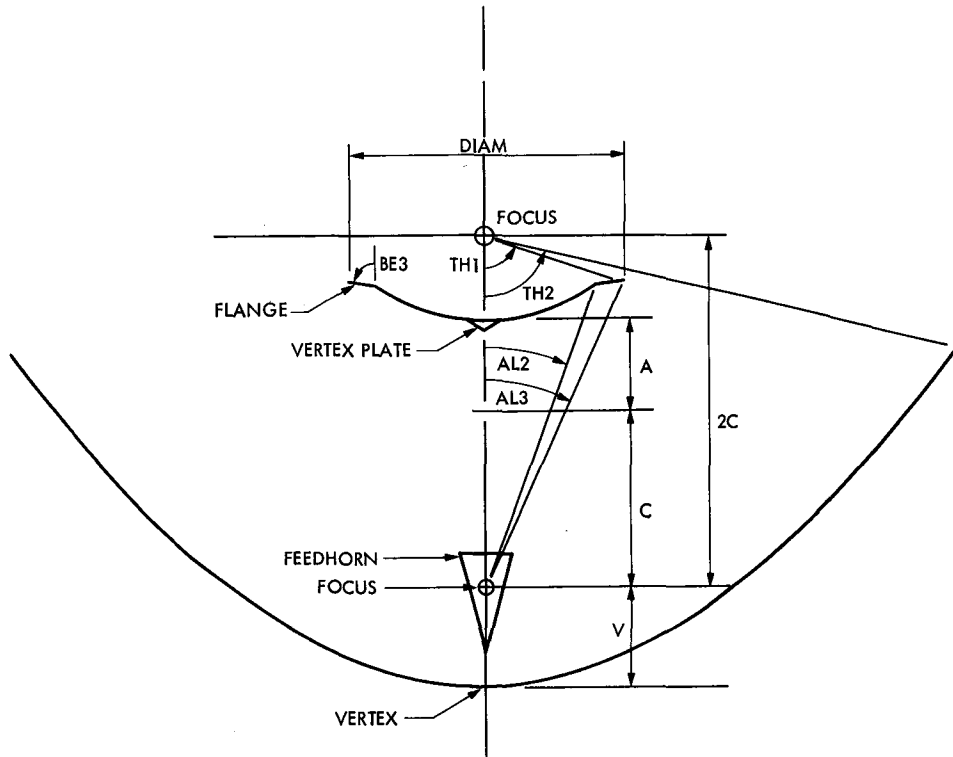


Fig. 2. Diagram of typical symmetric antenna configuration (cf. Table 1 for 34-meter antenna dimensions)

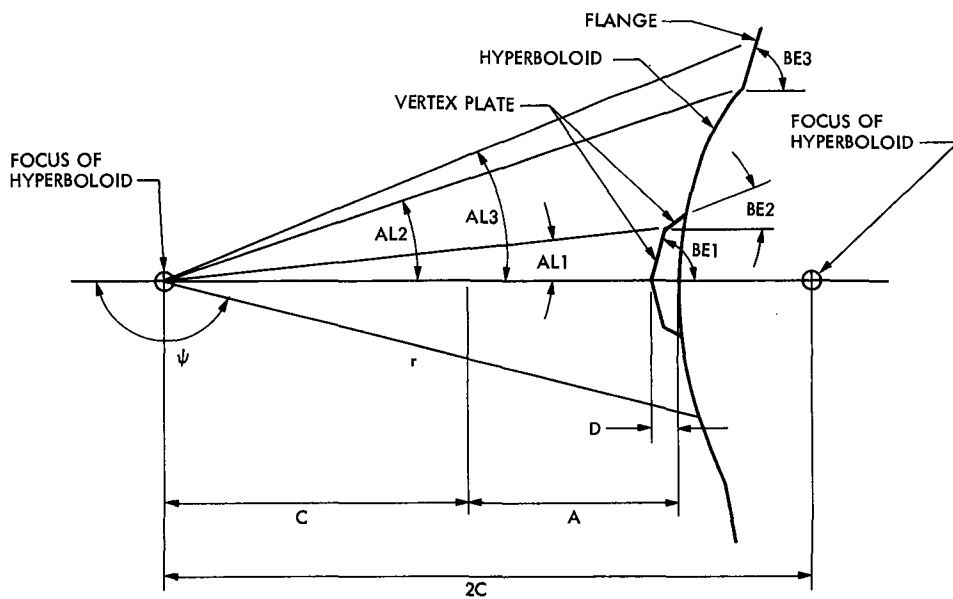


Fig. 3. Diagram of typical symmetric subreflector configuration (cf. Table 2 for 34-meter subreflector dimensions)

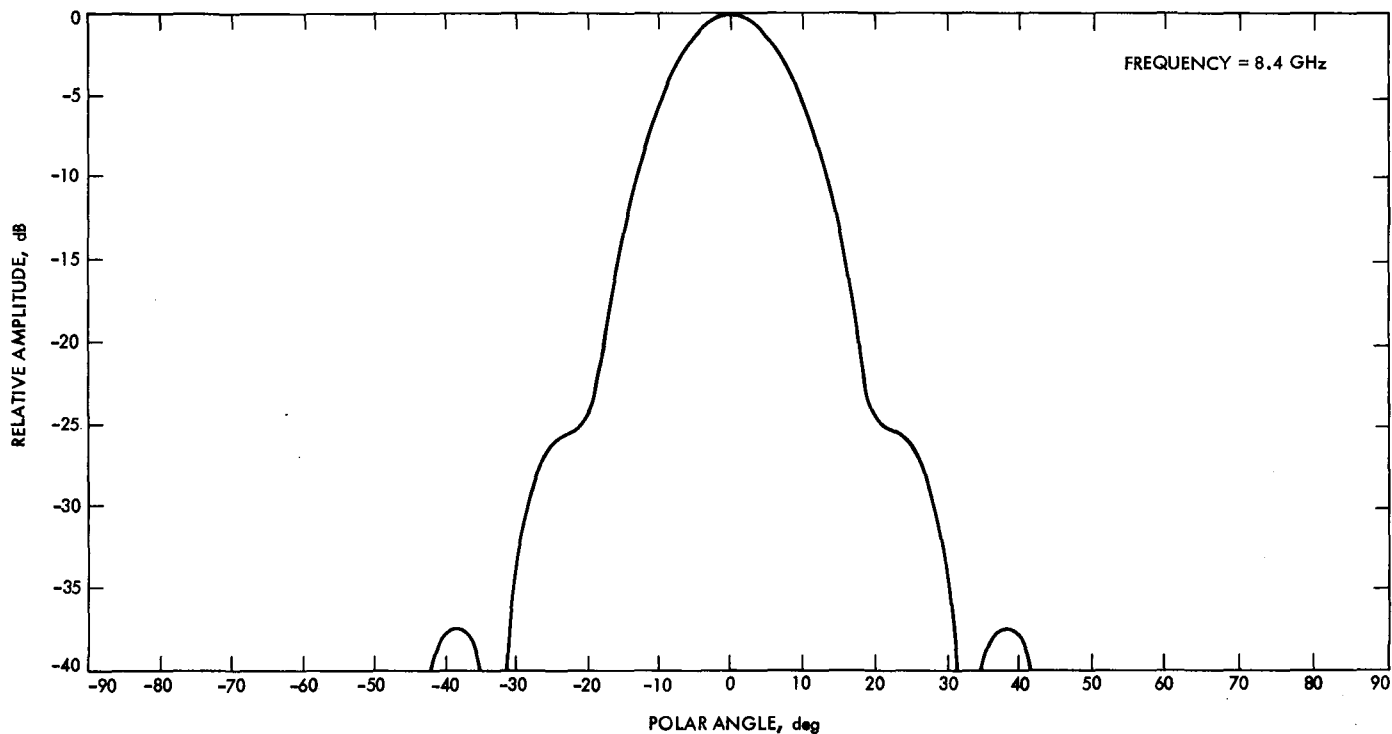


Fig. 4. Typical corrugated feedhorn amplitude pattern, S- and X-band (8.4 GHz shown)

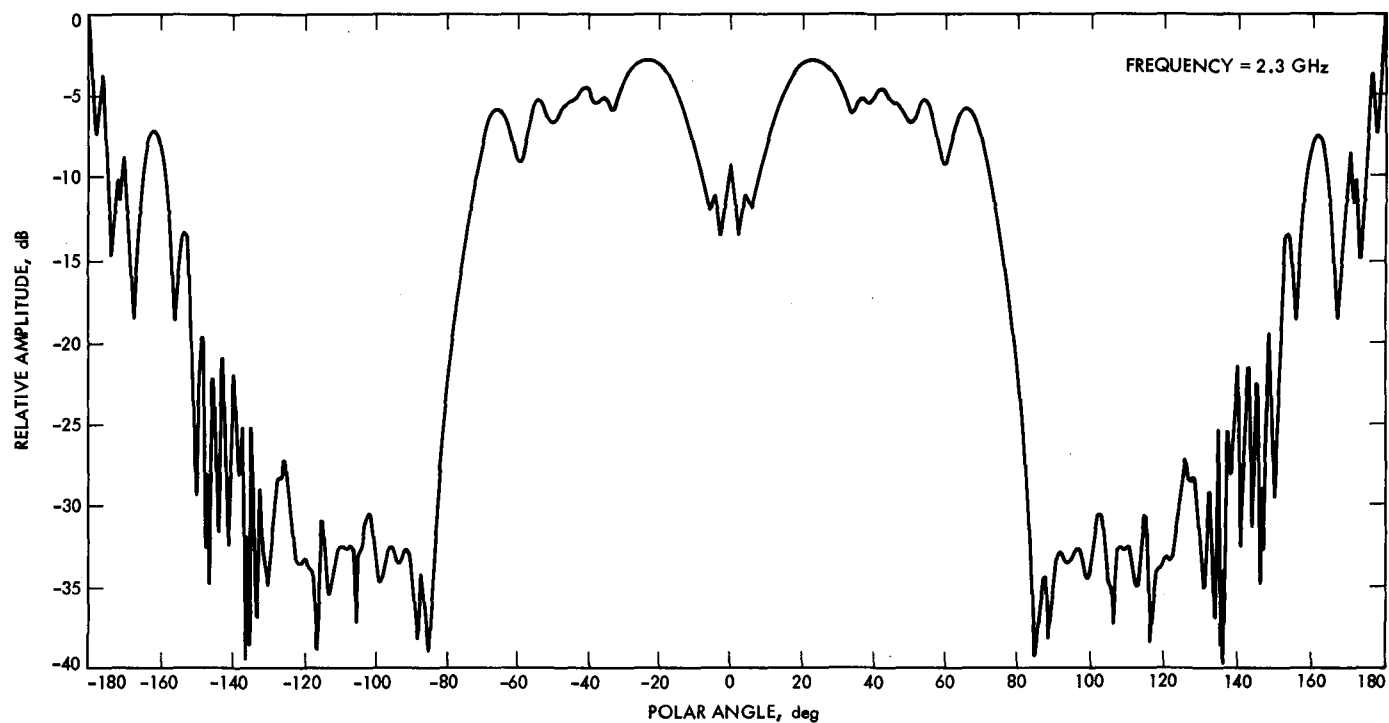


Fig. 5. Typical S-band scattered field from symmetric subreflector in 34-meter antenna configuration

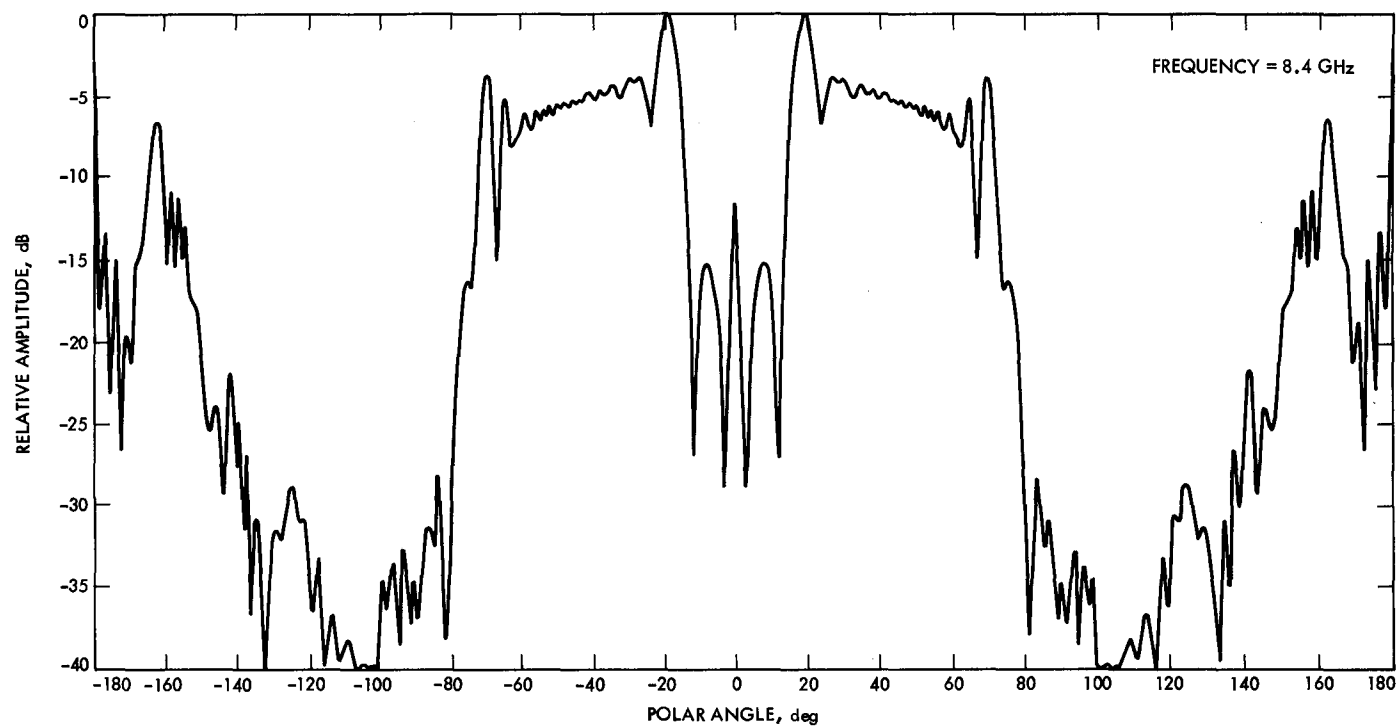


Fig. 6. Typical X-band scattered field from symmetric subreflector in 34-meter antenna configuration

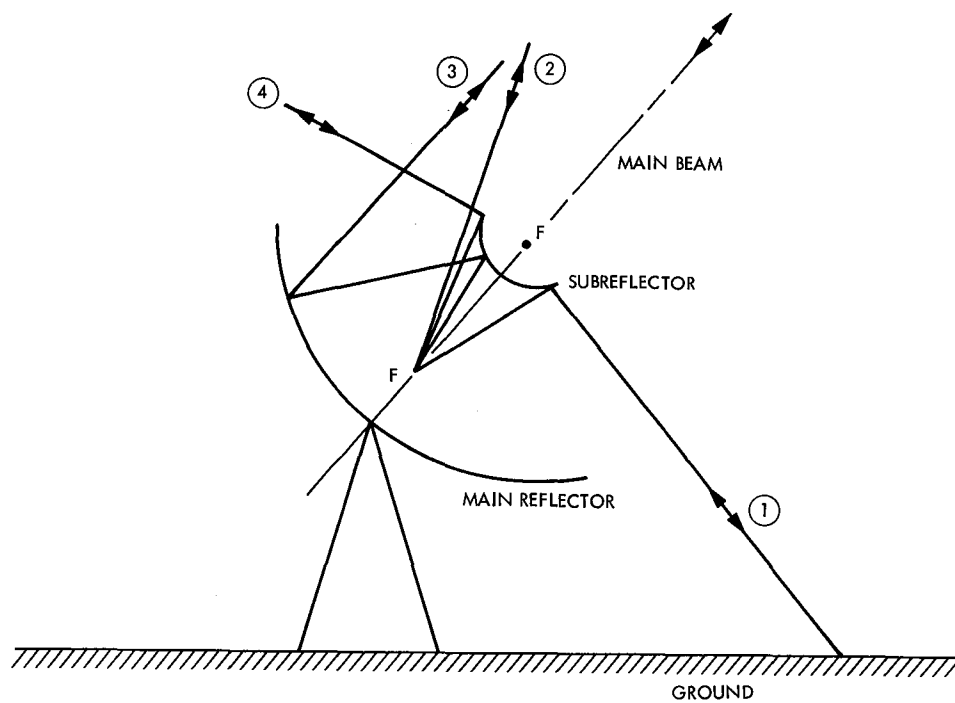


Fig. 7. Schematic view of ground and atmosphere contribution to system noise temperature

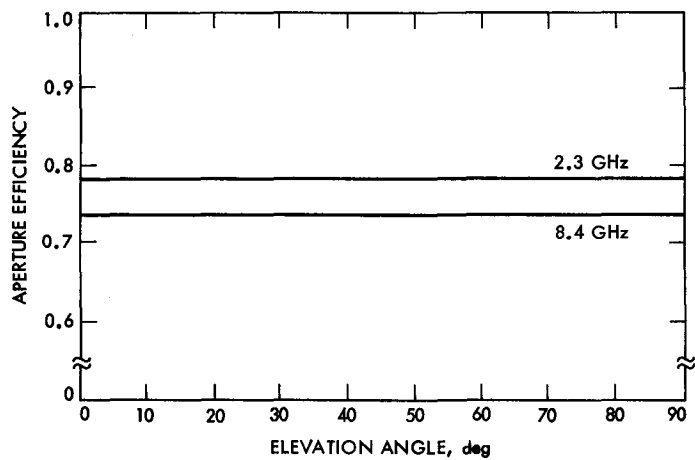


Fig. 8. Aperture efficiency at 2.3 and 8.4 GHz as a function of elevation angle

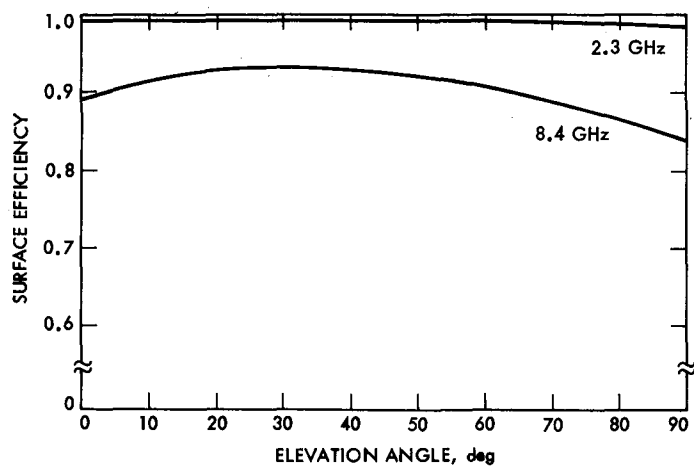


Fig. 9. Surface efficiency at 2.3 and 8.4 GHz as a function of elevation angle

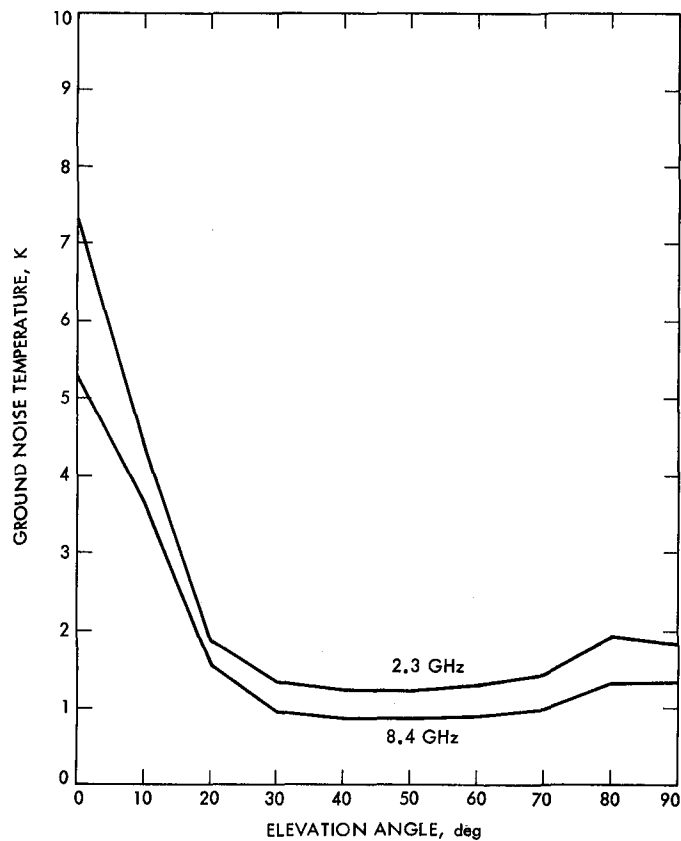


Fig. 10. Ground noise temperature at 2.3 and 8.4 GHz as a function of elevation angle

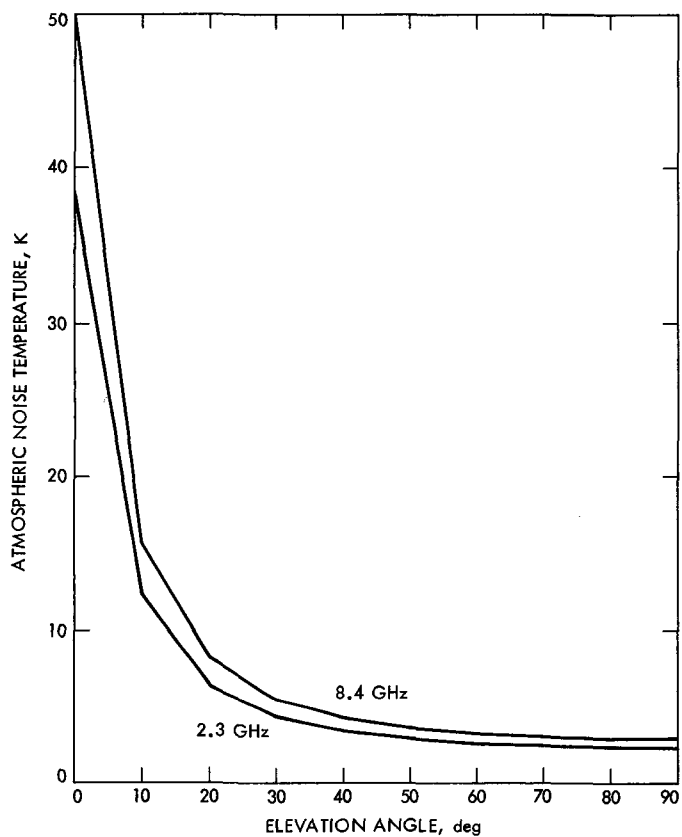


Fig. 11. Atmospheric noise temperature at 2.3 and 8.4 GHz as a function of elevation angle

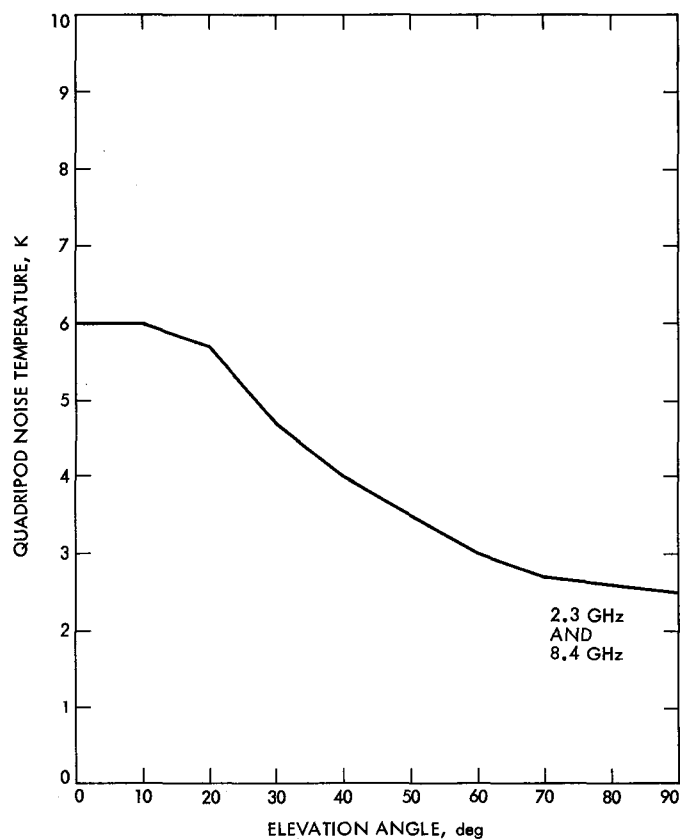


Fig. 12. Quadripod scatter noise temperature at 2.3 and 8.4 GHz as a function of elevation angle

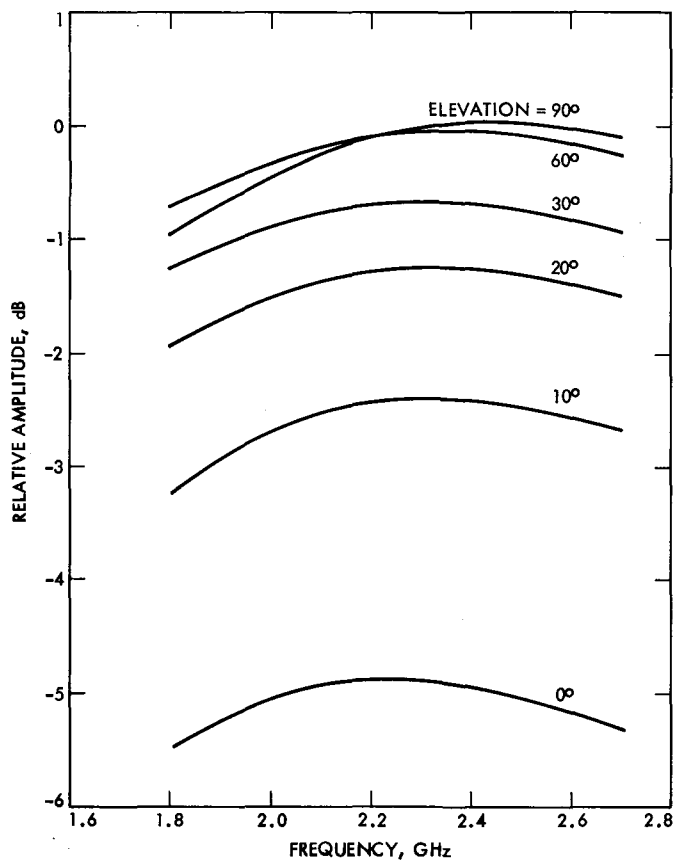


Fig. 13. G/T figure-of-merit for S-band relative to that at zenith and 2.3 GHz (cf. Table 15)

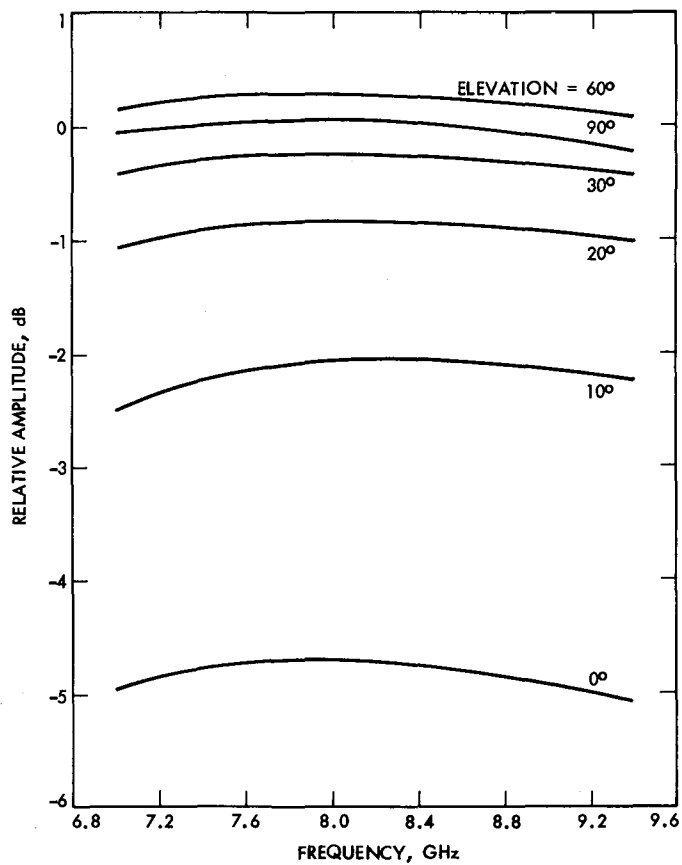


Fig. 14. G/T figure-of-merit for X-band relative to that at zenith and 8.4 GHz (cf. Table 15)

# Historical Cost Curves for Hydrogen Masers and Cesium Beam Frequency and Timing Standards

D. S. Remer

DSN Data Systems Section and Harvey Mudd College

R. C. Moore

DSN Data Systems Section

*Historical cost curves were developed for hydrogen masers and cesium beam standards used for frequency and timing calibration in the Deep Space Network. These curves may be used to calculate the cost of future hydrogen masers or cesium beam standards in either future or current dollars. The cesium beam standards have been decreasing in cost by about 2.3% per year since 1966, and hydrogen masers have been decreasing by about 0.8% per year since 1978 relative to the NASA inflation index.*

## I. Introduction

The Deep Space Network (DSN) at JPL is often faced with estimating the future cost of systems and hardware, but reliable cost estimating models have not been developed. Since many organizations outside JPL successfully use cost curves for doing estimates, it is concluded that it would be worthwhile to develop similar cost curves for the DSN. It is hoped that this study will be the first of many aimed at developing cost estimating tools for use in the DSN.

Some of the most important and extensively used hardware in the DSN are frequency and timing standards. JPL has purchased over thirty in the last two decades and is still in the process of acquiring more. Thus, they are an excellent test bed for cost analysis since there exists a cost history as well as a need for estimating future costs.

This report first describes briefly the various types of frequency and timing standards used at JPL. Second, there is a discussion of the sources we used for our historical data. Next, the actual cost curves are presented along with recommendations on correcting for inflation. Finally, we show several sample calculations.

## II. Types of Frequency Standards Used by the DSN

The DSN is the primary user of frequency and timing standards at JPL. A few standards are used for calibration throughout the Lab, but the majority are installed for use by the DSN at Goldstone, Spain, and Australia. The standards derive their extreme accuracy from transitions in the hyperfine



energy states of atoms. The three most commonly used elements are hydrogen, cesium and rubidium.<sup>1</sup>

### A. Hydrogen Maser

The hydrogen maser is the most stable and accurate standard available. It has a frequency stability on the order of  $10^{-15}$  parts per thousand, and it is a secondary standard which means it must be externally calibrated. A control panel of a hydrogen maser can be seen in Fig. 1 and a more detailed block diagram (Ref. 1) of the system is shown in Fig. 2. The hydrogen maser is manufactured for JPL by the Smithsonian Astrophysical Observatory and costs around \$500K today. A purchase order must be filed before construction will begin so delivery time may be several years.

### B. Cesium Beam Standard

The cesium beam standard is the second most stable frequency standard with a stability on the order of  $10^{-14}$  parts per thousand. Figure 3 shows the most commonly used cesium standard, and a simple schematic (Ref. 2) is given in Fig. 4. The cesium is a primary standard so it need not be calibrated externally. Hewlett Packard has manufactured most of the cesium standards for JPL.

### C. Rubidium Vapor Standard

Finally, the DSN uses the rubidium vapor standard. The stability of this device is much lower than either of the other two, on the order of  $10^{-13}$  parts per thousand. As a result, the DSN has no future plans for acquiring any more and those in existence will ultimately be replaced by cesium standards. For this reason, a cost analysis of the rubidium standards was not done.

## III. Input Data Sources

Historical data for developing the models were obtained from two major sources: property records at JPL and purchase orders from the DSN's Frequency and Timing Systems (FTS) group. In addition, the people involved with buying frequency and timing standards for the DSN were interviewed.

JPL's Property Section maintains a comprehensive list of Laboratory property acquired and kept for about the past 25 years. The list is indexed by JPL identification number, manufacturer, nomenclature and model number (see Table 1 for an example of property indexed by model number). The FTS group gave us the model numbers for the frequency and timing standards. With these, the remaining information

could be looked up including the date received and the initial value placed on the standard.

From the FTS group, we also obtained the original purchase orders for all of the hydrogen masers and for those cesium standards purchased after 1978. The prices from these purchase orders plus subsequent JPL memos were used to develop our cost curves. For those cesium standards purchased before 1978, property values were used as cost data. However, purchase order costs and property record values for the cesium standards bought after 1978 were cross checked, and the agreement was within 2%.

We then met with FTS personnel and were able to confirm that our list of standards was complete. In addition it was found that a few standards had been loaned or given to JPL, so they were not used as data points.

## IV. Historical Cost Data

### A. Hydrogen Masers

All of the hydrogen masers acquired before 1978 were either built by JPL or obtained from other government agencies.

Historical cost data for more recent hydrogen masers purchased from the Smithsonian Astrophysical Observatory (S.A.O) are given in Table 2. Of the S.A.O. masers, only one has been delivered to JPL. It was received in December, 1979. Three others are being constructed for the DSN; two of these are scheduled for delivery in early 1985 and the third is due a few months later. The DSN is also in the process of buying two more masers. Both of these are to be ready by 1986.

### B. Cesium Beam Standards

The cost data for the cesium beam standards cover a much longer time span, starting in 1966, as shown in Table 3. Since 1966, the DSN has continued to acquire them periodically up until 1981. It is probable that more will be purchased in the future.

## V. Cost Curves and Equations

From the historical data we developed a cost curve for each standard. In the case of the cesium standard, there are several options that have been available since 1973 which have improved its stability and versatility. These options include a high-performance tube, clock, battery and charger, and a rack mounting kit. These generally account for about 25% of the total cost. However, JPL has had those options included in all of its cesium standards since 1973 so we included them as part of the total cost.

<sup>1</sup>R. I. Sydnor, *Frequency and Timing White Paper - Draft*, Jet Propulsion Laboratory, Pasadena, Calif., June 20, 1984 (unpublished).

## A. Hydrogen Maser Cost Equation

In Fig. 5, we see the cost of a hydrogen maser from 1978 through 1983. A best fit approximation of this curve is given by:

$$y = 1.103 \exp(0.072x) \quad (1)$$

where  $x$  is the year, for example in 1983  $x = 83$ , and  $y$  is the cost in thousands of dollars.

This curve has a correlation coefficient of .982 which indicates that it is a relatively good approximation of the data. The effective annual cost increase,  $j_h$ , for the period of 1978 to 1983 can be calculated from the equation

$$j_h = \left( \frac{c_1}{c_2} \right)^{1/n} \quad (2)$$

where  $c_1$  represents the latest costs in 1983,  $c_2$  represents the earliest cost in 1978, and  $n$  equals the number of years between the two. For the hydrogen maser,  $n = 5$ ,  $c_1 = \$429,897$  and  $c_2 = \$305,173$ . Thus,  $j_h$  is calculated to be 1.071 for an effective annual increase of 7.1% from 1978 to 1983.

## B. Cesium Beam Standard Cost Equation

In Fig. 6 is a similar model developed for the cesium beam standard. Note that the best fit approximation is also exponential:

$$y = 342.1 \exp(0.056x) \quad (3)$$

where  $x$  is the year, for example in 1983  $x = 83$ , and  $y$  is the cost in dollars. The correlation coefficient of .947 for this curve is also very high so the fit here is quite good. We can again use Eq. (2) to calculate the effective annual cost increase. Thus,  $j_c = 1.056$  for an effective annual rate of 5.6%. For this case,  $n = 18.25$  years. The quarter of a year (0.25) comes as a result of the three month period in 1976 when the U.S. Government shifted the beginning of the fiscal year from July 1 to October 1.

We can now estimate the future cost for a frequency and timing standard system by using Eq. (1) for hydrogen masers and Eq. (3) for cesium beam standards or equivalently by extrapolating from Figs. 5 and 6. More accurate graphical extrapolations may be obtained by replotting Figs. 5 and 6 using the logarithm of cost as a function of the year. However, the calculation of the cost of a future system in today's dollars must consider inflation.

## VI. Inflationary Impact

Since the impact of inflation varies with the industry, it is important to choose the proper index. Each year the NASA Inflation Index is published with rates based on the space industry, Bureau of Labor Statistics data, and related information<sup>2</sup>. Although it is not considered an "official" index, it is the one most closely associated with the work that goes on in the DSN. Table 4 gives the yearly inflation rate from 1966 to 1984 from the NASA Index. "TQ" refers to the transition quarter in 1976. The effective annual NASA inflation rate for this period was calculated from Eq. (1) as 7.9%. The impact on the value of the dollar since 1966 because of this inflation is shown in Fig. 7. The equation of the curve is given by

$$y = 0.007 \exp(0.076x) \quad (4)$$

where  $x$  is the year, for example in 1983  $x = 83$ , and  $y$  is the cost of what one dollar would purchase in 1966.

A summary of the effective annual inflation rate along with the effective annual increase in cost for each of the frequency standards is shown in Table 5. Also included in this table is the Consumer Price Index (CPI) annual inflation rate for 1966 through 1983. Note that this is about 1% lower than the annual inflation from the NASA Index. From this table we can also see that even though the cost of timing and frequency standards is increasing in budgeted dollars, it is decreasing in real dollars. For hydrogen masers this amounts to a 0.8% per year decrease and for the cesium standards the figure is 2.3% per year.

The actual cost of a future system found from Eqs. (1) and (3) can now be adjusted for inflation. To find the cost in today's dollars, several methods could be used. One might simply use the past NASA rate of 7.9% as the calculated value of the projected annual effective inflation rate. Thus, to bring the cost back to 1984 dollars simply divide it by  $(1.079)^k$  where  $k$  is the number of years into the future for which the estimate is to be made. A variation on this method is to choose your own inflation rate. Calculating the final cost in 1984 dollars is identical to the procedure above.

## VII. Sample Calculations

This section shows some sample calculations using each of the curves to calculate the cost of future systems, and if desired, how to adjust for inflation to get those costs in today's dollars. Let's assume you wanted to calculate the

<sup>2</sup>W. E. Ruhland, Transmittal of NASA Inflation Index, JPL IOMs (internal documents), Feb. 8, 1978, and Feb. 7, 1984, Jet Propulsion Laboratory, Pasadena, Calif.

cost of both a hydrogen maser and a cesium standard for 1988 in future dollars and today's dollars. For the hydrogen maser we use Eq. (1) with  $x = 88$ . We find that  $y = \$623,000$ . Now if you wanted to calculate this cost in 1984 dollars, using an inflation rate of 7.9%,  $(1.079)^4 = 1.355$ . Dividing this into the 1988 cost yields about \$459,000. If instead we choose an inflation rate of say 10%, we would get a cost in 1984 dollars of \$425,000.

For the cesium beam standard, Eq. (3) is used with  $x = 88$ . We find that  $y = \$47,245$  in 1988 dollars. Thus, in 1984 dollars the result is given by:

$$1984 \text{ cost} = \frac{\$47,245}{1.355} = \$35,000$$

And with the 10% rate, the cost in 1984 dollars is about \$32,300.

## VIII. Conclusion

The cost curves developed in this paper are very useful for estimating future costs of timing and frequency standards. Costs can now be calculated in both future and present dollars. Just as important, however, is the fact that this methodology can be used for developing cost estimating curves for other systems of hardware and software in the DSN. For example, there may be the potential of developing similar curves for maser amplifiers and receivers. As more DSN cost curves are developed, the job of cost estimating will become easier and more accurate estimates will result.

## Acknowledgement

P. F. Kuhnle and R. L. Sydnor were very helpful in supplying information on hydrogen masers and cesium beam standards.

## References

1. *Operating and Maintenance Manual*, for the Model VLG-10B, Atomic Hydrogen Maser, February, 1979, Smithsonian Institution Astrophysical Observatory.
2. *Operating and Service Manual for a Cesium Beam Frequency Standard*, 5061A Hewlett Packard Corporation, July, 1974.

**Table 1. Example of property listing by model number**

Gov't. ID	Nomenclature	Manufacturer	Model/Type	Mfr. Serial No.	Value, dollars
J270F100605	Standard Freq.	H.P.	5061-A	2002A01637	24,863.85
J270F100961	Standard Freq.	H.P.	5061-A	2002A01694	28,451.45
J270F100972	Standard Freq.	H.P.	5061-A	2002A01695	29,296.60
J270F101702	Standard Freq.	H.P.	5061-A	2002A01717	28,046.60

**Table 2. Hydrogen maser historical cost data (1978–1983)**

Fiscal Year	Cost, dollars
1978	305,173
1979	312,325
1980	341,000
1983	429,897

**Table 3. Cesium beam frequency standard historical cost data (1966–1984)**

Fiscal Year	Cost, dollars	Units
1966	15,500	1
1967	15,035	1
1968	16,106	1
1972	17,248	1
1977	24,319	3
1978	25,576	2
1979	26,350	2
1980	33,597	4
1981	35,024	5
1984	41,745 <sup>a</sup>	1

<sup>a</sup>Based on 1984 Hewlett Packard catalog not including remote monitor equipment. Where more than one unit is indicated, the costs have been averaged.

**Table 4. NASA Index of annual inflation rate (1966–1984)**

Fiscal Year	Rate, %
1966	3.4
1967	4.1
1968	5.0
1969	6.0
1970	8.0
1971	8.4
1972	5.7
1973	5.7
1974	7.2
1975	10.8
1976	9.0
TQ	2.1
1977	8.5
1978	7.8
1979	9.5
1980	10.7
1981	10.9
1982	9.4
1983	6.1
1984	6.2 <sup>a</sup>

<sup>a</sup>Estimated by NASA

**Table 5. Summary of effective annual costs and inflation rates**

NASA Inflation Index	7.9% (1966 – 1984)
Consumer Price Index	6.8% (1966 – 1983)
Hydrogen Maser	7.1% (1978 – 1983)
Cesium Beam Standard	5.6% (1966 – 1984)

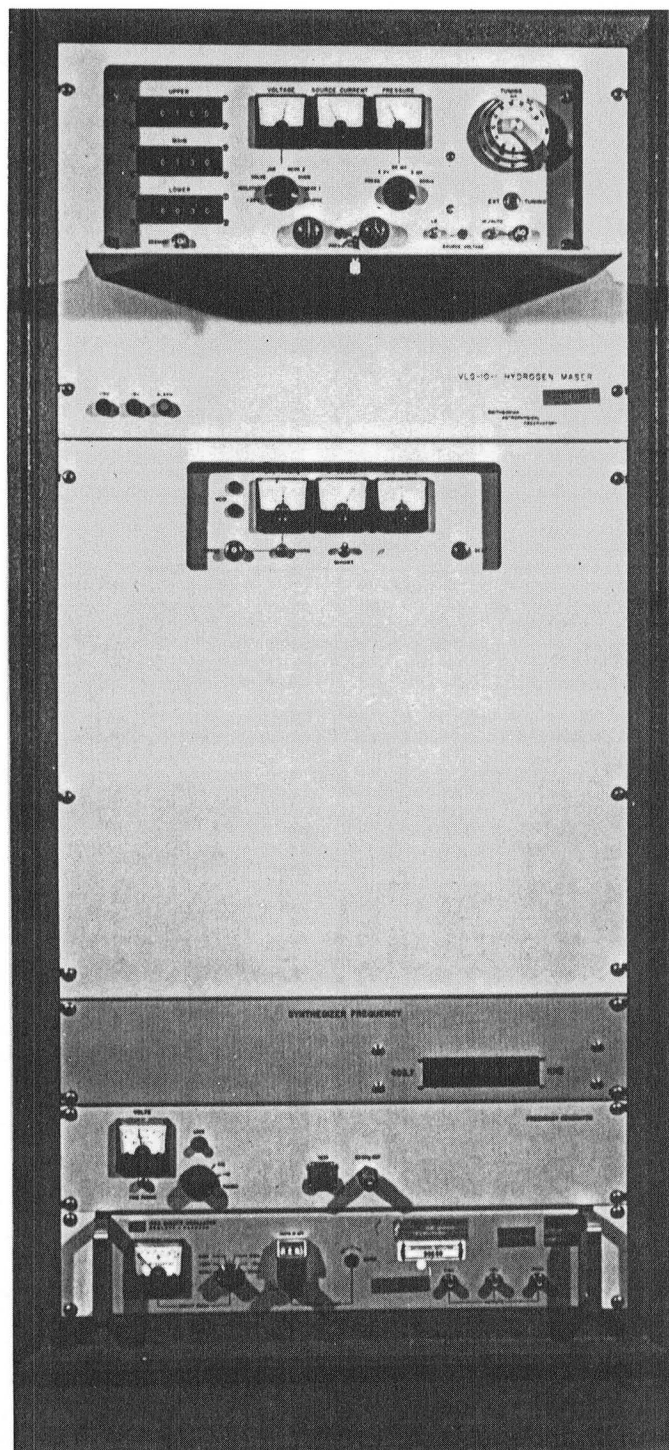
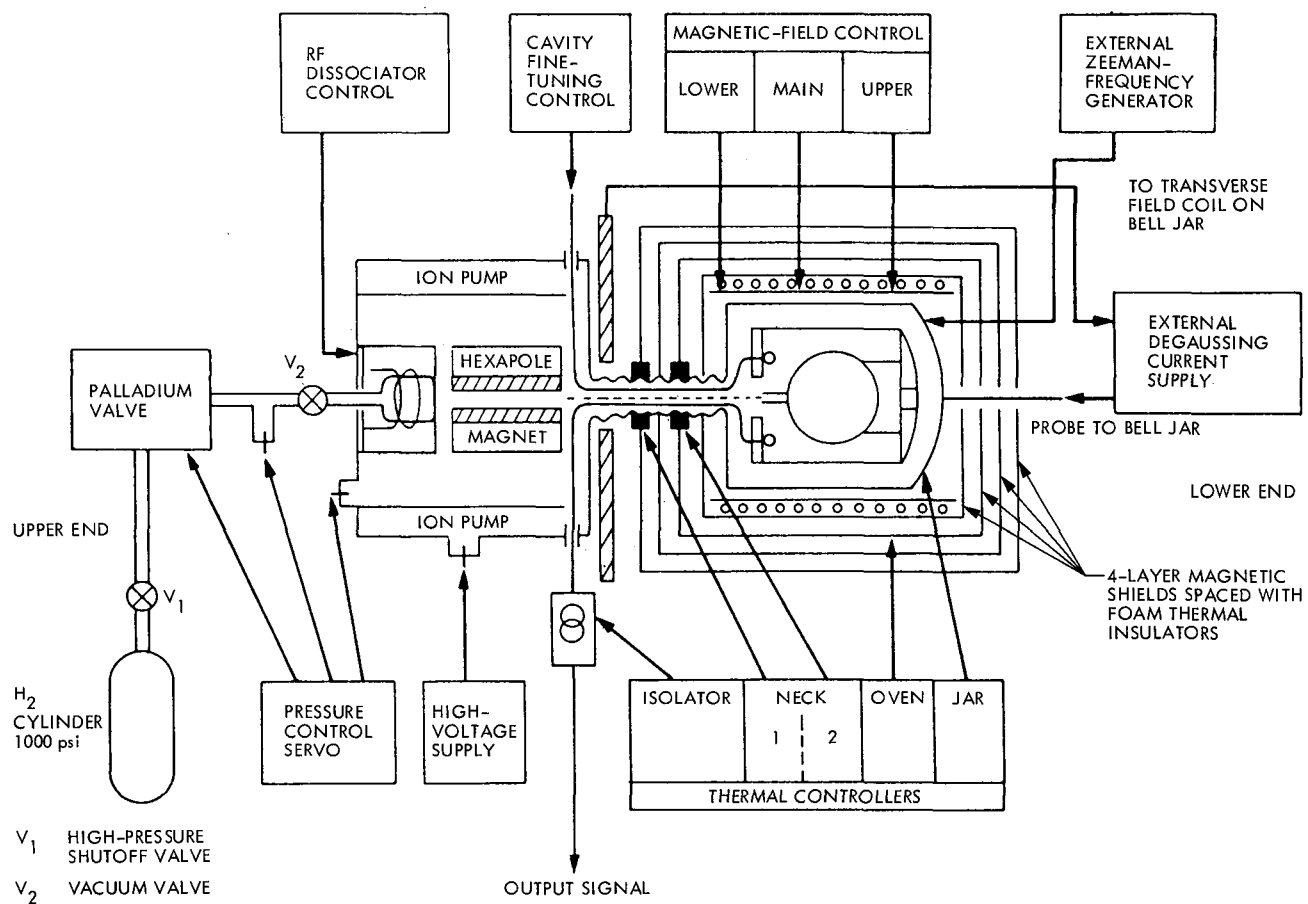


Fig. 1. Hydrogen maser control panel, Model VLG-10-0, Smithsonian Astrophysical Laboratory (from Smithsonian Astrophysical Laboratory)



**Fig. 2. Block diagram of the VLG-10B hydrogen maser system**

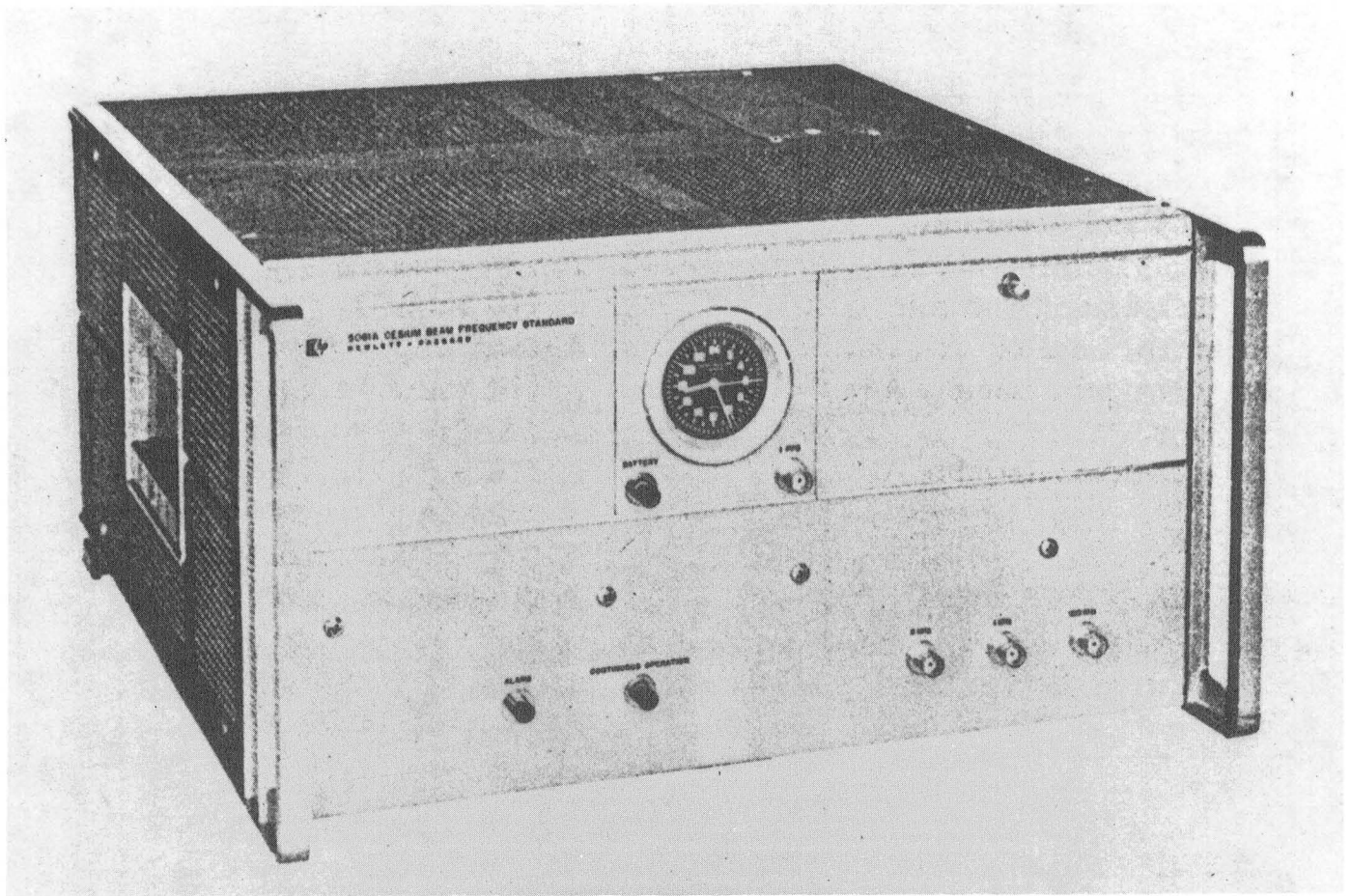


Fig. 3. Cesium beam frequency standard, Model 5061A, Hewlett Packard (from Ref. 2)

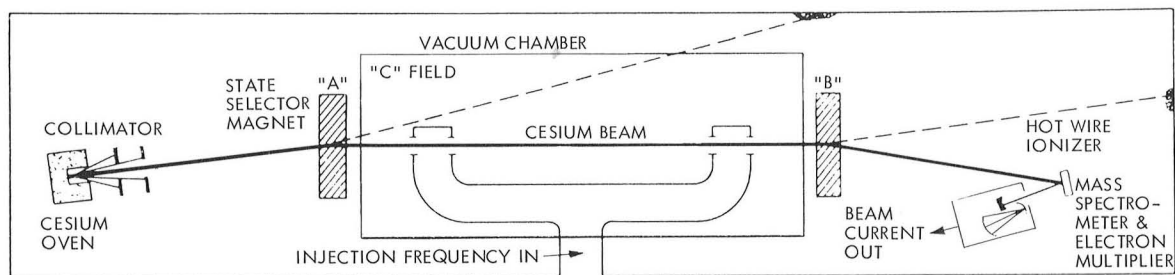


Fig. 4. Cesium beam tube schematic, Hewlett Packard, Model 5061A

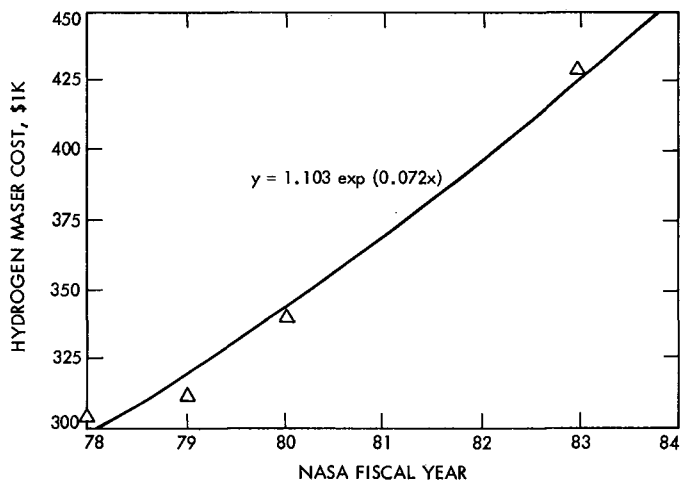


Fig. 5. Cost of a hydrogen maser from 1978 through 1983

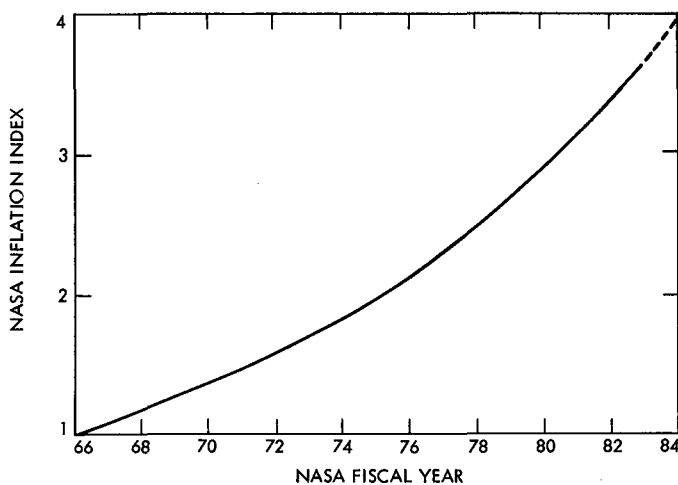


Fig. 7. NASA Inflation index for 1966 through 1984

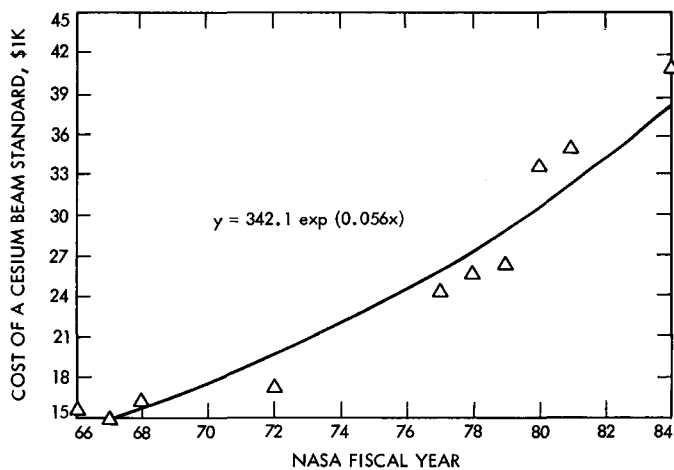


Fig. 6. Cost of a cesium beam standard from 1966 through 1984



# The Accuracy of Radio Interferometric Measurements of Earth Rotation

T. M. Eubanks, J. A. Steppe, and M. A. Spieth  
Tracking Systems and Applications Section

*The accuracy of VLBI earth rotation (UT1) measurements is examined by inter-comparing TEMPO and POLARIS data for 1982 and the first half of 1983. None of these data are simultaneous, and so a proper intercomparison requires accounting for the scatter introduced by the rapid, unpredictable, UT1 variations driven by exchanges of angular momentum with the atmosphere. A statistical model of these variations, based on meteorological estimates of the Atmospheric Angular Momentum (AAM) is derived, and the optimal linear (Kalman) smoother for this model is constructed. The scatter between smoothed and independent raw data is consistent with the residual formal errors, which do not depend upon the actual scatter of the UT1 data. This represents the first time that an accurate prediction of the scatter between UT1 data sets has been possible.*

## I. Introduction

Observations of extragalactic radio sources with VLBI between widely separated antennas can be used to make highly accurate measurements of the orientation and length of the vector between each pair of antennas (the baseline vector). Changes in baseline lengths are currently being monitored by several groups in the hope of eventually detecting tectonic motions over transcontinental or intercontinental distances. Changes in the baseline orientation are dominated by rotations of the earth as a whole. Independent Very Long Baseline Interferometry (VLBI) earth orientation estimates are now produced routinely by the POLARIS project of the National Geodetic Survey (NGS) (Ref. 1) and by the TEMPO program of the Deep Space Network (DSN) at the Jet Propulsion Laboratory (JPL) (Ref. 2). The VLBI data provide a

substantial reduction in the Root Mean Square (rms) scatter seen in previous UT1 intercomparisons (Refs. 3, 4, and 5).

Knowledge of the earth orientation is essential for accurate spacecraft navigation, and is of intrinsic geophysical interest (Refs. 6, 7, and 8). An understanding of the true errors in these VLBI measurements is essential to realizing their full potential. It is generally not possible to verify the full accuracy of baseline length measurements because of the lack of independent length determinations of comparable accuracy over the same baseline. Baseline orientation changes are dominated by changes in the total earth orientation, and it is thus possible to intercompare earth orientation results from widely separated baselines. The intercomparisons described in this article are thus of interest to all geodetic users of VLBI, as well as to those particularly interested in the UT1.

## II. VLBI Measurements of the UT1

The JPL TEMPO program monitors changes in earth orientation, together with station clock behavior, in support of interplanetary navigation by the DSN. TEMPO analyzes the results from two VLBI observing sessions per week, one each on the Spain-California (SC) and Australia-California (AC) DSN baselines. The SC baseline, with a latitude of only  $3^\circ$ , best determines the UT1, and only the TEMPO results from that baseline will be used in this article. The accuracy and density of these data have improved considerably since the lengthening of each observing session to a total of 3 hours in February 1982. Since some useful measurements are also available from January 1982, we started our intercomparison at the beginning of that year. Thirty TEMPO UT1 measurements are available for the period between 1982.0 and 1983.4. Two of these have formal errors  $> 2.0$  ms and comparable scatters; these had a negligible effect on our analysis and were excluded from further consideration. The remaining measurements have formal UT1 errors from 0.22 to 1.43 ms.

The POLARIS project was specifically established to monitor earth orientation changes with state-of-the-art VLBI equipment (Ref. 5). This project has conducted 24-hour observing sessions every week since June 1981, over the single baseline between the Westford Observatory in Massachusetts and the George R. Agassiz Station (GRAS) at Fort Davis, Texas. The latitude of this baseline is  $20^\circ$ . Some of the POLARIS experiments also involved simultaneous observations at the Onsala Space Observatory in Sweden. A total of 68 POLARIS UT1 measurements are available for the period between 1982.0 and 1983.4, with formal UT1 errors of 0.05 to 0.63 ms.

Any single-baseline VLBI experiment is sensitive to only two components of earth orientation. Since neither the TEMPO SC baseline nor the POLARIS Westford-GRAS baseline is exactly equatorial, neither can measure the UT1 directly. Both the TEMPO data and the POLARIS single-baseline UT1 estimates thus have a minor contribution from the Bureau International de L'Heure (BIH) smoothed Circular-D Polar Motion estimates. We assumed that these have a 10 milliarcsecond random error, found the induced UT1 error for each baseline, and found the rss of this error and the quoted formal error to better estimate the true formal error of each single-baseline UT1 estimate. The resulting formal errors are called the raw formal errors. We did not adjust the formal errors from the POLARIS multiple baseline experiments in any way.

Our null hypothesis is that the true measurement errors are independent random variables with standard deviations equal to the raw formal errors. The only way to test this hypothesis rigorously is by an intercomparison of independent

measurements. Since there are no simultaneous TEMPO and POLARIS measurements, any intercomparison will involve averaging or interpolating the data in some fashion. The scatter between a Kalman smoothing of one data set and independent raw data provides a useful test of both the data accuracy and the statistical model of the UT1. The various smoothings discussed in this analysis use data taken before 1982.0 to minimize any "edge effect" at the beginning of the intercomparison. The filter rapidly down-weights any old information, however, and the effect of including the pre-1982 data is small.

## III. Kalman Filtering and Smoothing of the UT1

The UT1 Kalman filter and smoother were developed at JPL as part of an effort to smooth and predict earth orientation changes for spacecraft navigation. The UT1 filter uses a statistical model of the unpredictable high-frequency UT1 fluctuations driven by exchanges of angular momentum with the atmosphere (Ref. 7). Meteorologically derived AAM data indicate that the UT1 power spectrum should be proportional to the frequency $^{-4}$  at periods  $< 100$  days (Ref. 8). A random process that obeys such a power law at all frequencies is an integrated random walk,

$$\frac{d^2 UT1}{dt^2} = W(t) \quad (1)$$

where  $W(t)$  is a white noise with a constant power spectral density,  $Q$ . (We are ignoring problems of existence of derivatives, etc., that can be handled rigorously, at the cost of loss of clarity (Ref. 9)). This model thus assumes that the torques on the solid earth can be described as a white noise, and that in the absence of these torques the rate of rotation of the solid earth would be a constant. For the filter to work properly, the UT1 model must provide realistic estimates of the UT1 signal-to-measurement-noise ratio (SNR), especially at frequencies where the true SNR is near unity. At frequencies where the true SNR is very large or very small, it is generally sufficient if the model SNR is also very large or very small, respectively. With modern measurement techniques and typical measurement densities, the SNR will be near unity for frequencies between 0.02 and 0.05 day $^{-1}$ . The seasonal variations in the UT1 are well above the noise, and the model SNR is also large at those frequencies, so we do not include these explicitly in the UT1 model. There are also predictable monthly and fortnightly UT1 oscillations of tidal origin. These are estimated from an a priori model (Ref. 10) and removed from all of the UT1 data before any further analysis.

Given a linear stochastic model, it is relatively straightforward to derive the corresponding Kalman filter (Refs. 9, 11, and 12). The forward filter, which estimates the UT1 based on

past and present data, is best described recursively in the state space formalism. The state vector corresponding to Eq. (1) is

$$\mathbf{X} = \begin{bmatrix} \text{UT1} \\ \frac{d\text{UT1}}{dt} \end{bmatrix} \quad (2)$$

Given estimates of the state  $\hat{\mathbf{X}}$ , and the covariance matrix  $\mathbf{P}$  at time  $T$ , the state estimate at a later time  $T + \Delta t$ , in the absence of measurements, is given by the state propagation equations:

$$\hat{\mathbf{X}}_{T+\Delta t} = \Phi(\Delta t) \hat{\mathbf{X}}(T) \quad (3a)$$

and

$$\mathbf{P}_{T+\Delta t} = \Phi(\Delta t) \mathbf{P}_T \Phi^T(\Delta t) + \int_T^{T+\Delta t} \Phi(T + \Delta t - t') \begin{bmatrix} 0 & 0 \\ 0 & Q \end{bmatrix} \Phi^T(T + \Delta t - t') dt' \quad (3b)$$

where

$$\Phi(\Delta t) = \begin{bmatrix} 1 & \Delta t \\ 0 & 1 \end{bmatrix}$$

is the state transition matrix. The integral in Eq. (3b) describes the increasing uncertainty induced by the unpredictable rapid fluctuations in UT1, and  $Q$  is thus a measure of the strength of these fluctuations. Based on our analysis of the AAM data, we adopted a value of  $0.0036 \text{ (ms/day)}^2/\text{day}$  for  $Q$ . Note that if  $Q$  is set to zero, the filter will simply fit a straight line to the data. When a new measurement is available, the optimum state estimate consists of the vector weighted average of the propagated state and the new measurement. This weighted average takes advantage of the correlation between the components of the state vector to determine both the UT1 and its derivative from a series of UT1 measurements. The optimal smoothing is the vector weighted average of the forward filter and a similar filter run backwards on the same data (Refs. 11 and 13).

## IV. Results

In our preliminary data analysis, we noticed a bias of 0.35 to 0.40 ms between the TEMPO and POLARIS data in all intercomparisons, including those with the pre-1982 data. Such biases arise from slight differences in the orientation of the reference frames used in the reduction of the two data

sets. We subtracted 0.375 ms from all of the TEMPO UT1 data used in this intercomparison. Figure 1 shows the raw TEMPO and POLARIS data, together with the Kalman smoothing of the combined data set, after subtracting the BIH smoothed Circular-D UT1, the tidal effects, and the TEMPO-POLARIS bias. One-sigma error bars are shown with the raw VLBI data. It is apparent that the TEMPO and POLARIS data agree at the ms level, and that there are UT1 fluctuations of up to 5 ms ignored by the Circular-D smoothing. The agreement between the two data sets is especially impressive considering that these are derived from completely independent efforts, using different equipment observing schedules, software, and procedures (Refs. 1 and 2).

Figure 2 shows our Kalman smoothing of the POLARIS data together with the raw TEMPO data, again after subtracting the BIH smoothed Circular-D data, the tidal model, and the TEMPO-POLARIS bias. The smoothing residuals (the difference between the raw and smoothed data in Fig. 2) are shown in Fig. 3, together with one-sigma error bars. Each residual formal error is the rss of the raw TEMPO formal error and the formal-error estimate of the POLARIS Kalman smoothing at that epoch. The rms scatter of these residuals is 0.57 ms, and the ensemble  $\chi^2$  is 35.4, for 28 degrees of freedom, which is consistent with the null hypothesis. The results of the  $\chi^2$  test should be regarded as an approximation of the true significance of the observed scatter since smoothing reduces the independence of the smoothing residuals. The rapid down-weighting of old information by the filter means that smoothing errors should have correlation times of a few weeks at most. The long-term correlation between the residuals in Fig. 3, if real, is thus probably not induced by the smoothing.

Any small random error not in the VLBI error budget would be most noticeable in the scatter of residuals with small formal errors. There are 17 residuals in Fig. 3 with formal error estimates  $< 0.5$  ms. These differences have an rms of 0.50 ms and a  $\chi^2$  of 26.5 with, of course, 17 degrees of freedom, again consistent with the null hypothesis. There do not seem to be any obvious outliers in this data set. In fact, none of the residuals in Fig. 3 are as much as three formal errors from zero. A similar analysis, with similar results, was conducted by comparing the smoothed TEMPO and the raw POLARIS data. The lower density of the TEMPO data introduces more correlation into the smoothing residuals, which complicates the interpretation of these results.

Since we implemented the Kalman smoother by a weighted average of forward and backward filters, it is easy to estimate the UT1 at the epoch of any measurement from an independent smoothing of all the other measurements. This

“excluded” smoothing thus provides a statistically independent estimate of the UT1 at the time of each measurement. We examined the scatter between each measurement, except the last, and the excluded smoothing of the combined VLBI data set. The residual formal error was again the rss of the raw data and smoothing formal errors. There are 95 such residuals, with an rms of 0.62 ms and a  $\chi^2$  of 123.9 (with 95 degrees of freedom). Of these differences, 44 have residual formal errors  $< 0.5$  ms, with a rms of 0.40 ms and a  $\chi^2$  of 44.1 with 44 degrees of freedom. Only one residual is more than three formal errors from zero. Although this point (at 4.6 formal errors from zero) is not likely to have occurred by chance, it is unclear if this is a true outlier or merely a symptom of unusually rapid changes in the UT1. There are enough excluded smoothing residuals to examine the scatter as a function of the residual formal errors for formal errors between 0.4 and 1.0 ms. Except for the possible outlier, the scatter is consistent with the formal error throughout this range. We attempted to estimate the variance (assumed to be a constant) of any unmodeled error in these residuals. The estimated variance was consistent with zero, and we think that it is unlikely that any such unmodeled random error could have a standard deviation as large as 0.4 ms.

An analysis of all three components of the earth orientation (Ref. 14), conducted after this paper was originally written, indicates that the POLARIS Westford Fort Davis single-baseline data have a substantial systematic error in one component. This error, which is partly seasonal in nature, is not present in the multiple-baseline POLARIS data. The

systematic error in the single-baseline data is probably due to tropospheric modeling errors and induces a systematic UT1 error with an rms scatter of  $\sim 0.34$  ms. The intercomparisons discussed in this article did not distinguish between multiple- and single-baseline results, and the temporal distribution of the available TEMPO data was not well suited for detecting seasonal systematic errors. It is not surprising that this error was not detected in the analysis presented in this paper.

## V. Conclusions

Our results show that VLBI determinations of the earth rotation from two independent efforts are consistent to within 0.4 to 0.5 ms (20 to 25 cm), and that the observed scatter is explained by the measurement formal errors and a statistical model for the rapid UT1 fluctuations driven by the atmosphere. These fluctuations will make it impossible to validate the subdecimeter VLBI formal errors without either a denser series of measurements or a set of exactly simultaneous data. The periods of intense activity planned during the MERIT campaign (Ref. 15) may provide the necessary raw material for such validations. Since this intercomparison uses only 1.3 years of data, it is insensitive to any long-period systematic errors. The accumulation and analysis of more VLBI data, as well as data from other techniques, will be necessary to fully understand the role of systematic errors in the earth rotation data. We plan to report on our analysis of all three components of the earth orientation in the future.

## Acknowledgments

We would like to thank W. E. Carter and D. S. Robertson for making the POLARIS data available and for their assistance. We would also like to thank J. O. Dickey, T. A. Herring, and R. W. King. The UT1 Kalman filter was implemented at JPL by D. C. Hernquist.

## References

1. Robertson, D. S., and Carter, W. E., in *Proc. Sym. No. 5*, NOAA Tech. Rep. 95, NGS 24, pp. 63-70. National Oceanic and Atmospheric Administration, Washington, D.C., 1982.
2. Eubanks, T. M., Roth, M. G., Esposito, P. B., Steppe, J. A., and Callahan, P. S., in *Proc. Sym. No. 5*, NOAA Tech. Rep. 95, NGS 24, pp. 81-90. National Oceanic and Atmospheric Administration, Washington, D.C., 1982.
3. Robertson, D. S., Carter, W. E., Eanes, R. J., Schutz, R. E., Tapley, B. D., King, R. W., Langley, R. B., Morgan, P. J., and Shapiro, I. I., *Nature*, Vol. 302, pp. 509-511, 1983.
4. Dickey, J. O., Williams, J. G., and Eubanks, T. M., in *Proceedings of the International Association of Geodesy (IAG) Symposia on Geodynamic Aspects of Earth Rotation*, International Union of Geodesy and Geophysics XVIIIth General Assembly, Hamburg, FRG, August 15-17, 1983, Ohio State University, 1984.
5. Carter, W. E., Robertson, D. S., Pettey, J. E., Tapley, B. D., Schutz, B. E., Eanes, R. J., and Lufeng, M., *Science*, Vol. 224, No. 4652, pp. 957-961, June 1, 1984.
6. Langley, R. B., King, R. W., Shapiro, I. I., Rosen, R. D., and Salstein, D. A., *Nature*, Vol. 294, pp. 730-733, 1981.
7. Hide, R., Birch, N. T., Morrison, L. V., Shea, D. J., and White, A. A., *Nature*, Vol. 286, pp. 114-117, 1980.
8. Eubanks, T. M., Steppe, J. A., Dickey, J. O., and Callahan, P. S., *J. Geophys. Res.*, in press, 1984.
9. Jazwinski, A. H., *Stochastic Processes and Filtering Theory*, Academic Press, New York, 1970.
10. Yoder, C. F., Williams, J. G., and Parke, M. E., *J. Geophys. Res.*, Vol. 86, No. B2, pp. 881-891, 1981.
11. Gelb A., Editor, *Applied Optimal Estimation*, The MIT Press, Cambridge, Mass., 1974.
12. Maybeck, P. S., *Stochastic Models, Estimation and Control*, Vol. 1, Academic Press, New York, 1979.
13. Maybeck, P. S., *Stochastic Models, Estimation and Control*, Vol. 2, Academic Press, New York, 1982.
14. Steppe, J. A., Eubanks, T. M., and Spieth, M. A., *EOS Trans. AGU*, Vol. 65, No. 45, p. 855, 1984.
15. Wilkins, G. A., *Project MERIT: A Review of the Techniques to be Used During Project MERIT to Monitor the Rotation of the Earth*. Joint Working Group on the Rotation of the Earth, IAU/IUGG. Royal Greenwich Observatory, Greenwich, England, 1980.

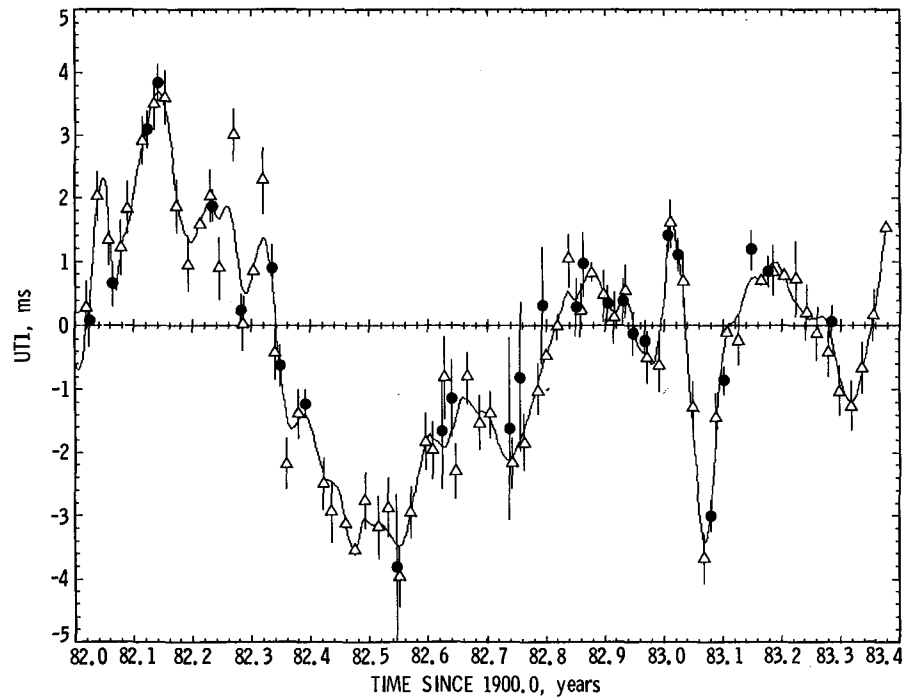


**Fig. 1.** The TEMPO (closed circles) and POLARIS (open triangles) UT1 estimates after subtracting the short-period tidal effects, the BIH smoothed Circular-D UT1, and the relative bias. One-sigma error bars are presented with each measurement. The solid line is the Kalman smoothing of the combined VLBI data set, also after subtraction of the Circular-D smoothing.

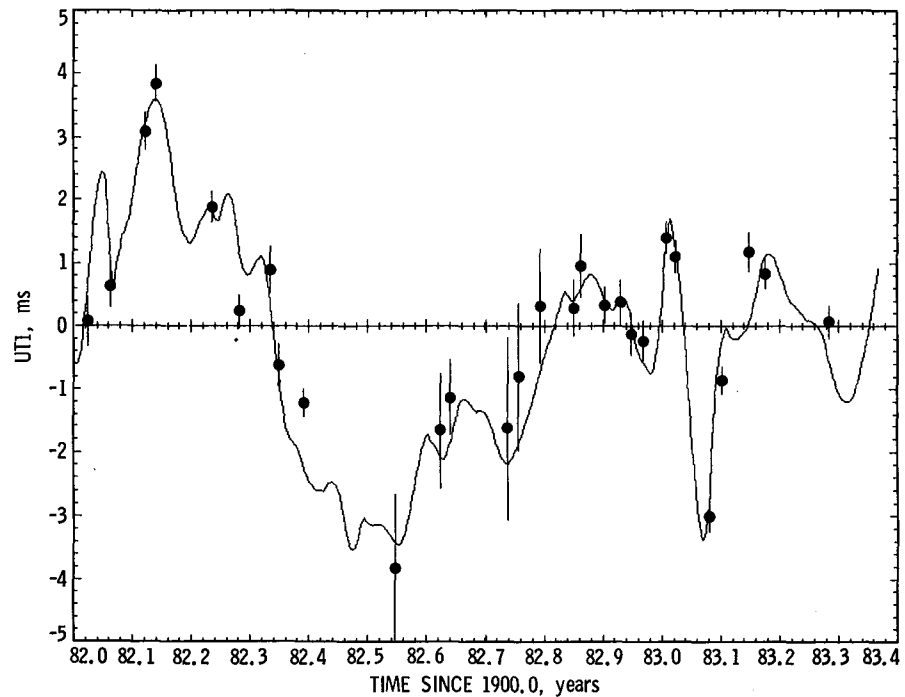


**Fig. 2.** The raw TEMPO data as given in Fig. 1, together with the Kalman smoothing of the POLARIS data, again after subtraction of the BIH smoothed Circular-D UT1 estimate, the tidal model, and the relative bias.

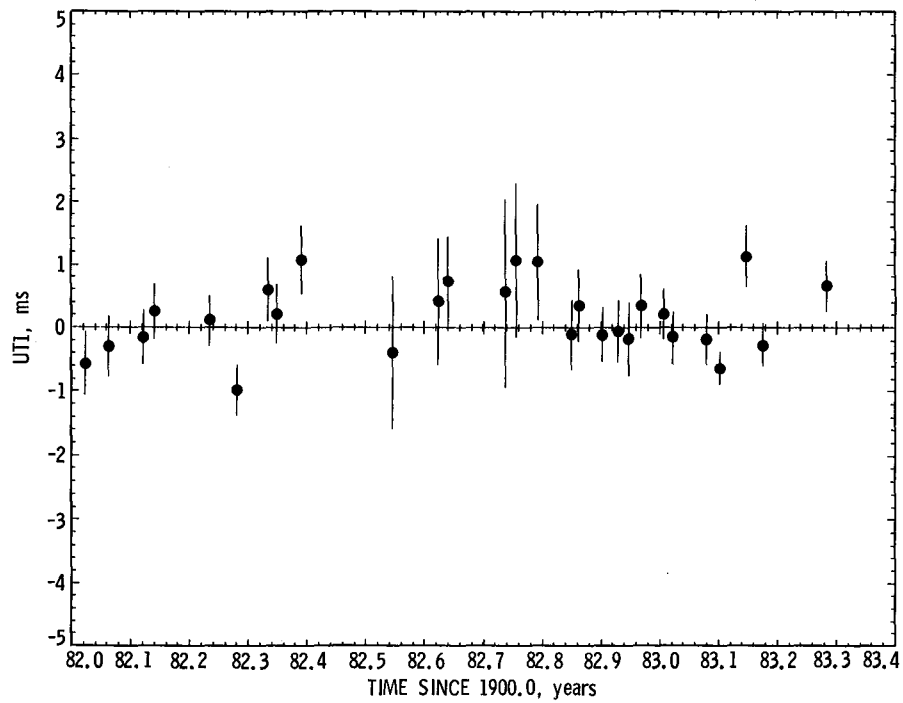


**Fig. 3.** The difference between the raw TEMPO data and the Kalman smoothed POLARIS data shown in Fig. 2. The error bars on these differences are the rss of the raw TEMPO formal errors and the error estimated by the POLARIS Kalman smoothing at the epoch of each TEMPO measurement.

# Codes With Parity Conditions on Subsets of Coordinates

E. C. Posner

Office of Telecommunications and Data Acquisition

Z. Reichstein

Harvard University, Graduate Student

*This article considers binary codes with the constraint that the codes restricted to certain subsets of columns must be contained in particular codes of the shorter lengths. In particular, we consider codes of even length  $2k$ , and of minimum distance  $\geq d$ , where the code obtained by restricting to the first  $k$  positions has even weight and at the same time the code obtained by restricting to the last  $k$  positions also has even weight. If  $k = 2n$ ,  $n$  odd, and  $d = 2n$ , we prove that the code has at most  $8n - 4$  codewords, and  $8n - 4$  is attainable for  $n = 3$ . This yields 20 binary words of length 12, distance  $\geq 6$ , where the number of 1's in the first six and the last six positions is even for every codeword in the code. This permits a file-transfer protocol control function assignment for personal computers to be chosen for 20 control functions using essentially just pairs of upper-case alphabetic ASCII characters where the Hamming distance between the binary forms of every two different control functions is at least six.*

## I. Introduction

In Ref. 1, the following problem was suggested: Find codes of the largest possible size with specified length and minimum Hamming distance where the shorter codes obtained by projecting the coordinates corresponding to a given partition of the coordinates are required to be contained in specified shorter codes. The examples in this paper require that the projection onto the first  $k$  coordinates must have even weight and similarity for the last  $k$ , where the length is  $2k$ .

The problem arose because simple file-transfer protocols for personal computers may have to be restricted for interbrand compatibility to just ASCII binary eight-tuples corresponding

to upper-case alphabetic characters, to avoid control characters that would be interpreted differently by machines of different manufacturers. Although the ASCII code is 8 bits, two of the bits are constant on the set of upper-case letters, and a third bit is parity. Hence, upper-case ASCII can be thought of as (26 of the 32) six-tuples of even weight. If we want control functions of two ASCII characters each, ignoring the constant 4 bits of the 16, our binary twelve-tuples are to have even weight in the first six positions and in the last, and we may want good distance properties to at least detect errors on noisy analog voice circuits. For example, we may want distance  $\geq 6$ , where the maximum distance possible is of course 12. Subject to the above, we find that a code of 20 codewords exists, and that this is the largest code possible with the above constraints.



The above result is a special case of the main result of this paper. Namely, for  $k$  an integer  $\geq 1$ , let:

- (1)  $A(2k, d)$  be the largest size of a binary code of length  $2k$  and minimum distance  $\geq d$ ;
- (2)  $B(2k, d)$  be the same as (a) but each codeword has an even number of 1's in its first  $k$  columns and in its last  $k$  columns;
- (3)  $C(2k, d)$  is the same as (a) but each codeword has an even number of 1's.

We see that, in general, for trivial reasons,

$$B(2k, d) \leq C(2k, d) \leq A(2k, d)$$

The function  $A$  is, of course, well known; the function  $B$  is much more interesting than  $C$  and is the main focus of this paper. (The  $C$ -values are trivially obtained from the  $A$ -values.) Above we said that we show  $B(12, 6) = 20$ . We will also show that for  $k = 2n$ ,  $n$  odd,  $B(4n, 2n) \leq 8n - 4$ , where  $B(12, 6)$  is the case  $n = 3$ . We present evidence that the  $8n - 4$  bound is the "right" one; if it fails for a certain  $n$  it is probably because certain Hadamard Matrices do not exist. We will also exhibit exact values or at least the tightest bounds we can for  $B(2k, d)$  and  $C(2k, d)$  for specific small values of  $k$  and  $d$ , and compare them with the well-known code sizes  $A(2k, d)$  obtained from published tables of error-correcting codes.

## II. Specific Values of $A$ , $B$ , and $C$

This section presents a table of the  $A$ ,  $B$ , and  $C$  functions for lengths  $2k$  up to 12 and all relevant  $d$ . Various techniques are used, some relying on later sections of this paper. The results are illustrated in Table 1. For simplicity, we call the  $A$ -function the *unconstrained* problem, the  $C$ -function the *even* problem, and the  $B$ -function the *even-even* problem. The most interesting even-even problems arise when the length is a multiple of 4, because then the code can contain antipodal codewords. References are given unless the result is obvious by inspection. Unreferenced values of  $A$  are taken from Ref. 2. Derivation of the results follow.

- (1)  $B(10, 4) = 32$ . If  $B(10, 4) > 32$ , there would be three "head" five-tuples with different "tails" in the code. The tails form a code of length 5, minimum distance  $\geq 4$ , but  $A(5, 4) = 2$ , not 3. So  $B(10, 4) \leq 32$ .

Here's how to get 32 even-even codewords of length 10 and mutual distance  $\geq 4$ , proving  $B(10, 4) = 32$ . Consider the length-five linear code of two elements 00000 and 11110, at distance 4. Calling this code  $G_1$ ,

let  $G_2, \dots, G_7$  be the seven other cosets of  $G_1$  in the vector space (group) of five-tuples of even weight.  $G_1$  is of dimension 4, so there are indeed eight cosets altogether. Our desired code is the set of  $32 = 8 \times 2 \times 2$  even-even ten-tuples  $\alpha_{ijk} = (\beta_{ij}, \beta_{ik})$ ,  $1 \leq i \leq 8$ ,  $1 \leq j, k \leq 2$ , where  $\beta_{ij}$  and  $\beta_{ik}$  are in  $G_i$ . Each  $G_i$  is, of course, a distance-4 code, in its own right.

Now if  $i_1 \neq i_2$ ,  $d(\beta_{i_1 j}, \beta_{i_2 k}) \geq 2$ , where  $d$  is Hamming distance. This is because  $\beta_{i_2 j} \neq \beta_{i_2 k}$  if  $i_1 \neq i_2$  because the cosets partition the space. And all nonzero distances are at least 2, being even. So  $d(\alpha_{i_1 j_1 k_1}, \alpha_{i_2 j_2 k_2}) \geq 2 + 2 = 4$  if  $i_1 \neq i_2$ .

Finally, if  $i_1 = i_2$ ,  $d(\alpha_{ijk}, \alpha_{ij'k'}) \geq 4$  if  $j' \neq j$  or  $k' \neq k$ , i.e., if the elements are distinct. For  $\alpha_{ijk}$  differs from  $\alpha_{ij'k'}$ , in either head or tail (or both), and we have observed that each  $G_i$  is a distance-4 code. This completes the proof that  $B(10, 4) = 32$ .

- (2)  $B(10, 6) = 5$ . The following five ten-tuples are at mutual distance 6 or greater:

00000	00000
11110	11000
11101	00110
00101	11011
10010	01111

This shows  $B(10, 6) \geq 5$ . We show  $B(10, 6) \leq 5$  as follows. By complementing an even number of columns in each half, we can assume the all-0 word is in the code. If there were three left halves of weight 4, and so mutual distance 2, then right halves would be at mutual distance 4, contradicting  $A(5, 4) = 2$ . So there are at most two four-tuples on the left and two on the right. If there were six codewords, then there would be three two-tuples on the left (and on the right). Two of these heads are at distance 2, because  $A(5, 4) = 2$ . Their tails are at distance 4. But their tails are of weight 4, for the distance of the entire codeword from the 0 codeword is at least 6. Two five-tuples of weight 4 if different are at distance 2. So we do not have three two-tuples as heads, and  $B(10, 6) \leq 5$ .

- (3)  $B(12, 4) = 128$ . There are  $32 = 2^5$  distinct even-weight six-tuples from which to choose our heads and tails. If one even-weight six-tuple occurred more than four times as a head, we would have five tail six-tuples at mutual distance  $\geq 4$ , contradicting  $A(6, 4) = 4$ . So  $B(12, 4) \leq 4 \times 32 = 128$ .

To show  $B(12, 4) \geq 128$ , we construct 128 even-even codewords of distance  $\geq 4$  analogous to the construction for  $B(10, 4)$  in (1) above. Here  $G_1$ , a constant-distance 4 linear code, is

000000  
111100  
001111  
110011

(It is the (3, 2) simplex code with columns doubled.) Again there are eight cosets altogether, and the even-even code of length 12 has  $8 \times 4 \times 4 = 128$  codewords. The rest is the same as before. So  $B(12, 4) \geq 128$ , and indeed  $B(12, 4) = 128$ .

- (4)  $B(12, 8) = 4$ . We know  $B(12, 8) \leq A(12, 8) = 4$ . Here is how to get four even-even twelve-tuples of mutual distance  $\geq 8$ : Use  $C(6, 4) = 4$ , and write each "1" as "11," each "0" as "00." This doubles the length to 12, doubles the minimum distance to 8, and insures an even number of ones in any even number of consecutive columns starting an odd number of columns from the left, such as column 1 or column 7 with six columns.

This completes verification of all the entries in Table 1 except  $B(12, 6) = 20$ , which will follow from subsequent results.

### III. $B(4n, 2n)$ When $n$ Is Even

First note that if  $n$  were even, and there happened to exist, as there usually does, a  $2n \times 2n$  Hadamard Matrix  $H$ , we could proceed as follows. We can make one row of  $H$  all 1's, by reversing columns. Then every row of  $H$  has an even number of -1's, either 0 (one row) or  $n$  ( $2n - 1$  rows). Let  $H_0$  be  $H$  under the mapping  $1 \rightarrow 0, -1 \rightarrow 1$ ; every row of  $H_0$  has an even number of 1's. The  $4n \times 4n$  matrix (or code) given by the well-known tensor product construction

$$H_{4n}^0 = \begin{pmatrix} H_0 & H_0 \\ H_0 & \bar{H}_0 \end{pmatrix}$$

is even-even. Here  $\bar{H}_0$  is the mod-2 complement of  $H_0$ , and is also even.

The distance between any two codewords of  $H_{4n}^0$  is found as follows. If their heads are identical, their tails are complementary, and the distance is  $2n$ . If they both lie in the top or bottom half, the distance is  $n + n = 2n$ . And if one is in the top half and one in the bottom half with unequal heads, the distance is also  $n + n = 2n$ . So  $H_{4n}^0$  is an even-even Hadamard Matrix, or an even-even code of length  $4n$  and distance  $2n$ . We can now throw in the mod-2 complements of the  $4n$  codewords as well, to get an even-even code of length  $4n$  with  $8n$  codewords of minimum distance  $2n$ ; each word is of distance  $4n$  from exactly one other word, its mode-2 complement. This construction shows  $B(4n, 2n) \geq 8n$  if  $n$  is even and a  $2n \times 2n$  Hadamard Matrix exists.

Even without the even-even condition, it is well-known (and easy) that  $A(4n, 2n) \leq 8n$  (Ref. 2, p. 43, Cor. 4, or Ref. 3, Thm. 1). Thus  $B(4n, 2n) = 8n$  when  $n$  is even if a  $2n \times 2n$  Hadamard Matrix exists. It is much more difficult to find  $B(4n, 2n)$  when  $n$  is odd, even if we are willing to assume that convenient Hadamard Matrices exist. We suspect that our upper bound of  $8n - 4$  is really the "right" answer, but we have been able to verify it only when  $n = 1$  ( $B(4, 2) = 4$ ) and  $n = 3$  ( $B(12, 6) = 20$ ). This we start to do in the next section.

### IV. $B(4n, 2n)$ When $n$ Is Odd

This section has some preliminary vector space results needed to upper bound  $B(4n, 2n)$  when  $n$  is odd. The  $n$ -odd case is considerably more difficult than the  $n$ -even case. We will show that  $B(4n, 2n) \leq 8n - 4$  when  $n$  is odd. In the following section, we show that the bound is attained when  $n = 3$ ; Table 1 shows that the bound is attained for  $n = 1$ . Specifically, we solve the following problem in the next few sections:

**Problem.** Let  $n$  be an odd integer, and let  $a_1, \dots, a_k$  be binary codewords of length  $4n$ . Suppose that each  $a_i$  has an even number of 1's among its first  $2n$  coordinates. Also suppose  $d(a_i, a_j)$  (the Hamming distance between  $a_i$  and  $a_j$ ) is equal to or greater than  $2n$  for all  $1 \leq i, j \leq k$ . Then  $k \leq 8n - 4$ .

**Definition:** Let  $F = \{f_1, \dots, f_k\}$  be a collection of vectors in the Euclidean space  $\mathbf{R}^s$ . Then we say that  $F$  satisfies:

Condition (1) if  $f_i \neq 0$  and  $f_i \cdot f_j \leq 0, 1 \leq i \neq j \leq k$ .

Condition (2) if all coordinates of  $f_1, \dots, f_k$  are  $\pm 1$  in some basis of  $\mathbf{R}^s$ .

Now suppose  $s$  is even and  $F$  satisfies Condition (2). Fix some basis such that the coordinates of  $f_1, \dots, f_k$  are  $\pm 1$  in that basis. Then we can define  $w(f_i) =$  the number of 1's among the first  $s/2$  coordinates of  $f_i$ . We say that  $F$  satisfies:

Condition (3) if it satisfies Condition (2),  $s$  is even and in some basis of  $\mathbf{R}^s$ , and  $w(f_i)$  is even for all  $i$ .

Using this terminology, our problem can be restated in the following way:

Let  $n$  be an odd integer. Then if  $\{f_1, \dots, f_k\}$  in  $\mathbf{R}^{4n}$  satisfies Conditions (1), (2), and (3), then  $k \leq 8n - 4$ .

To see that this statement is equivalent to the original problem, replace all zeros by -1's in the binary representation of  $a_i$ , and view the resulting  $4n$ -tuple as a vector  $f_i$  in  $\mathbf{R}^{4n}$ .

## V. Some Relevant Facts From Linear Algebra

In this section we shall study the properties of the collections of vectors  $F = \{f_1, \dots, f_k\}$  from  $\mathbf{R}^s$  satisfying Condition (1). The underlying space  $\mathbf{R}^s$  will play no role in this section, since it can always be replaced by  $\text{span}(F)$ . For this reason we will omit any references to it.

**Proposition 1:** Let  $F = \{f_i, \dots, f_k\}$  for  $k \geq 3$  satisfy Condition (1) and suppose the inner product  $f_{k-1} \cdot f_k < 0$ . Then  $\text{rank}(f_1, \dots, f_{k-2}) \leq \text{rank}(F) - 1$ .

**Proof:** Assume the contrary:  $f_1, \dots, f_{k-2}$  generate  $M = \text{span}(F)$ . Let  $\text{rank}(F) = \dim M = m$ . We can assume without loss of generality that  $f_1, \dots, f_m$  is a basis of  $M$ . We want to apply the Gram-Schmidt orthogonalization procedure to this basis. Let

$$e_1 = \frac{f_1}{\|f_1\|}$$

$$e_p = \left( f_p - \sum_{i=1}^p (f_p \cdot e_i) e_i \right) / \left\| f_p - \sum_{i=1}^p (f_p \cdot e_i) e_i \right\|$$

for  $p = 2, 3, \dots, m$

We claim that the collection  $F_p = \{e_1, e_2, \dots, e_p, f_{p+1}, \dots, f_k\}$  satisfies Condition (1) for  $p = 1, \dots, m$ .

We induce on  $p$ . For  $p = 1$  the claim is obvious. Suppose we know it for some  $1 \leq p \leq m$ . Then to prove it for  $p + 1$  we have to show that

- (1)  $e_{p+1} \cdot e_i \leq 0$  for  $i = 1, 2, \dots, p$ .
- (2)  $e_{p+1} \cdot f_j \leq 0$  for  $j = p + 2, \dots, m$ .

Here (1) is obvious, since  $e_{p+1}$  is orthogonal to  $e_i$  by construction. To prove (2), observe that

$$e_{p+1} \cdot f_j = \frac{1}{\left\| f_{p+1} - \sum_{i=1}^{p+1} (f_{p+1} \cdot e_i) e_i \right\|} \cdot \left( f_p \cdot f_j - \sum_{i=1}^p (f_p \cdot e_i) (e_i \cdot f_j) \right)$$

Here

$$f_p \cdot f_j \leq 0, f_p \cdot e_i \leq 0, e_i \cdot f_j \leq 0, i = 1, \dots, p$$

by our induction assumption. Hence, the expression on the right is nonpositive, as desired. This proves the claim.

Therefore,  $\{e_1, \dots, e_m, f_{m+1}, \dots, f_k\}$  satisfies Condition (1). By our assumption,  $f_{k-1}, f_k$  are in  $M = \text{span}(e_1, \dots, e_m)$ . Write

$$f_{k-1} = \sum_{i=1}^m a_i e_i$$

and

$$f_k = \sum_{i=1}^m b_i e_i$$

Then

$$f_{k-1} \cdot e_i \leq 0 \text{ implies } a_i \leq 0, i = 1, \dots, m$$

$$f_k \cdot e_i \leq 0 \text{ implies } b_i \leq 0, i = 1, \dots, m$$

From this, we see that

$$0 > f_{k-1} \cdot f_k = \sum_{i=1}^m a_i b_i \geq 0$$

a contradiction. Therefore,  $f_1, \dots, f_{k-2}$  cannot generate all of  $M$ . This proves Proposition 1.

Proposition 1 has the following well-known Corollary, which immediately implies the inequality  $A(4n, 2n) \leq 8n$  (Ref. 3, Thm. 1). Here we give a proof based on Proposition 1.

**Corollary 1:** Let  $F = \{f_i, \dots, f_k\}$  satisfy Condition (1) of the previous section. Then  $k \leq 2 \text{rank}(F)$ .

**Proof:** We induce on  $\text{rank}(F)$ . When  $\text{rank}(F) = 1$  the corollary is obvious. Now suppose we know it for  $\text{rank}(F) = 1, 2, \dots, m(m \geq 1)$ , and we want to prove it for  $\text{rank}(F) = m + 1$ . We can assume without loss of generality that  $k \geq 3$ . Suppose  $k > 2(m + 1)$ . Then clearly  $f_1, \dots, f_k$  cannot be mutually orthogonal; say  $f_{k-1} \cdot f_k < 0$ . Proposition 1 implies  $\text{rank}(f_1, \dots, f_{k-2}) \leq m$ . Hence, by our induction assumption,  $k - 2 \leq 2 \text{rank}(F) \leq 2m$ , i.e.,  $k \leq 2(m + 1)$ , a contradiction.

The same argument also proves the following:

**Corollary 2:** Let  $F = \{f_1, \dots, f_k\}$  satisfy Condition (1), and suppose  $k > \text{rank}(F)$ . Then  $F$  contains a subcollection of  $k - \text{rank}(F)$  mutually orthogonal vectors.

**Proposition 2:** Let  $F = \{f_1, \dots, f_k\}$ ,  $k > (3/2)m = (3/2)\text{rank}(F)$  satisfy Condition (1). Then there exists  $G = \{g_1, \dots, g_k\}$  with the following properties:

- (1)  $g_1, \dots, g_{k-m}$  are in  $F$  and are mutually orthogonal.
- (2)  $g_{k-m+1} = -g_1, \dots, g_{3k-4m} = -g_{2k-3m}$ .
- (3)  $g_{3k-4m}, \dots, g_k$  are in  $F$ .
- (4)  $G$  satisfies Condition (1).

**Proof:** By Corollary 2 we can assume that  $f_1, \dots, f_{k-m}$  are mutually orthogonal. Choose an orthonormal basis  $e_1, \dots, e_m$  in span  $(F)$  such that

$$e_i = \frac{f_i}{\|f_i\|} \text{ for } i = 1, \dots, k-m$$

Let  $f_j = (\alpha_j^1, \dots, \alpha_j^{k-m}, \dots, \alpha_j^m)$  in this basis for  $k-m+1 \leq j \leq k$ . Then  $f_j \cdot f_1 \leq 0, \dots, f_j \cdot f_{k-m} \leq 0$ , which implies that for all  $k-m+1 \leq j \leq k$ ,  $\alpha_j^1, \dots, \alpha_j^{k-m} \leq 0$ .

Let  $v_j = (\alpha_j^{k-m+1}, \dots, \alpha_j^m)$ . Then

$$v_{j_1} \cdot v_{j_2} = f_{j_1} \cdot f_{j_2} - \sum_{i=1}^{k-m} \alpha_{j_1}^i \alpha_{j_2}^i \geq f_{j_1} \cdot f_{j_2} \geq 0$$

Hence, the vectors  $\{v_j: j = k-m+1, \dots, k\}$  (or those of them that are nonzero, to be precise) satisfy Condition (1). Here  $\text{rank}\{v_j: j = k-m+1, \dots, k\} \leq m - (k-m) = 2m-k$ . Hence, by Corollary 1, at most  $4m-2k$  of the  $v_j$ 's are nonzero. So (permuting the  $f_j$ 's, if necessary), we have the following picture:

$$f_1 = (\|f_1\|, 0, 0, \dots, 0^{(k-m)}, 0, \dots, 0)$$

$$f_2 = (0, \|f_2\|, 0, \dots, 0, 0, \dots, 0)$$

.

.

.

$$f_{k-m} = (0, \dots, \dots, \|f_{k-m}\|, 0, \dots, 0)$$

$$f_{k-m+1} = (\beta_1^1, \dots, \dots, \beta_1^{(k-m)}, 0, \dots, 0)$$

.

.

.

$$f_{3k-4m} = (\beta_{2k-3m}^1, \dots, \dots, \beta_{2k-3m}^{(k-m)}, 0, \dots, 0)$$

$$f_{3k-4m+1} = (\gamma_1^1, \dots, \dots, \gamma_1^{(k-m)}, v_1)$$

.

.

.

$$f_k = (\gamma_{4m-2k}^1, \dots, \dots, \gamma_{4m-2k}^{(k-m)}, v_{4m-2k})$$

Here, as we showed above, all  $\beta_j^i$  and  $\gamma_j^i$  are  $\leq 0$ .

We claim the following. Suppose  $\beta_j^i < 0$  for some  $1 \leq i \leq k-m$ ,  $1 \leq j \leq 2k-3m$ . Then every other  $\beta$  and every other  $\gamma$  in the  $i$ th column must be equal to 0. Indeed, suppose  $\gamma_s^i < 0$  for some  $s$ . Then

$$0 \geq f_j \cdot f_s = \sum_{t=1}^{k-m} \beta_j^t \gamma_s^t > 0$$

(the  $i$ th term is  $> 0$  and the other terms are all  $\geq 0$ ) and we get a contradiction. The same argument shows that  $\beta_s^i = 0$  for  $s \neq j$ .

Now, since each  $f_j$  has at least one nonzero coordinate, we can assume that  $\beta_1^1 \neq 0, \beta_2^2 \neq 0, \dots, \beta_{2k-3m}^{2k-3m} \neq 0$ . Then our claim proves that the collection  $\{f_1, \dots, f_{k-m}, -f_1, \dots, -f_{2k-3m}, f_{3k-4m+1}, \dots, f_k\}$  satisfies Condition (1). This proves Proposition 2.

## VI. Linear Dependence of $(-1, 1)$ Vectors

In this section we shall study the collections  $F = \{f_1, \dots, f_k\}$  of  $\mathbf{R}^s$  satisfying Condition (2). Some elementary lemmas are in order.

**Lemma 1:** Let  $A = (a_{ij})$  be an  $n \times n$  matrix with all  $a_{ij} = \pm 1$ . Then

- (1) If  $n = 2$ ,  $\det A = 0, \pm 2$ .
- (2) If  $n = 3$ ,  $\det A = 0, \pm 4$ .
- (3) If  $n = 4$ ,  $\det A = 0, \pm 8, \pm 16$ .

**Proof:** If we subtract the first row of  $A$  from the other  $n-1$ , then the last  $n-1$  rows will have entries  $0, \pm 2$ . This shows that  $\det A$  is divisible by  $2^{n-1}$ . On the other hand, if we denote the row vectors of  $A$  by  $a_1, \dots, a_n$  then  $|\det A| \leq \|a_1\| \cdot \|a_2\| \cdot \dots \cdot \|a_n\|$  (because  $|\det A|$  = measure of the  $n$ -parallelopiped spanned by the  $a_i$ )  $= (\sqrt{n})^n$ . Combining these two properties ( $2^{n-1} \mid \det A$  and  $|\det A| \leq (\sqrt{n})^n$ ) we get (1), (2), and (3). This proves Lemma 1.

We recall the following standard terminology:

**Definition:**  $F = \{f_1, \dots, f_k\}$  is *minimally linearly dependent* if  $F$  is linearly dependent but any proper subcollection of  $F$  is linearly independent.

Clearly if  $F$  is minimally linearly dependent, then  $k = \text{rank}(F) + 1$ . We can now prove Lemma 2.

**Lemma 2:** Suppose  $F = \{f_1, \dots, f_k\}$  satisfies Condition (1) of Section 4 (nonpositive inner product). Then if

- (1)  $\text{Rank}(F) = 1$  with  $k = 2$ ,  $F$  is minimally linearly dependent if and only if  $f_1 = -f_2$ ;
- (2)  $\text{Rank}(F) = 2$ ,  $F$  cannot be minimally linearly dependent;
- (3)  $\text{Rank}(F) = 3$  with  $k = 4$ ,  $F$  is minimally linearly dependent if and only if  $f_1 = k_2 f_2 + k_3 f_3 + k_4 f_4$  with  $k_i = \pm 1$  for  $i = 2, 3, 4$ ;
- (4)  $\text{Rank}(F) = 4$  with  $k = 5$ ,  $F$  is minimally linearly dependent if and only if  $k_1 f_1 = k_2 f_2 + \dots + k_5 f_5$  with  $k_i$  chosen from  $\{\pm 1, \pm 2\}$ .

**Proof:** (1) is obvious. If  $F$  satisfies Condition (2) and is minimally linearly dependent, then we can write  $f_1$  as

$$\sum_{i=2}^k \alpha_i f_i, \quad \alpha_i \neq 0, \quad \text{all } i$$

In coordinates (using the basis that represents the  $f_i$ 's as  $(-1, 1)$  vectors), if  $f_i = (f_i^1, \dots, f_i^s)$ ,  $f_i^j = \pm 1$ , this equality becomes the system of linear equations

$$\sum_{i=2}^k \alpha_i f_i^j = f_1^j, \quad j = 1, 2, \dots, s$$

Since  $F$  is minimally linearly dependent,

$$\text{rank}(f_s^i)_{\substack{i=2, \dots, k \\ j=1, \dots, s}} = k - 1$$

and the  $\alpha_i$  can be computed (using Cramer's rule) as ratios of the determinants of two  $(k-1) \times (k-1)$  matrices whose entries are  $f_s^i$ , i.e.,  $\pm 1$ . Since  $F$  is minimally linearly dependent, none of the  $\alpha_i$ 's can be 0. Thus Lemma 1 gives (3) and (4).

To prove (2), observe that by Lemma 1, the only possibility is  $\alpha_1, \alpha_2 = \pm 1$ , i.e.,  $f_1 = \pm f_2 \pm f_s$ . The entries of  $\pm f_2 \pm f_s$  have to be 0,  $\pm 2$ , and the entries of  $f_1$  are  $\pm 1$ . This proves (2).

**Lemma 3:** Let  $F = \{f_1, \dots, f_k\}$  satisfy conditions (1) and (2) and be minimally linearly dependent with  $\text{rank } F = m$ .

Then

- (1) If  $m = 3, k = 4$ , then  $f_1 + f_2 + f_s + f_4 = 0$ ;
- (2) If  $m = 4, k = 5$  then  $k_1 f_1 + k_2 f_2 + \dots + k_5 f_5 = 0$  with  $k_1, \dots, k_5$  chosen from  $\{1, 2\}$ .

**Proof:** (1) Assume the contrary. Lemma 2 says that  $k_1 f_1 + k_2 f_2 + k_3 f_3 + k_4 f_4 = 0$ , where  $k_1, k_2, k_3, k_4 = \pm 1$ . We can assume without loss of generality that  $k_1 = k_2 = 1, k_4 = -1$ . Taking the inner product of both sides with  $f_4$ , we get  $f_1 \cdot f_4 + f_2 \cdot f_4 + k_3 f_3 \cdot f_4 - f_4 \cdot f_4 = 0$ . But  $f_4 \cdot f_4 = s$ , while  $f_1 \cdot f_4 \cdot f_2 \cdot f_4 < 0$ . Hence,  $k_3 (f_3 \cdot f_4) - s \geq 0$  so  $|f_3 \cdot f_4| \geq s$ . But  $\|f_s\| = \|f_4\| = \sqrt{s}$ . Hence,  $|f_s \cdot f_4| \leq s$ , with equality if and only if  $f_4 = -f_3$ . Since we assumed that  $\{f_1, \dots, f_4\}$  is minimally linearly dependent, this is impossible. This proves (1).

(2) Again, assume the contrary. Lemma 2 says that

$$\sum_{i=1}^5 k_i f_i = 0 \quad \text{with } k_i \text{ chosen from } \{\pm 1, \pm 2\}$$

We can assume without loss of generality that  $k_1, k_2, k_3 > 0$ ,  $k_5 < 0$ . If  $k_4 > 0$ , then take the inner product of

$$\sum_{i=1}^5 k_i f_i = 0$$

with  $f_5$  to get a contradiction.

If  $k_4 < 0$  then we can assume without loss of generality that  $|k_4| \geq |k_5|$ . Then taking the inner product of both sides with  $f_4$ , we get

$$k_4 s + k_5 (f_4 \cdot f_5) \geq 0, \quad \text{i.e., } |k_4| s \leq |k_5| \cdot |f_4 \cdot f_5|$$

This implies

$$|f_4 \cdot f_5| \geq s$$

and the same argument as in (1) leads to a contradiction.

**Corollary 1.** Let  $F = \{f_1, \dots, f_k\}$  satisfy Conditions (1) and (2).

- (1) If  $\{f_1, f_2\}$  are minimally linearly dependent, then  $f_i$  is orthogonal to  $f_j$  for  $i = 1, 2, j = 3, \dots, k$ .
- (2) If  $\{f_1, \dots, f_4\}$  are minimally linearly dependent, then  $f_i$  is orthogonal to  $f_j$  for  $i = 1, 2, \dots, 4, j = 5, \dots, k$ .
- (3) If  $\{f_1, \dots, f_5\}$  are minimally linearly dependent, then  $f_i$  is orthogonal to  $f_j$  for  $i = 1, \dots, 5, j = 6, \dots, k$ .

**Proof:** In (2), by Lemma 3,  $\sum_{i=1}^4 f_i = 0$ . Hence, for  $j \geq 5$ ,

$$0 = f_j \cdot \left( \sum_{i=1}^4 f_i \right) = \sum_{i=1}^4 (f_j \cdot f_i)$$

Each term  $(f_j \cdot f_i)$  is nonpositive. Hence, the above equality implies that they all must be 0. This proves (2). The same argument proves (1) and (3) (in (1),  $f_1 + f_2 = 0$ ).

**Corollary 2:** Let  $F = \{f_1, \dots, f_k\}$  of  $\mathbf{R}^s$  satisfy Conditions (1) and (2), and let  $m = \text{rank}(F)$ .

- (1) If  $m = 3$ ,  $k = 4$  and  $f_2, f_3$ , and  $f_4$  are mutually orthogonal, then  $F$  cannot be minimally linearly dependent.
- (2) If  $m = 4$ ,  $k = 5$ , and  $f_2, f_3, f_4, f_5$  are mutually orthogonal with  $F$  minimally linearly dependent, then  $f_1 = k_2 f_2 + \dots + k_5 f_5$  with  $k_2, \dots, k_5 = \pm 1/2$ .

**Proof.** To prove (1), observe that by Lemma 2,  $f_1 = k_2 f_2 + k_3 f_3 + k_4 f_4$  where  $k_2, k_3, k_4 = \pm 1$ . Then

$$s = f_1 \cdot f_1 = \left\| \sum_{i=2}^4 k_i f_i \right\|^2 = \sum_{i=2}^4 k_i^2 \|f_i\|^2 = \sum_{i=2}^4 s = 3s$$

a contradiction. To prove (2), by Lemma 2, we can write  $f_1$  as  $\sum_{i=2}^5 k_i f_i$  where the  $k_i$  are chosen from  $\{\pm 1/2, \pm 1, \pm 2\}$ . Now

$$s = \|f_1\|^2 = \sum_{i=2}^5 k_i^2 \|f_i\|^2 = \left( \sum_{i=2}^5 k_i^2 \right) s$$

Hence,  $\sum_{i=2}^5 k_i^2 = 1$ , which proves (2).

## VII. Maximal Orthogonal Systems Satisfying Condition (3)

The question of the existence of an orthogonal basis  $F$  of  $\mathbf{R}^s$  satisfying Condition (2) is the question of existence of an  $s \times s$  Hadamard Matrix. In this section we shall prove that when  $s = 4n$ ,  $n$  odd, no basis of  $\mathbf{R}^s$  can satisfy Condition (3), i.e.,  $s$  odd, weights even. Moreover, any orthogonal system  $F$  satisfying Condition (3) can have at most  $s - 2$  vectors (Proposition 3 below). To prove this result, we need the following Lemma from Ref. 4, stated here without proof.

**Lemma 4:** Let  $f_1, \dots, f_{4n-\alpha}$  be mutually orthogonal  $(1, -1)$  vectors in  $\mathbf{R}^{4n}$ . Then if  $\alpha = 1, 2$  or  $3$ , there exist  $\alpha$  more  $(1, -1)$  vectors  $g_1, \dots, g_\alpha$  such that  $\{f_1, \dots, f_{4n-\alpha}, g_1, \dots, g_\alpha\}$  is an orthogonal basis of  $\mathbf{R}^{4n}$ .

**Proposition 3:** Let  $F = \{f_1, \dots, f_{4n-1}\}$  satisfy Conditions (1), (2), and (3). Then the vectors  $f_1, \dots, f_{4n-1}$  cannot be mutually orthogonal.

**Proof.** Assume the contrary. Then by Lemma 4 there exists a  $(-1, 1)$  vector  $f_{4n}$  such that  $\{f_1, \dots, f_{4n-1}, f_{4n}\}$  is an orthogonal basis of  $\mathbf{R}^{4n}$ . Let  $w_i = w(f_i)$  for  $i = 1, \dots, 4n$ . By our assumption,  $w_i$  is even for  $i = 1, \dots, 4n - 1$ . Consider the vector  $c = (1, 1, \dots, 1^{(2n)}, 0, \dots, 0)$  (in the original basis). Then  $c \cdot f_i = 2(n - w_i)$  and  $\|f_i\|^2 = 4n$ . Hence,

$$c = \sum_{i=1}^{4n} \frac{2(n - w_i)}{4n} f_i$$

Knowing this, we see that

$$\begin{aligned} 2n &= \|c\|^2 = \left\| \sum_{i=1}^{4n} \frac{n - w_i}{2n} f_i \right\|^2 \\ &= \sum_{i=1}^{4n} \frac{(n - w_i)^2}{4n^2} \cdot \|f_i\|^2 \\ &= \sum_{i=1}^{4n} \frac{(n - w_i)^2}{n} \end{aligned}$$

Therefore,

$$2n^2 = \sum_{i=1}^{4n} (n - w_i)^2$$

Now we reduce this equality mod 4. Because  $n$  is odd,  $2n^2 \equiv 2 \pmod{4}$ . Similarly  $n - w_i$  is odd for  $i = 1, \dots, 4n - 1$ . Hence,

$$\sum_{i=1}^{4n-1} (n - w_i)^2 \equiv 4n - 1 \equiv -1 \pmod{4}$$

This leaves us with

$$(n - w_{4n})^2 \equiv 3 \pmod{4}$$

which is impossible, since  $a^2 \equiv 0$  or  $1 \pmod{4}$  for any integer  $a$ . This contradiction completes the proof of Proposition 3.

## VIII. The Main Theorem

We now have the necessary tools to upper bound  $B(4n, 2n)$  when  $n$  is odd. We start with another lemma.

**Lemma 5.** Suppose  $F = \{f_1, \dots, f_{5n-3}\}$  of  $\mathbf{R}^{4n}$  ( $n$  odd) satisfies Conditions (1), (2), and (3). Then  $F$  cannot have a minimally linearly dependent subset of four elements.

**Proof:** Suppose  $f_{8n-6}, f_{8n-5}, f_{8n-4}$ , and  $f_{8n-3}$  are minimally linearly dependent. Denote their span by  $M$ . By definition,  $\dim M = 3$ . Then by Corollary 1 (2) to Lemma 3,  $f_1, \dots, f_{8n-7}$  are in  $M^{\text{perp}}$ . Hence,  $\text{rank } \{f_1, \dots, f_{8n-7}\} \leq 4n - 3$ . By Proposition 2 (with  $k = 8n - 7$ ,  $m = 4n - 3$ ), we can assume (replacing  $\{f_1, \dots, f_{8n-7}\}$  by  $G$  if necessary) that  $f_1, \dots, f_{4n-5} (= 2k-3m)$  are mutually orthogonal and  $f_{4n-6} = -f_1, \dots, f_{8n-10} = -f_{4n-5}$ . Then Corollary 1 (1) to Lemma 3 forces  $f_{8n-9}, f_{8n-8}, f_{8n-7}$  to be in  $(\text{span } \{f_1, \dots, f_{4n-5}\})^{\text{perp}}$ . That is,  $\text{rank } (f_{8n-9}, f_{8n-8}, f_{8n-7}) \leq 2$ .

By Lemma 2 (2), (1) we can thus assume that  $f_{8n-8} = -f_{8n-9}$ , which again forces  $f_{8n-7}$  and  $f_{8n-9}$  to be orthogonal. Therefore,  $F = \{f_1, \dots, f_{4n-5}, f_{8n-9}, f_{8n-7}, f_{8n-6}\}$  is an orthogonal system satisfying Condition (2) and containing  $4n - 2$  vectors. Hence, by Lemma 4 there exist  $(-1, 1)$  vectors  $h_1$  and  $h_2$  such that  $F$  with  $h_1$  and  $h_2$  adjoined is an orthogonal basis of  $\mathbf{R}^{4n}$ . Since  $f_{8n-5}$  is orthogonal to  $f_i$  for  $i = 1, \dots, 8n - 7$ , we have that  $f_{8n-5}$  is in  $\text{span } \{f_{8n-6}, h_1, h_2\}$ . Then by Corollary 2(1) to Lemma 3,  $\{f_{8n-5}, f_{8n-6}, h_1, h_2\}$  cannot be minimally linearly dependent, i.e., it must have a pair of opposites.

But  $f_{8n-5} = -h_i$  ( $i = 1$  or  $2$ ) is impossible because then  $\{f_1, \dots, f_{4n-5}, f_{8n-7}, f_{8n-6}, f_{8n-5}\}$  would be an orthogonal system of  $4n - 1$   $(-1, 1)$  vectors, contradicting Proposition 3. And  $f_{8n-5} = -f_{8n-6}$  contradicts our assumption about minimal linear dependence of  $f_{8n-6}, f_{8n-5}, f_{8n-4}$ , and  $f_{8n-3}$ . And, finally, there cannot be any opposites among  $\{f_{8n-6}, h_1, h_2\}$  because these vectors are mutually orthogonal. This contradiction proves Lemma 5.

**Lemma 6.** Suppose  $F = \{f_1, \dots, f_{8n-3}\}$  of  $\mathbf{R}^{4n}$  ( $n$  odd) satisfies Conditions (1), (2), and (3). Then  $F$  cannot have a minimally linear dependent subset of 5 elements.

**Proof:** We use the same strategy. Assume the contrary, say  $f_{8n-7}, f_{8n-6}, \dots, f_{8n-3}$  are minimally linearly dependent. Let  $M = \text{span } \{f_{8n-7}, \dots, f_{8n-3}\}$ ,  $\dim(M) = 4$ . Then  $f_1, \dots, f_{8n-8} \in M^{\text{perp}}$  by Corollary 1(3) to Lemma 3. Hence,  $\text{rank } \{f_1, \dots, f_{8n-8}\} \leq 4n - 4$ . Then by Corollary 2 to Proposition 1 we can assume that  $f_1, \dots, f_{4n-4}$  are mutually orthogonal. Then  $\{f_1, \dots, f_{4n-4}, f_{8n-7}\}$  is an orthogonal system of  $4n - 3$  vectors. By Lemma 4 there exist three  $(-1, 1)$  vectors  $h_1, h_2$ , and  $h_3$  such that  $\{f_1, \dots, f_{8n-7}, h_1, h_2, h_3\}$  is an orthogonal basis of  $\mathbf{R}^{4n}$ .

Note that  $f_{8n-7}, f_{8n-6}, f_{8n-5}, f_{8n-4}, f_{8n-3}$  are in  $\text{span } \{f_{8n-7}, h_1, h_2, h_3\}$ . We claim that there is an orthogonal pair

among  $\{f_{8n-7}, \dots, f_{8n-3}\}$ . For proof assume the contrary:  $f_i \cdot f_j < 0$  for all  $i \neq j$  in  $\{8n - 7, \dots, 8n - 3\}$ . Denote  $f_{8n-8+i}$  by  $g_i$  for  $i = 1, \dots, 5$ . For  $i = 2, 3, 4, 5$  write  $g_i$  as

$$\alpha_i g_1 + \sum_{j=1}^3 \beta_j^i h_j$$

Since  $\alpha_i = (g_i \cdot g_1)/4n$ , it must be negative by our assumption, for  $i = 2, 3, 4, 5$ . On the other hand,  $\alpha_i \neq -1$ , because we assume that  $\{g_i; i = 1, 2, \dots, 5\}$  is minimally linearly dependent. Hence, by Corollary 2 to Lemma 3 and Lemma 2 (2),  $\alpha_i = -1/2, \beta_j^i = \pm 1/2$  for all  $i, j$ .

We can assume without loss of generality that  $\beta_2^2$  and  $\beta_2^3$  have the same sign. Then

$$\begin{aligned} 0 &> \frac{g_2 \cdot g_3}{4n} = \frac{-\frac{1}{2}g_1 + \sum_{j=1}^3 \beta_j^2 h_j \cdot \left(-\frac{1}{2}g_1 + \sum_{j=1}^3 \beta_j^3 h_j\right)}{4n} \\ &= \left(\frac{1}{4} + \beta_2^1 \beta_3^1\right) + \left(\beta_2^2 \beta_3^2 + \beta_2^3 \beta_3^3\right) \\ &= \frac{1}{2} + \left(\beta_2^2 \beta_3^2 + \beta_2^3 \beta_3^3\right) \\ &\geq \frac{1}{2} + \left(-\frac{1}{4} - \frac{1}{4}\right) = 0 \end{aligned}$$

a contradiction. This contradiction proves the claim.

Now (using the same notation as in the proof of the claim) we can assume that  $g_1$  and  $g_2$  are orthogonal. By Lemma 4, we can complete the orthogonal system  $\{f_1, \dots, f_{4n-4}, g_1, g_2\}$  to an orthogonal basis by adding two new  $(-1, 1)$  vectors  $t_1$  and  $t_2$ . Write

$$g_i = p_i^1 g_1 + p_i^2 g_2 + p_i^3 t_1 + p_i^4 t_2$$

By Corollary 2 to Lemma 3 and Lemma 2, for each  $i$ , there are only two possibilities for the  $p_i^j$ 's:

- (1) One of the coefficients  $p_i^1, p_i^2, p_i^3, p_i^4$  is  $\pm 1$  and the other three are 0;
- (2)  $p_i^1, \dots, p_i^4 = \pm 1/2$ .

Let us consider each of these two possibilities.

- (1)  $p_i^1, p_i^2$  cannot be  $\pm 1$ , since we assume that  $\{g_1, \dots, g_5\}$  are minimally linearly dependent. If  $p_i^3 = \pm 1$  then

$\{f_1, \dots, f_{4n-4}, g_1, g_2, g_i\}$  would be an orthogonal system of  $4n - 1$   $(-1, 1)$  vectors, contradicting Proposition 3. Similarly  $p_i^4 \neq \pm 1$ . Thus (1) is impossible for any  $i = 3, 4, 5$ .

(2) In this case  $p_i^1 = p_i^2 = -1/2$ , since

$$p_i^j = \frac{g_i \cdot g_j}{4n} \leq 0 \text{ for } i = 3, 4, 5, j = 1, 2$$

We can assume without loss of generality that  $\beta_3^3$  and  $\beta_3^4$  have the same sign. Then

$$\begin{aligned} \frac{g_3 \cdot g_4}{4n} &= \left( -\frac{1}{2}g_1 - \frac{1}{2}g_2 + \beta_3^3 t_1 + \beta_3^4 t_2 \right) \\ &\quad \cdot \left( -\frac{1}{2}g_1 - \frac{1}{2}g_2 + \beta_4^4 t_1 + \beta_4^4 t_2 \right) \\ &= \left( \frac{1}{4} + \frac{1}{4} + \beta_3^3 \beta_3^4 \right) + \beta_4^4 \beta_3^4 = \left( \frac{1}{4} + \frac{1}{4} + \frac{1}{4} \right) + \beta_4^4 \beta_3^4 \\ &\geq \frac{3}{4} - \frac{1}{4} = \frac{1}{2} > 0 \end{aligned}$$

This contradiction proves Lemma 6.

Now we at last reach the main theorem of this paper.

**Theorem:** Suppose  $F = \{f_1, \dots, f_k\}$  of  $\mathbf{R}^{4n}$  ( $n$  odd) satisfies Conditions (1), (2), and (3). Then  $k \leq 8n - 4$ . That is,  $B(4n, 2n) \leq 8n - 4$  ( $n$  odd).

**Proof:** It is sufficient to prove that  $F = \{f_1, \dots, f_{8n-3}\}$  cannot satisfy Conditions (1), (2), and (3). Assume the contrary. Then by Proposition 2, we can assume (replacing  $F$  by  $G$  if necessary) that  $f_1, \dots, f_{4n-6}$  are mutually orthogonal and  $f_{4n-5} = -f_1, \dots, f_{8n-12} = -f_{4n-6}$  (here  $k = 8n - 3, m \leq 4n$ ). By Corollary 2 (1), the remaining nine vectors (denote them by  $g_1, \dots, g_9; g_i = f_{8n-12+i}$ ) lie in the orthogonal complement of  $\text{span}\{f_1, \dots, f_{4n-6}\}$ . Hence,  $\text{rank}\{g_1, \dots, g_9\} \leq 6$ . So  $g_1, \dots, g_9$  cannot be mutually orthogonal, and we can assume that  $g_1 \cdot g_2 < 0$ .

By Proposition 1, we can now conclude that  $\text{rank}\{g_3, \dots, g_9\} \leq 5$ . Again (permuting the  $g_i$ 's if necessary, we can assume that  $g_3 \cdot g_4 < 0$ . Then by Proposition 1,  $\text{rank}\{g_5, \dots, g_9\} \leq 4$ . By Lemma 6,  $\{g_5, \dots, g_9\}$  cannot be minimally linearly dependent. By Lemma 5, no subcollection of this collection

containing four elements can be minimally linearly dependent. By Lemma 2 (2), no subcollection of three elements can be minimally linearly dependent.

All this means that  $\{g_5, \dots, g_9\}$  contains a pair of opposites, say  $g_8 = -g_9$ . Then by Corollary 1 (1) to Lemma 3,  $g_i$  is orthogonal to  $g_8$  for  $i = 1, \dots, 7$ . Hence,  $\text{rank}\{g_3, \dots, g_7\} \leq 4$ . Using the same argument as above, we see that the collection  $\{g_3, \dots, g_7\}$  must contain a pair of opposites, say  $g_6 = -g_7$ . By Corollary 1 (1) to Lemma 3,  $g_i$  is orthogonal to  $g_6$  for  $i = 1, \dots, 5$ . Hence,  $\text{rank}\{g_1, \dots, g_5\} \leq 4$ .

Again Lemmas 5, 6, and 2 (2) imply that this collection, too, must contain a pair of opposites, say  $g_4 = -g_5$ . But then by Corollary 2 (1) to Lemma 3,  $g_1, g_2$ , and  $g_3$  are orthogonal to  $g_4$ . Therefore,  $\{f_1, \dots, f_{4n-6}, g_2, g_4, g_6, g_8\}$  is an orthogonal collection of  $4n - 2$   $(-1, 1)$  vectors. By Lemma 4, there exist  $(-1, 1)$  vectors  $h_1$  and  $h_2$  such that  $\{f_1, \dots, f_{4n-6}, g_2, g_4, g_6, g_8, h_1, h_2\}$  is an orthogonal basis of  $\mathbf{R}^{4n}$ .

Since  $g_1$  is orthogonal to  $f_1, \dots, f_{4n-6}$ , then  $g_4, g_6, g_8, g_1$  must all lie in  $\text{span}\{g_2, h_1, h_2\}$ . Since  $g_2, h_1$ , and  $h_2$  are mutually orthogonal, Corollary 2 (1) to Lemma 3 says that  $g_1, g_2, h_1$ , and  $h_2$  cannot be minimally linearly dependent. Then by Lemma 2 (2), (1), this collection must have a pair of opposites. Since  $g_2, h_1$ , and  $h_2$  are mutually orthogonal, there are only two possibilities, each of which we rule out:

- (1)  $g_1 = -g_2$ . Then by Corollary 2 (1) to Lemma 3, every other vector in the original collection will be orthogonal to  $g_1$  and  $g_2$ . Hence,  $\{f_1, \dots, f_{4n-6}, g_2, g_4, g_6, g_8, g_3\}$  will be an orthogonal collection of  $4n - 1$  vectors, contradicting Proposition 3.
- (2)  $g_1 = -h_i$  ( $i = 1$  or  $2$ ). Then  $\{f_1, \dots, f_{4n-6}, g_1, g_2, g_4, g_6, g_8\}$  will be an orthogonal collection, which again contradicts Proposition 3. This contradiction at last proves the Theorem:  $B(4n, 2n) \leq 8n - 4$  if  $n$  is odd.

## IX. Determining $B(12, 6)$

We have left determination of  $B(12, 6)$  to the end, because we need the upper bound  $B(12, 6) \leq 8 \cdot 3 - 4 = 20$  of the preceding section. Table 2 is a particular code meeting the upperbound, showing that  $B(12, 6) = 20$ .

This example has some additional structure that helped us find it and that may generalize. Note that  $A_2, \dots, A_{10}$  are at distance 4 from  $A = (000000111111)$ . Also note that  $A_{k+10} = A_k$ ,  $1 \leq k \leq 10$ . It may be that whenever  $B(4n, 2n) = 8n - 4$  with  $n$  odd, the code consists of  $4n - 2$  orthogonal vectors and their complements. We can now readily check by inspection that for  $k < m$ ,  $1 \leq k \leq 10$ ,



$$d(A_k, A_m) = \begin{cases} 12 & \text{if } m - k = 9 \ (2 \leq k \leq 10) \text{ or } k = 1, m = 20; \\ 6 & \text{otherwise.} \end{cases}$$

so that the code of Table 2 has minimum distance 6.

Some additional structure that helped us find the code is as follows. If we consider the middle 18 rows of Table 2 as

decomposed into four 9-row by 6-column blocks, there are three 1's in each column of the two diagonal blocks, each of which consists of six-tuples of weight 2, and six 1's in each column of the antidiagonal blocks. One can show in the case  $n = 3$  that, once we know that there is a pair of codewords at distance 12, all the additional structure follows. Knowing all this, Table 2 was easy to derive.

## References

1. Posner, Edward C., and Zinvoy Reichstein, "Minimum-Distance Problems in Protocol Design," TDA Progress Report 42-77, January-March 1984. Jet Propulsion Laboratory, Pasadena, California.
2. MacWilliams, F. J., and N. J. A. Sloane, *The Theory of Error-Correcting Codes*, North Holland, Amsterdam, 1977.
3. Rankin, R. A., "The Closest Packing of Spherical Caps in  $n$  Dimensions," *Proc. Glasgow Math. Assoc.*, Vol. 2 (1955), pp. 139-144.
4. Hall, Marshall, and Herbert J. Ryser, "Normal Completions of Incidence Matrices," *Amer. Jour. Math.*, Vol. 76 (1954), pp. 581-589.

**Table 1. Largest codes<sup>a</sup> of even lengths  $2k \leq 12$**

$2k = 2$			
$d$	$A(2, d)$	$C(2, d)$	$B(2, d)$
1	4	2	1
2	2	2	1

$2k = 4$			
$d$	$A(4, d)$	$C(4, d)$	$B(4, d)$
1	16	8	4
2	8	8	4
3	2	2	2
4	2	2	2

$2k = 6$			
$d$	$A(6, d)$	$C(6, d)$	$B(6, d)$
1	64	32	16
2	32	32	16
3	8	4	4
4	4	4	4
5	2	2	1
6	2	2	1

$2k = 8$			
$d$	$A(8, d)$	$C(8, d)$	$B(8, d)$
1	256	128	64
2	128	128	64
3	20	$16^b$	$16^b$
4	16	$16^b$	$16^b$
5	4	2	2
6	2	2	2
7	2	2	2
8	2	2	2

$2k = 10$			
$d$	$A(10, d)$	$C(10, d)$	$B(10, d)$
1	1024	512	256
2	512	512	256
3	72-80	38-40 <sup>c</sup>	32 <sup>d</sup>
4	38-40	38-40 <sup>c</sup>	32 <sup>d</sup>
5	12	6 <sup>c</sup>	5 <sup>d</sup>
6	6	6 <sup>c</sup>	5 <sup>d</sup>
7	2	2	2
8	2	2	2
9	2	2	1
10	2	2	1

$2k = 12$			
$d$	$A(12, d)$	$C(12, d)$	$B(12, d)$
1	4096	2048	1024
2	2048	2048	1024
3	256	144-160 <sup>e</sup>	128 <sup>d</sup>
4	144-160	144-160 <sup>e</sup>	128 <sup>d</sup>
5	32	24 <sup>e</sup>	20 <sup>f</sup>
6	24	24 <sup>e</sup>	20 <sup>f</sup>
7	4	4 <sup>g</sup>	4 <sup>d</sup>
8	4	4 <sup>g</sup>	4 <sup>d</sup>
9	2	2	2
10	2	2	2
11	2	2	2
12	2	2	2

$A$ : unconstrained,

$C$ : even

$B$ : even-even.

<sup>a</sup>A-Values from Ref. 2, App. A, p. 674, Fig. 1.

<sup>b</sup>Biorthogonal (8, 4) linear codewords for  $C(8, 4)$  ( $= C(8, 3)$ )  $= B(8, 4)$   $= 16$ .

<sup>c</sup>From Ref. 2,  $A(9, 5) = 6$ , and append an even parity bit; likewise  $38 \leq A(9, 3) \leq 40$ .

<sup>d</sup>Derived in this Section:  $B(2k, 2t - 1) = B(2k, 2t)$  because all distances are even.

<sup>e</sup>Same reasoning as footnote c, where  $144 \leq A(11, 3) \leq 160$ ,  $A(11, 5) = 24$ .

<sup>f</sup>Derived in Section 9.

<sup>g</sup>Use  $B(12, 8) = 4$ .

**Table 2.  $B(12, 6) \geq 20$**

	$A_k(1)$						$A_k(2)$					
$A_1$	0	0	0	0	0	0	0	0	0	0	0	0
$A_2$	0	0	1	0	0	1	1	1	1	1	0	0
$A_3$	0	1	0	0	0	1	1	1	0	0	1	1
$A_4$	1	0	0	0	0	1	0	0	1	1	1	1
$A_5$	0	0	1	0	1	0	1	0	1	0	1	1
$A_6$	0	1	0	0	1	0	0	1	1	1	1	0
$A_7$	1	0	0	0	1	0	1	1	0	1	0	1
$A_8$	0	0	1	1	0	0	0	1	0	1	1	1
$A_9$	0	1	0	1	0	0	1	0	1	1	0	1
$A_{10}$	1	0	0	1	0	0	1	1	1	0	1	0
$A_{11}$	1	1	0	1	1	0	0	0	0	0	1	1
$A_{12}$	1	0	1	1	1	0	0	0	1	1	0	0
$A_{13}$	0	1	1	1	1	0	1	1	0	0	0	0
$A_{14}$	1	1	0	1	0	1	0	1	0	1	0	0
$A_{15}$	1	0	1	1	0	1	1	0	0	0	0	1
$A_{16}$	0	1	1	1	0	1	0	0	1	0	1	0
$A_{17}$	1	1	0	0	1	1	1	0	1	0	0	0
$A_{18}$	1	0	1	0	1	1	0	1	0	0	1	0
$A_{19}$	0	1	1	0	1	1	0	0	0	1	0	1
$A_{20}$	1	1	1	1	1	1	1	1	1	1	1	1

# Utilization of Mobile VLBI for Geodetic Measurements

J. M. Davidson and D. W. Trask

Tracking Systems and Applications Section

*Three mobile VLBI systems have been fabricated under the direction of JPL for the NASA Crustal Dynamics Project. These systems include the 9-meter-diameter MV-1 telescope, the 3.7-meter-diameter MV-2 telescope and the 5-meter-diameter MV-3 telescope. Since 1980, mobile systems have been operated in conjunction with several fixed base stations in the western United States as part of a geodetic survey program to determine relative motions and regional strain fields near the tectonic plate boundaries in California and Alaska. In this article, we present a description of the three mobile systems and the environment in which they must function. The inherent accuracy of mobile VLBI measurements is assessed, based on a consideration of major sources of error. Some recent results are presented which serve to illustrate various aspects of the error model and are of geodetic interest as they span the broad region surrounding the surface trace of the San Andreas Fault. These results indicate that baseline measurements utilizing the current mobile VLBI systems have attained an accuracy of 2 cm or better in the horizontal plane. Since average geological rates of horizontal motion are on the order of 5 cm/yr across the plate boundary regions being studied, it is likely that crustal motions will be detected within the next few years, provided they are presently occurring at the geological rates.*

## I. Introduction

Over the past fifteen years, considerable progress has been made in the application of very long baseline interferometry (VLBI) to the measurement of Earth orientation and global crustal motion (see, e.g., Refs. 1, 2, 3, and 4). However, in order to study crustal motion on a regional scale (baselines of lengths less than 1000 km), mobile systems are required for spatial densification. To meet this need, MacDoran and others (Refs. 5, 6, and 7), beginning in the early 1970s, undertook the development of a 9-meter-diameter mobile VLBI system (now known as MV-1). Tests of this mobile system were conducted from 1974 to 1979 in order to demonstrate the feasi-

bility of the mobile VLBI concept and to initiate a program of regional deformation studies in the western United States. The success of this effort subsequently led to the construction of two additional mobile VLBI systems. These were fabricated under the direction of JPL for the Crustal Dynamics Project (CDP; see Ref. 8) of the NASA Geodynamics Program. These newer MV (for mobile VLBI) systems include the 3.7-meter MV-2 telescope, which began data collection in 1980, and the 5-meter MV-3 telescope, which began data collection in 1982. The newer systems are smaller, are more easily transportable and take advantage of the technological insights gained in the experience with MV-1 (Refs. 9 and 10). These three MV units are presently being operated in conjunction with several fixed

based stations in the western United States as part of a geodetic surveying program, to determine relative motions and regional strain fields near tectonic plate boundaries in California and Alaska. All data and results from this observing program are regularly archived in the CDP Data Information System (DIS) located at the Goddard Space Flight Center (GSFC), Greenbelt, Maryland (Refs. 11 and 12), where it is in the public domain. All results presented herein are available in the DIS (Ref. 13).

In this article, we present a description of the three mobile VLBI systems and the difficult environment in which they must function. The inherent accuracy of the mobile VLBI measurements is assessed for the example of the 883-km baseline between Monument Peak and Quincy in California, based on a consideration of major sources of error and on the internal consistency of the mobile VLBI results. Some recent results are presented which serve to illustrate various aspects of mobile system's inherent accuracy and are of geodetic interest as they span the broad region surrounding the surface trace of the San Andreas Fault. The current single-measurement (24 hours of data collection) accuracy in the length and horizontal transverse components of baselines of lengths 500 km or less appears to lie in the range of 1–2 cm. For baselines of lengths 500–1000 km, the accuracy of the transverse component degrades to the 2–3 cm range, because of uncertainties in currently available Earth orientation calibrations. The accuracy in the baseline vertical component is considerably worse than this, falling in the range of 8–10 cm. Anticipated improvements by 1986 in troposphere and earth orientation calibration (M. A. Janssen and J. O. Dickey, private communication) will improve single-measurement accuracies to 1–2 cm and 3–4 cm for the transverse and vertical components, respectively. Since average geological rates of horizontal motion are on the order of 5 cm/yr across the plate boundary regions being studied (Ref. 14), it is likely that crustal motions will be detected within the next few years, provided they are presently occurring at the geological rates.

## **II. The Mobile VLBI Systems**

### **A. The Interferometry Technique**

In interferometry measurements, the random broad-band emission of an extra-galactic radio source (usually a quasar) is simultaneously recorded on a magnetic medium at two widely separated radio antennas (Ref. 4). Subsequent cross-correlation of the recorded data at a centrally located special-purpose computer (known as a "correlator") leads to a determination of the difference in arrival time of the radio wavefront at the two antennas. This difference (or delay) depends on, among other things, the direction of the source and the vector separation of the two antennas. Hence, it is pos-

sible to estimate these and other quantities by measuring the delays and their rates of change for many different sources, preferably on several baselines simultaneously, and then passing these delays and delay rates through a multiparameter least-squares fitting code in which geophysical and astrometric quantities are adjustable parameters. For a complete description of the interferometry techniques, see, e.g., Refs. 15 and 16.

### **B. The Mobile Environment**

It has long been foreseen that interferometric baseline measurements using large, permanent radio telescopes would eventually attain an accuracy in length of two centimeters or better. However, it was not clear that mobile systems were capable of this same level of performance. The reasons for this reservation are simple, having to do with the environment in which mobile systems operate. In this subsection, we present a description of these environmental conditions.

The most severe penalty imposed by the requirement of high mobility is the reduction of the quasar signal-to-noise ratio (SNR). This is a simple consequence of the small aperture size of the transportable telescopes. The smaller SNR lowers the inherent system precision and limits the number of sources usable for mobile VLBI interferometry. For observations in North America, the available number of sources of adequate strength is only about a dozen. The small size of this catalogue tends to distort the experimental geometry and observing strategy and may lead to high correlations between estimated geodetic and other parameters. This latter problem becomes especially serious in the event of poor behavior of the time and frequency standards.

Of almost equal importance is the lack of such strict environmental control as is routinely available in permanent radio observatories. This may have serious consequences in regard to the performance of the MV stations' hydrogen masers and other electronics, which are particularly sensitive to thermal, magnetic and mechanical perturbations. Further, the electronic equipment in an MV unit must withstand vibrations from hundreds of miles of highway driving and many miles of driving on rough off-highway roads. Dust and grit are pervasive under field conditions, in stark contrast to the conditions for in-house data collection, where even cigarette smoke is considered a hazard to computer magnetic tape and disk drives.

When a remote site is reoccupied, the mobile antenna is parked as near as possible (usually within 10 cm of horizontal displacement) to a monumented ground reference point, the official CDP "location" of that site. The survey tie vector between the antenna intersection of axes and the monument is measured using conventional surveying techniques. The error

in this measurement further degrades the quality of mobile VLBI baseline results. (This is discussed further in Section III.)

There are important personnel or "human" considerations that are unique to the mobile environment. For example, the field crews often do not have convenient access to normal eating, sleeping and sanitary facilities. The nature of field work tends to be fatiguing. Mobile VLBI field exercises (or "bursts") may last up to two weeks and involve several thousand miles of driving and considerable heavy physical labor. In addition, field crews may have to contend with dense swarms of mosquitoes, rattlesnakes and even bears in the course of data collection. Although these human factors are impossible to include explicitly in the computation of formal uncertainties, they may strongly affect the quality, and quantity, of data taken in the field and thus may in effect lower mobile VLBI accuracy.

Several other problems unique to the mobile environment pose challenges, albeit indirectly, to the goal of two-centimeter accuracy. For example, the remote sites often do not have electricity and telephone service. Hence, the MV units must provide their own power and communications capability. Catastrophic station failures may require the hurried shipment by air of a particular part (or technician) to the scene of a disabled MV unit. Validation of remote station operation by quick correlation of a test tape may be difficult or impossible. Magnetic tape logistics in the field are a major problem, as the tapes for one MV unit for a single burst may weigh several thousand pounds. Special highway permits are required for the heavy vehicles that make up an MV "caravan," and travel restrictions in certain local areas may present problems. For example, on one occasion a field crew's unfamiliarity with heavy-vehicle regulations led to the arrest of the MV-2 antenna in Northern California, resulting in the loss of over twelve hours of geodetic data.

### C. Mobile Station Description

Three mobile VLBI stations have been fabricated and are currently involved in the ongoing collection of data for the Crustal Dynamics Project. These are the 9-meter-diameter MV-1 station, the 3.7-meter MV-2 station and the 5-meter MV-3 station. The MV-1 and MV-2 antennas, but not electronics, were initially obtained as U.S. Army surplus equipment. All MV-3 components were designed and built specifically for the Crustal Dynamics Project. MV-1 was developed as a proof-of-concept effort, with high mobility as a lesser priority. It requires four men and fourteen working days (not including transit time) to relocate. MV-2 was developed to establish the concept of high mobility; this MV station has, in the course of actual field exercises, been relocated in 5 hours, plus transit time, using a crew of four (although more typical relocation

times range from 24 to 48 hours in consideration of field crew fatigue and safety). MV-3 can also be relocated in five hours, plus transit time, with only a minimum crew of two needed. Station calibration equipment includes water vapor radiometers (WVRs) and surface meteorology sensors, recording temperature, barometric pressure, and relative humidity. The water vapor radiometers are attached to the telescopes themselves and point with the telescopes in the direction of the quasar line-of-sight.

Many aspects of MV station design have taken into account the mobile environmental factor discussed in the previous subsection. To optimize the SNR, all three of these stations are equipped to operate in a standard CDP configuration. That is, data are recorded using a computer-controlled Mark III terminal (up to 112 Mbits/s record rate), with dual-frequency (X-band and S-band) recording. This is a substantial improvement over the 4 Mbits/s rate of the Mark II recording system (X-band only) that was used through 1980, and reduces the penalty imposed by the small aperture diameters. (Indeed, the need to optimize SNR in the mobile systems was a major justification for the development of the Mark III system.) Spanned bandwidths are approximately 400 MHz at X-band (approximately 8.4 GHz) and 100 MHz at S-band (approximately 2.4 MHz). The broad-banding of the receivers also improves precision of the delay measurements. The hydrogen masers, used as time and frequency standards in all the MV units, are housed in double-walled environmental control enclosures, within which the temperature is regulated to within 0.1 Kelvin. The walls of this enclosure are lined with magnetic shielding. Each MV unit is equipped with a radio telephone and 50-kVA electric generator; MV-3 has two such generator units. Each unit has a walk-in trailer housing the station electronics. These electronics have been hardened against damage from highway vibrations so that data loss from in-transit equipment damage is minimal with the current systems. The trailer for MV-3 also contains cooking, sleeping and sanitary facilities for the field crews.

An MV station in transit between sites consists of a convoy or "caravan" of vehicles. The MV-1 caravan includes a crane for telescope assembly. The MV-1 and MV-2 caravans include a pick-up truck site-vehicle. The transit configurations of the three mobile stations are shown schematically in Fig. 1. MV-3 is shown in both its in-transit and deployed configurations in Fig. 2.

### D. Field Operations

In their normal operating modes, the mobile VLBI units are deployed in observing campaigns or bursts, which may last from one to two weeks. MV-1 operates as a quasi-fixed station, while MV-2 and MV-3 tour the mobile VLBI sites which have

been scheduled. From one to four fixed base stations may operate in conjunction with the MV-units to strengthen network geometry and SNR. Typical site occupation times range from 24 to 36 hours. Current deployment plans, as set up by the Crustal Dynamics Project, call for four bursts per year, three in the western United States and one in Alaska. From the present through 1988, MV-1 will be stationed semi-permanently at Vandenberg Air Force Base, California, while MV-2 and MV-3 will occupy about thirty sites in California and Alaska on an annual basis.

### III. Sources of Error

In this section, we discuss the major sources of error in mobile VLBI measurements. These sources include: Earth orientation calibration, propagation media calibration, mobile survey tie, source positions, system noise, processing scatter, and other (unmodeled) error sources. A summary of the error model inputs is given in Table 1 for the mobile systems of 1980, for the current (1984) mobile systems and as anticipated for the mobile systems of 1986. The impact of these inputs on baseline accuracy, in all three components, is illustrated in Figs. 3, 4, and 5 for the example of the Monument Peak to Quincy baseline. Although the impact of calibration errors varies considerably as a function of baseline length and orientation and other factors, such as local meteorology, the example of this baseline is chosen as illustrative of many features of the mobile VLBI sources of error.

#### A. Earth Orientation

The VLBI technique provides a very accurate measurement of a baseline vector within the reference frame of the quasi-stellar radio sources (Refs. 17, 18, and 19). However, expression of the baseline in an Earth-fixed frame requires an accurate knowledge of the orientation of the Earth in space, that is, in the quasar frame. In principle, this calibration could be extracted from the mobile VLBI data themselves. However, the relatively short length of the mobile VLBI baselines would provide calibrations inferior to those which are now available from a number of external sources. Over the past several years, several different sources have been used. Initially, calibrations based primarily (although not exclusively) on classical astrometry (Ref. 20 and M. Feissel, private communication) were used. In the past several years, calibrations from a number of other sources (R. W. King, private communication) have been applied, with greatly improved results. In the current processing of mobile VLBI data, calibrations for UT1-UTC are those of Eubanks et al. (Ref. 21), in which data from Lunar Laser Ranging (LLR; see Ref. 22), VLBI-based data from the POLARIS project of the National Geodetic Survey (Ref. 23), DSN observations (Ref. 4), and data from the TEMPO project at JPL (Ref. 24) were combined with a Kalman filter based

upon studies of atmospheric angular momentum. Within the next two years, improved calibrations based on Kalman filter combinations for all components of Earth orientation will be available (Ref. 21) as additional LLR stations come on-line and more frequent VLBI-based measurements are made. With these new calibrations, Earth orientation errors will become a negligible component in the mobile VLBI error budget (see Table 1 and Figs. 4 and 5).

#### B. Propagation Media

The total observed delay contains contributions due to the propagation media traversed by the radio waves. For individual stations, the total contributions for sources near the zenith may be as large as 120 cm for the ionosphere for X-band data recording, 220 cm for the dry troposphere at sea level and 30 cm for atmospheric water vapor; for sources at low elevations, these effects may be larger by factors of three or more. Clearly, the careful calibration of propagation media effects is one of the most challenging and important tasks requisite to attaining two-cm accuracy in mobile VLBI measurements.

Calibration of the ionosphere with the current mobile systems is obtained from simultaneous recording of data at S-band and X-band frequencies and combining of the separate delay (and delay rate) observables, based on an assumed inverse-squared frequency dependence for ionosphere dispersion. To the extent that higher-order terms in the dispersive relation are negligible, this approach provides an exact calibration of ionosphere effects. Prior to the implementation of the dual-frequency recording capability, data were recorded at X-band only. For these data, corrections to baseline solutions and covariances were determined empirically using data from a number of recent experiments with dual-frequency data recording (see Table 1 and Figs. 3, 4, and 5).

Calibration of the dry troposphere at the local zenith is obtained directly from the surface barometric pressure, corrected to the intersection of axes of the antenna. Mapping of the dry air mass from the zenith of the quasar line-of-sight is done using the mapping function of Chao (Ref. 25). Although the impact of error from mapping is minimized because of the relatively high (17 degrees) elevation angle cutoff used in mobile VLBI observations, the line-of-sight error may be as large as 1 cm for the Chao model (G. A. Lanyi and R. N. Treuhaft, private communication). This may cause shifts in the baseline vertical on the order of 1 cm. The combined error from the pressure measurement, the presence of horizontal pressure gradients, dynamic contributions to the barometric pressure, and from the mapping is approximately 1.5 cm for regional baselines.

Calibration of the atmospheric water vapor is obtained from water vapor radiometer (WVR) data. These data are used

to extract the additional sky brightness along the quasar line-of-sight due to microwave emission from free water molecules. The WVR data are currently reduced using an algorithm developed by Claflin, Wu and Resch (Ref. 26). These calibrations, corrected to zenith, are accurate to about 2 cm (G. M. Resch, private communication). When WVR data are unavailable, calibrations are derived from an atmospheric model with surface meteorology (SM) data as input (Ref. 25). The SM-based calibrations are taken to be accurate to one-half the mean total value at zenith, which is typically in the range from 5 to 10 cm. The atmospheric water vapor dominates the error budget for the baseline vertical component, particularly when SM calibrations are used, as they were routinely in 1980.

The calibration of water vapor is expected to improve substantially in the next two years as new WVRs, developed by a CDP team made up of members from JPL, GSFC and the Bendix Corporation, become available (M. A. Janssen, private communication). Using these new WVRs, the calibration of atmospheric water vapor, corrected to zenith, will be accurate to about 0.5 cm, and this error source will no longer dominate the error budget for any one baseline component.

## C. Mobile Survey Tie

The locations reported (see, e.g., Ref. 13) for the mobile VLBI sites are monumented ground reference points. The offset vector from the monument to the antenna intersection of axes (usually less than 10 cm in the horizontal plane) is measured using conventional surveying techniques. The consistency of repeated measurements of these vectors indicates that their accuracy is approximately 2 mm.

## D. Source Positions

The positions of the radio sources that are used in the mobile VLBI observations in principle may be estimated from the mobile VLBI data itself. However, this source catalogue would be inferior in accuracy to several available catalogues which are based on larger data bases accumulated from large, fixed observatory antennas. Moreover, the estimation of source coordinates from the mobile VLBI data would weaken the solutions for the baseline coordinates.

The radio source positions and uncertainties adopted in the processing of the mobile VLBI data were derived from ten years of NASA DSN intercontinental VLBI data (Refs. 18 and 19). Positional uncertainties in the current DSN catalogue are on the order of 5 milliarcsec; these are expected to decrease by about a factor of five over the next two years (O. J. Sovers, private communication).

## E. System Noise

The theoretical precision of the raw delay and delay rate observables is dependent on a combination of factors (see, e.g.,

Ref. 3), including telescope diameter, system temperature and receiver spanned bandwidth. As discussed earlier, the aperture sizes of the mobile systems may be smaller by an order of magnitude than that of fixed observatory telescopes used in geodetic measurements, resulting in decreased SNR and baseline measurement precision. To mitigate this problem, the CDP has provided two important system improvements to enhance the SNR of the mobile stations. One of these is the computer-controlled Mark III data recording system, which provides an increased bandwidth of up to 56 MHz, compared to 2 MHz for the Mark II system. The other is the installation of cooled field-effect transistor (FET) receivers to replace the traveling wave maser (TWM) receivers at the antenna feed. The FET receivers permit a spanned bandwidth at X-band of 400 MHz, whereas the TWM receivers were generally limited to 40 MHz. These two upgrades in principle can reduce system noise errors by greater than an order of magnitude, and in fact the improvement realized is about a factor of ten.

## F. Other Random Errors

After parameter estimation, the RMS scatter of the delay residuals (i.e., observed delay minus theoretical delay) is invariably found to be substantially larger than expected based on system noise errors. This phenomenon is normally accommodated in the routine processing by addition in quadrature of white noise to the system noise errors of the individual observations, such that the normalized chi-square after parameter adjustment is one. Clearly, there are significant contributions to the total delay which are not represented in the theoretical delay model. Although it is for the present largely conjectural, it seems likely that these unmodeled random errors arise from high frequency instabilities in the time and frequency distribution (and other instrumental) systems and in the troposphere. In addition, there may be contributions from the effects of ocean loading, and radio source structure, which are not fully modeled in the current software, although mis-modeling of these may lead to a mixture of random and systematic errors.

## G. Processing Scatter

It has long been known that, in the course of routine data processing of VLBI data, there exist problems with repeatability in the cross-correlation process and in the estimation of geodetic parameters from a given set of observables. Both of these have historically come to be viewed as sources of random error. However, recent investigations by R. N. Treuhaft (private communication) and A. E. E. Rogers (private communication) indicate that the first of these phenomena is a simple consequence of random data loss during input to the correlator, attributable to the poor quality of the magnetic tapes used, and that once the data have been successfully read from the tapes, the cross-correlation and observable extraction



processes proceed without error. Hence, correlator nonrepeatability is not an error source; rather, it is in effect a loss of signal-to-noise ratio, but one which is properly modeled in the extraction of observables and for which no additional error modeling is necessary or even appropriate. In the case of geodetic parameter estimation, as with correlation, there is data loss, in this case resulting from analysts' subjective decisions in the deletion of spurious data points. (In addition, the analyst may make decisions regarding modeling of station clock behavior.) Although the character of this data loss depends somewhat on the skill of the analysts and on the quality of the data, it would appear for the current mobile systems that this process too is effectively random. Hence, nonrepeatability in parameter estimation, as with correlation, is not an error source and no additional error modeling is necessary. Both of these problems have been reduced substantially by improvements in the quality of magnetic recording tapes available for use in mobile VLBI experiments and by overall improvements in quality of data produced by the mobile systems, reducing the need for human intervention in the processing of data.

## H. Other Systematic Errors

Systematic errors are more difficult to detect than random errors, because they generally have no first-order effect on the size of the residual scatter. Further, they may have no effect on the consistency of repeated measurements made using the same technique, at least over short time spans. Moreover, systematic errors which vary on annual, or longer, time scales may be indistinguishable from actual tectonic motions. One way of testing for systematic errors is by comparing measurements made using different techniques of comparable precision. A preliminary comparison of VLBI (mobile and observatory-based) results with results from collocated satellite laser ranging (SLR) measurements (J. Ryan, private communication) shows consistency between the two techniques at about the level of the quadratically summed formal errors. Since there are few error sources common to both techniques, it is unlikely that there are unmodeled systematic errors in either technique which are as large as the formal errors themselves. Nevertheless, there are several mechanisms which may give rise to systematic errors on the order of one centimeter in the mobile VLBI results. These include: incomplete phase calibration, antenna flexure effects, interaction of the Earth's magnetic field with the receiver, the effects of ocean loading, radio source structure and mapping of the zenith dry troposphere to quasar elevation. To acknowledge the presence of these error sources, and in lieu for the time being of a more concise estimate of their significance, we have included these in Table 1 and in Figs. 3, 4, and 5 for the current mobile VLBI systems as 1 centimeter for the baseline length and horizontal transverse components and 2 centimeters for the baseline vertical component.

## IV. Comparison to Results

In this section, we examine current baseline results (Ref. 13) for the Owens Valley Radio Observatory (OVRO)—JPL (335 km) and OVRO—Quincy (383 km) baselines and evaluate them for internal consistency. Based on these results, we conclude that the repeatability of multiple baseline measurements is consistent with the uncertainties derived from the error model presented in the previous section. This is consistent with the claim that the current estimates are realistic and that the mobile VLBI systems have attained an accuracy in the horizontal plane of better than 2 cm, overcoming the challenge posed by the mobile environment.

### A. The OVRO—JPL Baseline

The mobile VLBI site at JPL has been occupied fifteen times between January of 1980 and the present. These occupations have resulted in eighteen separate measurements of the baseline between JPL and the 40-meter-diameter radio telescope of the OVRO, Big Pine, California. As has been pointed out in preceding sections of this paper, the mobile systems have undergone a substantial evolution in terms of system engineering over this period. Thus, the JPL—OVRO baseline is a good case in point to illustrate the effect of system improvements and to test consistency for the mobile VLBI baseline results.

Results from the current Mobile VLBI data base (Ref. 13) for the JPL—OVRO baseline are presented in Figs. 6a to 6c. These figures show error ellipsoids (one standard deviation) in the horizontal plane. The temporal history of this baseline is divided into three periods. The first is from January of 1980 through May of 1981 (shown in Fig. 6a). All of those data were collected using the "original" mobile VLBI system of 1980, that is, using Mark II data recording; 40-MHz, narrow-passband TWM receivers; and single-frequency X-band data recording. The second period is from August through November of 1981 (shown in Fig. 6b). These data were collected using Mark III data recording, and 400-MHz, passband, cooled FET receivers; however, only X-band data were recorded. In the third period, from October 1982 through February 1983, we show examples of data recorded using the fully upgraded, current mobile VLBI systems, including Mark III data recording; 400-MHz, passband, cooled FET receivers; and dual-frequency (S-X) data recording.

These figures contain several features which illustrate the effect of system improvements. First, it is clear from inspection that there is a considerable decrease in the size of the formal errors from 1980 to 1983. Moreover, there is a corresponding decrease in the scatter of these repeated measurements. To assess the consistency of the scatter and the

formal errors, chi-square has been calculated for each coordinate of each figure. The results of these calculations are presented in Table 2, along with the probabilities for obtaining chi-square of that size or larger.

Before discussing the results of these calculations, it should be noted that there are three assumptions implicit in the way these tests were made:

- (1) First, we assume that there is no significant contribution to the scatter in the repeated measurements arising from actual short-term (or episodic) tectonic motions within any of the three time periods. Although there is no *a priori* reason to make this assumption, we note that such motions would tend to make chi-square anomalously large, whereas it actually tends to be somewhat smaller than expected. Further, there is no evidence for significant long-term motion on this baseline (see Section V).
- (2) A second implicit assumption is that a meaningful chi-square may be calculated separately for each baseline coordinate, thus assuming, in effect, that there is no correlation between their errors.
- (3) A third assumption is that there is no correlation between Earth orientation errors in separate experiments. This assumption is almost certainly incorrect for experiments separated by periods of less than a week. Hence we issue the caution that assumptions (2) and (3) may make chi-square anomalously small.

With the above in mind, we now consider the results of these tests. In Table 2, we see that for most cases, the scatter in the repeated solutions is reasonably representative of the formal errors, although there is some indication (in the length in Fig. 6a and the transverse in Fig. 6c) that the scatter is smaller than expected. (Possibly this is a breakdown of either or both of assumptions (2) and (3).) Hence, we conclude that the realistic uncertainties (one standard deviation) in horizontal components of the OVRO-JPL baselines are no worse (and possibly better) than the current formal errors, which are on the order of 1.5 cm in the horizontal plane. Similar plots for the baseline vertical coordinate (not included here because of space constraints) show essentially the same agreement with the error model.

## B. The OVRO—Quincy Baseline

The mobile VLBI remote site at Quincy in Northern California has been occupied by the Mobile VLBI stations in October 1982 and June 1983. (An additional occupation occurred in April of 1984, but those data are not yet available from the Crustal Dynamics Data Information System (Ref. 11).) The monitoring of crustal motions involving the

Quincy site is of particular interest because of its reported southward motion of  $6.5 \pm 1.5$  cm/yr with respect to the Monument Peak site, some 883 km away in the extreme south of California, based on SLR measurements made between 1970 and 1979 (Ref. 27). Although the mobile VLBI surveying history for these two sites as of this writing is too short to make a confirmation of the published SLR result, it is nevertheless of great interest to examine the first-epoch measurements to evaluate their accuracy.

Results from the current mobile VLBI data base (Ref. 13) for the OVRO—Quincy baseline are presented in Fig. 6d for the October 1982 occupation (experiments 82E and 82G) and the June 1983 occupation (experiment 83F). As inspection of this figure shows, the three measurements have formal errors on the order of 1 cm in the horizontal plane. Chi-square calculations for these data (Table 2) lead to the same basic conclusion as in the case of the OVRO—JPL baseline. First-epoch measurements of the OVRO—Monument Peak baseline (not shown) give results of similar accuracy. Thus, if the motion reported from observations between 1970 and 1979 in the SLR-based measurements (Ref. 27) is still occurring, then it will be easily detected within the next two years, as current CDP observing plans (R. J. Coates, private communication) call for annual reoccupations of both of these sites.

## V. Discussion

In this article, we have presented a description of the mobile VLBI systems and the engineering and technical steps that were taken to optimize their performance under field conditions. An error model was presented and its predictions were found to be consistent with the observed scatter in repeated measurements. This suggests that the error model is realistic and that the accuracy in the horizontal plane of mobile VLBI measurements has reached the level of 2 cm or better.

This accuracy should improve further within the next two years as improved calibrations for Earth orientation and atmospheric water vapor become available. The anticipated accuracy at that time for regional baselines (up to 1000 km in length) will be approximately 1.5 cm in the length and horizontal transverse and 3.5 cm in the baseline vertical. The most important remaining error sources at that time will be random errors, probably from unmodeled troposphere and station clock (and other instrumental) behavior. These problems are currently being studied at JPL and other VLBI centers; however, they may ultimately prove to be difficult to eliminate entirely from the mobile VLBI error budget.

One possible means of increasing mobile system precision by possibly an order of magnitude, in effect circumventing the problems described above, lies in the use of the phase delay

observable, rather than the presently used group delay, as the input to parameter estimation. Preliminary results for very short baseline (length  $< 20$  km) phase-delay measurements (K. M. Liewer, private communication, and Ref. 28) are extremely encouraging. However, it remains to be seen whether the phase delay data type can be used routinely on regional baselines, using the small-diameter mobile VLBI telescopes.

These remaining problems notwithstanding, it should be emphasized that the current mobile systems have a sensitivity

to crustal motion, over a four-year period of monitoring, of about 0.5 cm/year (one standard deviation), assuming even a rather modest observing scenario of only one site occupation per year. More frequent monitoring will lead to even higher sensitivity. Since the geological rates of horizontal motion are on the order of 5 cm/yr across the plate boundary regions being studied in California and Alaska (Ref. 14), it seems likely that crustal motions will be detected using the mobile systems within the next few years, provided they are presently occurring at the geological rates.

## Acknowledgment

This article consists partially of materials representing the personal accomplishments of the authors, both of whom have been involved in the mobile VLBI project at JPL for many years. However, the bulk of the materials and results presented herein represent the multi-year efforts of dozens of individuals, some of whom we list here. The mobile VLBI project was initially founded at JPL under the name of Project ARIES by Peter F. MacDoran, George M. Resch and Arthur E. Niell. Development of the MV-3 mobile VLBI system, initially known by the name of Project ORION, was led by Charles J. Vegos and Gary S. Parks. The mobile VLBI field operations were coordinated and directed by Charles J. Vegos. The extensive software system, containing Earth model and matrix inversion routines, used in the reduction of mobile VLBI data was conceived and written by John L. Fanelow. Considerable physical insight into the workings of mobile VLBI systems and understanding of error sources was provided by a number of analysts, including Arthur E. Niell, John L. Fanelow, J. Brooks Thomas and Steven L. Allen. The Mobile VLBI Project is a part of the JPL Geodynamics Project, managed by Dr. Nicholas A. Renzetti.

## References

1. J. W. Ryan, T. A. Clark, R. J. Coates, B. E. Corey, W. D. Cotton, C. C. Counselman, III, H. F. Hinteregger, C. A. Knight, C. Ma, D. S. Robertson, A. E. E. Rogers, I. I. Shapiro, A. R. Whitney, and J. J. Wittels, "Precision Surveying Using Radio Interferometry," *J. Surveying and Mapping Div., Proc. ASCE*, vol. 104, no. SU1, pp. 25-34, 1978.
2. T. A. Herring, B. E. Corey, C. C. Counselman, III, I. I. Shapiro, B. O. Ronnang, O. E. H. Rydbeck, N. R. Vandenberg, H. F. Hinteregger, C. A. Knight, A. E. E. Rogers, A. R. Whitney, D. S. Robertson, and B. R. Schupler, "Geodesy by Radio Interferometry: Intercontinental Distance Determinations with Subdecimeter Precision," *J. Geophys. Res.*, 86, pp. 1647-1651, 1981.
3. A. R. Whitney, A. E. E. Rogers, H. F. Hinteregger, C. A. Knight, J. I. Levine, S. Lippincot, T. A. Clark, I. I. Shapiro, and D. S. Robertson, "A Very-Long-Baseline Interferometer System for Geodetic Applications," *Rad. Sci.*, 11, pp. 421-432, 1976.
4. O. J. Sovers, J. B. Thomas, J. L. Fanselow, E. J. Cohen, G. H. Purcell, Jr., D. H. Rogstad, L. J. Skjerve, and D. J. Spitzmesser, "Radio Interferometric Determination of Intercontinental Baselines and Earth Orientation Utilizing Deep Space Network Antennas," *J. Geophys. Res.* (in press).
5. J. B. Thomas, J. L. Fanselow, P. F. MacDoran, L. J. Skjerve, D. J. Spitzmesser, and H. F. Fliegel, "A Demonstration of an Independent-Station Radio Interferometry System with 4-cm Precision on a 16-km Baseline," *J. Geophys. Res.*, 81, pp. 995-1005, 1976.
6. A. E. Niell, K. M. Ong, P. F. MacDoran, G. M. Resch, D. D. Morabito, E. S. Claflin, and J. F. Dracup, "Comparison of a Radio Interferometric Differential Baseline Measurement with Conventional Geodesy," *Tectonophysics*, 52, pp. 49-58, 1979.
7. K. M. Ong, P. F. MacDoran, J. B. Thomas, H. F. Fliegel, L. J. Skjerve, D. J. Spitzmesser, P. D. Batelaan, and S. R. Paine, "A Demonstration of a Transportable Radio Interferometric Surveying System with 3-cm Accuracy on a 307-m Base Line," *J. Geophys. Res.*, 81, pp. 3587-3593, 1976.
8. "Application of Space Technology to Crustal Dynamics and Earthquake Research," NASA Technical Paper 1464, GSFC, Greenbelt, MD, August 1979.
9. D. W. Trask, M. L. Brunn, E. J. Cohen, J. M. Davidson, J. L. Fanselow, P. F. MacDoran, R. B. Miller, A. E. Niell, G. S. Parks, G. M. Resch, L. J. Skjerve, C. J. Vegos, and K. S. Wallace, "Mobile VLBI Surveying: Instrumentation, Operating Procedures, and Survey Results of ARIES," *Proceedings of Symposium No. 5: Geodetic Applications of Radio Astronomy*, ed. William Carter, U. S. Department of Commerce, National Oceanic and Atmospheric Administration, Washington, D.C., pp. 120-133, 1982.
10. D. W. Trask, M. L. Brunn, J. M. Davidson, J. L. Fanselow, A. E. Niell, G. M. Resch, and K. S. Wallace, "Response of the Mobile VLBI Design to Error Sources," *Proceedings of Interferometry*, Centre National d'Etudes Spatiales, Toulouse, France, pp. 88-108, 1982.
11. H. G. Linder, and C. E. Noll, "Crustal Dynamics Data Information System User's Guide," NASA/GSFC Document X-931-82-14, GSFC, Greenbelt, MD, October 1982.

12. C. E. Noll, E. A. Creamer, R. J. Allenby, H. G. Linder, and G. D. Mead, "Crustal Dynamics Catalogue of Site Information (Review Copy)," NASA/GSFC Document X-904-83-14, GSFC, Greenbelt, MD, September 1983.
13. P. M. Kroger, S. L. Allen, B. C. Beckman, J. M. Davidson, J. E. Patterson, M. A. Slade, J. S. Spitler, and F. P. Wieland, "Current Mobile VLBI Data Base Submitted to the NASA Crustal Dynamics Data Information System," GSFC, Greenbelt, MD, 4 July 1984.
14. J. B. Minster and T. H. Jordan, "Present-Day Plate Motions," *J. Geophys. Res.*, 83, pp. 5331-5354, 1978.
15. J. B. Thomas, "An Analysis of Long Baseline Radio Interferometry," DSN Progress Report, JPL Technical Report 32-1526, Vol. VII, pp. 37-50, Vol. VIII, pp. 29-38, and Vol. XVI, pp. 47-64, Jet Propulsion Laboratory, Pasadena, California, 1972.
16. I. I. Shapiro, "Estimation of Astrometric and Geodetic Parameters from VLBI Observations," *Methods of Experimental Physics*, ed. M. L. Meeks, Academic Press, New York, pp. 261-276, 1976.
17. S. L. Allen, "Earth Orientation Effects on Mobile VLBI Baselines," TDA Progress Report 42-78, pp. 202-215, Jet Propulsion Laboratory, Pasadena, California, 1984.
18. J. B. Thomas, O. J. Sovers, J. L. Fanelow, E. J. Cohen, G. H. Purcell, Jr., D. H. Rogstad, L. J. Skjerve, and D. J. Spitzmesser, "Radio Interferometric Determination of Source Positions, Intercontinental Baselines, and Earth Orientation with Deep Space Network Antennas—1971 to 1980," TDA Progress Report 42-73, pp. 128-155, Jet Propulsion Laboratory, Pasadena, California, 1983.
19. J. L. Fanelow, O. J. Sovers, J. B. Thomas, G. H. Purcell, Jr., E. J. Cohen, D. H. Rogstad, L. J. Skjerve, and D. J. Spitzmesser, "Radio Interferometric Determination of Source Positions Utilizing Deep Space Network Antennas—1971 to 1980," *Astron. J.* (in press).
20. M. Feissel, BIH (Bureau International de l'Heure) Annual Report, 1982.
21. T. M. Eubanks, J. A. Steppe, and M. A. Spieth, "The Accuracy of Radio Interferometric Measurements of Earth Rotation," TDA Progress Report 42-80, Jet Propulsion Laboratory, Pasadena, California, 1984.
22. J. O. Dickey and J. G. Williams, "Earth Rotation from Lunar Laser Ranging," *Astron. Astrophys. Suppl. Ser.*, 54, pp. 519-540, 1983.
23. W. E. Carter, D. S. Robertson, J. E. Pettay, B. D. Tapley, B. E. Schutz, R. J. Eanes and M. Lufeng, "Variations in the Rotation of the Earth," *Science*, 224, pp. 957-961, 1984.
24. T. M. Eubanks, M. G. Roth, P. B. Esposito, J. A. Steppe and P. S. Callahan, "An Analysis of TEMPO Earth Orientation Results," *Proceedings of Symposium No. 5: Geodetic Applications of Radio Astronomy*, ed. William Carter, U.S. Department of Commerce, National Oceanic and Atmospheric Administration, Washington, D.C., pp. 152-162, 1982.
25. C. C. Chao, "A New Method to Predict Wet Zenith Range Correction from Surface Measurements," DSN Progress Report 32-1526, Vol. XIV, pp. 33-41, Jet Propulsion Laboratory, Pasadena, California, 1973; and A. L. Berman, "The Prediction of Zenith Range Refraction from Surface Measurements of Meteorological Parameters," JPL Technical Report 32-1602, Jet Propulsion Laboratory, Pasadena, California, 1976.

26. E. S. Claflin, S. C. Wu, and G. M. Resch, "Microwave Radiometer Measurement of Water Vapor Path Delay: Data Reduction Techniques," DSN Progress Report 42-48, pp. 22-30, Jet Propulsion Laboratory, Pasadena, California, 1978; and S. C. Wu, "Optimum Frequencies of a Passive Microwave Radiometer for Tropospheric Path Length Correction," IEEE Transactions on Antennas and Propagation, Vol. AP-27, No. 2, pp. 233-239, 1979.
27. D. E. Smith, R. Kolenkiewicz, P. J. Dunn, and M. H. Torrence, "The Measurements of Fault Motion by Satellite Laser Ranging," Tectonophysics, Vol. 52, pp. 59-67, 1979.
28. A. E. E. Rogers, C. A. Knight, H. F. Hinteregger, A. R. Whitney, C. C. Counselman, III, I. I. Shapiro, S. S. Gourevitch, and T. A. Clark, "Geodesy by Radio Interferometry: Determination of a 1.24 km Baseline with  $\sim 5$ -mm Repeatability," J. Geophys. Res., 83, pp. 325-334, 1978.

**Table 1. Error model inputs<sup>a</sup>**

Error Source	Assumed Uncertainty in Year		
	1980 <sup>b</sup>	1984	1986
Earth Orientation			
UT1-UTC	2 milliseconds	0.2 milliseconds	0.07 milliseconds
X-pole	10 milliarcsec	7 milliarcsec	2.0 milliarcsec
Y-pole	10 milliarcsec	7 milliarcsec	1.5 milliarcsec
Transmission Media			
Water Vapor (Zenith)	5 cm	2 cm	0.5 cm
Dry Air (Zenith)	1 cm	1 cm	1 cm
Dry Air (Mapping) <sup>c</sup>	1 cm	1 cm	1 cm
Ionosphere <sup>d,e</sup>			
Length	1.1 cm/500 km	0 cm	0 cm
Transverse	2.4 cm	0 cm	0 cm
Vertical	6.2 cm	0 cm	0 cm
Mobile Survey Tie	0.5 cm	0.2 cm	0.2 cm
Source Positions	20-50 milliarcsec	5 milliarcsec	1 milliarcsec
System Noise	300 picoseconds	50 picoseconds	50 picoseconds
Other Random (Clocks, troposphere, other)	150 picoseconds	50 picoseconds	50 picoseconds
Other Systematic <sup>d</sup>			
Length, Transverse	2 cm	2 cm	1 cm
Vertical	5 cm	5 cm	2.5 cm

<sup>a</sup>Except where otherwise indicated (see footnote c), the quoted value denotes the error in the calibration or error source, not the resulting error in the baseline component.

<sup>b</sup>Current (1984) uncertainties for Earth orientation and source positions permit reprocessing of 1980 data with improved accuracy. The values presented here serve to illustrate improvements in the quality of mobile VLBI results in a historical perspective.

<sup>c</sup>This is the error in the Chao mapping function at 17 degrees, which is the elevation angle cutoff for the mobile systems.

<sup>d</sup>The quoted value is not the error in the calibration or error source itself; it is the empirically determined error in the baseline resulting from this error source.

<sup>e</sup>An average level of  $1.0 \times 10^{17}$  electrons/cm<sup>2</sup> is assumed for the zenith columnar ionosphere content.

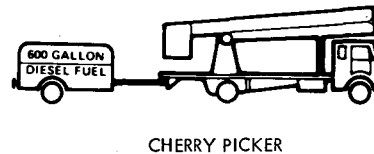
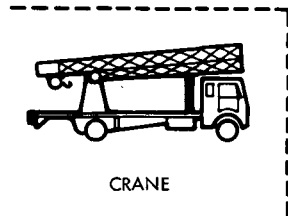
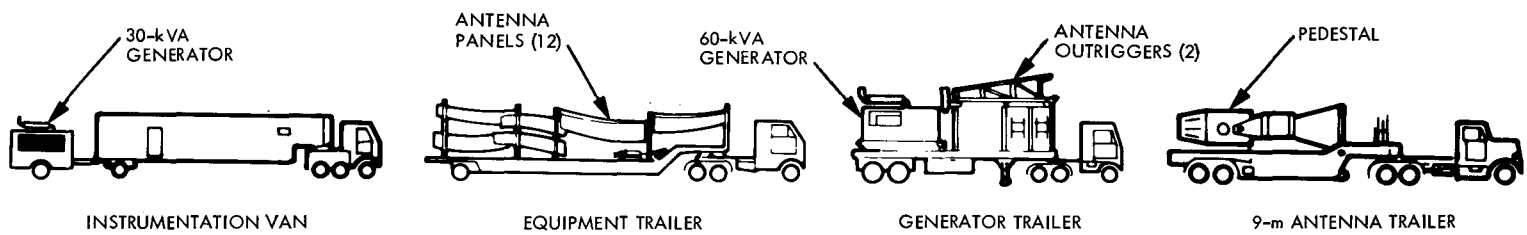
**Table 2. Chi-square calculations<sup>a</sup>**

Baseline	Dates	Degrees of Freedom	Chi-square		Probability <sup>b</sup>	
			Length	Transverse	Length	Transverse
OVRO-JPL	1/80- 5/81	6	1.3	5.9	97	56
OVRO-JPL	8/81- 11/81	3	0.84	1.8	83	62
OVRO-JPL	10/82- 2/83	3	2.4	0.12	49	99
OVRO-Quincy	10/82 6/83	2	1.3	0.24	52	89

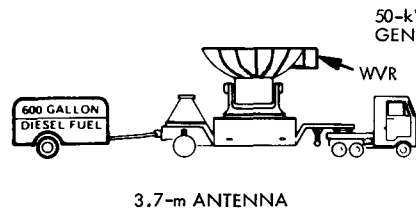
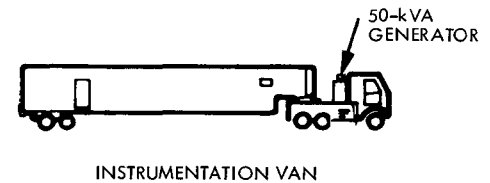
<sup>a</sup>The data from which these are calculated are graphically displayed in Fig. 6.

<sup>b</sup>The listed values give probability (units of percentage) of obtaining chi-square that large or larger.

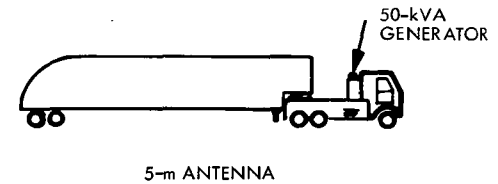
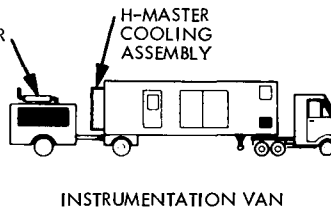




MV 1 CARAVAN  
(ARIES 9-m)



MV 2 CARAVAN  
(ARIES 3.7-m)



MV 3 CARAVAN  
(ADVANCED ARIES OR ORION)

**Fig. 1. Schematic depictions of the transit configurations of the three mobile VLBI stations**

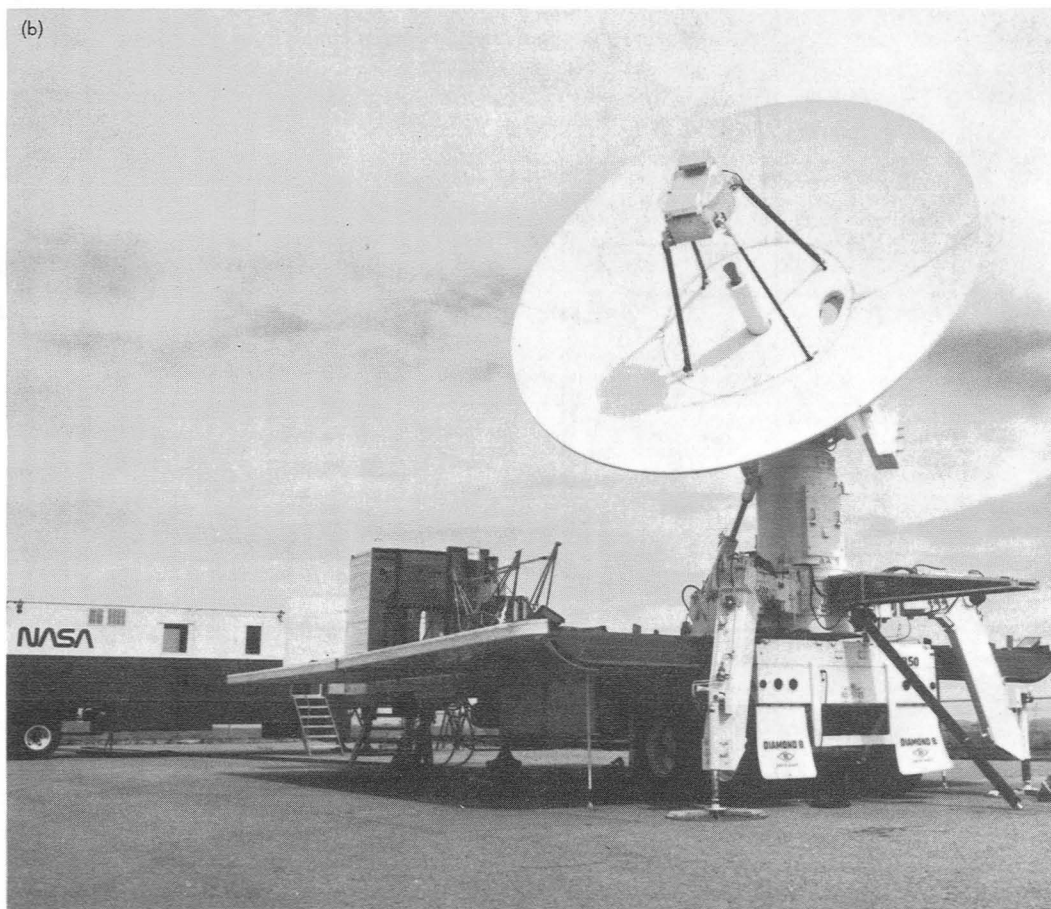
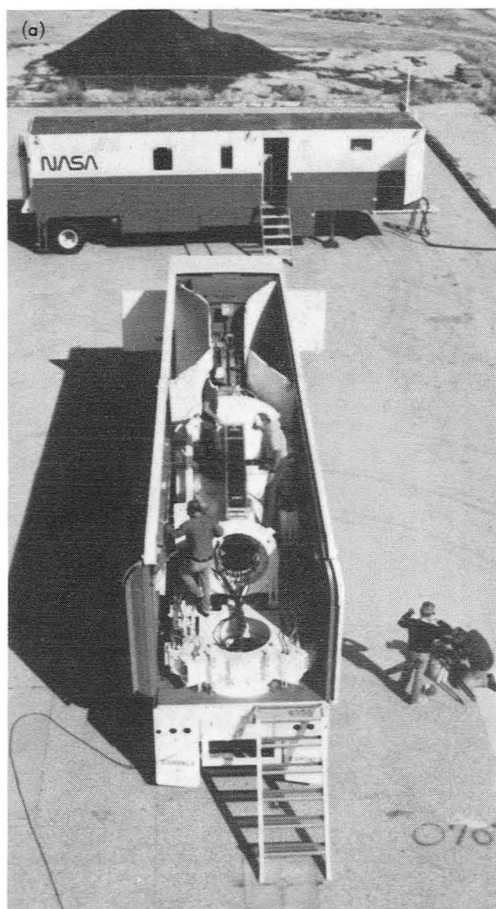


Fig. 2. MV-3 in: (a) its transit configuration and (b) its deployed configuration

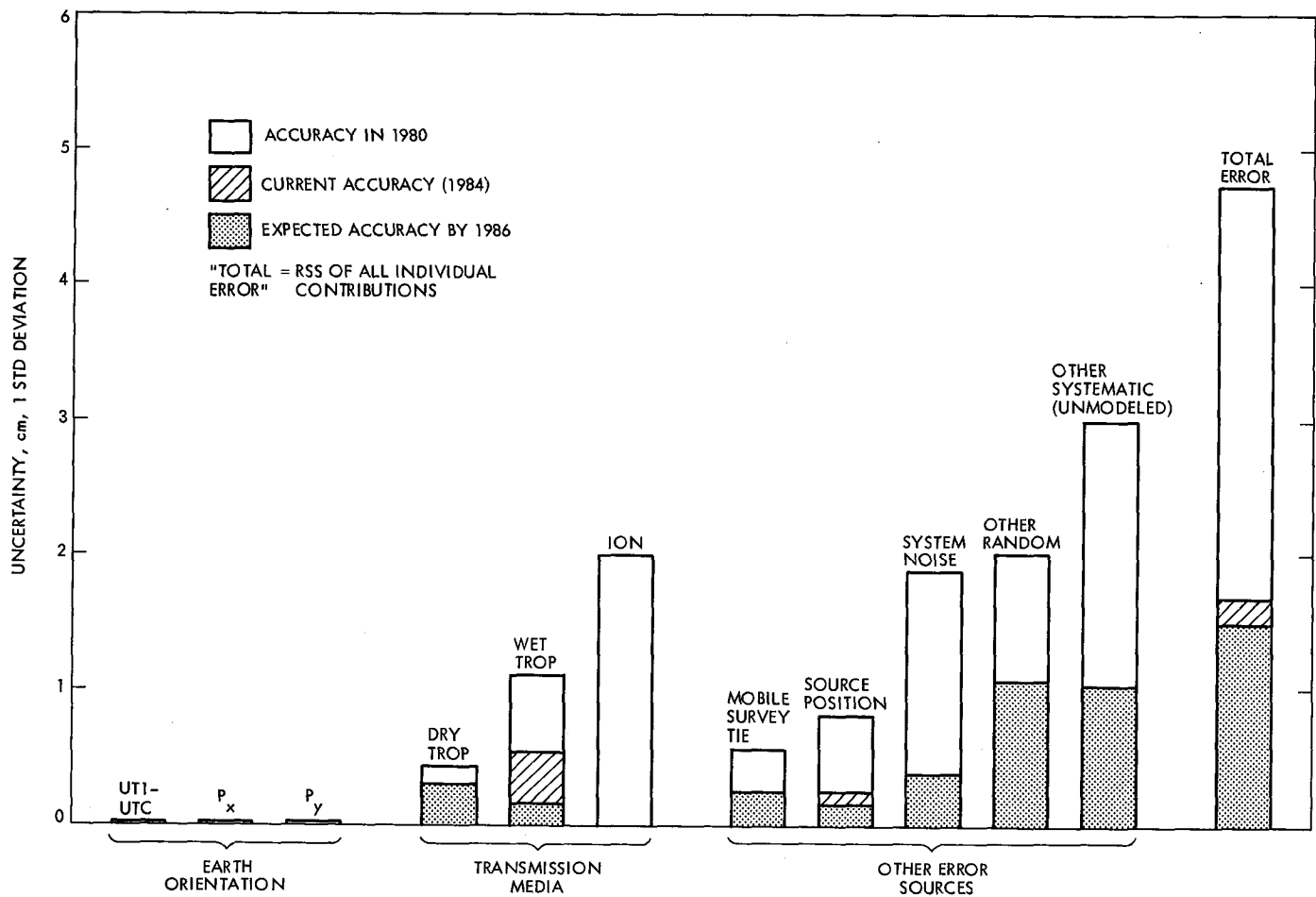


Fig. 3. The error budget for the length component for the example of the Monument Peak—Quincy baseline

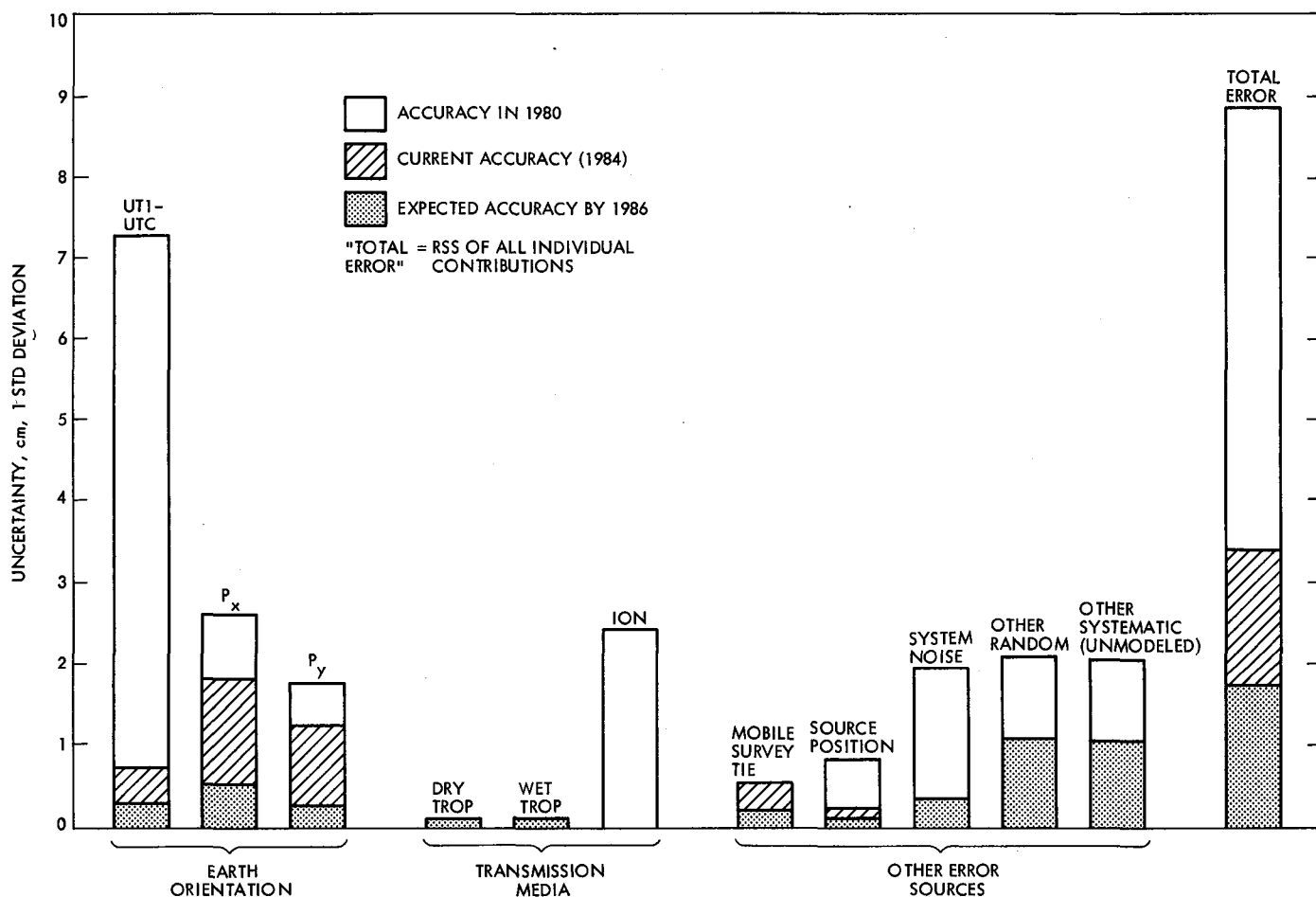


Fig. 4. The error budget for the horizontal transverse component for the example of the Monument Peak—Quincy baseline

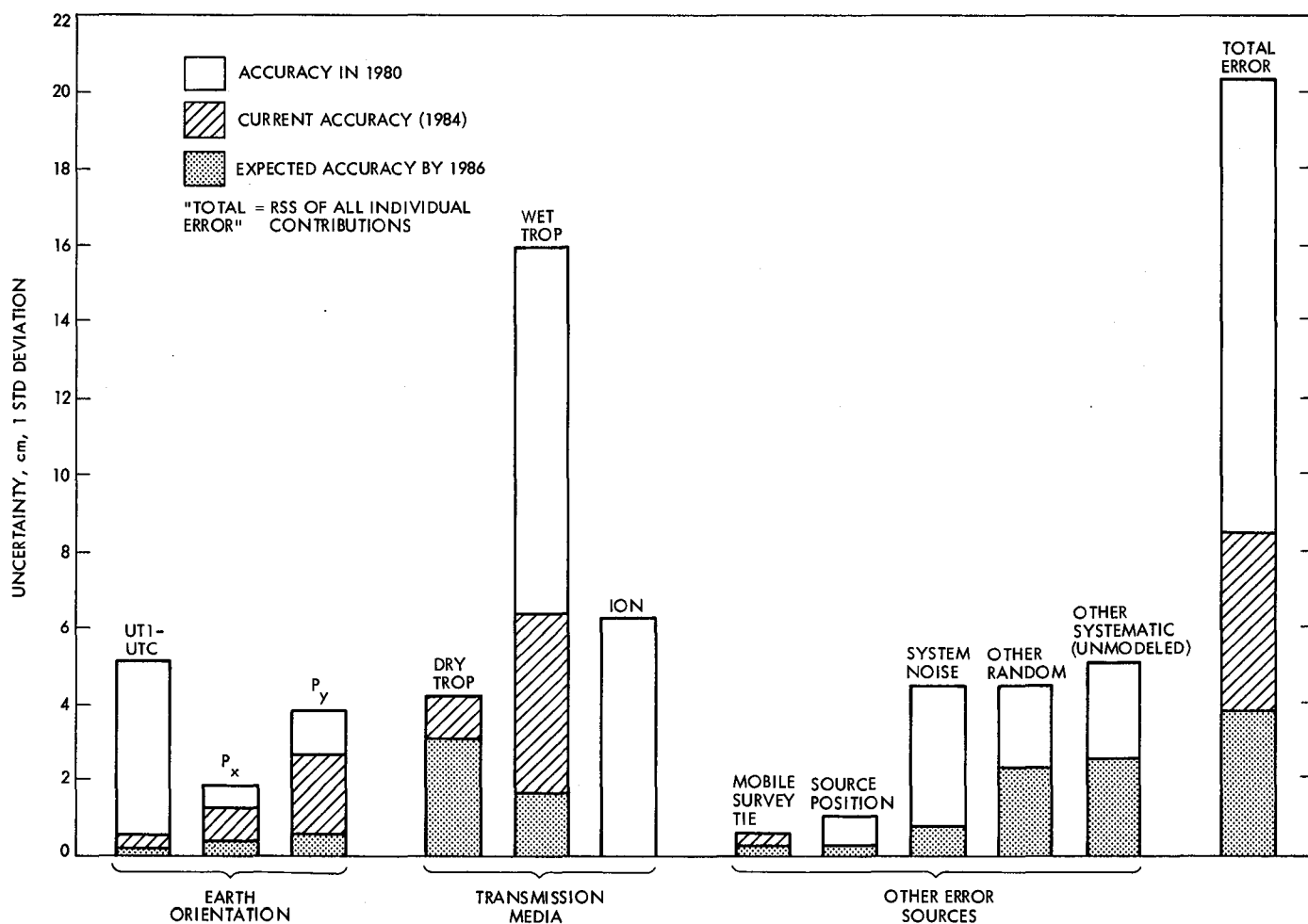
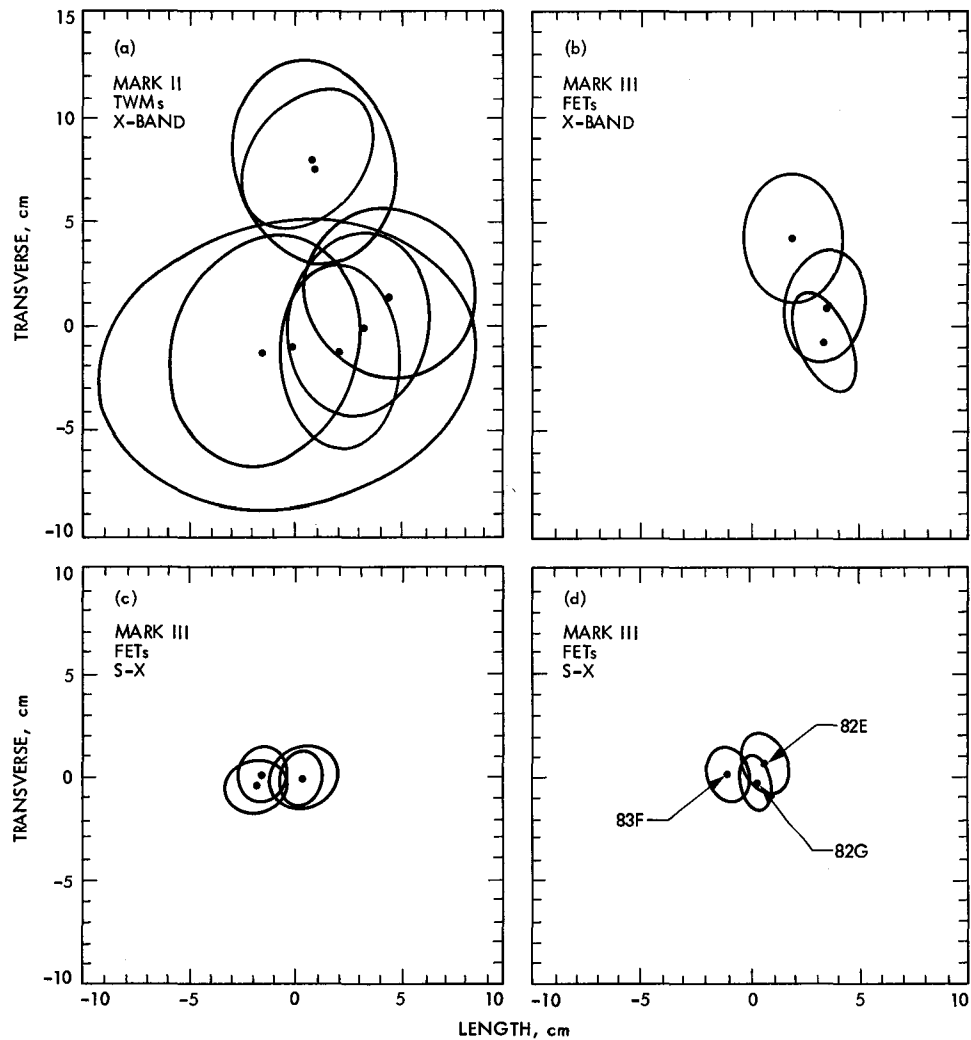


Fig. 5. The error budget for the baseline vertical component for the example of the Monument Peak—Quincy baseline



**Fig. 6. Error ellipsoids in the horizontal plane for: (a) the OVRO—JPL baseline from January 1980 to May 1981, (b) the OVRO—JPL baseline from August 1981 to November 1981, (c) the OVRO—JPL baseline from October 1982 to February 1983, and (d) the OVRO—Quincy baseline from October 1982 to June 1983. These error ellipsoids illustrate various stages of mobile VLBI system development over the past four years. Consistency of the measurements made using the current system (see Figs. 6c and 6d) appears to be on the order of 2 cm or better.**

## Author Index,<sup>1</sup> 1984

### *The Telecommunications and Data Acquisition Progress Report*

42-77, January–March, May 15, 1984

42-78, April–June, August 15, 1984

42-79, July–September, November 15, 1984

42-80, October–December, February 15, 1985

#### **Aguirre, S.**

- 42-78 Coherent Digital Demodulation of a Residual Carrier Signal Using IF Sampling, pp. 135-142.

See Sfeir, R.

- 42-79 Design and Performance of Sampled Data Loops for Subcarrier and Carrier Tracking, pp. 81-95.

S. Aguirre and W. J. Hurd

#### **Allen, S. L.**

- 42-78 Earth Orientation Effects on Mobile VLBI Baselines, pp. 202-215.

#### **Bathker, D. A.**

- 42-80 Microwave Surface Resistivity of Several Materials at Ambient Temperature, pp. 8-11.

See Reilly, H. F.

#### **Bautista, J. J.**

- 42-79 Superconducting NbTi and Pb(Cu) Bandpass Filters, pp. 62-68.

J. J. Bautista and S. M. Petty

- 42-80 Microwave Surface Resistivity of Several Materials at Ambient Temperature, pp. 8-11.

See Reilly, H. F.

#### **Bhanji, A. M.**

- 42-78 High Power Ka-Band Transmitter for Planetary Radar and Spacecraft Uplink, pp. 24-48.

A. M. Bhanji, D. J. Hoppe, R. W. Hartop, E. W. Stone, W. A. Imbriale, D. Stone, and M. Caplan

- 42-80 The Effects of Mode Impurity on Ka-Band System Performance, pp. 12-23.

See Hoppe, D. J.

#### **Brazil, S.**

- 42-78 Intermodulation Product Levels in Flame-Sprayed Materials, pp. 79-98.

See Yung, C. S.

#### **Brokl, S. S.**

- 42-77 Demodulator and Accumulator for the High-Speed Data Acquisition System, pp. 97-103.

- 42-77 The Goldstone R/D High Speed Data Acquisition System, pp. 87-96.

See Deutsch, L.

#### **Caplan, M.**

- 42-78 High Power Ka-Band Transmitter for Planetary Radar and Spacecraft Uplink, pp. 24-48.

See Bhanji, A. M.

#### **Chang, J. J.**

- 42-79 VLSI Architectures for the Multiplication of Integers Modulo a Fermat Number, pp. 136-141.

J. J. Chang, T. K. Truong, I. S. Reed, and I. S. Hsu

<sup>1</sup>In the case of joint authorship, the reader is referred to the citation under the first author where all authors of the article are listed.

**Chian, C. T.**

- 42-78 NASTRAN Structural Model for the Large 64-Meter Antenna Pedestal Part III — Applications to Hydrostatic Bearing Oil Film, pp. 172-183.

C. T. Chain and D. Schonfeld

**Cormier, R.**

- 42-79 Development and Testing of a 20-kW X-Band Transmitter With High Phase Stability, pp. 47-61.

R. Cormier and T. Tesarek

**Davidson, J. M.**

- 42-80 Utilization of Mobile VLBI for Geodetic Measurements, pp. 248-266.

J. M. Davidson and D. W. Trask

**Deardorff, D. D.**

- 42-78 Magnetic Refrigeration Development, pp. 49-58.

D. D. Deardorff and D. L. Johnson

**Deutsch, L.**

- 42-77 The Goldstone R/D High Speed Data Acquisition System, pp. 87-96.

L. Deutsch, R. F. Jurgens, and S. S. Brokl

- 42-77 Effects of NRZ-M Modulation on Convolution Codes Performance, pp. 33-40.

L. Deutsch, F. Pollara, and L. Swanson

- 42-80 Reed-Solomon Code Synchronization Revisited, pp. 91-96.

**Duff, L. W.**

- 42-78 64-m Antenna Automatic Subreflector Focusing Controller, pp. 73-78.

See Guiar, C. N.

**Eubanks, T. M.**

- 42-80 The Accuracy of Radio Interferometric Measurements of Earth Rotation, pp. 229-235.

T. M. Eubanks, J. A. Steppe, and M. A. Spieth

**Fanselow, J. L.**

- 42-79 VLBI Solutions for the Time Variation of DSN Baselines: 1978 to 1983, pp. 25-34.

See Treuhaft, R. N.

**Farazian, K. H.**

- 42-79 Programmable Digital Baud Integrators for the Radar High-Speed Data Acquisition System, pp. 142-151.

K. H. Farazian and R. F. Jurgens

**Faulkner, J.**

- 42-80 Arcsecond Positions for Milliarcsecond VLBI Nuclei of Extragalactic Radio Sources, Part III: 74 Sources, pp. 1-7.

See Morabito, D. D.

**Galindo-Israel, V.**

- 42-80 Interpolation Methods for GTD Analysis of Shaped Reflectors, pp. 62-67.

V. Galindo-Israel, W. Imbriale, Y. Rahmat-Samii, and T. Veruttipong

**Gordon, D. D.**

- 42-79 Mark IVA DSN 26-Meter Subnet, pp. 152-159.

**Gosline, R. M.**

- 42-77 DSS 13 Microprocessor Antenna Controller, pp. 64-74.

**Greenhall, C. A.**

- 42-77 Time Interval Errors of a Flicker-Noise Generator, pp. 126-135.

**Grimm, M. J.**

- 42-78 A Simple Algorithm for the Metric Traveling Salesman Problem, pp. 108-114.

**Guiar, C. N.**

- 42-78 64-m Antenna Automatic Subreflector Focusing Controller, pp. 73-78.

C. N. Guiar and L. W. Duff



- 42-78 Potential Surface Improvements by Bump Removal for 64-m Antenna, pp. 59-72.  
See Katow, S.
- Gulkis, S.**
- 42-77 Note on the Optimum Search Strategy for Uniformly Distributed CW Transmitters, pp. 144-150.
- Ham, N. C.**
- 42-79 VLBI System (BLK I) IF-Video Down Conversion Design, pp. 172-188.
- Hartop, R. W.**
- 42-78 High Power Ka-Band Transmitter for Planetary Radar and Spacecraft Uplink, pp. 24-48.  
See Bhanji, A. M.
- Hoppe, D. J.**
- 42-78 High Power Ka-Band Transmitter for Planetary Radar and Spacecraft Uplink pp. 24-48.  
See Bhanji, A. M.
- 42-80 The Effects of Mode Impurity on Ka-Band System Performance, pp. 12-23.  
D. J. Hoppe, W. A. Imbriale, and A. M. Bhanji
- Hsu, I. S.**
- 42-79 VLSI Architectures for the Multiplication of Integers Modulo a Fermat Number, pp. 136-141.  
See Chang, J. J.
- Hughes, R. D.**
- 42-80 Design Procedure for the New 70-Meter Antenna Subreflector Positioner, pp. 68-82.
- 42-80 Subreflector Focusing Techniques Applied to New DSS-15 and DSS-45 34-Meter Antennas, pp. 83-90.  
R. D. Hughes and M. S. Katow
- Hurd, W. J.**
- 42-78 Symbol-Stream Combiner: Description and Demonstration Plans, pp. 115-121.  
W. J. Hurd, L. J. Reder, and M. D. Russell
- 42-78 Coherent Digital Demodulation of a Residual Carrier Signal Using IF Sampling, pp. 135-142.  
See Sfeir, R.
- 42-79 Design and Performance of Sampled Data Loops for Subcarrier and Carrier Tracking, pp. 81-95.  
See Aguirre, S.
- 42-79 Improved Carrier Tracking by Smoothing Estimators, pp. 96-106.  
See Pomalaza Ruez, C. A.
- Imbriale, W. A.**
- 42-78 High Power Ka-Band Transmitter for Planetary Radar and Spacecraft Uplink, pp. 24-48.  
See Bhanji, A. M.
- 42-80 Interpolation Methods for GTD Analysis of Shaped Reflectors, pp. 62-67.  
See Galindo-Israel, V.
- 42-80 The Effects of Mode Impurity on Ka-Band System Performance, pp. 12-23.  
See Hoppe, D. J.
- Jauncey, D. L.**
- 42-77 Arcsecond Positions for Milliarcsecond VLBI Nuclei of Extragalactic Radio Sources, Part II: 207 Sources, pp. 1-11.  
See Morabito, D. D.
- 42-80 Arcsecond Positions for Milliarcsecond VLBI Nuclei of Extragalactic Radio Sources, Part III: 74 Sources, pp. 1-7.  
See Morabito, D. D.
- Johnson, D. L.**
- 42-78 Magnetic Refrigeration Development, pp. 49-58.  
See Deardorff, D. D.
- Jurgens, R. F.**
- 42-77 The Goldstone R/D High Speed Data Acquisition System, pp. 87-96.  
See Deutsch, L.

- 42-79 Programmable Digital Baud Integrators for the Radar High-Speed Data Acquisition System, pp. 142-151.

See Farazian, K. H.

**Katow, M. S.**

- 42-78 Potential Surface Improvements by Bump Removal for 64-m Antenna, pp. 59-72.

S. Katow and C. N. Gujar

- 42-80 Subreflector Focusing Techniques Applied to New DSS-15 and DSS-45 34-Meter Antennas, pp. 83-90.

See Hughes, R. D.

**Koerner, M. A.**

- 42-77 Effect of RF Filtering on the Performance of Uncoded PCM/PM Telemetry Channels, pp. 104-125.

**Koscielski, C. G.**

- 42-78 Mojave Base Station Implementation, pp. 216-223.

**Lansing, F.**

- 42-78 Intermodulation Product Levels in Flame-Sprayed Materials, pp. 79-98.

See Yung, C. S.

**Lanyi, G.**

- 42-78 Tropospheric Delay Effects in Radio Interferometry, pp. 152-159.

**Lee, G.**

- 42-77 Magnetically Enhanced Hydrogen Gas Dissociator: A Progress Report, pp. 19-23.

G. Lee, T. K. Tucker, and L. Maleki

**Lee, P. J.**

- 42-77 New Short Constraint Length, Rate  $1/N$  Convolution Codes Which Minimize Required  $E_b/N_o$  for Given Bit Error Rate, pp. 41-56.

- 42-79 Analysis of a Coded,  $M$ -ary Orthogonal Input Optical Channel With Random-Gain Photomultiplier Detection, p. 107-113.

- 42-79 A Very Efficient Transfer Function Bounding Technique on Bit Error Rate for Viterbi Decoded, Rate  $1/N$  Convolutional Codes, pp. 114-123.

- 42-80 Further Results on Rate  $1/N$  Convolutional Code Constructions With Minimum Required SNR Criterion, pp. 97-102.

**Levy, R.**

- 42-78 Optimization of Antenna Structure Design, pp. 9-23.

- 42-80 Condensed Antenna Structural Models for Dynamics Analysis, pp. 40-61.

**Liewer, K. M.**

- 42-79 VLBI Solutions for the Time Variation of DSN Baselines: 1978 to 1983, pp. 25-34.

See Treuhaft, R. N.

**Linfield, R. P.**

- 42-80 Arcsecond Positions for Milliarcsecond VLBI Nuclei of Extragalactic Radio Sources, Part III: 74 Sources, pp. 1-7.

See Morabito, D. D.

**Lokshin, A.**

- 42-77 An Investigation of the Effects of Scan Separation on the Sensitivity of the SETI All Sky Survey for the Case of Gaussian Noise, pp. 151-158.

A Lokshin and E. T. Olsen

**Maleki, L.**

- 42-77 Magnetically Enhanced Hydrogen Gas Dissociator: A Progress Report, pp. 19-23.

See Lee, G.

**Marshall, W. K.**

- 42-80 Detection and Symbol Synchronization for Multiple-Bit per Photon Optical Communications, pp. 24-30.

**McClure, D. H.**

- 42-79 64-Meter to 70-Meter Antenna Extension, pp. 160-164.

D. H. McClure and F. D. McLaughlin

**McEliece, R. J.**

- 42-77 An Easy-to-Implement Coding Scheme for Multi-frequency PPM, pp. 57-63.

R. J. McEliece and L. Swanson

**McGinness, H. D.**

- 42-80 Antenna Axis Drive Torques for the 70-Meter Antenna, pp. 121-126.

- 42-80 Characteristics of the Elevation Drive Suspension of the 64-Meter Antennas, pp. 146-175.

- 42-80 Elevation Bearing Maximum Load, 70-Meter Antenna, pp. 142-145.

- 42-80 An Evaluation of the 64-Meter Antenna Radial Bearing for Use on the 70-Meter Antenna, pp. 127-141.

- 42-80 Hydrostatic Bearing Pad Maximum Load and Overturning Conditions for the 70-Meter Antenna, pp. 176-179.

**McLaughlin, F. D.**

- 42-79 64-Meter to 70-Meter Antenna Extension, pp. 160-164.

See McClure, D. H.

**Meeker, J. G.**

- 42-77 X-Band Uplink Technology Demonstration at DSS-13, pp. 24-32.

J. G. Meeker and C. T. Timpe

**Merkey, P.**

- 42-78 GCF Compatibility With Packets and Data Compression, pp. 199-201.

See Posner, E. C.

**Mileant, A.**

- 42-80 Performance of the DSA's Subcarrier Demodulation Digital Loop, pp. 180-194.

See Simon, M. K.

**Moore, R. C.**

- 42-80 Historical Cost Curves for Hydrogen Masers and Cesium Beam Frequency and Timing Standards, pp. 220-228.

See Remer, D. S.

**Morabito, D. D.**

- 42-77 Submilliarcsecond VLBI Observations of the Close Pair GC 1342+662 and GC 1342+663, pp. 12-18.

- 42-77 Arcsecond Positions for Milliarcsecond VLBI Nuclei of Extragalactic Radio Sources, Part II: 207 Sources, pp. 1-11.

D. D. Morabito, R. A. Preston, M. A. Slade, D. L. Jauncey, and G. D. Nicolson

- 42-79 Submilliarcsecond VLBI Using Compact Close Pairs of Radio Sources: Error Analysis, pp. 1-16.

- 42-80 Arcsecond Positions for Milliarcsecond VLBI Nuclei of Extragalactic Radio Sources, Part III: 74 Sources, pp. 1-7.

D. D. Morabito, R. A. Preston, R. P. Linfield, M. A. Slade, A. E. Wehrle, J. Faulkner, and D. L. Jauncey

**Moultrie, B.**

- 42-79 The Performance of Differential VLBI Delay During Interplanetary Cruise, pp. 35-46.

B. Moultrie, P. J. Wolff, and T. H. Taylor

**Nicolson, G. D.**

- 42-77 Arcsecond Positions for Milliarcsecond VLBI Nuclei of Extragalactic Radio Sources, Part II: 207 Sources, pp. 1-11.

See Morabito, D. D.

**Niell, A. E.**

- 42-79 VLBI Solutions for the Time Variation of DSN Baselines: 1978 to 1983, pp. 25-34.

See Treuhaft, R. N.

**Olsen, E. T.**

- 42-77 An Investigation of the Effects of Scan Separation on the Sensitivity of the SETI All Sky Survey for the Case of Gaussian Noise, pp. 151-158.

See Lokshin, A.

**Parsons, P. L.**

- 42-79 Antenna Microwave Subsystem, pp. 165-171.

**Petty, S. M.**

- 42-79 Superconducting NbTi and Pb(Cu) Bandpass Filters, pp. 62-68.  
See Bautista, J. J.

**Pollara, F.**

- 42-77 Effects of NRZ-M Modulation on Convolution Codes Performance, pp. 33-40.  
See Deutsch, L.

**Pomalaza Raez, C. A.**

- 42-79 Improved Carrier Tracking by Smoothing Estimators, pp. 96-106.  
C. A. Pomalaza Raez and W. J. Hurd

**Posner, E. C.**

- 42-77 Minimum-Distance Problems in Protocol Design, pp. 136-143.  
E. C. Posner and Z. Reichstein
- 42-77 TDA Assessment of Recommendations for Space Data System Standards, pp. 75-84.  
E. C. Posner and R. Stevens
- 42-78 GCF Compatibility With Packets and Data Compression, pp. 199-201.  
E. C. Posner and P. Merkey
- 42-80 Codes With Parity Conditions on Subsets of Coordinates, pp. 236-247.  
E. C. Posner and Z. Reichstein

**Preston, R. A.**

- 42-77 Arcsecond Positions for Milliarcsecond VLBI Nuclei of Extragalactic Radio Sources, Part II: 207 Sources, pp. 1-11.  
See Morabito, D. D.
- 42-80 Arcsecond Positions for Milliarcsecond VLBI Nuclei of Extragalactic Radio Sources, Part III: 74 Sources, pp. 1-7.  
See Morabito, D. D.

- 42-80 The Venus Balloon Project, pp. 195-201.

R. A. Preston, J. H. Wilcher, and C. T. Stelzried

**Rahmat-Samii, Y.**

- 42-80 Interpolation Methods for GTD Analysis of Shaped Reflectors, pp. 62-67.  
See Galindo-Israel, V.

**Rauch, L. L.**

- 42-79 On Estimating the Phase of a Periodic Waveform in Additive Gaussian Noise — Part II, pp. 17-24.

**Reder, L. J.**

- 42-78 Symbol-Stream Combiner: Description and Demonstration Plans, pp. 115-121.  
See Hurd, W. J.

**Reed, I. S.**

- 42-78 Error-Trellis Syndrome Decoding Techniques for Convolutional Codes, pp. 122-134.  
I. S. Reed and T. K. Truong
- 42-79 VLSI Architectures for the Multiplication of Integers Modulo a Fermat Number, pp. 136-141.  
See Change, J. J.
- 42-79 Sequential Syndrome Decoding of Convolutional Codes, pp. 124-135.  
I. S. Reed and T. K. Truong

**Reichstein, Z.**

- 42-77 Minimum-Distance Problems in Protocol Design, pp. 136-143.  
See Posner, E. C.
- 42-80 Codes With Parity Conditions on Subsets of Coordinates, pp. 236-247.  
See Posner, E. C.

**Reilly, H. F.**

- 42-80 Microwave Surface Resistivity of Several Materials at Ambient Temperature, pp. 8-11.  
H. F. Reilly, J. J. Bautista, and D. A. Bathker

**Remer, D. S.**

- 42-80 Historical Cost Curves for Hydrogen Masers and Cesium Beam Frequency and Timing Standards, pp. 220-228.

D. S. Remer and R. C. Moore

**Riewe, Jr., A. A.**

- 42-78 Investigation and Rehabilitation to Extend Service Life of DSS-13 Antenna Concrete Foundation, pp. 160-171.

**Russell, M. D.**

- 42-78 Symbol-Stream Combiner: Description and Demonstration Plans, pp. 115-121.

See Hurd, W. J.

**Schonfeld, D.**

- 42-78 NASTRAN Structural Model for the Large 64-Meter Antenna Pedestal Part III — Applications to Hydrostatic Bearing Oil Film, pp. 172-183.

See Chian, C. T.

**Sfeir, R.**

- 42-78 Coherent Digital Demodulation of a Residual Carrier Signal Using IF Sampling, pp. 135-142.

R. Sfeir, S. Aguirre, and W. J. Hurd

**Simon, M. K.**

- 42-80 Performance of the DSA's Subcarrier Demodulation Digital Loop, pp. 180-194.

M. K. Simon and A. Mileant

**Sipes, Jr., D. L.**

- 42-80 Highly Efficient Nd:YAG Lasers for Free-Space Optical Communications, pp. 31-39.

**Slade, M. A.**

- 42-77 Arcsecond Positions for Milliarcsecond VLBI Nuclei of Extragalactic Radio Sources, Part II: 207 Sources, pp. 1-11.

See Morabito, D. D.

- 42-80 Arcsecond Positions for Milliarcsecond VLBI Nuclei of Extragalactic Radio Sources, Part III: 74 Sources, pp. 1-7.

See Morabito, D. D.

**Slobin, S. D.**

- 42-80 DSN 34-Meter Antenna Optics Analysis for Wide-band SETI Investigations, pp. 202-219.

**Sovers, O. J.**

- 42-79 VLBI Solutions for the Time Variation of DSN Baselines: 1978 to 1983, pp. 25-34.

See Treuhaft, R. N.

**Spieth, M. A.**

- 42-80 The Accuracy of Radio Interferometric Measurements of Earth Rotation, pp. 229-235.

See Eubanks, T. M.

**Stelzried, C. T.**

- 42-80 The Venus Balloon Project, pp. 195-201.

See Preston, R. A.

**Steppe, J. A.**

- 42-80 The Accuracy of Radio Interferometric Measurements of Earth Rotation, pp. 229-235.

See Eubanks, T. M.

**Stevens, G. L.**

- 42-78 A High-Performance Hybrid RF Isolation Amplifier, pp. 1-8.

**Stevens, R.**

- 42-77 TDA Assessment of Recommendations for Space Data System Standards, pp. 75-84.

See Posner, E. C.

- 42-78 Availability of the DSN Telemetry Data System and Its Major Elements, Including the TWM Assemblies, pp. 184-191.

- 42-78 A Study of DSN Traveling Wave Maser System Reliability, pp. 192-198.

R. Stevens and C. P. Wiggins

**Stoller, F.**

- 42-78 Intermodulation Product Levels in Flame-Sprayed Materials, pp. 79-98.

See Yung, C. S.

**Stone, D.**

- 42-78 High Power Ka-Band Transmitter for Planetary Radar and Spacecraft Uplink, pp. 24-48.

See Bhanji, A. M.

**Stone, E. W.**

- 42-78 High Power Ka-Band Transmitter for Planetary Radar and Spacecraft Uplink, pp. 24-48.

**Swanson, L.**

- 42-77 Effects of NRZ-M Modulation on Convolution Codes Performance, pp. 33-40.

See Deutsch, L.

- 42-77 An Easy-to-Implement Coding Scheme for Multi-frequency PPM, pp. 57-63.

See McEliece, R. J.

- 42-78 A Strategy for Successful Deep Space Information Transmission in Bad Weather, pp. 143-151.

L. Swanson and J. H. Yuen

**Tan, H. H.**

- 42-79 Avalanche Photodiode Statistics in Triggered-Avalanche Detection Mode, pp. 69-80.

**Tausworthe, R. C.**

- 42-80 Concepts and Tools for the Software Life Cycle, pp. 103-120.

**Taylor, T. H.**

- 42-79 The Performance of Differential VLBI Delay During Interplanetary Cruise, pp. 35-46.

See Moultrie, B.

**Tesarek, T.**

- 42-79 Development and Testing of a 20-kW X-Band Transmitter With High Phase Stability, pp. 47-61.

See Cormier, R.

**Thomas, J. B.**

- 42-79 VLBI Solutions for the Time Variation of DSN Baselines: 1978 to 1983, pp. 25-34.

See Treuhaft, R. N.

**Timpe, C. T.**

- 42-77 X-Band Uplink Technology Demonstration at DSS-13, pp. 24-32.

See Meeker, J. G.

**Trask, D. W.**

- 42-80 Utilization of Mobile VLBI for Geodetic Measurements, pp. 248-266.

See Davidson, J. M.

**Treuhaft, R. N.**

- 42-79 VLBI Solutions for the Time Variation of DSN Baselines: 1978 to 1983, pp. 25-34.

R. N. Treuhaft, J. L. Fanelow, K. M. Liewer, A. E. Niell, O. J. Sovers, J. B. Thomas, and K. S. Wallace

**Truong, T. K.**

- 42-78 Error-Trellis Syndrome Decoding Techniques for Convolutional Codes, pp. 122-134.

See Reed, I. S.

- 42-79 VLSI Architectures for the Multiplication of Integers Modulo a Fermat Number, pp. 136-141.

See Chang, J. J.

- 42-79 Sequential Syndrome Decoding of Convolutional Codes, pp. 124-135.

See Reed, I. S.

**Tucker, T. K.**

- 42-77 Magnetically Enhanced Hydrogen Gas Dissociator: A Progress Report, pp. 19-23.

See Lee, G.

**Veruttipong, T.**

- 42-80 Interpolation Methods for GTD Analysis of Shaped Reflectors, pp. 62-67.

See Galindo-Israel, V.

**Vo, Q. D.**

- 42-78 Performance Simulation for Unit-Memory Convolutional Codes With Byte-Oriented Viterbi Decoding Algorithm, pp. 99-107.

**Wallace, K. S.**

- 42-79 VLBI Solutions for the Time Variation of DSN Baselines: 1978 to 1983, pp. 25-34.

See Treuhaft, R. N.

**Wehrle, A. E.**

- 42-80 Arcsecond Positions for Milliarcsecond VLBI Nuclei of Extragalactic Radio Sources, Part III: 74 Sources, pp. 1-7.

See Morabito, D. D.

**Wiggins, C. P.**

- 42-78 A Study of DSN Traveling Wave Maser System Reliability, pp. 192-198.

See Stevens, R.

**Wilcher, J. H.**

- 42-80 The Venus Balloon Project, pp. 195-201.

See Preston, R. A.

**Wolff, P. J.**

- 42-79 The Performance of Differential VLBI Delay During Interplanetary Cruise, pp. 35-46.

See Moultrie, B.

**Yuen, J. H.**

- 42-78 A Strategy for Successful Deep Space Information Transmission in Bad Weather, pp. 143-151.

See Swanson, L.

**Yung, C. S.**

- 42-78 Intermodulation Product Levels in Flame-Sprayed Materials, pp. 79-98.

C. S. Yung, F. Stoller, F. Lansing, and S. Brazil

